

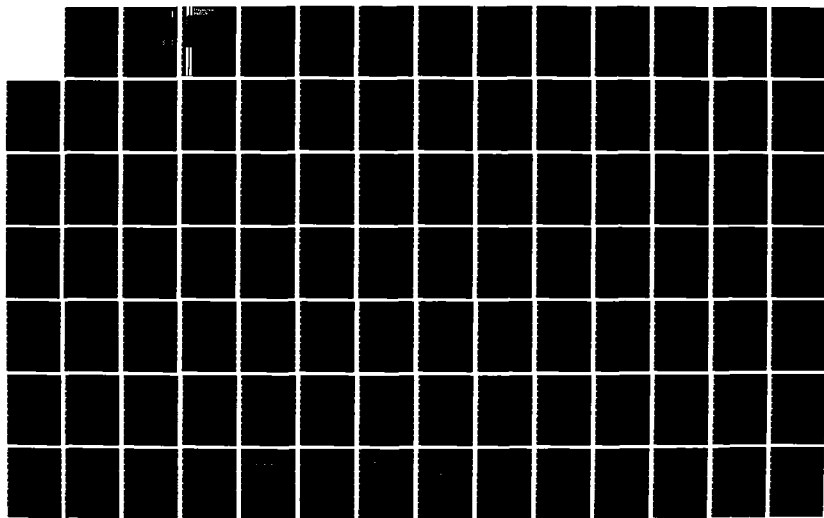
AD-A136 906

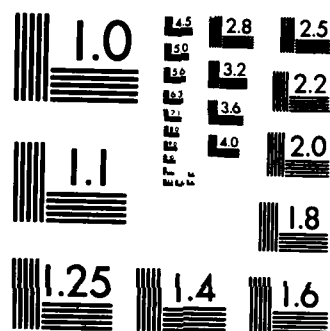
TRANSVERSE AND QUANTUM EFFECTS IN LIGHT CONTROL BY
LIGHT; (A) PARALLEL BE. (U) POLYTECHNIC INST OF NEW
YORK BROOKLYN DEPT OF MECHANICAL AND A. F P MATTAR
1983 POLY-M/RE-83-4 N00014-80-C-0174 F/G 20/6

1/6

UNCLASSIFIED

NL





MICROCOPY RESOLUTION TEST CHART
NATIONAL BUREAU OF STANDARDS-1963-A

AD A 136906

DTIC ACCESSION NUMBER

II

LEVEL

PHOTOGRAPH THIS SHEET

INVENTORY

Final Rpt., Dec. '79 - 31 July 83
Rpt. No. Poly M/AE 83-4

DOCUMENT IDENTIFICATION

Contract N00014-80-C-0174

DISTRIBUTION STATEMENT A

Approved for public release;
Distribution Unlimited

DISTRIBUTION STATEMENT

ACCESSION FOR

NTIS GRA&I

DTIC TAB

UNANNOUNCED

JUSTIFICATION



BY

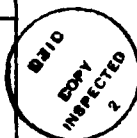
DISTRIBUTION /

AVAILABILITY CODES

DIST

AVAIL AND/OR SPECIAL

A/1



DISTRIBUTION STAMP

DTIC
ELECTE
S JAN 17 1984 D
D

DATE ACCESSIONED

DATE RETURNED

84 01 16 052

DATE RECEIVED IN DTIC

REGISTERED OR CERTIFIED NO.

PHOTOGRAPH THIS SHEET AND RETURN TO DTIC-DDAC

Polytechnic Institute of New York

AD A136906

TRANSVERSE AND QUANTUM EFFECTS IN
LIGHT CONTROL BY LIGHT (a) PARALLEL
BEAMS: PUMP DYNAMICS FOR THREE-
LEVEL SUPERFLUORESCENCE; (b) COUN-
TERFLOW BEAMS: AN ALGORITHM FOR
TRANSVERSE, FULL TRANSIENT EFFECTS
IN OPTICAL BI-STABILITY IN A FABRY-
PEROT CAVITY

F. P. MATTAR

Mechanical & Aerospace Engineering
and Spectroscopy Lab, M.I.T.

U.S. Office of Naval Research

Contract N000-14-80-C-0174

Poly M/AE 83-4

DISTRIBUTION STATEMENT A

Approved for public release;
Distribution Unlimited

FINAL REPORT

FOR CONTRACT N000-14-80-C-0174
(From Dec., 1979 to Spring, 1983)

on

TRANSVERSE AND QUANTUM EFFECTS IN
LIGHT CONTROL BY LIGHT

(a) PARALLEL BEAMS: THREE LEVEL SUPERFLUORESCENCE
CALCULATIONS;

and

(b) COUNTERFLOW BEAMS:
AN ALGORITHM FOR OPTICAL BISTABILITY

to

Physics Program

The U.S. Office of Naval Research

by

Farres P. Mattar
Department of Mechanical & Aerospace Engineering
Polytechnic Institute of New York
Brooklyn, New York 11201

and

Spectroscopy Laboratory
Massachusetts Institute of Technology
Cambridge, Massachusetts 02139

Table of Contents

1. Abstract.
2. Collaborators.
3. Acknowledgement to Joint Sponsorship by ARO.
4. Official Presentation at Meetings.
5. Refereed Papers.
6. Adaptive Stretching and Rezoning Techniques for the Solution of Paraxial Maxwell - Bloch Equations.
7. Simplified Analytical Solutions for Double Coherent Transients.
8. Two Beam CW Moment Theory.
9. Small Trend Calculations for SIT.
10. Perturbation Treatment of Two Parallel Beams Interaction: One Strong Beam and One Weak Beam.
11. Best Estimate for One Dimensional Equivalent to Diffraction Loss.
12. Swept-gain Superradiance in Two and Three-level Systems with Transverse Effects and Diffraction.
13. Transient Counter-Beam Propagation in a Nonlinear Fabry-Perot.
14. High Intensity Laser Beam Propagation and Fluid Approach.
15. Transverse Effects in Swept-gain Superradiance Evolution from the Superradiant State.
16. Effects of Propagation Transverse Mode Coupling and Diffraction on Nonlinear Light Pulse Evolution.
17. Transverse and Phase Effects in Light Control by Light: Pump Dynamics in Superfluorescence.
18. A Production System for the Management of a Results Function Bank and a Special Application: The Laser Project.
19. Light Control by Light with an Example in Coherent Pump Dynamics, Propagation, Transverse and Diffraction Effects in Three-level Superfluorescence.
20. Coherent Pump Dynamics Propagation, Transverse and Diffraction Effect in Three-level Superfluorescence and Control of Light by Light.
21. Fresnel Dependence of Quantum Fluctuation in Two-color Superfluorescence (SF) from Three-level Systems.
22. Fresnel Variation of Deterministic and Quantum Initiation in Two and Three-level Superfluorescence.

23. Comments on P.D. Drummonds's Central Partial Difference Propagation Algorithm.
24. The Perturbation Theory of the Self-Focusing of a CW Optical Beam On-Resonance.
25. On the Perturbative Theory of the Onset of the Self-Focusing in the Purely Absorptive CW Optical Beam Propagation (Short).
26. On the Perturbative Theory of the Onset of the Self-Focusing in the Purely Absorptive CW Optical Beam Propagation (long).
27. Quantum Fluctuation in Two-color Superfluorescence from Three-level Systems.
28. Perturbation Interaction of Counterflow Propagation: One strong and one weak beam.
29. Report Documentation Page.

Transverse and Quantum Effects in
Light Control by Light
(a) Parallel Beams:
Three-Level Superfluorescence Calculations;
and
(b) Counterflow Beams: An Algorithm for Optical Bistability

F.P. Mattar

Abstract

1. Methodology

Computational methodologies were developed to treat rigorously (i) transverse boundary in an inverted (amplifying) media; (ii) to treat quantum fluctuations in an initial boundary condition in the light-matter interactions problem; (iii) construct a two-laser three-level code to study light control by light effect; (iv) construction of a data base that (a) would manage the production of different types of laser calculations: cylindrical, cylindrical with atomic frequency broadening, cartesian geometry; (all of the above with quantum mechanical initiation), (b) allow parametric comparison within the same type of calculations, by establishing a unifying protocol of software storage, of the various refinements of the model could be contrasted among themselves and with experiment; (v) construct an algorithm for counterbeam transient studies for optical bistability and optical oscillator studies.

A. Transverse propagation effects in an inverted medium were studied. Special care had to be taken to treat the boundary reflection conditions. If ill-posed, they can obscure the emergence of any new physical results. The two transverse effects considered are (1) the

'spatial averaging' associated with the ~~in~~ⁱⁿ atomic inversion density being radially dependent (since the pump which inverts the sample has typically a Gaussian-like profile); and (2) the "diffraction coupling" (which permits the various parts of the cylindrical cross-section to communicate, interact and emit at the same time). The first effect is important for large Fresnel numbers, whereas the second is predominant for small Fresnel numbers.

The study of output energy stabilization between diffraction spreading and nonlinear self-action due to the non-uniform gain of the active media was also carried out to reach an understanding of the various physical processes that take place in coherent resonant amplifiers.

B. Physical Results

i. The Study of three-level systems exhibited that injected coherent-pump initial characteristic (such as on-axis area, temporal and radial width and shape) injected at one frequency can have significant deterministic effects on the evolution of the superfluorescence at another frequency and its pulse delay time, peak intensity, temporal width and shape. The importance of Resonant Coherent Raman processes was clearly demonstrated in an example where the evolving superfluorescence pulse temporal width t_s is much less than the reshaped coherent pump width t_p even though the two pulses temporarily overlap (i.e., the superfluorescence process gets started late and terminates early with respect to the pump time duration). The results of the three-level calculations are in quantitative agreement with observation in CO_2 pumped CH_3F by A.T. Rosenberg and T.A. DeTemple (Phys. Rev., A24, 868 (1981)).

ii. Additional calculations incorporating fluctuations in both pump and superfluorescence transitions were carried out to study the output pulse delay statistics. The fluctuations operators were introduced as langevin operators in the matter (density matrix) operators. In the average c-number semi-classical regime the fluctuations appear as additional driving forces in the Bloch equations acting for all p , z and t .

iii. Two color superfluorescence was subsequently studied in collaboration with Professor F. Haake. The propagation theory of M. Feld was shown to prevail over the Mean-Field theory of Bonifacio et al. The main result of the calculation displayed for the plane wave regime is a pulse synchronisation which ascertains Eberly et al's theory of 'simultons.' However for quantum fluctuations during the initiation and strong phase evolution in the beam (i.e., large Fresnel number) the synchronisation decreases and the standard deviation of the delay difference between the two peaks normalized to the average delay becomes larger.

iv. Elucidating the physical processes [namely, (a) the dynamic diffraction, (b) the non-uniform absorption (i.e., refraction) and (c) beam stripping] that lead to the on-axis manifestation predicted by Boshier and Sandle calculation [see Optic Commu., 42, 371 (1982)]. This effort was carried out in collaboration with Professor J. Teichmann.

V. The development of an implicit algorithm which self-adaptive non-uniform computational grids. This effort was carried out in collaboration with Dr. B.R. Suydam. These new codes represent a combination of Snyder code in Los Alamos and Mattar stretching and rezoning techniques to treat self-lensing effects.

Collaborations:

(i) Physics

- A. Dr. Charles M. Bowden (MICOM)
 - Two-level amplifier output stabilisation and three-level pump dynamics
- B. Professor Michael S. Feld (MIT) - The 'gaussian radial average' or 'shell model' as an important transverse variation included in the modeling (private communication)
 - The 'tipping angle' (average uniform) initiation of the superfluorescence process [J.R.R. Lerte, R.S. Sheffield, M. Incloy, R.D. Sharma and M.S. Feld, Phys. Rev. A, 14, 1151 (1976)]
- C. Professor Fritz Haake (Essen, F. R. Germany) - two colour superfluorescence
- D. Professor Jiri Teichmann and Mr. Yve Claude (University of Montreal)
 - Development of analytical perturbative treatment which elucidates the onset of on-resonant CW self-focusing of very intense laser beams in a two-level atoms

(ii) Numerics

- Prof. Gino Moretti (Polytechnic Institute of New York) for the Counter beam propagation
- Dr. B.R. Suydam (T7 - Los Alamos National Lab) for the Implicit code

(iii) Structure software and system programming

- Richard E. Francoeur (Mobil International Division)
- Pierre Cadieux (system routine for data bases)
- Michel Cormier (user interface for data base)
- Yve Claude (pagination of the program to simulate on CDC the virtual memory facility existing on IBM)

ACKNOWLEDGEMENT

The counterbeam algorithm development as well as the co-propagation code and the software programs for the data base were jointly sponsored by the Army Research Office, DAAG 29-79-C-0148.

The hospitality of Dr. H.M. Gibbs at Bell Lab, that of Professor M.S. Feld at the spectroscopy Lab and that of Dr. C.M. Bowden at MICOM is greatly appreciated. Their energetic and enthusiastic collaboration have accelerated the rate of progress of my research. The hospitality of Professor Jiri Teichmann in the Physics Department of the University of Montreal is also appreciated.

The continuous encouragements of Professor G. Moretti and H.A. Haus is joyfully acknowledged.

Official Presentations at Meetings during the Tenure of the Contract

- 1 - The International Conference on Laser 80, New Orleans, Dec. 30 (two papers), proceedings published by STS, MacLean, Virginia, 1982).
- 2 - The International Conferences on Excited States and Multiresonant Nonlinear Optical Processes in Solid, Aussois, France, March, 1981, (Abstract digest, ed. by D. Chemla published for CNET by les Editions de Physique, France
- 3 - The European Conference on Atomic Physics, Bielberg, April, 1981, (Abstract digest ed. by J. Kowalski, G. Zuputlitz and K.G. Weber, European Physical Society, Geneva, Switzerland, 1981).
- 4 - Los Alamos Conference on Optics, Los Alamos, 1981, Proceedings published by the Society of Photo-Optic Instrumentation Engineers (SPIE), Bellingham, Washington, 1981, vol. 288, pp. 353-363 and pp. 364-371.
- 5 - The Twelfth Annual Pittsburg Modeling and Simulation Conference (May, 1981), ed. W. Vogt and M. Mickle, Proceedings published by the Instrument Society of America, Pittsburg, Pennsylvania.
- 6 - The International Conference on Optical Bistability Proceedings, ed. by C.M. Bowden, M. Cifan and H.R. Robl (Plenum Press, New York, 1981), p. 503, (invited).
- 7 - U.S. Army Research Office Workshop On Coupled Nonlinear Oscillators, Los Alamos Center for Nonlinear Series, 1981, (invited).
- 8 - The Fifth International Laser Spectroscopy Meetings, VICOLS (two post-deadlines), Jasper, Alberta, Canada, 1981, ed. by B. Stoicheff et al., (Springer Verlag, 1982).
- 9 - The Annual Meeting of the Optical Society at Orlando, Florida, 1981 (two papers), see abstracts in J. Opt. Soc. Am., 71, 1589 (1981).
- 10 - The Annual Meeting DEAP of the APS, New York, December, 1981, three abstracts.
- 11 - The International Conference on Laser 81, New Orleans, December, 1981 (one invited, three contributed), proceedings published by STS, MacLean, Virginia, 1982.
- 12 - The Maxborn Centenary Conference, Edinburgh, Scotland, September, 1982 (three papers), ed. by the Institute of Physics, United Kingdom, proceedings to be published by SPIE, Bellingham, Washington, 1983.

- 13 - The Fourth International Symposium of Gas-Dynamic Lasers by M. Onorato, the Polytechnic Institute of Torino (two papers), Proceedings in press.
- 14 - The XII International Conference on Quantum Electronics, Munich, June, 1982 (one invited paper, one contributed paper), see Appl. Phys. (Springer Verlag) June and December issues, 1982.
- 15 - The International Conference for Raser (December, 1982) in New Orleans (three contributed papers).
- 16 - The Los Alamos Conference of Optics, Los Alamos National Lab, Spring, 1983, Proceedings to be published by SPIE (one review paper and one computational paper).
- 17 - Fifth Rochester Coherent and Quantum Optics Conference (June, 1983) (four contributed papers), Proceedings to be published by Plenum Press.
- 18 - Annual Meeting of the Canadian Association of Physicist and Canadian Astrophysics Society. Victoria, British Columbia, Canada (June, 1983).

Refereed Papers from the work and methodologies developed during the tenure of the research

1. Adaptive Stretching and Rezoning As Effective Computational Techniques for Two-Level Paraxial Maxwell-Bloch Simulation; Computer Physics Communications 20 (1980) 139-163, North Holland Publishing Company (with M.C. Newstein).
2. Coherent Propagation Effects in Multilevel Molecular Systems; Proceedings of the International Conference on Lasers '80, December 15-19, 1980 p. 270-279 (with C.D. Cantrell, F.A. Rebentrost, and W.H. Louisell).
3. Swept-gain Superradiance in Two- and Three-level Systems with Transverse Effects and Diffraction; International Conference on Excited States and Multiresonant Nonlinear Optical Processes in Solids pub. Les editiousde Physique, France (with C.M. Bowden).
4. Transverse Effects in Burnham-Chiao Ringing and Superfluorescence; Proceedings of the International Conference on Lasers '80, December 15-19, 1980 (with H.M. Gibbs and Optical Sciences Center, University of Arizoa, p. 777, 782 Tuscon, AZ).
5. Transverse Effects in Superfluorescence; Vol. 46, No. 17, p. 1123-1126 Physical Review Letters, April, 1981 (with H,M, Gibbs, S.L. McCall and M.S. Feld).
6. Transient Counter-Beam Propagation in a Nonlinear Farby-Perot Cavity; Computer Physics Communications 23 (1981) 1-17, North-Holland Publishing Company (with G. Moretti and R.E. Franceour).
7. Fluid Formulation of High Intensity Laser Beam Propagation Using Lagrangian Coordinates; Computer Physics Communications 22 (1981) 1-11 North-Holland Publishing Company (with J. Teichmann).
8. Effects of Propagation, Transverse Mode Coupling, Diffraction, and Fluctuations on Superfluorescence Evolution; SPIE Vol. 288-Proceedings of the Los Alamos Conference on Optics, 1981, p. 353,363 by the Society of Photo-Optical Instrumentation Engineers, Box 10, Bellingham, WA.
9. Transverse Effects in Swept-gain Superradiance: Evolution from the Superradiant State; SPIE Vol. 288-Proceedings of the Los Alamos Conference on Optics, 1981, p. 364,371 by the Society of Photo-Optical Instrumentation Engineers, Box 10, Bellingham, WA (with C.M. Bowden).

10. Effects of Propagation, Transverse Mode Coupling and Diffraction on Nonlinear Light Pulse Evolution; Optical Bistability (1981) Edited by Charles M. Bowden, Mikael Ciftan and Herman R. Robl, Pub. Plenum, NY p. 503,555.
11. Transverse and Phase Effects in Light Control By Light: Pump Dynamics in Superfluorescence; Proceedings of the International Conference on Lasers '81, December 14-18, 1981.
12. A Production System for the Management of a Results Functions Bank and a Special Application: The Laser Project ; Published in the proceedings of the International Conference on Laser '81, ed. by C.B. Collins (STS, MacLean Virginia 1982) pp. 1055-1115 (with M. Cormier, Y. Claude and P. Cadieux).
13. Light Control by Light with an Example in Coherent Pump Dynamics, Propagation, Transverse & Diffraction Effects in Three-Level Superfluorescence; IEEE International Quantum Electronics Conference, Munich (1982), Abstracts Digest Appl. Physics Dec (1982) Springer-Verlag (with C.M. Bowden).
14. Distortions of a CW Light Beam Propagating Through Gas: Self Lensing and Spatial Ringings; Max Born Centenary Conference, Edinburgh (Sep. 1982), (paper 36901), proceedings to be published by SPIE, Bellingham WA (1983) (with M. LeBerre, E. Ressayre and A. Tallet).
15. Coherent Pump Dynamics, Propagation, Transverse, and Diffraction Effects in Three-Level Superfluorescence and control of light by light; Physical Review A, Vol. 27, No. 1, Jan. 1983, p. 345-359 (with C.M. Bowden).
16. Quantum Fluctuations and Transverse Effects in Superfluorescence; Physical Review A, Vol. 27, No. 3, March, 1983 p. 1427-1434 (with E.A. Watson, H.M. Gibbs, M. Cormeier, Y. Claude, S.L. McCall and M.S. Feld).
17. Coherent Pump Dynamics, Propagation, Transverse, and Diffraction Effects in Three-Level Superfluorescence and control of light by light; Topics of current physicsL Multiple Photou Dissociation of Polyatomic Molecules, ed. C.D. Cantrell, Springer Verlag (In Press, 1983).

ADAPTIVE STRETCHING AND REZONING AS EFFECTIVE COMPUTATIONAL
TECHNIQUES FOR TWO-LEVEL PARAXIAL MAXWELL-BLOCH SIMULATION*

F.P. Mattar[†] and M.C. Newstein^{††}

Polytechnic Institute of New York
Brooklyn, NY 11201 USA

Received 6 December 1979, MS 867

The coherent interaction of short optical pulses with a nonlinear active resonant medium is calculated. The rigorous and self-consistent solution of the coupled nonlinear Maxwell-Bloch equations including transverse and time-dependent phase variations predicts in absorbers the onset of an on-resonance self-focusing and predicts in amplifiers beam degradation. The self-focusing result agrees very well with a previous perturbation treatment and with recent experiments in sodium and neon, whereas the severe beam distortion was observed in high power lasers utilized in inertial fusion experiments. The formation of dynamic self-action effects is elucidated as being due to the combined effects of diffraction and the inertial response of the active media.

Accuracy and computational economy are achieved simultaneously by redistributing the computational grid points according to the physical requirements of the problem. Evenly spaced computational grids are related to variable grids in physical space by a range of stretching and rezoning techniques including adaptive rezoning where the coordinate transformation is determined by the actual physical solution.

SUMMARY: The mathematical modeling of the coherent transmission of ultra-short optical pulses in a two-level atomic gaseous media, which can sustain amplification and/or absorption, is presented. The main motivation was to achieve an understanding of the inertial (cumulative temporal history) nonlinearity on the propagation of intense ultra-short light beams. Previously, this effect had been untractable and unapproachable.

The results of this analysis served as a guidance to real-life coherent light-matter interaction experiments. The equations with both radial and phase variations included, are implemented using a two-dimensional time-dependent finite difference computer code with two population densities, an inertial medium polarization density and adaptive propagation capabilities. The importance of dynamic transverse effects in the evolution of both initial ground-state and inverted media with different Fresnel numbers has also been assessed.

The memory requirements for a two-dimensional calculation are greater than those in a one-dimensional case, consequently, the computational mesh is predictably coarser. Unfortunately, this may cause a lack of fine resolution. But through the innovative implementation of stretching and rezoning techniques as outlined below, the coarse nature of the Eulerian code is adapted to a most sensitive and economical grid.

Calculations using this code have predicted and elucidated an on-resonance transient whole-beam self-lensing phenomenon in absorbers. This effect was subsequently ascertained

by experimental observations in sodium and neon. On the other hand, calculations concerning amplifiers depicted longitudinal pulse break-up, which degraded the beam quality, as substantiated in high power laser experiments. The significant phase modulation and transverse spreading may explain the mechanism that limits the useful output of long amplifiers. Parametric computations illustrated that these self-action phenomena can be controlled by tuning the various system parameters.

Accuracy and computational economy are achieved simultaneously by redistributing the computational Eulerian grid points according to the physical requirements of the nonlinear interaction. Evenly spaced computational grids are related to variable grids in a physical space by a range of stretching and rezoning techniques. This mapping consists of either an a priori coordinate transformation or an adaptive transformation based on the actual physical solution. Both stretching transformation in time and rezoning techniques in space are used to alleviate the computational effort. The propagation problem is then reformulated in terms of appropriate coordinates that will automatically accommodate any change in the beam profile.

The dynamic grid obtained through the self-adjusted mapping techniques removes the main disadvantage of insufficient resolution from which Eulerian codes generally suffer. Furthermore, the advantages of grid sensitivity are obtained while circumventing the traditional impediments associated with the Lagrangian methods. Thus, the convenience of an Eulerian formulation has been combined with the desirable zoning features of a Lagrangian code in a systematic and simple way.

* Work jointly supported by F.P. Mattar, the Research Corporation, the International Division of Mobil, the University of Montreal and the U.S. Army Research Office.

[†] Aerodynamics Laboratories

^{††}Electrical Engineering

I. INTRODUCTION

When an intense laser beam propagates through a resonant active medium, the absorptive and dispersive properties of the medium will affect the shape of the laser beam profile, which, consequently, alters the characteristic structure of the medium [1-6]. This modified matter will reffect, in turn, the field profile. The resulting cross-modulation of light by matter and matter by light is a continuous self-sustained phenomenon.

The subject of optical transmission is an interdisciplinary one. It draws on certain aspects of wave propagation, fluid flow, atomic physics and on both geometrical and physical optics. In addition, because many aspects of the problems of interest are analytically intractable, one finds that a complete study often requires extensive computer analyses of coupled optical field-matter equations; more specifically, the coupled optical propagation and atomic dynamics equations. The coherent behavior predicted on this model is in several important respects, quite different from that given by earlier treatments.

The current research was undertaken in an effort to answer more detailed questions relating to the coherent exchange of energy, nonlinear phase distortion and beam quality in high power laser transmission; the method was chosen to develop a suitable theory and realistic numerical computer code based on close collaboration with experimentalists [8-38]. The motivation of this work arises from the belief that real life experiments would depart from the predictions of previous plane wave analysis as it is sketched in Figures (1a) and (1b). The interplay of diffraction coupling and the medium coherent response will inevitably redistribute the beam energy both spatially and temporally [39-43]. This transient beam reshaping can profoundly affect a device that relies on this nonlinear interaction effect.

Essentially, this study seeks to minimize the number of simplifying assumptions associated with previous analyses. Specifically, this modeling encompasses self-phase modulation, dynamic longitudinal and transverse reshaping and coherent energy exchange in an inertial medium. Effective mathematical transformations which are consistent with the physics make attainable a heretofore unachievable solution [44-74].

When light propagates in free space, it experiences diffraction spreading which alters the beam shape [75, 77]. In the more complicated nonlinear problem, the interaction intertwines the various parts of the beam; the transverse dimensions of the beam change drastically. As the transmission distance increases from the launching aperture; one is faced inevitably with substantial numerical difficulties. For example, a numerical paraxial code using a uniform radial grid can suffer a serious drawback which would make the cost of the calculation prohibitive. Namely, the number of

points required would need to be increased tremendously if the transient beam undergoes severe self-divergence (self-expansion) or self-convergence (self-narrowing). It is therefore imperative that the transverse mesh be sufficiently small to correctly sample the oscillations of the field amplitude and phase.

If, for self-focused beams, a fixed transverse mesh is used, there may be in the vicinity of the focal region a lack of resolution as displayed in Figure (2a) and Figure (2b). A non-negligible loss of computational effort in the wings of the beam will also occur. The total required computer storage could become quite large. In an effort to maintain accuracy and efficiency, it has been decided to integrate the governing equations using a simple coordinate transformation which was revised at suitable intervals to allow the numerical grid to follow the pulsed-beam behavior. The mesh network will expand or contract accordingly. The successive implementations of coordinate mappings, which redistribute the points in the most appropriate manner, correspond to a series of renormalization procedures.

The interdependent nature of each aspect of the problem requires a thorough comprehension of the total relevant physics. In setting up variable grids there is an important factor to be considered: one must address simultaneously any transverse energy distribution while analyzing the longitudinal alterations as shown in Figure (3) and Figure (4). If a variable longitudinal mesh, $\Delta\eta$, is introduced without carrying a variable radial mesh, Δ , to handle large increments along the direction of propagation, one inevitably faces a steadily decreasing $\Delta\eta$ step as the beam becomes more perturbed and starts to break up. This effect will intensify to such an extent that $\Delta\eta$ crashes [162] to an increasingly smaller value and the calculation must be discontinued.

In addition to the coordinate modification, a change in the dependent variables is introduced in terms of the renormalizing factors (such as the reference beam waist, wave-front curvature and field amplitude) to extract the radial dependence of the phase front and any important source of amplitude variation. As a result of the factorization of the radial phase, the new dependent functions vary more gradually in the new coordinate system: what one calculates, therefore, is a deviation from a reference Gaussian beam; any troublesome radial phase oscillation is hence removed. As soon as the localized computational mesh departs significantly from the physical beam waist, the renormalization procedure is refreshed and redefined using pertinent moment properties of the physical quantities. The new grid coincides with the actual expansion and contraction of the beam. Thus, the grid can be coarser, less extensive and more efficient.

Another major obstacle to circumvent is the cumulative memory effect in the response of the medium to the laser beam. For computa-

tional efficiency, the temporal grid will be non-uniformly stretched as indicated in Figure (5). To conduct such a study one must resort to machine calculation as the equations are far too complicated for any known analytic methodologies. In such a large and involved computational problem the calculational efficiency of the algorithm chosen is of crucial importance; it can well make the difference whether the physical problem is actually solvable or not. A brute force finite difference treatment of the governing equations is not feasible. Instead, by judiciously making the salient details of the physical processes the determinant factors of where to concentrate the computational effort, one can achieve both accuracy and economy.

The adoption of non-uniform meshing techniques defined in connection with aerodynamics problems has proved to be a very foresighted decision. In particular, these numerical methods, designed by Moretti [50, 59], discriminate between different domains of dependence of different physical parameters; as a result a higher degree of accuracy in the actual physical problem became feasible.

II. PHYSICAL BACKGROUND

The great interest in understanding the transmission of intense ultra-short pulses through a nonlinear medium is due to their application in laser-induced energy release via fusion of hydrogen isotopes. The pulses of interest are assumed to be so short that no appreciable pumping (or other energy-exchange processors) can occur during the pulse. The resonant medium is thus left in a non-equilibrium state after the pulse passes. The behavior of the pulse is therefore different and more complex. When designing a high power laser system, one must verify that no beam distortion could evolve. Any departure from the desired uniform illumination of the target could prevent the fusion mechanism from taking place. One should control the cumulative interplay of beam diffraction with the medium inertia to avoid triggering the onset of any substantial self-action phenomena, such as temporal and radially dependent phase modulation and associated transverse energy current and self-lensing phenomena. This chain reaction can contribute to undesired self-induced aberrations of the beam. The focal properties of the laser pulse on target will inevitably be degraded.

This model is readily deduced from the Maxwell-Bloch equations while taking into account the mutual influence of the transient beam and the resonant two-level atoms. The intense traveling electric field is treated classically, whereas, the two-level system is analyzed quantum mechanically. In particular, the medium response is described using the density matrix formalism [76]. Furthermore, only a forward wave (i.e., moving in the direction of the incident wave), is present in this analysis; backward waves are neglected. Consequently, we shall not be concerned with stand-

ing-wave effects. The effect of the dynamic transverse variation, the time-dependent phase, the boundary conditions for the propagating field are also included. None of the simplifying approximations (such as adiabatic following, rate equation or mean-field limit), is introduced; instead an exact numerical approach is developed. This investigation is accomplished by using a novel algorithm inspired by a similar line of attack in complicated studies in Fluid Dynamics which has achieved substantial success. Such self-consistent methodologies have permitted the construction of a computer code capable of being physically meaningful at every node point.

This first non-planar study simulates more accurately the experimental configurations than the previous restrictive one-dimensional theoretical attempts. This complete model takes into account rigorously the interplay of diffraction, nonlinear atomic inertia and both initial matter and field boundary conditions.

This modeling, which evolved from a close collaboration with different experimentalists, can lead to a better understanding of the basic and fundamental cooperative effects in light-matter interactions. A quantitative evaluation and clarification of some of the recent experimental advances has been reached. This study helped define novel laboratory experiments which yield additional subtleties in the physical processes. Also, extensions of this study may help select optimum design configuration for superfluorescence [79-82], X-ray lasers [86-91], optical bi-stability [92-100], double coherent transients [101-109] and real-time holography [110-117]. Further benefits may include the development of new methods to generate ultra-short pulses as required for optical information transmission and optical communication [118].

III. EQUATIONS OF MOTION

In the slowly varying envelope approximation the dimensionless field-matter equations [8, 39, 42] which describe our system, in a cylindrical geometry with azimuthal symmetry, are:

$$-iF \nabla_T^2 e + \frac{\partial e}{\partial \eta} = \quad (1)$$

$$\partial / \partial \tau = eW - (i\Delta\Omega + 1/\tau_2) \quad (2)$$

and

$$\partial W / \partial \tau = -1/2(e^* + e) - (W - W_0)/\tau_1 \quad (3)$$

where

$$e = (2\mu/\hbar)\tau_p e', \quad \text{and} \quad = (2/\mu)',$$

$$E = \text{Re} \{ e' \exp [i(k/c)z - \omega t] \};$$

with $k/c = \omega$ and $\nabla_T^2 e = \left[\frac{1}{\rho} \frac{\partial}{\partial \rho} \left(\rho \frac{\partial e}{\partial \rho} \right) \right]$; after applying L'Hopital's rule, the on-axis Laplacian reads:

$$\nabla_T^2 e = 2 \frac{\partial^2 e}{\partial \rho^2} \quad ; \text{ and}$$

$$P = i \operatorname{Re} [e \exp \{ (k/c)z - kt \}].$$

The complex field amplitude e , the complex polarization density, and the energy stored per atom W , are normalized functions of the transverse coordinate $\rho = r/r_p$, the longitudinal coordinate $\eta = z/a_{\text{eff}}$, and the retarded time $\tau = (t - zn/c)/\tau_p$. The time scale is normalized to a characteristic time of the input pulse, τ_p and the transverse dimension scales to a characteristic spatial width of the input pulse r_p . The longitudinal distance is normalized to the effective absorption length, $(a_{\text{eff}})^{-1}$, where

$$a_{\text{eff}} = \left[\frac{\mu N}{n \Delta \omega} \right] \tau_p + [\sigma \tau_p] \quad (4)$$

In this expression, ω is the angular carrier frequency of the optical pulse, μ is the dipole moment of the resonant transition, N is the number density of resonant molecules, and n is the index of refraction of the background material. The dimensionless quantities $\Delta \omega = (\omega - \omega_0)\tau_p$, $\tau_1 = T_1/\tau_p$, and $\tau_2 = T_2/\tau_p$ measure the offset of the optical carrier frequency ω from the central frequency of the molecular resonance ω_0 , the thermal relaxation time T_1 , and the polarization dephasing time T_2 , respectively.

It is perhaps worthwhile pointing out that, even in their dimensionless forms, the various quantities have a direct physical significance. Thus F is a measure of the component of the transverse oscillating dipole moment (μ has the proper phase for energy exchange with the radiation field). In a two-state system, in the absence of relaxation phenomena, a resonant field will cause each atom to oscillate between the two states, $W = -1$ and $W = +1$, at a Rabi circular frequency $f_R = e/\tau_p = (\mu/h)e$. Thus F measures how far this state-exchanging process proceeds in a FWHM pulse length τ_p .

The dimensionless parameter, F , is given by $F = \lambda(a_{\text{eff}})^{-1}/(4\pi r_p^2)$. The reciprocal of F is the Fresnel number associated with an aperture radius r_p and a propagation distance $(a_{\text{eff}})^{-1}$.

The magnitude of F determines whether or not it is possible to divide the transverse dependence of the field into "pencils", (one pencil for each radius ρ), which may be treated in the plane-wave approximation. The diffraction coupling term and the nonlinear interaction terms alternately dominate depending on whether $F > 1$ or $F < 1$.

As outlined by Haus et al [38], the acceptance of equation (3), as describing the coupling of the material to the electric field, implies cer-

tain assumptions and approximations. Equation (3) shows clearly that the product 'e' of the electric field, e , and the polarization, P , causes a time rate of change of the population difference (or equivalently, of medium energy) leading to saturation effects: Inertial effects are considered.

IV. ENERGY CONSIDERATION

From the field-matter relations (1)-(3) one obtains the energy current equation:

$$+iF \nabla_T (e \nabla_T e^* - e^* \nabla_T e) + \partial_\eta e^2 = (e^* + e^*)$$

$$\nabla \cdot \mathbf{I} = -2[\partial_\tau W + (W - W_0)/\tau_1] \quad (5)$$

where, using the polar representation of the complex envelope, we have

$$e = A \exp[i\phi] \quad (6)$$

$$J_z = A^2; \text{ and} \quad (7)$$

$$J_T = 2F \lambda A^2 \frac{\partial \phi}{\partial \rho} \quad (8)$$

The components J_z and J_T represent the longitudinal and transverse energy current flow. Thus, the existence of transverse energy flow is clearly associated with the radial variation of the phase of the complex field amplitude e . When J_T is negative [i.e., $\partial \phi / \partial \rho > 0$], self-induced focusing dominates diffraction spreading. Since $\partial \phi / \partial \rho$ determines the direction and speed of energy flow, it is reasonable to monitor either a phase gradient or the transverse energy current for a central diagnostic as the calculation proceeds.

One may rewrite the continuity equation (5) in the laboratory frame to recover its familiar form:

$$\nabla \cdot \mathbf{I} = -\frac{\partial}{\partial t} [2W + \frac{n}{c\tau_p a_{\text{eff}}} A^2] - 2 \frac{W - W_0}{\tau_1} \quad (9)$$

SMALL TRENDS CALCULATION AND SIMPLE PHYSICAL PICTURE

There are at least two ways of visualizing the coherent transient on-resonance self-lensing phenomena. The first is to see that phase variations can lead to a frequency offset, so that index arguments used for off-resonance self-focusing apply. By Eq. (1) the in-phase component of the polarization leads to phase changes with propagation. If the input is transversely uniform and on resonance (hence also unchirped), the in-phase component of always vanishes, even when integrated over a symmetrical inhomogeneous line width, so no intensity-dependent phase changes or focusing

occur. If the input is transversely nonuniform, the in-phase is initially zero. Through the ordinary diffraction term, however, phase variations begin immediately. These phase changes lead to defocusing. They also lead to chirps which appear as a frequency offset. This allows for an intensity-dependent in-phase to arise which can result in focusing or defocusing.

To establish a second argument based on more physical intuition let us derive the relative dependence of pulse velocity on the input field area for a given pulse length in the uniform plane wave limit. The diffractionless field equation reads as follows:

$$\partial_{\eta} e_{ID} = \quad (10)$$

while the energy equation

$$\partial_{\eta} e_{ID}^2 = 2e_{ID} \quad (11)$$

using the Bloch equations, obtained from the density matrix, one obtains

$$\partial_{\eta} e_{ID}^2 \approx \pm 2 e_{ID} \sin \theta_{ID} \quad (12)$$

$$\text{with } \theta_{ID} = \int_{-\infty}^{\tau} e_{ID} d\tau' \quad (13)$$

The minus/plus sign refers to absorber/amplifier. If one assumes that for small propagation distances the induced polarization, P , is driven by the field at the input plane, e_a , an analytic expression for the field energy can be obtained as follows:

$$e_{ID}^2 \approx e_a^2 \pm 2\eta e_a \sin \theta_a \quad (14)$$

with e_a and θ_a the field and its time-integrated area at the input, (or aperture plane), respectively. For large values of τ , e_a tends to zero causing e_{ID} to be bound and finite.

The electric field is now given by:

$$e_{ID} \approx (e_a^2 \pm 2\eta e_a \sin \theta_a)^{1/2} \quad (15)$$

By direct integration, one finds that in the case of the absorber the peak is delayed relative to the speed of light, whereas in the amplifier it is advanced. This follows because in the first case, the leading edge is absorbed and in the second situation it is amplified. In the case of the 2π pulse the behavior in the trailing edge for either media is the reverse of the leading edge. This leads to the possibility of distortionless 2π pulses traveling with a velocity greater or less than c/n , the speed of light in amplifiers and absorbers respectively. The speed of the peak of a smaller area, in both types of media, is less than the speed of the peak of the larger 2π pulse. A way to express it mathematically is to determine the change in the field from one plane to the next as determined by the polarization. The contribution of the field radiated by the polarization

is given by the second term on the right hand side of the equation (14). The behavior in an amplifier is illustrated in Figure (6a) where the 2π , e_a , field and total field e_{ID} after a small distance η are compared with the corresponding pair, $e_a' = 1.6\pi$ and e_{ID}' . The advance of the peak is less in the smaller area. The corresponding curves for an absorber are shown in Figure (6b). In contrast, the delay for the peak is greater for the smaller area.

Thus, in each case, absorber or amplifier, the smaller area pulse moves more slowly than that of the larger area pulse.

It is noteworthy that the relative delay for adjacent pulses in resonant absorbers is larger than the relative advance for adjacent pulses in amplifying media as illustrated in Figure (7a) and Fig. (7b).

V. PERTURBATION APPROACH TO THE INITIAL BEHAVIOR

The three-dimensional beam can be thought of as a composite set of one-dimensional plane-wave pencils (a pencil for each radius). This idea may be used to construct a picture of the physical processes that produce the phenomenon of transverse reshaping, as in the following example. A comparison of the distinct temporal evolution of two separate pencils will be made for short propagation distances. One pencil is on-axis, where the intensity is at maximum, while the second, which is just off-axis has a smaller intensity. The induced nonlinear polarization that results will make the group velocity of the pulse peak at the center pencil exceed the corresponding off-axis group velocity. This is sketched in Figure (7a) for a pre-excited medium and in Figure (7b) for an absorber. For the particular instant of time τ_0 , the off-axis field is larger than the on-axis field.

Associated with this relative motion between adjacent pencils, there is a variation in the sign of the on-axis transverse coupling (Laplacian) term. At the input plane its contribution is negative. As the pulse propagates along η , at a later instant of time τ_0 the transverse coupling term eventually vanishes. Still further away, its contribution for time τ_0 becomes positive. Thus the sign of the Laplacian is a function of time. Its value at the front of the pulse is different from that at the tail of the pulse. Along with these changes in amplitude, the phase also varies. These amplitude, A , variations and phase, ϕ , delays lead to larger phase accumulation on-axis. Radial variations of the phase will induce a dynamic transverse energy current, (defined by $J_T = 2 F i A^2 \partial \phi / \partial \rho$), flowing inwardly at some times and outwardly at others.

The parameter F , which is the coefficient of the Laplacian term, is a small number $O(10^{-3})$. Its reciprocal is the Fresnel number per active characteristic length. F corresponds also to the reciprocal of the on-resonance small signal gain given in a diffraction length as defined by Lax et al in their paper on the analysis of the paraxial approximation [118]. Furthermore, the small longitudinal field that Lax has found as a first order correction to the purely transverse field is negligible for our case.

It is therefore suitable to use F as an expansion parameter for the relevant variables. When keeping only the first order term, one obtains:

$$\begin{aligned} e &= e_0 + F(e_{1p} + ie_{1l}); \\ &= 0 + F(1_r + i1_l) \text{ and} \\ W &= W_0 + FW_{1r} \end{aligned} \quad (16a)$$

where e_0 and 0 are the numerical real (phaseless) solutions of the uniform plane-wave propagation problem.

Thus, when substituting in the coupled wave-material equations and separating the zeroth and first order, one gets:

$$\begin{aligned} \partial_\eta e_0 &= 0; \\ \partial_\tau 0 &= e_0 W_0; \text{ and} \\ \partial_\tau W_0 &= -e_0 0 \end{aligned} \quad (16b)$$

$$\begin{aligned} \partial_\eta e_{1r} &= 1_r \\ \partial_\tau 1_r &= W_0 e_{1r} + e_0 W_{1r} \\ \partial_\tau W_{1r} &= (e_{1r} 0 + e_0 1_r) \\ \nabla_T^2 e_0 + \partial_\eta e_{1r} &= 1_l \\ \partial_\tau 1_l &= W_0 e_{1l} \end{aligned} \quad (16c)$$

It is easy to see that if initially, (for all η and for $\tau < 0$), and at the input plane (for $\eta = 0$ and all τ) the perturbations terms are zero, the real parts will remain zero all the time. As the pulse propagates, the imaginary parts of both the three-dimensional field and the induced polarization grow.

Thus, we have from (16c)

$$1_l = \int_0^\tau dt' W_0 e_{1l} \quad (17)$$

Equations (16c) can be integrated to obtain the perturbed field e_{1l} in terms of the known solutions of the one-dimensional problem: e_0 and W_0 . By making a further approximation

$$1_l \ll \nabla_T^2 e_0 \quad (18)$$

which is certainly true for small enough η , we get our working equations:

$$e_{1l} = \int_0^\eta d\eta' [\nabla_T^2 e_0] \quad (19a)$$

The rate of growth of e_{1l} and its sign depend on the radial variation of e_0 .

$$\phi = \tan^{-1} [Fe_{1l}/e_0] \quad (19b)$$

Numerical computation showed that the latest approximation (18) is a valid one. The new value of the perturbation field and of the related phase are in very good agreement with those evaluated previously. By taking iteratively into account the effect of 1_l , one obtains:

$$e_{1l}^C = \int_0^\eta d\eta' [\nabla_T^2 e_0 + \int_0^\tau dt' (W_0 e_{1l})] \quad (20a)$$

and

$$\phi^C = \tan^{-1} (F e_{1l}^C / e_0) \quad (20b)$$

The second term in the right-hand side of (20a) being a functional of W_0 , will change sign according to the initial stage of the medium. Should the medium be initially at ground state, W_0 is negative; on the other hand, if the medium is pre-excited, the population is inverted, and W_0 is positive. Accordingly, the sign and the value of the phases will vary. This contribution will be reflected in the transverse energy current, J_T .

Thus, the wavefront curvature is directly attributable to the on-axis pencil moving faster than the off-axis rays, as sketched in Figure (8), inducing the Laplacian to alternate sign as a function of all the independent variables.

The validity of this procedure is limited to the range of propagation distances where one-dimensional pulses do not differ significantly from their three-dimensional counterparts.

A significant prediction of the perturbation theory is the development of a substantial focusing curvature of the wavefront in the tail of the pulse. This occurs well within the reshaping region before any substantial focusing (or defocusing) begins to occur. The results of the perturbation theory are in good agreement with the corresponding rigorous three-dimensional results [39, 41]. This is illustrated for absorber in Figure (9a) and for amplifier in Figure (9b). These graphs refer to a situation well within the reshaping region where no substantial self-lensing has yet

occurred. Nevertheless, there is already substantial phase variation on the tail of the pulse. This is indicated by the curves labeled $\phi(3D; \rho=0)$ and $\phi(3D; \rho=\Delta\rho)$. These give the phase variation for the three dimensional case (3D) as determined by the full numerical calculation for two values of ρ . In the input plane, the pulse area is 2π at $\rho = 0$ and is 1.8π at $\rho = \Delta\rho$.

The fact that in absorbers the phase is smaller at $\rho = \Delta\rho$ than at $\rho = 0$ shows that energy is flowing radially toward $\rho = 0$ in the tail of the pulse, whereas, in amplifiers, the phase decreases as a function of r , and this decrease is stronger at $\rho = 0$ than at $\rho = \Delta\rho$. The absorber and the amplifier appear to behave in inverse ways in the reshaping region; the tail of the absorber focuses and the tail of the amplifier defocuses. The reciprocity is lost as the light pulse continues to propagate. This is because the pulse in absorbers moves with a speed less than the velocity of light in the medium, c/n , while the pulse in the amplifier moves with a speed greater than c/n (this fact does not contradict special relativity since the energy flow rate never exceeds c/n). Thus, when focusing does occur in the absorber, the peak pulse intensity corresponds to a value r , where the phase curvature was significant in a previous plane. In the case of the amplifier, the peak field moves away from the tail of the pulse. Therefore, even though the on-axis phase indicates defocusing in the tail, there is no time-flow of energy into this region. The energy in the tail of the beam wings remain at the same place for a considerable propagation distance. Furthermore, in an amplifier the medium represents a continuous source of energy; this is in contrast to the absorber situation where only the initial electric field represents the total available energy. Thus, a defocusing effect in an amplifier will always be competing against this amplifying action, and therefore no significant self-defocusing could reasonably be observed.

Instead, focusing does occur in the time tail of a coherent pulse propagating in the same amplifying medium. As it will be shown subsequently in this paper, a pulse break-up occurs on-axis; only the second pulse of the double peak seems to be associated with focusing. The three-dimensional numerical calculation for the amplifier indicate that longitudinal pulse break-up occurs, but the first pulse is indistinguishable from the corresponding one-dimensional pulse. This is consistent with our theory since phase modulation does not become significant during the passage of the first pulse.

One sees that the phase variations due to transverse coupling are not only a function of the space coordinates but also evolve in time. As a result, if the propagation beyond the reshaping regime (where field phase builds up), occurred in free space, the beam at the

temporal peak cut would only focus after $\alpha_{eff}^2 = 38.75$, which is in the far field of the input aperture. On the other hand, if the propagation continues in the nonlinear medium, the focus occurs much sooner, at $\alpha_{eff}^2 = 8.875$, which is the near field. Thus, the presence of the active medium triggers the self-lensing mechanism sooner. The reciprocity between the physical processes in absorbers and in amplifiers, is further lost, as the transverse boundary begins playing an important role for amplifiers.

As a summary note, one finds that the movement in time of the pulse's energy (i.e., peak amplitude) relative to the focusing (or defocusing) phase is the most critical mechanism for the development of any self-action phenomenon.

It is particularly appropriate to study the origin and evolution of the energy current since it determines the appropriate conditions responsible for the onset and development of the coherent self-lensing phenomena.

VI. FURTHER ANALYTICAL WORK

By combining the previous small trends calculation and pencils approach, one obtains a completely analytic expression for the phase ϕ as well as for J_T , the transverse energy current [41,43].

From equation (19) to equation (30) namely

$$\phi \approx Fe_{11}^C/e_{1D} \quad (21)$$

$$J_T \approx Fe_{1D}^2 (\partial_p \phi) = F \{ e_{1D} (\partial_p e_{11}^C) - e_{11}^C (\partial_p e_{1D}) \} \quad (22)$$

The various self-action processes arise through the combined effects of diffraction and the nonlinear inertial response of the medium.

For illustration, an absorber example is considered. The specific dependence of the pulse delay on the input area is shown in Figure (10a) and Figure (10b). Consequently, one expects that little focusing occurs in the reshaping region while each annular ring of the input Gaussian profile evolves (see Figure (10c) and Figure (10d)) according to the uniform plane wave theory; the conventional outward energy flow takes place (as shown in Figure (11a)). However, as the three-dimensional calculation will show, since the more intense rings propagate more rapidly, the tail of the pulse has more intensity in the outer rings (causing the appearance of an indentation near the axis). However, linear diffraction will fill the profile as displayed in Figure (11b). Light diffracting towards the axis from the trailing edge of the pulse in the rim of the beam (at larger radius) interacts with those atoms which were excited by the preceding pulse (which was closer to the axis) and can experience net ampli-

cation as illustrated in Figure (12a) and (12b). Because of this always-present interaction with population-inverted atoms, the amount of energy arriving in the absorber at the axis is significantly higher than what it would be if the remaining medium were linear. This boosting mechanism continues as energy flows towards the axis, making a positive contribution to the center of the beam. The leading portion of the pulse in the rim of the beam continually sees an absorber and thus experiences net absorption.

Consequently, the resulting expression for J_T is a power series in η with coefficients of alternate sign. For small enough η (where higher order terms of η can be neglected), the energy current is positive indicating an outward transverse energy flow in agreement with the spreading due to a near-field diffraction effect. As η increases, the second term must be considered also. Since its contribution is, in absorbers, a negative quantity, J_T eventually changes sign and begins flowing inward towards the axis forming a converging lens. The latter may counteract and overcome the diffraction, giving rise eventually to the coherent self-focusing. If η increases further, the third term contribution becomes important; its effect will tend to reduce the inward transverse energy flow associated with the second term. The third term can be interpreted as the manifestation of additional diffraction due to the narrowing of the optical beam. In amplifier, however, the second term is flowing outwardly enhancing the diffraction spreading.

In Figure (13a) and Figure (13b) J_T is displayed for absorber and amplifying media respectively.

Due to the approximations used, the expressions obtained can at best suggest trends of what really occurs, which can only be studied by rigorous three-dimensional numerical computations. However, the present results were found to be qualitatively consistent with the full three-dimensional calculation results.

VII. SUMMARY OF THE PHYSICS

We have verified that in an amplifier, energy is transferred from the medium to the electric field in the front of the pulse, and back to the medium in the tail of the pulse; and that the converse applies for absorbers. Only for the case of a '2 π ' pulse is all the energy returned to its sources.

The propagation speed of the peak of the pulse exceeds the speed of light in amplifying media; whereas, it is less than the speed of light in absorbers. In both cases, the propagation speed is greater for the more intense pulse than for the weaker pulse. The difference in speed among adjacent radii is less in

amplifiers than in absorbers. As the beam propagates into the medium, its characteristics may significantly change temporarily causing a larger field off-axis than on-axis.

In the reshaping region, the radial field distribution in the tail of the amplifier differs from that in the absorbers. In the amplifier pulse tail, the field remains peaked on-axis whereas in the absorber pulse tail, a depression develops on-axis. Thus outward diffraction continues to dominate in the amplifier pulse tail, whereas inward energy flow starts to occur in the tail of the absorbing pulse.

This trend to focusing in nonlinear absorbers is significant in that it is opposite to the effect shown by a conventional diffracting free-space signal. In amplifiers, a stronger diffraction is set up at the front of the beam. Light that thereby diffracts outwardly, experiences nonlinear amplification by the pre-excited resonant medium which has not yet interacted with the slower moving pulse off-axis as shown in Figure (14). The subsequent behavior of this diffracted light will be strongly influenced by the boundary conditions at the edge of the medium.

VIII. OUTLINE OF NUMERICS

The retarded time τ refers to the actual time in a stationary frame of the time of arrival of the front of the pulse at the position z . The advantage of this coordinate transformation, from t to τ , illustrated in Figure (15a) is that it allows an accurate numerical scheme to be developed for which the increment in η and τ need not be related in any special way.

Herein, the equations of motion are solved in the near-field region of an optical pulse, initially Gaussian in both ρ and τ . This amounts to a mixed initial boundary-value problem. The initial configurations of the laser beam and the resonant medium are specified subject to certain conditions for $\tau \geq 0$ which must be satisfied at all space points. Furthermore, the field boundary condition at $\eta = 0$ is time-dependent. This is sketched in Figures (15b) and (15c). For the numerical solution, a temporal-spatial mesh of grid points is used to represent the ρ - η - τ space. At a given plane η , the values of the various dependent variables are obtained for all stations. This procedure is repeated until the desired propagation length has been traversed.

The basic numerical algorithm consisted of a combined explicit and implicit method. The MacCormack [48] two-level predictor-corrector non-symmetrical finite-differencing scheme is used to advance the field equation along the direction of propagation, η , while the modified Euler three-level, predictor-corrector scheme is used to update the material variable in time-retarded time τ . The mutual light-matter influence is a mixture of a boundary value (for advancing the field) and an initial value problem (for calculating the atomic responses)

[11]. To improve accuracy and to speed up the convergence, cross-coupling is accentuated. With such steps, the scheme becomes as flexible as a strongly-implicit algorithm. The final field value, rather than the predicted one as done classically [8-11, 25, 39-40], is used to correct the material variable, and the final material values instead of the predicted ones are used to correct the field. The final variables are obtained as solutions of a set of five, simultaneous, algebraic equations.

IX. DETAILS OF NUMERICAL PROCEDURE

An outline of the numerical method is illustrated using two simplified equations that are representative of the full set describing the propagation and atomic dynamics effects. In this context, the material variables are denoted by M , whereas either of the electric field variables is denoted by F . Both variables are complex quantities which are functions of η , the propagation coordinate, η , the transverse spatial coordinate and τ , the retarded time. With M_e , the equilibrium value of M , one can write the representative equations as:

$$-i \nabla_T^2 F + \frac{\partial F}{\partial \eta} = M \quad (23)$$

$$\text{with } \nabla_T^2 F = \frac{1}{\rho} \left\{ \frac{\partial}{\partial \rho} \left(\rho \frac{\partial F}{\partial \rho} \right) \right\} \quad (24)$$

$$\frac{\partial M}{\partial \tau} = FM + M + M_e \quad (25)$$

subjected to the initial and boundary conditions.

1. for $\tau \geq 0$: $F = 0$, $M = M_0$ known function to take into account the pumping effects;
2. for $\eta = 0$: F is given as known function of τ and ρ ;
3. for all η and τ : $[\partial F / \partial \rho]_{\rho=0}$ and $[\partial F / \partial \rho]_{\rho=\rho_{\max}}$ vanishes as with ρ_{\max} defining the extent of the region over which the numerical solution is to be determined).

The derivatives appearing in (23) are only with respect to space variables; in this equation, time enters only implicitly, through the right-hand side terms. On the other hand, the derivative in (25) is a time derivative only, and the space influence is provided by the right-hand side terms. This situation entitles us to consider the two equations as somewhat uncoupled and to adopt special integration procedures for each of them separately. This assumption, though not rigorously correct, has proven to be very useful in practice. We cannot be sure that the accuracy of the integration procedure is of the second order in $\Delta \eta$ and $\Delta \rho$ as well as in $\Delta \tau$ for the material variables. A similar remark may be made for the field variable with respect to $\Delta \tau$. In this algorithm (which uses the two-level nonsymmetric MacCormack explicit predictor-corrector finite difference scheme for

marching the electric field F along η and the three-level modified Euler scheme to integrate along τ the material variables), special attention is given to ensure second-order accuracy in all space and time increment steps simultaneously for all the dependent physical, field and material variables.

This goal is achieved by using the final field F instead of the predicted F to evaluate the final M ; and the final M instead of the predicted M to correct the field variable F . A set of two transformed simultaneous, nonlinear, algebraic equations in two complex variables is obtained and can be easily solved. For simplification a well-known quasi-linearization, an example of which can be found in Moretti's treatment of the chemical kinetics problem [53], is introduced as follows:

$$FM = -F_i M_i + F_i M + F M_i \quad (26)$$

where i means the "initial value" and can reasonably be denoted by the predicted values. This approach follows readily the Taylor expansion of the product 'FM':

$$FM = (FM)_i + \left[\frac{\partial}{\partial F} (FM) \right]_i (F - F_i) + \left[\frac{\partial}{\partial M} (FM) \right]_i (M - M_i) + \dots \quad (27)$$

truncated at first-order terms.

Mathematically, this algorithm reads as follows: with

$$F(j, \Delta \eta, m \Delta \rho, k \Delta \tau) \equiv F_{m,k}^j \quad (28)$$

$$LF = i \nabla_T^2 F = (i/\rho) \{ \partial \rho (\rho F) \} \quad (29)$$

The predicted field can be written as:

$$F_{m,k}^{j+1} = F_{m,k}^j + \Delta \eta [M_{m,k}^j - L^F F_{m,k}^j] \quad (30)$$

whereas the corrected field reads as follows:

$$F_{m,k}^{j+1} = \frac{1}{2} [(F_{m,k}^j + F_{m,k}^{j+1}) + \Delta \eta (M_{m,k}^{j+1} - L^B F_{m,k}^{j+1})] \quad (31)$$

L^F and L^B are the forward and backward differencing of the transverse Laplacian operator cylindrical coordinates with azimuthal symmetry.

The material variables are integrated in the following manner. The predicted values are defined as:

$$M_{m,k+1}^{j+1} = M_{m,k-1}^{j+1} + 2(\Delta \tau) [F_{m,k}^{j+1} M_{m,k}^{j+1} - M_{m,k}^{j+1} M_e] \quad (32)$$

while the corrected values are given by:

$$\begin{aligned}
M_{m,k+1}^{j+1} = & \frac{1}{2}(M_{m,k}^{j+1} + \tilde{M}_{m,k+1}^{j+1}) \\
+ \Delta \tau \{ & (-F_{m,k+1}^{j+1} \tilde{M}_{m,k+1}^{j+1}) + F_{m,k+1}^{j+1} \tilde{M}_{m,k+1}^{j+1} \\
+ & F_{m,k+1}^{j+1} M_{m,k+1}^{j+1} + (\tilde{M}_{m,k+1}^{j+1} + M_e^{j+1}) \} \quad (33)
\end{aligned}$$

Rearranging, one has

$$F_{m,k+1}^{j+1} = a_1 + b_1 F_{m,k+1}^{j+1} + q_1 M_{m,k+1}^{j+1} \quad (34)$$

$$M_{m,k+1}^{j+1} = a_2 + b_2 F_{m,k+1}^{j+1} + q_2 M_{m,k+1}^{j+1} \quad (35)$$

which is a set of "linear algebraic equations" (with locally constant coefficients) that can readily be solved by straightforward elimination.

It is noteworthy that when this differencing procedure forward-predictor, backward-correction at 'j+1', is followed, at 'j+2', by its corresponding reverse backward predictor-forward corrector, the overall amplification of the error wavelets is smaller. This results from the fact that when one alternates the two reverse procedures, the amplification matrices (one for each procedure), have different eigenvalues and eigenvectors for the same Fourier component of the solution [49].

The numerical code has been tested systematically by insuring the reproduction of analytical results of problems such as free-space propagation [76], Gaussian beams propagation through lenslike media [77], Bloch's solution at the input plane for an on-resonance real field [8] and coupled uniform plane-wave calculations for an input $2\frac{1}{2}$ hyperbolic secant [8]. Identical results were obtained solving these problems expressed in the eikonal and transport form [1], and the three-dimensional results have been compared qualitatively and quantitatively with an analytic perturbation in the reshaping region [39,40].

X. IMPORTANCE OF BOUNDARY CONDITIONS

In this section we will discuss the role played by the boundary conditions in the solution of the problem. Previously, the importance of careful handling of boundary conditions was not stressed. For all physical problems, particularly those in fluid mechanics, that have been treated numerically so far, acceptable results have been achieved only by coupling an accurate analysis of the internal points with a careful numerical treatment of the boundary points [54].

When the laser beam travels through an amplifier, the transverse boundary has an increasingly crucial effect in contrast to the absorber situation. In particular, the laser field, which resonates with the pre-excited transition will experience gain; whereas, the laser which encounters a transition initially at ground

state, experiences resonant absorption and losses. A more significant portion of the pulse energy is diffracted outwardly in the amplifier than in the absorber. This point has been previously discussed in the section on perturbation.

In resonant, nonlinear, light-matter interactions, the velocity profile will not be uniform across the beam. The local intensity at a particular radius as well as the initial state of the transition (pre-excited as opposed to ground state) will dictate the distinct delay/advance that the "pencil" [pulse] will experience at a particular radius. Consequently, these boundary reflection conditions tends to play a substantial role in the amplifier calculations and could, if ill-posed, obscure the emergence of any new physical effects. One has, therefore, to be particularly careful in simulating amplifiers.

Special care is required to reduce the boundary effect to a minimum. By using non-uniform grids (in all physical variables), and confining the active medium by radially-dependent, absorbing shells one can construct an effective and reliable algorithm that is locally consistent with the physics of the problem.

More specifically, the boundary condition to be discussed below describes, in effect, an absorbing surface. This condition is a representation of an actual experimental approach in which the laser amplifier is coated to circumvent any spurious reflections. Various attempts have been made to simulate this absorbing surface.

Mathematically, this approach is implemented by introducing a radially-dependent loss distribution. The loss coefficients obey a Gaussian dependence peaking at the wall itself.

Three forms of losses were studied: an Ohmic linear form, a cubic Kerr loss, and a reduction in the nonlinear gain of the active medium.

For strongly amplifying media, the transverse boundary could still cause computational difficulties for self-diverging beams, because it is difficult to select, beforehand, the functional location of the boundary. An alternate approach to the problem would be to extend the transverse grid to infinity as displayed in Figure (16a) and Figure (16b). With this new mapping method, the mesh density is reasonably uniform in the region occupied by the beam, while outside this region the mesh density falls off rapidly with the final point occurring at infinity. In practice, the most effective treatment of the dynamic, transverse, boundary consists of implementing an absorbing surface while concurrently considering an infinite physical domain and mapping it on a finite computation region.

Hence, the desired transformation process for the transverse coordinate is similar to that used in constructing the nonuniform temporal grid.

Specifically,

$$\xi = \tanh(\beta\rho) \quad 0 < \xi < 1; N_B > N_A \quad (36)$$

$$\xi = (k-1)/N_B \quad 1 < k < N_B \quad (37)$$

$$\rho_{\max} = \rho(N_A), \quad (38)$$

$$\rho = \left(\frac{1}{2\beta}\right) \log\left(\frac{1+\xi}{1-\xi}\right) \quad (39)$$

$$\text{with } \beta = \frac{1}{2\rho(N_A)} \log\left[\frac{1+\xi(N_A)}{1-\xi(N_A)}\right] \quad (40)$$

with $\rho(N_A)$ denoting the actual maximum radius where the active medium is still present. In the region extending from $\rho(N_A)$ to $\rho(N_B)$ there is no amplifying medium; instead, there is an absorbing layer.

The derivatives of the mapping can also be defined analytically as follows:

$$\frac{\partial \xi}{\partial \rho} = \beta (1-\xi^2) = \beta \operatorname{sech}^2(\beta\rho) \quad (41a)$$

and

$$\frac{\partial^2 \xi}{\partial \rho^2} = -2\beta \xi (1-\xi^2). \quad (41b)$$

$$\text{on axis } \nabla_{\rho}^2 \xi \rightarrow 0 \quad (41c)$$

Therefore, the diffraction coupling term becomes:

$$\nabla_T^2 e = \frac{\partial^2 e}{\partial \xi^2} \frac{\partial \xi^2}{\partial \rho} + \frac{\partial e}{\partial \xi} (\nabla_{Tp}^2 \xi); \quad (41d)$$

with the on-axis contribution reading as

$$\begin{aligned} \nabla_T^2 e \big|_{\rho=0} &= \frac{\partial^2 e}{\partial \xi^2} + \lim_{\rho \rightarrow 0} \frac{1}{\rho} \frac{\partial e}{\partial \rho} \frac{\partial \xi}{\partial \rho} \\ &= 2 \frac{\partial^2 e}{\partial \xi^2} \frac{\partial \xi^2}{\partial \rho} \end{aligned} \quad (41e)$$

In Figure (17a), Figure (17b), Figure (17c) and the first, second radial derivation and the Laplacian term are drawn. Figure (18) contrasts in the stretched radial coordinate system, the transverse coupling and the electric field.

One can appreciate the sensitivity of the numerical domain and the dependence of the physical parameters to the boundary conditions.

XI. PRESCRIBED STRETCHING

A proper handling of the differential equations of motion is possible provided that there are

enough mesh points to assure proper resolutions where phase gradients (wavefront curvature) change very rapidly.

While there is no maximum amount of mesh points that can be used, it would be costly to reduce the entire mesh size to assure values which allow sufficient accuracy at the critical plane.

A compromise solution can be found, however, in a variable mesh that is defined by widely-spaced computational nodes in the area most distant from the plane of interest and densely clustered nodes in the critical region of rapid change; the latter being in the neighborhood of maxima and minima or, for multi-dimensional problems, in the vicinity of saddle points.

Consequently, resolution is sought after only where it is needed. The costs involving computer time and memory size will dictate the maximum number of points that can be economically employed. In planning the use of such a variable mesh size, the following points, outlined by Moretti [50] in connection with aero-dynamics shock calculations, must be kept in mind:

- (A) The stretching of the mesh should be defined analytically so that all the additional weight coefficients appearing in the equations of motion in the computational space and their derivatives can be evaluated exactly at each node. This avoids the introduction of additional truncation errors in the computation.
- (B) To assure a maximum value of ΔT , the mathematical grid step, the minimum value of Δt , the physical time increment, should be chosen at each step according to necessity. This means that the minimum value of Δt must be a function of the steepness of the pulse function.
- (C) The minimum value of Δt should occur inside the region of the highest gradient which occurs near the peak of the pulse.

To reiterate the above discussion, the most suitable nonlinear transformation is one in which more points are concentrated near the peak of the pulse. The derivatives with respect to τ are greatest around the peak rather than in the wings. By this choice, the desired fineness of the mesh is achieved with a minimum number of points. For example, following Moretti's approach, if $T = \tanh(\alpha\tau)$ (42a) and α must be larger than 1, the entire semi-axis τ greater than zero can be mapped on the interval 0 F T F 1 with a clustering of points in the vicinity of $\tau = 0$, for evenly-spaced nodes in t . Mapping of this kind has several advantages. They introduce into the equations of motion new coefficients which are defined analytically and have no singularities. They also avoid interpolation at the common border of meshes differently spaced. From the viewpoint of coding, not much additional work

is required. The computation is formally the same in the 'T' space as it was in the τ space. Some additional coefficients, due to the presence of the stretching function, appear and are easily defined by coding the stretching function in the main program. Obviously, by a proper choice of the function and by letting some of their parameters (such as α , above) vary as functions of the propagation distance according to the physical needs, the accumulation of points can be obtained where necessary at any distance of propagation. In the laser problem, we use a slightly modified stretching function:

$$\tau = \tau_c + (\alpha/2) \log(T/(1-T)) \quad (42b)$$

where α is a stretching factor which makes points more dense around τ_c , the center of gravity of the transformation. In particular,

$$\alpha = \tau_{\text{window}} / \log(N_{\text{up}} - 2) \quad (43)$$

with N_{up} is the number of uniform points in the mathematical grid, and τ_{window} is the temporal window (duration of shutter opening)

$$\tau_{\text{window}} = (\tau_{\text{max}} - \tau_{\text{min}}) \quad (44)$$

τ_c is an arbitrary point used to define the center of transformation so that the change of the coordinate will be optimum for more than one plane along the direction of propagation. Figure (19) illustrates the transformation and its different dependence on the particular choice of its parameters.

It is noteworthy that derivatives of the mapping functions produced by the gradual variation along the 'T' axis is also defined analytically namely $\partial\tau/\partial T = (\alpha/2) [T(1-T)]^{-1}$ (44b).

The computational grid in response to these transformations remains unchanged while the physical grid (and the associated weighting factors) can change appreciably. In particular, it is noteworthy that τ_c , which can be a

function of Z , defines the location of the minimum ' $\Delta\tau$ ' and its value. Consequently, the stretching can be adjusted, in centering and strength, at every step according to specification. While τ_{window} defines the extent of the physical region to be computed using the nonuniform stretching, the same adequate resolution around the peak of the pulse can be obtained with only one fifth of the points should their distribution have been uniform. The improvement is dramatic. In contrast, the uniform grid would have required five times the computer time and significant extra storage.

Should one need to study the laser field build-up due to either initial random noise polarization (for super-radiance), or due to an initial tapping angle (for super-fluorescence), one must utilize a different stretching [173]. This

desired stretching is similar to the one defined for treating the radial boundary conditions. The mesh points are clustered near the beginning (small τ); their density decreases for large value of τ (near the end of the temporal window).

XII. ADAPTIVE STRETCHING IN TIME

Due to the continuous shifting of energy from the field into the medium and then back from the medium to the field, the velocity of the pulse is modified disproportionately across the beam cross-section. This retardation/advance phenomenon in absorber/amplifier can cause energy to fall outside the temporal window. Furthermore, due to nonlinear dispersion, the various portions of a pulse can propagate with different velocities, causing pulse compression. This temporal narrowing can lead to the formation of optical shock waves. The quality of the temporal resolution becomes critical. To maintain computational accuracy a more sophisticated stretching than that described in Section XI is needed. It is therefore necessary that the center of accumulation of the nonlinear transformation used to stretch the time coordinate be made to vary along the direction of propagation. This adaptive stretching will insure that the redistribution of mesh points properly matches the shifted pulse. It is displayed in Figure (20).

This time, the transformation (42) from τ to T is applied about a center τ_c which is a function of η :

$$\tau = \tau_c(\eta) + \frac{\alpha}{2} \log \frac{T}{1-T} \quad (45)$$

The stretching factor α could also be a function of η as illustrated in Figure (19b).

The equations are very similar to those of Section III, except that an extra term is added:

$$-iF \nabla_{T\rho}^2 e + \partial_{\eta} e + \frac{\partial e}{\partial T} \left[-\frac{\partial T}{\partial} \right]_{\tau_c} \frac{d\tau_c}{d\eta} = \quad (46)$$

The role played by the time coordinate is different. Previously the field equation did not contain an explicitly dependent term.

$$\tau_c(\eta + \Delta\eta) = \tau_c(\eta) + [\tau_{pk}(\eta) - \tau_{pk}(\eta - \Delta\eta)], \quad (47)$$

where $\tau_{pk}(\eta)$ is determined from the previous plane η as the time at which the electric field on axis is a maximum. The time delay/advance accumulated in the interval $\Delta\eta$

$$\Delta\tau = \tau_{pk}(\eta) - \tau_{pk}(\eta - \Delta\eta) \quad (48)$$

measures the velocity of the peak relative to the speed of light:

$$\frac{v}{c} = \frac{1}{c(\Delta\tau/\Delta\eta) + 1} \quad (49)$$

XIII. REZONING

The main difficulty in modeling laser propagation through inhomogeneous and nonlinear media stems from the difficulty of pre-assessing the mutual influence of the field on the atomic dynamics and the effect of the induced polarization on the field propagation. Strong beam distortions are expected to occur based on a perturbational treatment of initial trends. Hence, in practice, any rigorous, self-consistent algorithm requires particularly flexible numerical strategies to avoid insufficient resolution within a reasonable number of grid points. Thus, one must normalize the various, critical oscillations to overcome the economical burden of an extremely fine mesh size. To insure such accuracy and speed in the computation, a judicious choice of coordinate system and appropriate changes in the dependent variables must be considered as plotted in Figure (21). Evenly-spaced grid points in a computational space are related to variable grids in the physical space. The paraxial equation is, thereby, transformed into a more suitable form for computation. These numerical strategies can either be chosen a priori and prescribed at the start of the computation or automatically redefined and adapted during the computation.

The basic rationale behind the transformations is to restrict the computation to the departures on the Gaussian beam rather than requiring calculation of the complete amplitude. This procedure removes the necessity for sampling the high frequency oscillations induced in the phase by self-lensing phenomena. The coordinate transformation alters the independent variables and thereby causes the dependent variables to take a different functional form. The new dependent variables are numerically identical to the original physical amplitudes at equivalent points in space and time in the two coordinate systems.

The requirements of spatial rezoning will be satisfied by simultaneously selecting a coordinate transformation (from the original coordinates ρ and η to new coordinates ξ and z) and an appropriate phase and amplitude transformation. The chosen transformation will share the analytical properties of an ideal Gaussian beam propagating in a vacuum. Using Kogelnik and Li's notation [75], the Gaussian solution of the free-space (≈ 0) equation

$$2i \partial_{\eta} e + \nabla_{\rho}^2 e = 0 \quad (50)$$

is well known and may be written as:

$$e(\rho, \eta, \tau) = a(\eta, \tau)^{-1} \exp\{\psi(\eta, \tau) - \rho^2 \left(\frac{1}{a^2(\eta, \tau)} + \frac{ik n_0}{2R(\eta, \tau)} \right)\} \quad (51)$$

where

$$\psi(\eta, \tau) = \arctan(\eta/ka_0^2) \quad (52)$$

$$a(\eta, \tau) = a_0 \sec \psi \quad (53)$$

and

$$R(\eta, \tau) = \eta \operatorname{cosec} \psi \quad (54)$$

The parameter a is the measure of the transverse scale, and

$$a_0 = a(0, \tau) \quad (55)$$

is the width of the initial intensity distribution. The parameter " a " shrinks or expands as the beam converges or diverges from the focus. It is logical to require the transverse mesh to vary as a varies. Therefore, the variable

$$\xi = \rho/a(\eta, \tau) \quad (56)$$

is introduced. It is displayed in Figures (21a) and (21b). To reiterate, it is well known that a linear stability analysis of the numerical discretization of the propagation equation imposes a pertinent condition relating two spatial meshes $\Delta\rho$ and $\Delta\eta$. This stability condition must be satisfied so that the numerical solution asymptotically approaches the analytical solution of the linearized partial-differential equation. More specifically, stability and convergence are assured if the ratio $[\Delta\eta/(\Delta\rho)^2]$ is appropriately defined and kept constant throughout the calculation.

For this purpose it is necessary to introduce a new axial variable z so that this parameter automatically remains constant as ρ varies. This should increase the density of η planes around the focus of the laser field where the irradiance sharply increases in magnitude causing a more extensive and severe field-material interaction to occur. The above is accomplished by introducing

$$z = \psi \quad (57)$$

and using a constant Δz . This transformation has the effect of making the extent of real space related to the size of the vacuum beam. It may be worthwhile to recognize that $[\Delta z/(\Delta\xi^2)]^{-1}$ is just the Fresnel number associated with a range Δz with respect to the aperture of radius $\Delta\xi$.

In terms of ξ and z the field equation now appears as

$$\frac{1}{a^2(z)} \{ 2i \partial_z e - 2i\xi(\tan z) \partial_{\xi} e + \nabla_{\xi}^2 e \} = ic_1 \quad (58)$$

where c_1 is a constant.

It is imperative to remove these rapid oscillations that would necessitate very fine mesh samplings in the transverse direction. For the field and polarization envelopes, the variables B and S are defined as:

$$\{e\} = \{a_0^{-1} \cos z\} \{S\} \exp[i \frac{kz}{2} \tan z - iz] \quad (59)$$

The quadratic phase and amplitude variation have been removed. The new field then takes the form:

$$\{1/a^2(z)\} \{2i \partial_z B + \nabla_T^2 B + (2 - \xi^2) B\} = ic_1 S \quad (60)$$

B and S vary more slowly in their functional values than their predecessors allowing the numerical procedure to march the solution forward in a more economical fashion by using larger meshes. They are numerically treated in an almost identical fashion to e and η [170]. However, for strongly nonlinear media, those a priori changes in the basic equations are not sufficient. A more sophisticated approach is needed. The desired method should automatically adjust the coordinate system in compliance with the local wavefront surfaces and actual beam features.

XIV. ADAPTIVE REZONING

The concepts of the previous section may be generalized by repeating the simple coordinate and analytical function transformations along the direction of propagation at each integration step. Figure (22a) and Figure (22b) illustrate this self-adjusted mapping in both planar and isometric graphs. The resolution of the computational grid is thereby defined according to the actual requirements of the physical problem.

The feasibility of such automatic rezoning has been demonstrated, without requiring any guesswork, by Hermann and Bradley in their CW analysis of thermal blooming [60] and by Moretti in supersonic flow calculations [51, 52, 57].

In particular, the change of reference wavefront technique consists of tracking the actual beam features and then readjusting the coordinate system. An adaptation of Hermann and Bradley's technique to a cylindrical geometry is presented herein.

The transverse mesh is forced to follow more exactly the actual expansion or contraction of the beam. The reference phase front is altered at each integration step (and for every instant of time) in the propagation direction, hence coinciding more precisely with the physical wavefront at that point; moreover, by locally referring the wavefront to a new focal point one has smaller phase changes with which to contend.

The new axial coordinate z is defined, as before, as

$$z = \arctan(\eta/ka_0^2); \quad (61)$$

$$\text{and } \partial_z z = (1/ka_0^2). \quad (62)$$

Previously, the center of the transformation where the radial mesh points were most tightly bunched, was at the focus ($z = \eta = 0$). Now this will no longer be the case, and the transformation will be defined in terms of an auxiliary axial variable z_ξ as a function of z , which is calculated adaptively in a way that reflects and compensates the changing physical situation. For the moment, the relationship $z_\xi(z)$ will be defined later in this section.

The radial coordinate ξ is then defined similarly as

$$\xi = \rho/a_\xi(z_\xi) \quad (63)$$

with an auxiliary axial coordinate z_ξ different from z . For stability reasons, it is required that $(\Delta z_\xi / \Delta \xi^2)$ should be a constant from $z_\xi = \psi$ (64). This leads to:

$$a_\xi(z_\xi) = a_{0\xi} / \cos z_\xi \quad (65)$$

$$d\eta = ka_0^2 [\tan(z+dz) - \tan z] \quad (66)$$

$$= ka_{0\xi}^2 [\tan(z_\xi + dz_\xi) - \tan z_\xi] \quad (67)$$

which gives:

$$\partial_z z_\xi = a^2/a_\xi^2 \quad (68)$$

and also leads to an expression for " dz_ξ ":

$$\tan(dz_\xi) = a^2 \tan(dz) / \{a_\xi^2 + \tan(dz)[a^2 \tan z_\xi - a_\xi^2 \tan z]\} \quad (69)$$

This enables one to find appropriate values for a^2/a_ξ^2 . $a_{0\xi}$ is then defined by writing:

$$a_\xi(z_\xi + dz_\xi) = a_{0\xi} / \cos(z_\xi + dz_\xi) \quad (70)$$

In this adaptive rezoning scheme, the physical solution near the current z plane is described better by a Gaussian beam of neck radius $a_{\xi 0}$ whose focal point is a distance z away than by an initially assumed Gaussian beam with parameters a_0 and z . With this transformation the field equation (50) in terms of z and ξ becomes

$$2i \partial_z e + \frac{a}{a_\xi^2} [\nabla_T^2 e - 2i \xi \tan z (\partial_z e)] = ic_1 a_\xi^2 \quad (71)$$

To remove the unwanted oscillations, new dependent variables B and S are introduced by $e = GB$ and $\eta = GS$ where

$$G = a^{-1} \xi \exp\left\{+\frac{i}{2} \xi^2 \tan z_\xi - i z_\xi\right\}. \quad (72)$$

all the values at the end of the previous interval (η plane) are indicated with a subscript p. The electric field e is given in the old representation as $e = G_p B_p$, and in the new representation as $e = GB$; where G_p is dependent on $z_{\xi p}$ and G on z_ξ , and B is given by

$$B_p = B \exp\{+i(\alpha \xi^2 + \beta \xi^4)\} \quad (73)$$

The best match is obtained by requiring that $\phi(B)$, the phase of B , should vary radially as little as possible.

$$\begin{aligned} \phi(b) &= \phi(B_p) + \phi(G_p) - \phi(G) \\ &= (\alpha \xi^2 + \beta \xi^4 + \dots) + ((1/2)\xi^2 \tan z_{\xi p} - z_{\xi p}) \\ &\quad - ((1/2)\xi^2 \tan z_\xi - z_\xi) \end{aligned} \quad (74)$$

where α is the curvature.

α and β are determined in an appropriate manner from B_p so that a new variable B has no curvature. It is clear that the new value of z_ξ at the present new plane under consideration is derived from the old value by

$$z_\xi = \arctan(2\alpha + \tan z_{\xi p}) \quad (75)$$

with the new neck radius $a_{0\xi}$

$$a_{0\xi} = a_\xi \cos z_\xi \quad (76)$$

The equation for B is then:

$$2i\partial_z B + \frac{a^2}{a_\xi^2} \{\nabla_T^2 B + (2-\xi^2)B\} = ic_1 a^2 S \quad (77)$$

By using this final differential equation, significant improvements in numerical computational cases have been achieved: i.e., this new equation varies less in its functional values than does the original one.

The instantaneous local parameters α and β of the quadratic wave front are determined by fitting the calculated $\phi(\xi)$ of B_p to a quartic in ξ ; a reasonable approach is that the intensity weighted square of the phase gradient

$$\int B^2 [\partial_p (\alpha \xi^2 + \beta \xi^4 + \psi)]^2 \xi d\xi = \text{minimum} \quad (78)$$

where ψ is the phase of the field variable $B = A \exp(-i\psi)$ [79]. The minimization of this phase gradient is weighted by the beam intensity. Consequently, the curvature at the highest intensity portion of the beam controls the phase transformation. The following different moment integrals are introduced, such as B_p , that would otherwise

$$\begin{aligned} M_1 &= \int \{\xi^2 B^2\} \xi d\xi; \\ M_2 &= \int \{\xi^4 B^2\} \xi d\xi; \\ M_3 &= \int \{\xi^6 B^2\} \xi d\xi; \\ Y_1 &= \int \{B^2 \xi \partial_\xi \psi\} \xi d\xi \\ Y_2 &= \int \{B^2 \xi^3 \partial_\xi \psi\} \xi d\xi \end{aligned} \quad (80)$$

using the relation

$$B^2 \partial_\xi \psi = -\text{Im}\{B^* \partial_\xi B\} \quad (81)$$

by taking partial derivatives with respect to the α 's and β 's, one obtains

$$\begin{aligned} Y_1 &= -\text{Im}\{B^* \partial_\xi B\} \xi d\xi, \\ Y_2 &= -\text{Im}\{B^* \partial_\xi B \xi^3\} \xi d\xi, \\ \alpha &= -(M_2 Y_2 - M_3 Y_1)/E, \text{ and} \\ \beta &= (M_1 Y_2 - M_2 Y_1)/2E, \end{aligned}$$

$$\text{where } E = 2(M_2^2 - M_1 M_3). \quad (82)$$

The distinctive advantage of these stretching and adjustable rezoning techniques stems, as suggested by Moretti, from the fact that they automatically define the mapping and all related derivatives analytically (that is, exactly) as it is determined by the calculation itself.

XV. NON-GAUSSIAN REFERENCE BEAMS

The phase transformation was readily generalized by Breaux [64] to be as convenient as possible. Consequently one is not restricted to a Gaussian beam as a reference. The transformations utilized for adaptive coordinates and phase removal become:

$$\rho = \rho/a(z) \quad (83)$$

$$e = B G = [B/a(z)] \exp\{[(1/2)\beta \rho^2 \{(\partial a/\partial z)/a(z)\}]\} \quad (84)$$

$$z = \int_{\eta_0}^{\eta} (\beta a^2)^{-1} d\eta \quad (85)$$

the application of these transformations to the free space wave equation results in:

$$2i \frac{\partial B}{\partial z} + \nabla_T^2 B + g(\rho, z) B = 0 \quad (86)$$

where

$$g(\rho, z) = -\beta^2 \rho^2 (a^3 \frac{\partial^2 a}{\partial z^2}) \quad (87)$$

appear in the transformed equation have been eliminated by this particular choice of variables. These specific transformations are a simple generalization of the transformation designed by Hermann and Bradley [60].

Furthermore, for strongly self-lensing beams, it appears that the relation

$$a(z) = [(1-z)^2 + (Nz/\beta)^2]^{1/2} \quad (50)$$

has all the prerequisite characteristics necessary for the treatment of a self-expanding beam. In particular, this form is similar to the z-dependent beam waist for a focused Gaussian beam. However, its scale expands N times larger than that of an ordinary Gaussian beam. The equation relating η and z becomes

$$z = N^{-1} \arctan[N\eta/\beta(1-\eta)] \quad (88)$$

and

$$\eta = \beta \tan z / (N + \beta \tan z) \quad (89)$$

XVI. NUMERICAL RESULTS

In this section we outline some basic results, which have been obtained with and without the use of rezoning and stretching, and which illustrate why the more sophisticated techniques required less computational efforts.

The first part of this investigation which dealt with absorbing material has led to the discovery of interesting new physical phenomena which promises to have significant applications to proposed optical communications systems. It had been shown that spontaneous focusing can occur in the absence of lenses, and that the focusing can be controlled by varying the medium parameters. The second part of this analysis dealt with amplifiers.

A. Pertinent Parameters

Since the Fresnel number F^{-1} associated with a characteristic length, the "area" of the input pulse on axis, the relaxation times and the off-line center frequency shift are the pertinent parameters describing the temporal and transverse evolution of these coherent pulses in the absorbing media, we have studied the dependence of the propagation characteristics on these parameters. In particular, the dependence of the location of the focusing in absorbers and the sharpness of its threshold, as well as the appearance of the multiple foci on-axis along the direction of propagation, are dependent on the specific choice of the following characteristics:

(1) The reciprocal of the Fresnel number associated with a characteristic absorbing length through its different constituents:

(i) The temporal length of the pulse t_p ;

(ii) The spatial beam width of the (perfectly smooth) Gaussian profile ρ_0 (to avoid any additional diffraction from the edge as well as possible small ripples that could cause beam distortion and small-scale self-focusing);

(iii) The absorbing length per unit time $(\sigma')^{-1}$ that enters the gain of the active medium;

(iv) The carrier wave length λ .

(2) The material relaxation times τ_1 and τ_2 (the effect of atomic memory).

(3) The carrier frequency offset $\Delta\Omega$.

(4) The input on-axis (time integrated field amplitude) area.

Furthermore, prior to the experiment in sodium [119], a family of calculations was made to verify that the coherent self-focusing predicted for a sharp line would remain in a broad-line atomic system.

In furtherance to this study, the transmission characteristics in pre-excited media was analyzed by varying the previously cited parameters. The effect of the boundary condition was carefully investigated.

The computed pulse-breakup on axis agrees with laboratory observations carried out on high power laser chains for fusion [153, 154, 155].

B. Scaling

In order to facilitate the interpretation of our numerical results, we have considered a class of problems in which the input field has a given functional variation in time, τ , and transverse coordinate, ρ , namely a Gaussian in each variable with the additional input condition $\int_{-\infty}^{\infty} d\tau e(\rho=0, \eta=0, \tau) = 2\pi$, i.e., a 2π

pulse on axis. Once one specifies the relaxation times, the resonance frequency offset and the pulse area on axis, the factor F becomes the sole parameter distinguishing one family of physical situations from another. Since the mathematical expression in normalized coordinates ρ , η and t for all input fields characterizing different situations is the same, this gives us the ability to interpret the numerical results with some flexibility.

By studying the numerical results, one can identify several physical effects which seem to play important roles in the evolution of the focusing process by affecting the relative motion (among adjacent pencils) and the transverse energy flow. Some of these effects have been separately studied by others, e.g., adiabatic following [33], strong self-phase

modulation [6,25], spectral broadening [25] and self-steepening [27], but in our problem they combine to affect the behavior during different parts of the pulse evolution, both in space and time.

C. Choice of Parameters

Finally, since the imaginary part of the electric field grows in proportion to the product of the diffraction term and the factor F (as outlined by the perturbation approach), it follows that the sign of this quantity and its value changes as the pulse propagates in the resonant medium. Eventually, this forces a curvature in the wave-front of the electric field to occur. The latter is the mechanism that induces transverse energy flow that underlines the self-focusing phenomenon in absorbers and the beam degradation in amplifier. The coherent self-action processes may be repeated at other sites as the pulse continues to propagate and interact further.

By changing the parameters constituting F , one alters the growth and development of the field phase. For example, reducing F will tend to retard the threshold of the focusing phenomenon in absorbers while increasing it will stimulate the focusing sooner and strengthen it. These remarks are not intended to imply that the physical mechanisms are simple and well-defined. The effect of this particular variation in F is a rather complicated matter. The competition between refraction (through the inertial response of the resonant absorber), and normal near-field diffraction (as in free-space) results in a transverse energy flow. The latter may lead to self-focusing or self-expansion. This means that for a limited useful range of F , the resonant absorber acts as a nonlinear converging lens; whereas, the pre-excited medium, by effectively behaving as a diverging lens, limits the useful output of the incoming laser beam. Each of these three mechanisms (near-field diffraction, refraction and nonlinear absorption) will strongly affect the relative motion among the different adjacent pencils.

While it may be useful to consider each of these three physical processes as independent units. Each mechanism plays an overlapping role in the overall physical picture. Hence, the precise dependence of the focusing behavior on a particular physical parameter such as τ_p , ρ_0 , λ , T_1 , T_2 , α' , Δ and on the input area is difficult to predict beforehand with any elementary system. For example, let us attempt to predict the influence of a decrease in the pulse duration τ_p (i.e., an increase in F) on the self-focusing. If the interaction between adjacent pencils is ignored, one may arrive at the erroneous conclusion that adjacent pencils fall out of step faster for narrower pulses than for broader ones. In reality, for short pulses the exchange of energy is very fast, so that the relative time delays

between adjacent radii is greatly reduced. The pencils tend to move together and the resulting interaction grows weaker. A reduction in τ_p translates into a broadening of the pulse frequency spectrum. This will make the resonant propagation look more like the free-space solution since the interaction is substantially reduced. For exceptionally short pulses, the question of the validity of the slowly varying envelope approximation arises [23-25].

D. Sample Cases

(i) ABSORBERS

(1) One-dimension effects in Absorbers

In our discussion of absorbers, we first consider the case of one-dimensional pulse propagation with the pulse duration much shorter than both T_1 and T_2 . Analytic distortionless solutions of the material-field equations are known [9] of the form

$$\frac{\mu e'}{h} = \frac{2}{\tau_p} \operatorname{sech} \left[\frac{t-(z/v)}{\tau_p} \right] \quad (90)$$

(equivalently $e = 2 \operatorname{sech}(\tau)$) where v is the pulse velocity given in terms of the pulse length τ_p by

$$\frac{1}{v} = \frac{n}{c} + \alpha_{\text{eff}} \tau_p \quad (91)$$

This is the 2π pulse:

$$\int_{-\infty}^{\infty} d\tau \left[\left(\frac{2\mu}{h} e' \tau_p \right) \right] = \int_{-\infty}^{\infty} dt e = 2\pi \quad (92)$$

In Figure (23) we present the results of numerical integration of the one-dimensional field equation for the case that the input pulse is a Gaussian in time of input area 2π .

Figures (23a) through (23d) show the pulse reshaping. As defined earlier in Section III, the symbol τ stands for the time counted from the instant when a signal traveling at the speed of light in the medium reaches the point z , normalized to the pulse length τ_p thus

$$\tau = (t - \frac{n}{c} z) / \tau_p \quad (93)$$

The units of τ_p are nanoseconds. After 300 cm the pulse shape closely matches the sech form. From the measured width after 300 cm the analytic expression for the pulse velocity is $(v/c) = 0.7$. In Figure (23e), we have plotted the integrated intensity (Energy/cm² = $\int dt e^2$), pulse area, and time delay of the peak all against the propagation distance z . The time delay is the difference between the local and input plane values of τ at the peak of the pulse. This quantity measures the velocity of the peak relative to the speed of light.

$$\frac{v}{c} = \left[\frac{1}{c(\Delta\tau/\Delta\eta) + 1} \right] \quad (94)$$

where $\Delta\tau$ is the time delay accumulated in the interval $\Delta\eta$. We note that the pulse area remains at the input value 2π and the pulse energy decreases linearly with distance as the pulse reshapes from Gaussian toward sech. This decrease is associated with the non-vanishing (but small) value of $(1/T_1)$. The

pulse peak moves more slowly than the speed of light. After 300 cm, the numerical pulse velocity is 0.7 times the speed of light. This corresponds to the speed of sech pulse of the same width.

(2) Three-dimension effects in Absorbers

We present the results for a typical calculation of a 2π pulse area on-axis. The temporal and transverse variations of the electric field are Gaussian. The chosen parameters were consistent with: $F \approx 1.592 \times 10^{-3}$, $(\lambda = 10^{-3} \text{ cm})$, $\rho_{\text{eff}} = 1/20 \text{ cm}^{-2}$, $\rho_0 = 1 \text{ cm}$; $\Delta\eta = 0.0$; $\tau_1 = 10$; $\tau_2 = 20$ and $\tau_3^* = \infty$.

The effect of coherent self-focusing is illustrated in Figure (24). The time integrated pulse 'energy' per unit area is plotted for various values of the transverse coordinate, as a function of the propagation distance. Two orientations are shown to display the energy redistribution as the laser beam is transmitted in the nonlinear resonant absorber. The necessity of non-uniform mesh is quite evident. At the input plane, on the left of the figure, the profile is Gaussian. After a reshaping period, during which the relative retardation of adjacent pencils leads to the development of a curvature of the phase front, strong focusing occurs which leads to substantial magnifications of the on-axis energy per unit area. There appears to be a rapid attenuation of the total field energy after the focal plane is passed. Most of this attenuation is due to substantial pure diffraction spreading of the narrowed beam while some is due to the temporal retardation in the peak of the pulse associated with the coherent interaction. For later distances, not all of the pulse energy (or pulse area) falls within the time interval in the co-moving frame over which the numerical integration was performed; (alternatively expressed, the tail of the pulse could escape from the temporal window).

Furthermore, with uniform radial nodes the transverse sampling was not as good in the focal region as it is in the input plane. The calculation was repeated with twice as many transverse sampling points (58 instead of 29) and obtained consistent results. When rezoning was implemented only 32 points were sufficient to adequately sample the rapid variations associated with the self-lensing phenomena.

Figure (25) gives the pulse characteristics as a function of the propagation distance: the

on-axis time-integrated 'energy' per unit area, the total field energy (integrated over the beam cross-section), and a quantity that characterizes the beam cross-section. This quantity ρ_{eff} is the ratio of the total field energy to the on-axis field energy per unit area:

$$\rho_{\text{eff}} = \frac{\int_0^{r_m} dp \rho \int_{-\infty}^{\infty} e(\rho, \eta, \tau)^2 d\tau}{\int_{-\infty}^{\infty} e(\rho, \eta, \tau)^2 d\tau} \quad (95)$$

Here r_m defines the extent of the region over which the numerical solution is to be determined.

This graph represents the most striking description of coherent self-focusing since the contraction of the beam produces a considerably amplified field intensity on-axis of the focal region and its immediate vicinity.

It is noteworthy that the total field energy per transverse plane is a smooth decaying function of the propagation distance in the resonant absorber. This is in agreement with the physics of the problem even in the presence of strong magnification on-axis and provides additional confidence in the computation.

Figure (26) contrasts the transverse distribution of the time integrated energy per unit area at the focal plane with the one at the input plane to illustrate the coherent narrowing of the beam. The development of self-focusing is clearly evident.

The three-dimensional numerical calculations [39,40] substantiate the physical picture based on time changes in the phase. In Figure (27) the field amplitude is plotted versus the retarded time for three stages of the propagation process: (a) the reshaping region; (b) the build-up region; and (c) the focal region. The transverse energy current is plotted versus the retarded time for the same three distances in Figure (27d), (27e) and (27f). In each case the plots are given for several values of the transverse coordinate ρ . Positive values of the transverse energy flow correspond to outward flow and negative values correspond to inward flow. Figure (27) clearly illustrates the following features of the self-focusing. In the earliest stages of the propagation (Figures (27) and (28)) the near axis energy current is outward for most of the pulse time, but becomes inward (self-focusing) toward the rear ($\tau \sim 2.4$). For this value of t the field amplitude (Figure (29a)) is already past its peak and has a small value. As we proceed beyond the reshaping region (Figures (29b) and (29c)), the near axis peak amplitude moves back in time (corresponding to the fact that the group velocity is less than c/n) while the temporal location of the change from focus-

ing to defocusing energy flow remains the same. This leads to a large increase in the value of the transverse energy. In Figures (29c) and (29f) (in the focal plane) the peak amplitude occurs at $\tau = 2.4$.

In graphs (a), (b) and (c) in Figure (27) and Figure (28) the profile of the field amplitude is plotted for several instants of time in the leading part of the pulse or in the lagging parts of the pulses respectively, for the same three stages of the propagation process. In the plots of Figure (28a), (28b), (28c) one can notice the distinct deviation of the profile from the input Gaussian shape. The beam splits into more than one lobe, indicating the different concentration of energy in more than one ring around the axis outwardly due to diffraction. The quantitative agreement of the hole formation and in filling up (see Figure (29)) with the simplified physical picture predictions presented earlier is evident. Graphs (d), (e) and (f) of Figure (29) and in Figure (29) display the transverse energy current for earlier and later instants of time, respectively, at the main stages of the propagation process. In the earlier stage of propagation, the energy current flows outwardly (see Graph (d) of Figures (27), (28), (29) according to traditional diffraction spreading (Figure (11a)). Once a sufficient relative motion between neighboring pencils arises, a burn in the profile appears. By diffraction radial energy flows in both directions, outwards and inwards. Consequently, part of the beam experiences self-focusing whereas another part shows self-defocusing. More specifically, diffraction (from the tail of the pulse in the wings of the beam), into the forward central region, still in an amplifying mode, results in a continuous boost of the inward flow of energy. This interaction with those atoms which were excited by the preceding pulse, that was closer to the axis, make the inwardly diffracting light experiences a net amplification. Moreover, this boosting phenomenon continues as energy flows more towards the axis; it leads to a positive contribution to the center of the beam. This means that the leading portion of the pulse in the rim of the beam in an initially ground-state medium sees an absorber and thus experiences net absorption (as shown in Figure (12a) and Figure (12b)). Because of this always-present interaction with population-inverted atoms, the amount arriving at the axis is significantly much higher than it would be if the remaining medium was linear. This energy intensification on axis is the new coherent self-focusing phenomenon. Immediately after the focal plane, both inward and outward transverse energy flow occur within the same pulse at different slices of time; the outward occurs in the leading portion resulting from the diffraction of the focused beam while the inward flow occurs and prepares the second (but weaker) focusing.

This intuitive physical picture is clearly reinforced by the projection graphs illustrating the rigorous three-dimensional calculation.

This same pattern of pulse compression and beam narrowing was clearly observed in the first experiment conducted in Na, illustrating SIT-SF with transverse energy flow. The drastic changes in spatial and temporal profiles are shown in Figure (30) for the maximum off-resonance (a and a1) and on-resonance (b and b1) coherent self-focusing. Figure (31) displays clearly the observed longitudinal reshaping. The significant contribution of the transverse effects in SIT experiments is clearly displayed in Figure (32) where we contrast the temporal behavior for both uniform-plane wave SIT and non-uniform SIT.

For additional clarity, in Figures (33a), (33b), (33c), (33d) the field energy is isometrically plotted against the retarded time for various transverse coordinates at four specific regions of the propagation process: (A) the reshaping region where the perturbation treatment holds (b) the build-up region; (C) the focal region; and (D) the post-focal region. A rotation of the isometric energy plots is displayed in Figure (34a), (34b), (34c) and (34d) versus ρ for various instants of time to emphasize the radially dependent delay resulting from the coherent interaction. Graphs (34e), (34f), (34g) and (34h) describe the same position illustrated previously. The plots a, b, c, d, of Figure (33) and Figure (34) are contrasted against their counterplotted isometric representation of the transverse energy current for the same four distances. Plots (34e)-(34h), however, are displayed in Figure (35) in contrast to the rotated isometric drawings of the energy current. Positive values of the transverse energy current correspond to outward flow and negative values correspond to inward flow. The results of Figure (33a), (34a) and (33e), (34e) are in agreement with the physical picture associated with the analytic perturbation previously discussed in this paper.

The computational grid has to be shaped around each cross-section (ρ , τ) to optimize the calculation: Therefore the spatial mapping which is needed is complicated and must be continuously changing, (i.e., adapting locally to the physics). A proper pattern of grids indicating temporal stretching and spatial rezoning provides the necessary resolution.

The burn pattern, iso-irradiance level contours (against τ and ρ) for different propagation distances are shown in Figure (35). Severe changes in the beam cross-section are taking place as a function of the propagating distance. At the launching front, the beam is smooth and symmetric; as the beam propagates into the nonlinear resonant medium the effect of the nonlinear inertia takes place: relative velocities across the beam (for different radii) arise causing tails to occur in the wings. The strong pulse propagates faster than the weak pulse. Consequently, a hole near the axis appears, but linear diffraction causes the beam to gradually fill. Due to a boosting mechanism the inward flowing energy current gets magnified. This is clearly an initial self-focusing

phenomena followed by a beam expansion. The temporal shift of the beam gravity illustrates the delay associated with the coherent exchange of energy between the field and active medium.

(iii) EXPERIMENTAL VERIFICATION

We have studied these processes numerically: Change in shape, temporal length, spatial width and amplitude of the input pulse were considered. Pulse development, when the inhomogeneous broadening τ_2 , the characteristic length α_{eff}^{-1} and the frequency offset $\Delta\omega$ are varied, was observed. We have compiled universal output curves illustrating the expected output from the absorber as one modifies the characteristics of the input field and the active media [42,43].

As an example, from Figure (36), we predict the observation of coherent self-focusing (an on-axis magnification of axial energy per unit area of 10) when the F parameter has the value 0.4×10^{-3} . The distance to the focal plane will then be $10(\alpha_{\text{eff}}^{-1})$.

Until quite recently, the work whose physical parameters most closely match the situation in our computations was the experiment of Gibbs and Slusher [9]. Unfortunately, the length of their cell and the range of operating pressures were such that the focal distance exceeded their effective cell length.

More recently, the SIT near-resonance SF and defocusing was first observed by Gibbs and Bolger at Philips Laboratory [119] in inhomogeneously broadened Na. An increase in energy per unit area (fluency) at the center of the beam was used as definition of focusing as shown in Figure (32). The experimental dependence of coherent transient SF upon absorption and magnetic detuning in Na is shown in Figure (38); CW light has no transient SF and focuses for $\Delta\omega < 0$ and defocuses for $\Delta\omega > 0$ (Figure (37), curve g) [122]. For 2-ns pulses and $\alpha L > 3$, slight SF occurs peaked on-resonance (Figure (37), curve a). At higher absorption the maximum SF occurs for $\Delta\omega > 0$ but SF is still seen on resonance (Figure (37), curve a-d). Only for very high absorption ($\alpha L \sim 20$) is there no magnification on resonance (Figure (37), curves e and f); presumably absorption destroys the pulse after it passes its focus. The observation of focusing on resonance for coherent pulses and not for CW light clearly illustrates that coherent transient self-focusing is different from previous self-focusing [123,125]. This coherent contribution has been disregarded in the past in the analysis of High Power Laser. This Na observation has shown that the disregard of this inertial term is not justified in a system within which the pulse length is comparable with the inverse linewidth. This dependency on the frequency mismatch agrees perfectly with the trend predicted theoretically.

The experimental F value of 10^{-2} corresponds to a Fresnel number of about 3, i.e., strong enough diffraction to provide radial communications, but weak enough that the induced nonlinear self-lensing effect overcomes the spreading associated with diffraction. Numerical simulations predict, for sharp-line atomic systems, maximum magnification of almost 10 for $F = 4 \times 10^{-4}$ and $\alpha L \sim 18$ (~ 44). All self-focusing calculations were done in sharp line. Experiments deal only with essential broad-line. To predict whether or not the experiment will work, it would be necessary to repeat all the calculations with a broad line system, which is a very expensive proposition, since it involves an additional dimension. Therefore, a sufficient number of broad line simulations were done, from which was derived a calibration curve to correlate the essential features of both families of calculations. Based on this curve, the main feature of is effective absorption, we can deduce the properties of self-focusing in broad line. In particular, if one adjusts the absorption in the numerical simulation for sharp line two-level atomic systems, in such a manner that it is equal to the effective absorption that one gets in the broad line case (which is the situation of most of the experiments), one would find that on-resonance coherent SF does indeed occur at an αL of 7.5 with a magnification of about 2.45. This is an astonishingly good qualitative and quantitative agreement between theory and the Na experiments for the observed magnification of $\alpha L = 10$ and $F = 10^{-2}$.

Attempts to observe on-resonance magnifications greater than 2 with large-diameter beams resulted in hot spots in the output even for $\alpha L > 15$. These probably result from focusing of smaller diameter regions with $F \sim 10^{-2}$ initiated by input phase and intensity variations (small ripples) differing from the theoretically assumed perfect Gaussian input. Consequently, SIT self-focusing is unavoidably important in the propagation of coherent optical pulses through thick absorbers ($\alpha L > 15$) even when large-diameter beams (large λ) are used on resonance.

The second experiment was conducted in Heidelberg by Toschek [120] et al. They investigated the propagation of linearly polarized $1.15 \mu\text{m}$ light pulses in an absorbing inhomogeneously broadened quasi-non-degenerate neon discharge ($\alpha L < 9$) and observed both SIT and SF. The transmission T (or magnification) is determined by graphic integration of about forty superimposed pulses. Particular care is taken to produce a perfect Gaussian beam with less than 3% variation of diameter along the absorber (as shown in Figure (38)) to avoid small-scale self-focusing [121,126]. Comparison with numerical simulations of uniform-plane-wave Maxwell-Schrödinger equations with $T_1 = 33$ ns and $T_2 = 10$ ns calibrates the squared pulse area θ^2 , in agreement with power measurements. Data and simulations are compared in Figure

(39). For $\tau_p = 3$ ns, experimental T's slightly exceed those^p from uniform-plane-wave theory; for 1-ns pulses the discrepancy is even larger. This increase in SF with increased T_2/τ_p agrees perfectly with the three-dimensional calculations [128] and emphasizes the coherent nature of the effect. The shorter the pulse length τ_p compared to the relaxation times T_1 and T_2 , the stronger the SIT-SF will be. Magnifications up to 40% and more recently up to 60% [129] were seen (see Figure (40)). Note that the experimental transmissions increase and the uniform plane-wave simulations decrease with increasing αL .

Data and theory agree that coherent SF can be as large on resonance as off; on-resonance SF can occur, for a wide range of input areas above π , SF is most effective with the relaxation times are long compared to the pulse length. There is no doubt that the recently experimentally observed SF [122,127] is the new mechanism recently predicted numerically. Coherent transient SF may explain previously not understood observed transverse effects.

Perhaps the reason this effect has not been seen clearly before and hence received due attention, is that it becomes significant only after the reshaping region, i.e., $\alpha_{eff}^2 \leq 5$, on which most SIT experiments have concentrated. Much higher absorption ($\alpha_{eff}^2 \sim 25$) was used by McCall and Hahn [8] in the first SIT experiment; they reported bright spots in the output (also seen in the Na experiment for large input diameters) which they attributed to transverse instabilities. The experiment of Zembrud and Gruhl [22] was characterized by $\alpha_{eff}^2 \sim 11$ and $F \sim 10^{-2}$ so self-focusing should be beginning; their Figure 1c has an output about 14% higher than the input and most of their data have higher transmissions than that expected by uniform plane-wave simulations. Rhodes and Szoke [28] also reported transverse effects seen in SF₆ for $\alpha_{eff}^2 \sim 20$ which may have resulted once again from self-focusing.

Further experimental and theoretical studies of coherent self-focusing could thus clarify the best procedures for maintaining near-uniform wavefronts in thick absorbers.

ii) AMPLIFIERS

1) Background

The main difficulties encountered in high power laser construction are due to small scale and whole beam self-focusing. To achieve fusion one needs a perfect uniformity of target illumination [126]. This requirement is so critical that even the slightest phase variation must be avoided. Thus, the major design problem challenge could be summarized as follows: how to keep the shape together while minimizing the small-scale self-focusing? Any phase gradient would lead to an energy redistribution and self-lensing phenomenon which are detrimental to optimum target illumination.

This could be expressed in another manner: how to keep the fill factor high without generating diffraction fringes at the edges. Thus, one would want to determine the effects of nonlinear propagation on the spatial and temporal profile of the output, (to be focused on target), laser beam.

To minimize a crucial loss of focusable output power, various experimental strategies have been implemented. The use of spatial filtering allows control of the growth of phase variation [131, 132, 153, 154]. More specifically, long path spatial filtering [120], pinhole spatial filtering [123] and, more recently, apodisation [131], and optical imaging relay [131] seem to be the key schemes in maintaining as smooth a beam shape as possible. The performance of present and committed laser systems can be greatly improved by compensating for [132] any departure from the desired equi-phase uniform plane wavefronts. Furthermore, the development of new types of material, such as phosphate glass [132], have helped in reducing the nonlinear properties which are responsible for damaging the light beam. If the beam is not perfectly smooth initially, the fluctuation amplitudes may oscillate, decay or grow exponentially with spatial and temporal rates determined by the nonlinearities and the nature of the initial fluctuations. Furthermore, fluctuations may lead to further self-action phenomena before the beam collapses as a whole. It is this type of theoretical analysis (that was performed initially by Bespalov and Talanov [134-136], and later by Suydam [137-139] and others [140,155], which has gained importance in studies of high power laser performance. To reach definite answers such as the location of self-focusing filaments for a fluctuation of given amplitude, one has to treat the nonlinear growth more accurately than this linearized analysis. The latter was generalized into several possibilities: First, by considering nonsinusoidal transverse fluctuation profiles, Suydam [137] has proven that any eigenfunction of the transverse Laplacian such as a Bessel function, can be a solution. Clearly, such solutions form a complete set. These are referred to as normal modes of the perturbation. Thus, any linear combination will constitute a solution. Among these modes, certain ones are unstable and grow exponentially. However, beyond certain characteristic growth lengths, the most rapidly growing mode will outstrip the others and ultimately be the only significant one [137]. Recently, a useful physical picture of small-scale self-focusing, based on the idea of interference between a strong background and a weak wave launched at an angle, was presented by Trenholme in his reviews of the state of the art [144]. The degree of nonlinear phase accumulation (B : break-up integral) determines the useful output power. Further investigations (a) have extended the theories to handle any polarization state [141] in the background beam; and (b) allowed the inclusion of additional effects such as linear gain [133], saturable gain [142], or stimulated Brillouin or Raman scatter-

ing [143]. More recently, using Vlasov et al's moment theory [155], Suydam [139] intuitively extended the plane-wave theory for small-scale self-focusing to describe finite-apertured beams that can initially converge or diverge.

The two types of self-focusing are not mutually exclusive [145]; they can be complementary. None of these theories are complete. Remarkably enough, experimental observations by Campillo et al [149-151] confirm the soundness of Suydam's work. Suydam realized the interplay of both whole-beam nonlinear lensing and small-scale self-focusing [137]. He concluded, however, his analysis by pointing out that since temporal effects were not included, it was impossible to quantitatively predict beam degradation. Independently, Fleck has developed a cw numerical code, which treated simultaneously small-scale and whole-beam self-focusing, that he used to study transverse variations in the beam evolution of Cyclops [154]. Combining Suydam's elegant generalization of Bessel and Talanov's linear stability to Frantz-Nodvik's [147] flux saturation equation, Elliot [147,148] provides another refinement description of uniform pulse-wave small-scale self-focusing. We believe it would be advantageous to combine Elliot's work with Suydam's most recent analysis of finite effects.

Since the extent of this profile distortion varies with time, as the pulse intensity rises and falls on each shot, complications occur when pulses are used. The temporal distortion is hence produced beam filaments which grow in intensity at the expense of the main beam; the main beam gets depleted by the scattering process which transfers most of the energy to filaments. Therefore, some energy may be lost completely from the beam, and get absorbed nonlinearly. Present theoretical efforts are unable to predict and estimate the beam quality degradation as observed by experimentalists at Livermore (Bliss et al [41]) and at Rochester by (Soures et al [43]). Figures (41) and Figure (42) represent an example of the severe temporal distortion which can be caused by nonlinear propagation. One reaches the unavoidable conclusion that beam breakup in laser systems containing optically thick nonlinear material can lead to a severe reduction in the fraction of the output which can be usefully focused.

In some extreme cases of advanced stages of self-focusing, essentially all of the power can be scattered out of the primary beam and become unfocusable for a fusion-size target. Furthermore, since the nonlinear propagation of instabilities causes growth of small-scale amplitude perturbations which reduces the focusing properties of such beams, rigorous computer calculations with real-life parameters are necessary. Quantitative analytic predictions are too complicated to be easily characterized in detail. Much of this complexity arises from the fact that sources for dust particles, small damage sites and various material imperfections. Now that Suydam has

commendably recognized the relevance of interplay of small-scale and whole beam self-focusing, it is logical as recently summarized by Brown [146] to address the temporal dependence of active medium with inertial memory on the beam evolution. This analysis can be done first separately and then as an addition to previous analysis a la Suydam [139] and a la Fleck [154]. One ought to expect that (since the modulation of the beam profile grows exponentially with intensity and the loss from the focal spot increases nonlinearly with modulation depth), the fraction lost from the temporal and spatial peak of the pulse is considerably larger than the average over the whole pulse. In other words, severe temporal or spatial distortion could occur as a result of preferentially depleting the high intensity parts of the pulse, thus, when coherent transient effects are additionally present, self-action phenomena arise at distances less than those predicted by either theory considered separately [119, 120].

2) One dimension effects in Amplifiers

We present the one-dimensional propagation data and summaries then the contrasting three-dimensional calculations for the same parameters. Like the absorber, observations relevant to the theory of self-action will be noted. The numerical solutions are presented and discussed for the three-situations where the on-axis ray has area π , 2π and 3π .

Figure (43) shows the one-dimensional propagation in amplifying medium of a pulse whose input area is π . The relaxation times T_2 and T_1 are ten and twenty times the FWHM τ_p (4 nsec) Gaussian shaped input field. After five linear amplifying lengths ($1/\alpha_{eff} = 40$ cm), several characteristic features are apparent.

The pulses "real area" $\int e(t,z)dt$ remains at

2π even though the energy is increasing. The electric field envelope is real but can become negative. The "absolute area" (replace e by $|e|$), which is always the area referred to in the figures, does increase with distance z as does the energy. The development of the second pulse is the result of leaving the medium in a partially amplifying state after most of the pulse has past. The tendency is the same as a ringing linear oscillator circuit. Introducing a larger damping term T_1 suppresses the phenomenon.

3) Transverse Effects in Amplifiers

The general format for presenting three-dimensional coherent pulse propagation in amplifying medium will be the same as part A for the absorber. We now propose results of the three-dimensional computation corresponding to the one-dimensional case just discussed. In Figures (44) and (45) the field energy amplitude and the transverse energy current

are displayed as a function of retarded time τ for various small and larger radii. The profile is plotted for small instants of time in Figure (46) and in large instants of time in Figure (47).

In Figure (48) the field energy and radial current are displayed isometrically against the retarded time for various radii at the previously defined four critical regions of propagation; their profile is plotted in Figure (49) for various instants of time. In Figure (50) from the contour energy level, one sees clearly that the peak of the pulse is advanced with respect to a frame moving with the velocity of light. It is seen that the smaller area propagates slower than the stronger areas. From the energy current graphs, one finds out that a focusing phase is not an exclusive property of a resonant absorber.

The effect of the radial boundary is illustrated in Figure (51) to Figure (57). Non-uniform radial stretching was adopted during the computation. Projections of the field energy and the energy current are plotted versus τ for different radii in Figures (51) and (52), and versus ρ for small instants of time in Figure (53) and large instants of time in Figure (54). The four characteristic regions of propagation are clearly illustrated in isometric plots in Figure (55) and Figure (56); whereas Figure (57) displays the contour energy level.

XVII. MODIFICATION OF THE BLOCH EQUATION ALGORITHMIC SOLVER

This work is not, as it has appeared, a model of any restricted specific situation. Rather, what we have attempted to study is a situation where coherent interaction leads to strong deviation from the conditions in plane-wave propagation. We first dealt with a simplified model (scalar-wave equation coupled to a two-level sharp-line atomic system without degeneracy) where transverse effects will enhance inhomogeneities, and lead to nonlinear dispersion and nonlinear absorption. The significant role of the dynamic transverse energy flow is expected to play the same physical role in more realistic situations, where it might be somehow modified by other effects but still will not be washed out. Coherent phenomena are not confined just to the situation where the pulse duration is much shorter than the relaxation time: They will also appear whenever the field is large enough so that significant exchange of energy between the light pulse and matter takes place in a time short compared to a relaxation time. When this situation is combined with a sufficiently rapid spatial variation in the input plane, significant self-action phenomena are expected.

More specifically, for certain laser fusion chains, such as the Los Alamos CO_2 system and the Garching Iodine laser system, the

pulse length is not much shorter than the medium relaxation times. This situation is an intermediate one between the coherent and rate-equation-approximation limit. It enables one to consider an alternative more implicit method to solve the Bloch equations. The numerical integration method is based on an exact formal solution of the equations in question. This method is a generalization of an approach previously used by Suydam [68], Goldstein and Dickman [159], to solve the four-level CO_2 atomic dynamics in the rate equation limit. This technique is particularly appropriate when the rate constant can become very large. It was subsequently realized [162] that Fleck [163] has independently reached the same conclusion when studying Q-switching of pulse lasers.

In particular, one can attempt to express the differential variable appearing on the left-hand side of a given material in terms of an integral over the right-hand side. The integral can then be handled formally and exactly. The scheme is implicit and has been linearized by assuming that the field is known. The field can be guessed at the new time then corrected through iteration. γ , σ and W can be readily evaluated as the solution to three simultaneous linear algebraic equations. Even though this implicit method takes longer to calculate, it is particularly advantageous since its stability does not limit its usefulness to a restricted range of parameters.

In particular, this method can be easily outlined in the following manner: The material coupled differential equation has the form

$$\frac{\partial A}{\partial \tau} + \gamma A = f(\tau) \quad (96)$$

where γ can be either a real or a complex decay constant. By introducing

$$A = B \exp(-\gamma\tau), \quad (97)$$

$$\text{i.e., } B = A \exp(+\gamma\tau), \quad (98)$$

one obtains

$$\frac{\partial A}{\partial \tau} + \gamma A = \frac{\partial B}{\partial \tau} \exp(-\gamma\tau) = f(\tau) \quad (99)$$

integrating both sides:

$$[A \exp(\gamma\tau)]_{\tau}^{\tau+\Delta\tau} = \int_{\tau}^{\tau+\Delta\tau} f(\xi) \exp(\gamma\xi) d\xi \quad (100)$$

$$\exp(\gamma\tau)[A(\tau+\Delta\tau) \exp(\gamma\Delta\tau) - A(\tau)]$$

$$= [1/\gamma] \int_{\tau}^{\tau+\Delta\tau} f(\xi) d[\exp(\gamma\xi)] \quad (101)$$

$$= [1/\gamma] [f(\xi) \exp(\gamma\xi)]_{\tau}^{\tau+\Delta\tau} - [1/\gamma] \int_{\tau}^{\tau+\Delta\tau} \exp(\gamma\xi) f'(\xi) d\xi$$

$$A(\tau+\Delta\tau) \exp(\gamma\Delta\tau) - A(\tau) = [f(\tau+\Delta\tau) \exp(\gamma\Delta\tau) - f(\tau)]/\gamma$$

$$- (\exp(-\gamma\tau)/\gamma^2) \int_{\tau}^{\tau+\Delta\tau} f'(\xi) d[\exp(\gamma\xi)] \quad (102)$$

$$= [f(\tau+\Delta\tau) - f(\tau)]/\gamma - (f'(\tau+\Delta\tau) \exp(\gamma\Delta\tau) - f'(\tau)/\gamma)$$

$$+ [\exp(-\gamma\tau)/\gamma^2] \int_{\tau}^{\tau+\Delta\tau} f''(\xi) \exp(\gamma\xi) d\xi \quad (103)$$

These formal solutions, which are exact, will be the basis of the finite difference approximation scheme. Assuming that $f(\tau)$ is a linear function of τ between τ and $\tau+\Delta\tau$ (hence, $f''(\tau)$ vanishes), one can stop carrying the process of integration by part further.

Using f_{n+1} for $f(\tau+\Delta\tau)$ and f_n for $f(\tau)$ and the approximation:

$$f'_{n+1} = f'_n = (f_{n+1} - f_n)/\Delta\tau \quad (104)$$

one can evaluate the integral explicitly with the result:

$$A_{n+1} = \exp(-\gamma\Delta\tau) A_n + [f_{n+1} - f_n \exp(-\gamma\Delta\tau)]/\Delta\tau - \{[1 - \exp(-\gamma\Delta\tau)]/\gamma^2\} (f'_{n+1} - f'_n)/\Delta\tau \quad (105)$$

$$A_{n+1} = \exp(-\gamma\Delta\tau) A_n + \{[(1 - \exp(-\gamma\Delta\tau))/\gamma\Delta\tau] - \exp(-\gamma\Delta\tau)/\gamma\} f'_n + \{[1 - (1 - \exp(-\gamma\Delta\tau))/\gamma\Delta\tau]/\gamma\} f'_{n+1} \quad (106)$$

as $((\gamma\Delta\tau)^{-1})$ is allowed to approach 0, (i.e., $(\gamma\Delta\tau) \rightarrow \infty$), A_{n+1} approaches $[f_{n+1}/\gamma]$. This means that in the limit of large time increments, the numerical solution of the Bloch equations can approach their 'rate-equation' form.

Using this approach to solve the Bloch equations, one can identify the driving term ' f ' as ' $-1/2(e^* + e^*)$ ' for the population inversion equation, and ' f ' as ' e^*w ' the polarization equation.

The result is three linear equations for the three unknown quantities:

$$j+1, \quad *j+1 \quad \text{and} \quad w^{j+1} \\ m, k+1, \quad m, k+1, \quad m, k+1$$

Assuming that the field is known, one can solve this system in a straightforward manner.

Nonuniform stretching from τ to T can also be implemented. If the stretching weighting function is $g(\tau, T)$, the new source becomes ' $f(\tau)g(\tau, T)$ ' while the time decay constant becomes ' $\gamma g(\tau, T)$ '. The procedure remains the same; only the algebra becomes more tedious [165].

XVIII. CONCLUDING REMARKS

Most of the features of the numerical model used to study temporal and transverse reshaping effects of short optical pulses propagating in active non-linear resonant media have been presented. The motivation for choosing the various numerical techniques was explained on physical grounds. The rigorous analysis of this non-linear interaction was attempted to be achieved with maximum accuracy and minimum computational effort. The applicability of computational methods developed in gas and fluid dynamics to the detailed evolution of optical beams in non-linear media has been demonstrated. The introduction of adaptive stretching and rezoning transformations considerably improved the calculations.

In particular, self-adjusted rezoning and stretching techniques consisting of repeated applications of the same basic formula were reviewed as a convenient device for generating computational grids for complex nonlinear interaction such as in coherent light-matter energy exchanges. The techniques are well-suited for easy programming mainly because the mapping functions and all related derivatives (weighting factors) are defined as much as possible analytically. Enhancement of accuracy of speed was realized by improving the integration technique/algorithm which turned out to be general and extremely simple in its application when compared with its analogue, the two-dimensional Lagrangian approach [172]. Furthermore, this method has been applied to a number of situations with and without homogeneity in the broadening properties of the resonant medium. It may be worthwhile to mention that theoretical predictions defined with this code, when applied to absorbing media, were quantitatively ascertained by independent experimental observations [119, 120] and recent independent perturbational [166, 167] and computational analysis [168]. One should also re-emphasize that the self-action phenomena predicted with the algorithm described here are distinct from that discussed by other researchers. The main characteristics that distinguish this system are (1) the non-instantaneous polarization response; (2) the fact that this coherent interaction can occur at exact line center (while all the other theories exclude the possibility of self-lensing action whenever the pulse wavelength is exactly tuned to the center of a resonant absorption line), and (3) that the angle of the slowly varying electric field phasor depends on time as well as position.

Although the topic of this paper has been most widely received in optical radiation physics, it our belief that this methodology, drawn from aerodynamics, will prove functional for a wide variety of nonlinear time-dependent equations in such fields as chemical kinetics and oil reservoir simulations.

ADDENDUM

It is noteworthy that a recent research effort which dealt with resonant light beam interaction has been recently reported [169]. Rezon-ing was also incorporated; however, an implicit Crank-Nickson, algorithm was used for marching the field; whereas the multi-line atomic dynamic were solved using Heun method. No temporal stretching was used.

For details of the numerics, kindly refer to Reference [170]; for the physics, please refer to [171].

ACKNOWLEDGMENTS

F.P. Mattar would like to express in particular his appreciation to his thesis advisor Professor M.C. Newstein and to his mentors Professor H.A. Haus and Professor Gino Moretti for their unselfish guidance to the physics and numerics of the work. He has benefitted from enlightening discussions with Dr. H.M. Gibbs, Dr. S.L. McCall, Professor J.H. Marburger, Dr. D.C. Brown, Professor P.E. Toschek, in the physics and Dr. J. Herrman, Dr. B.R. Suydam and Dr. J. Fleck on the numerics. He is indebted to H.M.G. for his faith in the work that led to the first experimental verification of the coherent on-resonance self-focusing. The hospitality of Professor J. Teichman at University of Montreal and Dr. T.C. Cattrall at Mobil which makes the computations possible, is gratefully acknowledged. F.P. Mattar wishes to thank in particular Dr. C. Hazzi and D.J. Steele for their extended patience, unselfish support and encouragements during his convalescence. Furthermore, the editing efforts of D.J. Steele (which clarified the manuscript); the art work of Kerop Studio in Cairo and P. Florence in New York; and the skillful and laborious word processing effort of E. Cummings are joyfully appreciated.

REFERENCES

1. S.A. Akhmanov, A.P. Sukhorukov, and P.V. Kokhirov, Laser Handbook, F. Arrechi, Ed., Amsterdam, The Netherlands: North Holland, 1972, pp. 1151-1228.
2. G. Askary'yan, Sov. Phys. JET P42, 1568 (1962) Moscow; and Usp. Fiz. Nauk, vol. 111, pp. 249-260, October 1973.
3. B.R. Suydam, "Self-focusing in passive media I," Los Alamos Scientific Lab., Tech. Rep. L4-S003-MS, March 1973, pp. 1-19.

4. O. Svelto, Progress in Optics XII, E. Wolf, Ed. Amsterdam, The Netherlands: North Holland, 1974, pp. 1-52.
5. J. Marburger, Progress in Quantum Electron., vol. 4, pp. 35-110, Pergamon Press, 1975.
6. J.A. Fleck, Jr., and C. Layne, Appl. Phys. Lett., 22, pp. 467-469, 1973; and Appl. Phys. Lett. 22 pp. 546-548 (1975).
7. E.L. Hahn, Phys. Rev. 80, 580 (1950).
8. S.L. McCall and E.L. Hahn, Bull. Am. Phys. Soc. 10, 1189 (1965).
Phys. Rev. Lett. 18, 908 (1967).
Phys. Rev. 183, 457-485 (1969).
Phys. Rev. A2, 870 (1970).
9. H.M. Gibb and R.E. Slusher, Appl. Phys. Lett. 18, 505 (1971).
Phys. Rev. A3, 1634 (1972).
Phys. Rev. A6, 2326 (1972).
10. F.A. Hopf and M.O. Scully, Phys. Rev. 179, 399 (1969).
11. A. Icsevigi and W.E. Lamb, Jr., Phys. Rev. 185, 517-545 (1969).
12. E. Courtens, In Proc. 1969 Chania Conference (unpublished), and in Laser Handbook, ed. by F. Arrechi (North Holland, Amsterdam, 1972).
13. G. Lamb, Rev. Mod. Phys. 43, pp. 99-124 (1971).
14. R.E. Slusher, Progress in Optics XII, E. Wolf, Ed. Amsterdam, The Netherlands: North Holland, 1974, pp. 53-100.
15. I.A. Poluektov, Yu. M. Popov, and V.S. Roitoeig, Sov. Phys Usp., Vol. 17, pp. 673-690, 1975.
16. P. Kryukow and V. Letokov, Sov. Phys. Usp., Vol. 12, pp. 641-672, 1970.
17. D. Dialetis, Phys. Rev. A2, 599 (1970).
18. R. Bonifacio and P. Schwendimann, Lett. al Nuovo Cimento, 3, 509 and 512 (1970).
19. R. Bonifacio, P. Schwendimann, and F. Haake, Phys. Rev. A4, 302 (1971) and A4, 854 (1971).
20. F.T. Arrecchi and E. Courtens, Phys. Rev. A2, 1730 (1970).
21. S. Chi, Theory of the generation and propagation of ultrashort pulses in laser systems, Ph.D. dissertation, Polytechnic Institute of Brooklyn, 1972.
22. A. Zembrod and T. Gruhl, Phys. Rev. Lett. 27, 287-290 (1971).

23. R. Marth, Theory of chirped optical pulse propagation in resonant absorbers, Ph.D. dissertation, Polytechnic Institute of Brooklyn, 1971.
24. E. Courtens, Proc. 6th IEEE Int. Conf. Quantum Electronics (Kyoto, Japan, 1970), pp. 298-299.
25. J.C. Diels and E.L. Hahn, Phys. Rev. A, vol. 8, pp. 1084-1110, 1973; and Phys. Rev. A, 10, pp. 2501-2509, 1974.
26. N.D. Wright, Pulse Propagation in Non-linear Resonant Media, Ph.D. dissertation, Polytechnic Institute of New York, February 1974.
27. a) T. Gustafson, J. Taran, H.A. Haus, J. Lifszitz and P. Kelley, Phys. Rev., vol. 117, pp. 306-313 (1969)
b) F. Demartini, C. Townes, T. Gustafson and P. Kelley, Phys. Rev. Vol. 164 pp. 312-323 (1967).
28. a) C.K. Rhodes and A. Szoke, Phys. Rev., vol. 184, pp. 25-37, 1969.
b) C.K. Rhodes, A. Szoke, and A. Javan, Phys. Rev. Lett., vol. 21, pp. 1151-1155, 1968.
c) F.A. Hopf, C.K. Rhodes and A. Szoke, Phys. Rev. B, vol. 1, pp. 2833-2842.
29. a) G.J. Salamo, H.M. Gibbs, and G.G. Churchill, Phys. Rev. Lett., vol. 33, pp. 273-276, 1974.
b) H.M. Gibbs, S.L. McCall, and G.J. Salamo, Phys. Rev. A, vol. 12, pp. 1032-1033, 1975.
30. J.A. Armstrong and E. Courtens, Quantum Electron., Vol. QE-4, pp. 411-419 (1968); Quantum Electron., vol. QE-5, pp. 249-259, 1969.
31. E.L. Gieselmann, Chirped pulses in laser amplifier, Opt. Sci. Center, Univ. Arizona, Tucson, AZ, Tech. Rep. 80, June 1973, pp. 1-106.
32. M. Sargent, Higher Energy Lasers and Their Applications, S. Jacobs et al., Ed. Reading, MA: AddisonWesley, 1975, pp. 1-50.
33. D. Grischkowsky, Phys. Rev. Lett., vol. 24, pp. 866-869, 1970; and D. Grischkowsky and J. Armstrong in Proc. 3rd Conf. Quantum Optics (Univ. of Rochester 1972, pp. 829-831).
34. A. Javan and P.L. Kelley, IEEE J. Quantum Electron., vol. QE-2, pp. 470-473, 1966.
35. T.J. Bridges, H.A. Haus, P.W. Hoff, IEEE J. Quantum Electron., vol. QE-4, 777-782 (1968).
36. C.P. Christensen, C. Freed, and H.A. Haus, IEEE J. Quantum Electron., QE-5, 276-283 (1969).
37. H.A. Haus and T.K. Gustafson, IEEE J. Quantum Electron., QE-4, 519-522 (1968).
38. W.G. Wagner, H.A. Haus and K.T. Gustafson, IEEE J. Quantum Electron., QE-4, 267-273 (1968).
39. N. Wright and M.C. Newstein,
a) Opt. Commun., vol. 9, pp. 8-13, 1973.
b) IEEE J. Quantum Electron., vol. QE-10, p. 743, 1974.
40. M.C. Newstein and F.P. Mattar, Proc. 7th Conf. Numerical Simulation of Plasmas (Courant Institute, New York Univ., June 1975), p. 223.
41. M.C. Newstein and F.P. Mattar, 10th Congress of the International Commission of Optics, Prague, Czechoslovakia (1975), Recent Advances in Optical Physics, p. 199, et. B. Havelka and J. Blabla, distributed by the Soc. of Czechoslovak Math. and Phys. (1976).
42. F.P. Mattar and M.C. Newstein, IX International Conference of Quantum Electronics, Amsterdam (1976), see Opt. Comm. 18, 70 (1976), and IEEE J. Quantum Electron., QE-13, 507-518 (1977).
43. F.P. Mattar and M.C. Newstein, Cooperative Effects in Matter and Radiation, edited by C.M. Bowden, D.W. Howgate and H.R. Robl, p. 139-193 (Plenum Press, New York, 1977).
44. G. Moretti, Floating Shock-Fitting Technique for Imbedded Shocks in Unsteady, Multidimensional Flow Fields, Proceedings of the 1974 Heat Transfer and Fluid Mechanics Institute, ed. by L.R. Davis and R.E. Wilson, Stanford University Press, 1974, POLY-AE/AM Report No. 74-9.
45. G. Moretti, Transonic Flows and Numerical Analysis, published in "Omaggio a Carlo Ferrari," Libreria Editrice Universitaria, Levretteo & Bella, Torino, Italy, pp. 539-548, December 1974 (POLY-AE/AM Report No. 74-23).
46. G. Moretti, Thoughts and Afterthoughts About Shock Computations, PIBAL Report No. 73-18, August, 1973.
47. G. Moretti, An Old Integration Scheme for Compressible Flows Revisited, Refurbished and Put to Work, POLY M/AE Report No. 73-22 in Computers & Fluids, under title "The λ -Scheme."

23. R. Marth, Theory of chirped optical pulse propagation in resonant absorbers, Ph.D. dissertation, Polytechnic Institute of Brooklyn, 1971.
24. E. Courtens, Proc. 6th IEEE Int. Conf. Quantum Electronics (Kyoto, Japan, 1970), pp. 298-299.
25. J.C. Diels and E.L. Hahn, Phys. Rev. A, vol. 8, pp. 1084-1110, 1973; and Phys. Rev. A, 10, pp. 2501-2509, 1974.
26. N.D. Wright, Pulse Propagation in Non-linear Resonant Media, Ph.D. dissertation, Polytechnic Institute of New York, February 1974.
27. a) T. Gustafson, J. Taran, H.A. Haus, J. Lifshitz and P. Kelley, Phys. Rev., vol. 117, pp. 306-313 (1969)
b) F. Demartini, C. Townes, T. Gustafson and P. Kelley, Phys. Rev. Vol. 164 pp. 312-323 (1967).
28. a) C.K. Rhodes and A. Szoke, Phys. Rev., vol. 184, pp. 25-37, 1969.
b) C.K. Rhodes, A. Szoke, and A. Javan, Phys. Rev. Lett., vol. 21, pp. 1151-1155, 1968.
c) F.A. Hopf, C.K. Rhodes and A. Szoke, Phys. Rev. B, vol. 1, pp. 2833-2842.
29. a) G.J. Salamo, H.M. Gibbs, and G.G. Churchill, Phys. Rev. Lett., vol. 33, pp. 273-276, 1974.
b) H.M. Gibbs, S.L. McCall, and G.J. Salamo, Phys. Rev. A, vol. 12, pp. 1032-1033, 1975.
30. J.A. Armstrong and E. Courtens, Quantum Electron. Vol. QE-4, pp. 411-419 (1968); Quantum Electron., vol. QE-5, pp. 249-259, 1969.
31. E.L. Gieselmann, Chirped pulses in laser amplifier, Opt. Sci. Center, Univ. Arizona, Tucson, AZ, Tech. Rep. 80, June 1973, pp. 1-106.
32. M. Sargent, Higher Energy Lasers and Their Applications, S. Jacobs et al., Ed. Reading, MA: Addison-Wesley, 1975, pp. 1-50.
33. D. Grischowsky, Phys. Rev. Lett., vol. 24, pp. 866-869, 1970; and D. Grischowsky and J. Armstrong in Proc. 3rd Conf. Quantum Optics (Univ. of Rochester 1972, pp. 829-831).
34. A. Javan and P.L. Kelley, IEEE J. Quantum Electron., vol. QE-2, pp. 470-473, 1966.
35. T.J. Bridges, H.A. Haus, P.W. Hoff, IEEE J. Quantum Electron., vol. QE-4, 777-782 (1968).
36. C.P. Christensen, C. Freed, and H.A. Haus, IEEE J. Quantum Electron., QE-5, 276-283 (1969).
37. H.A. Haus and T.K. Gustafson, IEEE J. Quantum Electron., QE-4, 519-522 (1968).
38. W.G. Wagner, H.A. Haus and K.T. Gustafson, IEEE J. Quantum Electron., QE-4, 267-273 (1968).
39. N. Wright and M.C. Newstein,
a) Opt. Commun., vol. 9, pp. 8-13, 1973.
b) IEEE J. Quantum Electron., vol. QE-10, p. 743, 1974.
40. M.C. Newstein and F.P. Mattar, Proc. 7th Conf. Numerical Simulation of Plasmas (Courant Institute, New York Univ., June 1975), p. 223.
41. M.C. Newstein and F.P. Mattar, 10th Congress of the International Commission of Optics, Prague, Czechoslovakia (1975), Recent Advances in Optical Physics, p. 199, et. B. Havelka and J. Blabla, distributed by the Soc. of Czechoslovak Math. and Phys. (1976).
42. F.P. Mattar and M.C. Newstein, IX International Conference of Quantum Electronics, Amsterdam (1976), see Opt. Comm. 18, 70 (1976), and IEEE J. Quantum Electron., QE-13, 507-518 (1977).
43. F.P. Mattar and M.C. Newstein, Cooperative Effects in Matter and Radiation, edited by C.M. Bowden, D.W. Howgate and H.R. Robl, p. 139-193 (Plenum Press, New York, 1977).
44. G. Moretti, Floating Shock-Fitting Technique for Imbedded Shocks in Unsteady, Multidimensional Flow Fields, Proceedings of the 1974 Heat Transfer and Fluid Mechanics Institute, ed. by L.R. Davis and R.E. Wilson, Stanford University Press, 1974, POLY-AE/AM Report No. 74-9.
45. G. Moretti, Transonic Flows and Numerical Analysis, published in "Omaggio a Carlo Ferrari," Libreria Editrice Universitaria, Levrette & Bella, Torino, Italy, pp. 539-548, December 1974 (POLY-AE/AM Report No. 74-23).
46. G. Moretti, Thoughts and Afterthoughts About Shock Computations, PIBAL Report No. 73-18, August, 1973.
47. G. Moretti, An Old Integration Scheme for Compressible Flows Revisited, Refurbished and Put to Work, POLY M/AE Report No. 78-22 in Computers & Fluids, under title "The λ -Scheme."

48. R.W. MacCormack, AIAA Hypervelocity Impact Conference 1969 (paper 69-354).
49. R.W. MacCormack, Lecture notes in Physics, Springer Verlag, p. 151, (1971).
50. G. Moretti, A Critical Analysis of Numerical Techniques: The Piston-Driven Inviscid Flow. PIBAL Report No. 69-25, July 1969.
51. G. Moretti, The Choice of a Time-Dependent Technique in Gas Dynamics. PIBAL Report No. 69-26, July 1969.
52. G. Moretti, Transient and Asymptotically Steady Flow of an Inviscid, Compressible Gas Past a Circular Cylinder. PIBAL Report No. 70-20, April 1970.
53. G. Moretti, The Chemical Kinetics Problem in the Numerical Analyses of Nonequilibrium Flows, Proceedings of the IBM Scientific Computing Symposium on Large Scale Problems in Physics, December 1963, IBM Research Center, Yorktown Heights, New York).
54. G. Moretti, Importance of Boundary Conditions in the Numerical Treatment of Hyperbolic Equations, PIBAL Report No. 68-15 (1968).
55. G. Moretti and M.D. Salas, Numerical Analysis of the Viscous Supersonic Blunt Body Problem - Part I. PIBAL Report No. 70-48, November 1970.
56. G. Moretti, Complicated One-Dimensional Flows. PIBAL Report No. 71-25, September 1971.
57. G. Moretti, A Pragmatical Analysis of Discretization Procedures for Initial - and Boundary-Value Problems in Gas Dynamics and Their Influence on Accuracy, Or Look Ma, No Wiggles! POLY-AE/AM Report No. 74-15, September 1974.
58. G. Moretti, Accuracy and Efficiency in the Numerical Analysis of Transonic Flows. Proc. Symposium Transsonicum II, Gottingen Germany, Sept. 8-13, 1975, ed. by K. Oswatitsch and D. Rues, Springer-Verlag, Berlin, pp. 439-448, 1976. (POLYAE/AM Report No. 76-06).
59. G. Moretti, Conformal Mappings for Computations of Steady, Three-Dimensional, Supersonic Flows. Proceedings of the ASME Symposium on Numerical/Laboratory Computer Methods in Fluid Mechanics, published by ASME, December 1976. POLY M/AE Report No. 76-06.
60. L. Bradley and J. Hermann, MIT-Lincoln Lab Tech report LTP-10 (July 1971) and internal note on Change of reference wavefront in the MIT CW Nonlinear Optics Propagation Code (Fall 1974) private communication to F.P. Mattar for which he is grateful.
61. P.B. Ulrich, A Numerical Calculation of Thermal Blooming of Pulsed, Focused Laser Beams, Naval Research Lab., Tech. Report NRL 7382 (December 1971).
62. P.B. Ulrich and J. Wallace, J. Opt. Soc. Am. **63**, 8 (1973).
63. P.B. Ulrich, PROP-1: An Efficient Implicit Algorithm for Calculating Nonlinear Scalar Wave Propagation in the Fresnel Approximation, NRL Report 7706 (May 1974).
64. H.J. Breaux, An Analysis of Mathematical Transformations and a Comparison of Numerical Techniques for Computation of High-Energy CW Laser Propagation in an Inhomogeneous Medium, Ballistic Research Laboratories, Aberdeen Proving Ground, Maryland; BRL Report 1723 (1974).
65. J.A. Fleck, Jr., J.R. Morris and M.D. Feit, Time Dependent Propagation of High-Energy Laser Beams through the Atmosphere, Lawrence Livermore Laboratory, Livermore, CA, Part I: LLL Report UCRL-51372 (1975).
66. J.A. Fleck, Jr., J.R. Morris and M.D. Feit, Time Dependent Propagation of High-Energy Laser Beams through the Atmosphere: II, Preprint of Technical Report, Lawrence Livermore Laboratory, University of California, UCRL-52071 (May 1976).
67. K.G. Whiteney, G.L. Mader, and P.B. Ulrich, SSParam: A Nonlinear Wave-optics Multipulse (and CW) Steady-State Propagation Code with Adaptive Coordinates, Naval Research Laboratory, Washington, DC, NRL Report 8074 (1977).
68. B.R. Suydam, A Laser Propagation Code, Los Alamos Scientific Laboratory, LA-5607-MS, Informal Report (1974).
69. F.P. Mattar, Appl. Phys. **17**, 53-62 (1978), Springer-Verlag.
70. A.J. Glass, The Method of Trajectories, Lawrence Livermore Lab., Annual Laser Fusion Report, Basic Studies 1973-1974.
71. L.R. Bissonette, A Study of the Thermally Induced Nonlinear Propagation of a Laser Beam in an Absorbing Fluid Medium, Defence Research Establishment, Valcartier, Quebec, Canada, Technical Note DREV TN-2049/72 (1972).
72. L.R. Bissonette, Appl. Optics **12**, 719-728 (1973).

73. O. Rossignol, Simulation numerique de la defocalisation thermique d'un faisceau laser intense, DREV R-4029 (1976).
74. J.A. Fleck, Jr., J. Comp. Phys. **16**, 324-341 (1974).
75. H. Kogelnik and T. Li, Appl. Opt. **5**, 1550 (1969).
76. H. Kogelnik, Appl. Opt. **4**, 1562-1569 (1965); P.K. Tien, J.P. Gordon and J.R. Whinnery, Proceedings of IEEE **53**, 129-136 (1965); and A. Yariv, Quantum Electronics, Interscience (1975).
77. W. Lamb, Jr., Phys. Rev. **134A**, 1429 (1964).
78. M. Sargent, M.O. Scully and W. Lamb, Jr., Laser Physics, Addison-Wesley (1974).
79. J.H. Eberly, Am. J. Phys. **40**, 1374 (1972).
80. For a pedagogical review on superfluorescence/superradiance, see L. Allen and J.H. Eberly, Optical Resonance and Two-Level Atoms (Wiley, New York 1975).
81. R.H. Dicke, Phys. Rev. **93**, 99 (1954) and in Quantum Electronics: Proceedings of the Third International Congress, Paris, edited by P. Grivet and N. Bloembergen (Dunod, Paris and Columbia Univ. Press, New York, 1965).
82. N.E. Rehler and J.H. Eberly, Phys. Rev. **A3**, 1735 (1971).
83. Q.H.F. Vrehen, H.M.J. Hikspoors and H.M. Gibbs, Phys. Rev. Lett. **38**, 764 (1977).
84. H.M. Gibbs, Q.H.F. Vrehen and H.M.J. Hikspoors, Phys. Rev. Lett. **39**, 547 (1977).
85. H.M. Gibbs, Q.H.F. Vrehen and H.M.J. Hikspoors, in Laser Spectroscopy III, edited by J.L. Hall and J.L. Carlsten, (Springer-Verlag, 1977).
86. M.S. Feld in Fundamental and Applied Laser Physics: Proceedings of the Esfahan Symposium, edited by M.S. Feld, N.A. Kurnit and A. Javan (Wiley, New York, 1973).
87. N. Skribanowitz, I.P. Herman, J.C. MacGillivray and M.S. Feld, Phys. Rev. Lett. **30**, 309 (1973).
88. I.P. Hermann, J.C. MacGillivray, N. Skribanowitz and M.S. Feld, in Laser Spectroscopy, edited by R.G. Brewer and A. Mooradian (Plenum Press, New York, 1974).
89. J.C. MacGillivray and M.S. Feld, Phys. Rev. **A14**, 1169 (1976).
90. M.S. Feld in Frontiers of Laser Spectroscopy, edited by R. Balian, S. Haroche and S. Liberman (North-Holland, Amsterdam, 1977).
91. J.C. MacGillivray and M.S. Feld, to be published in Phys. Rev. A; Fall 1979.
92. H. Seidel, Bistable optical circuits using saturable absorber within a resonant cavity, U.S. Patent 3 610 731.
93. A. Szoke, V. Daneau, J. Goldhar and N.A. Kurnit, Appl. Phys. Lett. Vol. **15**, pp. 376-379, 1969.
94. S.L. McCall, Phys. Rev. A, Vol. **9**, pp. 1515-1523, 1974.
95. S.L. McCall, H.M. Gibbs, G.G. Churchill and T.N.C. Venkatesan, Bull. Amer. Phys. Soc., vol. **20**, p. 636, 1975.
96. S.L. McCall, H.M. Gibbs, and T.N.C. Venkatesan, J. Opt. Soc. Amer., vol. **65**, p. 1184, 1975.
97. H.M. Gibbs, S.L. McCall, and T.N.C. Venkatesan, Phys. Rev. Lett., vol. **36**, pp. 1135-1138, 1976.
98. T.N.C. Venkatesan and S.L. McCall, Appl. Phys. Lett., vol. **30**, pp. 282-284, 1977.
99. P.W. Smith and E.H. Turner, Appl. Phys. Lett., vol. **30**, pp. 280-281, 1977.
100. F.S. Felber and J.H. Marburger, Appl. Phys. Lett., vol. **28**, pp. 731-733, 1976.
101. R. Brewer and E.L. Hahn, Phys. Rev. **A11**, 1641 (1975).
102. M. Sargent III, and P. Horwitz, Phys. Rev. **A13**, 1962 (1976).
103. B.W. Shore and S. AcKerhalt, Phys. Rev. **A15**, 1640 (1977).
104. J.T. Ackerhalt, J.H. Eberly and B.W. Shore, Phys. Rev. **A19**, 248 (1977).
105. Z. Biatynicka-Birala and I. Biatynicki-Birala, J.H. Eberly and B.W. Shore, Phys. Rev. **A16**, 2038 (1977).
106. F.P. Mattar and J.H. Eberly, Proceeding of the Physics and Chemistry of Laser-Induced Process in Molecules, Edinburgh (1978) ed. by K.L. Kompa and S.C. Smith, pp. 61-65, Springer-Verlag (1979).
107. M. Konopnicki and J.H. Eberly, 10th Pittsburg Annual Simulation and Modeling Conference, Pittsburg (1979).

108. M.S. Feld, Frontiers in Laser Spectroscopy, Vol. 2, pp. 203-238 (Les Houches Lectures 195-75), Ed. R. Balian, S. Haroche and S. Liberman, North Holland (1977).
109. C.R.C. Stroud, Jr., Notes on Double Resonant Interaction (private communication to F.P.M.) Spring 1979.
110. A. Yariv, Compensation for Optical Propagation Distortion through Phase Adaptation (preprint, Caltech 1979).
111. A. Yariv, IEEE J. Quantum Electron., QE-14, 650-660 (1978).
112. R.W. Hellwarth, J. Opt. Soc. Am. 67, 1-3 (1977).
113. R.W. Hellwarth, IEEE J. Quantum Electron., QE-15, 101-109 (1979).
114. S.M. Jensen and R.W. Hellwarth, Appl. Phys. Lett. 32, 166-168 (1978).
115. J.C. Diels, Study of a Ring Laser Cavity with a Wave-Front Conjugating turning mirror (preprint of proposal-USC; private communication for which the authors are grateful).
116. J.H. Marburger, Theory of Self-focusing with counter-propagating beams (USC preprint, Fall 1979); and Theory of degenerate Four-Wave Mixing I. Stationary Linear Theory on Non-Resonant Media (USC preprint, Fall 1979).
117. G. Gould and J.T. LaTourrette, Novel Wide-Angle Low-Noise Laser Receiver BALAD: Progress Report No. 37 to JSTAC, Polytechnic Institute of Brooklyn (now of New York) pp. 117-120 (1972).
118. M. Lax, W.M. Louisell and W.B. McKnight, Phys. Rev. A, 1365-1370 (1975).
119. H.M. Gibbs, B. Bolger and L. Baade, IX International Conference of Quantum Electronics (1976), see Opt. Comm. 18, 199-200 (1976).
120. G. Forster and P.E. Toschek, post-deadline paper of the Quantum Optics Session of the Spring Annual Meeting of the German Physical Society, Hanover, F.R. Germany (February 1976).
121. W. Krieger, G. Gaida and P.E. Toschek, Z. Physik B 25, 297 (1976).
122. H.M. Gibbs, B. Bolger, F.P. Mattar, M.C. Newstein, G. Forster and P.E. Toschek, Phys. Rev. Lett. 37, 1743-1747 (1976) (prepared by H.M. Gibbs).
123. J.E. Bjorkholm and A. Ashkin, Phys. Rev. Lett. 32, 28-32 (1974).
124. A. Javan and P.L. Kelley, IEEE J. Quant. Electr. 2, 470-473 (1966).
125. D. Grischkowsky and J. Armstrong, in Coherence and Quantum Optics (Plenum Press, New York 1973), Ed. by L. Mandel and E. Wolf, p. 829-837.
126. F.P. Mattar, G. Forster and P.E. Toschek, Spring meeting of the German Physical Society, Mainz, F.R. Germany (February 1977). (Prepared by P.E. Toschek.)
127. F.P. Mattar, M.C. Newstein, P. Serafim, H.M. Gibbs, B. Bolger, G. Forster and P. Toschek, Fourth Rochester Conference of Coherence and Quantum Optics, Rochester, New York (June 1977), Plenum Press, ed., R. Mandel and E. Wolf, p. 143-164 (1978). (Prepared by H.M. Gibbs.)
128. F.P. Mattar, Kvantovaya Elektronika (Moscow) 4, 2520-2532 (1977).
129. F.P. Mattar, G. Forster and P.E. Toschek, Kvantovaya Elektronika (Moscow) 5, 1819-1824 (1978). (Prepared by P.E. Toschek.)
130. J.L. Emmett, IEEE J. Quantum Electron/QE-9, 709 (1973).
131. J. Soures, University of Rochester, Laboratory for Laser Energetics (private communication, Fall 1976-Spring 1977).
132. D. Brown (private communication) University of Rochester, Lab for Laser Energetics, University of Rochester, Rochester, NY Fall 1976, Spring 1977).
133. ERDA Review of BETA, Laser Fusion Prototype, University of Rochester, Lab for Laser Energetics, Rochester, NY (January 1977).
134. V.I. Bespalov and V.I. Talanov, Soviet Phys., JETP letters, 3, 471 (1966), English Translation 3, 307.
135. V.I. Talanov, Soviet Phys., JETP Letters 2, 218 (1965) English Translation 2, 138.
136. V.I. Talanov, Zh. Eksp. Teor. Fiz. Pisma. Red. 11, pp. 303-305, English Translation pp. 133-201, JETP letters, March 20, 1970.
137. B.R. Suydam, Laser Induced Damage in Optical Material, 1973 NBS special publication 387, p. 42.
138. B.R. Suydam, IEEE J. Quantum Electronics, 10, 837 (1974).
139. B.R. Suydam, IEEE J. Quantum Electronics 11, 225 (1975).

140. A.J. Glass, Laser Induced Damage in Optical Material, 1973, NBS special publication 287, p. 36.
141. J. Marburger, R. Jokipii, A. Glass and J. Trenholme, Laser Induced Damage in Optical Material 1973, NBS special publication 387, p. 49.
142. K.A. Brueckner and J.E. Howard, Laser Induced Damage in Optical Material 1975, NBS special publication 387, p. 57.
143. K.A. Brueckner and S. Jorna, Phys. Rev. Lett. **17**, 78 (1966).
144. J.B. Trenholme, Lawrence Livermore Laboratory, (LLL) Laser Fusion program 2nd 1973 semi-annual program report, p. 47-49 (UCRL-50021-73-2).
145. N.B. Baranova, N.E. Bykovskii, B. Ya. Zel'Dovich and Yu.V. Senatskii, Kvant, Elektron, Vol. 1, pp. 2435-2443 (1974).
146. D.C. Brown, The Physics of High Peak Power Nd-Glass Lasers, Springer-Verlag (to be published in the Fall 1980).
147. L.M. Frantz and J.S. Nodvik, J. Appl. Phys. **34**, 2346-2349 (1963).
148. C.J. Elliot, Appl. Phys. Lett. **24**, 31 (1974).
149. C.J. Elliot and B.R. Suydam, IEEE J. Quantum Electronics **11**, 863 (1975).
150. A.J. Campillo, R.A. Fisher, R.C. Hyer and S.C. Shapiro, Appl. Phys. Lett. **25**, 408 (1974).
151. A.J. Campillo, S.L. Shapiro and B.R. Suydam, Appl. Phys. Lett. **23**, 628 (1973); Appl. Phys. Lett. **24**, 178 (1974).
152. J.F. Holzrichter and D.R. Speck, J. Appl. Phys. **47**, 2459 (1976).
153. E.S. Bliss, J.T. Hunt, P.A. Renard, G.E. Sommargren and H.J. Weaver, IEEE J. Quantum Electron. **12**, 402 (1976).
154. J.A. Fleck, J.R. Morris and E.S. Bliss, IEEE J. Quantum Electron., **14**, 353 (1978).
155. S.M. Vlasov, V.A. Petrishev and V.I. Talanov, Soviet Phys. Radio Fizika, **14**, 1353 (1971).
156. E.S. Bliss, Proceedings of 1974 Symposium on Damage in Laser Materials, Boulder, Colorado ASTM/NBS/ONR NBS Special publication 414.
157. E.S. Bliss, D.R. Speck, J.F. Holzrichter, J.H. Erkkila and A.J. Glass, Applied Phys. Lett. **25**, 448 (1974).
158. A.J. Glass, LLL MALAPORP code (private communication to F.P. Mattar, Dec. 1976).
159. J.B. Trenholme, LLL BALLS code in Laser Propagation. Private communication to F.P. Mattar, Dec. 1976.
160. J. Goldstein and D. Dickman, LAPU2, write-up describing the upgrading of Suydam laser pulse propagation to handle multi-types of media with the insertion of various beam diagnostics, Los Alamos Scientific Lab, New Mexico, 1978.
161. R.A. Fisher, "Computer code to follow the growth of various (transverse) Fourier components of a light beam through a laser system using the small scale self-focusing growth rate formula and modifications to the spectrum caused by various optical (passive) components," private communication. (See also Los Alamos Scientific Laboratory Laser Program 1975 Annual report Rep. LA-6050-PR p. 8-10.)
162. J.A. Fleck, "LAMP code" r,z,t (LLL Technical report UCID-16525 (1974)) code and "FOUR-D FAST FOURIER CODE x,y,z and t as well, Lawrence Livermore Laboratory, Theoretical Physics Group - Private communication. UCRL-1826 (1975), UCRL-50-2071 (1976), UCRL-77719 (1976).
163. B. Feldman (private communication, Fall 1978).
164. J. Fleck, Phys. Rev. **B1**, 84-100, 1970.
165. F.P. Mattar, Proceedings of the Eighth Conf. of Numerical Methods in Plasmas, Monterey, June 1979 (with the assistance of B.R. Suydam).
166. L.A. Bol'shov, V.V. Likhanskii and A.O. Napartovich, Zh. Eksp. Teor. Fiz. **72**, 1769-1774 (1977) Moscow.
167. M.J. Ablowitz and Y. Kodama (Clarkson College preprint, Fall 1978, to be published by Phys. Lett.).
168. L.A. Bol'shov, T.K. Kirichenko, A.P. Favolsky, Numerical Analysis of the Small Scale Instability of the Coherent Interaction of the Light Impulses with the Resonant Absorbing Medium, (U.S.S.R. Academy of Sciences - Mathematics Division, preprint, Fall 1978), Institute of Applied Mathematics 1978, 53 (3A).
169. M.E. Riley, T.D. Padrick and R.E. Palmer, IEEE J. Quantum Electron., **QE-15**, 178-179 (1979).
170. F.P. Mattar, Application of the MacCormack Scheme and the Rezoning Techniques to the Transient Propagation of Optical Beam in Active Media, n-10 Technical Note #63, March 1976, Lab for Laser Energetics, Univ. of Rochester, Rochester, NY.

171. F.P. Mattar, Transverse Effects Associated with the Propagation of Coherent Optical Pulses in Resonant Absorbing Media, Ph.D. dissertation, Polytechnic Institute of New York, NY, December 1975 (available from Ann Arbor, Michigan).
172. F.P. Mattar and J. Teichman, Fluid Formulation of Intense Laser Beam CW Propagation in Nonlinear Media Using the Lagrangian Description, Technical Report, Laboratoire de la Physique des Plasmas, Université de Montreal, Montreal, Canada (Fall 1979) submitted to Computer Physics Communication.
173. F.P. Mattar and H.M. Gibbs, Rigorous Computations of Dynamic Transverse Effects in Superfluorescence Experiments, in preparation for XI Quantum Electronics Conference, Boston (1979).

FIGURE CAPTIONS

Figure 1 The state of the art in coherent pulse propagation is displayed. The theoretical effort was restricted to uniform plane wave prior to Newstein et al's efforts; whereas the usual experiment was carried out using Gaussian beam. To simulate a uniform plane wave, the detector diameter was selected as small as possible when compared to the Gaussian beam diameter.

Figure 2 (a) Isometric representation of the beam cross-section as it experiences self-focusing: The cross-section decreases as a function of the propagation distance.

(b) An isometric display of the time integrated field energy as a function of ρ and η to illustrate the resolution limitation associated with uniform mesh.

Figure 3 Two-dimensional prescribed rezoning for ρ and η . As the beam narrows the density of transverse points and the transmission planes increase simultaneously.

Figure 4 Self-adjusted two-dimensional rezoning for ρ and η to follow more closely the actual beam characteristics. The (normalizing) Gaussian reference beam is redefined during the calculation.

Figure 5 Non-uniform prescribed temporal stretching.

Figure 6 The smaller area, 1.6π , moves more slowly than the larger area 2π in both (a) amplifier and (b) absorbers. The peak of the pulse propagates with a speed larger than the velocity of light in amplifier and smaller in absorbers.

Figure 7 Relative motion among adjacent pencils propagating coherently in resonant (a) amplifiers, and (b) absorbers.

Figure 8 Isometric representation illustrating the relative motion among adjacent pencils after a certain propagation distance η .

Figure 9 Comparison of pencil perturbation theory with rigorous three-dimensional calculation for (a) absorbers, and (b) amplifier. (Curve 9b from Wright dissertation, ref.[16]).

Figure 10 Graph (a) illustrates the pulse delay to be experienced by the peak of the pulse when propagating in a resonant absorber. Graph (b) displays the dependency of τ_D on the input area; corresponding value of the input energy is given at the top horizontal scale. The solid curve is for the case $T_2 > \tau_p$, $T_1 > \tau_p$ and zero detuning. The dot-dash curve is for $T_1 = 150$ nsec and the dashed curve is for $T_2 = 50$ nsec. Other parameters are the same as for the solid curve.

Graphs (c) and (d) display distortionless pulse propagation in absorbers. Isometric plots of a family of 2π hyperbolic-secant pulses with radially-dependent pulse-widths (equivalent to some pulse-length τ_p but of different area strengths). In graph (c) the relative motion is displayed whereas in graph (d) the hole formation near the axis at the trailing edge of the pulse is clearly substantiated.

Figure 11 Graph (a) illustrates the spreading effects of linear diffraction on the propagation of a Gaussian beam profile.

Whereas Graph (b) illustrates the effects of linear diffraction on the propagation of an intensity profile with a hole near the axis. This input profile is achieved by the subtraction of two Gaussians with different beam widths.

The propagation follows the analytical work of Kogelnik and Li.

Figure 12 (a) An isometric time evolution for three distinct radii representing three 2π hyperbolic-secant pulses (with radially-dependent pulse-width) after a propagation distance η . This plot illustrates the relative motion as well as the boosting operation that the light diffracted from the tail of the pulse on the rim of the beam, experiences while flowing toward the axis.

(b) Results of rigorous three-dimensional computations illustrating the hole formation at the trailing edge and its successive filling through boosted diffraction by nonlinear interaction.

Figure 13 Analytic predictions of energy current J_T evolution for (a) absorber and (b) amplifiers.

Figure 14 As the light diffracts outwardly in the leading edge of the pulse, it interacts with the slower moving pulse off-axis and experiences gain.

Figure 15 Graph (a) displays the retarded time concepts.

Graph (b) outlines the numerical approach: a marching problem along η for the field simultaneously with a temporal upgrading of the material variables along τ .

Figure 16 Graph (a) shows non-uniform stretching of the transverse coordinate.

Graph (b) contrasts the Gaussian beam dependence with the non-uniform physical radius.

Figure 17 This graph illustrates the dependence of the radial mapping and the derivation on the different parameters versus the uniform mathematical radius.

Figure 18 This figure contrasts the Laplacian dependence for a given Gaussian profile for various non-uniform radial point densities.

Figure 19 Dependence of prescribed stretching and its derivatives on the point densities and the center of transformation.

Figure 20 Adaptive stretching with different centers of transformation.

Figure 21 The concept of the prescribed rezoning are presented in Graph (a); whereas Graph (b) is a close-up of the non-uniform mapped grid of Figure 2(b).

Figure 22 Graph (a) illustrates the self-adjusted rezoned grid.

Graph (b) illustrates the usefulness of the adaptive two-dimensional mapping through an isometric representation of the field fluency.

Figure 23 One-dimensional propagation in absorbers. Figures (a) to (d) illustrate the time behavior of a 2π input pulse at various planes. The retarded time is measured in nanoseconds. Figure (e) gives the time integrated intensity ($\text{energy}/\text{cm}^2 = \int dt e^2$), pulse area, and time delay at the peak all against the propagation distance.

Figure 24 The energy per unit area

$$\int_0^{\tau} e(\rho, \eta, \tau')^2 d\tau'$$

the fluency is displayed as a function of the distance in the direction of propagation for various values of the coordinates transverse to the direction of propagation. To illustrate the gradual inward energy flow the $\pi/2$ reorientation is also displayed. The longitudinal orientation illustrates the gradual boosting mechanism that the field energy experiences as it flows radially towards the beam axis (while η increases). The second angle displays the severe beam distortion in its cross-section as a function of η .

Figure 25 The principal characteristics plotted against the dimensionless propagation distance for a particular value of F : the on-axis energy density, the total field energy and an effective radius defined as the square root of the total field energy divided by the on-axis energy density.

Figure 26 The profile of the energy per unit area for both the input and focal planes.

Figure 27 The absorber field amplitude (a,b,c) and the transverse energy current (d,e,f) for several radii versus the retarded time for three stages of the propagation: the reshaping region, the build-up region and the focal region (as a function of the transverse coordinate).

Figure 28 The profile of the absorber field amplitude (a,b,c) and the profile of the transverse energy current (d,e,f) for several earlier (small) instants of time for three stages of the propagation: the reshaping region, the build-up region and the focal region, as a function of earlier retarded time (slices in the front of the pulse).

Figure 29 The profile of the absorber field amplitude (a,b,c) and the profile of the transverse energy current (d,e,f) for several later (subsequent) instants of time for the three stages of the propagation: the reshaping region, the build-up region and the focal region as a function of subsequent retarded times (slices in the trailing edge of the pulse).

Figure 30 Changes in spatial and temporal profiles for pulses undergoing self-induced-transparency with transverse energy flow, that lead to coherent self-focusing, a and a1, maximum off-resonance SF; b and b1, on-resonance.

Figure 31 Temporal behavior of pulses. Break-up of a 4π input pulse is shown under (a) self-focusing and (b) uniform plane-wave conditions in Na. In (a) the integrated output is 35% larger than the input.

Figure 32 Cross-section of beam at cell exit in the first experiment: curve a, without Na, and curve b, with Na on-resonance, with input area of 3π to 4π and magnetic field of 3.5 kG.

Figure 33 Isometric plots of the absorber field energy and transverse energy flow, against the retarded time for various transverse coordinates at four regions: (a) reshaping, (b) build-up region, (c) focal region, (d) post-focal region.

Figure 34 Isometric plots of the absorber field energy and transverse energy flow profile for various time slices at the four regions of interest.

Figure 35 Absorber field energy contour plots for the four propagation regions of interest. Notice the temporal delay associated with the coherent exchange of energy between light and matter, as well as the beam cross-section narrowing.

Figure 36 Principal characteristics of the focal plane as a function of the parameter F : the dimensionless focal length ($\alpha_{\text{eff}} \cdot L(\text{focal}) = \Lambda(\text{focal})$); the ratio M of the axial energy per unit area at the focal plane to that at the input plane; the time delay at the focal plane of the peak of the pulse on axis; the ratio of the total field energy to the axial energy per unit area πp_{eff}^2 .

Figure 37 Experimental energy-density magnification and diameter reduction in Na as a function of detuning. Curves a to f are for 2-ns, 5 pulses of $125\mu\text{m}$ diam in an 11-mm cell. The absorption increases from curve a to curve f; curve g is self-focusing of CW light; curve h shows the atomic absorption. Above, Curve a is the diameter for the conditions of curve a, etc.

Figure 38 Experimental Gaussian profile carefully prepared to eliminate any ripple larger than 3% variation to avoid the additional small-scale self-focusing to the transient whole beam break-up under study.

Figure 39 Pulse energy transmission (output per input in Ne vs. squared pulse area for 3ns (full dots) and 1ns (open dots) pulses. Curves are the corresponding plane-wave computer simulations.

Figure 40 Energy-density magnification vs. peak intensity for 0.8ns pulses, showing increase of self-focusing with Ne absorption αL . Curves are plane wave computer simulations with $T_2 = 10\text{ns}$.

Figure 41 Graph (a) displays an example of the severe temporal distortion which can be caused by nonlinear propagation in the Lawrence Livermore Labs Cyclops laser chain.

Graph (b) displays the corresponding plots of the fraction of the pulse power which is focused through two different diameter apertures as a function of the break-up integral B (see Bliss et al, IEEE J. Quantum Electron, July 1976).

The focused output beam does not contain all the energy which entered the experiment.

Figure 42 Example of the temporal distortion due to small-scale beam break-up on the Beta prototype of the University of Rochester Laser Fusion Laboratory (LLE) (see LLE program report to ERDA, January 1977).

Figure 43 One-dimensional amplifier: Graph (a) shows the input pulse as being a 4 nsec Gaussian with integrated area 2π . Graphs (b) and (c) correspond to the pulse propagated to 40 and 200 cm. Graph (d) is the summarized propagation data of the pulse versus the amplifier length ($\alpha_{\text{eff}} = 200\text{ cm}$).

Figure 44 Longitudinal projection of amplifier energy field amplitude and transverse current for near-axis (small) radii at the four critical regions (a) reshaping, (b) build-up, (c) focal region, and (d) post-focal.

Figure 45 Longitudinal projection of amplifier energy field amplitude for large (off-axis) radii at the four critical regions.

Figure 46 The profile of amplifier energy field amplitude and transverse energy current for small slices of time (in the front of the pulse) at the four critical propagation regions of interest.

Figure 47 The profile of amplifier energy amplitude and transverse energy current for large slices of time (in the trailing edge of the pulse) at the four critical propagation regions of interest.

Figure 48 Isometric plots of the amplifier field energy and transverse energy flow, against the retarded time for various transverse coordinates at four regions: (a) reshaping, (b) build-up region, (c) focal region, (d) post-focal region.

Figure 49 Isometric plots of the amplifier field energy and transverse energy flow profile for various time slices at the four regions of interest.

Figure 50 Amplifier field energy contour plots for the four propagation regions of interest. Notice the temporal advance associated with the coherent exchange of energy between light and matter, as well as the beam cross-section narrowing.

Figure 51 Longitudinal projection of amplifier energy field amplitude and transverse current for near-axis (small) radii at the four critical regions, with stretched radial coordinate for proper accounting of the transverse boundary condition.

Figure 52 Longitudinal projection of amplifier energy field amplitude for large (off-axis) radii at the four critical regions, with stretched radial coordinate for proper accounting of the transverse boundary condition.

Figure 53 The profile of amplifier energy field amplitude and transverse energy current for small slices of time (in the front of the pulse) at the four critical propagation regions of interest, with stretched radial coordinate for proper accounting of the transverse boundary condition.

Figure 54 The profile of amplifier energy amplitude and transverse energy current for large slices of time (in the trailing edge of the pulse) at the four critical propagation regions of interest, with stretched radial coordinate for proper accounting of the transverse boundary condition.

Figure 55 Isometric plots of the amplifier field energy and transverse energy flow, against the retarded time for various transverse coordinates at four regions: (a) reshaping, (b) build-up region, (c) focal region, (d) post-focal region, with stretched radial coordinate for proper accounting of the transverse boundary condition.

Figure 56 Isometric plots of the amplifier field energy and transverse energy flow profile for various time slices at the four regions of interest, with stretched radial coordinate for proper accounting of the transverse boundary condition. No severe reflection or abrupt variation in the field energy, at the wall boundary, is observed.

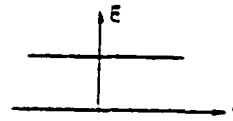
Figure 57 Amplifier field energy contour plots for the four propagation regions of interest. Notice the temporal advance associated with the coherent exchange of energy between light and matter, as well as the beam cross-section narrowing, with stretched radial coordinate for proper accounting of the transverse boundary condition. No severe reflection or abrupt variation in the field energy, at the wall boundary, is observed.

Coherent Pulse Propagation

I. Usual Theory

1 Dim. $\xi = \xi(\rho)$

'Uniform Plane Wave'



II. Usual Experiment

$\xi = \xi(\rho) \cdot e^{i\phi}$

'Gaussian'

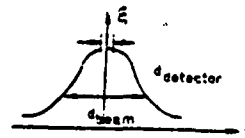


Fig. 2

Figure 1 The state of the art in coherent pulse propagation is displayed. The theoretical effort was restricted to uniform plane wave prior to Newstein et al's efforts; whereas the usual experiment was carried out using Gaussian beam. To simulate a uniform plane wave, the detector diameter was selected as small as possible when compared to the Gaussian beam diameter.

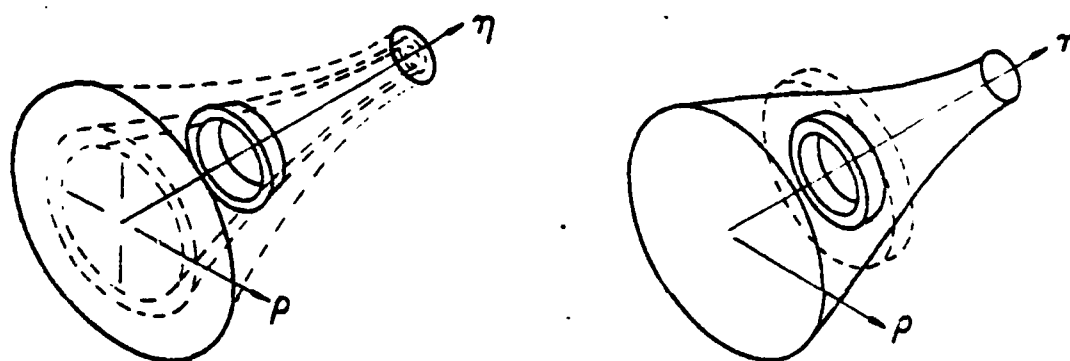


Fig 2

Figure 2 (a) Isometric representation of the beam cross-section as it experiences self-focusing: The cross-section decreases as a function of the propagation distance.

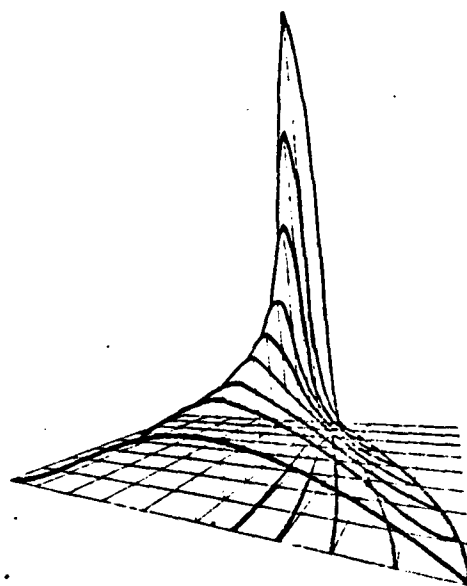


Fig 2(b)

- (b) An isometric display of the time integrated field energy as a function of p and q to illustrate the resolution limitation associated with uniform mesh.

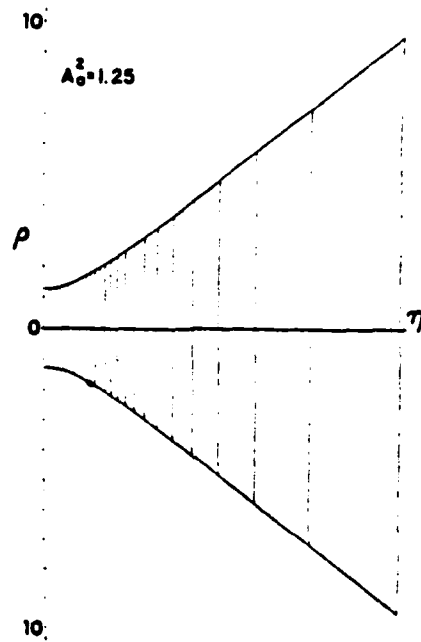


Fig-3

Figure 3 Two-dimensional prescribed rezoning for ρ and η . As the beam narrows the density of transverse points and the transmission planes increase simultaneously.

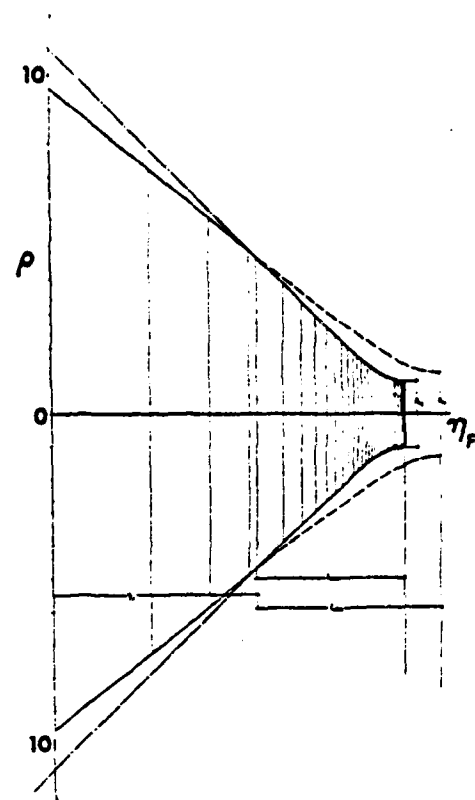


FIG. 4

Figure 4 Self-adjusted two-dimensional rezoning for ρ and η to follow more closely the actual beam characteristics. The (normalizing) Gaussian reference beam is redefined during the calculation.

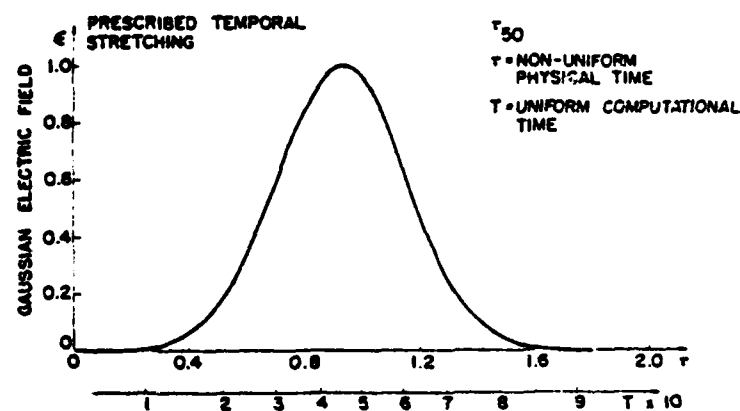


Fig 5

Figure 5 Non-uniform prescribed temporal stretching.

AMPLIFIER

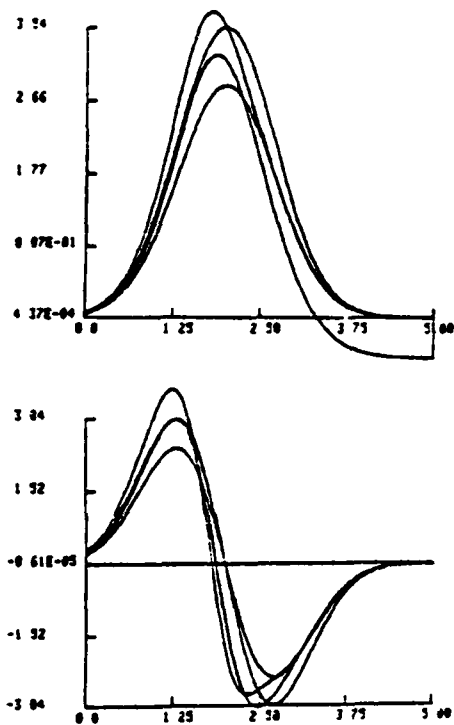


Fig 6(a)

ABSORBER

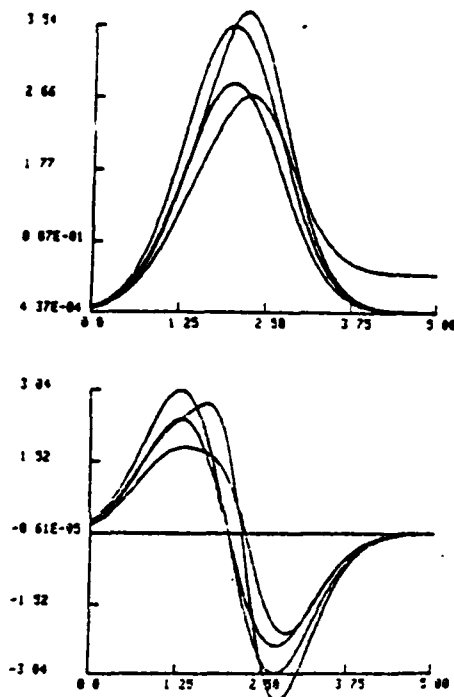


Fig 6(b)

Figure 6 The smaller area, 1.6π , moves more slowly than the larger area 2π in both (a) amplifier and (b) absorbers. The peak of the pulse propagates with a speed larger than the velocity of light in amplifier and smaller in absorbers.

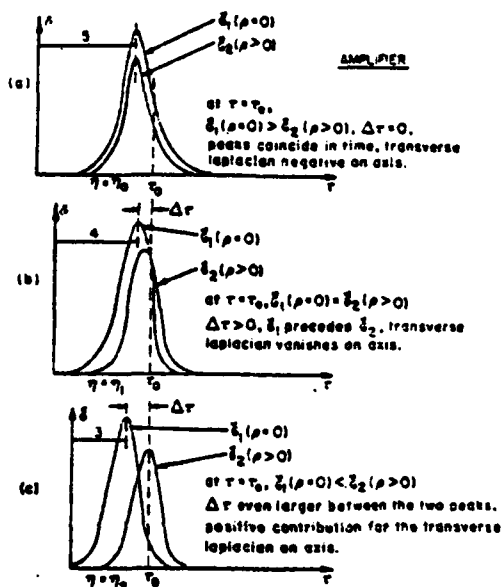


Fig 7(a)

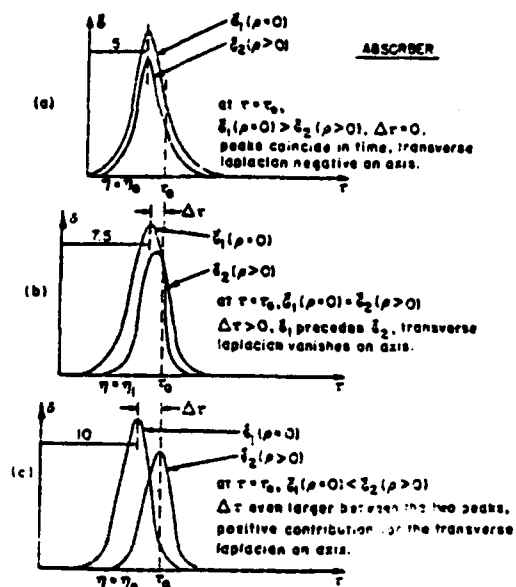


Fig 7(b)

Figure 7 Relative motion among adjacent pencils propagating coherently in resonant (a) amplifiers, and (b) absorbers.

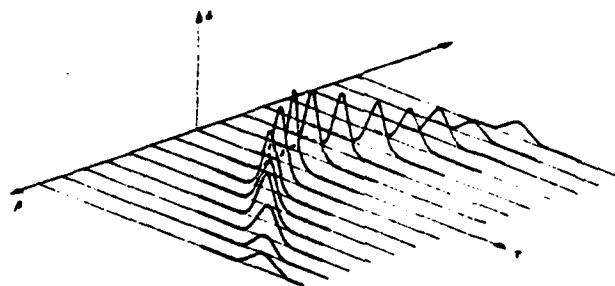


Fig- 8

Figure 8 Isometric representation illustrating the relative motion among adjacent pencils after a certain propagation distance η .

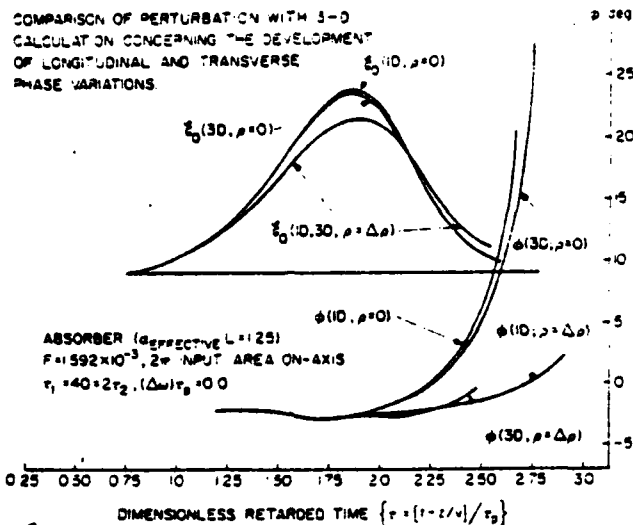


Fig 9(a)

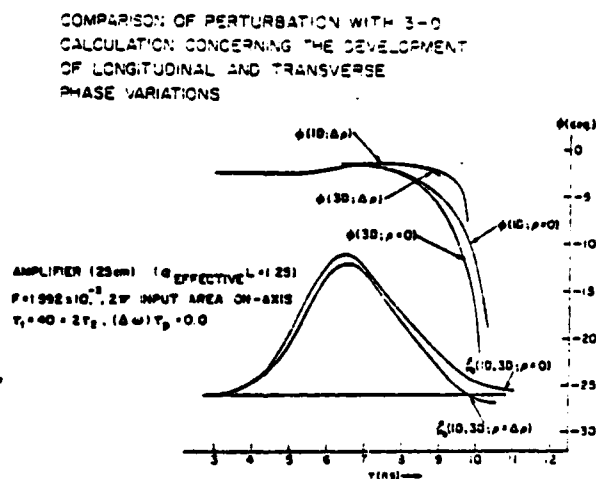


Fig 9(b)

Figure 9 Comparison of pencil perturbation theory with rigorous three-dimensional calculation for (a) absorbers, and (b) amplifier. (Curve 9b from Wright dissertation, ref. [18]).

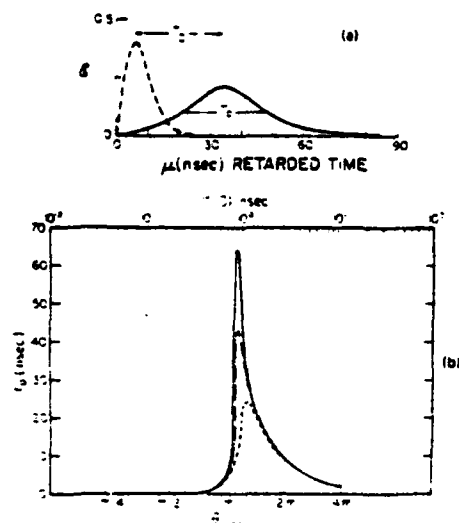


Fig.
10(a,b)

Figure 10 Graph (a) illustrates the pulse delay to be experienced by the peak of the pulse when propagating in a resonant absorber. Graph (b) displays the dependency of τ_p on the input area; corresponding value of the input energy is given at the top horizontal scale. The solid curve is for the case $T_2 > \tau_p$, $T_1 > \tau_p$ and zero detuning. The dot-dash curve is for $T_1 = 150$ nsec and the dashed curve is for $T_2 = 50$ nsec. Other parameters are the same as for the solid curve.

Graphs (c) and (d) display distortionless pulse propagation in absorbers. Isometric plots of a family of 2π hyperbolic-secant pulses with radially-dependent pulse-widths (equivalent to some pulse-length τ_p but of different area strengths). In graph (c) the relative motion is displayed whereas in graph (d) the hole formation near the axis at the trailing edge of the pulse is clearly substantiated.

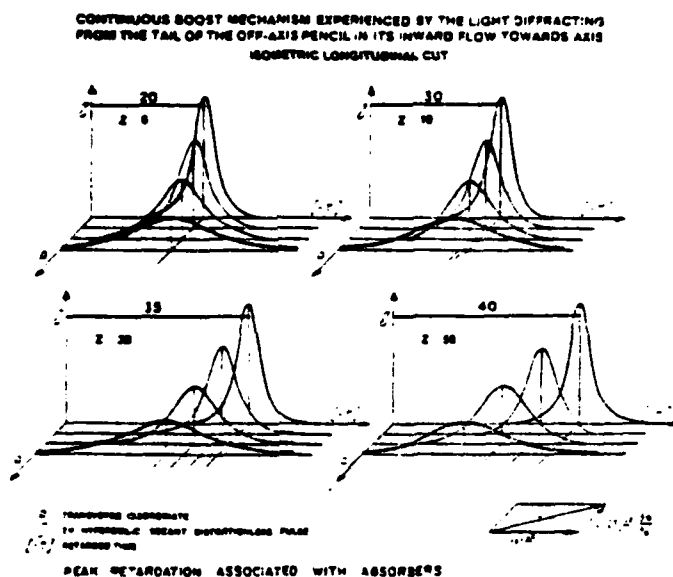


Fig 10(c)

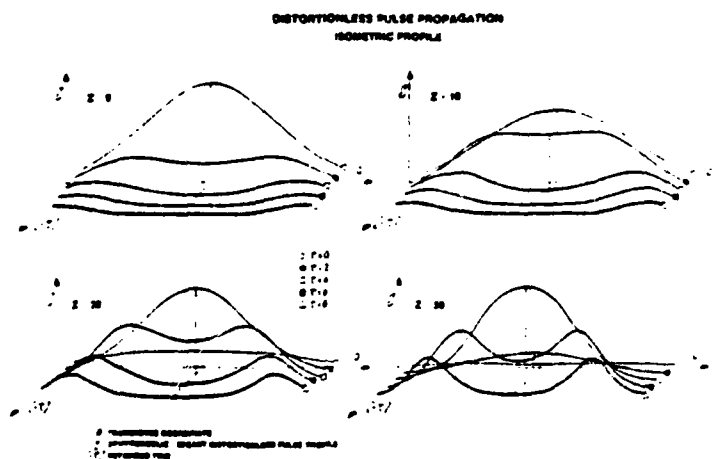


Fig 10(d)

Figure 11 Graph (a) illustrates the spreading effects of linear diffraction on the propagation of a Gaussian beam profile.

Whereas Graph (b) illustrates the effects of linear diffraction on the propagation of an intensity profile with a hole near the axis. This input profile is achieved by the subtraction of two Gaussians with different beam widths.

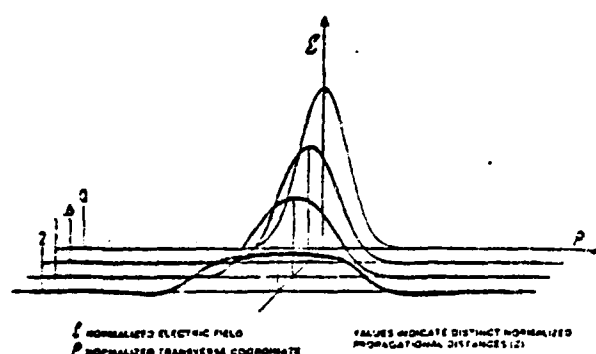


Fig 11(a)

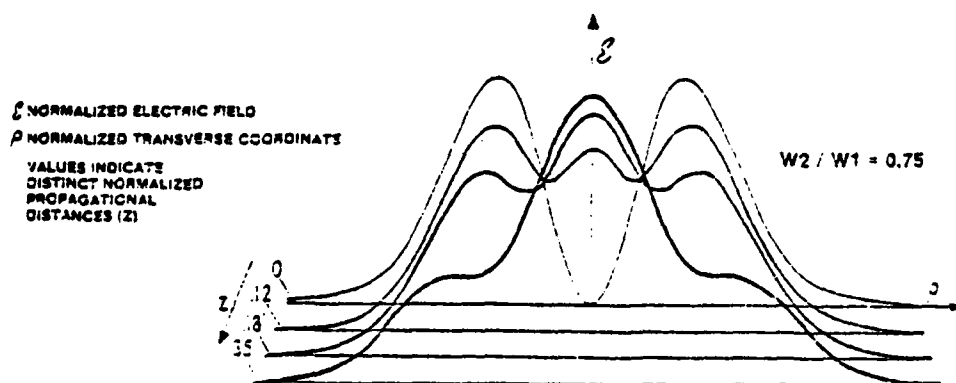


Fig 11(b)

LINEAR DIFFRACTION OF A BEAM WITH A NULL ON-AXIS

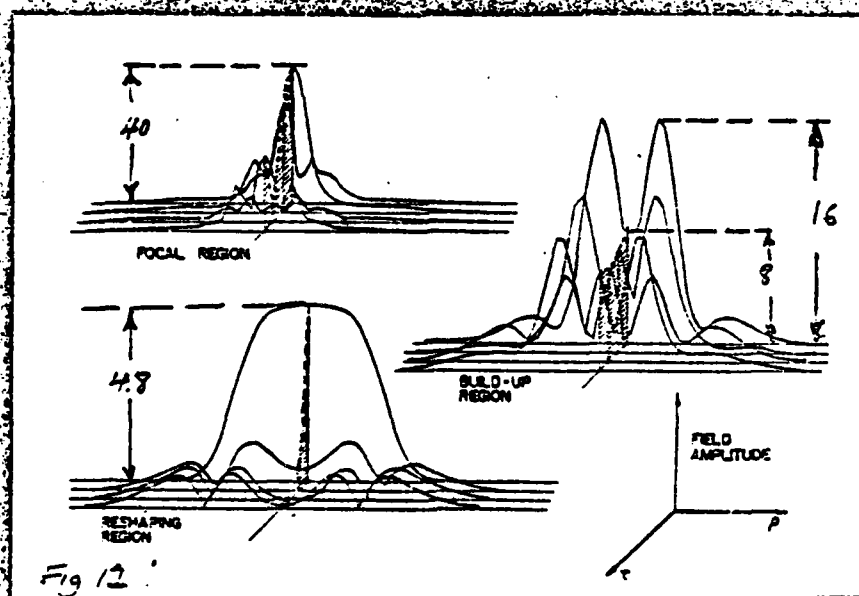
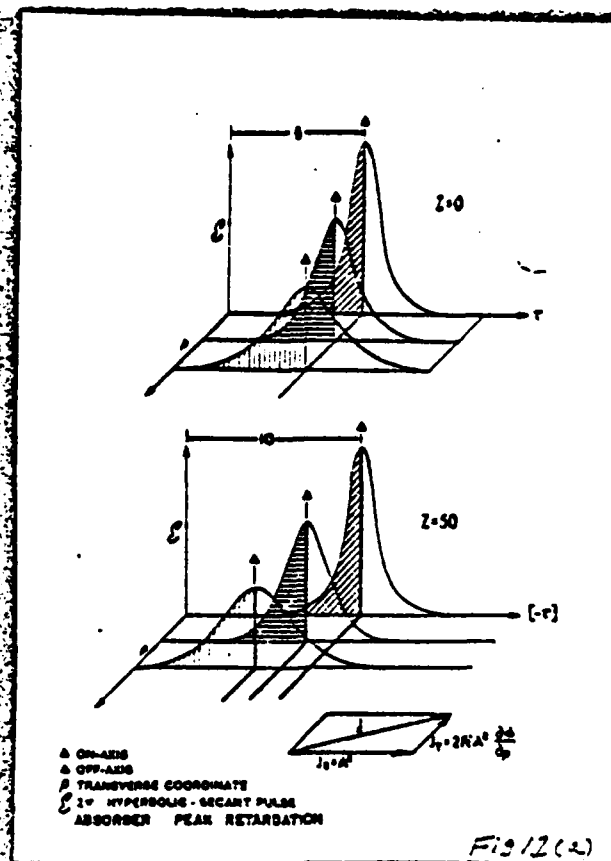


Figure 12 (a) An isometric time evolution for three distinct radii representing three 2π hyperbolic-secant pulses (with radially-dependent pulse-width) after a propagation distance η . This plot illustrates the relative motion as well as the boosting operation that the light diffracted from the tail of the pulse on the rim of the beam, experiences while flowing toward the axis.

(b) Results of rigorous three-dimensional computations illustrating the hole formation at the trailing edge and its successive filling through boosted diffraction by nonlinear interaction.

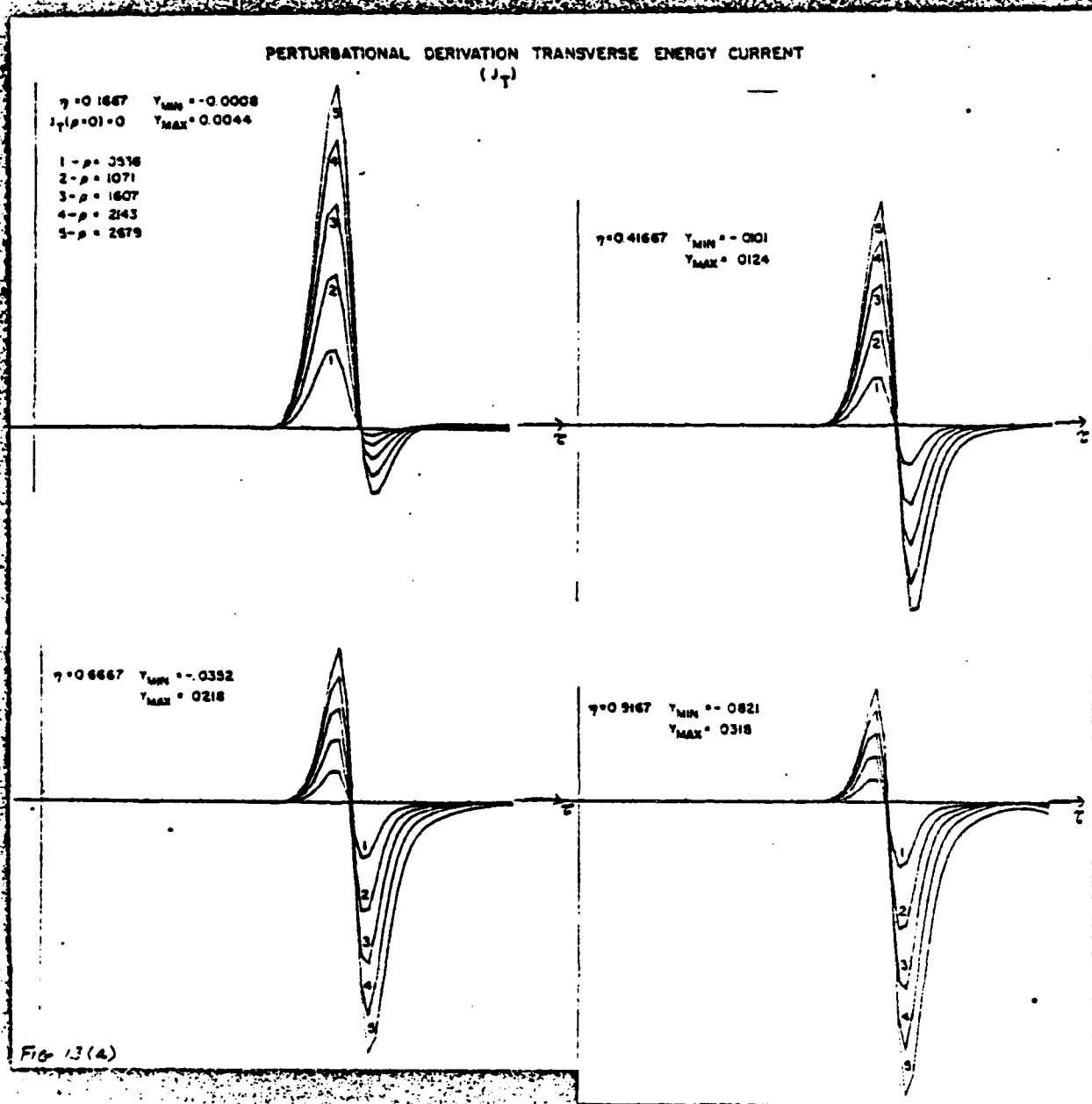


Figure 13 Analytic predictions of energy current J_T evolution for (a) absorber.

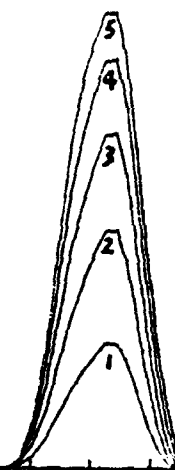
Fig 156

PERTURBATIONAL DERIVATION OF TRANSVERSE ENERGY CURRENT J_T (b) AMPLIFIERS

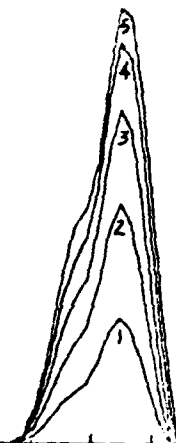
ETA = 0 1667 YMIN = 0 0000 YMAX = 0 0039

1- ρ = .0536
2- ρ = .1071
3- ρ = .1607
4- ρ = .2143
5- ρ = .2679

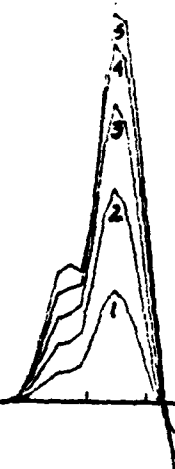
$J_T(\rho=0) = 0.0$



ETA = 0 4167 YMIN = 0 0007 YMAX = 0 0127



ETA = 0 6667 YMIN = 0 0048 YMAX = 0 0238



ETA = 0 9167 YMIN = 0 0137 YMAX = 0 0358



FIG 13(b)

13(b)

Analytic prediction of energy current J_T evolution for amplifier. Note that diffraction is greater here than in the absorber - counterpart situation (13a). For illustration purposes the current was derived beginning with the field equations as opposed to the energy equations. Only when the energy equation is used is the expression J_T valid for large \mathcal{Z} . (Plots constructed beginning with the energy equation can be found in ref. [171; 1975]).

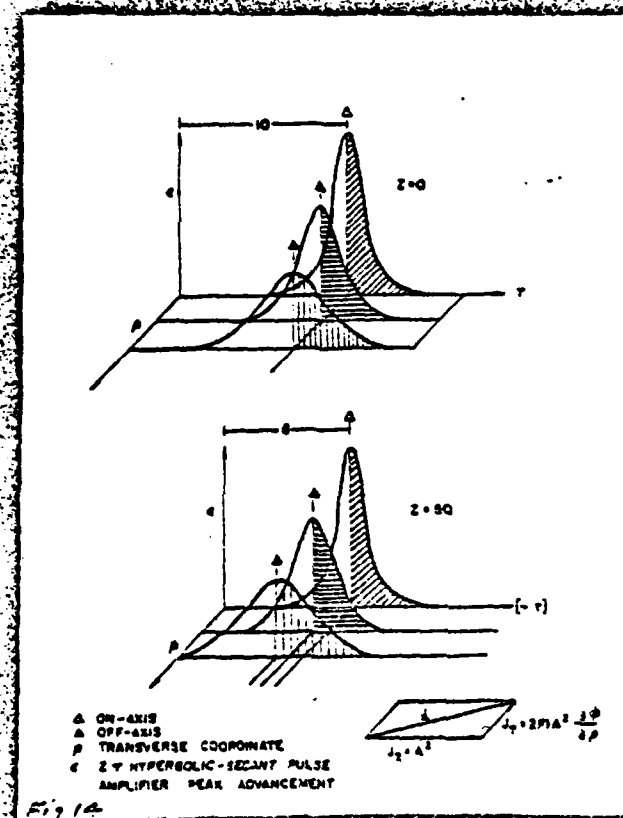


Figure 14 As the light diffracts outwardly in the leading edge of the pulse, it interacts with the slower moving pulse off-axis and experiences gain.

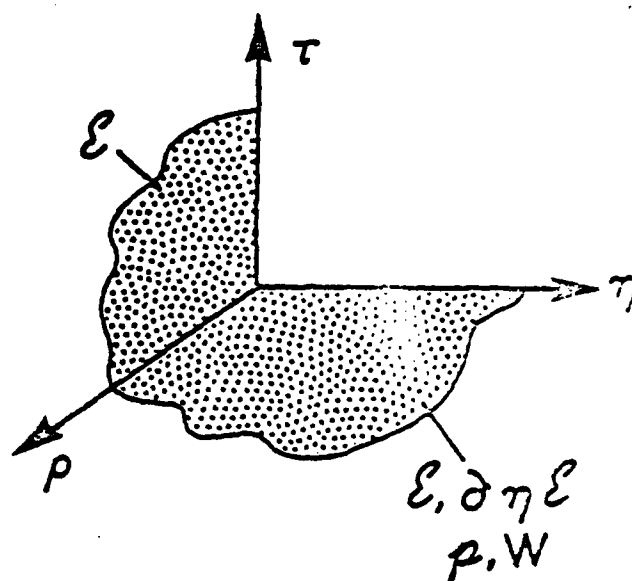
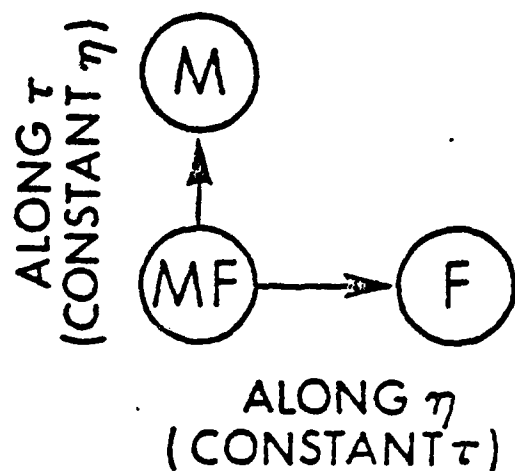
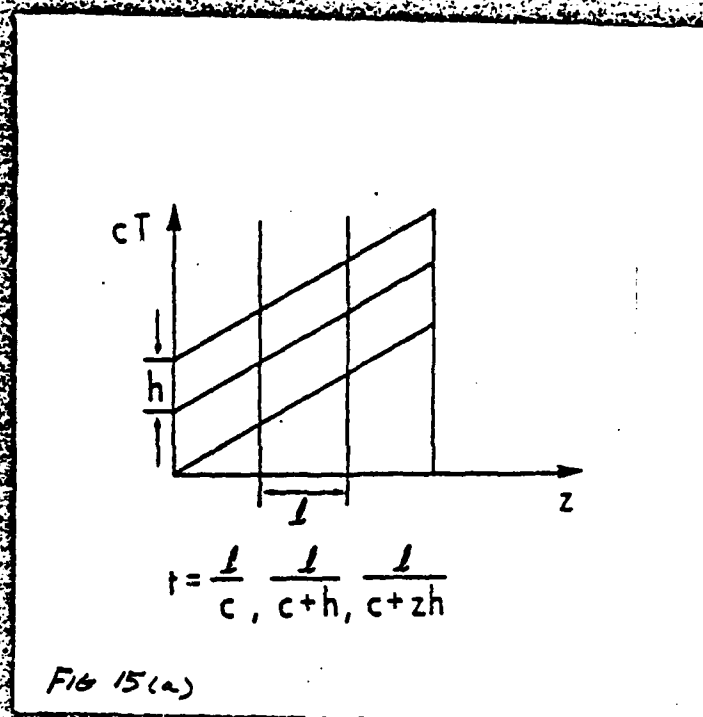


Figure 15 Graph (a) displays the retarded time concepts.

Graph (b) outlines the numerical approach: a marching problem along η for the field simultaneously with a temporal upgrading of the material variables along τ .

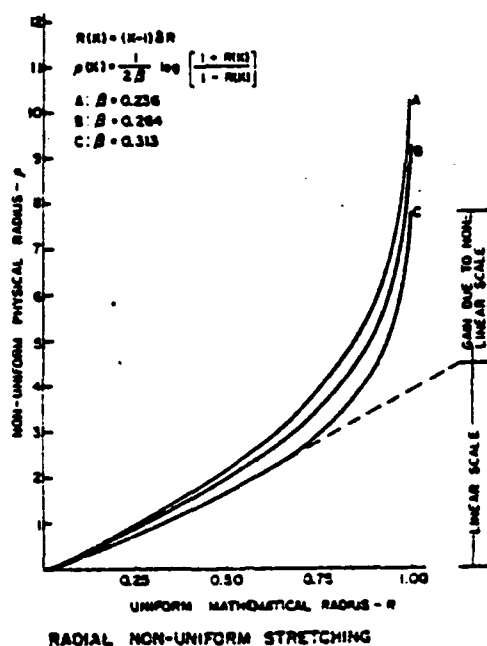


Fig 16(a)

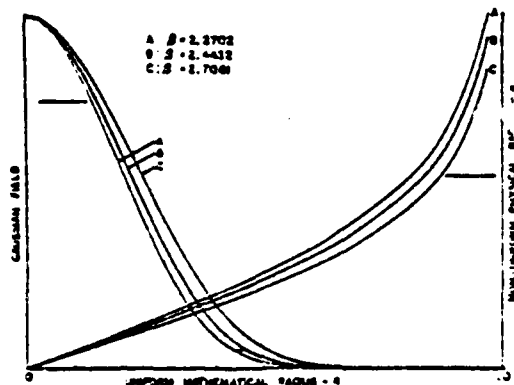


Fig 16(b)

Figure 16 Graph (a) shows non-uniform stretching of the transverse coordinate.

Graph (b) contrasts the Gaussian beam dependence with the non-uniform physical radius.

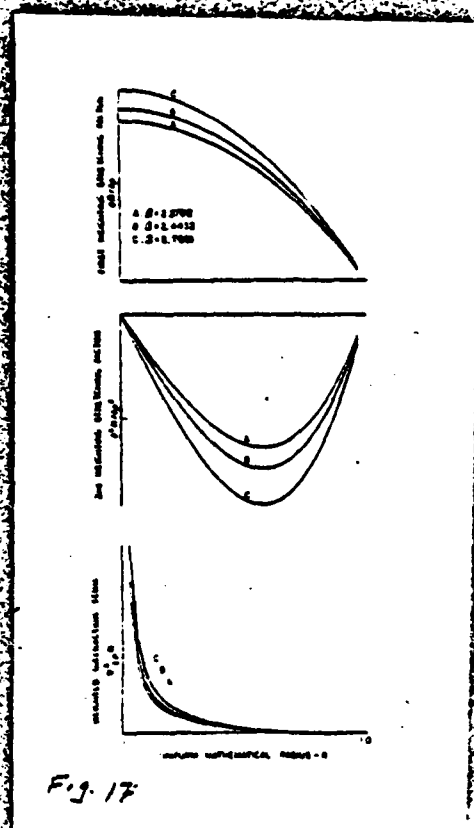


Figure 17 This graph illustrates the dependence of the radial mapping and the derivation on the different parameters versus the uniform mathematical radius.

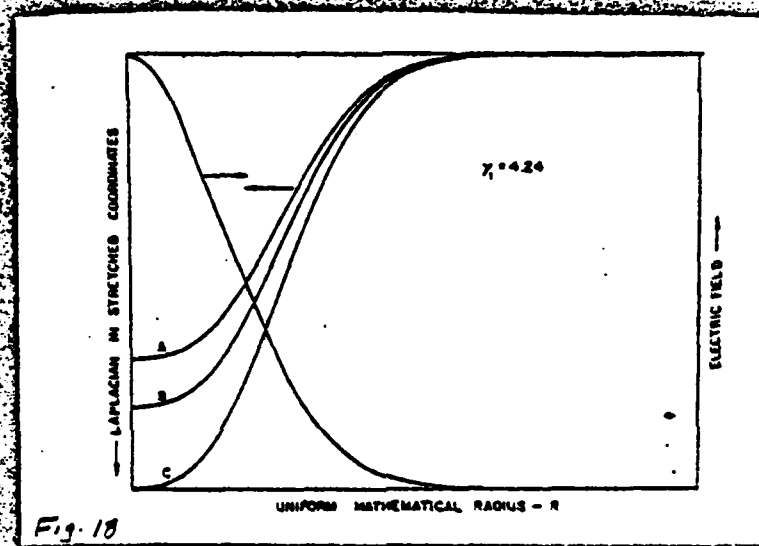


Fig. 18

Figure 18 This figure contrasts the Laplacian dependence for a given Gaussian profile for various non-uniform radial point densities.

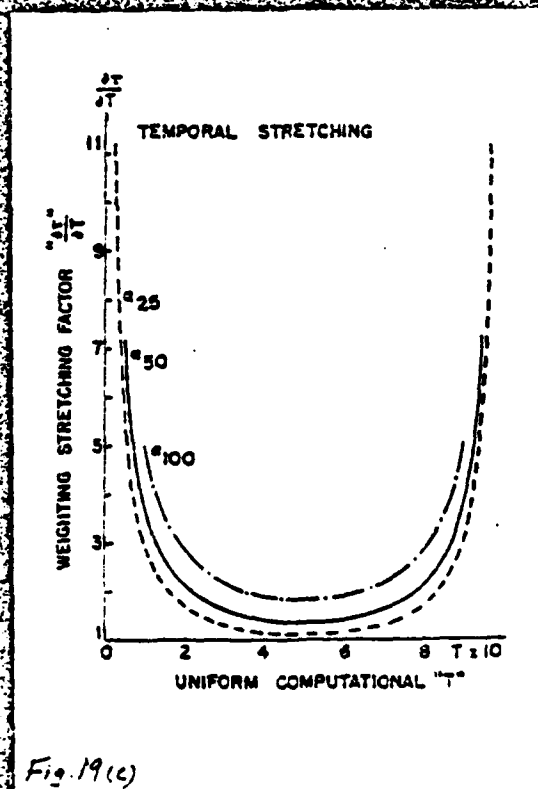
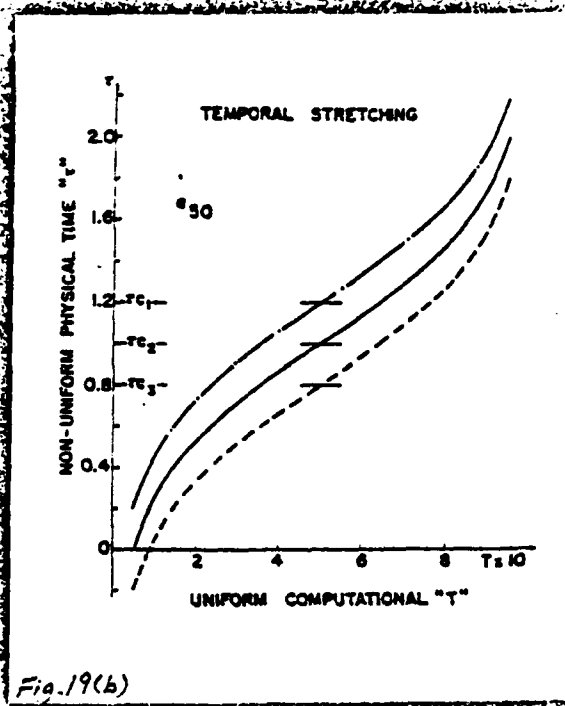
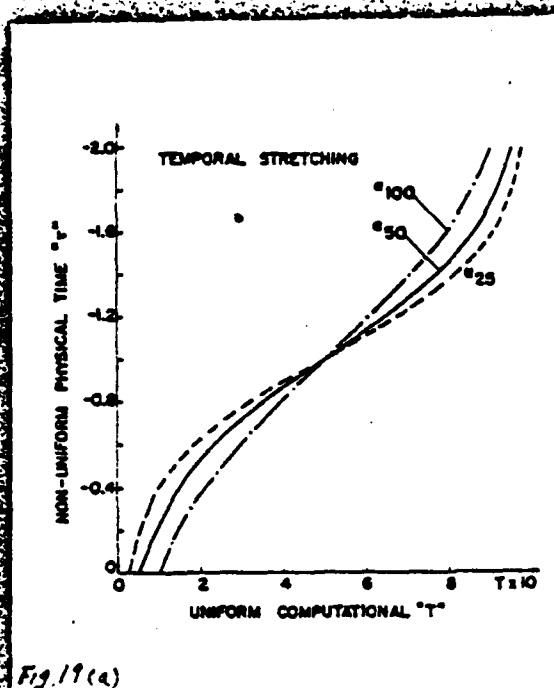


Figure 19 Dependence of prescribed stretching and its derivatives on the point densities and the center of transformation.

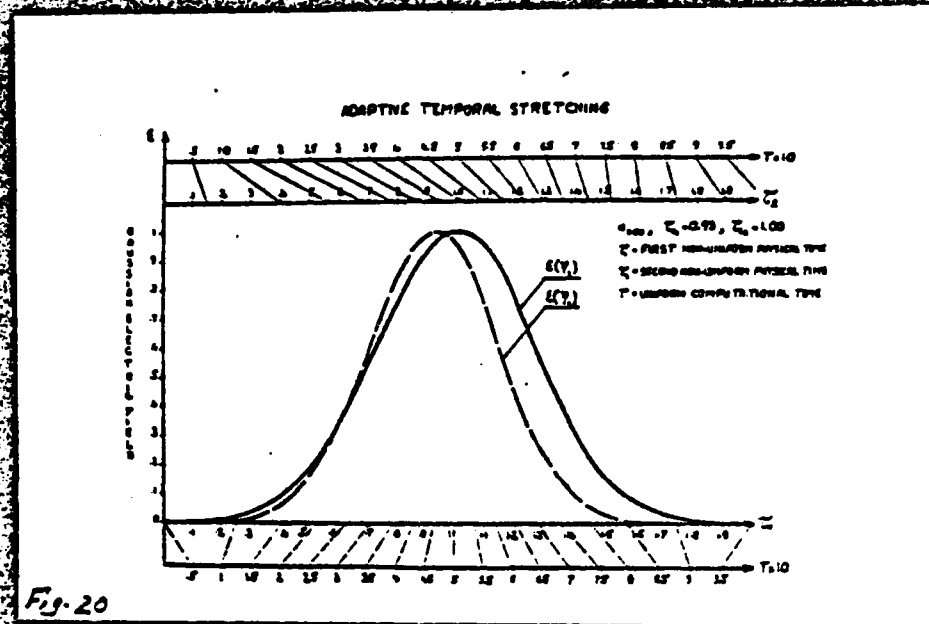


Figure 20 Adaptive stretching with different centers of transformation.

RESONING PRESCRIBED GAUSSIAN

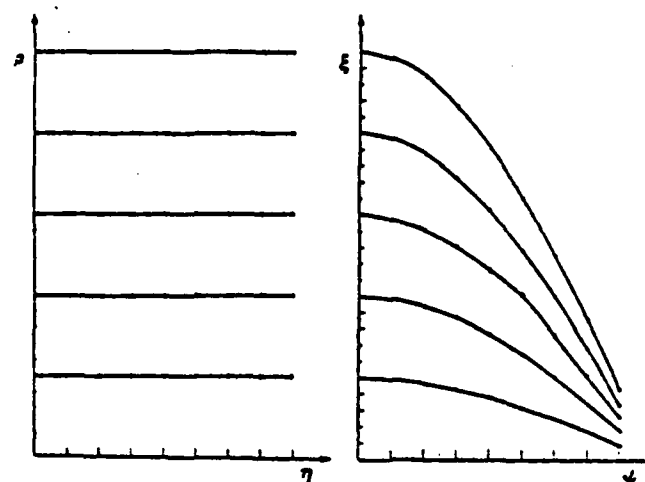


Fig 21(a)

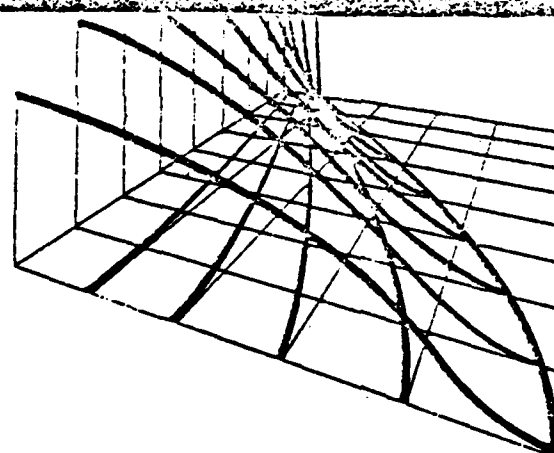


Fig 21(b)

Figure 21 The concept of the prescribed rezoning are presented in Graph (a); whereas Graph (b) is a close-up of the non-uniform mapped grid of Figure 2(b).

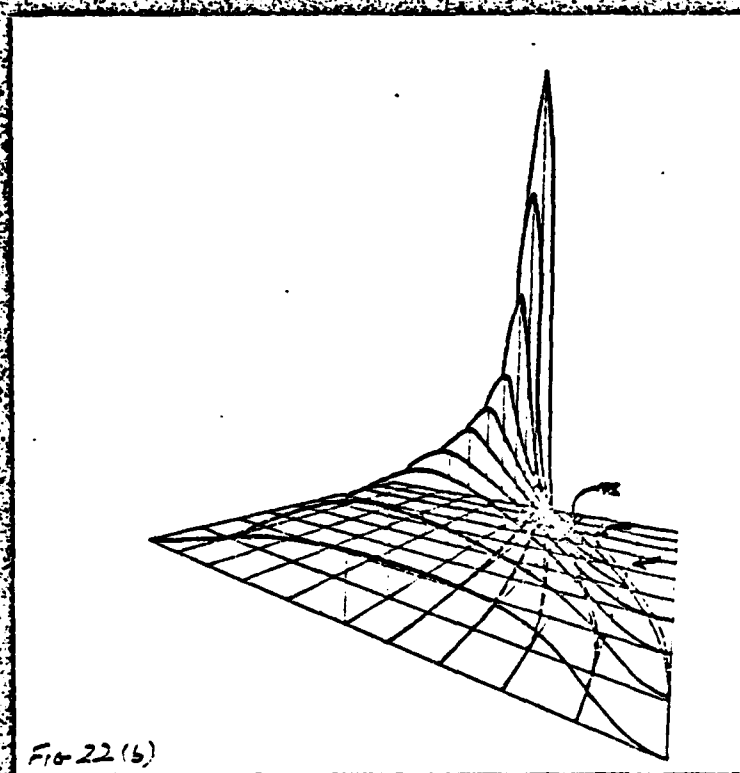
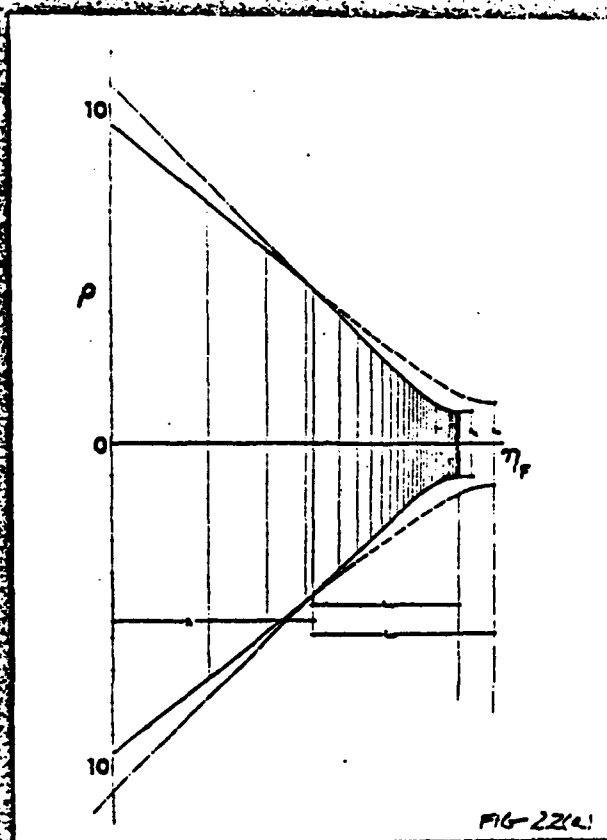


Figure 22 Graph (a) illustrates the self-adjusted rezoned grid.

Graph (b) illustrates the usefulness of the adaptive two-dimensional mapping through an isometric representation of the field fluency.

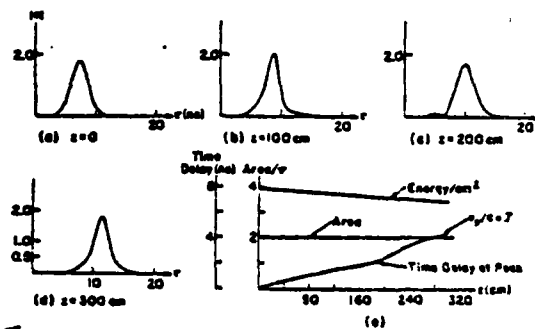


Fig 23

Figure 23 One-dimensional propagation in absorbers. Figures (a) to (d) illustrate the time behavior of a 2π input pulse at various planes. The retarded time is measured in nanoseconds. Figure (e) gives the time integrated intensity (energy/cm² = $\int dt e^2$), pulse area, and time delay at the peak all against the propagation distance.

FIG 24 (a)

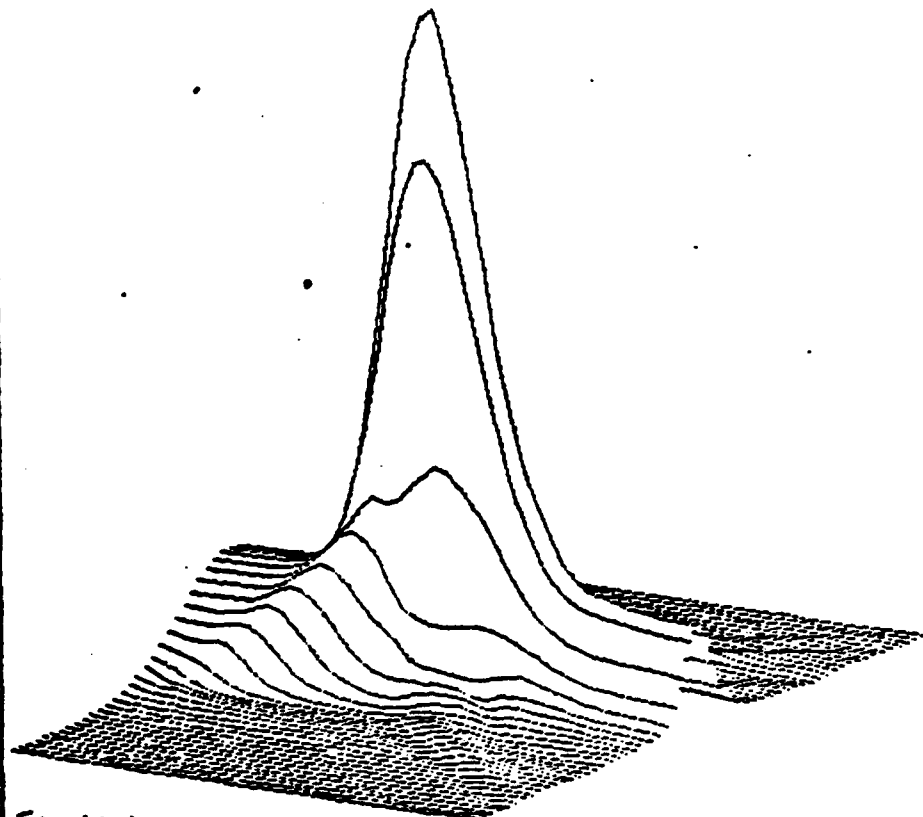
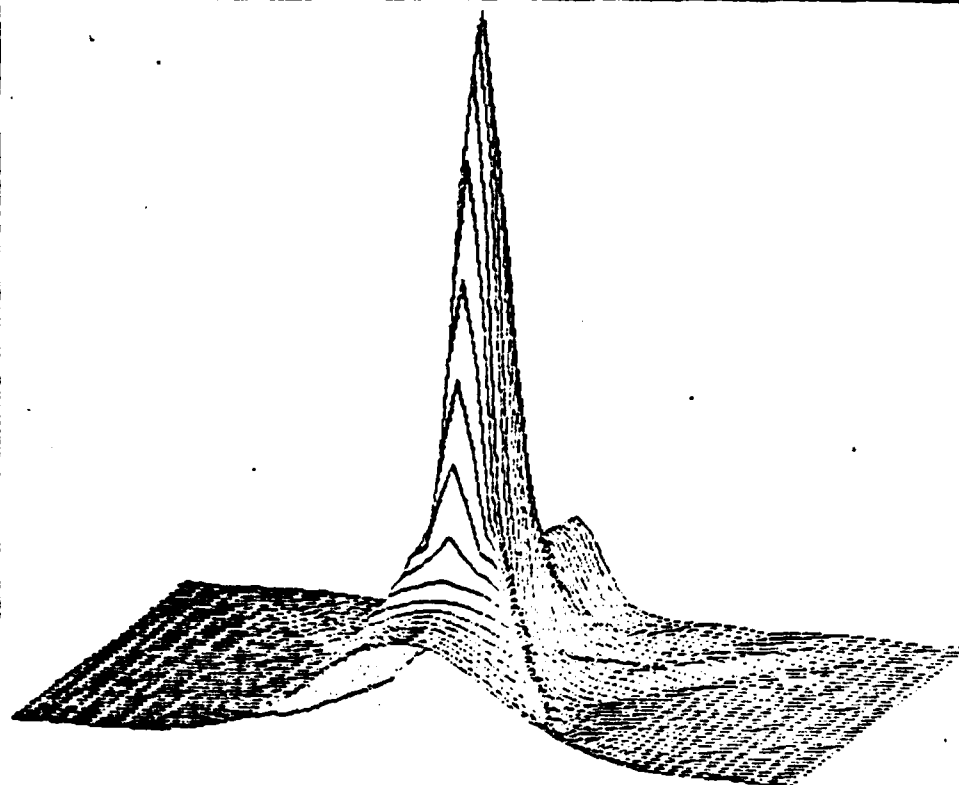


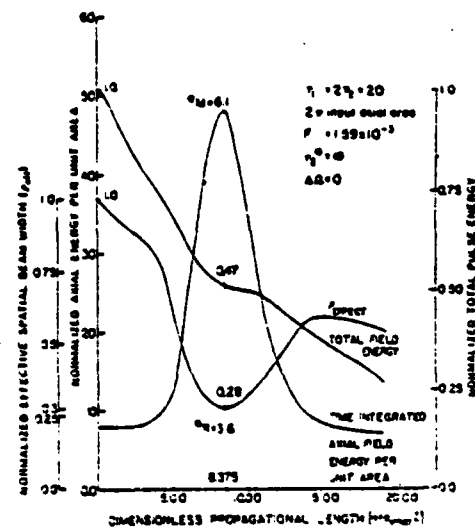
Figure 24 The energy per unit area

$$\int_0^r e(\rho, \eta, r')^2 dr'$$

the fluency is displayed as a function of the distance in the direction of propagation for various values of the coordinates transverse to the direction of propagation. To illustrate the gradual inward energy flow the $\pi/2$ reorientation is also displayed. The longitudinal orientation illustrates the gradual boosting mechanism that the field energy experiences as it flows radially towards the beam axis (while η increases). The second angle displays the severe beam distortion in its cross-section as a function of η .

24(b)





The principal characteristics plotted against the dimensionless propagation distance for a particular value of F : the on-axis energy density, the total field energy, and an effective radius defined as the square root of the total field energy divided by the on-axis energy density.

FIG 25

Figure 25 The principal characteristics plotted against the dimensionless propagation distance for a particular value of F : the on-axis energy density, the total field energy and an effective radius defined as the square root of the total field energy divided by the on-axis energy density.

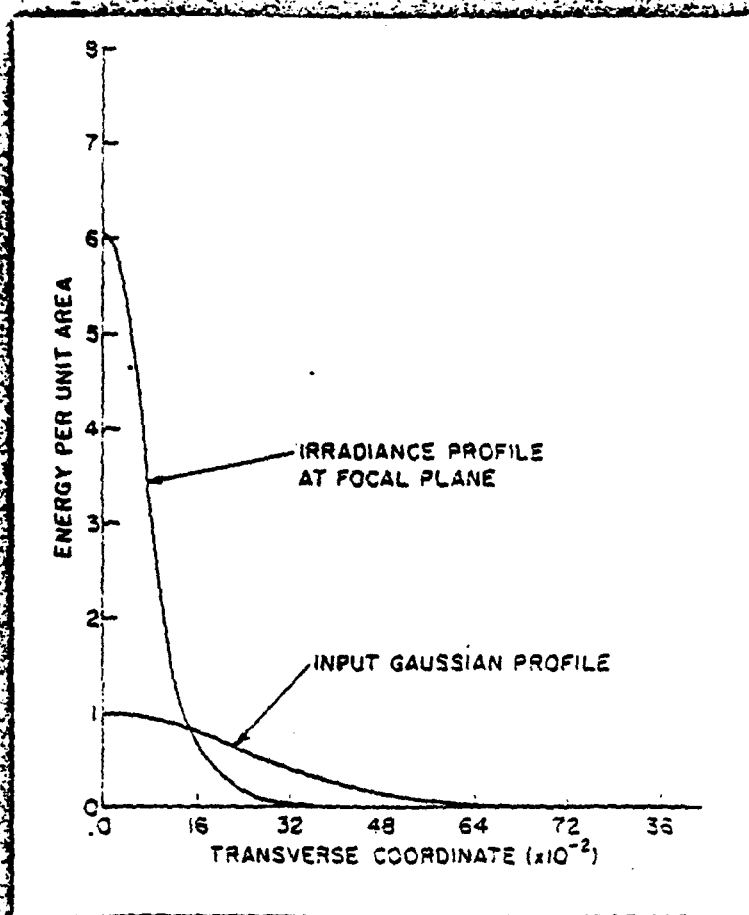


Figure 26 The profile of the energy per unit area for both the input and focal planes.

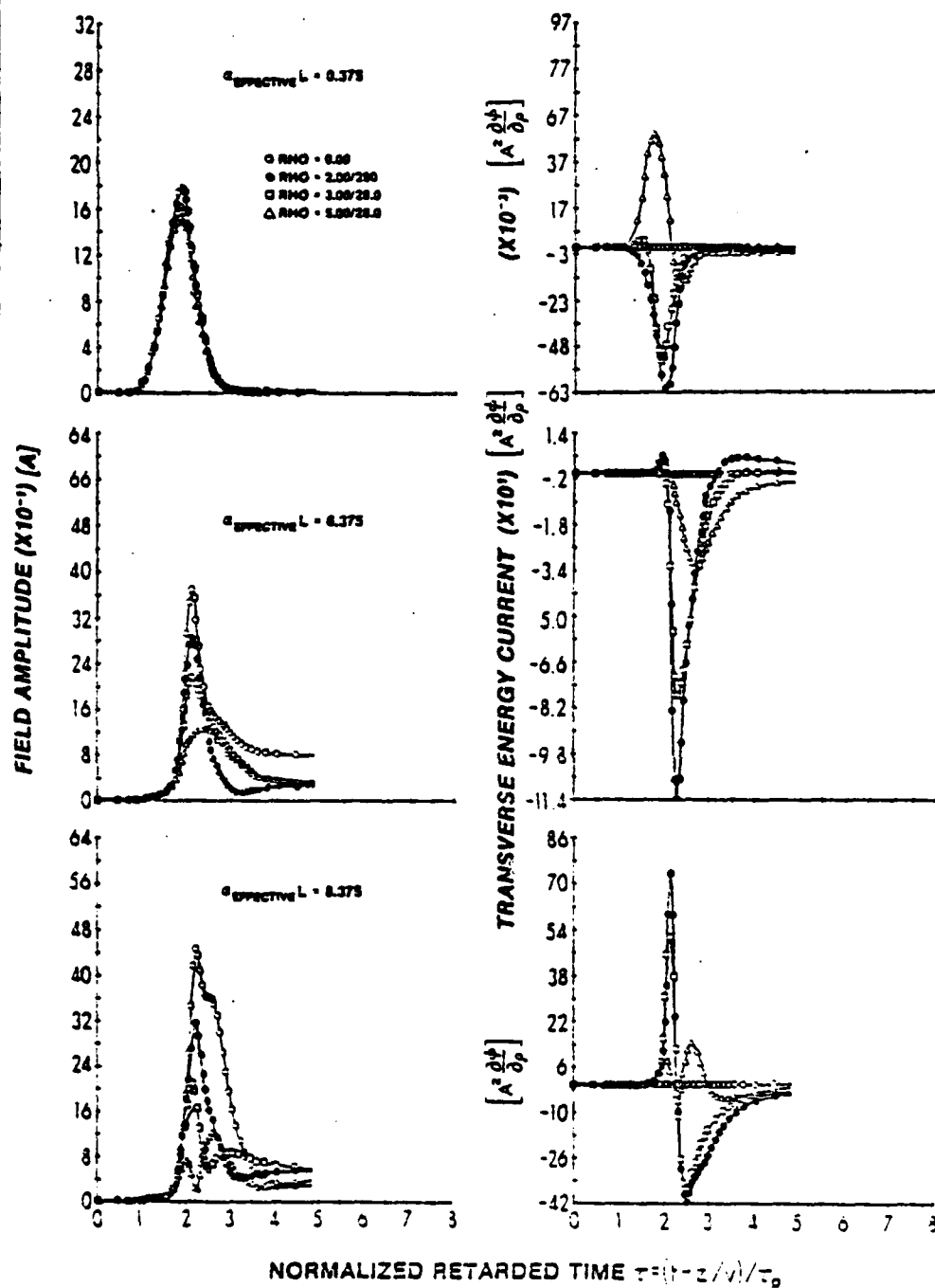


Figure 27 The absorber field amplitude (a,b,c) and the transverse energy current (d,e,f) for several radii versus the retarded time for three stages of the propagation: the reshaping region, the build-up region and the focal region (as a function of the transverse coordinate).

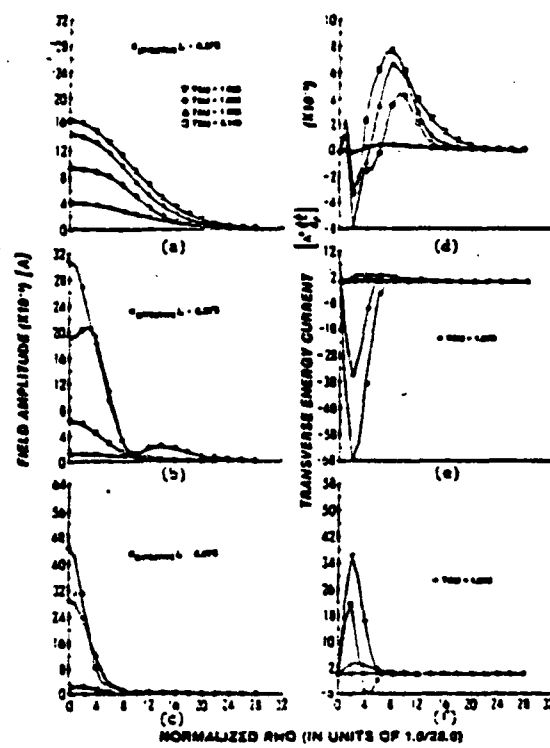


Figure 28 The profile of the absorber field amplitude (a,b,c) and the profile of the transverse energy current (d,e,f) for several earlier (small) instants of time for three stages of the propagation: the reshaping region, the build-up region and the focal region, as a function of earlier retarded time (slices in the front of the pulse).

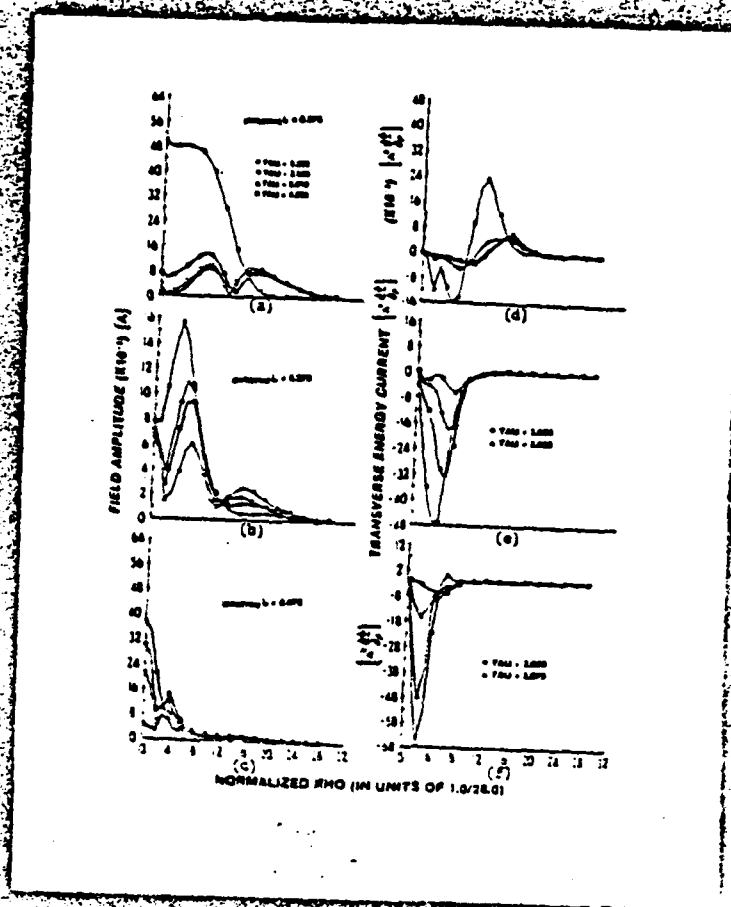


Figure 29 The profile of the absorber field amplitude (a,b,c) and the profile of the transverse energy current (d,e,f) for several later (subsequent) instants of time for the three stages of the propagation: the reshaping region, the build-up region and the focal region as a function of subsequent retarded times (slices in the trailing edge of the pulse).

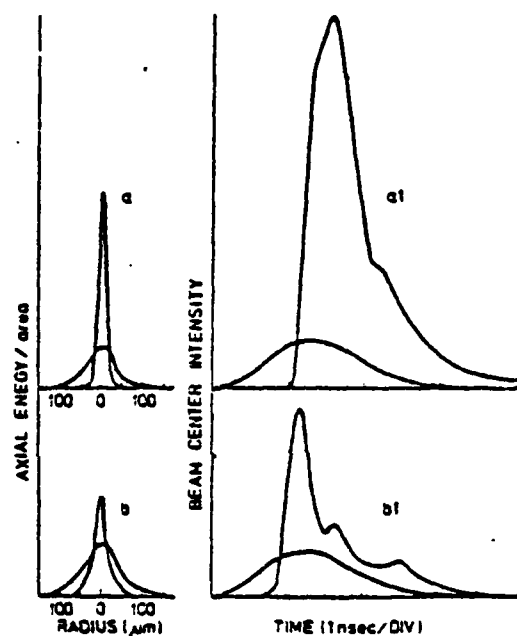


Fig 30

Figure 30 Changes in spatial and temporal profiles for pulses under going self-induced-transparency with transverse energy flow, that lead to coherent self-focusing, a and a1, maximum off-resonance SF; b and b1, on-resonance.

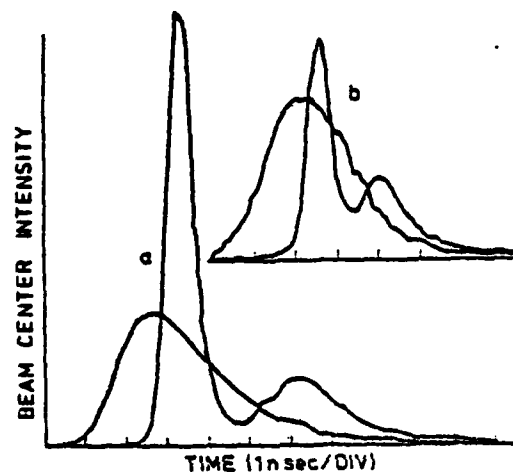


FIG 31

Figure 31 Temporal behavior of pulses. Break-up of a 4π input pulse is shown under (a) self-focusing and (b) uniform plane-wave conditions in Na. In (a) the integrated output is 35% higher than the input.

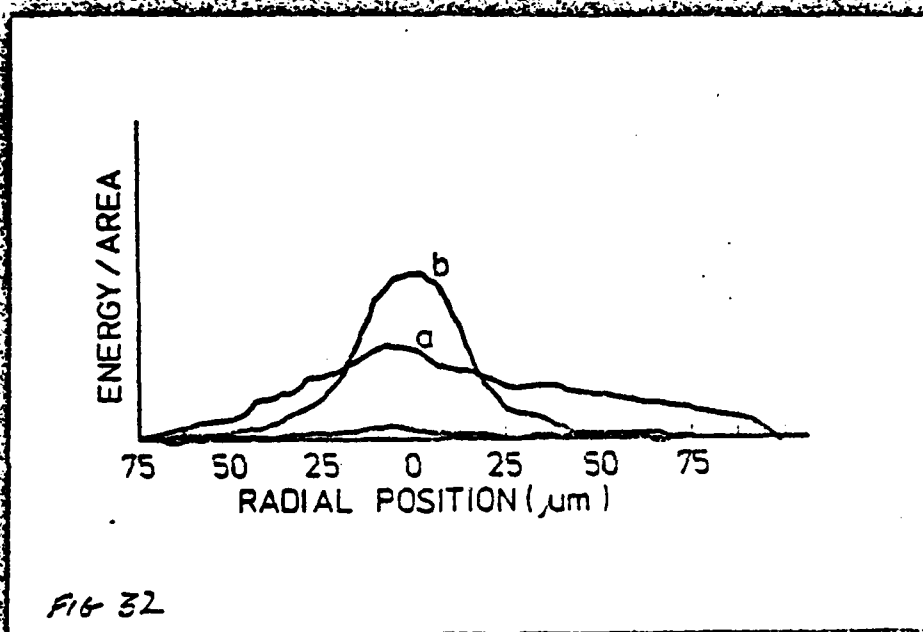


Fig 32

Figure 32 Cross-section of beam at cell exit in the first experiment: curve a, without Na, and curve b, with Na on-resonance, with input area of 3π to 4π and magnetic field of 3.5 kG.

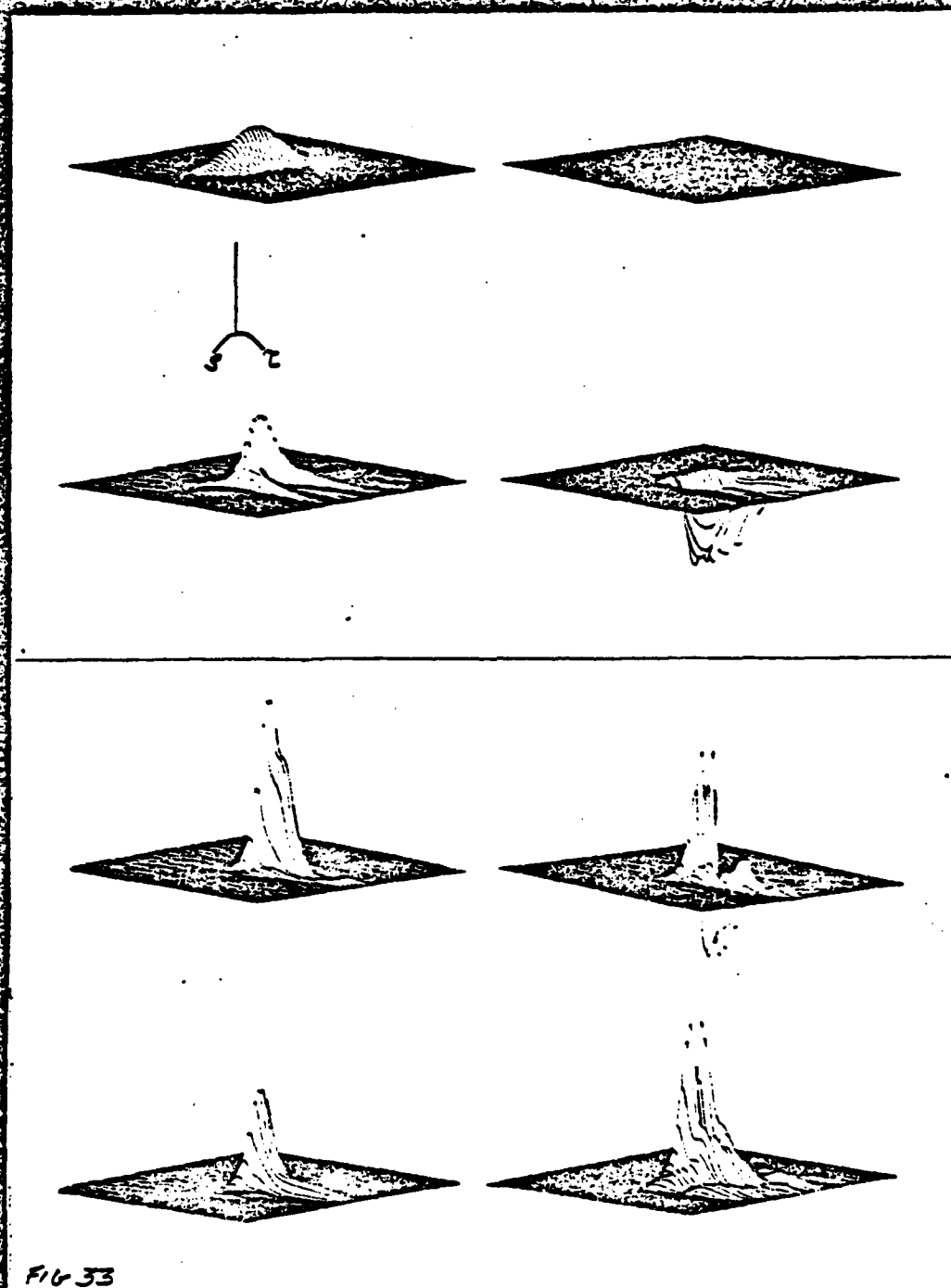


FIG 33

Figure 33 Isometric plots of the absorber field energy and transverse energy flow, against the retarded time for various transverse coordinates at four regions: (a) reshaping, (b) build-up region, (c) focal region, (d) post-focal region.

ELECTRIC FIELD AMPLITUDE & TRANSVERSE ENERGY CURRENT AT THE THREE STAGES
OF PROPAGATION: RESHAPING, BUILD-UP AND POST-FOCAL REGIONS

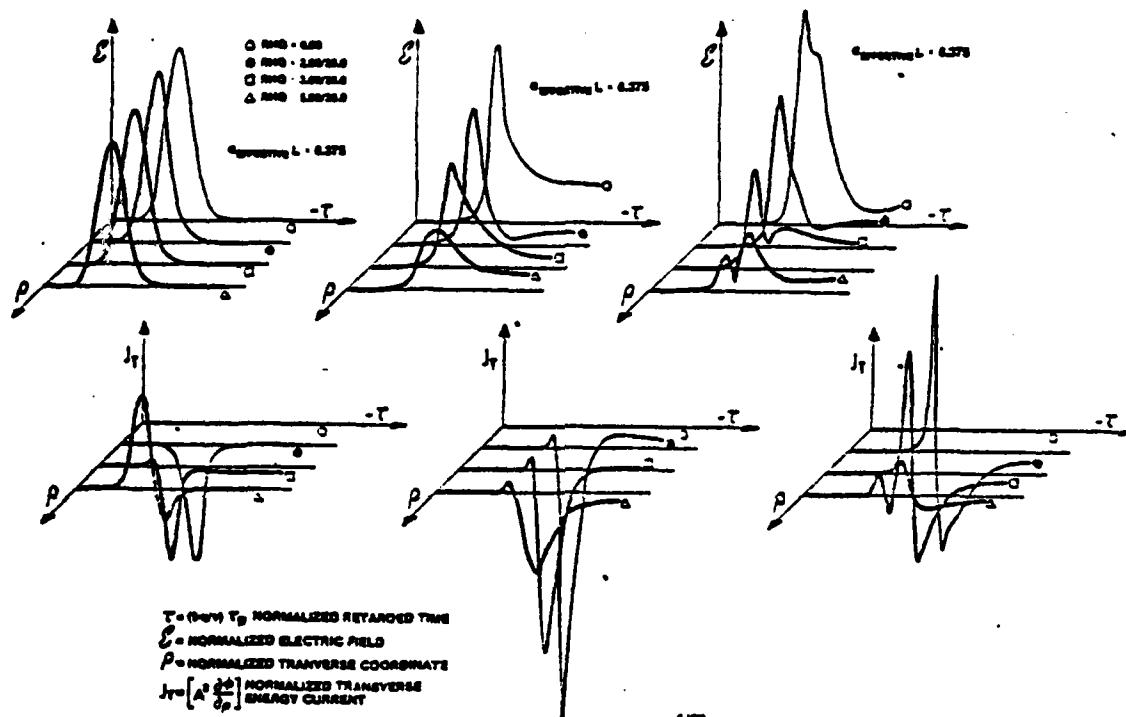


Fig 33(a)

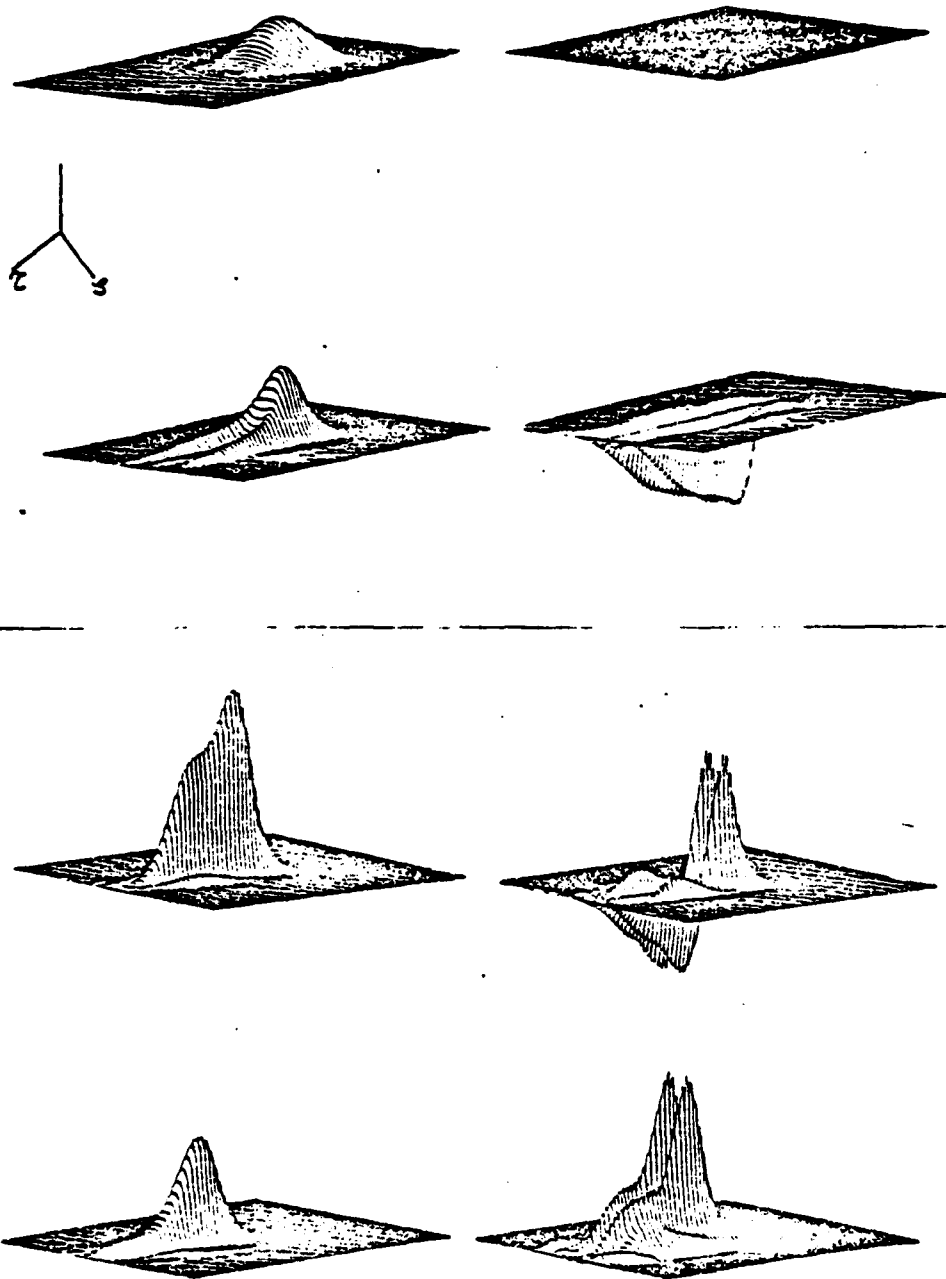


FIG 34

Figure 34 Isometric plots of the absorber field energy and transverse energy flow profile for various time slices at the four regions of interest.

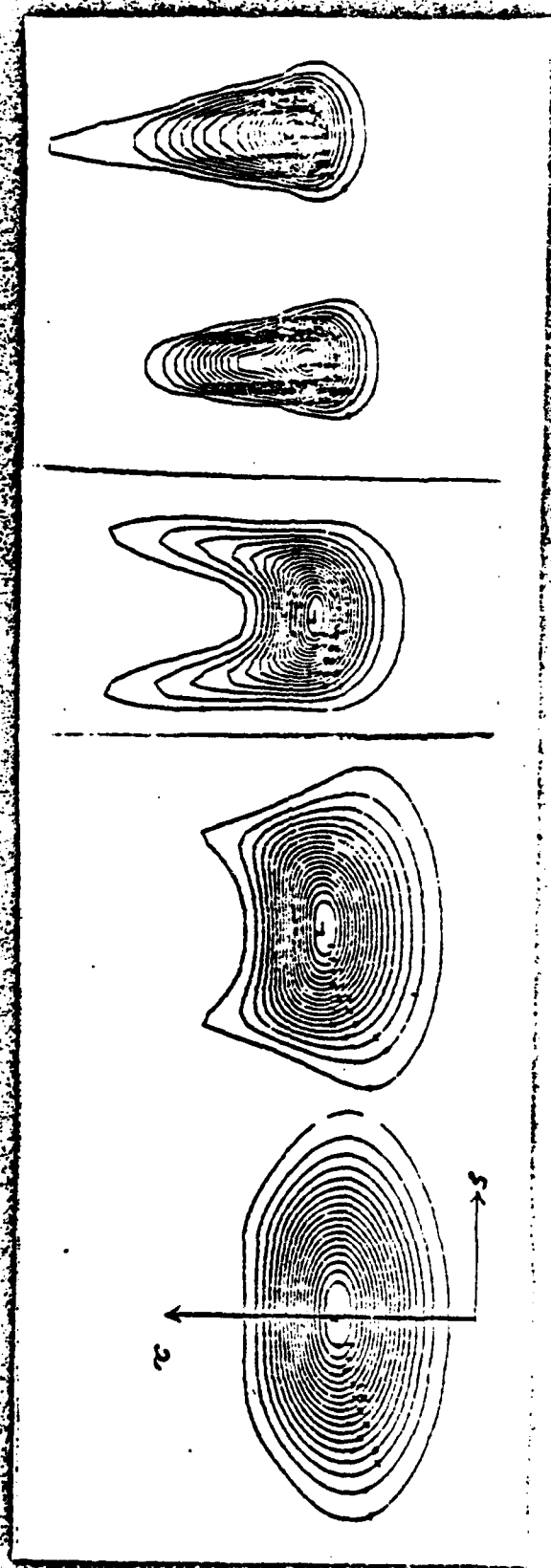


Figure 35 Absorber field energy contour plots for the four propagation regions of interest. Notice the temporal delay associated with the coherent exchange of energy between light and matter, as well as the beam cross-section narrowing.

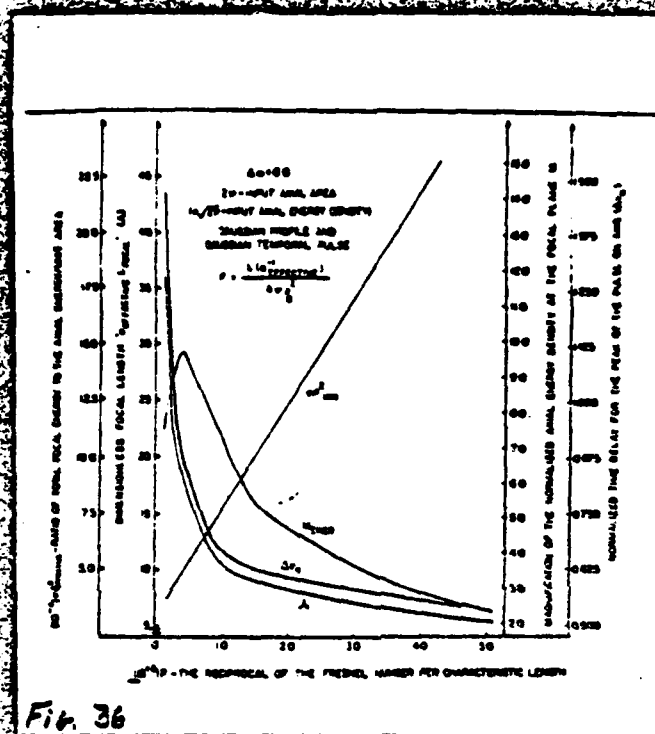


Fig. 36

Figure 36 Principal characteristics of the focal plane as a function of the parameter F : the dimensionless focal length ($\alpha_{\text{eff}} \cdot L(\text{focal}) = \Lambda(\text{focal})$; the ratio M of the axial energy per unit area at the focal plane to that at the input plane; the time delay at the focal plane of the peak of the pulse on axis; the ratio of the total field energy to the axial energy per unit area π^2).

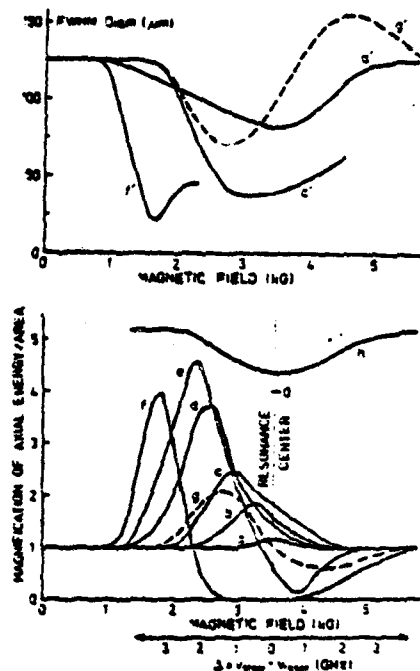


Fig 37

Figure 37 Experimental energy-density magnification and diameter reduction in Na as a function of detuning. Curves a to f are for 2-ns, 5 pulses of 125μm diam in an 11-mm cell. The absorption increases from curve a to curve f; curve g is self-focusing of CW light; curve h shows the atomic absorption. Above, Curve a is the diameter for the conditions of curve a, etc.

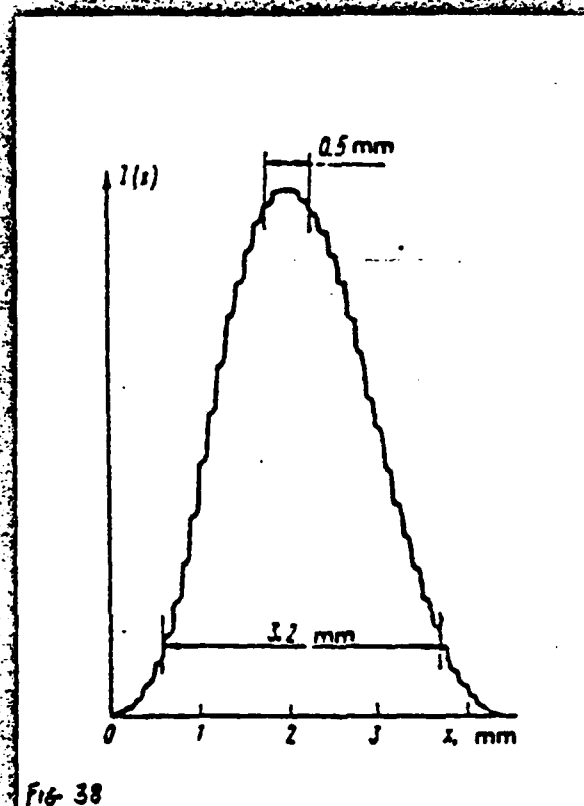


Fig 38

Figure 38 Experimental Gaussian profile carefully prepared to eliminate any ripple larger than 3% variation to avoid the additional small-scale self-focusing to the transient whole beam break-up under study.

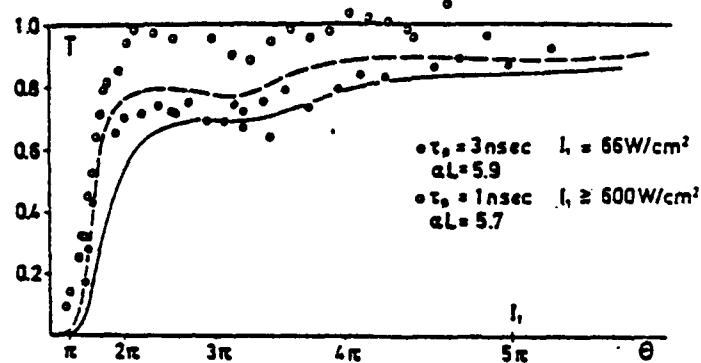


Fig 39

Figure 39 Pulse energy transmission (output per input in Ne vs. squared pulse area for 3ns (full dots) and 1ns (open dots) pulses. Curves are the corresponding plane-wave computer simulations.

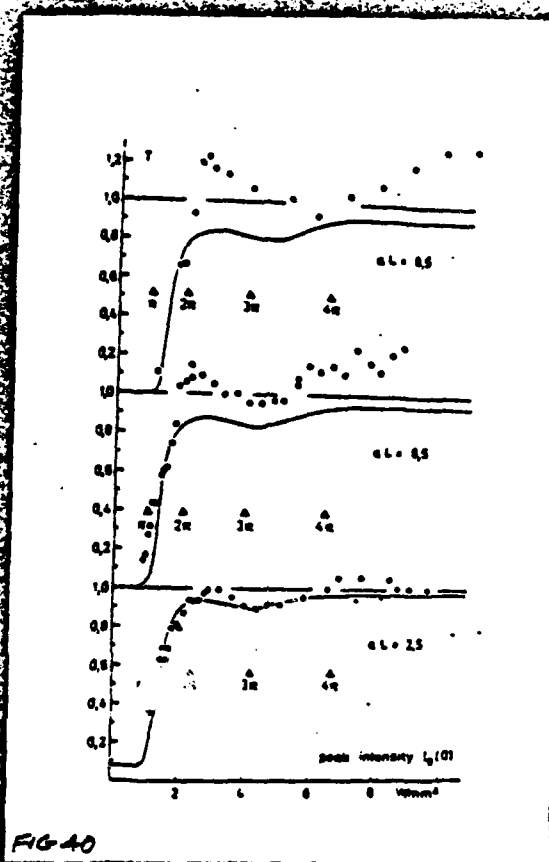


FIG 40

Figure 40 Energy-density magnification vs. peak intensity for 0.8ns pulses, showing increase of self-focusing with Ne absorption αL . Curves are plane wave computer simulations with $T_2' = 10\text{ns}$.

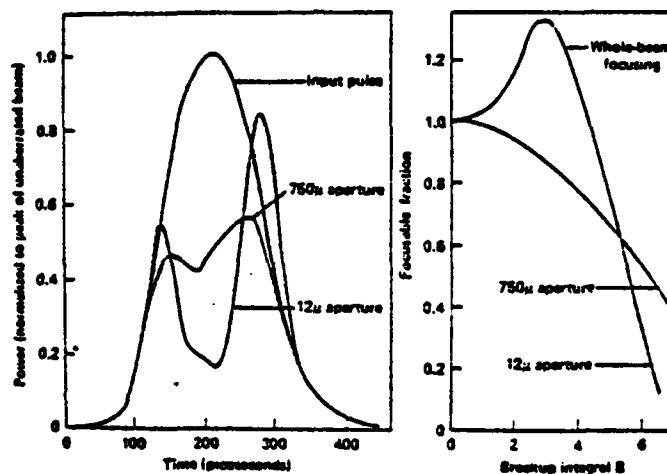


FIG. 41

Figure 41 Graph (a) displays an example of the severe temporal distortion which can be caused by nonlinear propagation in the Lawrence Livermore Labs Cyclops laser chain.

Graph (b) displays the corresponding plots of the fraction of the pulse power which is focused through two different diameter apertures as a function of the break-up integral B (see Bliss et al, IEEE J. Quantum Electron, July 1976).

The focused output beam does not contain all the energy which entered the experiment.

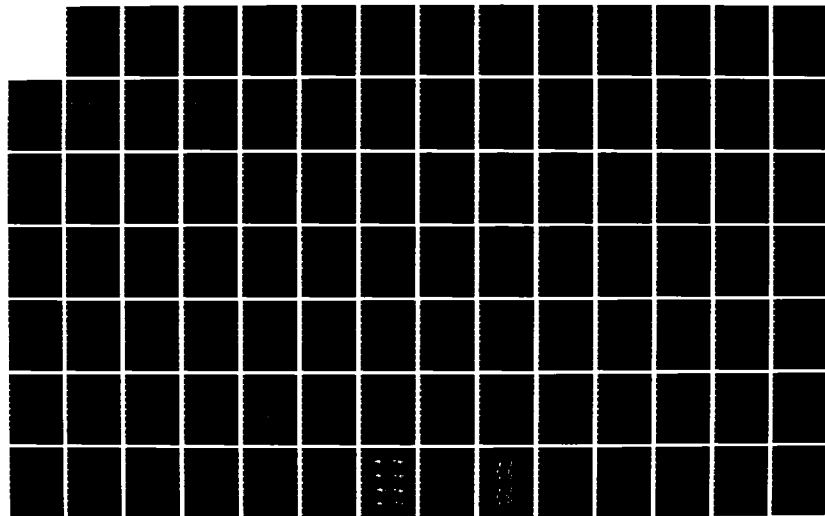
AD-A136 906

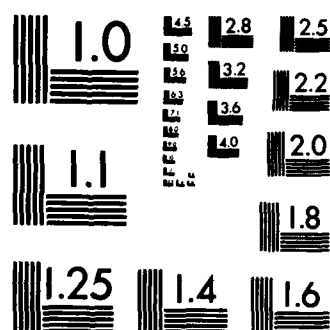
TRANSVERSE AND QUANTUM EFFECTS IN LIGHT CONTROL BY
LIGHT: (A) PARALLEL BE. (U) POLYTECHNIC INST OF NEW
YORK BROOKLYN DEPT OF MECHANICAL AND A. F P MATTAR
1983 POLY-M/AE-83-4 N00014-80-C-0174 F/G 20/6

2/6

UNCLASSIFIED

NL





MICROCOPY RESOLUTION TEST CHART
NATIONAL BUREAU OF STANDARDS-1963-A

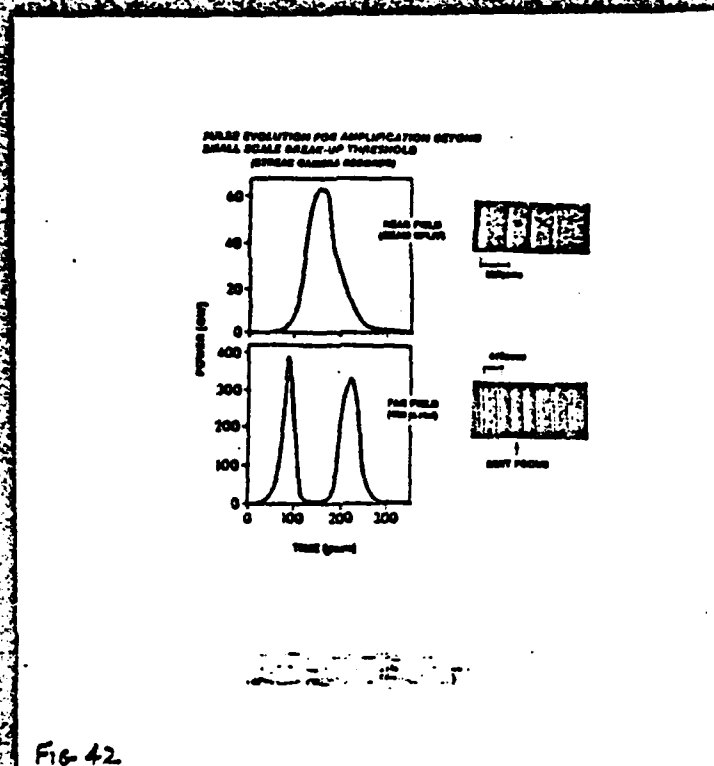


Fig 42

Figure 42 Example of the temporal distortion due to small-scale beam break-up on the Beta prototype of the University of Rochester Laser Fusion Laboratory (LLE) (see LLE program report to ERDA, January 1977).

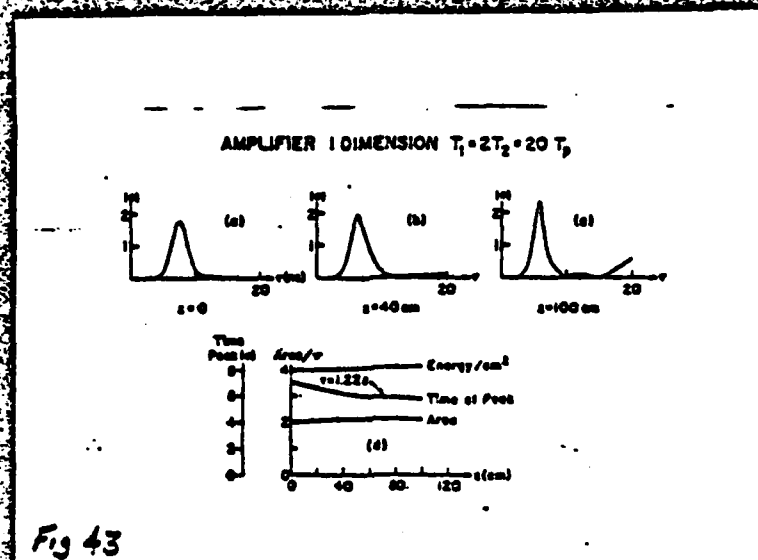


Fig 43

Figure 43 One-dimensional amplifier: Graph (a) shows the input pulse as being a 4 nsec Gaussian with integrated area 2π . Graphs (b) and (c) correspond to the pulse propagated to 40 and 200 cm. Graph (d) is the summarized propagation data of the pulse versus the amplifier length ($\alpha_{eff} = 200$ cm).

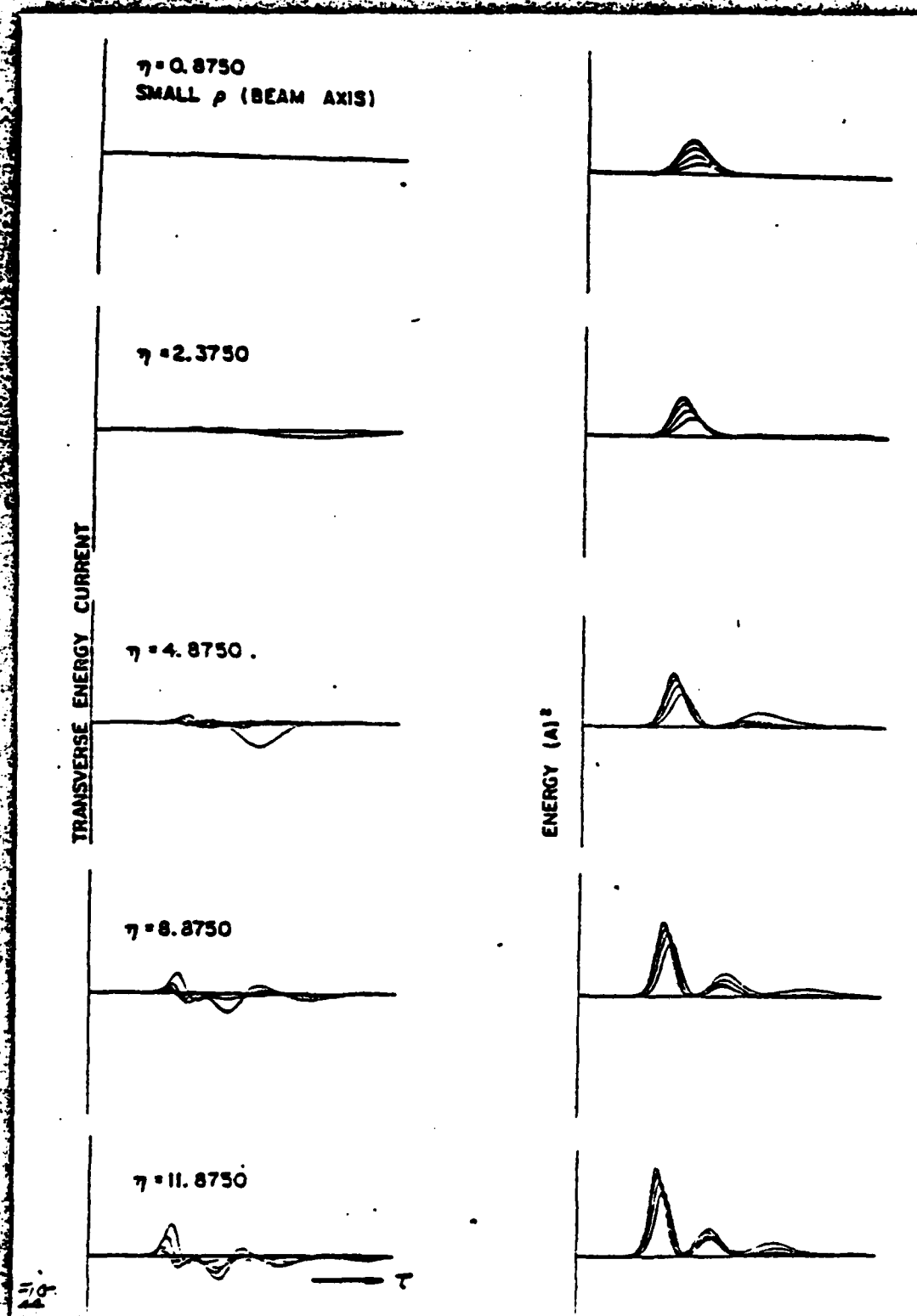


Figure 44 Longitudinal projection of amplifier energy field amplitude and transverse current for near-axis (small) radii at the four critical regions (a) reshaping, (b) build-up, (c) focal region, and (d) post-focal.

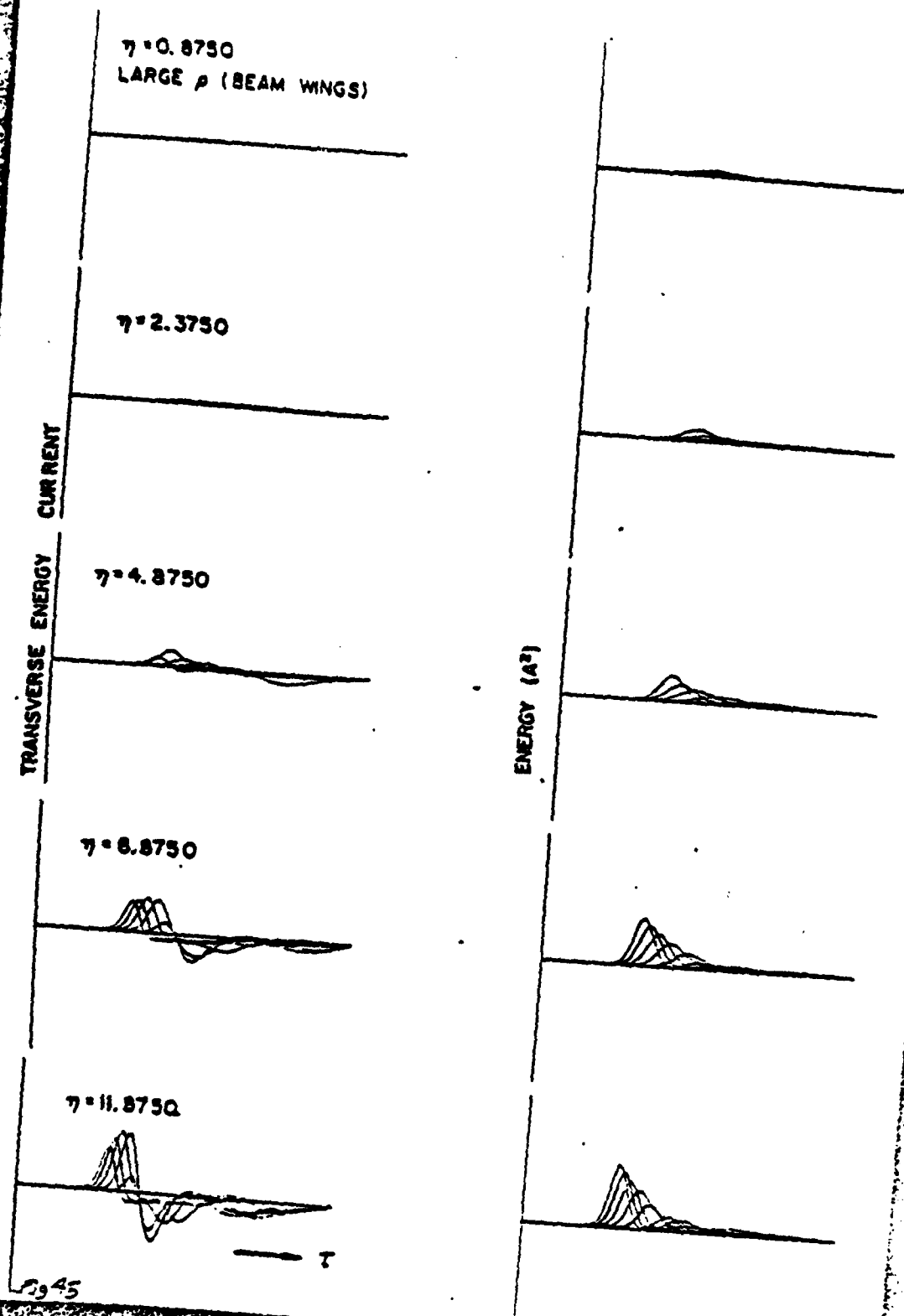


Figure 45 Longitudinal projection of amplifier energy field amplitude for large (off-axis) radii at the four critical regions.

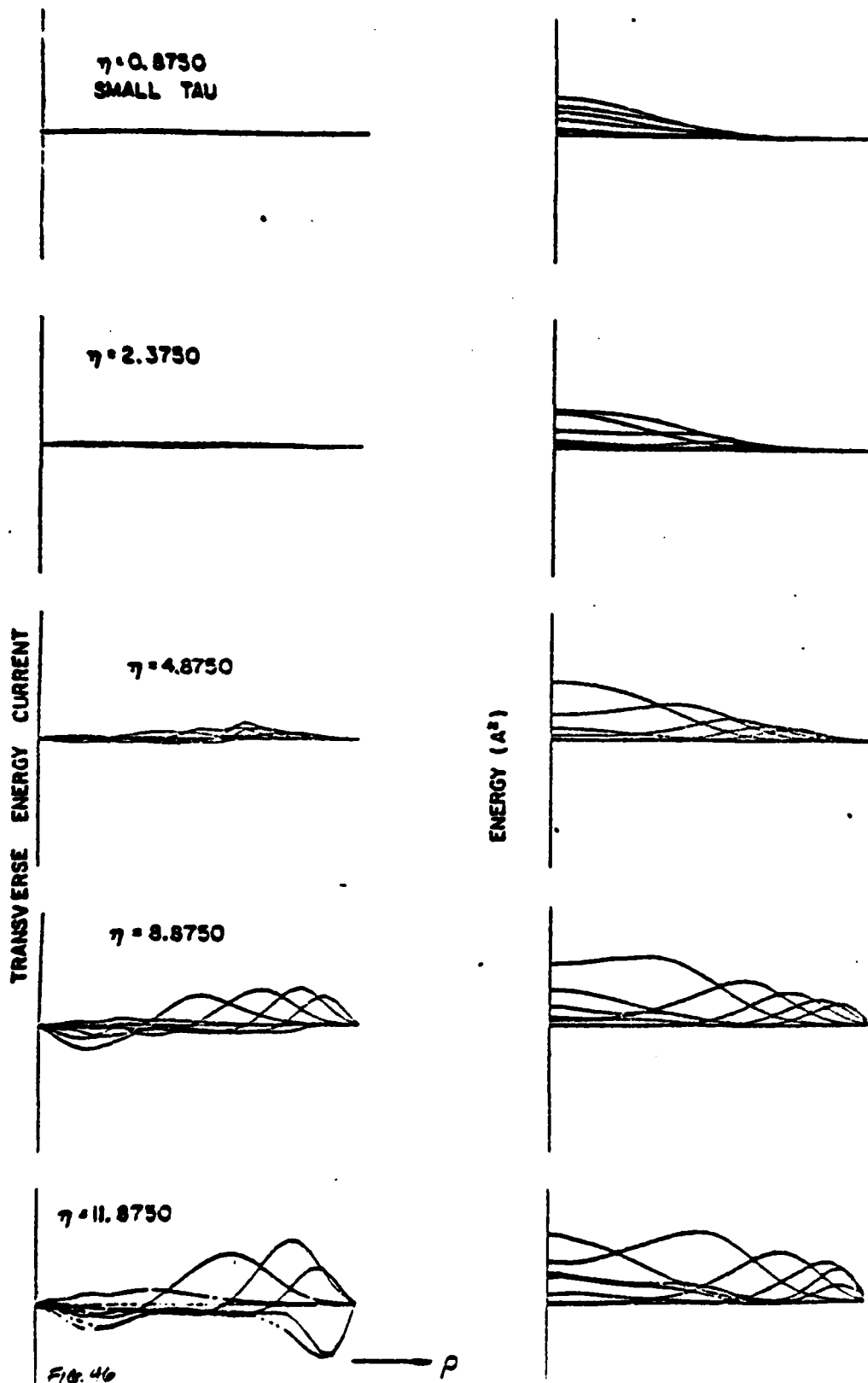


Figure 46 The profile of amplifier energy field amplitude and transverse energy current for small slices of time (in the front of the pulse) at the four critical propagation regions of interest.

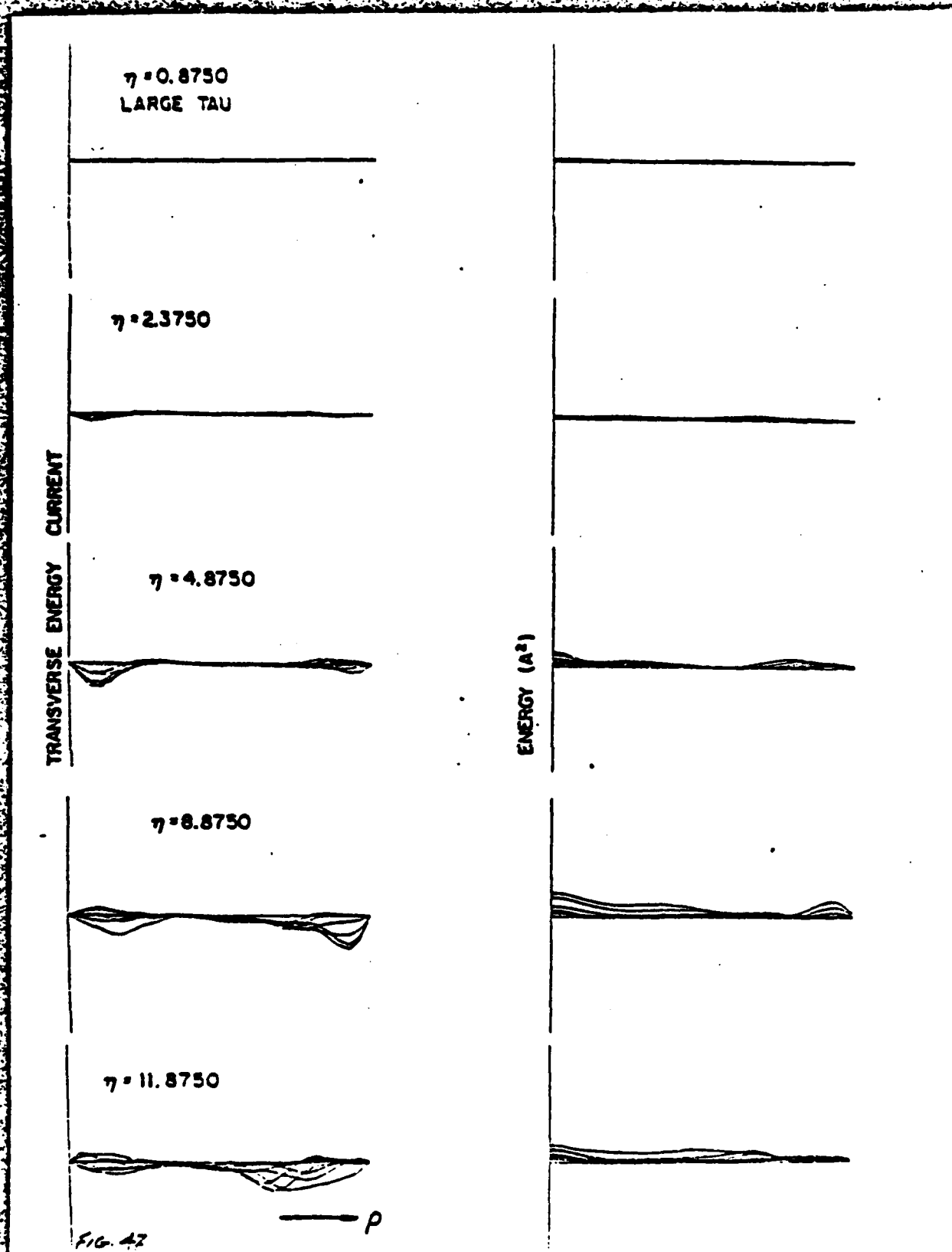


Figure 47 The profile of amplifier energy amplitude and transverse energy current for large slices of time (in the trailing edge of the pulse) at the four critical propagation regions of interest.

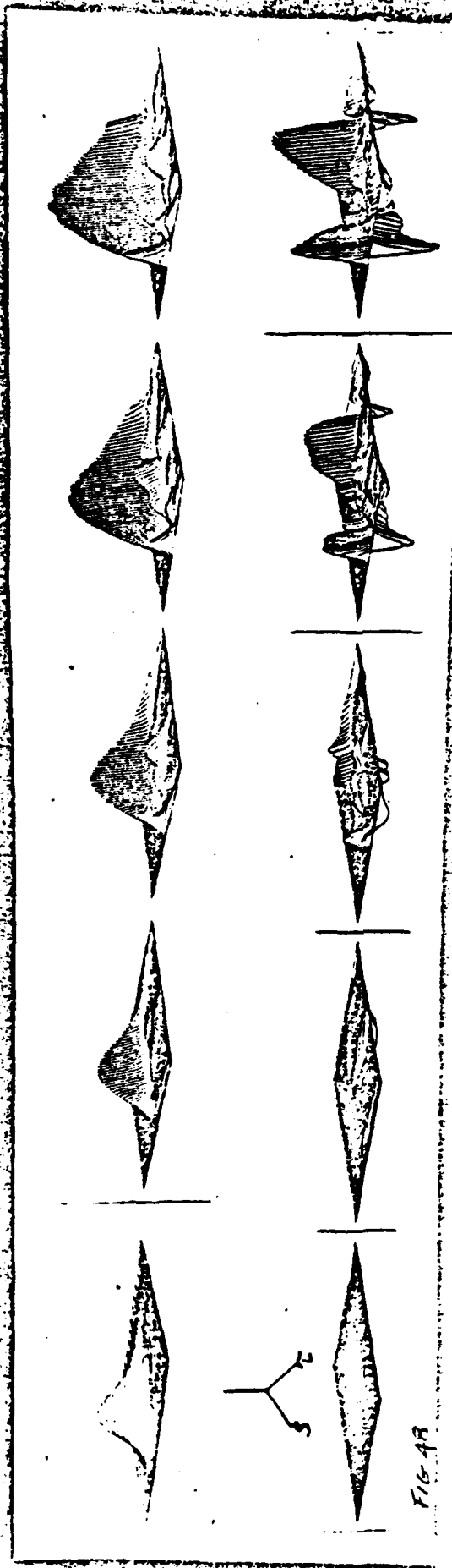


Figure 48 Isometric plots of the amplifier field energy and transverse energy flow, against the retarded time for various transverse coordinates at four regions: (a) reshaping, (b) build-up region, (c) focal region, (d) post-focal region.

FIG 48

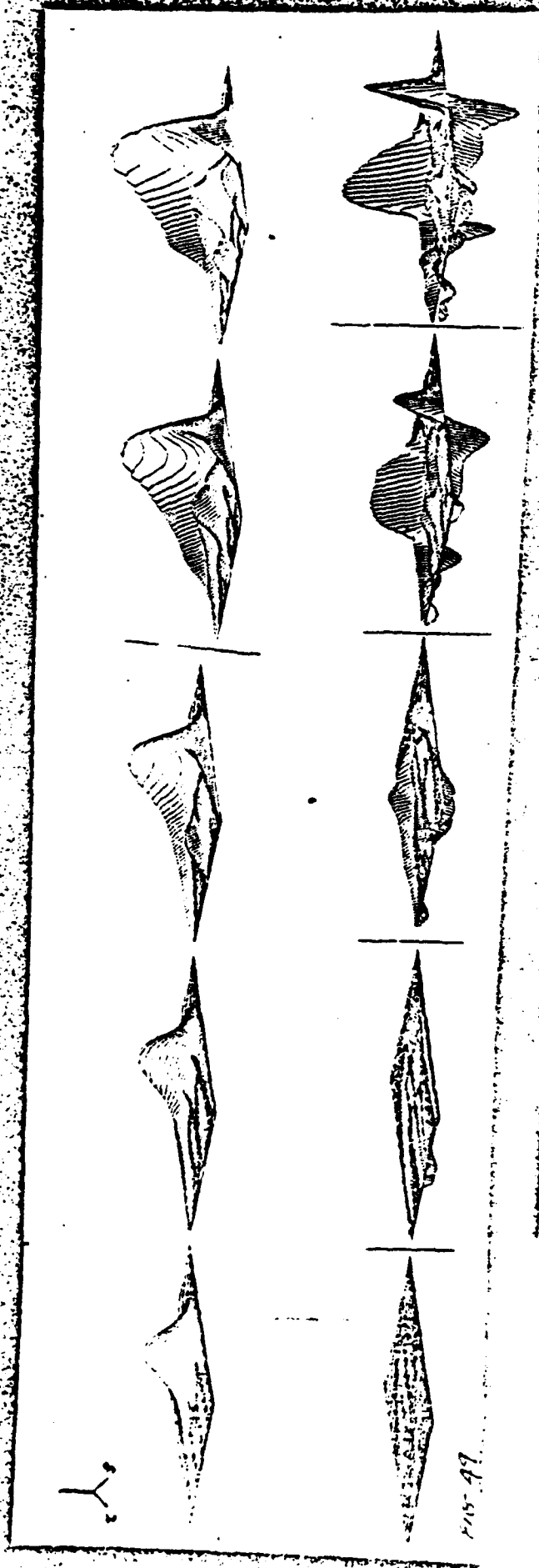


Figure 49 Isometric plots of the amplifier field energy and transverse energy flow profile for various time slices at the four regions of interest.



Figure 50 Amplifier field energy contour plots for the four propagation regions of interest. Notice the temporal advance associated with the coherent exchange of energy between light and matter, as well as the beam cross-section narrowing.

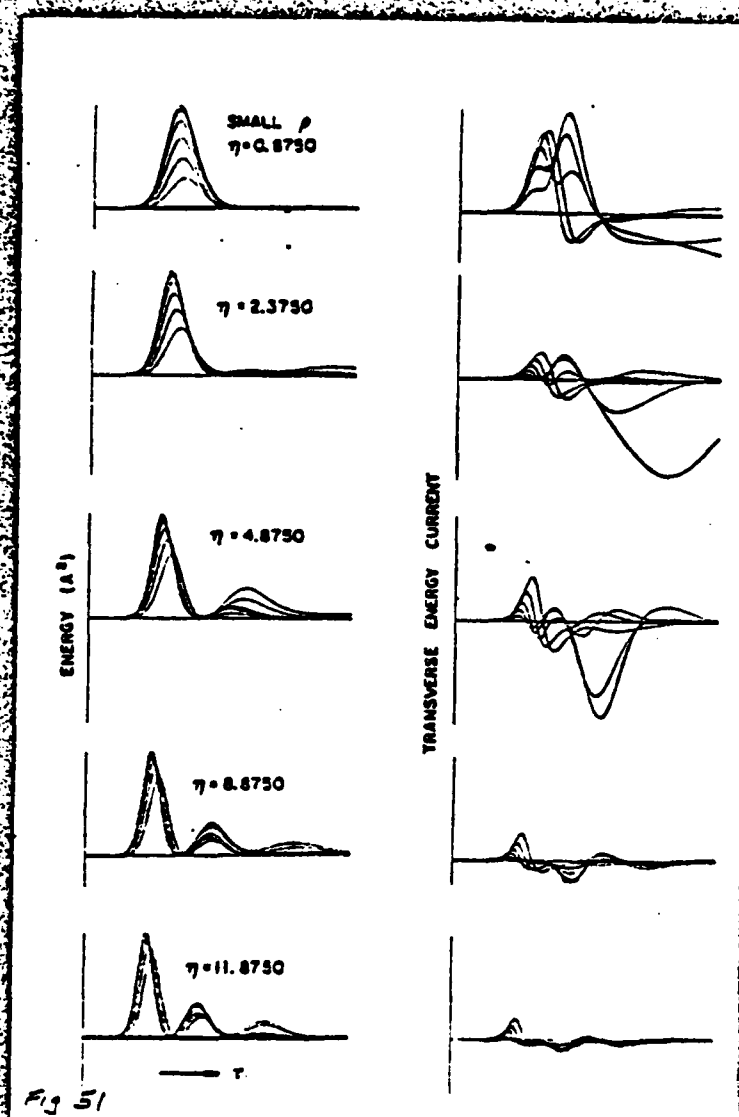


Fig 51

Figure 51 Longitudinal projection of amplifier energy field amplitude and transverse current for near-axis (small) radii at the four critical regions, with stretched radial coordinate for proper accounting of the transverse boundary condition.

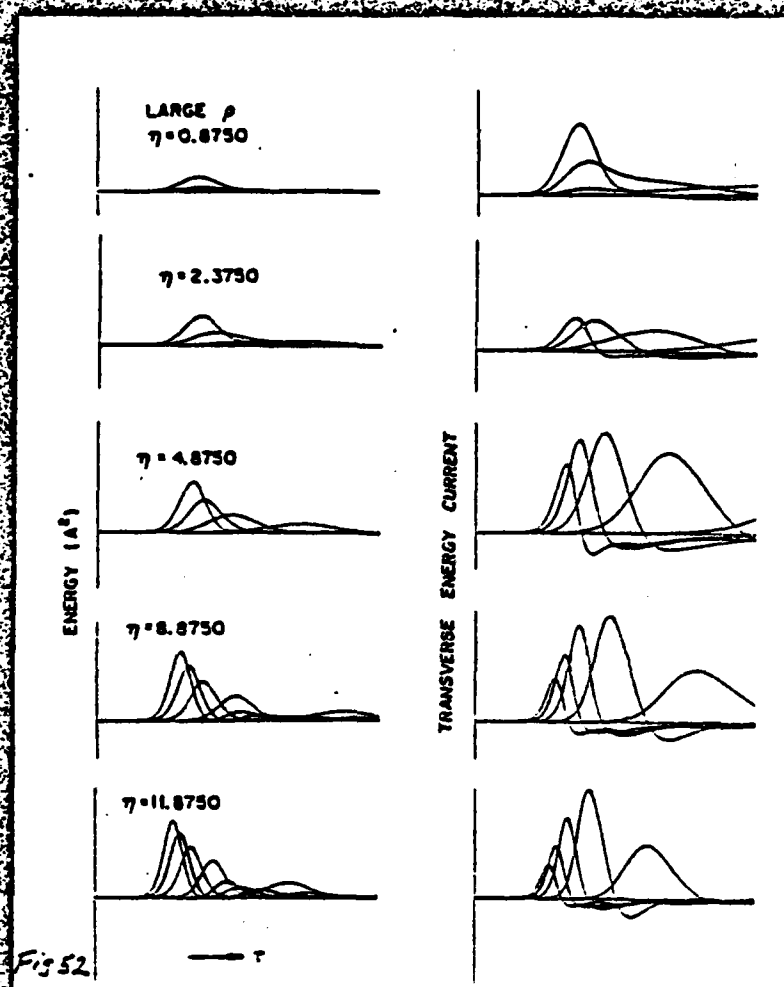


Figure 52 Longitudinal projection of amplifier energy field amplitude for large (off-axis) radii at the four critical regions, with stretched radial coordinate for proper accounting of the transverse boundary condition.

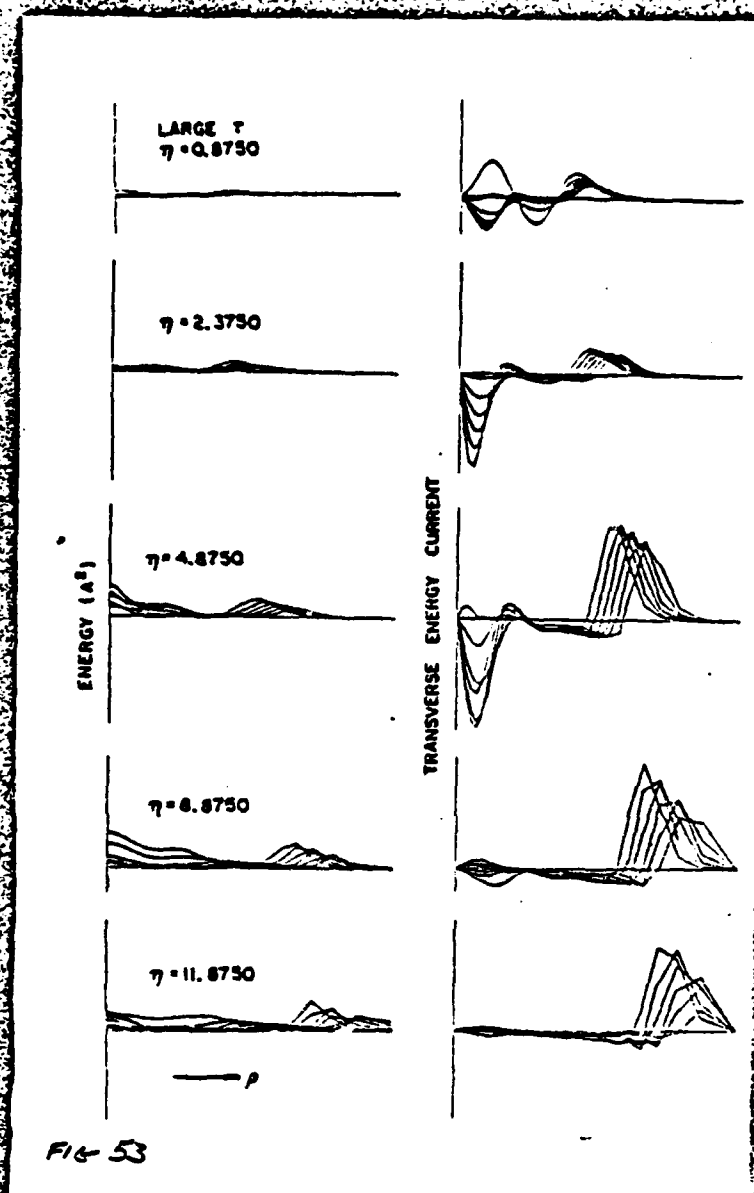


Figure 53 The profile of amplifier energy field amplitude and transverse energy current for small slices of time (in the front of the pulse) at the four critical propagation regions of interest, with stretched radial coordinate for proper accounting of the transverse boundary condition.

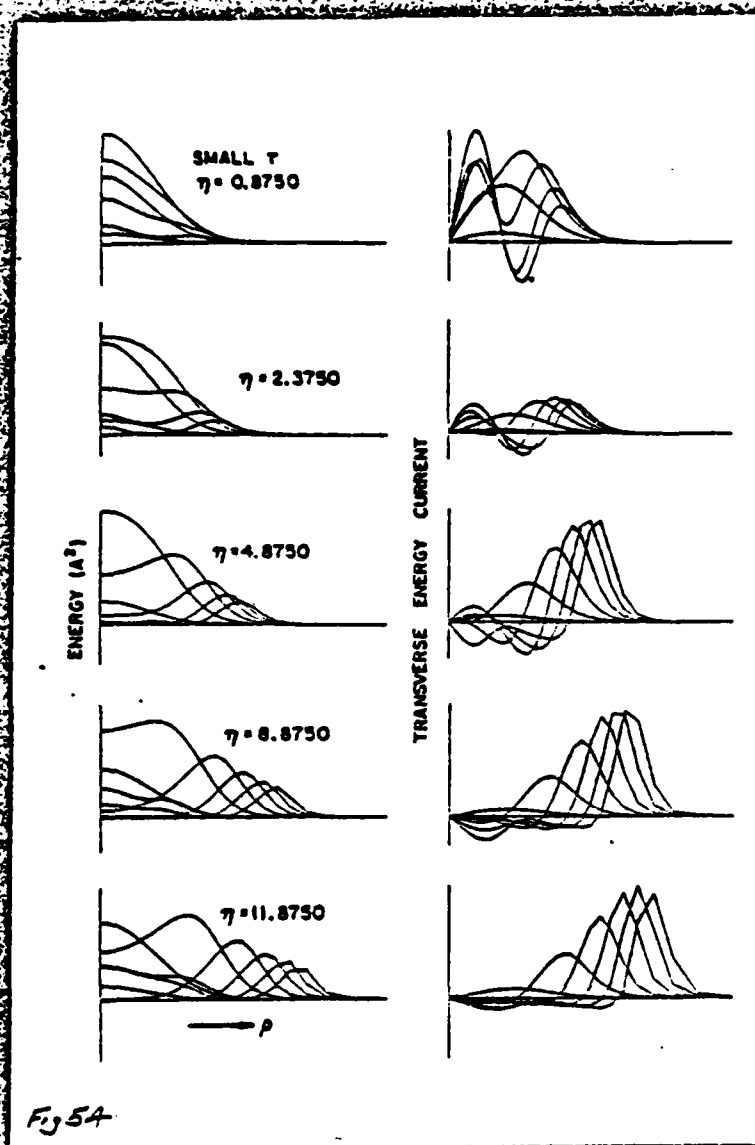
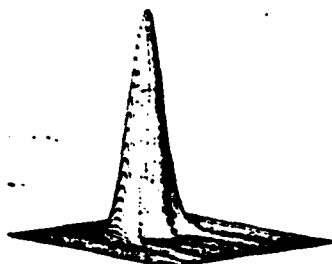
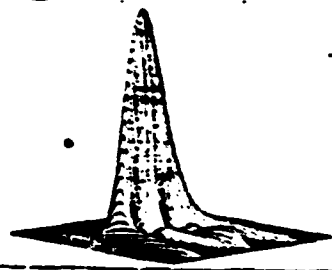
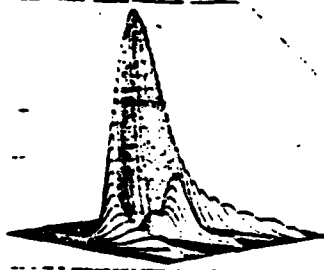
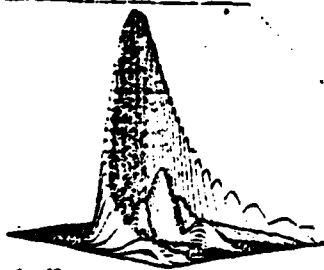
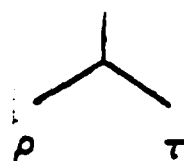
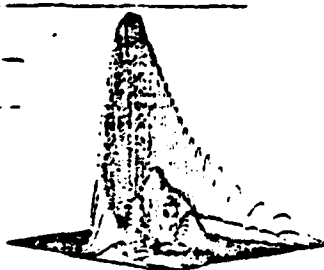
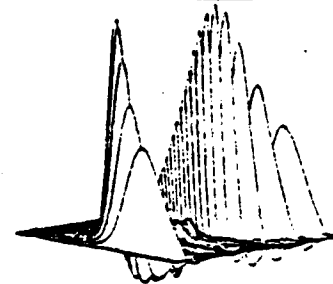
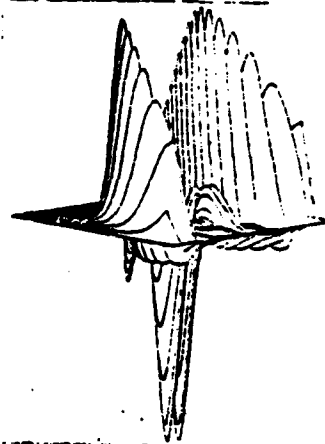
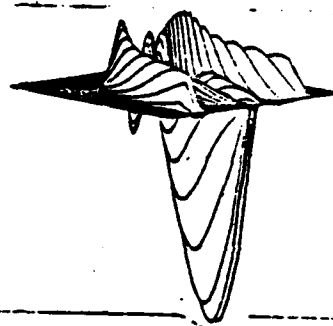
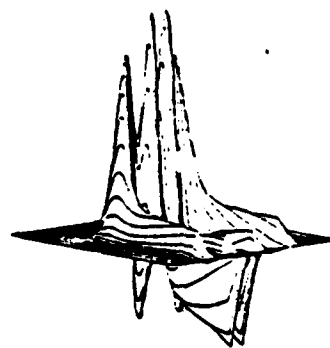


Figure 54 The profile of amplifier energy amplitude and transverse energy current for large slices of time (in the trailing edge of the pulse) at the four critical propagation regions of interest, with stretched radial coordinate for proper accounting of the transverse boundary condition.

ENERGY (A)

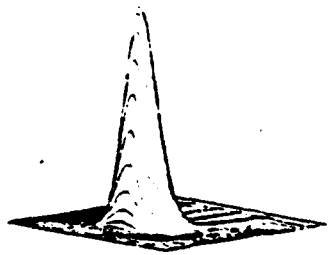
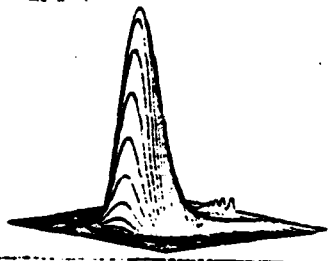
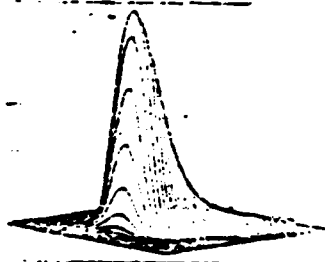
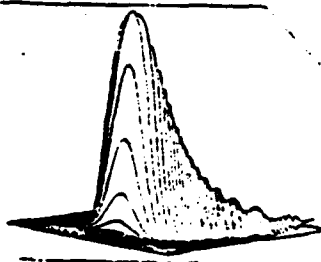
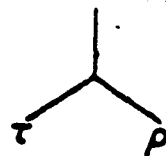
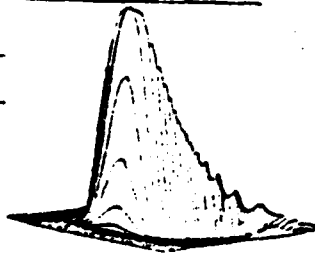
 $\eta = 0.8750$  $\eta = 2.3750$  $\eta = 4.8750$  $\eta = 8.8750$  $\eta = 11.8750$ 

TRANSVERSE ENERGY CURRENT

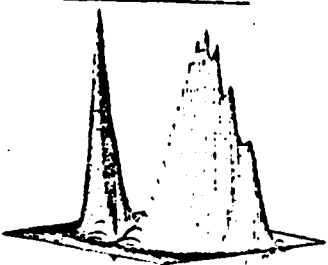
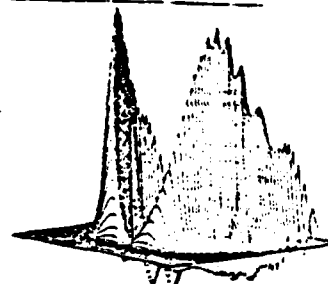
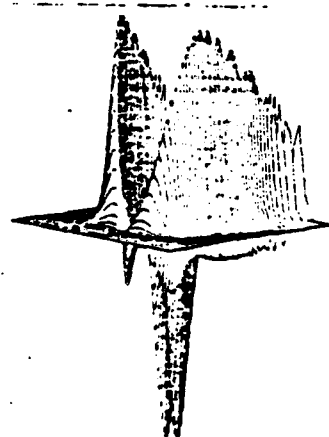
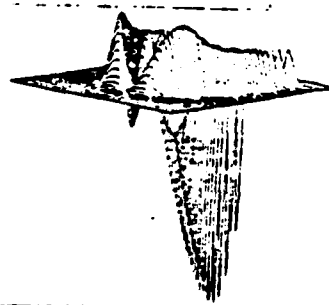
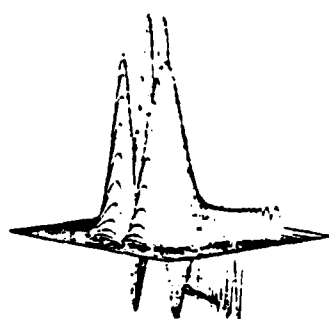


ETA	TPOYIN		ENERGY	
	YMAX	YMIN	YMAX	YMIN
0.8750	0.1212	-0.0524	3.2780	0.0
2.3750	0.6170	-1.6608	3.8555	0.0
4.8750	3.0621	-3.3117	5.1225	0.0
8.8750	15.0163	-3.1394	7.0939	0.0
11.8750	30.3785	-5.0060	8.3751	0.0

Figure 55 Isometric plots of the amplifier field energy and transverse energy flow, against the retarded time for various transverse coordinates at four regions: (a) reshaping, (b) build-up region, (c) focal region, (d) post-focal region, with stretched radial coordinate for proper accounting of the transverse boundary condition.

$\eta = 0.8750$  $\eta = 2.3750$  $\eta = 4.8750$  $\eta = 8.8750$  $\eta = 11.8750$ 

TRANSVERSE ENERGY CURRENT



ETA	TPOYIN		ENERGY	
	YMAX	YMIN	YMAX	YMIN
0.8750	0.1212	-0.0524	3.2780	0.0
2.3750	0.5170	-1.6608	3.8555	0.0
4.8750	3.0621	-3.3117	5.1225	0.0
8.8750	15.0163	-3.1394	7.0939	0.0
11.8750	30.3785	-5.0060	8.3751	0.0

Figure 56 Isometric plots of the amplifier field energy and transverse energy flow profile for various time slices at the four regions of interest, with stretched radial coordinate for proper accounting of the transverse boundary condition. No severe reflection or abrupt variation in the field energy, at the wall boundary, is observed.

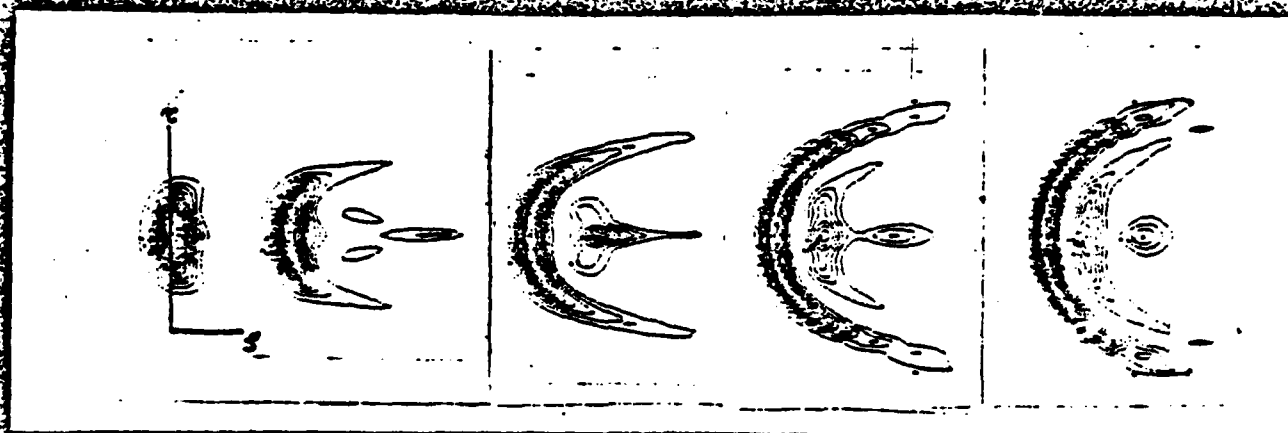


Figure 57 Amplifier field energy contour plots for the four propagation regions of interest. Notice the temporal advance associated with the coherent exchange of energy between light and matter, as well as the beam cross-section narrowing, with stretched radial coordinate for proper accounting of the transverse boundary condition. No severe reflection or abrupt variation in the field energy, at the wall boundary, is observed.

Figure 58 Status of joint effort, Fall 1973, between theory & experiment

SIT calculations	Proposed Sodium Experiment
$P = 1.98 \times 10^{-3}$	$P = 1.98 \times 10^{-3}$ chosen because calculations show that this is good for transient white-beam self-focusing
$\lambda = 10 \text{ cm.}$	$\lambda = 0.05 \times 10^{-3} \text{ (S beam)}$
$P_0 = 1 \text{ cm.}$	$P_0 = 0.005 \text{ cm. (from } g_0^2 = \frac{\lambda^2 d^2 \text{ off}}{4\pi^2} \text{)}$
$d_{\text{off}} = (1/20) \text{ cm.}^{-1}$	$d_{\text{off}} = \frac{d_{\text{off}}^2}{L} = \frac{8}{0.5} = 16$
Focus occurs at $L=0$	$d_{\text{off}} = 16$ chosen because focus occurs there and because one can't go much beyond $d_{\text{off}} L=10$
$L = 160 \text{ cm.}$	$L=0.5 \text{ cm. length of the experimental tube.}$

Situation:

When inhomogeneous broadening due to this choice of parameters is hard to say. Gibbs and Belger [119: 1976] 3000. These pulses through SIT reshaping give laser pulse, i.e., a 125 MHz wide pulse in a 2000MHz wide absorber. Surely, the coherent self-focusing effect would still be there, but the question is to what degree? Therefore, one must assess by a few set of calculations — this time in the broad line regime — if this experiment would work or not. When using circularly polarized light in high field ($M = -1/2, M = 1/2, M = 3/2, M = 5/2$), one is faced with four M transitions, which are about 400MHz apart. So one would not be in the center of a single transition, but in the center of four transitions. Still on the average, the atomic sodium vapor should look like a simple inhomogeneous broad line, since M is another form of inhomogeneous broad line in this context.

Fig 50

Figure 58 Choice of parameters of the proposed sodium experiment and related discussion prior to carrying out the experiment.

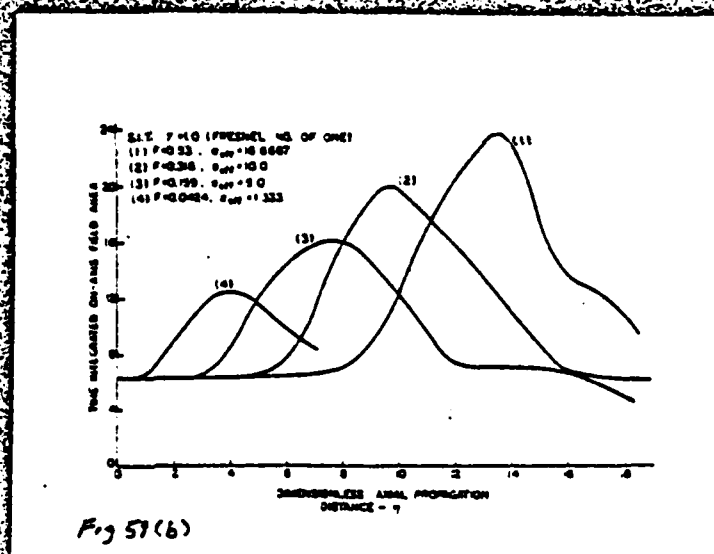
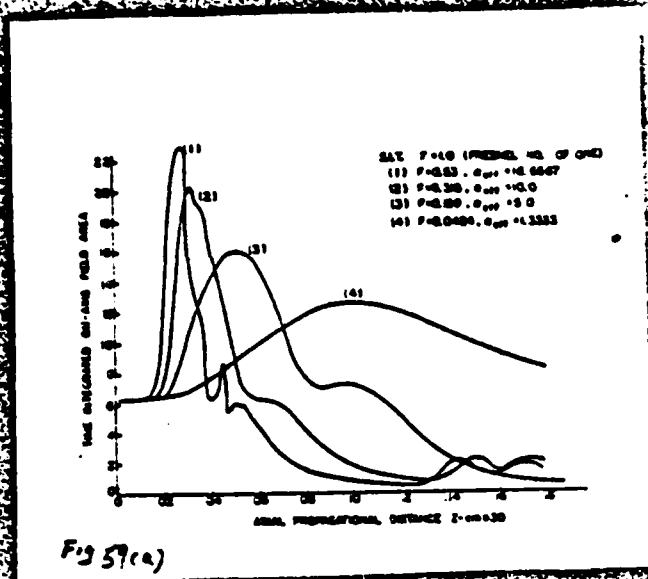


Figure 59 Self-induced-transparency for a unity Fresnel number ($F=1$): On-axis time-integrated area under the electric field as a function of the propagation distance [(a) in physical centimeters; (b) in normalized coordinate to α^{-1}] for different effective absorption lengths.

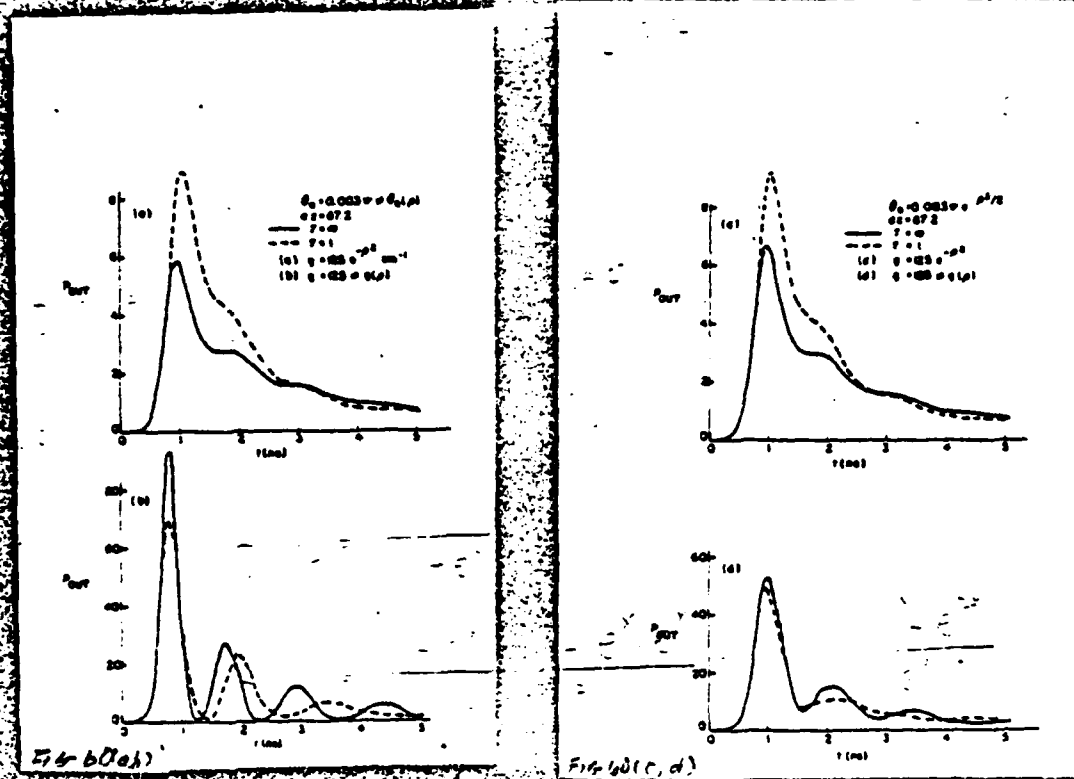


Figure 60 Super-fluorescence in a pre-excited medium for uniform plane wave and for non-planar wave with unity Fresnel number: Output power (averaged across the beam area) buildup over an axial distance of $L=87.2$ from an initial tipping angle θ_{eff}

$\theta=0.00037$ graph (a) contrast the situation of a uniform plane wave $F=0$ and $F=1$ with a radially dependent gain. In graph (b) the gain is radially independent while the tipping angle has a Gaussian profile. Graph (c) and graph (d) respectively share the physical situation of graphs (a) and (b) but with an additional radial dependence on the tipping angle.

$$\partial_{\tau} u_c = (\Delta_a + \Delta_b) v_c - u_c / \tau_{2ab} - \frac{1}{2}(X_a v_b + Y_a u_b) + \frac{1}{2}(X_b v_a + Y_b u_a)$$

$$\partial_{\tau} v_c = -(\Delta_a + \Delta_b) u_c - v_c / \tau_{2ab} + \frac{1}{2}(X_a u_b - Y_a v_b) - \frac{1}{2}(X_b u_a - Y_b v_a)$$

Perturbation:

e_a strong beam; e_b weak beam $|e_b| \ll |e_a|$

$$X_b + iY_b = e(\alpha + i\beta)(X_a + iY_a) = e(\alpha X_a - \beta Y_a) + ie(\beta X_a + \alpha Y_a)$$

where $e \ll 1$; α, β, e real; $\alpha, \beta, e > 0$

$(\alpha + i\beta)$ the polarization constant

Then

$$X_a = X_{a0} + eX_{a1} + e^2 X_{a2} + \dots$$

$$Y_a = Y_{a0} + eY_{a1} + e^2 Y_{a2} + \dots$$

$$X_b = \quad + eY_{b1} + e^2 X_{b2} + \dots$$

$$Y_b = \quad + eY_{b1} + e^2 Y_{b2} + \dots$$

$$u_a = u_{a0} + eu_{a1} + e^2 u_{a2} + \dots$$

$$v_a = v_{a0} + ev_{a1} + e^2 v_{a2} + \dots$$

$$u_b = \quad + eu_{b1} + e^2 u_{b2} + \dots$$

$$v_b = \quad + ev_{b1} + e^2 v_{b2} + \dots$$

$$u_c = \quad + eu_{c1} + e^2 u_{c2} + \dots$$

$$v_c = \quad + ev_{c1} + e^2 v_{c2} + \dots$$

$$W_a = W_{a0} + eW_{a1} + e^2 W_{a2} + \dots$$

$$W_b = \quad + eW_{a2} + e^2 W_{b2} + \dots$$

Zero order e^0

(single stream S.I.T.)

$$\partial_{\eta} X_{ao} + F \nabla_T^2 Y_{ao} = g_a u_{ao}$$

$$\partial_{\eta} Y_{ao} - F \nabla_T^2 X_{ao} = g_a v_{ao}$$

$$\partial_{\tau} u_{ao} = X_{ao} W_{ao} + \Delta_a v_{ao} - u_{ao}/\tau_{2a}$$

$$\partial_{\tau} v_{ao} = Y_{ao} W_{ao} - \Delta_a u_{ao} - v_{ao}/\tau_{2a}$$

$$\partial_{\tau} W_{ao} = -(X_{ao} u_{ao} + Y_{ao} v_{ao}) - (W_a - W_a^0)/\tau_{1a}$$

First order e^1

$$\partial_{\eta} X_{a1} + F \nabla_T^2 Y_{a1} = g_a u_{a1}$$

$$\partial_{\eta} Y_{a1} - F \nabla_T^2 X_{a1} = g_a v_{a1}$$

$$\partial_{\eta} X_{b1} + F \nabla_T^2 Y_{b1} = g_b u_{b1}$$

$$\partial_{\eta} Y_{b1} - F \nabla_T^2 X_{b1} = g_b v_{b1}$$

$$\partial_{\tau} u_{a1} = X_{a1} W_{ao} + X_{ao} W_{a1} + \Delta_a v_{a1} - u_{a1}/\tau_{2a}$$

$$\partial_{\tau} v_{a1} = Y_{a1} W_{ao} + Y_{ao} W_{a1} + \Delta_a u_{a1} - v_{a1}/\tau_{2a}$$

$$\partial_{\tau} W_{a1} = -(X_{ao} u_{a1} + X_{a1} u_{ao} + Y_{ao} v_{a1} + Y_{a1} v_{ao}) - (W_{a1} - W_{a1}^0)/\tau_{1a}$$

$$\partial_{\tau} u_{b1} = \Delta_b v_{b1} - \frac{1}{2} (X_{ao} u_{c1} + Y_{ao} v_{c1}) - u_{b1}/\tau_{2b}$$

$$\partial_{\tau} v_{b1} = -\Delta_b u_{b1} - \frac{1}{2} (X_{ao} v_{c1} - Y_{ao} u_{c1}) - v_{b1}/\tau_{2b}$$

$$\partial_{\tau} W_{b1} = \frac{1}{2} (X_{ao} u_{a1} + X_{a1} u_{ao} + Y_{ao} v_{a1} + Y_{a1} v_{ao}) - (W_{b1} - W_{b1}^0)/\tau_{1b}$$

$$\begin{aligned}\partial_{\tau} u_{c1} &= (\Delta_a + \Delta_b) v_{c1} - u_{c1}/\tau_{2ab} - \frac{1}{2} (X_{ao} v_{b1} + Y_{ao} u_{b1}) \\ &+ \frac{1}{2} [(\alpha X_{ao} - \beta Y_{ao}) v_{ao} + (\beta X_{ao} + \alpha Y_{ao}) u_{ao}]\end{aligned}$$

$$\begin{aligned}\partial_{\tau} v_{c1} &= -(\Delta_a + \Delta_b) u_{c1} - v_{c1}/\tau_{2ab} + \frac{1}{2} (X_{ao} u_{b1} - Y_{ao} v_{b1}) \\ &- \frac{1}{2} [(\alpha X_{ao} - \beta Y_{ao}) u_{ao} - (\beta X_{ao} + \alpha Y_{ao}) v_{ao}]\end{aligned}$$

$$\text{with } w_{a1}^0 = w_{b1}^0 = 0$$

Second Order ε^2 :

$$\partial_{\eta} X_{a2} + F \nabla_T^2 Y_{a2} = g_a u_{a2}$$

$$\partial_{\eta} Y_{a2} - F \nabla_T^2 X_{a2} = g_a v_{a2}$$

$$\partial_{\eta} X_{b2} + F \nabla_T^2 Y_{b2} = g_b u_{b2}$$

$$\partial_{\eta} Y_{b2} - F \nabla_T^2 X_{b2} = g_b v_{b2}$$

$$\begin{aligned}\partial_{\tau} u_{a2} &= (X_{ao} W_{a2} + X_{a1} W_{a1} + X_{a2} W_{ao}) + \Delta_a v_{a2} - (u_{a2}/\tau_{2a}) \\ &+ \frac{1}{2} (X_{b1} u_{c1} + Y_{b1} v_{c1}) = (X_{ao} W_{a2} + X_{a1} W_{a1} + X_{a2} W_{ao}) \\ &+ \Delta_a v_{a2} - (u_{a2}/\tau_{2a}) + \frac{1}{2} (\alpha X_{ao} - \beta Y_{ao}) u_{c1} - \frac{1}{2} (\beta X_{ao} + \alpha Y_{ao}) v_{c1}\end{aligned}$$

$$\begin{aligned}\partial_{\tau} v_{a2} &= (Y_{ao} W_{a2} + Y_{a1} W_{a1} + Y_{a2} W_{ao}) - \Delta_a u_{a2} - (v_{a2}/\tau_{2a}) \\ &+ \frac{1}{2} (X_{b1} v_{c1} - Y_{b1} u_{c1}) = (Y_{ao} W_{a2} + Y_{a1} W_{a1} + Y_{a2} W_{ao}) \\ &+ \Delta_a u_{a2} - (v_{a2}/\tau_{2a}) + \frac{1}{2} (\alpha X_{ao} - \beta Y_{ao}) v_{c1} - \frac{1}{2} (\beta X_{ao} + \alpha Y_{ao}) u_{c1}\end{aligned}$$

$$\begin{aligned}\partial_{\tau} W_{a2} &= - (X_{a2} u_{ao} + X_{a1} u_{a1} + X_{ao} u_{a2} + Y_{a2} v_{ao} + Y_{a1} v_{a1} + Y_{ao} v_{a2}) \\ &+ \frac{1}{2} (\alpha X_{ao} - \beta Y_{ao}) u_{b1} + \frac{1}{2} (\beta X_{ao} + \alpha Y_{ao}) v_{b1} - [W_{a2}/\tau_{1a}]\end{aligned}$$

$$\begin{aligned}\partial_{\tau} u_{c2} &= (\alpha X_{ao} - \beta Y_{ao}) W_{b1} + \Delta_b v_{b2} - [v_{b2}/\tau_{2b}] \\ &- \frac{1}{2} [X_{ao} u_{c2} + X_{a1} u_{c1} + Y_{ao} v_{c2} + Y_{a1} v_{c1}]\end{aligned}$$

$$\begin{aligned}\partial_{\tau} v_{c2} &= (\beta X_{ao} + \alpha Y_{ao}) w_{b1} - \Delta_b u_{b2} - [v_{b2}/\tau_{2b}] \\ &- \frac{1}{2}(X_{ao} v_{c2} + X_{a1} v_{c1} - Y_{ao} u_{c2} - Y_{a1} u_{c1})\end{aligned}$$

$$\begin{aligned}\partial_{\tau} w_{b2} &= - [(\alpha X_{ao} - \beta Y_{ao}) u_{b1} + (\beta X_{ao} + \alpha Y_{ao}) v_{b1}] - (w_{b2}/\tau_{1b}) \\ &+ \frac{1}{2}[(X_{a2} u_{ao} + X_{a1} u_{a1} + X_{ao} u_{a2}) + (Y_{a2} v_{ao} + Y_{a1} v_{a1} + Y_{ao} v_{a2})]\end{aligned}$$

$$\begin{aligned}\partial_{\tau} u_{c2} &= (\Delta_a + \Delta_b) v_{c2} - u_{c2}/\tau_{2ab} - \frac{1}{2}[(X_{ao} v_{b2} + X_{a1} v_{b1}) \\ &+ (Y_{ao} u_{b2} + Y_{a1} u_{b1})] + \frac{1}{2}(\alpha X_{ao} - \beta Y_{ao}) v_{a1} + \frac{1}{2}(\beta X_{ao} + \alpha Y_{ao}) u_{a1}\end{aligned}$$

$$\begin{aligned}\partial_{\tau} v_{c2} &= - (\Delta_a + \Delta_b) u_{c2} - [v_{c2}/\tau_{2ab}] + \frac{1}{2}[(X_{ao} u_{b2} + X_{a1} u_{b1}) \\ &- (Y_{ao} v_{b2} + Y_{a1} v_{b1})] - \frac{1}{2}(\alpha X_{ao} - \beta Y_{ao}) u_{a1} \\ &+ \frac{1}{2}(\beta X_{ao} + \alpha Y_{ao}) v_{a1}\end{aligned}$$

UNIFORM PLANE SITUATION

2 lasers

$$\begin{array}{c} e_a \xrightarrow{\quad \epsilon_1 \quad} \\ \quad \downarrow \quad w_a \\ e_b \xrightarrow{\quad \epsilon_2 \quad} \\ \quad \downarrow \quad w_b \\ \quad \quad \quad \epsilon_3 \end{array}$$

$$\begin{array}{c} e_{a,b}, \quad P_{a,b}, \quad W_{ab} \\ \text{B.C.} \quad e_{a,b}, \quad P_{a,b} \rightarrow 0 \quad \tau \rightarrow \infty \end{array}$$

$$W_{a,b} \rightarrow W_{a,b}^{(0)} = (\text{const.}) \quad \tau \rightarrow \infty$$

with infinite relaxation time

$$\partial_\eta e_{a,b} = g_{a,b} P_{a,b} \quad (g_{a,b} \text{ real constants}) \quad (\text{A})$$

$$\partial_\tau P_a = e_a W_a - \frac{i}{2} e_B^* Q \quad (\text{B})$$

$$\partial_\tau P_b = e_b W_b + \frac{i}{2} e_B^* Q$$

$$\partial_\tau Q = \frac{i}{2} (e_a P_b - P_a e_b) \quad (\text{C})$$

$$\partial_\tau W_a = -\frac{1}{2}(e_a^* P_a + e_a P_a^*) + \frac{1}{4}(e_b^* P_b + P_b^* e_b) \quad (\text{D})$$

$$\partial_\tau W_b = -\frac{1}{2}(e_b^* P_b + e_b P_b^*) + \frac{1}{4}(e_a^* P_a + P_a^* e_a)$$

I. Real Solution

$$e_{a,b}, \quad P_{a,b}, \quad Q = i\phi$$

for steady-state solution assume

$$E_{a,b} = \alpha_{a,b} \text{sech}(K_1 \xi_1) \quad \text{with} \quad \xi_1 = \tau - \lambda_1 \eta$$

using (A), (D), we get

$$g_{a,b} P_{a,b} = K_1 \lambda_1 \alpha_{a,b} \text{sech}(K_1 \xi_1) \tanh(K_1 \xi_1)$$

$$W_{a,b} = W_{a,b}^{(0)} + \frac{\lambda}{2} \beta_{a,b} \text{sech}^2 K_1 \xi_1 \quad (\text{D}')$$

where $\beta_{a,b} = \frac{\alpha_{a,b}^2}{g_{a,b}} - \frac{\alpha_{b,a}^2}{2g_{b,a}}$

From (C) we assume $Q = i\Phi$

$$\Phi = \Gamma_1 \operatorname{sech}^2 K_1 \xi_1 + \Gamma_2$$

and get

$$\begin{aligned} & \frac{-2\Gamma_1 K_1 \operatorname{sech}^2 K_1 \xi_1 \tanh K_1 \xi_1}{\lambda_1 K_1^2 \frac{\alpha_a}{g_a} = \alpha_a W_a^{(0)} + \frac{1}{2} \alpha_b \Gamma_2} \\ & = \frac{\lambda_1 K_1}{2} \alpha_a \alpha_b \left(\frac{1}{g_b} - \frac{1}{g_a} \right) \operatorname{sech}^2 (K_1 \xi_1) \tanh (K_1 \xi_1) \\ \Rightarrow & \Gamma_1 = (\lambda_1/4) \alpha_a \alpha_b \left(\frac{1}{g_b} - \frac{1}{g_a} \right) \end{aligned} \quad (1)$$

From (B1)

$$-\lambda_1 K_1^2 \frac{\alpha_a}{g_a} = \alpha_a W_a^{(0)} + \frac{1}{2} \alpha_b \Gamma_2 \quad (2)$$

$$2\lambda_1 K_1^2 \frac{\alpha_a}{g_a} = \frac{\lambda_1}{2} \alpha_a \cdot \beta_a + \frac{1}{2} \alpha_b \Gamma_1 \quad (3)$$

From (B2)

$$-\lambda_1 K_1^2 \frac{\alpha_b}{g_b} = \alpha_b W_b^{(0)} - \frac{1}{2} \alpha_a \Gamma_2 \quad (4)$$

$$2\lambda_1 K_1^2 \frac{\alpha_b}{g_b} = \frac{\lambda_1}{2} \alpha_b \cdot \beta_b - \frac{1}{2} \alpha_a \Gamma_1 \quad (5)$$

$K_1, \lambda_1, \alpha_a, \alpha_b, \Gamma_1, \Gamma_2$ 6 parameters

5 equations = > so one parameter, say K_1 is free.

Note: By combining (3) and (5) get Γ_1 and comparing with (1) one obtains:

$$\frac{\alpha_b^2}{g_b} + \frac{\alpha_a^2}{g_a} \quad (\text{unless } g_a = -g_b)$$

II. Complex Solution

Assume:

$$e_{a,b} = \alpha_{a,b} \operatorname{sech} K_1 \xi_1 \exp[\mp i K_2 \xi_2]$$

Using A

$$g_{a,b} P_{a,b} = \alpha_{a,b} [\lambda_1 K_1 \operatorname{sech} K_1 \xi_1 \tanh K_1 \xi_1 \pm i K_2 \lambda_2 \operatorname{sech} [K_1 \xi_1] \exp [\mp i K_2 \xi_2]]$$

Using D, A

$$w_{a,b} = w_{a,b}^{(0)} + \frac{\lambda_1}{2} \beta_{a,b} \operatorname{sech}^2 K_1 \xi_1$$

From (C) one can assume

$$Q = i[\Gamma_1 \operatorname{sech}^2 K_1 \xi_1 + \Gamma_2] + \Gamma_3 \tanh K_1 \xi_1$$

Consistency conditions (using B and C):

$$\alpha_a \alpha_b \lambda_1 \left(\frac{1}{g_b} - \frac{1}{g_a} \right) = -4\Gamma_1 \quad (1)$$

$$\alpha_a \alpha_b \lambda_1 K_2 \left(\frac{1}{g_b} - \frac{1}{g_a} \right) = 2\Gamma_3 K_1 \quad (2)$$

$$\frac{\alpha_a}{g_a} (\lambda_1 + \lambda_2) K_1 K_2 = \frac{\alpha_b}{2} \Gamma_3 \quad (3)$$

$$\frac{\alpha_a}{g_a} (K_2^2 \lambda_2 - K_1^2 \lambda_1) = \alpha_a W_a^{(0)} + \frac{\alpha_b}{2} \Gamma_2 \quad (4)$$

$$\frac{\alpha_a}{g_a} \cdot (2\lambda_1 K_1^2) = \frac{\alpha_a \lambda_1}{2} \left[\frac{\alpha_a^2}{g_a} - \frac{\alpha_b^2}{2g_b} \right] + \frac{\alpha_b}{2} \Gamma_1 \quad (5)$$

$$(\lambda_1 + \lambda_2) K_2 K_1 \frac{\alpha_b}{g_b} = \frac{\alpha_a}{2} \Gamma_3 \quad (6)$$

$$\frac{\alpha_b}{g_b} (\lambda_2 K_2^2 - \lambda_1 K_1^2) = \alpha_b W_b^{(0)} - \frac{\alpha_a}{2} \Gamma_2 \quad (7)$$

$$\frac{\alpha_b}{g_b} \cdot (2\lambda_1 K_1^2) = \frac{\alpha_b \lambda_1}{2} \left[\frac{\alpha_b^2}{g_b} - \frac{\alpha_a^2}{2g_a} \right] + \frac{\alpha_a}{2} \Gamma_1 \quad (8)$$

Note: From (3) and (6), one gets as for the situation of real solutions

$$\frac{\frac{\alpha_b^2}{g_b} + \frac{\alpha_a^2}{g_a}}{\quad} \quad (\text{unless } g_a = -g_b) \quad (9)$$

Here instead we have 9 parameters:

$$\alpha_a, \alpha_b, \lambda_1, \lambda_2, K_1, K_2, \Gamma_1, \Gamma_2, \Gamma_3$$

and 8 equations. We expect to have two free parameters, hence 2 equations must be equivalent.

Indeed from (1) = >

$$\Gamma_1 = - \frac{\alpha_a \alpha_b \lambda_1}{4} \left(\frac{1}{g_b} - \frac{1}{g_a} \right) \quad (10)$$

And combining (5) and (8): , (using (q)) we get the same equation.

$$\Gamma_1 = - \frac{\alpha_a \alpha_b \lambda_1}{4} \left(\frac{1}{g_b} - \frac{1}{g_a} \right) \quad (10)$$

So we can discard either (5) or (8) and hence we have 7 equations and 9 parameters \Rightarrow 2 free parameters correspond to complex solution. Namely,

K_1, K_2 are free parameters.

If $K_2=0$ then the solution tends to real solution as before.

Physically this solution may be explained as two pendulum coupled to each other. At some point, levels are excited by each other.

By simplifying, one gets:

$$4K_1 = \frac{\alpha_a^2 + \alpha_b^2}{4}$$

$$\Gamma_1 = - \frac{\lambda_1 \alpha_a \alpha_b}{4} \left(\frac{1}{g_b} - \frac{1}{g_a} \right)$$

$$\lambda_2 = \frac{\lambda_1 + \lambda_2}{4} \Rightarrow \underline{\underline{3\lambda_2 = \lambda_1}}$$

$$\Gamma_3 = 8\lambda_2 K_1 K_2 \cdot \frac{\alpha_a}{\alpha_b \cdot g_a}$$

$$\frac{\alpha_a}{g_a} \cdot \frac{g_b}{\alpha_b} = \frac{\alpha_a W_a^{(0)} + \frac{\alpha_b}{2} \Gamma_2}{\alpha_a W_a^{(0)} + \frac{\alpha_b}{2} \Gamma_2}$$

$$\Gamma_2 = \frac{2\alpha_a}{\alpha_b g_a} (K_2^2 \lambda_2 - K_1^2 \lambda_1) - \frac{2\alpha_a}{\alpha_b} W_a^{(0)}$$

$$\frac{\alpha_a^2}{g_a} = \frac{\alpha_b^2}{g_b}$$

Note that if $K_2=0 \Rightarrow \Gamma_3=0$

Summary

$$\partial_{\eta} e_{a,b} = g_{a,b} P_{a,b}$$

$$\partial_{\tau} P_a = e_a W_z - \frac{1}{2} e_b^* Q$$

$$\partial_{\tau} P_b = e_b W_z - \frac{1}{2} e_a^* Q$$

$$\partial_{\tau} Q = \frac{1}{2} (e_a P_b - e_b P_a)$$

$$\partial_{\tau} W_a = -\frac{1}{2} (e_a^* P_a + e_a P_a^*) + \frac{1}{4} (e_b^* P_b + e_b P_b^*)$$

$$\partial_{\tau} W_b = -\frac{1}{2} (e_b^* P_b + e_b P_b^*) + \frac{1}{4} (e_a^* P_a + e_a P_a^*)$$

Conservation Laws:

$$\partial_{\tau} \{ |P_a|^2 + |P_b|^2 + |Q|^2 + \frac{4}{3} (W_a^2 + W_a W_b + W_b^2) \} = 0$$

$$\partial_{\eta} |e_a|^2 + \frac{4}{3} g_a \partial_{\tau} (2W_a + W_b) = 0$$

$$\partial_{\eta} |e_b|^2 + \frac{4}{3} g_b \partial_{\tau} (2W_b + W_a) = 0$$

Consider Real solution

$$e_{a,b}, \quad P_{a,b}, \quad Q = i\phi, \quad W_{a,b}$$

From the previous note, the steady propagating solution has the property

$$\frac{E_a^2}{g_a} + \frac{E_b^2}{g_b} = \text{constant}$$

This implies $W_a = W_b$.

So if we apply $W_a = W_b \equiv W$, (or $e_a P_a = e_b P_b$) then defining

$$\begin{aligned} e_a &\equiv \sqrt{g_a} e, & e_b &\equiv \sqrt{g_b} e \\ P_a &\equiv \sqrt{g_b} P, & P_b &\equiv \sqrt{g_a} P \end{aligned} \quad (\text{consistent})$$

one can reduce the original equations to

$$\partial_{\eta} e = \sqrt{g_a g_b} e$$

$$\partial_{\tau} P = \frac{1}{2} \frac{g_a + g_b}{\sqrt{g_a g_b}} W e$$

$$\partial_{\tau} W = - \frac{1}{2} \sqrt{g_a g_b} e P$$

This is equivalent to a single laser problem.

From the conservation laws:

$$P^2 + \frac{g_a + g_b}{g_a g_b} W^2 = \text{const.}$$

Define

$$\begin{aligned} P &\equiv P_0 \sin \phi \\ W &\equiv W_0 \cos \phi \end{aligned} \quad \rightarrow \quad P_0^2 = \frac{g_a + g_b}{g_a g_b} W_0^2$$

$$\frac{\partial^2 \phi}{\partial \tau \partial \eta} = \alpha \sin \phi : \quad \text{Sine-Gordon eq.}$$

$$\alpha \equiv \frac{1}{2} (g_a + g_b) W_0$$

Complex case: If one applies $W_a = W_b = W$

$$\Rightarrow \text{i.e., } e_a^* P_a + e_a P_a^* = e_b^* P_b + e_b P_b^*$$

and then define

$$\begin{aligned} e_a &= \sqrt{g_a} e, & e_b &= \sqrt{g_b} e \\ P_a &= \sqrt{g_a} P, & P_b &= \sqrt{g_a} P \end{aligned} \quad \text{consistent.}$$

One reduces the original equations to:

$$\partial_{\eta} e = \sqrt{g_a g_b} P$$

$$\partial_{\tau} P = \frac{1}{2} \left(\sqrt{\frac{g_b}{g_a}} + \sqrt{\frac{g_a}{g_b}} \right) W e$$

$$\partial_{\tau} Q = \frac{i}{2} (g_a - g_b) e P$$

$$\partial_{\tau} W = - \frac{1}{4} \sqrt{g_a g_b} (e P^* + e^* P)$$

$$iQe^* = (\sqrt{\frac{g_a}{g_b}} - \sqrt{\frac{g_b}{g_a}}) We$$

Since the number of eq. is one more than the number of unknown function, the last equation has to be derived from the first four equations. But this situation is not, only steady propagation solution case. O.K. as shown before.

Particular case $|e_a|^2 = |e_b|^2$

$$\underline{\partial} \cdot (\underline{J} + \sigma \underline{J}) = -\underline{\nabla} \cdot (\underline{J} + \underline{J}) \quad \Rightarrow \underline{\partial} \cdot \underline{w} = \underline{\nabla} \cdot \underline{J}$$

$$J_{a//} = |e_a|^2 \quad J_{b//} = |e_b|^2 (= J_{a//})$$

$$J_{a-} = -\frac{1}{2}k_i \quad (e_a \nabla_T e_a^* - e_a^* \nabla_T e_a)$$

$$J_{b-} = -\frac{1}{2}k_i \quad (e_b \nabla_T e_b^* - e_b^* \nabla_T e_b)$$

$$\underline{\partial} \cdot (\underline{J}_{aT} + \sigma \underline{J}_{bT}) = \underline{\nabla} \cdot \underline{T}$$

$$\begin{aligned} T_{ij} = & \frac{1}{2k^2} \{ (\nabla_i e_a) (\nabla_j e_a^* + (\nabla_i e_a^*) (\nabla_j e_a) \\ & + (\nabla_i e_b) (\nabla_j e_b^*) + (\nabla_i e_b^*) (\nabla_j e_b) \} \\ & + \frac{1}{4k^2} \nabla_T^2 [|e_a|^2 + |e_b|^2]_{ij} + \frac{3\gamma_{lim}}{2k} [|e_a|^4 + |e_b|^4] \end{aligned}$$

i.e. the superposition of $(T_{ij})_a + (T_{ij})_b$, iff one renormalize γ^{im} , the constant

$$\tilde{\gamma}_{im} = 3\gamma_{im}$$

$$\text{Trace } T_{ij} = \frac{1}{2k^2} \sum_{a,b} \{ (\nabla_T^2 e_a) e_a^* + (\nabla_T^2 e_a) e_a \} + \frac{\gamma_{im}}{k} |e_a|^4$$

$$\frac{\partial}{\partial z} \text{Trace } T_{ij} = - \nabla \cdot Q?$$

$$\begin{aligned} \frac{\partial}{\partial z} \text{Trace } T_{ij} &= \frac{\gamma_{im}}{ik^2} \nabla_T \cdot [|e_a|^2 (e_a \nabla_T e_a^* - e_a^* \nabla_T e_a)] + \frac{i}{4k^3} \nabla_T \cdot \{ e_a \nabla_T (\nabla_T^2 e_a) \\ &+ (\nabla_T^2 e_a) (\nabla_T^2 e_a^*) - e_a \nabla_T (\nabla_T^2 e_a^*) - (\nabla_T^2 e_a^*) (\nabla_T^2 e_a) \} \\ &+ \frac{\gamma_{im}}{ik^2} \sigma \nabla_T [|e_b|^2 (e_b \nabla_T e_b^* - e_b^* \nabla_T e_b)] \\ &+ \frac{i}{4k^3} \sigma \nabla_T \cdot \{ e_b^* \nabla_T (\nabla_T^2 e_b) + (\nabla_T^2 e_b) (\nabla_T^2 e_b^*) \\ &- e_b \nabla_T (\nabla_T^2 e_b^*) - (\nabla_T^2 e_b^*) (\nabla_T^2 e_b) \} \end{aligned}$$

$$\begin{aligned} Q &= \frac{1}{4ik^3} \{ \{ e_a^* \nabla_T (\nabla_T^2 e_a) + (\nabla_T^2 e_a) (\nabla_T^2 e_a^*) - e_a \nabla_T (\nabla_T^2 e_a^*) - (\nabla_T^2 e_a^*) (\nabla_T^2 e_a) \} \\ &+ \sigma \{ e_b^* \nabla_T (\nabla_T^2 e_b) + (\nabla_T^2 e_b) (\nabla_T^2 e_b^*) - e_b \nabla_T (\nabla_T^2 e_b^*) - (\nabla_T^2 e_b^*) (\nabla_T^2 e_b) \} \\ &+ 4 \tilde{\gamma}_{im} k |e_a|^2 (e_a^* \nabla_T e_a - e_a \nabla_T e_a^*) \\ &+ 4 \tilde{\gamma}_{im} k |e_b|^2 (e_b^* \nabla_T e_b - e_b \nabla_T e_b^*) \} \end{aligned}$$

One can write an analytic expression for the average beam waist as a function of the

$$a_{\text{eff}}^2 = a_0^2 + 2 c_1 z + c_2 z^2$$

$$\text{with } a_0^2 = a^1(z=0)$$

$$\begin{aligned} C_1 &= \frac{1}{W_0} \int \vec{n} \cdot \vec{j} dv \\ &= \frac{1}{2ki} \frac{1}{W_0} \int dV r \{ e_a \nabla_T e_a^* - e_a^* \nabla_T e_a + \sigma (e_b \nabla_T e_b^* - e_b^* \nabla_T e_b) \} z = 0 \end{aligned}$$

$$C_2 = - \frac{1}{w_0} \frac{1}{2k^2} \int dV \{ (\nabla_T^2 e_a) e_a^* + (\nabla_T^2 e_a^*) e_a + 2\tilde{\gamma}_{im} |e_a|^4 \\ + (\nabla_T^2 e_b) e_b^* + (\nabla_T^2 e_b^*) e_b + 2\tilde{\gamma}_{im} |e_b|^4 \} \quad z = 0$$

$$w_0 = \int_{\Sigma} |e_a|^2 \, dS'$$

F. P. Mattar
Extension of the Vlasov et al
and Sugden moment theory
from one beam to two beams

Theory of moments

2 Beams

$$\frac{-i}{2k} \nabla_T^2 e_a + \frac{\partial}{\partial z} e_a = \gamma_a \{|e_a|^2 + 2|e_b|^2\} e_a$$

$$\frac{-i}{2k} \nabla_T^2 e_b + \sigma \frac{\partial}{\partial z} e_b = \gamma_b \{|e_a|^2 + 2|e_b|^2\} e_b$$

$\sigma = \pm 1$ +1 parallel beam (concomitant propagation)

-1 counterwave (antiparallel propagation)

First moment equation:

$$\frac{-i}{2k} e_a^* \nabla_T^2 e_a + e_a^* \frac{\partial}{\partial z} e_a = \gamma_a \{|e_a|^2 + 2|e_b|^2\} |e_a|^2$$

$$\frac{+i}{2k} e_a \nabla_T^2 e_a^* + e_a \frac{\partial}{\partial z} e_a^* = \gamma_a^* \{|e_a|^2 + 2|e_b|^2\} |e_a|^2$$

$$\frac{-i}{2k} (e_a^* \nabla_T^2 e_a - e_a \nabla_T^2 e_a^*) + \frac{\partial}{\partial z} |e_a|^2 = \gamma_a \{|e_a|^2 + 2|e_b|^2\} |e_a|^2$$

$$+ \gamma_a^* \{|e_a|^2 + 2|e_b|^2\} |e_a|^2$$

$$\frac{-i}{2k} \nabla_T (e_a^* \nabla_T^2 e_a - e_a \nabla_T^2 e_a^*) + \frac{\partial}{\partial z} |e_a|^2 = (\gamma_a + \gamma_a^*) \{|e_a|^2 + 2|e_b|^2\} |e_a|^2$$

Similarly

$$\frac{-i}{2k} \nabla_T (e_b^* \nabla_T^2 e_b - e_b \nabla_T^2 e_b^*) + \sigma \frac{\partial}{\partial z} |e_b|^2 = (\gamma_b + \gamma_b^*) [2|e_b|^2 + 2|e_a|^2] |e_b|^2$$

defining energy currents

$$J_{aT} \triangleq -\frac{1}{2kI} (e_a \nabla_T e_a^* - e_a^* \nabla_T e_a); \quad J_{a//} = |e_a|^2$$

$$J_{bT} \triangleq -\frac{1}{2kI} (e_b \nabla_T e_b^* - e_b^* \nabla_T e_b); \quad J_{b//} = |e_b|^2$$

with J_{aT} , J_{bT} the transverse current and $J_{a//}$ and $J_{b//}$ the longitudinal currents.

Introducing

$$\gamma_a \triangleq \gamma_{ar} + i \gamma_{ai}$$

$$\gamma_b \triangleq \gamma_{br} + i \gamma_{bi}$$

substituting one gets

$$\frac{\partial}{\partial z} J_{a//} + \nabla_T \cdot J_{aT} = 2\gamma_{ar} [|e_a|^2 + 2|e_b|^2] |e_a|^2$$

$$\sigma \frac{\partial}{\partial z} J_{b//} + \nabla_T \cdot J_{bT} = 2\gamma_{br} [2|e_b|^2 + |e_a|^2] |e_b|^2$$

$$\begin{aligned} \frac{\partial}{\partial z} [J_{a//} + \sigma J_{b//}] + \nabla_T \cdot (J_{aT} + J_{bT}) &= 2[\gamma_{ar} |e_a|^4 + 2\gamma_{ar} |e_a|^2 |e_b|^2 \\ &+ 2\gamma_{br} |e_a|^2 |e_b|^2 + \gamma_{br} |e_b|^4] \end{aligned}$$

$$\begin{aligned} \frac{\partial}{\partial z} [J_{a//} + \sigma J_{b//}] + \nabla_T \cdot [J_{aT} + J_{bT}] &= 2\{\gamma_{ar} |e_a|^4 \\ &+ 2\gamma_{ar} |e_a|^2 |e_b|^2 + 2\gamma_{br} |e_a|^2 |e_b|^2 + \gamma_{br} |e_b|^4\} \end{aligned}$$

For $\gamma_{ar} = \gamma_{br} = 0$

The equations reduce to:

$$\frac{\partial}{\partial z} [J_{a//} + \sigma J_{b//}] = -\nabla_T \cdot (J_{aT} + J_{bT})$$

Talanov

$$\Rightarrow \frac{\partial}{\partial z} w = -\nabla \cdot J$$

2nd moment equation:

$$\frac{\partial J}{\partial z} c^2 = \nabla \cdot T$$

$$\text{using } J_{aT} \equiv -\frac{i}{2k\ell} (e_a \nabla_T e_a^* - e_a^* \nabla_T e_a)$$

$$\frac{\partial J_{aT}}{\partial z} = [1/(2k\ell)] \left\{ -\frac{\partial e_a}{\partial z} \nabla_T e_a^* - e_a \left[\nabla_T \left(\frac{\partial e_a^*}{\partial z} \right) \right] + \frac{\partial e_a^*}{\partial z} \nabla_T e_a + e_a^* \left[\nabla_T \left(\frac{\partial e_a}{\partial z} \right) \right] \right\}$$

Using $\gamma_{ar} = \gamma_{br} = 0$

$$\text{and } \frac{\partial}{\partial z} e_a = (i/2k) \nabla_T^2 e_a + i \gamma_{ai} [|e_a|^2 + 2|e_b|^2] e_a$$

$$\frac{\partial J_{aT}}{\partial \tau} = \frac{1}{(2ki)} \{ -i/2k (\nabla_T e_a)(\nabla_T e_a) - i \gamma_{ai} (|e_a| e_a)(\nabla_T e_a)$$

$$-2(i \gamma_{ai}) |e_b|^2 e_a (\nabla_T e_a^*) - e_a \left(\frac{-i}{2k} \nabla_T (\nabla_T^2 e_a^*) + i \gamma_{ai} |e_a| \nabla_T (|e_a|^2 e_a^*) \right)$$

$$+ i \gamma_{ai} e_a \nabla_T (2|e_b|^2 e_a^*) - \frac{i}{2k} (\nabla_T^2 e_a^*) (\nabla_T e_a) - i \gamma_{ai} |e_a|^2 e_a^* (\nabla_T e_a)$$

$$- i \gamma_{ai} [2|e_b|^2 e_a^* (\nabla_T e_a)] + e_a^* \frac{i}{2k} \nabla_T (\nabla_T^2 e_a) + i \gamma_{ai} [e_a^* \nabla_T (|e_a|^2 e_a)]$$

$$+ i \gamma_{ai} [e_a^* \nabla_T (2|e_b|^2 e_a)] \}$$

$$\frac{\partial J_{aT}}{\partial z} = \frac{1}{4k^2} \{ -(\nabla_T e_a^*) (\nabla_T^2 e_a) - (\nabla_T e_a) (\nabla_T^2 e_a^*) + e_a \nabla_T (\nabla_T^2 e_a^*)$$

$$+ e_a^* \nabla_T (\nabla_T^2 e_a) \} + \frac{\gamma_{ai}}{2k} \{ -(|e_a|^2 e_a) (\nabla_T e_a^*) - (|e_a|^2 e_a^*) (\nabla_T e_a) \}$$

$$+ e_a \nabla_T (|e_a|^2 e_a^*) + e_a^* \nabla_T (|e_a|^2 e_a) \} + \frac{\gamma_{ai}}{2k} \{ -(|e_b|^2 e_b) (\nabla_T e_a^*)$$

$$- (|e_b|^2 e_a^*) (\nabla_T e_a) + e_a \nabla_T (|e_b|^2 e_a^*) + e_a^* \nabla_T (|e_b|^2 e_a) \}$$

$$\text{1st term} = (1/(4k^2)) \nabla_T [\nabla_T^2 (e_a e_a^*)]$$

$$- (1/2k^2) \nabla_T [(\nabla_i e_a)(\nabla_j e_a^*) + (\nabla_i e_a^*)(\nabla_j e_a)]$$

$$\text{2nd term} = \frac{\gamma_{ai}}{2k} \nabla_T |e_a|^4$$

$$\begin{aligned}
\text{3rd term} &= \frac{\gamma_{ai}}{k} \{-|e_b|^2 e_a (\nabla_T e_a^*) - |e_b|^2 e_a^* (\nabla_T e_a) + |e_a|^2 \nabla_T |e_b|^2 + e_a |e_b|^2 \nabla_T e_a^* \\
&\quad + |e_a|^2 \nabla_T |e_b|^2 + e_a^* |e_b|^2 \nabla_T e_a\} \\
&= \frac{\gamma_{ai}}{k} \{-|e_b|^2 e_a (\nabla_T e_a^*) - |e_b|^2 e_a^* (\nabla_T e_a) + |e_a|^2 e_b (\nabla_T e_b^*) \\
&\quad + |e_a|^2 e_b^* (\nabla_T e_b) + e_a |e_b|^2 (\nabla_T e_a^*) + |e_a|^2 e_b (\nabla_T e_b^*) \\
&\quad + |e_a|^2 e_b^* (\nabla_T e_b) + e_a^* |e_b|^2 (\nabla_T e_a)\} \\
&= \frac{\gamma_{ai}}{k} \{2|e_a|^2 e_b (\nabla_T e_b^*) + 2|e_a|^2 e_b^* (\nabla_T e_b)\} \\
&= 2 \frac{\gamma_{ai}}{k} |e_a|^2 (\nabla_T |e_b|^2)
\end{aligned}$$

$$\begin{aligned}
\therefore \frac{\partial J_{aT}}{\partial z} &= [(\frac{1}{4k^2}) \nabla_T (\nabla_T^2 |e_a|^2) - (\frac{1}{2k^2}) \nabla_T [(\nabla_i e_a)(\nabla_j e_a^*) + (\nabla_i e_a^*)(\nabla_j e_a)]] \\
&\quad + [\frac{\gamma_{ai}}{2k} \nabla_T |e_a|^4] + [\frac{2\gamma_{ai}}{k} |e_a|^2 \nabla_T |e_b|^2]
\end{aligned}$$

by analogy

$$\begin{aligned}
\sigma \frac{\partial J_{bT}}{\partial z} &= [\frac{1}{4k^2} \nabla_T^2 [\nabla_T |e_b|^2 \delta_{ij}] - \frac{1}{2k^2} \nabla_T [(\nabla_i e_b)(\nabla_j e_b^*) + (\nabla_i e_b^*)(\nabla_j e_b)]] \\
&\quad + [\frac{\gamma_{bi}}{2k} \nabla_T |e_b|^4] + [2 \frac{\gamma_{bi}}{k} |e_b|^2 \nabla_T |e_a|^2]
\end{aligned}$$

$$\text{but } \nabla_T [|e_a|^2 |e_b|^2] = |e_a|^2 \nabla_T |e_b|^2 + |e_b|^2 \nabla_T |e_a|^2$$

$$\begin{aligned}
\frac{\partial}{\partial z} (J_{aT} + \sigma J_{bT}) &= \frac{1}{4k^2} \nabla_T \cdot \nabla_T^2 (|e_a|^2 + |e_b|^2) \\
&- \frac{1}{2k^2} \nabla_T [(\nabla_i e_a)(\nabla_j e_a^*) + (\nabla_i e_a^*)(\nabla_j e_a)] \\
&- \frac{1}{2k^2} \nabla_T [(\nabla_i e_b)(\nabla_j e_b^*) + (\nabla_i e_b^*)(\nabla_j e_b)] \\
&+ \left\{ \frac{\gamma_{ai}}{2k} \nabla_T |e_a|^4 + \frac{\gamma_{bi}}{2k} \nabla_T |e_b|^4 \right\} \\
&+ \frac{2}{k} \gamma_{ai} \{ |e_b|^2 \nabla_T |e_b|^2 + \gamma_{bi} |e_b|^2 \nabla_T |e_a|^2 \}
\end{aligned}$$

NOTE: This can be expressed in form of $\nabla_T \cdot \underline{T}$ only by $\gamma_{a2} = \gamma_{b2} = \gamma_i$

Then

$$\begin{aligned}
\frac{\partial}{\partial z} (J_{aT} + \sigma J_{bT}) &= \nabla_T \cdot \underline{T} \\
\text{where } \underline{T}_{ij} &= -\frac{1}{2k^2} \{ (\nabla_i e_a)(\nabla_j e_a^*) + (\nabla_i e_a^*)(\nabla_j e_a) + (\nabla_i e_b)(\nabla_j e_b^*) + (\nabla_i e_b^*)(\nabla_j e_b) \} \\
&+ \frac{1}{4k^2} \nabla_T^2 \{ |e_a|^2 + |e_b|^2 \} \delta_{ij} + \frac{\gamma_{im}}{2k} [|e_a|^4 + |e_b|^4] \delta_{ij} \\
&+ \frac{2\gamma_{im}}{k} |e_a|^2 |e_b|^2 \delta_{ij}
\end{aligned}$$

$$\text{iff } \gamma_{ai} = \gamma_{bi} = 0, \quad \gamma_{bi} = \gamma_{ai} = \gamma_{im}$$

3rd moment relation

$$\frac{\partial}{\partial z} [\text{Trace } \underline{T}_{ij}] = - \nabla_T \cdot \underline{Q}.$$

$$\begin{aligned}
\text{Trace } \underline{T}_{ij} &= \left(\frac{1}{2k^2} \right) \{ (\nabla_T^2 e_a) e_a^* + (\nabla_T^2 e_a^*) e_a \} + \frac{\gamma_{im}}{k} |e_a|^4 \\
&+ \frac{1}{2k^2} \{ (\nabla_T^2 e_b) e_b^* + (\nabla_T^2 e_b^*) e_b \} + \frac{\gamma_{im}}{k} |e_a|^4 \\
&+ \frac{4\gamma_{im}}{k} |e_a|^2 |e_b|^2
\end{aligned}$$

1st term \rightarrow

$$\begin{aligned} & \frac{\partial}{\partial z} \left[\frac{1}{2k^2} \{ (\nabla_T^2 e_a) e_a^* + (\nabla_T^2 e_a^*) e_a \} + \frac{\gamma_{im}}{k} |e_a|^4 \right] \\ &= \frac{\gamma_{im}}{ik^2} \nabla_T \cdot [|e_a|^2 (e_a \nabla_T e_a^* - e_a^* \nabla_T e_a)] \\ &+ \frac{i}{4k^3} \nabla_T \cdot \{ e_a^* \nabla_T (\nabla_T^2 e_a) + (\nabla_T e_a) (\nabla_T^2 e_a^*) \\ &- e_a \nabla_T (\nabla_T^2 e_a^*) - (\nabla_T e_a^*) (\nabla_T^2 e_a) \} \end{aligned}$$

2nd term \rightarrow

$$\begin{aligned} & \frac{\partial}{\partial z} \left[\frac{1}{2k^2} \{ (\nabla_T^2 e_b) e_b^* + (\nabla_T^2 e_b^*) e_b \} + \frac{\gamma_{im}}{k} |e_b|^4 \right] \\ &= \frac{1}{2k^2} \left\{ \frac{\partial e_b}{\partial z} (\nabla_T^2 e_b^*) + e_b \nabla_T^2 \left(\frac{\partial e_b^*}{\partial z} \right) + \frac{\partial e_b^*}{\partial z} (\nabla_T^2 e_b) + e_b^* \nabla_T^2 \left(\frac{\partial e_b}{\partial z} \right) \right\} \\ &+ \frac{\gamma_{im}^\sigma}{ik^2} |e_b|^2 \nabla_T (e_b \nabla_T e_b^* - e_b^* \nabla_T e_b) \\ &= \frac{\sigma \gamma_{im}}{ik^2} \nabla_T \cdot [|e_b|^2 (e_b \nabla_T e_b^* - e_b^* \nabla_T e_b)] \\ &+ \frac{i\sigma}{4k^3} [\nabla_T \cdot \{ e_b^* \nabla_T (\nabla_T^2 e_b) + (\nabla_T e_b) (\nabla_T^2 e_b^*) - e_b \nabla_T (\nabla_T^2 e_b^*) - (\nabla_T e_b^*) (\nabla_T^2 e_b) \}] \end{aligned}$$

$$\therefore \frac{4\gamma_{im}}{k} \frac{\partial}{\partial z} [|e_a|^2 |e_b|^2] = \frac{4\gamma_{im}}{k} \{ |e_a|^2 \frac{\partial}{\partial z} |e_b|^2 + |e_b|^2 \frac{\partial}{\partial z} |e_a|^2 \}$$

$$\frac{\partial}{\partial z} |e_a|^2 = - \frac{i}{2k} \nabla_T \cdot (e_a \nabla_T e_a^* - e_a^* \nabla_T e_a)$$

$$\frac{\partial}{\partial z} |e_b|^2 = - \sigma \frac{i}{2k} \nabla_T \cdot (e_b \nabla_T e_b^* - e_b^* \nabla_T e_b)$$

$$\begin{aligned}
\therefore \quad & \frac{4y_{im}}{k} \frac{\partial}{\partial z} [|e_a|^2 |e_b|^2] = \frac{4y_{im}}{2ik^2} \{ |e_b|^2 \nabla_T \cdot (e_a \nabla_T e_a^* - e_a^* \nabla_T e_a) \\
& + |e_a|^2 \nabla_T \cdot (e_b \nabla_T e_b^* - e_b^* \nabla_T e_b) \} \\
& = \frac{4y_{im}}{i2k^2} \nabla_T (??)
\end{aligned}$$

if $|e_a|^2 \neq |e_b|^2$, it seems to be impossible, so far, to convert the third term into the desired form derived for one beam by Talanov.

SIT- Small Trench Calculations

F.P. Mathew

$$\partial_{\eta} e(\rho, \eta, \tau) = P(\rho, \eta, \tau) \quad (1)$$

$$e(\rho, \eta, \tau) = e(\rho, 0, \tau) + g \int_0^{\eta} P(\rho, \eta', \tau) d\eta' \quad (2)$$

$$e(\rho, \eta, \tau) = e(\rho, 0, \tau) - g \int_0^{\eta} \left\{ \sin \left[\int_0^{\tau} e(\rho, \eta', \tau') d\tau' \right] \right\} d\eta' \quad (3)$$

$$\tilde{e}(\rho, \eta, \tau) = e(\rho, 0, \tau) - g \int_0^{\eta} d\eta' \cdot \sin \int_0^{\tau} e(\rho, 0, \tau') d\tau' \quad (4)$$

$$= e(\rho, 0, \tau) - g \eta \left[\sin \int_0^{\tau} e(\rho, 0, \tau') d\tau' \right] \quad (5)$$

$$\tilde{e}(\rho, \eta, \tau) = e(\rho, 0, \tau) - g \eta \int_0^{\tau} e(\rho, 0, \tau') d\tau' \quad (6)$$

$$e(\rho, 0, \tau) = A_0 \exp[-(\tau - \tau_0)^2] \exp[-\rho^2] \quad (7)$$

$$\theta = \int_{-\infty}^{\infty} e(\rho, 0, \tau) = 2\pi \quad (8)$$

$$A_0 = 2\sqrt{\pi} \quad (9)$$

$$e(\rho, \eta, \tau) = 2\sqrt{\pi} \exp[-\rho^2] \{ \exp[-(\tau - \tau_0)^2] - g \eta \int \exp[-(\tau' - \tau_0)^2] d\tau' \} \quad (10)$$

$$e(\rho, \eta, \tau) = e(\rho, 0, \tau) - g \int_0^{\eta} d\eta' \left\{ \sin \left[\int_0^{\tau} (e(\rho, 0, \tau') - g\eta' \sin \int_0^{\tau'} e(\rho, 0, \tau'') d\tau'') d\tau' \right] \right\} =$$

$$= e(\rho, 0, \tau) - g \int_0^{\eta} d\eta' \left\{ \sin \theta(\tau) \cdot \cos \left(g\eta' \int_0^{\tau} d\tau' [\sin \theta(\tau')] \right) - \right.$$

$$\left. - \cos \theta(\tau) \cdot \sin \left(g\eta' \int_0^{\tau} d\tau' [\sin \theta(\tau')] \right) \right\} =$$

$$= e(\rho, 0, \tau) - g \sin \theta(\tau) \int_0^{\eta} d\eta' \cdot \cos \left[g\eta' \int_0^{\tau} d\tau' \sin \theta(\tau') \right] +$$

$$+ g \cos \theta(\tau) \int_0^{\eta} d\eta' \cdot \sin \left[g\eta' \int_0^{\tau} d\tau' \sin \theta(\tau') \right] \quad (12)$$

$$e_{10} = e_0 - g\eta \sin\theta + g^2 \frac{\eta^2}{2} \beta_1 \cos\theta \quad (22)$$

$$e_0 = 2\sqrt{\pi} \exp(-\rho^2) \exp[-(\tau'-\tau_0)^2] \quad (22)$$

$$e_0 = 2\sqrt{\pi} \exp(-\rho^2) \int_0^\tau \exp[-(\tau'-\tau_0)^2] d\tau' \quad (23)$$

$$\theta = 2\sqrt{\pi} \exp(-\rho^2) \int_0^\tau \exp[-(\tau'-\tau_0)^2] d\tau' \quad (24)$$

$$\beta_1 = \int_0^\tau \sin\theta d\tau' \quad (25)$$

$$\beta_2 = \int_0^\tau \theta \cos\theta d\tau' \quad (27)$$

$$\beta_3 = \int_0^\tau [-(\sin\theta) \cdot \theta^2 + (\cos\theta)\theta] d\tau' \quad (27)$$

$$\beta_4 = \int_0^\tau [\cos\theta(\theta-\theta^3) + \sin\theta(-3\theta^2)] d\tau' \quad (28)$$

$$e_1 = -4(1-\rho^2)\eta + g \frac{\eta^2}{2} [4(1-\rho^2)\theta \cos\theta + 4\rho^2 \eta^2 \sin\theta] +$$

$$- \frac{2}{3} g^2 \eta^3 \{ \beta_2 \cos\theta - \beta_1 \theta \sin\theta + \rho^2 [\theta \sin\theta (2\beta_2 + \beta_1) +$$

$$+ \cos\theta (\theta^2 \beta_1 - \beta_3)] \} \quad (29)$$

$$\partial \rho e_1 = 8\rho \{ (2-\rho^2) e_0 \eta - g \frac{\eta^2}{2} \{ \theta \cos\theta [(2-\rho^2) + \rho^2 \theta^2] - \theta^2 \sin\theta (2-3\rho^2) \} +$$

$$+ \frac{1}{6} g^2 \eta^3 [\cos\theta (-2\beta_1 \theta^2 + 2\beta_3) - 2 \sin\theta (\beta_1 \theta + 2\beta_2 \theta) +$$

$$+ \rho^2 (\sin\theta (\beta_1 \theta + 3\beta_2 \theta + 3\beta_3 \theta - \beta_1 \theta^3) +$$

$$+ \cos\theta (3\beta_1 \theta^3 + 3\beta_2 \theta^2 - \beta_4)) \} \} \quad (30)$$

$$\partial_{\rho} e_{1D} = -2\rho e_0 + 2g\eta\rho\theta\cos\theta + g^2 \frac{\eta^2}{2} (-2\rho\beta_2\cos\theta + 2\rho\beta_1\theta\sin\theta)$$

$$J_T = F(e_{1D} \cdot \partial_{\rho} e_1 - e_1 \cdot \partial_{\rho} e_{1D})$$

$$\phi = \tan^{-1}(Fe_1/e_{1D})$$

$$e_{1D} = \sqrt{e_0^2 - 2\eta e_0 \sin\theta} \quad (49)$$

$$\partial_{\rho} e_{1D} = -2\rho(e_0^2 - \eta f)/e_{1D} \quad (51)$$

$$f = e_0(\sin\theta + \theta\cos\theta) \quad (52)$$

$$\partial_{\rho} f = (-2\rho)f_1 \quad (53)$$

$$f_1 = e_0[3\theta\cos\theta - (1-\theta^2)\sin\theta] \quad (54)$$

$$\partial_{\rho} f_1 = (-2\rho)f_2 \quad (55)$$

$$f_2 = e_0[(7\theta-\theta^3)\cos\theta - (1-6\theta^2)\sin\theta] \quad (56)$$

$$\nabla_T^2 e_{1D} = -4 \frac{e_0^2 - \eta f}{e_{1D}} + 4\rho^2 \left[\frac{2e_0^2 - \eta f_1}{e_{1D}} - \frac{(e_0^2 - \eta f)^2}{e_{1D}^3} \right] \quad (57)$$

$$\begin{aligned} \nabla_T^2 e_{1D} = & 4 \frac{e_0^2}{e_{1D}} \cdot [-1 + 2\rho^2] - 4 \frac{e_0^4}{e_{1D}^3} \rho^2 + \\ & + \eta \left[\frac{4f}{e_{1D}} - 4\rho^2 \left(-\frac{2e_0^2}{e_{1D}} f + \frac{f_1}{e_{1D}} \right) \right] - \eta^2 \left[\rho^2 \frac{(4f^2)}{e_{1D}^3} \right] \end{aligned} \quad (58)$$

$$e_1 = \int_0^{\eta} (\nabla_T^2 e_{1D}) d\eta' \quad (59)$$

$$\begin{aligned} e_1 = & [4e_0^2(-1+2\rho^2)] I_1 - [4\rho^2 e_0^4] I_2 + [4(f-\rho^2 f_1)] I_4 + \\ & + [4\rho^2(2e_0^2 f)] I_5 - [\rho^2(4f^2)] I_7 \end{aligned} \quad (60)$$

$$e_{1D}^2 = a + b\eta \quad (61)$$

$$a = e_0^2 \quad (62)$$

$$b = -2e_0 \sin\theta \quad (63)$$

$$\begin{aligned}
\partial_{\rho} e_1 = & [32\rho e_0^2(1-\rho^2)]I_1 + [4e_0^2(-1+2\rho^2)]\partial_{\rho} I_1 + \\
& - [8\rho e_0^4(1-2\rho^2)]I_2 - [4\rho^2 e_0^4]\partial_{\rho} I_2 + \\
& + [8\rho(-2f_1+\rho^2 f_2)]I_4 + [4(f-\rho^2 f_1)]\partial_{\rho} I_4 + \\
& + [16\rho e_0^2(f-2\rho^2 f-\rho^2 f_1)]I_5 + [8\rho^2 e_0^2 f]\partial_{\rho} I_5 \\
& - [8\rho f(f-2\rho^2 f_1)]I_7 - [4\rho^2 f^2]\partial_{\rho} I_7
\end{aligned}$$

Perturbation

e^+ Strong Beam e^- Weak Beam

Mathematically, this translates

$$e^-/e^+ = \square(\delta) ; \quad P_{2p+1}^-/P_{2p+1}^+ = \square(\delta);$$

$$P_{2p+3}^\pm/P_{2p+1}^\pm = \square(\delta); \quad W_{2p}/W_{2(p+1)} = \square(\delta),$$

$$\text{and } P_{2p+3}^-/P_{2p+1}^+ = \square(\delta^2)$$

Case A. (In the diffractionless limit ($F = 0$, ∞) e_0^+ , P_{10}^+ $\propto W_0$ represent the S.I.T. limit.)

$$e^+ = e_0^+ + \delta e_1^+ + \delta^2 e_2^+ + \delta^3 e_3^+ + \dots$$

$$e^- = \delta w_1^- + \delta^2 e_2^- + \delta^3 e_3^- + \dots$$

$$P_1 = P_{10}^+ + \delta P_{11}^+ + \delta^2 P_{12}^+ + \delta^3 P_{13}^+ + \dots$$

$$P_1^- = \delta P_{11}^- + \delta^2 P_{12}^- + \delta^3 P_{13}^- + \dots$$

$$P_3^+ = \delta P_{31}^+ + \delta^2 P_{32}^+ + \delta^3 P_{33}^+ + \dots$$

$$P_5^+ = \delta^2 P_{52}^+ + \delta^3 P_{53}^+ + \dots$$

$$P_3^- = \delta^2 P_{32}^- + \delta^3 P_{33}^- + \dots$$

$$P_5^- = \delta^3 P_{53}^- + \dots$$

$$W_0 = W_{00} + \delta W_{01} + \delta^2 W_{02} + \delta^3 W_{03} + \dots$$

$$W_2 = \delta W_{21} + \delta^2 W_{22} + \delta^3 W_{23} + \dots$$

$$W_4 = \delta^2 W_{42} + \delta^3 W_{43} + \dots$$

Zero order of δ : $\square(\delta^0)$ as in S.I.T.

$$\partial_\tau e_0^+ + \partial_2 e_0^+ = g^+ P_{10}^+$$

$$\partial_\tau P_{10}^+ + P_{10}^+/\tau_2 = W_{00} e_0^+$$

$$\partial_\tau W_{00} + (W_{00} - W_{00}^e)/\tau_1 = -\frac{1}{2}(e_0^{+*} P_{10}^+ + e_0^+ P_{10}^{+*})$$

First order of δ : $\square(\delta)$

$$\partial_\tau e_1^+ + \partial_2 e_1^+ = g^- P_{11}^+$$

$$\partial_\tau e_1^- - \partial_2 e_1^- = g^- P_{11}^-$$

$$\partial_\tau P_{11}^+ + P_{11}^+/\tau_2 = W_{01} e_0^+ + W_{00} e_1^+$$

$$\partial_\tau P_{11}^- + P_{11}^-/\tau_2 = W_{00} e_1^- + W_{21}^* e_0^+$$

$$\partial_\tau P_{31}^+ + P_{31}^+/\tau_2 = W_{21} e_0^+$$

$$\partial_\tau W_{01} + W_{01}/\tau_1 = -\frac{1}{2}(e_0^{+*} P_{11}^+ + e_1^{+*} P_{10}^+ + \text{c.c.})$$

$$\partial_\tau W_{21} + W_{21}/\tau_1 = -\frac{1}{2}(e_0^{-*} P_{10}^+ + e_1^{+*} P_{31}^+ + e_1^+ P_{11}^{-*} e_0^+ P_{11}^+ + e_0^+ P_{10}^+)$$

2nd order of δ : $\square(\delta^2)$

$$\partial_\tau e_2^+ + \partial_2 e_2^+ = g^+ P_{12}^+$$

$$\partial_\tau e_2^- - \partial_2 e_2^- = g^- P_{12}^-$$

$$\partial_\tau P_{12}^+ + P_{12}^+/\tau_2 = W_{02} e_0^+ + W_{01} e_1^+ + W_{00} e_2^+ + W_{21} e_1^-$$

$$\partial_\tau P_{12}^- + P_{12}^-/\tau_2 = W_{00} e_2^- + W_{01} e_1^- + W_{21}^* e_1^{+-} + W_{22}^* e_0^+$$

$$\partial_\tau P_{32}^+ + P_{32}^+/\tau_2 = W_{22} e_0^+ + W_{21} e_1^+$$

$$\partial_{\tau} P_{52}^{+} + P_{52}^{+}/\tau_2 = W_{42} e_0^{+}$$

$$\partial_{\tau} P_{32}^{-} + P_{32}^{-}/\tau_2 = W_{22}^{*} e_0^{-}$$

$$\partial_{\tau} W_{22} = -\frac{1}{2} [(e_2^{+*} P_{10}^{+} + e_1^{+*} P_{11}^{+} + e_0^{+*} P_{12}^{+}) + (e_1^{-*} P_{11}^{-}) + \text{c.c.}]$$

$$\partial_{\tau} W_{22} = -\frac{1}{2} [(e_1^{-*} P_{11}^{+} + e_2^{-*} P_{10}^{+}) + (e_0^{+*} P_{32}) + (e_1^{+*} P_{11}^{-*} + e_0^{+*} P_{12}^{-})]$$

$$\partial_{\tau} W_{42} = -\frac{1}{2} (e_1^{-*} P_{31}^{+} + e_0^{+} P_{32}^{+} + e_1^{+} P_{31}^{+})$$

Steady State

$$\partial_z e_o^+ = g^+ P_{10}^+$$

$$P_{10}^+ = \tau_2 W_{oo} e_o^+$$

$$W_{oo} - W_{oo}^e = -\tau_1/2 [e_o^{+*} P_{10}^+ + e_o^+ P_{10}^{+*}]$$

$$W_{oo} = W_{oo}^e - \frac{\tau_1}{2} [e_o^{+*} (\tau_2 W_{oo} E_o^+) + e_o^+ (\tau_2 W_{oo} e_o^{+*})]$$

$$= W_{oo}^2 - \frac{\tau_1}{2} [\tau_2 W_{oo} |e_o^+|^2 + \tau_2 W_{oo} |e_o^+|^2]$$

$$= W_{oo}^2 - \tau_1 \tau_2 W_{oo} |e_o^+|^2$$

$$W_{oo} = W_{oo}^2 / [1 + \tau_1 \tau_2 |e_o^+|^2]$$

$$\partial_z e_o^+ = g^+ \tau_2 \frac{W_{oo}^e e_o^+}{1 + \tau_1 \tau_2 |e_o^+|^2}$$

with $e_S = (\tau_1 \tau_2)^{-1/2}$ and e_o^+ real

$$\partial_z e_o^+ = \tau_2 W_{oo}^e e_o^+ / [1 + (e_o^+ / e_S)^2]$$

$$d e_o^+ [1 + (e_o^+ / e_S)^2]^{+1} = [\tau_2 W_{oo}^2 e_o^+] dz$$

$$[(1/e_o^+) + (e_o^+ / e_S^2)] d e_o^+ = \tau_2 W_{oo}^2 dz$$

$$\ln \left[\frac{e_o^+}{e_S} \right] + \frac{[e_o^+(z)]^2 - e_o^+(0)]^2}{2 e_S} = \tau_2 (W_{oo}^2 dz)$$

$$+ \frac{\partial e_1^+}{\partial z} = g^+ P_{11}^+$$

$$- \frac{\partial e_1^-}{\partial z} = g^- P_{11}^-$$

$$P_{11}^+ = \tau_2 (W_{01} e_0^+ + W_{00} e_1^+)$$

$$P_{11}^- = \tau_2 (W_{00} e_0^- + W_{21}^* e_0^+)$$

$$P_{31}^+ = \tau_2 W_{21} e_0^+$$

$$W_{01} = -\tau_1/2 (e_0^{+*} P_{11} + e_1^{+*} P_{10} + \text{c.c.})$$

$$W_{21} = -\tau_1/2 (e_1^{-*} P_{10}^+ + e_0^{+*} P_{31}^+ + e_0^+ P_{11}^{-*})$$

$$W_{21} = -\tau_1/2 (e_1^{-*} P_{10}^+ + e_0^{+*} \tau_2 W_{21} e_0^+ + e_0^+ + e_0^+ P_{11}^*)$$

$$W_{21} = -\tau_1/2 (e_1^{-*} P_{10}^+ + \tau_2 W_{21} |e_0^+|^2 + e_0^+ P_{11}^{-*})$$

$$\therefore W_{21} = \frac{e_1^{-*} P_{10}^+ + e_0^+ P_{11}^{-*}}{1 + \frac{\tau_1 \tau_2}{2} |e_0^+|^2} = \frac{e_1^{-*} P_{10}^+ + e_0^+ P_{11}^{-*}}{1 + \frac{1}{2} \frac{|e_0^+|^2}{e_5^2}}$$

BEST ESTIMATE FOR ONE DIMENSIONAL EQUIVALENT
TO DIFFRACTION LOSS κ

$$-(i/F) \nabla_{\rho}^2 \xi \equiv \kappa \xi$$

$$\kappa = - (i/F) (\nabla_{\rho}^2 \xi) / \xi$$

$$\langle \kappa \rangle = (-i/\rho_{\max}) \int_0^{\rho_{\max}} (1/F) [\nabla_{\rho}^2 \xi / \xi] d\rho$$

$$\langle \bar{\kappa} \rangle = (-i/\langle F \rangle \rho_{\max}) \int_0^{\rho_{\max}} (1/\partial \xi) \frac{\partial}{\partial \rho} \left(\rho \frac{\partial \xi}{\partial \rho} \right) d\rho$$

$$= (-i/\langle F \rangle \rho_{\max}) \int_0^{\rho_{\max}} (1/\rho \xi) d[\rho \frac{\partial \xi}{\partial \rho}]$$

$$= (i/\langle F \rangle \rho_{\max}) \left[(1/\xi) \frac{\partial \xi}{\partial \rho} \right]_{\rho=\rho_{\max}} - \left[(1/\xi) \frac{\partial \xi}{\partial \rho} \right]_{\rho=0}$$

$$- \int_0^{\rho_{\max}} \rho \frac{\partial \xi}{\partial \rho} d[1/\rho \xi]$$

Since by cylindrical symmetry the on-axis field gradient vanishes, the second term is zero.

$$\langle \kappa \rangle = (i/\langle F \rangle \rho_{\max}) \left[(1/\xi) \frac{\partial \xi}{\partial \rho} \right]_{\rho=\rho_{\max}} + \int_0^{\rho_{\max}} \rho \left(\frac{\partial \xi}{\partial \rho} \right) \left(\frac{1}{\rho^2 \xi^2} \right) d(\rho \xi)$$

$$= - (i/\langle F \rangle \rho_{\max}) (1/\xi) \frac{\partial \xi}{\partial \rho} \Big|_{\rho=\rho_{\max}} + \int_0^{\rho_{\max}} (1/\xi^2 \rho) \left(\frac{\partial \xi}{\partial \rho} \right) d(\rho \xi)$$

$$\langle \kappa \rangle \simeq - (i/\langle F \rangle \rho_{\max}) \left[(1/\xi) \frac{\partial \xi}{\partial \rho} \right]_{\rho=\rho_{\max}}$$

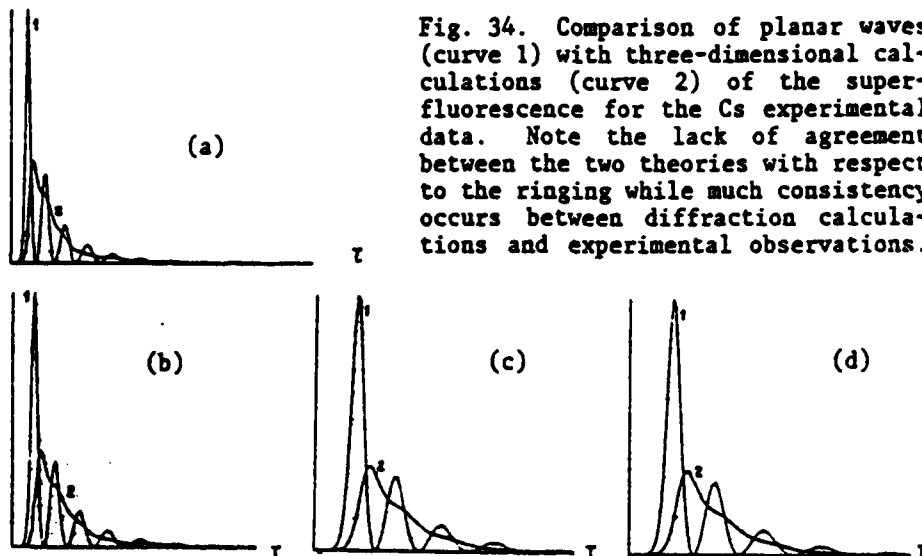
$$\xi = \xi_z \exp [i \phi (\rho)]$$

one obtains

$$\langle \kappa \rangle = (i/\langle F \rangle \rho_{\max}) \left[\frac{\partial \phi}{\partial \rho} \right]_{\rho=\rho_{\max}}$$

$$\text{i.e. } \langle \kappa \rangle = [\lambda/A] \quad (1/\rho_{\max} \langle g \rangle) \frac{\partial \phi}{\partial \rho} \Big|_{\rho=\rho_{\max}}$$

with $\langle g \rangle$ the average gain across the beam.



is needed to reduce the asymmetry and pulse width. But when relaxation terms are also included in the analysis and the densities are adjusted within quoted experimental uncertainties, a rather good agreement, (see Fig. (34)) is obtained between theory and experiments for a unity \mathcal{T} . These radial effects explain why the observed ringing in superfluorescence is less than that predicted by plane-wave simulations (see Fig. 34). Extensions of the present simulations to two-way propagation and random fluctuation of the tipping angle are planned. The agreement with experimental observations should be improved. [Recently, Bonifacio et al.^{1d} also reported the suppression of the ringing by using coupled-mode mean-field theory. However, their model does not encompass the propagational effects substantiated by both experimental observation and rigorous three-dimensional Maxwell-Bloch analysis.]

X. FLUID DESCRIPTION

Consider the polar representation of the field

$$e = A \exp (+i\phi) \quad (13)$$

with A and ϕ real amplitude and phase. Also let the nonlinear polarization of the RHS of equation (1) be written as

$$P^{NL} = (\chi_R + i \chi_I) e + \chi_{NL} e, \quad (14)$$

where χ_R and χ_I are real functions of A . Using equation (13), one gets from equation (1) the transport and the eikonal equations ($n_0 = k_0 c / \omega_0$)

$$K_0 \frac{\partial}{\partial \eta} A^2 + \nabla_T \cdot [A^2 \nabla_T \phi] = - \frac{4\pi\omega_0^2}{c^2} \chi_I A^2, \quad (15)$$

$$2k_0 \frac{\partial}{\partial \eta} \phi + (\nabla_T \phi)^2 - \left[\frac{A \cdot \nabla_T^2 A}{A^2} \right] = \frac{4\pi\omega_0^2}{c^2} \chi_R \quad (16)$$

The transport equation (15) expresses conservation of beam energy over the transverse plane. When $\chi_I = 0$, total power is conserved along the direction of propagation. The eikonal equation (16) describes the evolution of the surface of constant phase. It has the form of the Hamilton-Jacobi equation for the two-dimensional motion of particles having unit mass and moving under the influence of a potential⁴⁹ given by

$$V = - \frac{1}{2k_0^2} \cdot (\nabla_T^2 A) A^{-1} - \frac{2\pi}{n_0^2} \chi_R$$

if $k_{0z}z$ is regarded as time coordinate and $k_{0x}x$, $k_{0y}y$ as spatial coordinates. Furthermore, if one adopts A^2 and $\nabla_T \phi$ as new dependent variables, the equations of motion become similar to the continuity and momentum transport equations of ordinary hydrodynamics^{25,26}. By defining

$$\underline{v} = k_0^{-1} \nabla_T \phi, \quad \text{and} \quad (17)$$

$$\rho = A^2 \quad (18)$$

and supposing $\chi_I = 0$, equations (15) and (16) can be written as

$$\frac{\partial \underline{v}}{\partial \eta} + (\underline{v} \cdot \nabla_T) \underline{v} = \frac{1}{2k_0} \nabla_T [\rho^{-1/2} (\nabla_T^2 \sqrt{\rho})] + \frac{\gamma_2}{k_0} (\nabla_T \rho) \quad (19)$$

$$\frac{\partial \rho}{\partial \eta} + \nabla_T \cdot (\rho \underline{v}) = 0. \quad (20)$$

These equations are the momentum and continuity transport equations of a fluid with a pressure

$$P = (\nabla_T^2 \sqrt{\rho}) / \sqrt{\rho}). \quad (21)$$

It should be emphasized that this pressure depends here solely on the "fluid density" and not on the "velocity". Equation (19) and (20) can be rearranged into

$$\begin{aligned} \frac{\partial}{\partial t} (\rho \underline{v}) + \nabla_T \cdot (\rho \underline{v} \underline{v}) &= \frac{1}{2k_0^2} \left[\frac{1}{2} (\nabla_T^2 \rho) \underline{I} - \right. \\ &\left. - \frac{1}{2\rho} (\nabla_T \rho) (\nabla_T \rho) \right] + \frac{\gamma_2}{k_0} \rho (\nabla_T \rho), \end{aligned} \quad (22)$$

where \underline{I} is the unit tensor.

XI. EQUATIONS OF MOTION FOR OPTICAL BISTABILITY

In the slowly varying envelope approximation, the dimensionless field-matter equations* are

$$-iF\nabla_T^2 e^+ + \frac{\partial e^+}{\partial t} + \frac{\partial e^+}{\partial z} = +g^+ \langle P^* \exp(ikz) \rangle \quad (23)$$

$$-iF\nabla_T^2 e^- + \frac{\partial e^-}{\partial t} - \frac{\partial e^-}{\partial z} = +g^- \langle P \exp(+ikz) \rangle \quad (24)$$

with g^+ , g^- as the nonlinear form of the gain experienced by the forward (e^+) and backward (e^-) traveling waves associated with the pump. The quantities in the R.H.S. undergo rapid spatial variations; $\langle \dots \rangle$ spatial average of these quantities with a period of half a wavelength

$$\frac{\partial P}{\partial t} + (-i\Delta\Omega) + \tau_2^{-1} P = + \{W(e^+ + e^-)\} \quad (25)$$

$$\frac{\partial W}{\partial t} + \tau_1^{-1} (W^e - W) = - \frac{1}{2} (P^+ + P^-) (e^+ + e^-) \quad (26)$$

Equivalently,

$$\frac{\partial P}{\partial t} + (-i(\Delta\Omega) + \tau_2^{-1}) P = W[e^+ \exp(-ikz) + e^- \exp(+ikz)] \quad (27)$$

*As an aside, the nonlinear interface bistability effect^(e), though potentially important, is not considered.

$$\frac{\partial W}{\partial t} + \tau_1^{-1}(W^e - W) = \frac{1}{2}(Pe^{+*} \exp(ikz) + Pe^{-*} \exp(-ikz) + \text{c.c.}) \quad (28)$$

with

$$e^{\pm} = (2\mu\tau_p/\hbar)e^{\pm} \quad (29)$$

$$P = (p'/2\mu), \quad (30)$$

$$E^{\pm} = \text{Re}\{e^{\pm} \exp[i(\omega t \mp kz)]\} \quad (31)$$

and

$$P = \text{Re}\{i p' \exp(i\omega t)\} \quad (32)$$

The complex field amplitude e^{\pm} , the complex polarization density p and the energy stored per atom W are functions of the transverse coordinate

$$\rho = r/r_p, \quad (33)$$

the longitudinal coordinate

$$z = \alpha_{\text{eff}} z' \quad (34)$$

and the physical time

$$\tau = t/\tau_p. \quad (35)$$

In the standing-wave problem, the two waves are integrated simultaneously along the physical time, as contrasted to S.I.T. retarded time.⁵⁰ Otherwise the physical parameters and variables have the same meaning.

The presence of opposing waves leads to a quasi-standing wave pattern in the field intensity over a half-wave length. To effectively deal with this numerical difficulty one decouples the material variables using Fourier series^{18,19} namely,

$$P = \exp(-ikz) \sum_{p=0}^{\infty} P_{(2p+1)}^{+} \exp(-i2pkz) + \exp(+ikz) \sum_{p=0}^{\infty} P_{(2p+1)}^{-} \exp(+i2pkz) \quad (36)$$

$$W = W_0 + \sum_{p=1}^{\infty} [W_{2p} \exp(-i2pkz) + \text{c.c.}] \quad (37)$$

with W_0 a real number. Substituting in the traveling equation of motion⁰, one obtains

$$\partial_t P_1^+ + P_1^+/\tau_2 = W_0 e^+ + W_2 e^-; \quad (38)$$

$$\partial_t P_3^+ + P_3^+/\tau_2 = W_2 e^+ + W_4 e^-; \quad (39)$$

... ..

$$\partial_t P_{(2p+1)}^+ + P_{(2p+1)}^+/\tau_2 = W_{2p} e^+ + W_{2(p+1)} e^-; \text{ and} \quad (40)$$

$$\partial_t P_1^- + P_1^-/\tau_2 = W_0 e^- + W_2^* e^+ \quad (41)$$

$$\partial_t P_3^- + P_3^-/\tau_2 = W_2 e^- + W_4^* e^+ \quad (42)$$

... ..

$$\partial_t P_{(2p+1)}^- + P_{(2p+1)}^-/\tau_2 = W_{2p}^* e^- + W_{2(p+1)}^* e^+ \quad (43)$$

$$\partial_t W_0 + (W_0 - W_0^e)/\tau_1 = -\frac{1}{2}(e^{-*} P_1^- + e^{+*} P_1^+ + \text{c.c.}) \quad (44)$$

$$\partial_t W_2 + W_2/\tau_1 = -\frac{1}{2}(e^{-*} P_1^+ + e^{+*} P_3^+ + e^+ P_1^{-*} + e^- P_3^{-*}) \quad (45)$$

$$\partial_t W_{2p} + W_{2p}/\tau_1 = -\frac{1}{2}(e^{-*} P_1^+ + e^+ P_{2p+1}^+ + e^+ P_{2p+1}^{-*} + e^{-*} P_{2p+1}^{-*}) \quad (46)$$

The field propagation and atomic dynamic equation are subjected to the following initial and boundary conditions:

1. INITIAL:

$$\begin{aligned} \text{for } t &\geq 0 \\ e^\pm &= 0 \end{aligned} \quad (47)$$

$$W_0 = W_0^e, \quad (48)$$

where W_0^e is a known function to take into account the pumping effects. For S.I.T. or soliton collision

$$P_{(2p+1)}^\pm = 0, \quad \text{for all } p \quad (49)$$

while for the superfluorescence problem

$$P_{(2p+1)}^{\pm} \quad (50)$$

is defined in terms of an initial tipping angle θ_R .

2. LONGITUDINAL

For $z=0$ and $z=L$: e^+ and e^- are given in terms of a known incident function

$$e_{I0} \quad (51)$$

and

$$e_{IL} \quad (52)$$

of τ and ρ .

If enclosing mirrors delineating the cavity are used in the analysis, one must observe the longitudinal boundary equations

$$e^+ = \sqrt{(1-R_1)} e_{I0} + \sqrt{R_1} e^- \quad \text{at } z = 0 \quad (53)$$

$$e^- = \sqrt{(1-R_2)} e_{IL} + \sqrt{R_2} e^+ \quad \text{at } z = L \quad (54)$$

where R_1 , R_2 , $(1-R_1)$ and $(1-R_2)$ are the respective reflectivity and transmitting factor associated with each left and right mirror.

3. TRANSVERSE

For all z and τ $[\partial e^{\pm}/\partial \rho]_{\rho=0}$ and $[\partial e^{\pm}/\partial \rho]_{\rho=\rho_{\max}}$ vanish. The previously described transverse boundary conditions (Section II) apply here for each of the fields.

It is noteworthy that the presence of the longitudinal mirrors will enhance the mutual influence of the two beams. Variations in polarization and population over wave-length distances are treated by means of expansions in spatial Fourier series, which are truncated after the third or fifth harmonic. The number of terms needed is influenced by the relative strength of the two crossing beams and by the importance of pumping and relaxation processes in restoring depleted population differences.

XII. CONCEPT OF TWO-WAY CHARACTERISTICS

An easy way to visualize the mutual influence of the two counter-propagating beams is to imagine their respective information carriers in the traveling wave description.

For a light velocity normalized to unity ($c/n = 1$), by introducing

$$\xi = \frac{1}{2} (t-z) \quad \text{and} \quad \eta = \frac{1}{2} (t+z) \quad (55)$$

or equivalently

$$t = \eta + \xi \quad \text{and} \quad z = \eta - \xi, \quad (56)$$

one obtains the new derivative as

$$\frac{\partial}{\partial t} = \frac{1}{2} \left(\frac{\partial}{\partial \eta} + \frac{\partial}{\partial \xi} \right) \quad \text{and} \quad \frac{\partial}{\partial z} = \frac{1}{2} \left(\frac{\partial}{\partial \eta} - \frac{\partial}{\partial \xi} \right) \quad (57)$$

Consequently

$$\frac{\partial}{\partial t} + \frac{\partial}{\partial z} = \frac{\partial}{\partial \eta}, \quad \frac{\partial}{\partial t} - \frac{\partial}{\partial z} = \frac{\partial}{\partial \xi}. \quad (58a)$$

The field equation reduces to

$$\frac{\partial e^-}{\partial \xi} = i \nabla_T^2 e^- + P^-; \quad \frac{\partial e^+}{\partial \eta} = i \nabla_T^2 e^+ + P^+. \quad (58b)$$

This means that the field is integrated along its directional characteristic path. With the polarization having a dynamic functional dependence on the total field the full Bloch equations are required. Furthermore the two oppositely traveling waves must be integrated simultaneously.

$$P^\pm = P^\pm(P_1^\pm, \dots, P_n^\pm, e^+, e^-) \quad (59)$$

An example of one of the material (Bloch) equations is

$$\frac{\partial P_k^\pm}{\partial \xi} + \frac{\partial P_k^\pm}{\partial \eta} + \gamma_k P_k = S_k(P_1^\pm, \dots, P_{k1}^\pm, P_{k+1}^\pm, \dots, P_n^\pm, e^+, e^-) \quad (60)$$

By identifying as outlined in Courant and Hilbert [50], the characteristics variable, namely

$$\xi = \xi(s) \quad \text{and} \quad \eta = \eta(s), \quad (61)$$

or equivalently

$$\xi = \xi_0 + s \quad \text{and} \quad \eta = \eta_0 - s. \quad (62)$$

one obtains

$$\frac{\partial \xi}{\partial s} = +1 \quad \text{and} \quad \frac{\partial \eta}{\partial s} = -1 \quad (63)$$

which simplifies the Bloch equations as follows:

$$\frac{\partial P_k}{\partial s} + \gamma_k P_k = S_k \quad (64)$$

which can be rigorously^{54,55} integrated to give

$$P_k(s+\Delta s) = P_k(s) \exp(-\Delta s/\gamma s) + \int_s^{s+\Delta s} \{ \exp[-(s-s')\gamma] S_k(s') ds' \} \quad (65)$$

Illustrating the method of solution (see Fig. (35)), arrows indicate integration paths for reducing differential equations to finite difference equations. Paths AB are used for Field Equations, and while Paths CB are used for Material Equations.

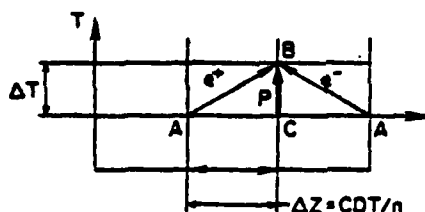


Fig. 35. Illustrates the two-way characteristic and the basis of the computational algorithm.

XIII. THE LAW OF FORBIDDEN SIGNALS

The effect of the physical law of forbidden signals on two-stream flow discretization problems was applied by Moretti to the integration of Euler equations^{24,43}.

For causality reasons, only directional resolution for spatial derivatives of each stream (forward and backward field) must be sought. This is achieved by using one-sided discretization techniques. The spatial derivative of the forward field is discretized using points lying to the left as all preceding forward waves have propagated in the same left-right direction; while the backward field is approximated by points positioned to the right. As a result, each characteristic (information carrier) is related to its respective directive history. Thus, violation of the law of forbidden signals is prevented.

In any wave propagation problem, the equations describe the physical fact that any point at a given time is affected by signals

sent to it by other points at previous times. Such signals travel along lines known as the "characteristics" of the equations. For example a point such as A in Figure (36) is affected by signals emanating from B (forward wave) and from C (backward wave), while point A' will receive signals launched from A and D. Similar wave trajectories appear in the present problem, but the slopes of the lines can change in space and time.

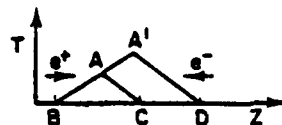


Fig. 36 Displays the role of characteristics as information carriers.

The slopes of the two characteristics carrying necessary information to define the forward and backward propagating variables at every point, are of different sign and are numerically equal to $\pm c/n$. For such a point A, Figure (37), the domain of dependence is defined by point B and C, the two characteristics being defined by AC and AB, to a first degree of accuracy. When discretizing the partial differential equations, point A must be made dependent on points distributed on a segment which brackets BC; e.g., on points D, E and F in Figure (38). This condition is necessary for stability but must be loosely interpreted. Suppose that one uses a scheme where a point A is made dependent on D, E and F, indiscriminately (this is what happens in most schemes currently used, including the MacCormack method). Suppose now, that the physical domain of dependence of A is the segment BC of Figure (38). The information carried to A from F is not only unnecessary;

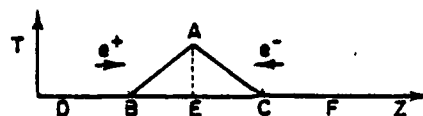


Fig. 37. Illustrates the concept of the law of forbidden signal for two-stream with characteristics of different sign.

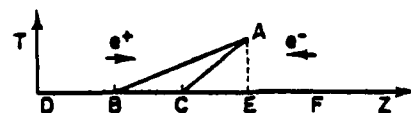


Fig. 38. Illustrates the concept of the causality for two-stream flow with characteristics of same (identical) sign.

it is also undue. Consequently, the numerical scheme, while not violating the Courant-Friedrick-Levy⁵⁴ (CFL) stability rule, would violate the law of forbidden signals. Physically, it is much better to use only information from D and E to define A, even if this implies lowering the nominal degree of accuracy of the scheme.

The sensitivity of results to the numerical domain of dependence as related to the physical domain of dependence explains why computations using integration schemes, like MacCormack's⁵², show a progressive deterioration as the AC line of Figure (38) becomes parallel to the T-axis ($\lambda_1 \rightarrow 0$), even if λ_1 is still negative. The information from F actually does not reach A; in a coarse mesh, such information may be quite different from the actual values (from C) which affect A. On the other hand, since the CFL rules must be satisfied and F is the nearest point to C on its right, the weight of such information should be minimized. Moretti's λ -scheme, relying simultaneously on the two field equations provides such a possibility. Every spatial derivative of the forward field is approximated by using points lying on the same side of E as C, and every derivation of the backward-scattered field is approximated by using points which lie on the same side of E as B. By doing so, each characteristic relates with information found on the same side of A from which the characteristic proceeds also such information is appropriately weighted with factors dependent on the characteristic's slopes, so the contribution of points located too far outside the physical domain of dependence is minimized.

A one-level scheme which defines

$$\frac{\partial e^+}{\partial z} = (e_E^+ - e_D^+)/\Delta z \quad (\text{forward wave}) \quad (66)$$

$$\frac{\partial e^-}{\partial z} = (e_F^- - e_E^-)/\Delta z \quad (\text{backward wave}) \quad (67)$$

is Gordon's scheme [53], accurate to the first order. To obtain a scheme with second-order accuracy, Moretti considered two levels, in a manner very similar to MacCormack's. More points, as in Fig. (39) must be introduced. At the predictor level following Moretti's scheme one defines

$$\frac{\partial \tilde{e}^+}{\partial z} = (2e_E^+ - 3e_D^+ + e_G^+)/\Delta z \quad (\text{forward wave}) \quad (68)$$

$$\frac{\partial \tilde{e}^-}{\partial z} = (e_F^- - e_E^-)/\Delta z \quad (\text{backward wave}) \quad (69)$$

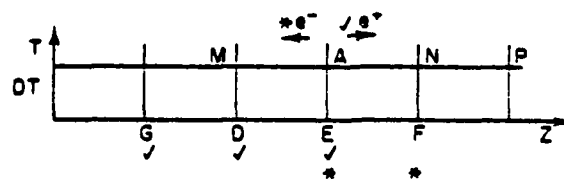


Fig. 39. Displays the computational grid for the λ -scheme.

At the corrector level, one defines

$$\frac{\partial \hat{e}^+}{\partial z} = (\tilde{e}_A^+ - \tilde{e}_M^+)/\Delta z \quad (\text{forward wave}) \quad (70)$$

and

$$\frac{\partial \hat{e}^-}{\partial z} = (-2\tilde{e}_A^- + 3\tilde{e}_N^- + \tilde{e}_P^-)/\Delta z \quad (71)$$

It is easy to see that, if any function f is updated as

$$\tilde{f} = f + f_t \Delta t \quad (72)$$

at the predictor level, with the t -derivatives defined as in (23) and (24) and the z -derivatives defined as in (68) and (69) and as

$$f(t+\Delta t) = \frac{1}{2} (f + \tilde{f} + f_t \Delta t) \quad (73)$$

at the corrector level, with the t -derivatives defined again as in (23) and (24), and the z -derivatives defined as in (70) and (71), the value of f at ' $t+\Delta t$ ' is obtained with second order accuracy. The updating rule (72) and (73) is the same as in the MacCormack scheme.

At the risk of increasing the domain of dependence, but with the goal of modularizing the algorithm, three- and four-point estimators were used for each first and second derivative respectively. Moretti's algorithm was also extended to non-uniform mesh to handle the longitudinal refractive left and right mirrors: the same one-sided differencing is used for both predictor and corrector steps. Nevertheless, the weights derived, using the theory of estimation, (presented by Hamming⁵³), have improved the order of accuracy of the spatial derivative estimator at both predictor and corrector levels. In particular, the derivative estimators are of second order instead of first order as in Moretti's λ -scheme. Specifically, these weights are derived using a development in terms as a sum of Lagrangian polynomials at a set of points. As a result, the overall accuracy of Moretti's predictor/corrector scheme was increased⁵⁶ from second to third order. Either forward or backward longitudinal derivatives at both predictor and corrector stages are given for the point x_1 , x_2 and x_3 as:

$$D_1 = \left(\frac{2x_1 - x_2 - x_3}{\pi_1(x_1)} , \quad \frac{x_1 - x_3}{\pi_2(x_2)} , \quad \frac{x_1 - x_2}{\pi_3(x_3)} \right) \quad (74)$$

$$D_2 = \left(\frac{x_2 - x_3}{\pi_1(x_1)} , \quad \frac{2x_2 - x_1 - x_3}{\pi_2(x_2)} , \quad \frac{x_2 - x_1}{\pi_3(x_3)} \right) \quad (75)$$

$$D_3 = \left(\frac{x_3 - x_2}{\pi_1(x_1)}, \quad \frac{x_3 - x_1}{\pi_2(x_2)}, \quad \frac{2x_3 - x_1 - x_2}{\pi_3(x_3)} \right) \quad (76)$$

$$\text{with } \pi_j(x) = \prod_{i \neq j=1}^3 (x - x_i) \quad (77)$$

Here D_1 , D_2 and D_3 represents forward, central and backward differencing estimators for the (first-order longitudinal spatial) derivative.

XIV. TREATMENT OF LONGITUDINAL BOUNDARY

When treating any point within the cavity or at either longitudinal boundary (where a partially reflecting mirror is situated), there is no problem. For example, at $z = 0$, e^+ is determined by equation (53) and not through previous predictor/corrector formulas (68-71), as only e^- is calculated at $z = 0$ in that predictor/corrector manner (68-71). However, for a point one increment ($\delta = \Delta z$) from the left mirror, one encounters difficulties calculating the forward wave. The second needed point, which is vital to the formulas, would fall outside the cavity. An identical difficulty arises from the counterpart backward wave with respect to the right hand mirror. The field traveling from the right is defined at $z = L$ by equation (54).

To deal with this situation one has to modify the predictor/corrector schemes so the increment " δ^2 " is used instead of δ . The loss of that second point reduces the accuracy of the derivative estimator. To maintain the same order of accuracy near the mirror, one must compensate for this loss by reducing the mesh size.

XV. NUMERICAL PROCEDURE FOR SHORT OPTICAL CAVITY

An alternate procedure to carry out the computation is to integrate the field along the longitudinal propagational distance. This approach is particularly attractive for a short cavity. It was developed with the help of McCall⁵⁷ as an attempt to relax the restrictive relation between the temporal t and spatial meshes z and r . It is presently being implemented and will be outlined here.

The reflecting effect of the partially refracting mirror can be built into the determining equations. Forward and backward field and polarization terms will appear explicitly as driving

sources in each traveling field equation (see Fig. 40). One can readily contrast the two physical situations of long and short cavity. To illustrate the methodology the diffraction is neglected. For no reflection, the fields are described by

$$e^+(t+\Delta t, z) = e^+(t, z-c\Delta t) + \int_{z-c\Delta t}^z dz' P^+(t+\Delta t - \frac{z-z'}{c}, z') \quad (78)$$

which applies if $z > c\Delta t$. Also

$$e^-(t+\Delta t, z) = e^-(t, z+c\Delta t) + \int_z^{z+c\Delta t} dz' P^-(t+\Delta t + \frac{z-z'}{c}, z') \quad (79)$$

applies if $L-z > c\Delta t$. For one reflection, the fields are obtained by

$$\begin{aligned} e^+(t+\Delta t, z) = & \sqrt{T} e_{I0}(t+\Delta t - z/c) + \int_0^z dz' P^+(t + \Delta t - \frac{z-z'}{c}, z') \\ & + \sqrt{R} e^-(t, c\Delta t - z) + \sqrt{R} \int_0^{c\Delta t - z} dz' P^-(t+\Delta t - \frac{z+z'}{c}, z') \end{aligned} \quad (80)$$

whenever $z < c\Delta t$, and if $L-z < c\Delta t$, then one reflection

$$\begin{aligned} e^-(t+\Delta t, z) = & \sqrt{T} e_{IL}(t+\Delta t - \frac{L-z}{c}) + \sqrt{R} e^{i\beta} e^+(t, 2L-z-c\Delta t) \\ & + \int_z^L dz' P^-(t+\Delta t + \frac{z-z'}{c}, z') \\ & + \sqrt{R} e^{i\beta} \int_{2L-z-c\Delta t}^L dz' P^+(t+\Delta t - \frac{2L-z-z'}{c}, z') \end{aligned} \quad (81)$$

In all of the above it is assumed that $c\Delta t < L$ (so that two reflections cannot occur in time Δt). To correctly include the influence of diffraction, appropriate weighting coefficients must be used as summarized below:

(1) For no reflection-correct by $\frac{1}{2} \nabla_T^2(e^+ c\Delta t)$, $\frac{1}{2} \nabla_T^2(e^- c\Delta t)$

(2) For one reflection-

(a) Term $\sqrt{T} e_{I0}$ only propagates z ($c\Delta t > z$) so correct only by $\frac{1}{2} \nabla_T^2$

- (b) Term $\int_0^z dz' P^+$ goes a distance of an average of $(\frac{1}{2})z$; correct by $\frac{z}{2} \frac{v_T^2}{v_T^2}$
- (c) Term $e^-(t, c\Delta t - z)$ goes a distance of $c\Delta t$; full correction by $c\Delta t - z$
- (d) Term $\sqrt{R} \int_0^{c\Delta t - z} dz' P^-$ goes $\frac{c\Delta t - z}{c} + z$; correct by a distance of $\frac{c\Delta t + z}{2} \frac{v_T^2}{v_T^2}$
- (e) Term \sqrt{T} goes $\frac{e}{IL}$ goes a distance of $(L - z)$; correct by $(1/2)(L - z) \frac{v_T^2}{v_T^2}$
- (f) Term $\sqrt{R} e^{i\beta} e^+$ goes full distance; correct $\frac{1}{2} c\Delta t \frac{v_T^2}{v_T^2}$
- (g) Term $\int_0^L dz' P^-$ goes a distance of $\frac{L - z}{2}$; correct by $\frac{1}{2} (L - z) \frac{v_T^2}{v_T^2}$
- (h) Term $\sqrt{R} e^{i\beta} \int_0^L dz' P^+$ goes a distance of $\frac{(L - z) + c\Delta t}{2}$ on the average; correct $\frac{L - z + c\Delta t}{2} \frac{v_T^2}{v_T^2}$

and similarly for any time correction.

Instead of the usual predictor/corrector weighting of 1/2 for each of predicted and corrected values, a more complicated procedure must be used.

XVI. TWO-LASER THREE-LEVEL ATOM

An extension of the SF calculations presented in Section IX should include such pump dynamics and its depletion on a three-level system similar to the model suggested by the Bowden et al.⁵⁹. The simulation of the dynamic interactions of two intense, ultra-short laser pulses propagating simultaneously through a gas of three-energy level atoms was considered⁶⁰. The rigorous diffrac-

tion and cross-modulation interplay of the two laser beams with the inertial response of the doubly resonant medium is studied using an extension of the numerical algorithm developed for SIT analysis. It is expected that by altering the pump characteristics, one encodes information in the pulse that evolves in the nonlinear media resulting in a light by light control. An intermediate study will be Double Coherent Transients^{61,62}. Another benefit of this study would be an analysis of Wall's⁶³ scheme for optical bistability in a coherently-driven three-level atomic system. However, some material equation modifications must be made as the novel mechanism relies on the nonlinear absorption resonances associated with a population trapping, coherent superposition of the ground sublevel. When one defines dimensionless variables in a parallel manner to SIT, the physical problems are described by the following equations: τ_{pa} and τ_{pb} are the pulse τ_p of laser a and laser b respectively. Q is the quadrupole slowly varying envelope.

$$-iF \nabla_T^2 e_{a,b} + \partial_\eta e_{a,b} = g_{a,b} P_{a,b} \quad (82)$$

with

$$g_{a,b} = (\mu_a/\mu_b) (\tau_{pa}/\tau_{pb})^{1/2} \quad (83)$$

$$\partial_\tau P_a = e_a W_a - i(\Delta\Omega_a) P_a - P_a/\tau_{2a} + \frac{i}{2} e_b^* Q \quad (84)$$

$$\partial_\tau P_b = e_b W_b - i(\Delta\Omega_b) P_b - P_b/\tau_{2b} - \frac{i}{2} e_a^* Q \quad (85)$$

$$\partial_\tau Q = -i[(\Delta\Omega_a + \Delta\Omega_b)]Q + \frac{i}{2} (e_a P_b - e_b P_a) - Q/\tau_{2ab} \quad (86)$$

$$\partial_\tau W_a = -\frac{i}{2}(e_a^* P_a + e_a P_a^*) - (W_a - W_a^e)/\tau_{1a} + \frac{1}{4}(e_b^* P_b + e_b P_b^*) \quad (87)$$

$$\partial_\tau W_b = -\frac{i}{2}(e_b^* P_b + e_b P_b^*) - (W_b - W_b^e)/\tau_{1b} + \frac{1}{4}(e_a^* P_a + e_a P_a^*) \quad (88)$$

If one uses the identity

$$W_a + W_b = W_{ab} \quad (89)$$

a further equation (not absolutely necessary) is introduced:

$$\partial_\tau W_{ab} = +1/4[(e_a^* P_a + e_a P_a^*) + (e_b^* P_b + e_b P_b^*)] - (W_{ab} - W_{ab}^e)/\tau_{ab} \quad (90)$$

when $W_{a,b}^e$ and W_{ab}^e are the equilibrium values of $W_{a,b}$ and W_{ab} , subjected for infinite relaxation times to a conservation of probability

$$\partial_t \{|P_a|^2 + |P_b|^2 + |Q|^2 + (W_a^2 + W_b^2 + W_{ab}^2)\} = \text{zero}. \quad (91)$$

Equivalently:

$$\begin{aligned} & |P_a|^2 + |P_b|^2 + |Q|^2 + 2/3(W_a^2 + W_b^2 + W_{ab}^2) \\ &= |P_{a,i}|^2 + |P_{b,i}|^2 + |Q_i|^2 + 2/3(W_{a,i}^2 + W_{b,i}^2 + W_{ab,i}^2). \end{aligned} \quad (92)$$

Figure (40) illustrates W_a , W_b and W_{ab} as a function of time for a particular radius in the reshaping region.

$J = 4$

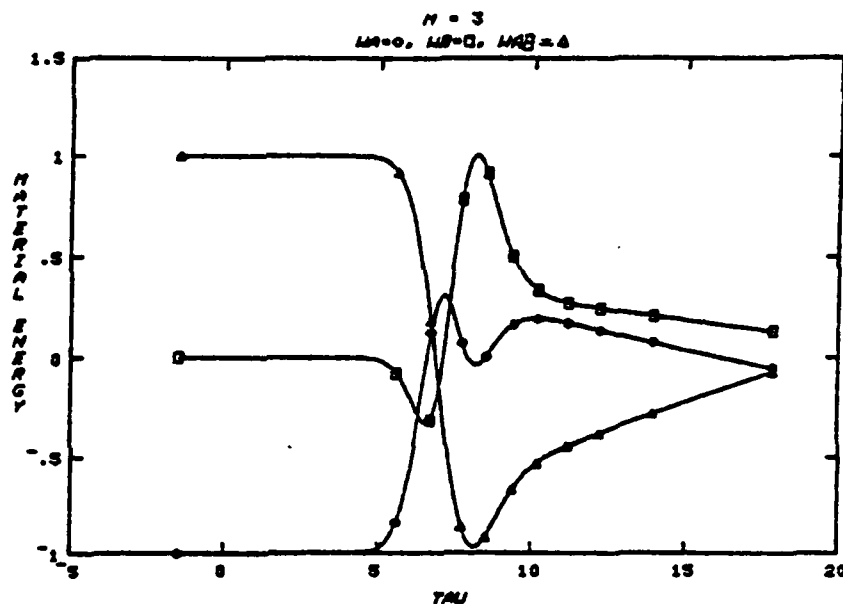


Fig. 40. Contrast of the material energy for a double self-induced transparency calculation.

Numerical Refinements

If the two laser beams which propagate concomitantly are severely disparate from each other, the normal stretching technique must be generalized into a double stretching transformation^{60c} to ensure that the nonuniform temporal grids simultaneously match the two different pulses. No spatial rezoning is as yet designed.

Prescribed Double Stretching

Due to the essential nonlinear nature of the cooperative effects associated with a coherent light-matter interaction, dif-

ferent speeds are associated with pulses of different strengths. So particular attention must be given to deal effectively with two concomitant longitudinal speeds (one for each laser). Mathematically this is

$$T = a\tau + b \sin \omega_s \tau$$

$$\frac{\partial T}{\partial \tau} = a + b \omega_s \cos \omega_s \tau$$

and is shown in Fig. 41. Evenly spaced grid points in T are clearly related to non-uniform variable grid points in the physical time τ .

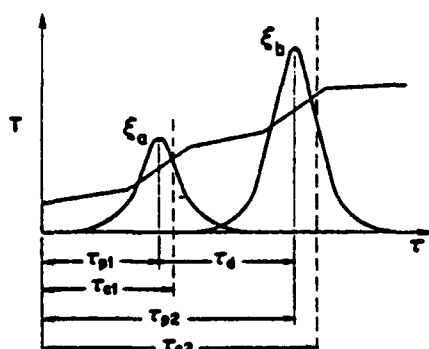


Fig. 41. Displays the prescribed double stretching.

ω_s	0	$\pi/2$	π	$3\pi/2$	2π
$\cos \omega_s \tau$	1	0	-1	0	1
$\partial T / \partial \tau$	$a + b\omega_s$	a	$a - b\omega_s$	a	$a + b\omega_s$

For $\omega_s \tau = \pi$, $\partial T / \partial \tau$ is minimum.

Several noteworthy facts must not be overlooked, i.e., (i) ω_s is related to the frequency of oscillations; and (ii) the steepness of the slopes must depend on the concentration points.

The various stretching parameters are given by

$$a = 1/2 \left[\frac{\partial T}{\partial \tau} \Big|_{\max} + \frac{\partial T}{\partial \tau} \Big|_{\min} \right]$$

$$b = \{1/2 \omega_s\} \left[\frac{\partial T}{\partial \tau} \Big|_{\max} - \frac{\partial T}{\partial \tau} \Big|_{\min} \right]$$

$$\omega_s (\tau_{c2} - \tau_{c1}) = 2\pi \Rightarrow \omega_s \tau_d = 2\pi$$

If τ_d increases, ω_s decreases - a smaller frequency yields to a larger b , if τ_d decreases, ω_s increases - a larger frequency yields to a smaller b parameter.

To ensure monotonicity of the function T in τ (so that multi-valued possibilities are excluded), an important condition which must never be violated (see Fig. 42), is

$$z = \frac{\partial T}{\partial \omega} \Big|_{\min} \equiv (a - b\omega) > 0$$

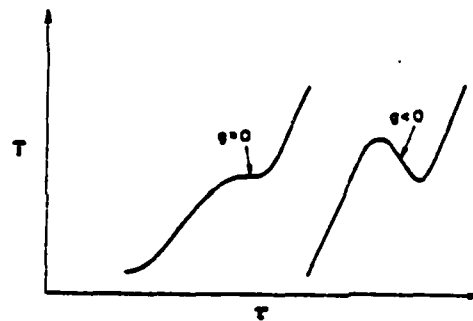


Fig. 42. Displays the limitations on the parameter choice to the double stretching transformation.

Adaptive Double Stretching

Following the spirit of adjusted stretching for a single pulse, described in Section V, the sampling frequency ω_s can vary along the direction of propagation η .

Prescribed Triple Stretching

For a correct treatment of the pulses propagating concomitantly while one of the two lasers may have broken up into two small pulses, successive double stretchings are applied

Step 1 $\zeta = A x^2 + Bx$

$$\begin{aligned}
 \text{from} \quad & x = x_2, \quad \zeta = \zeta_0 = Ax_2^2 + Bx_2 \\
 & x = x_3, \quad \zeta = 2\zeta_0 = Ax_3^2 + Bx_3 \\
 \text{and} \quad & x = 0, \quad \zeta = 0. \\
 & \zeta_1 - \zeta_2 = \zeta_2 - \zeta_3 = 0 - \zeta_1
 \end{aligned}$$

$$\text{one gets,} \quad A = \frac{\zeta_0(x_3 - 2x_2)}{x_3x_2(x_2 - x_3)} \quad \text{and} \quad B = \frac{\zeta_0(2x_2^2 - x_3^2)}{x_2x_3(x_2 - x_3)} ;$$

$$\text{Step 2} \quad Y = a\zeta + b \sin \omega_s \zeta$$

$$\text{Cumulative step} \quad Y = a(Ax^2 + Bx) + b \sin \omega_s (Ax^2 + Bx)$$

$$\begin{aligned}
 Y_x &= a(2x A + B) + b\omega_s (2Ax + B) \cos (Ax^2 + B) \\
 &= (2Ax + B) (a + b\omega_s \cos (Ax^2 + B)) .
 \end{aligned}$$

The coefficients are readily found (see Fig. 43).

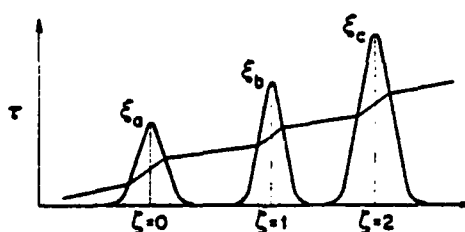


Fig. 43. Illustrates a prescribed triple stretching.

XVII. CONCLUDING REMARKS

Most of the features of the numerical model used to study temporal and transverse reshaping effects of single and multiple short optical pulses propagating concomitantly in active, nonlinear, resonant media have been presented. The calculations strive to achieve a rigorous analysis of this nonlinear interaction with maximum accuracy and minimum computational effort. The applicability of computational methods developed in gas and fluid dynamics to the detailed evolution of optical beams in nonlinear media have been demonstrated.

By introducing adaptive stretching and rezoning transformations wherever possible, the calculations improved considerably.

In particular, self-adjusted rezoning and stretching techniques consisting of repeated applications of the same basic formulae were reviewed as a convenient device for generating computational grids for complex nonlinear interactions. The techniques are well-suited for each programming because the mapping functions and all related derivatives are defined analytically as much as possible. Enhancement of speed and accuracy was realized by improving the integration technique/algorithm which was general and simple in its application compared with its analogue, the two-dimensional Lagrangian approach⁴².

This method was applied to a number of SIT situations with and without homogeneity in the resonant properties of the atomic medium. Note that the theoretical predictions defined with the single stream SIT code, when applied to absorbing media, were quantitatively found⁶⁴ by independent experimental observations⁶⁵, and recent independent perturbational⁶⁶ and computational analysis⁶⁷. The design of the first of these experiments dealing with sodium vapor, was based on qualitative ideas, quantitative analysis and numerical results obtained with the code described in this paper. More recently, King et al also reported⁶⁸ the experimental observation in iodine atomic vapor of the coherent on-resonance self-focusing. This is a novel manifestation of the phenomenon as it deals with a magnetic dipole instead of an electric dipole moment.

Also, the severe beam distortion and on-axis pulse break-up, when the problem of transverse boundary is rigorously addressed, was observed in high power lasers used in Laser Fusion experiments.

With the help of Gibbs and McCall, we have resolved the major discrepancies between planar calculations (as done by Hopf et al⁶⁹) and the Cs experimental observations. The main sources of these discrepancies⁶⁰ were the occurrence of transverse effects in the experiments and the uncertainty in the tipping angle values.

Optical bistability shares with the previous SIT and SF the same basic physical features; however, the initial and boundary conditions are different and complicate the problem. Nevertheless, the similarities predominate; therefore, a unified numerical description with some modifications can apply to all these problems. This new computational approach, based on the concept of absolute consistency of the numerics with the physics, should be successful.

ADDENDUM

An alternate solution to eliminate rapid oscillations from the two-mode Bloch equation without recourse to harmonic expansion could be to adopt Moore and Scully⁷¹ multiple-scaling perturbation

expansion. They have applied the techniques of multiple-scaling perturbation theory, described in hydrodynamics textbooks, to the free-electron laser problem and the pico-second transient phenomena.

ACKNOWLEDGMENTS

F.P. Mattar thanks his thesis advisor Professor M.C. Newstein, his mentors Professors H.A. Haus and Gino Moretti, for their guidance in the physics and numerics of the work. He has benefitted from discussions with Drs. H.M. Gibbs, S.L. McCall, J.H. Marburger, D.C. Brown, P.E. Toschek, and M.S. Feld in the physics; and J. Hermann, B.R. Suydam and J. Fleck, on the numerics. He is indebted to Dr. Gibbs for his faith in the work that led to the first experimental verification of the coherent on-resonance self-focusing. The hospitality of Dr. J. Teichman at the Univ. of Montreal and Dr. T.C. Catrall at Mobil, (which made the computations possible), is gratefully acknowledged. F.P. Mattar particularly thanks Dr. C. Hazzi and D.J. Steele for their patience, support and encouragement during his convalescence. Furthermore, the editing efforts of D.J. Steele the artwork of Kerop Studio in Cairo, W. Roberts and D.J. Steele in New York; and the skillful and laborious word processing efforts of E. Cummings are joyfully appreciated.

REFERENCES

1. (a) R.H. Dicke, *Phys. Rev.* **93**, 99 (1954) and in *Proc. Third Int. Conf. on Quant. Elec.*, Paris, 1963, ed. by P. Grivet and N. Bloembergen (Columbia University Press, N.Y., 1964); (b) D.C. Burnham and R.Y. Chiao, *Phys. Rev.* **188**, 667 (1979) and S.L. McCall, Ph.D. thesis, Univ. of California, Berkeley (1968); (c) J.C. MacGillivray and M.S. Feld, *Phys. Rev. A* **14**, 1169 (1976); (d) R. Bonifacio and L.A. Lugiato, *Phys. Rev. A* **11**, 1507 and 12 587 (1975).
2. (a) *Cooperative Effects in Matter and Radiation*, ed. by C.M. Bowden, D.W. Howgate and H.R. Robl (Plenum Press, N.Y., 1977), and (ii) panel discussion compiled by M. Konopnicki and A.T. Rosenberg, p. 360, (ii) H.M. Gibbs, p. 61 and (iii) Q.H.F. Vrehen, p. 79; (b) lecture on Superfluorescence experiments, 1977 NATO/ASI on Coherence in Spectroscopy and Modern Physics (Plenum Press, N.Y., 1977); (c) Q.H.F. Vrehen, *Coherence and Quantum Optics IV*, ed. by L. Mandel and E. Wolf (Plenum Press, N.Y., 1978), pp. 78 and *Laser Spectroscopy IV*, ed. H. Walther and I.W. Rothe; (d) Q.H.F. Vrehen, H.M.J. Hiksloops and H.M. Gibbs, *Phys. Rev. Lett.* **38**, 764 (1977), *Phys. Rev. Lett.* **39**, 547 (1977) and *Laser Spectroscopy III*, ed. by J.I. Hall and J.I. Carlsten, Springer-Verlag (1977);

- (e) Q.H.F. Vreken and M.F.H. Schuurmans, *Phys. Rev. Lett.* **42**, 224 (1979).
3. (a) H. Seidel, Bistable optical circuits using saturable absorber within a resonant cavity, U.S. Patent 3 610 731 (1969); (b) H.M. Gibbs, S.L. McCall and T.N.C. Venkatesan, *Optics News* **5**, 6 (1979), *J. Opt. Soc. Am.* **65**, 1184 (1975), *Phys. Rev. Lett.* **36**, 1135 (1976) (U.S. patents #012,699 [1975] and #121,167 [1976], lecture on Optical Bistability and Differential Gains at 1977 NATO/ASI on Coherence in Spectroscopy and Modern Physics (Plenum Press, 1977); (c) A. Szöke, V. Daneu, J. Goldher, and N.A. Kurint, *Appl. Phys. Lett.* **15**, 376 (1969).
 4. (a) T.N.C. Venkatesan and S.L. McCall, *Appl. Phys. Lett.* **30**, 282 (1977), H.M. Gibbs, S.L. McCall, T.N.C. Venkatesan, A.C. Gossard, A. Passner and W. Wiegmann, CLEA/1978 (IEEE J. Quantum Electronics **15**, 108D [1979]) and *Appl. Phys. Lett.* **35**, 451 (1979); S.L. McCall and H.M. Gibbs (to be published in *Opt. Comm.* 1980) and H.M. Gibbs, S.L. McCall and T.N.C. Venkatesan (to be published in special issue on Optical Feedback in *Opt. Eng.*); (b) T. Bischofberger and Y.R. Shen, *Appl. Phys. Lett.* **32**, 156 (1978), *Opt. Lett.* **4**, 40 & 175 (1979) and *Phys. Rev. A* **19**, 1169 (1979); (c) P.W. Smith, J.P. Hermann, W.J. Tomlinson and P.J. Maloney, *Appl. Phys. Lett.* **35**, 846 (1979); (d) Proc. of the Int'l Optical Bistability Conf., Asheville, North Carolina (June 1980), ed. C.H. Bowden, M. Ciftan and M.R. Robl, to be published (to be published) by Plenum Press.
 5. R. W. Hellwarth, *J. Opt. Soc. Am.* **67**, 1 (1977) and *IEEE J. Quantum Electron.*, **15**, 101 (1979).
 6. A. Yariv, *IEEE J. Quantum Electron.*, **14**, 650 (1978) and Compensation for Optical Propagation Distortion through Phase Adaptation (preprint Caltech 1979).
 7. (a) S.L. McCall, Ph.D. thesis, Univ. of California, Berkeley (1968); (b) J.-C. Diels, Ph.D. thesis, Univ. of Calif. Berkeley (1973); (c) A. Icsevgi and W.E. Lamb, Jr., *Phys. Rev.* **185**, 517 (1969).
 8. D.W. Dolfi and E.L. Hahn (to appear in *Phys. Rev. a*, 1980).
 9. H.M. Gibbs, B. Bölger, F.P. Mattar, M.C. Newstein, G. Forster and P.E. Toschek, *Phys. Rev. Lett.* **37**, 1743 (1976).
 10. F.P. Mattar, M.C. Newstein, P. Serafim, H.M. Gibbs, B. Bölger, G. Forster and P. Toschek, Fourth Rochester Conf. of Coherence and Quantum Optics, Rochester, NY (June 1977), Plenum Press, ed., L. Mandel and E. Wolf, p. 143-164 (1978).
 11. F.P. Mattar, H.M. Gibbs, Laser 1980, New Orleans (1980).
 12. S.L. McCall, F.P. Mattar, and H.M. Gibbs, Optics in Four-Dimensions, Encenade, Mexico (1980).
 13. F.P. Mattar, H.M. Gibbs, S.L. McCall and M.S. Feld submitted to *Phys. Rev. Lett.* and *Phys. Rev. A*.

14. N. Wright and M.C. Newstein, Opt. Commun., 9, 8 (1973) and IEEE J. Quantum Electron., 10, 743 (1974).
15. M.C. Newstein and F.P. Mattar, Proc. 7th Conf. Numerical Simulation of Plasmas (Courant Institute, NYU, June 1975, p. 223; and Proc. of 10th Congress of the Int'l Commission of Optics, Prague, Czechoslovakia (1975), Recent Advances in Optical Physics, p. 199, B. Havelka and J. Blabla, distributed by the Soc. of Czechoslovak Math. and Phys. (1976); IX Int'l Conf. of Quantum Electronics, Amsterdam (1976), see Opt. Comm. 18, 70 (1976), and IEEE J. Quantum Electron., 13, 507 (1977) and see ref. 2(a) 139.
16. J.C. Diels and E.L. Hahn, Phys. Rev. A 8, 1084 (1973) and Phys. Rev. A 10, 2501 (1974).
17. (a) S.L. McCall and E.L. Hahn, Phys. Rev. Lett. 28, 308 (1967), Phys. Rev. 183, 487 (1969) and Phys. Rev. A 2 (1970); (b) A. Icsevgi and W.E. Lamb, Jr., Phys. Rev. 185, 517 (1969).
18. S.L. McCall, Phys. Rev. A 9, 1515 (1974).
19. (a) J.A. Fleck, Jr., Appl. Phys. Lett. 13, 365 (1968); (b) J.A. Fleck, Jr., Phys. Rev. B 1, 84 (1970); (c) See Ref. 1(c) and ref. (11)
20. (a) S.L. McCall and H.M. Gibbs (to be published in Optics Comm. 1980); (b) H.J. Carmichael (to be published in Optica Acta (1980) and H.J. Carmichael and G.P. Agrawal, Inhomogeneous Broadening and Mean Field Approximation for Optical Bistability in a Fabry-Perot (preprint 1979); Steady State Formulation of Optical Bistability for a Doppler Broadened Medium in a Fabry-Perot (preprint 1980); (c) J.H. Marburger and F.S. Felber, Appl. Phys. Lett. 28, 831 (1976) and Phys. Rev. A 17, 335 (1978); (d) R. Sanders and R.K. Bullough in Cooperative Effects in Matter and Radiation, ed. by C.M. Bowden, D.W. Howgate and H.R. Robl, 209, Plenum Press (1977); and R. Saunders, S.S. Hassan and R.K. Bullough, J. Phys. A 9, 1725 (1976); (e) J.H. Eberly, K.G. Whitney and M. Konopnicki, unpublished Final Research Report to ONR (Fall 1977) Rochester, NY; (f) P. Meystre, Opt. Comm. 26, 277 (1978) and R. Bonifacio and P. Meystre, Opt. Comm. 27, 147 (1978); and F.A. Hopf and P. Meystre (to be published in Opt. Comm.).
21. (a) C.M. Bowden and C.C. Sung, Phys. Rev. A 18, 1558 (1978) and Phys. Rev. A 20, 2033 (1979); (b) R. Brewer and E.L. Hahn, Phys. Rev. A 11, 1641 (1975); (c) M. Sargent III and P. Horwitz, Phys. Rev. A 13, 1962 (1976); (d) N.S. Feld, Frontiers in Laser Spectroscopy, 2, 203 (Les Houches Lectures 1976), Ed. R. Balian, S. Haroche and S. Liberman, North Holland (1977); (e) F.P. Mattar and J.H. Eberly, Proc. of the Physics and Chemistry of Laser-Induced Process in Molecules, Edinburgh (1978) ed. by K.L. Kompa and S.C. Smith, 61, Springer-Verlag (1979); (f) M. Konopnicki and J.H. Eberly, Proc. 10th Pittsburgh Annual Simulation and Modeling Conf., Pittsburgh (1979) ed. Vogt and Publ. Instrument Soc. of America (ISA), Pittsburgh, PA.

22. G. Moretti, Polytechnic Institute of New York Rept 69-25, 1969; Polytechnic Institute of New York Rept 69-26, 1969; Proc. of the 1974 Heat Transfer and Fluid Mechanics Inst., Stanford Univ. Press, 1974, Polytechnic Institute of New York-AE/AM Rept 74-9; (POLY-AE/AM Rept 74-23); Polytechnic Institute of New York Rept 73-18, 1973; Polytechnic Institute of New York Rept 69-26, 1969; Polytechnic Institute of New York Rept 70-48, 1970; Polytechnic Institute of New York Rept 71-25, 1971; POLY-AE/AM Rept 74-15, 1974; Proc. Symposium Transsonicum II, Gottingen, Germany, September 8-13, 1975, Springer-Verlag, Berlin, 439 (1976); (Polytechnic Institute of New York-AE/AM Rept 76-06).
23. G. Moretti, The Chemical Kinetics Problem in the Numerical Analyses of Nonequilibrium Flows, Proc. of the IBM Scientific Computing Symposium on Large Scale Problems in Physics, Dec. 1963, IBM Research Ctr, Yorktown Heights, NY; and Polytechnic Institute of New York Rept 68-15 (1968). Polytechnic Institute of New York-AE/AM Rept 74-15, 1974.
24. G. Moretti, AIAA 14, 834 (1976), and Computers and Fluids 7, 191 (1979).
25. (a) E. Madelung, Z. Physik 40, 322 (1966). (b) H.E. Wilhelm, Phys. Rev. D1, 2278 (1970). (c) M. Jammer, The Philosophy of Quantum Mechanics 21, J. Wiley (1974).
26. (a) F.P. Mattar, Proc. of the Ninth Conf. of Numerical Methods in Plasma, Monterey, California (June 1978). Lawrence Livermore Lab. (LLL) Tech. Rept 78-004. (b) F.P. Mattar, J. Teichman, L. Bissonnette and R.W. MacCormack, Proc. of the Second Int'l Symp. on Gas Flow and Chemical Lasers, ed. J. Wendt, Western Hemisphere Pub. (1979).
27. R.P. Feynman, F.L. Vernon, Jr. and R.W. Hellwarth, J. Appl. Phys. 28, 43 (1957); and E.L. Hahn, Heritage of the Bloch Equations in Quantum Optics, to appear in The Felix Bloch Festschrift 75 Birthday.
28. (a) G. Askary'yan, Sov. Phys. JET P42, 1568 (1962) Moscow; and Usp. Fiz. Nauk., 111, 249, October 1973. (b) S.A. Akhmanov, A-P. Sukhorukov, and P.V. Kokhlov, Laser Handbook, F. Arrechi, Ed., Amsterdam, The Netherlands: North Holland, 1972, 1151. (c) B.R. Suydam, Self-Focusing in passive media I, Los Alamos Scientific Lab, Tech. Rep. L4-5002-MS, March 1973, and IEEE J. Quant. Elec. 10, 837 (1974), and IEEE J. Quant. Elec. 11, 225 (1975).
29. (a) J.H. Marburger, Progress in Quantum Electronics, 4, 35 ed. J.M. Sanders and Stenholm, Pergamon Press (1975), and Theory of Self-focusing with Counter-propagating Beams, preprint (1979). (b) O. Svelto, Progress in Optics XII, E. Wolf, ed. Amsterdam, The Netherlands: North Holland, 1974, 1.
30. Ibid Ref. 16.
31. T. Gustafson, J.-P. Taran, H.A. Haus, J. Lifshitz and P. Kelley, Phys. Rev. 177, 60 (1969).

32. (a) F.P. Mattar, *Kvantovaya Elektronika* 4, 2520 (1977). (b) S.L. McCall and H.M. Gibbs (ibid ref. 20(a) and ref. 4(d)). (c) D.A.B. Miller and S.D. Smith, *Opt. Comm.* 31, 101 (1979) and D.A.B. Miller, S.D. Smith and A. Johnston, *Appl. Phys. Lett.* 35, 658 (1979). (d) M.S. Feld and J.C. MacGillivray in Advances in Coherent Nonlinear Optics, ed. M.S. Feld and V.S. Letokhov (to be published by Springer-Verlag, 1980). (e) R. Bonifacio, J.D. Farina and L.M. Narducci, *Opt. Commun.* 31, 377 (1979).
33. G. Moretti, Polytechnic Institute of New York Rept 69-25, 1960; Polytechnic Institute of New York Rept 69-26, 1969.
34. G. Moretti, Proc. of the ASME Symp. on Numerical/Laboratory Computer Methods in Fluid Mechanics, ASME, Dec. 1976. Polytechnic Institute of New York -M/AE Rept 76-06.
35. L. Bradley and J. Hermann, MIT-Lincoln Lab Tech. Rept LTP-10 (July 1971) and Internal note on Change of reference wavefront in the MIT CW Nonlinear Optics Propagation Code (Fall 1974) private communication.
36. P.B. Ulrich, NRL Rept 7706 (May 1974).
37. H.J. Breaux, Ballistic Research Labs, Aberdeen Proving Ground, Maryland; BRL Rept 1723 (1974).
38. J.A. Fleck, Jr., J.R. Morris and M.D. Feit, *Appl. Phys.* 10, 129 (1976) and 14, 99 (1977).
39. F.P. Mattar, *Appl. Phys.* 17, 53 (1968) Springer-Verlag.
40. K.G. Whiteney, G.L. Nader, and P.B. Ulrich, Naval Research Lab. Washington, DC, NRL Rept 8074 (1977).
41. W.A. Newcomb, Nuclear Fusion, Suppl. 2, 451 (1962).
42. F.P. Mattar and J. Teichmann, IEEE Conf. Plasma Science, Montreal (1979) and submitted to *Comp. Phys. Comm.*
43. (a) G. Moretti, *AIAA* 14, 894 (1976) and Poly-M/AE Tech. Rep. 78 (1980), PINY; (b) B. Gabutti, La stabilita de una schema alle differenze finite per le equazioni della fluide dinamica (preprint, Polytechnico di Milano).
44. H.M. Gibbs and R. E. Slusher, *Appl. Phys. Lett.* 18, 505 (1971), *Phys. Rev. A* 5, 1634 (1972) and *Phys. Rev. A* 6, 2326 (1972).
45. H.A. Haus and T.K. Gustafson, *IEEE J. Quant. Elec.* 4, 519 (1968).
46. F.P. Mattar and M.C. Newstein, PINY Rept. ADL-M/AE 79-63 (1979) (to be published in *Comp. Phys. Comm.* 1980).
47. G. Moretti, Polytechnic Institute of New York Rept 68-15 (1968). Polytechnic Institute of New York-AE. AM Rept 74-15, 1974.
48. (a) V.I. Bespalov and V.I. Talanov, *Soviet Phys., JETP letters*, 3, 471 (1966), *Eng. Trans.* 3, 307. (b) V.I. Talanov, *Soviet Phys. JETP Letters* 2, 218 (1965) *Eng. Trans.* 2, 138 and *Zh. Eksp. Teor. Fiz. Pisma. Red.* 11, 303, *Eng. Trans.* 133, *JETP letters*, 1970. (c) B.R. Suydam, Laser Induced Damage in Optical Material, 1973 NBS special publication 387, 42 and *IEEE J. Quant. Elec.* 10, 837 (1973) and *IEEE J. Quant. Elec.*

- 11, 225 (1975). (d) J.B. Trenholme, (LLL) Laser Fusion program 2nd 1973 semi-annual program report, 47 (UCRL-60021-73-2).
- (e) N.B. Baranova, N.E. Bykovskii, B. Ya. Zel'dovich and Yu. V. Senatskii, Kvant. Elektron. 1, 2435 (1974). (f) D.C. Brown, The Physics of High Peak Power Nd-Glass Lasers, Springer-Verlag (to be published in the Spring 1980). (g) L.A. Gol'shov, V.V. Likhanskii and A.O. Napartovich, Zh. Eksp. Teor. Fiz. 72, 769 (1977) Moscow. (h) M.J. Ablowitz and Y. Kodama, Phys. Lett. (1979). (i) L.A. Bol'shov, T.K. Kirichenko, A.P. Favolsky, U.S.S.R. Acad. of Sci., Math. Div. preprint, Fall 1978), Inst. of Appl. Math. 1978, 53 (3A) in Russian.
49. W.G. Wagner, H.A. Haus and J.H. Marburger, J. Phys. Rev. (1970).
50. R. Courant and K.O. Friedrichs, Supersonic Flow and Shock Waves, NY Interscience (1948).
51. F.A. Hopf and M.O. Scully, Phys. Rev. 179, 399 (1969).
52. R.W. MacCormack, AIAA Hypervelocity Impact Conf., 1969, paper 69-554 and Lecture Notes in Physics, Springer-Verlag, 151 (1971).
53. P. Gordon, General Electric Final Rep. NOL Contrace #N60921-7164 (1968).
54. R.W. Hamming, Numerical Methods for Scientists and Engineers, McGraw-Hill Book Co. (1962).
55. (a) B.R. Suydam, A Laser Propagation Code, Los Alamos Sci. Lab., LA-5607-MS Tech. Informal Rept (1974). (b) F.P. Mattar (with the help of Dr. B.R. Suydam, LASL) Eighth Conf. on Numerical Simulation of Plasmas, Monterey, Calif. (June 1978). Distributed by the Univ. of Calif./LLL, Livermore, Calif. (rept Conf-780612).
56. F.P. Mattar and R.E. Francoeur, Transient Counter-Beam Propagation in a Nonlinear Fabry Perot Cavity (Long Sample), PINY, ADL-M/AE Tech. Rept. 80-12 (1980) and Proc. of the Ninth Conf. of Numerical Simulation of Plasma (ed. G. Knorr and J. Denavit) Northwestern Univ. Evanston, IL, 1980.
57. F.P. Mattar and S.L. McCall, Transient Counter-Beam Propagation in a Nonlinear Fabry Perot Cavity II. Short Sample, PINY, ADL-M/AE Tech. Rept. 80-15 (1980).
58. (a) Ibid ref. 1(c); (b) Ibid ref. 2
59. Ibid ref. 21(a).
60. (a) Ibid ref. 21(d); (b) Ibid ref. 21(e); (c) F.P. Mattar, Proc. 10th Pittsburgh Annual Simulation and Modeling Conf., Pittsburgh (1979), ed. W. Vogt and M. Mickle, Publ. ISA, Pittsburgh, PA.
61. R.G. Brewer, (1975) in Frontiers in Laser Spectroscopy, ed. R. Balian, S. Haroche and S. Liberman 338 (North Holland 1977).
62. V.S. Letkhov and B.D. Sov. J. Quant. Elec. 4, 11 (1975).
63. D. Walls (ref. 4(d)).

64. (a) H.M. Gibbs, B. Bölger, F.P. Mattar, M.C. Newstein, G. Forster and P.E. Toschek, Phys. Rev. Lett. 37, 1743 (1976) (prep. by H.M. Gibbs); (b) Ref. (10); (c) F.P. Mattar, G. Forster and P.E. Toschek, Spring meeting of the German Phys. Soc., Mainz, F.R. Germany (Feb. 1977). Kvantovaya Elektronika 5, 1819 (1978).
65. (a) H.M. Gibbs, B. Bölger and L. Baade, IX Int'l Conf. of Quant. Elec. (1976), Opt. Comm. 18, 199 (1976). (b) G. Forster and P.E. Toschek, Quantum Optics Session of the Spring Annual Meeting of the German Phys. Soc., Hanover, F.R. Germany (Feb. 1976). (c) W. Krieger, G. Gaida and P.E. Toschek, Z. Physik B25, 297 (1976).
66. (a) L.A. Bol'shov, V.V. Likhanskii and A.O. Napartovich, Zh. Eksp. Teor. Fiz. 72, 1769 (1977) Moscow; (b) M.J. Ablowitz and Y. Kodama, Phys. Lett. A70, 83 (1979); (c) L.A. Bolshov and V.V. Likhansky, Zhurnal Eksperimental'noi i Teoreticheskii Fiziki, 75, 2947 (1978) in Russian (Eng. trans.: Sov. Phys. Jnl of Exp. and Theo. Phys. 48, 1030 (1979)).
67. L.A. Bol'shov, T.K. Kirichenko, A.P. Favolsky, (USSR Acad. of Sci., Math. Div. preprint, Fall 1978), Inst. of Appl. Math. 1978, 53 (3A) in Russian.
68. J.J. Bannister, H.J. Baker, T.A. King and W. G. McNaught, Phys. Rev. Lett. 44, 1062 (1980) and XI Int'l Conf. of Quant. Elec., Boston (1980).
69. F.A. Hopf (private communication).
70. (See *ibid* ref. 11-13.)
71. G.T. Moore and M.O. Scully, Coherent Dynamics of a Free-Electron Laser with Arbitrary Magnet Geometry. I-General Formulation, Opt. Sci. Ctr, Univ. of Arizona, preprint (brought to the author's attention by Professor F.A. Hopf).

TRANSVERSE AND PHASE EFFECTS IN LIGHT CONTROL BY LIGHT:
PUMP DYNAMICS IN SUPERFLUORESCENCE

F. P. Mattar*

Mechanical and Aerospace Engineering Dept., Polytechnic Institute of New York, Brooklyn, NY 11201
and Spectroscopy Laboratory, Massachusetts Institute
of Technology, Cambridge, MA 02139

and

C. M. Bowden

Research Directorate, US Army Missile Laboratory
US Army Missile Command, Redstone Arsenal, Huntsville, AL 35898

and

Y. Claude and M. Cormier

Dept d'Informatique, Université de Montreal, Montreal, PQ, Canada

Abstract

Calculational results and analysis are presented and discussed for the effects of coherent pump dynamics, propagation, transverse and diffraction effects on superfluorescent (SF) emission from an optically-pumped three-level system. The full, co-propagational aspects of the injected pump pulse together with the SF which evolves are explicitly treated in the calculation. It is shown that the effect of increasing the injection signal area exhibits a similar effect on the evolved SF delay time as either increasing the gain, or F^{-1} , (F is the Fresnel number per effective gain). All else being equal, it is demonstrated that alteration of the temporal as well as radial shape of the injected pump pulse has a profound effect upon the shape of SF as well as the sharpness of the rise of the pulse, its delay time, peak intensity and temporal width. For conditions of sufficiently large gain and large injection pulse area, SF which evolves and the propagating pump pulse eventually occur in the same time frame (overlap). It is shown that under these conditions the SF can be significantly temporally narrower than the pump and of significantly larger peak intensity. Thus, by choosing the shape of the injected pump envelope and/or its area, the SF shape, delay time, peak intensity and temporal duration can be altered. Thus, deterministic control of the characteristics of the evolving SF pulse is demonstrated by selecting appropriate characteristics of the injected pulse signal at a different frequency.

Introduction

Superfluorescence[1] (SF), is the dynamical radiation process which evolves from a collection of atoms or molecules prepared initially in the fully inverted state, and which subsequently undergoes collective, spontaneous relaxation[2]. Since Dicke's early work[2], much theoretical and experimental effort has been devoted to this subject[3].

With the exception of the more recent work of Bowden and Sung[4], all theoretical treatments have dealt exclusively with the relaxation process from a prepared state of complete inversion in a two-level manifold of atomic energy levels, and thus do not consider the dynamical effects of the pumping process. Yet, all reported experimental work[5-10] has utilized optical pumping on a minimum manifold of three atomic or molecular energy levels by laser pulse injection into the nonlinear medium, which subsequently superfluoresces.

It was pointed out by Bowden and Sung[4] that for a system otherwise satisfying the conditions for superfluorescent emission, unless the characteristic superradiance time[1], τ_R , is much greater than the pump pulse temporal duration, τ_p , i.e., $\tau_R \gg \tau_p$, the process of coherent optical pumping on a three-level system can have dramatic effects on the SF. This is a condition which has not been realized over the full range of reported data. Also, Bowden and Sung's analysis was restricted to the uniform plane wave regime; it cannot account for the inevitable spatial and temporal beam energy redistribution (as in physical system). Transverse fluency is associated with radial density variations and diffraction coupling, it leads to communication among the various parts of the beam.

In this paper, we present calculational results and analysis for the effects of coherent pump dynamics, propagation, transverse and diffraction effects on SF emission from an optically-pumped three-level system. The full, nonlinear, co-propagational aspects of the injected pump pulse, together with the SF which evolves are explicitly treated in the calculation. Not only do our results relate strongly to previous calculations and experimental results in SF, but we introduce and demonstrate a new concept in nonlinear light-matter

* Jointly supported by the US Army Research Office DAAG29-79-C-0148, the Office of Naval Research N000-14-80-C-0174, and Battelle Columbus

145
interactions, which we call light control by light. We show how characteristics of the SF can be controlled by specifying certain characteristics of the injection pulse.

Equations of motion

The model upon which the calculation is based is comprised of a collection of identical three-level atoms, each having the energy level scheme shown in Figure 1. The $1 \leftrightarrow 3$ transition is induced by a coherent electromagnetic field injection pulse of frequency ω_0 nearly tuned to the indicated transition. The properties of this pumping pulse are specified initially in terms of the initial and boundary conditions. The transition $3 \leftrightarrow 2$ evolves by spontaneous emission at frequency ω_0 . It is assumed that the energy level spacing is such that $\epsilon_3 > \epsilon_2 \gg \epsilon_1$ so that the fields at frequencies ω_0 and ω can be treated by separate wave equations. The energy levels $2 \leftrightarrow 1$ are not coupled radiatively due to parity considerations, and spontaneous relaxation from $3 \leftrightarrow 2$ is simulated by the choice of a small, but nonzero initial transverse polarization characterized by the parameter $\phi_0 \sim 10^{-4}$. Our results do not depend upon nominal deviations of this parameter. The initial condition is chosen consistent with the particular choice of ϕ_0 , with nearly all the population in the ground state, and the initial values of the other atomic variables chosen consistently [4,11].

We use the electric dipole and rotating wave approximations and couple the atomic dipole moments to classical field amplitudes which are determined from Maxwell's equations. The Hamiltonian which describes the field-matter interaction for this system [4] comprising N atoms, is,

$$H = \sum_{r=1}^3 \sum_{j=1}^N \epsilon_{rj} R_{rr}^{(j)} - \frac{i\hbar}{2} \sum_{j=1}^N [\Omega^{(j)} R_{32}^{(j)} e^{-i(\omega t - \mathbf{k} \cdot \mathbf{r}_j)} - \Omega^{(j)*} R_{23}^{(j)} e^{i(\omega t - \mathbf{k} \cdot \mathbf{r}_j)}] - \frac{i\hbar}{2} \sum_{j=1}^N [\omega_R^{(j)} R_{31}^{(j)} e^{-i(\omega_0 t - \mathbf{k}_0 \cdot \mathbf{r}_j)} - \omega_R^{(j)*} R_{13}^{(j)} e^{i(\omega_0 t - \mathbf{k}_0 \cdot \mathbf{r}_j)}], \quad (1)$$

The first term on the right-hand side of Eq. (1) is the free atomic system Hamiltonian, with atomic level spacings ϵ_{rj} , $r = 1, 2, 3$; $j = 1, 2, \dots, N$. The second term on the right-hand side describes the interaction of the atomic system with the fluorescence field associated with the $3 \leftrightarrow 2$ transition, whereas the last term on the right in (1) described the interaction between the atomic system and the coherent pumping field. The fluorescence field and the pumping field have amplitudes $\Omega^{(j)}$ and $\omega_R^{(j)}$, respectively, in terms of Rabi frequency, at the position of the j^{th} atom, \mathbf{r}_j . The respective wave vectors of the two fields are \mathbf{k} and \mathbf{k}_0 and the carrier frequencies are ω and ω_0 . It is assumed that the electromagnetic field amplitudes vary insignificantly over the atomic dimensions and that all of the atoms remain fixed during the time frame of the dynamical evolution of the system.

The atomic variables in (1) are the canonical operators [4] $R_{kl}^{(j)}$ which obey the Lie algebra defined by the commutation rules [12-14]

$$[R_{ij}^{(m)}, R_{kl}^{(n)}] = R_{ik}^{(m)} \delta_{lj} \delta_{mn} - R_{lj}^{(m)} \delta_{ik} \delta_{mn} \quad (2)$$

$i, j, = 1, 2, 3$; $m, n = 1, 2, \dots, N$. The Rabi rates, $\Omega^{(j)}$ and $\omega_R^{(j)}$ are given in terms of the electric field amplitudes $E^{(j)}$ and $E_0^{(j)}$, respectively, and the matrix elements of the transition dipole moments, $\mu_{32}^{(j)}$ and $\mu_{31}^{(j)}$ by

$$\Omega^{(j)} = \frac{E^{(j)} \mu_{32}^{(j)}}{\hbar}, \quad (3a)$$

$$\omega_R^{(j)} = \frac{E_0^{(j)} \mu_{31}^{(j)}}{\hbar}, \quad (3b)$$

where we have considered only one linear polarization for the two fields and propagation in the positive z direction.

It is convenient to canonically transform (1) to remove the rapid time variations at the carrier frequencies ω and ω_0 and the rapid spacial variations in the wave vectors \mathbf{k} and \mathbf{k}_0 . We assume that the field envelopes $\Omega^{(j)}$ and $\omega_R^{(j)}$ vary much more slowly than the periods ω^{-1} and ω_0^{-1} , respectively. In the trans-

formed representation, we are thus dealing with slowly varying field amplitudes and atomic operators. The desired transformation U is unitary and is described in ref. 12.

$$\tilde{H}_T = U H U^{-1}$$

The equations of motion for the atomic variables are calculated from the transformed Hamiltonian according to

$$i\hbar \dot{R}_{kl}^{(j)} = [H_T, R_{kl}^{(j)}] \quad (5)$$

This set of equations constitutes the equation of motion for the density operator ψ for the system in the slow-varying operator representation. By imposing the canonical unitary transformation, we, in fact, transformed to a slow-varying operator representation which is consistent with the slowly-varying enveloped approximation to be imposed later on in the Maxwell's equations coupled to the hierarchy of nonlinear, first-order equations, (5).

The following hierarchy of coupled nonlinear equations of motion is obtained for the atomic variables:

$$\dot{R}_{33}^{(j)} = \frac{1}{2} [\Omega^{(j)} R_{32}^{(j)} + \Omega^{*(j)} R_{23}^{(j)}] + \frac{1}{2} [w_R^{(j)} R_{31}^{(j)} + w_R^{*(j)} R_{13}^{(j)}] - \gamma_{11} [R_{33}^{(j)} - R_{33}^{(e)}], \quad (6a)$$

$$\dot{R}_{22}^{(j)} = -\frac{1}{2} [\Omega^{(j)} R_{32}^{(j)} + \Omega^{*(j)} R_{23}^{(j)}] - \gamma_{11} [R_{22}^{(j)} - R_{22}^{(e)}], \quad (6b)$$

$$\dot{R}_{11}^{(j)} = -\frac{1}{2} [w_R^{(j)} R_{31}^{(j)} + w_R^{*(j)} R_{13}^{(j)}] - \gamma_{11} [R_{11}^{(j)} - R_{11}^{(e)}], \quad (6c)$$

$$\dot{R}_{32}^{(j)} = i\delta^{(j)} R_{32}^{(j)} + \frac{1}{2} \Omega^{*(j)} [R_{22}^{(j)} - R_{33}^{(j)}] + \frac{1}{2} w_R^{*(j)} R_{12}^{(j)} - \gamma_1 R_{32}^{(j)}, \quad (6d)$$

$$\dot{R}_{12}^{(j)} = i\delta^{(j)} R_{12}^{(j)} - \frac{1}{2} [\Omega^{*(j)} R_{13}^{(j)} + w_R^{(j)} R_{32}^{(j)}] - \gamma_1 R_{12}^{(j)}, \quad (6e)$$

$$\dot{R}_{13}^{(j)} = i\delta^{(j)} R_{13}^{(j)} + \frac{1}{2} \Omega^{(j)} R_{12}^{(j)} - \frac{1}{2} w_R^{(j)} [R_{33}^{(j)} - R_{11}^{(j)}] - \gamma_1 R_{13}^{(j)}. \quad (6f)$$

In Eqs. (6), we have added phenomenological relaxation γ_{11} and dephasing γ_1 and taken these to be uniform, i.e., the same parameters for each transition. For the diagonal terms, $R_{kk}^{(j)}$, the equilibrium values are designated as $R_{kk}^{(e)}$, the same for all atoms.

Since the equations (6) are linear in the atomic variables $R_{kl}^{(j)}$, they are isomorphic to the set of equations of motion for the matrix elements of the density operator ψ . We shall treat the Eqs. (6) from this point as c-number equations. Further, we assume that all the atoms have identical energy level structure and also, we drop the atomic labels j , so it is taken implicitly that the atomic and field variables depend upon the special coordinates as well as the time.

It is convenient to introduce a new set of variables in terms of the old ones. We let

$$w_{kl} = R_{kl} - R_{ll} \quad , \quad k > l \quad , \quad (7a)$$

$$R_{kl} = \frac{1}{2} (U_{kl} + i V_{kl}) \quad , \quad k > l \quad , \quad (7b)$$

where U_{kl} , V_{kl} , and w_{kl} are real variables, and $U_{kl} = U_{lk}$, $V_{kl} = V_{lk}$,

$$\Omega = X + iY \quad , \quad (7c)$$

$$w_R = X_0 + iY_0 \quad , \quad (7d)$$

where X , Y , X_0 and Y_0 are real variables.

The resulting equations of motion for the real variables $\{w_{kl}, U_{kl}, V_{kl}\}$ are

$$\dot{w}_{31} = \frac{1}{2} \{X U_{32} - Y V_{32}\} + \{X_0 U_{31} - Y_0 V_{31}\} - \gamma_{11} [w_{31} - w_{31}^{(e)}], \quad (8a)$$

$$\dot{w}_{32} = \{X U_{32} - Y V_{32}\} + \frac{1}{2} \{X_0 U_{31} - Y_0 V_{31}\} - \gamma_{11} [w_{32} - w_{32}^{(e)}], \quad (8b)$$

$$\dot{U}_{32} = -\delta V_{32} - X w_{32} + \frac{1}{2} [X_0 U_{21} - Y_0 V_{21}] - \gamma_1 U_{32}, \quad (8c)$$

$$\dot{V}_{32} = \delta U_{32} + YW_{32} - \frac{1}{2} [X_o V_{21} + Y_o U_{21}] - Y_1 V_{32} \quad (8d)$$

$$\dot{U}_{31} = \delta V_{31} + \frac{1}{2} [XU_{21} + YV_{21}] - X_o W_{31} - Y_1 U_{31} \quad (8e)$$

$$\dot{V}_{31} = -\delta U_{31} + \frac{1}{2} [XV_{21} - YU_{21}] + Y_o W_{31} - Y_1 V_{31} \quad (8f)$$

$$\dot{U}_{21} = \delta V_{21} - \frac{1}{2} [XU_{31} - YV_{31}] - \frac{1}{2} [X_o U_{32} - Y_o V_{32}] - Y_1 U_{21} \quad (8g)$$

$$\dot{V}_{21} = -\delta U_{21} - \frac{1}{2} [XV_{31} + YU_{31}] + \frac{1}{2} [X_o V_{32} + Y_o U_{32}] - Y_1 V_{21} \quad (8h)$$

In obtaining Eqs. (8), we have made use of the invariant, $\text{tr } \psi = I$,

$$I = R_{11}^{(j)} + R_{22}^{(j)} + R_{33}^{(j)} \quad (9)$$

It is noted that $\dot{I} = 0$ is satisfied identically in (6a)-(6c) for $Y_{11} = 0$. For $Y_{11} \neq 0$, the condition (9) together with (6a)-(6c) constitutes the statement of conservation of atomic density, i.e., particle number.

The Eqs. (8) are coupled to Maxwell's equations through the polarizations associated with each transition field. It is easily determined that the Maxwell's equations in dimensionless form in the slowly-varying envelope approximation and in the retarded time frame can be written in the following form

$$\frac{1}{\epsilon_p} \nabla_\rho^2 \left\{ \begin{matrix} -X \\ Y_o \end{matrix} \right\} + \frac{\partial}{\partial \eta_p} \left\{ \begin{matrix} Y_o \\ X_o \end{matrix} \right\} = d \left\{ \begin{matrix} -U_{31} \\ V_{31} \end{matrix} \right\} \quad (10a)$$

$$\frac{1}{\epsilon_s} \nabla_\rho^2 \left\{ \begin{matrix} -X \\ Y \end{matrix} \right\} + \frac{\partial}{\partial \eta_s} \left\{ \begin{matrix} Y \\ X \end{matrix} \right\} = d \left\{ \begin{matrix} -U_{32} \\ V_{32} \end{matrix} \right\} \quad (10b)$$

In the above equations, we have assumed cylindrical symmetry, thus the transverse Laplacian which accounts for diffraction coupling is:

$$\nabla_\rho^2 = \frac{1}{\rho} \frac{\partial}{\partial \rho} \left(\rho \frac{\partial}{\partial \rho} \right) \quad (11)$$

The first term on the left-hand side in (10a,b) accounts for transverse communication effects across the beam with normalized radial coordinate $\rho = r/r_p$ where r is the radial distance and r_p is a characteristic spatial width. In (10), $\eta_{p,s} = z \alpha_{eff_{p,s}}$ where $\alpha_{eff_{p,s}}$ is the on-axis effective gain,

$$\alpha_{eff_{p,s}} = \frac{\left\{ \begin{matrix} \mu_{32} \\ \mu_{31} \end{matrix} \right\}^2}{n^2 A c} \left\{ \begin{matrix} \tau_p \\ \tau_s \end{matrix} \right\} \quad (12)$$

where $\left\{ \begin{matrix} \tau_p \\ \tau_s \end{matrix} \right\}$ are characteristic times for the system, N is the atomic number density (assumed longitudinally homogeneous) and n is the index of refraction (assumed identical for each transition wavelength). The quantity

$$d = \frac{N(r)}{N_o} \quad (13)$$

governs the relative radial population density distribution for active atoms and is taken as either Gaussian with full width r_p or uniform, in which case r_p corresponds to $\rho_{max} = 1$. The Gaussian distribution would be associated with an atomic or molecular beam with propagation along the beam axis. For the cases treated here, it was found that there is no significant difference in the results for a uniform density distribution with injection pulse of initial radial width at half maximum, r_o , and a Gaussian radial density variation with $r_o = r_p$. For the latter case, the effective gain g_{eff} is appropriately adjusted such that both the radially integrated gain and the total effective gain, $g_{eff}L$, remain invariant between the two cases, where L is the length of the medium in the direction of propagation. In obtaining (10-13), we have extended Matter et. al (14) Theoretical analysis for two-level SF. Equations (10) are written in the retarded time,

τ , frame where $\tau = t - nz/c$. From this point on, \cdot in Eqs. (8) is taken to be $\cdot = \partial/\partial\tau$. Finally, the first factors on the first terms in (10) are the reciprocals of the "gain length" Fresnel numbers defined by

$$F_{ps} = \frac{\pi r_p^2}{\lambda_{ps} s_{eff}^{-1}}, \quad (14)$$

where

$$s_{eff} = \frac{a_{eff}}{r_p} \quad (15)$$

It is seen from (10) that for sufficiently large Fresnel number, F , the corrections due to transverse effects become negligible. Note that F corresponds to a gain to loss ratio. The "gain length" Fresnel numbers F are related to the usual Fresnel numbers $\mathcal{F} = \pi r_p^2/\lambda L$, where L is the length of the medium by

$$F/\mathcal{F} = s_{eff} L. \quad (16)$$

i.e., the total gains of the medium. In the computation, diffraction is also explicitly taken into account by the boundary condition that $\rho = \rho_{max}$ corresponds to completely absorbing walls.

The initial conditions are chosen to establish a small, but nonzero transverse polarization for the $3 \rightarrow 2$ transition with almost the entire population in the ground state. This requires the specification of two small parameters, $\epsilon \sim 10^{-4}$, for the ground state initial population deficit, and $\delta \sim 10^{-4}$ for the tipping angle for the initial transverse polarization for the $3 \leftrightarrow 2$ transition. The derivation for the initial values for the various matrix elements is presented elsewhere [12], and the results are as follows:

$$W_{31} = 2\epsilon - 1 \quad (17a)$$

$$W_{32} = \epsilon \quad (17b)$$

$$U_{32} = 0 \quad (17c)$$

$$V_{32} = \epsilon\delta \quad (17d)$$

$$U_{31} = m \sin \phi_p \quad (17e)$$

$$V_{31} = m \cos \phi_p \quad (17f)$$

$$U_{21} = -2V_{31} \quad (17g)$$

$$V_{21} = 2U_{31} \quad (17h)$$

where $m = \cos^{-1}(2\epsilon - 1)$ and the phase ϕ_p is arbitrary, and we have chosen the phase ϕ_s to be zero.

Numerical Results

Calculational methods applied to this model and discussed elsewhere [13,15] were used to compute the effects on SF pulse evolution for various conditions for the injection signal, thus demonstrating control of the SF signal by control of the input signal. Some examples follow.

In Figure 2 is shown the transverse integrated SF pulse intensity vs. retarded time τ (curve 2) together with the transverse integrated pump pulse intensity vs. τ (curve 1) for a gain and propagation depth chosen so that the pulses temporally overlap. Under these conditions the two pulses strongly interact with each other via the nonlinear medium, and the two-photon process (resonant coherent Raman - RCR) which transfers population directly between levels 2 and 1, makes strong contributions to the mutual pulse development [4]. The importance of the RCR in SF dynamical evolution in an optically-pumped three-level system was pointed out for the first time in reference 4. Indeed, in the extreme case, the SF pulse evolution demonstrated here has greater nonlinearity than SF in a two-level system which has been prepared initially by an impulse excitation. What is remarkable is that this is an example where the SF pulse temporal width τ_s is much less than the pump width τ_p , i.e., the SF process gets started late terminates early with respect to the pump time duration. Pulses of this type have been observed [16] in CO_2 -pumped CH_3F .

Figure 3 is a comparison of the radially integrated SF pulses at equal propagation depth for three different values for the input pulse radial shape parameter v , where the initial condition for the pump transition field amplitude $X_0(\rho)$ is $X_0(\rho) = X_0(0) \exp[-(r/r_p)^v]$. Since all other parameters are identical

for the three curves, this shows that the peak intensity increases with increasing v whereas the temporal width and delay time decreases. Also, it is clear that the SF pulse shape varies with v . In connection with each of the SF curves shown, there is less than ten percent overlap with the injected pulse. These results thus demonstrate the control of the SF shape, delay time, peak intensity and temporal width by control of the injection pulse radial shape. In Figure 4, we contrast for different v (as in Fig. 3) isometric of the pump and superfluorescence outputs to display the importance of spatial profile ($v=1,2,3$: exponential, Gaussian and hyper-Gaussian).

The effect on the SF pulse of variation of the input pulse temporal shape parameter σ , is shown in Figure 5 which compares SF pulses at the same penetration depth as given in Figure 3, for two different values of σ . Here $X_0(\rho) = X_0(0) \exp[-(\frac{\rho}{r_p})^\sigma]$. It is seen that the variation from a Gaussian, $\sigma = 2$, to a

super-Gaussian, $\sigma = 4$, temporal input pump pulse shape causes almost a factor of two increase in the peak SF intensity with a significant reduction in temporal width and no discernible shift in the time delay. This situation is in marked contrast with that shown in Figure 3 for the effect of pump radial shape variation. As in the previous case, there is less than ten percent overlap between the SF pulses and the pump pulse.

Figure 6 shows the SF pulses at equal penetration for various values for the initial temporal width τ_p of the injected Gaussian π -pulses. All other parameters for the pulse propagation are equal. Again, there is less than ten percent overlap between the SF pulses shown and the pump pulse. Thus, reducing the initial temporal width of the injection pulse causes a shift of the SF delay time and temporal width to higher values, and a decrease in the SF peak intensity.

Figures 7 and 8 illustrates the Fresnel dependence of the SF buildings. Figure 7 represents the radially integrated output SF energy while Figure 8 displays isometrically, versus t and ρ , the SF energy. As the initial spatial width of the injected Gaussian pump increases r_p , the associated Fresnel number decreases, the delay strengthens, the SF peak intensity reduces and the SF pulse gets more symmetrical.

The effect on the SF pulse of the on-axis area of the Gaussian pump pulse is shown in Figure 9 for the same penetration depth as for Figure 3. It is seen here that the effect of increasing the initial on-axis area of the pump pulse is to decrease the SF pulse temporal width and delay time and to increase the intensity. As before, the overlap in this case between the SF and pump pulses is less than ten percent.

Figure 10 illustrates the dependence of SF output on the shape (form) of the input pump pulse whether it is full Gaussian pump, half-front Gaussian or reflected-half Gaussian. The shorter delay and the stronger SF output are associated with the full Gaussian followed by the reflected-half Gaussian pump and the (rising) front half Gaussian pump respectively.

In Fig. 11, the effect of varying N , the atomic density, on the SF build-up is shown. Note that N enters in the definition of σ_{eff} then in F_p . The more dense N becomes, (the larger is the effective gain),

the more intense is the SF build-up and the shorter becomes the relative delay. Thus, the overlap between the SF and the pump pulses increases with N . Furthermore, the nonlinear contribution of the two-photon effects increases significantly.

Conclusion

We have shown here eight ways of shaping the SF pulse by controlling corresponding properties of the injection pulse in coherent optical pumping on a three-level system, where propagation, transverse effects and diffraction are precisely taken into account. We have demonstrated also, in Figure 1, the highly nonlinear effect of generation of an SF pulse of much narrower temporal width and larger peak Rabi rate than the pump pulse under conditions where the two pulses completely temporally overlap after suitable propagation and pulse reshaping. An additional significant nonlinear to the SF emission in this case is due to the competing two-photon process with the direct process[4]. We have thus demonstrated by numerical simulation, the nonlinear control of light at one frequency with light of another frequency.

By changing the material characteristics such as the dipole moment of species on the associated transition frequency, one finds that the SF pump dynamics are modified [12]. The effect of increasing them is similar to the effects associated with augmenting N .

Acknowledgment

The diligent Word Processing efforts of Jerry Marciw are joyfully acknowledged.

REFERENCES

1. R. Bonifacio and L. A. Lugiatto, Phys. Rev. A11, 1507 (1975); 12, 587 (1975).
2. R. H. Dicke, Phys. Rev. 93, 99 (1954).

3. See papers and references contained in Cooperative Effects in Matter and Radiation, edited by C. M. Bowden, D. W. Howgate and H. R. Robl, (Plenum, New York, 1977).
4. C. M. Bowden and C. C. Sung, Phys. Rev. A18, 1558 (1978); Phys. Rev. A20, 2033 (1979).
5. N. Skribanowitz, I. P. Herman, J. C. MacGillivray and M. S. Feld, Phys. Rev. Lett. 30, 309 (1973).
6. H. M. Gibbs, Q. H. F. Vreken and H. M. J. Hickspoor, Phys. Rev. Lett. 39, 547 (1977).
7. Q. H. F. Vreken, in Cooperative Effects in Matter and Radiation, edited by C. M. Bowden, D. W. Howgate and H. R. Robl (Plenum, New York, 1977), p. 79.
8. M. Gross, C. Fabre, P. Pillet and S. Haroche, Phys. Rev. Lett. 36, 1035 (1976).
9. A. Flusberg, F. Mossberg and S. R. Hartmann, in Cooperative Effects in Matter and Radiation, edited by C. M. Bowden, D. W. Howgate and H. R. Robl (Plenum, New York, 1977), p. 37.
10. A. T. Rosenberger and T. A. DeTemple, Phys. Rev. A24, 868 (1981).
11. F. T. Hioe and J. M. Eberly, Phys. Rev. Lett. 47, 838 (1981).
12. F. P. Mattar and C. M. Bowden in preparation for Topics in Current Physics: Multiple Photon Dissociation of Polyatomic Molecules ed. C. D. Cantrell (Springer Verlag 1982).
13. F. P. Mattar, in Optical Bistability, edited by C. M. Bowden, M. Cifan and H. R. Robl (Plenum, New York, 1981), p. 503; in "Proceedings, 10th Simulation and Modeling Conference, Pittsburgh, 1978", edited by W. Vogt and M. Mickle, Publ. Inst. Soc. Am. (1979), Pittsburgh, PA; and in Appl. Phys. 17, 57 (1978).
14. F. P. Mattar, H. M. Gibbs, S. L. McCall and M. S. Feld, Phys. Rev. Lett. 46, 1123 (1981).
15. F. P. Mattar and M. C. Newstein, in Cooperative Effects in Matter and Radiation, edited by C. M. Bowden, D. W. Howgate and H. R. Robl, (Plenum, New York, 1977), p. 139.
16. T. A. DeTemple, private communication.

FIGURE CAPTIONS

- Figure 1. Model three-level atomic system and electromagnetic field tunings under consideration. For the results reported here, the injected pulse is tuned to the $1 \leftrightarrow 3$ transition.
- Figure 2. Radially integrated intensity profiles for the SF and injected pulse at $Z = 5.3$ cm penetration depth. The injected pulse is initially Gaussian in r and τ with widths $r_0 = 0.24$ cm and $\tau_p = 4$ nsec, respectively, and initial on-axis area $\theta = \pi$. Further, $(\epsilon_3 - \epsilon_1)/(\epsilon_3 - \epsilon_2) = 126.6$; $g_p = 17$ cm⁻¹; $g_s = 641.7$ cm⁻¹; $F_p = 8400$; $F_s = 2505$; $T_1 = 80$ nsec; $T_2 = 70$ nsec, where T_1 and T_2 are taken to be the same for each transition.
- Figure 3. Radially integrated intensity profiles of SF pulses at a propagation depth $Z = 5.3$ cm for three different values for the input radial shape parameter v . The injected pulse is initially Gaussian in τ , and has radial and temporal widths as for Figure 2 with initial on-axis area $\theta = 2\pi$. In this case, $g_p = 14.2$ cm⁻¹; $g_s = 758.3$ cm⁻¹; $F_s = 2960$; $F_p = 7017$, with all other parameters the same as for Figure 2. Here, curve 1, $v = 2$; curve 2, $v = 3$; curve 3, $v = 4$, (see text).
- Figure 4. Isometric SF intensity (τ versus ρ) at a propagation depth $Z = 5.3$ cm for three different values for use input radial shape parameter v . This figure complements Figure 3.
- Figure 5. Radially integrated intensity profiles of SF pulses at a propagation depth $Z = 5.3$ cm for two different values for the input pulse temporal shape parameter σ . The injected pulse is initially Gaussian in r , and has radial and temporal widths as for Figure 2 with initial on-axis area $\theta = 3\pi$. In this case, $g_s = 641.7$ cm⁻¹; $F_s = 2505$ and all other parameters are the same as for Figure 3. Here curve 1, $\sigma = 2$; curve 2, $\sigma = 4$ (see text).
- Figure 6. Radially integrated intensity profiles of SF pulses for five different values for the temporal width, τ_p of the injected signal: curve 1, $\tau_p = 4$ nsec; curve 2, $\tau_p = 3.3$ nsec; curve 3, $\tau_p = 2.9$ nsec; curve 4, $\tau_p = 2.5$ nsec; curve 5, $\tau_p = 2.2$ nsec.
- Figure 7. Radially integrated intensity profile of SF pulses at a propagation depth $Z = 5.3$ cm for five different values of the spatial width r_p of the injected pump (thus of the associated Fresnel number): curve 1, $\mathcal{F} = 0.69$; curve 2, $\mathcal{F} = 0.40$; curve 3, $\mathcal{F} = 0.24$; curve 4, $\mathcal{F} = 0.17$ and curve 5, $\mathcal{F} = 0.10$.

Figure 8. Contrast of SF (top line) and Pump (bottom line) Energy isometric versus τ and ρ at a propagation depth $Z = 5.3$ cm for different values of the Pump Fresnel number (associated with the initial spatial width of the injected signal): curve 1, $\mathcal{F} = 4.0$; curve 2, $\mathcal{F} = 2.26$; curve 3, $\mathcal{F} = 1.0$; curve 4, $\mathcal{F} = 0.69$; curve 5, $\mathcal{F} = 0.40$; curve 6, $\mathcal{F} = 0.27$ and curve 7, $\mathcal{F} = 0.10$.

Figure 9. Radially integrated intensity profiles of SF pulses for three different values for the initial on-axis injection pulse area θ_p ; curve 1, $\theta_p = \pi$; curve 2, $\theta_p = 2\pi$; curve 3, $\theta_p = 3\pi$. All other parameters are the same as for Figure 2, except for $g_s = 291.7 \text{ cm}^{-1}$ and $F_s = 1138.7$.

Figure 10. Radially integrated intensity profile of SF pulses for three different form of the injected pump: curve 1, front half Gaussian form; curve 2, full Gaussian and curve 3, reflected half Gaussian.

Figure 11. Radially integrated intensity profile of SF pulses for three different atomic density N . From curve a to curve d, the density ratios are: $b/a = 1.4$, $c/a = 1.8$, $d/a = 2.2$.

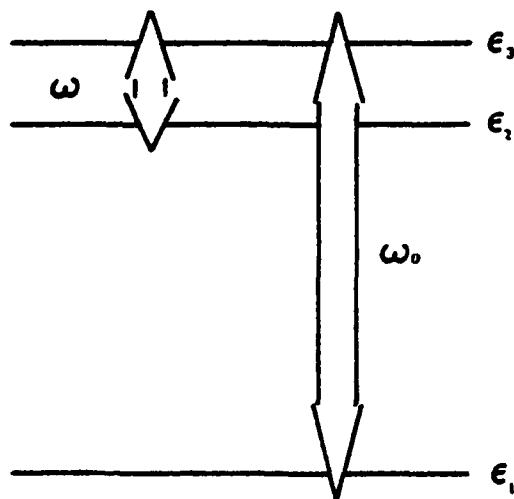


Figure 1

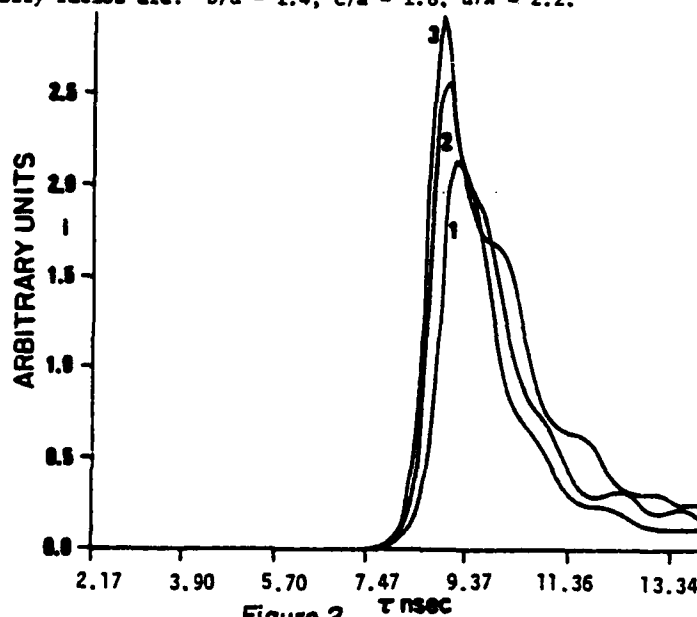
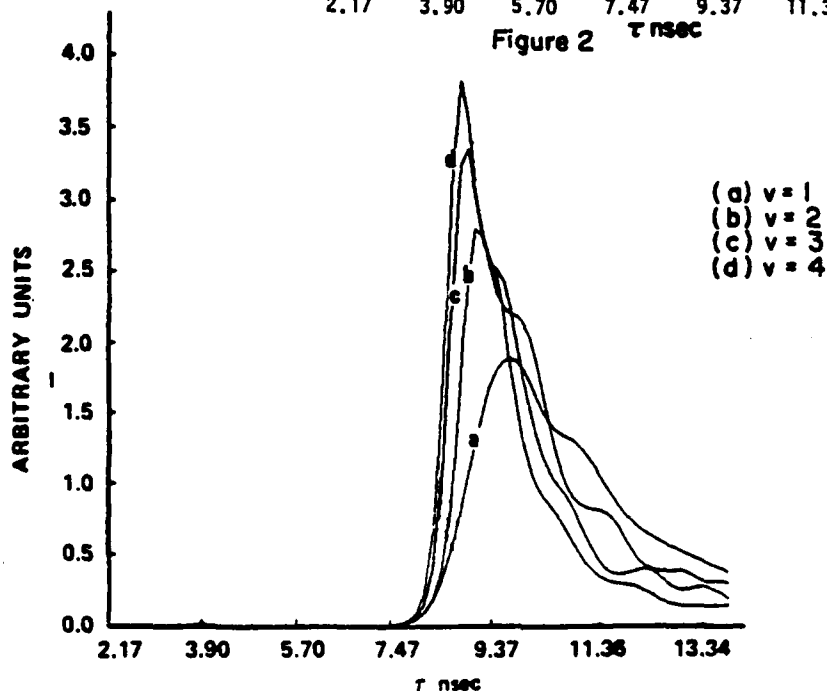


Figure 2

Figure 3



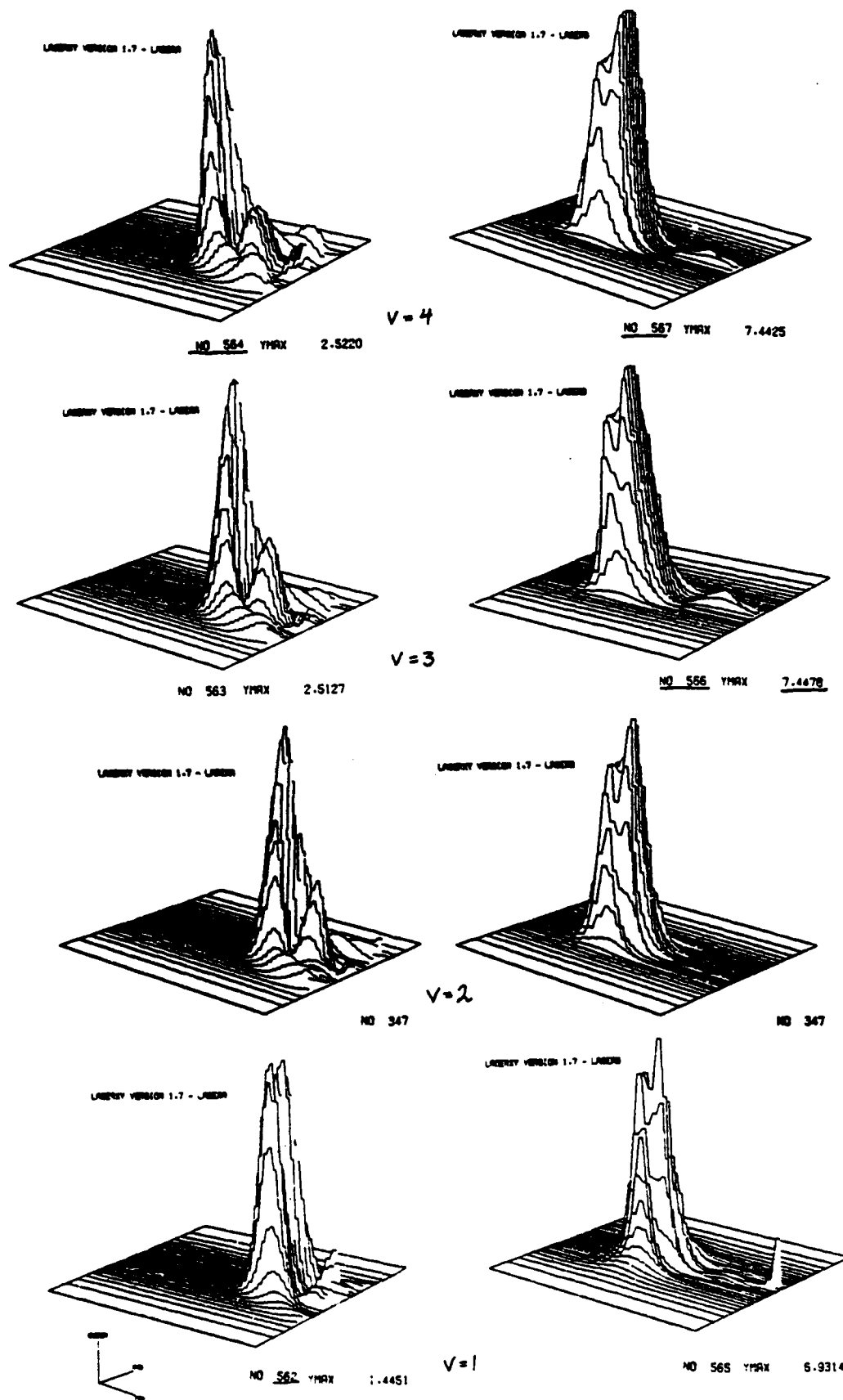


Figure 4

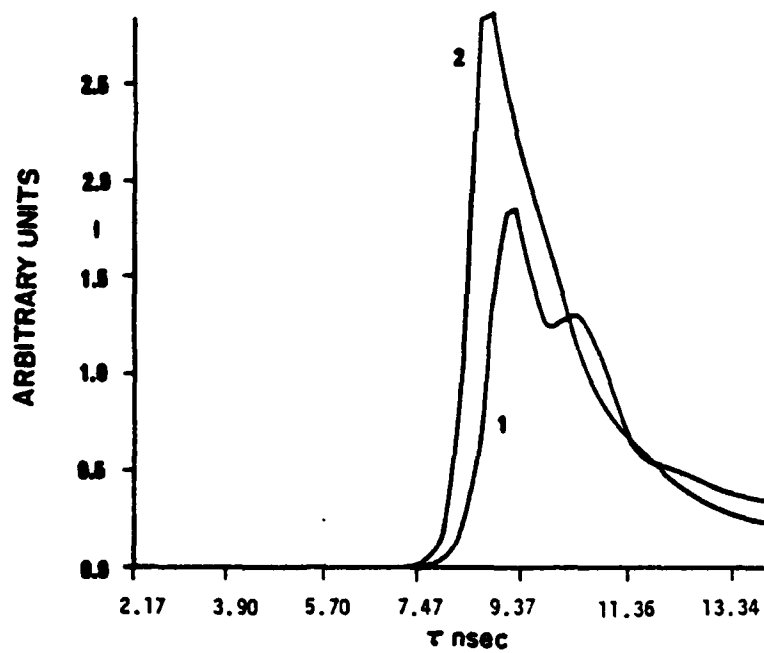


Figure 5

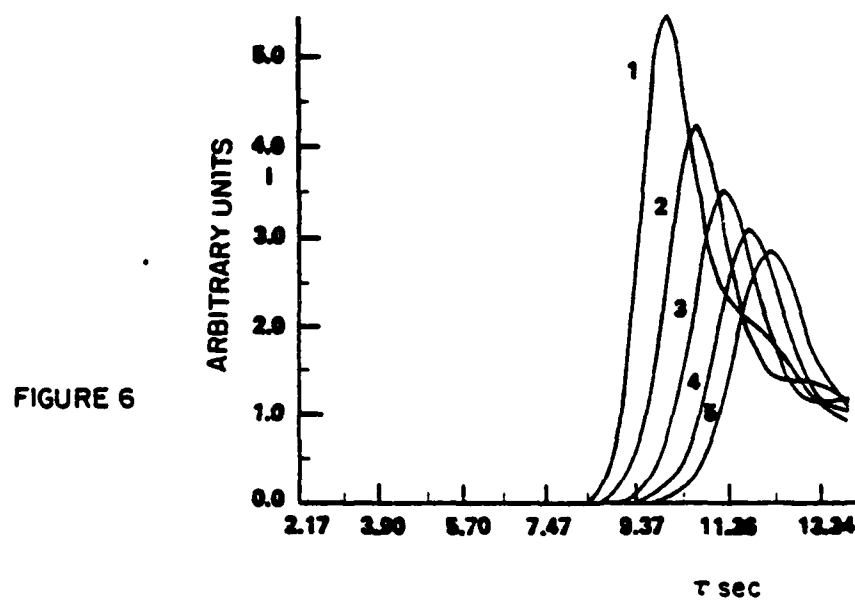


FIGURE 6

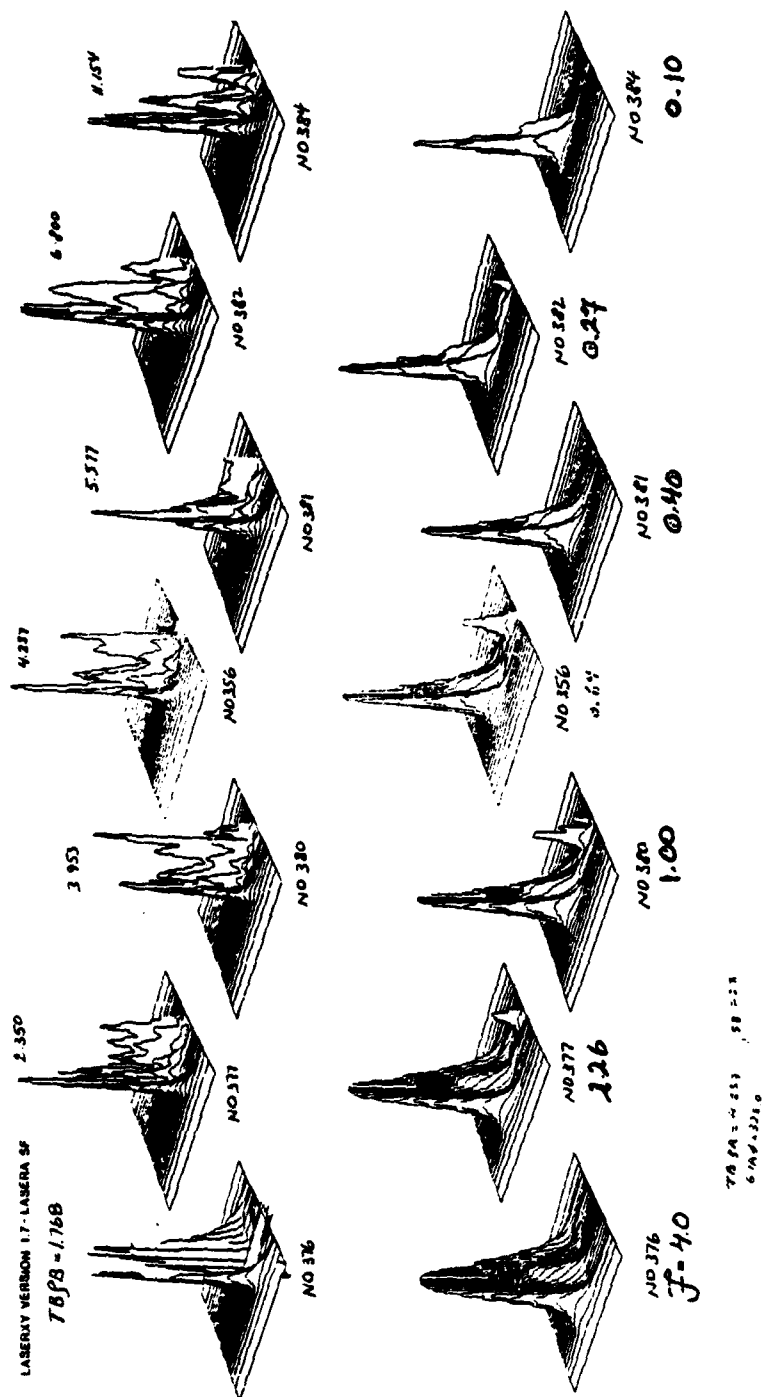
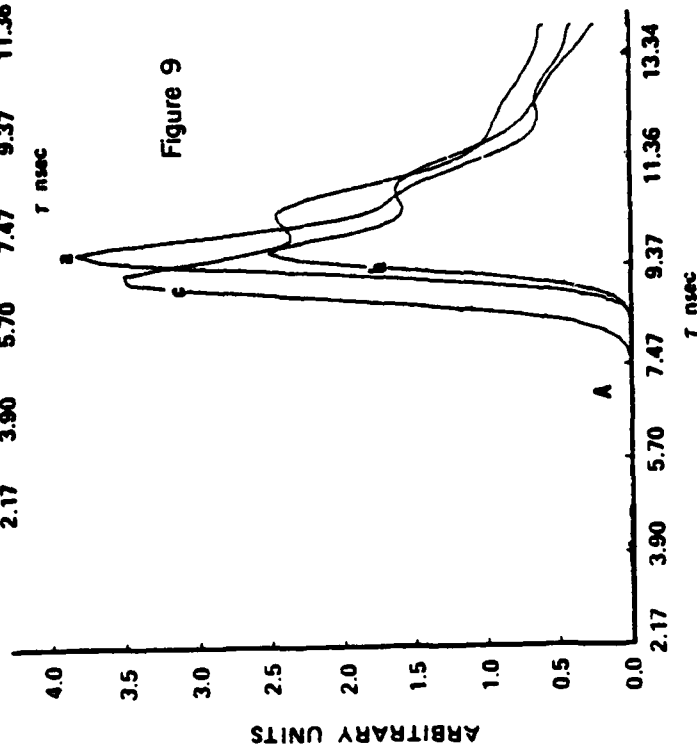
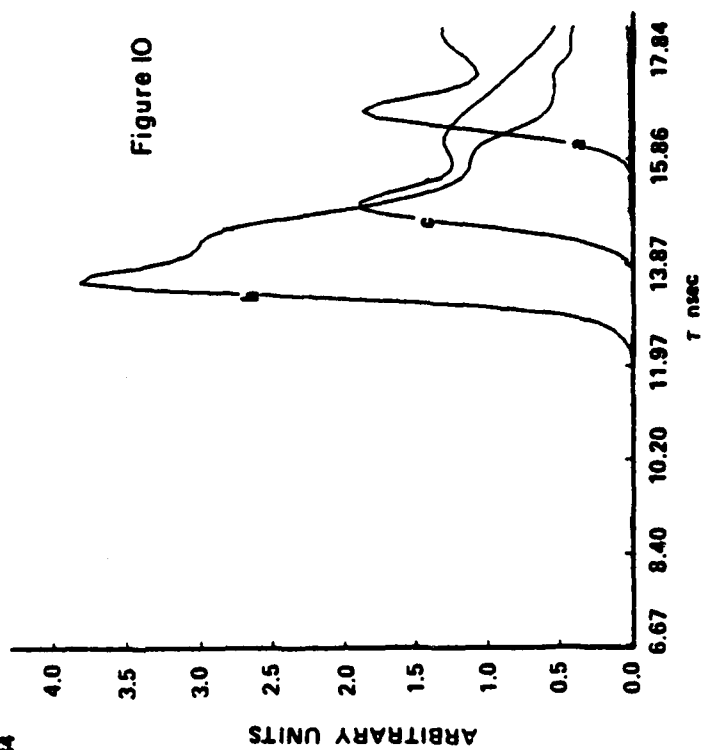
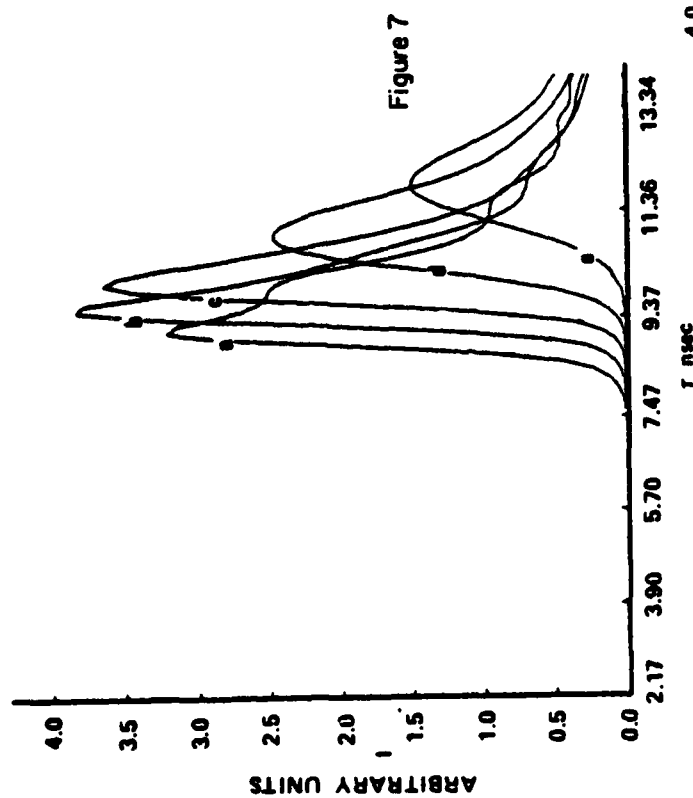


Figure 8



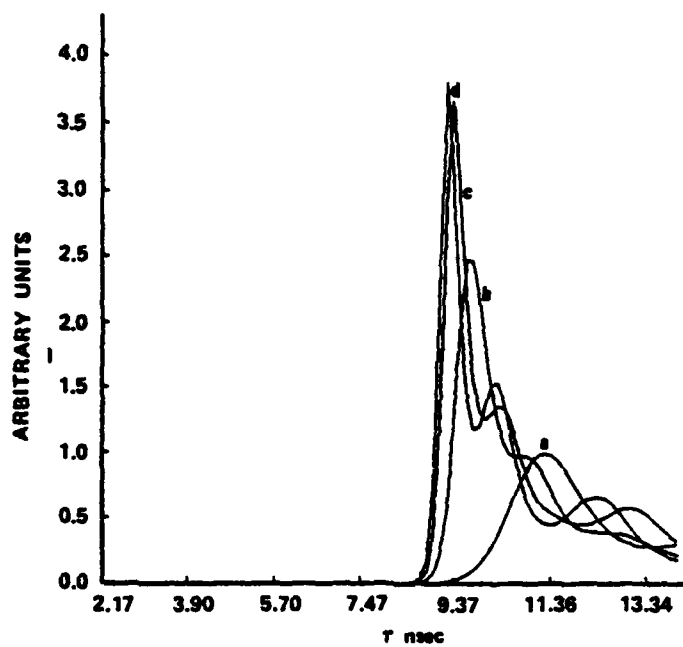


Figure II

DEPARTMENT OF MECHANICAL
AND AEROSPACE ENGINEERING

A PRODUCTION SYSTEM FOR THE MANAGEMENT
OF A RESULTS FUNCTIONS BANK AND A SPECIAL
APPLICATION: THE LASER PROJECT+

BY: M. CORMIER, P. CLAUDE, P. CADIEUX
AND P. MATTAR (POLYTECHNIC INSTITUTE
OF TECHNOLOGY AND SPECTROSCOPY
LABORATORY, MASSACHUSETTS INSTITUTE
OF TECHNOLOGY)

+ Presented at the International Conference
on Laser '81, New Orleans, Dec. 1981

AD-A136 986

TRANSVERSE AND QUANTUM EFFECTS IN LIGHT CONTROL BY
LIGHT; (A) PARALLEL BE. (U) POLYTECHNIC INST OF NEW
YORK BROOKLYN DEPT OF MECHANICAL AND A. F P MATTAR

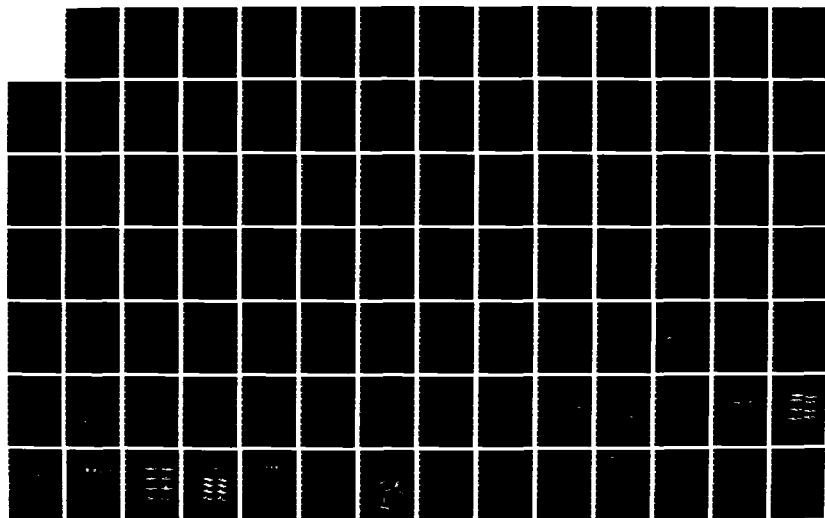
3/6

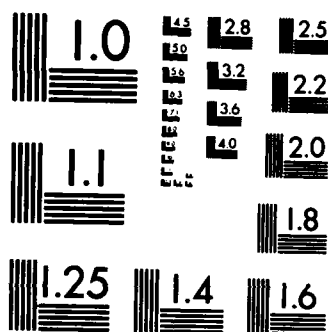
UNCLASSIFIED

1983 POLY-M/RE-83-4 N00014-80-C-0174

F/G 20/6

NL





A PRODUCTION SYSTEM FOR THE MANAGEMENT OF A
RESULTS FUNCTIONS BANK AND A SPECIAL APPLICATION:
THE LASER PROJECT

M. Cormier, Y. Claude, P. Cadieux
Dept. d'Informatique et Recherche operationnelle
Universite de Montreal, Montreal, Canada

&

F.P. MATTAR*
Dept. of Mechanical and Aerospace Engineering
Polytechnic Institute of New York, Brooklyn, New York 11201, U.S.A.
and
Spectroscopy Laboratory
Massachusetts Institute of Technology
Cambridge, Mass. 02139, U.S.A.

ABSTRACT

This document presents the system developed to support the numerical laser modeling project at the Universite de Montreal in conjunction with the Polytechnic Institute of New York. This tool represents a mechanism for practical parametric simulation studies of real-life experiments in quantum Electronics. The goal of this system is to offer a reliable, adaptable and easy tool to the production and study of laser simulations, a study mainly done through drawings and comparisons of functions. Organized around SIMRES and DATSIM type files, this system encompasses software packages which control file access, application programs and the very laser programs. The SIMRES files are self-descriptive and can store in the same direct access file all the information relative to a simulation. The SIMRES package is used to generate a SIMRES file while the XTRACT package permits the reading of the information stored on a SIMRES file. The DATSIM files regroup on one file, permanently located on disk, a summary of the SIMRES files (because of their size these must be filed away on a magnetic type). The DATSIM package permits the reading and the writing procedures of the DATSIM files. This document also presents three of the principal application programs: the DEFPARM program which helps the user to construct parameter games for the simulation programs, the DESRES program which plots the simulation results, and the SYNTH program which makes the comparisons. Finally, the document presents the different laser programs.

* Jointly supported by F.P.Mattar, the U.S. Army Research Office, the U.S. Office of Naval Research, the U.S. Science Foundation Research Corporation, Battelle Columbus Lab. and the Canadian Defense Research Establishment at Valcartier.

I - INTRODUCTION

The laser numerical modeling project began over three years ago at the University of Montreal. A first production system, which permitted generation of laser simulations and graphic representation of the results was then set up.

This first system was based on a fixed structure of the result files, and the programs using this structure were consequently not very flexible.

Eventually, new needs appeared (catalogs and comparisons) and their implementation made the system more complex and less efficient as these new possibilities could not always be adequately integrated. Finally, new models were introduced to the system for which the fixed format was not adequate.

A second system, more flexible and more powerful, was undertaken in May 1981. The object of this document is to present this new system. It consists, on the one hand, of a nucleus, made of general packages, which permits the creation and manipulation of result files consisting of functions of arbitrary dimensionality; and on the other, of a set of programs adapted to precise tasks (graphic representation of the results, comparisons).

The order of the sections goes from the general to the particular.

Section two presents the objectives which oriented the design and implementation of the system.

Section three gives a comprehensive view of the system.

Section four presents the different packages forming the nucleus.

Section five presents the programs which generate the various products (drawings, catalogs) of the laser modeling project.

The conclusion returns to the objectives presented in section two and discusses to what extent they have been attained.

II - OBJECTIVES

The design of the different packages composing the production system for the laser numerical modeling project has been elaborated from the following goals:

- modularity
- flexibility
- reliability
- efficiency
- transportability
- adequate documentation

2.1 MODULARITY

Modularity implies that a job is divided into tasks and that execution of a given task is confined within a set of routines.

By proceeding, such a task is isolated from the rest of the program. The use of packages is modular since they are independent from the programs and can therefore be used in various ways in various programs.

2.2 FLEXIBILITY

Flexibility is the quality of a software which not only answers a precise need but also adapts to a range of similar problems.

Software products must therefore be given a maximum of generality and flexibility in view of current and future needs. Ideally, a software should handle the general case.

But in reality, it is often neither possible nor desirable; and restrictions are necessary.

In such cases, flexibility is then measured by the facility with which the software can be modified in order to bypass its limitations or restrict their impact.

2.3 RELIABILITY

Reliability combines two major aspects.

The first aspect is that a software must give the control back to the operating system only if it wishes to do so. This means that a software must prevent conditions (such as memory overflow) where the operating system would otherwise force it to stop.

The second aspect is that when a routine or a program does return results, these must be correct; otherwise no results are produced and an error message is returned.

2.4 EFFICIENCY

When designing a software, the limited and often costly resources given by an operating system, often shared by many users, must be taken into account.

Techniques which minimize factors such as computation time, memory requirements and disk access are thus essential. Moreover, reduced use of the resources may have a positive impact on the turnaround time, and then again, these optimisations will directly benefit the user.

2.5 TRANSPORTABILITY

It is often difficult to produce perfectly transportable software products. Nevertheless, techniques can be used to increase software transportability. Thus, machine dependent and installation dependent features must be banned. In some cases, it is impossible to do so (such as in I/O routines) and critical actions must be isolated in routines which can easily be modified to adapt to other environments.

2.6 ADEQUATE DOCUMENTATION

Three types of documentation are necessary to describe a given system adequately:

Comments within the source code are necessary to maintain and modify the software.

A separate technical manual complements the internal documentation with a higher level description giving the overall design philosophy and indicating the global structure and interdependencies between the various procedures or programs.

Finally, a user's guide is needed to indicate clearly how the software is to be used.

III - A COMPREHENSIVE VIEW OF THE SYSTEM

The system supporting the laser modeling project has been developed on a pair of CDC CYBER 173 computers at the Centre de Calcul of the Université de Montréal. It consists of programs and packages written in FORTRAN IV. The three major tasks accomplished by the system are:

- generation of simulation results,
- drawings of the results of an individual simulation,
- comparisons of results between simulations.

3.1 GENERATION OF RESULTS

The study of lasers is done with programs simulating the spacial and temporal evolution of a laser impulse, in conformity with a given numerical model. Initially, there was only one program which was using a single laser cylindrical model. Eventually, with developments in the physics theory, the initial model was improved (it now takes into account Doppler effects, oscillatory phenomena, ...) and new models were developed (2-laser model, Cartesian model). There are now many laser simulation programs, each being the starting point of a data-base of results associated with the model.

Each simulation is controlled by a set of parameters defining the material and the field through which the laser impulse propagates. These parameters are given to the laser programs as FORTRAN NAMELISTs. For each model, simulations are identified through a unique number. This number is included in the NAMELISTs as a special parameter. The results of a simulation are written on SIMRES type files (SIMulation RESults). Each file is identified through a root to which a suffix is added; the root corresponds to the identifier of the program which produced the simulation, and the suffix is the simulation number.

SIMRES files contain general information (name of the originating program, version number of the program, creation date of the file, ...), the list of the simulation parameters, and the results of the simulation. The way results of a simulation are handled can be summarized in the following manner:

- The programs evaluate functions of varying dimensionality and the parameters of the simulation determine at what points these functions must be evaluated.
- Values of the functions are kept in SIMRES files for a given sample of evaluation points.

As can be seen, all the information relative to a simulation is kept on a single entity, i.e. the SIMRES file. In this basic scheme (NAMELISTs, simulation programs, SIMRES files), DATSIM type files and the program DEFPARM were added. The program DEFPARM (DEFinition PARAMeters) is used to assist the user in writing NAMELISTs. It is an interactive program which allows the user to describe a simulation of a family of simulations by using a compact syntax, and in return produces the corresponding NAMELISTs. Although this program may not be essential, its advantage is to relieve the user of the chore of writing often repetitive NAMELISTs.

It also avoids trivial errors such as syntax errors in NAMELISTs and errors in parameter names.

The emergence of DATSIM files is linked to a context of intense production. Moreover, to be efficient at a production level, it is necessary that any information concerning any given produced simulation be available. SIMRES files being too large and too numerous to be all kept on disk, a mechanism has been laid to transfer data between disk and tape. This archival system is essential, but it considerably slows the access to information. To be efficient, we must then compromise and keep on disk some high priority informations concerning all produced simulations.

The informations are gathered in a data base consisting of DATSIM type files (DATA SIMulation). DATSIM files contain, for every simulation produced by the program:

- general informations, identical to those on SIMRES files,
- values of the simulation parameters,
- evaluation points and values of the functions used in comparisons.

The program MAJOTS (Mise-A-Jour-update, DATSim) reads useful informations on a SIMRES file and writes them on the SIMRES file. It is noteworthy that the information contained in the DATSIM file is used by the program DEFPARM to get the numbers to be assigned to new simulations.

The configuration of the system, as regards to the production of simulations is given at figure 3.1.

The suffixes ICPS, ICPS, IPS, IP4S refer to the different laser models (these will be explained in Section 5).

Consider model LCFS (1-laser Cylindric Frequency Statistics model). The program DEFPARM takes the specifications from the user, validates them and writes on the file SXLCFS (Simulations to be eXecuted) the data needed to produce the simulations requested. Then, the program LRICFS (Laser) reads the appropriate data on the file SXLCFS, generates the simulation and produces a SIMRES file whose identifier is LRICFS (no) ((no): simulation number).

Finally, the file LRICFS (no) gives the program MAJOTS the information needed to register the simulation on the file DTLCFS (DaTsim) which contains a summary of the simulations carried out with the model LCFS.

3.2 DRAWINGS OF A SIMULATION

The study of the simulation results requires graphic support in order to visualize the profiles of the functions evaluated by the simulation programs. The program DESRES (dessin-drawing, simres) has been designed to offer such assistance. This program can be used either in batch or interactive mode.

Drawings needed are specified by using a syntax whose structure is similar to that of a program and allows inner loops on simulations, functions, selection criteria, etc. The user can thus indicate in a short way what drawings he wishes to have.

The commands given by the user are analysed by the program DESRES, which breaks them up in single units, using the package XTRACT. The SIMRES files then give all the information needed to identify and produce the drawings. There are four types of drawings available:

- 2-dimensional representation of a function,
- 3-dimensional representation of a function,
- 2-dimensional projection of a 3-d representation.

The 3-D projections and the level curves are performed by the program TRASURF (CACM sept /74).

Figure 3.2 presents the portion of the system which carries out the production of drawings.

3.3 COMPARISONS OF RESULTS BETWEEN SIMULATIONS

The program SYNTH (SYNTHesis) has been designed to allow comparisons of results between simulations. A comparison is done by superposing on one drawing 2-dimensional representations of either functions coming from different simulations or functions for which each point comes from a different simulation. The program SYNTH is a powerful tool; it can be used in both interactive and batch mode and its scope includes the three following applications:

- Comparison inside one simulation.
- Comparisons between simulations of a same model, bringing out the role of certain parameters in 2 or more laser models, and the role each laser plays.
- Comparisons between the different models to demonstrate their impact. The user specifies the work to be done either by defining the objects to be compared and the comparison criteria or by indicating where to search for the objects to be compared and how to organize the comparison. In this last case, part of the search procedure needed for the definition of the comparison is done by the SYNTH program.

After validating and accepting the request, the SYNTH program produces the necessary headings identifying the comparison (by isolating the fixed parameters from the variable ones) then effects the drawings corresponding to the comparison.

The running of a comparison requires all the information needed at the same time on one disk. It is at this level that the DATSIM files are useful as they give access to the parameter list of all the simulations already produced and to certain functions often used in the comparisons. Nevertheless, the data on the DATSIM files are not always sufficient, the user therefore must revert to the archival procedures of the needed SIMRES files.

This structure is presented in figure 3.3.

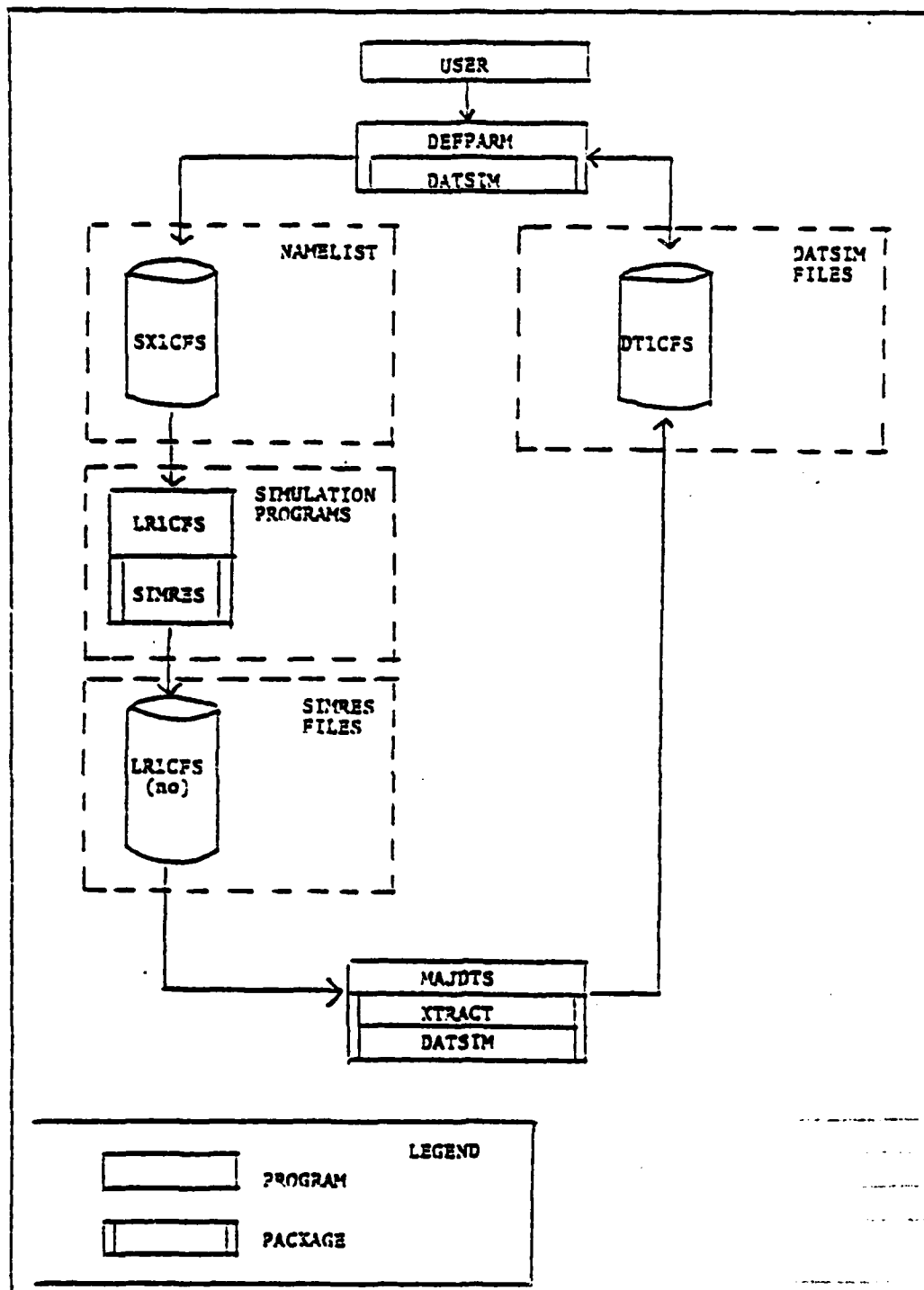


FIGURE 3.1 - SIMULATIONS PRODUCTION

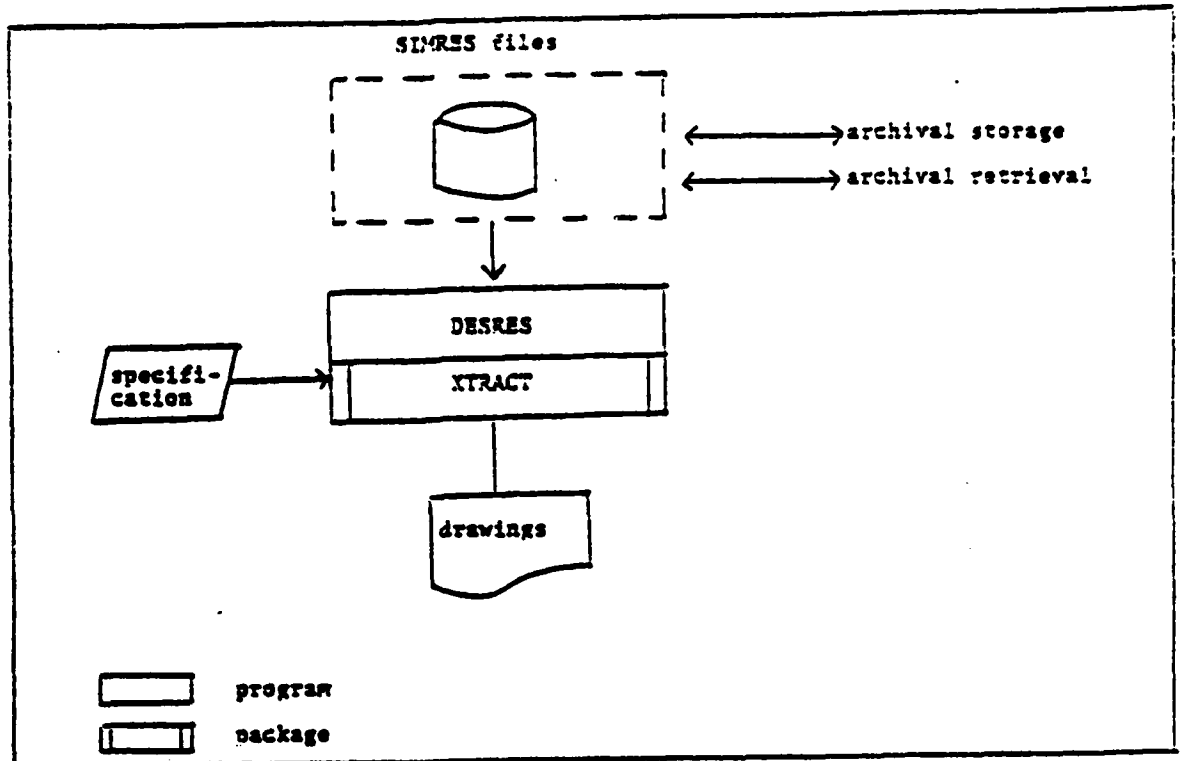


FIGURE 3.2 - PRODUCTION OF DRAWINGS

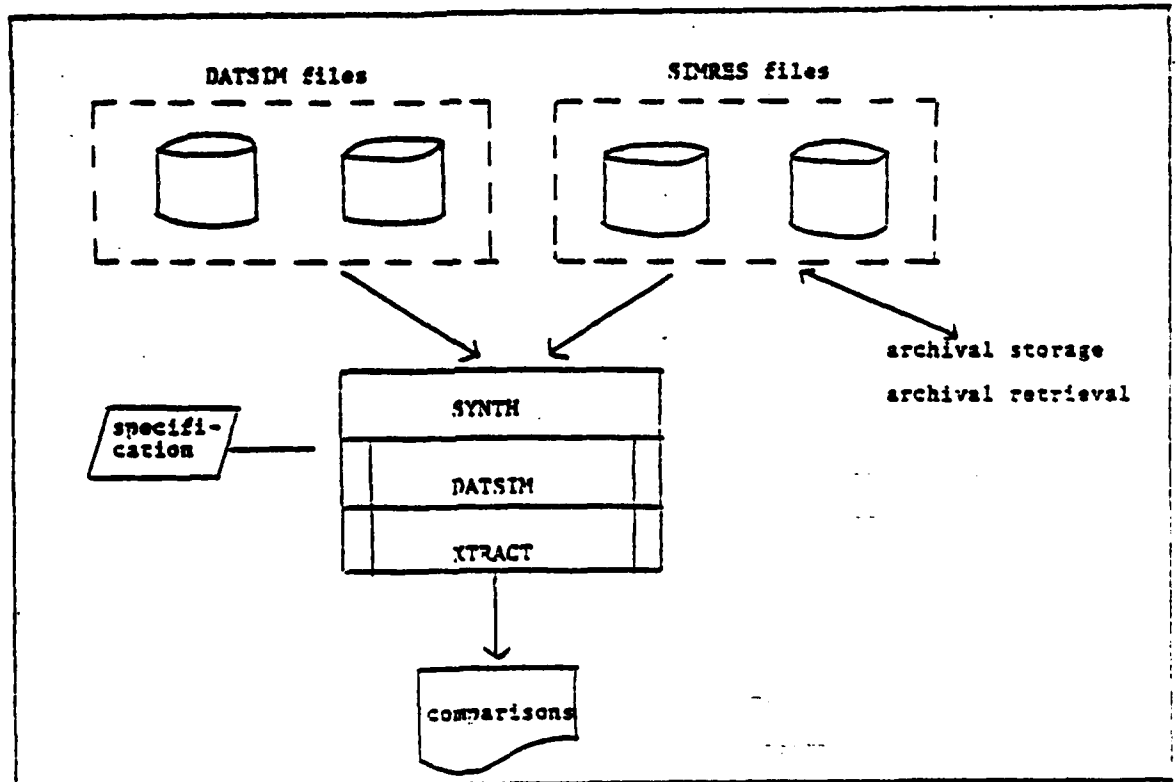


FIGURE 3.3 - PRODUCTION OF COMPARISONS

IV - THE PACKAGES

The packages are the lower level of the system. Beside answering a particular application, their role is to solve a problem in a general way. Each package is made up of several procedures accomplishing a precise task. The packages presented here are the following:

- SIMRES : generation of the SIMRES files;
- XTRACT : operation of the SIMRES files;
- DATSIM : generation and operation of the DATSIM files.

4.1 THE SIMRES PACKAGE

The SIMRES package aims, on the one hand, to keep on one single file all the information relative to a simulation and on the other, to provide self-descriptive files, or files that carry the necessary information to describe their organization. By proceeding this way, the integrity of the information is insured (all data relating to one simulation is concentrated in one file) and the system is given a greater flexibility when faced with changes (the organization of the file varies, the key is in its description).

4.1.1 DESIGN OF THE RESULTS FILES

The different simulation models describe the evolution of a laser pulse in a space of n dimensions. The value of n , the number of dimensions, depends on the model. To each dimension corresponds an axis identified by a name and by units. The simulation programs results are functions defined on the reals:

$$f_i = R^{d_i} - R$$

where $i = 1, 2, \dots, M$ (M = number of functions)

$0 \leq d_i \leq N$ (N = number of dimensions of the simulation space).

For instance, in the ICFS model involving a 4 dimension space defined by the STATISTIC, ETA, RHO and TAU axes, the O POWER function depends on the STATISTIC, ETA and TAU axes ($N = 4$ and $d_O \text{ POWER} = 3$).

The functions assessed by the simulation programs correspond to continuous phenomena. But the fact of using a computer makes it important to make them discrete. Thus, the points at which a function has to be assessed is determined by associating them to a sampling grid. When only one sampling grid is used for all the functions, it can be said that this grid constitutes the discrete space in which the simulation evolves.

It would be very costly to keep, for each value of a function, the value of its points of assessments. It is thus of prime importance to find a more compact method to describe the sampling grids.

The simplest sampling grid is the linear orthogonal grid which can be described by giving for each of the axes that make up that grid, a starting point, an increment and the number of points on the axis. Figure 4.1 shows such a grid.

However, the linear orthogonal grid offers little flexibility. Thus, in order to follow more adequately the phenomenon under study, there would be a need for a grid where the distance between the points, instead of being uniform, is smaller in certain areas than in others. This will define a finer grid where the phenomenon is more interesting. Such a grid is said to be "nonlinear orthogonal" and can be described by keeping for each of the axis the value of the chosen point: see figure 4.2.

Moreover, there may be a need for a grid even more adapted to the phenomenon under study, for instance for a grid without the constraints of orthogonality. In this case, the coordinate of the grid associated to an axis depends on the value on that axis and possibly on the values on other axes. A grid in R^N can thus be described by N sampling functions $f_{e1}, f_{e2}, \dots, f_{eN}$ each of these functions depending of an axis or on several axes for its assessment. What is stored to describe the grid is then the values of the functions. Thus, in figure 4.3, which illustrates a nonlinear orthogonal grid, the sampling grid f_{ey} , depending only on the y axis, is completely described by a 7 points vector and the function f_{ex} , depending on axes x and y , is described by a matrix of 7×7 points.

This last method is the most advantageous and thus, it is the one most used here. In fact, this method permits the description of grids as general as possible while avoiding the redundancy of the information at the level of the values of the points on the axes. For this method, the use of space is proportional to the "complexity" of the sampling functions.

The definition of a sampling grid often requires that the points be sufficiently close together and sufficiently numerous to assure the stability of the numerical techniques used. Thus, it is possible to store more information than is required to visualize the phenomena. Even more, it is possible that the results files may not be kept on the same disk unit: for instance, the complete Cartesian laser model assures four functions for more than a billion points (7 points for the STATISTIC axis x 500 for the ETA axis x 95 for the X axis x 95 for the Y axis x 54 for the TAU axis) which is far beyond the space capacity of a disk.

It is thus essential to reduce the volume of data to be put on file. This is done by introducing a selection mechanism which chooses those points of a sampling function for which the data is effectively being stored. This selection is done by specifying the number of the starting point and an increment in number of points. This simple way of proceeding, together with an as precise a grid as is required gives enough flexibility to make a pertinent choice of data for storage.

4.1.2 USAGE OF THE SIMRES PACKAGE

The procedures of the SIMRES package create the SIMTMP files (SIM for simulation and TMP for temporary) which will later be converted to SIMRES files. These procedures are:

- SIMDEB : initialization of the package;
- SIMAXE : definition of the axes;
- SIMTECH : definition of the sampling functions;
- SIMFCT : definition of the functions;
- SIMSEL : definition of the selectors;
- SIMVAL : writing of the values;
- SIMAVC : positioning of the selectors;
- SIMFIN : end of processing.

Figure 4.4 is a diagram showing the sequence of the package procedure calls and the uses of the special parameters, that is: those which identify the axes, the sampling functions, the results functions and those which build the dependencies between the sampling functions and the axes, between the results functions and the sampling functions. All this is explained more fully in the following paragraphs.

The SIMDEB procedure initializes the writing process of a SIMTMP file and records the identification and the main characteristics of the simulation. The parameters of the procedure are the following:

- ULSIM : unit number of E/S associated to the SIMTMP file;
- ULPRNT: unit number of E/S associated to the print file;
- IORI : name of the program creating the SIMTMP file;
- IVER : program version;
- NOSIM : simulation number;
- NAXE : axes number;
- NTECH : number of the sampling functions;
- NFCT : number of results functions.

Figure 4.5 shows an example of a program when 3 functions in a 2 dimension space is assessed. For this example, the call corresponding to SIMDEB would be the following:

```
CALL SIMDEB (1,6, 'SIMUL', '1.0', 1, 2, 2, 3)
```

The SIMAXE procedure is used to declare each of the axes defining the simulation space. The order in which the axes are declared determines the order in which the SIMVAL procedure will receive the values of the functions. The procedure receives in parameter the following information:

- IDAXE : the axis identifier;

- NPTAXE: the number of points of the axis;
- UNITAX: the MKSA units used for the graduation of the axis (meters, seconds, ...);
- EXPUNT: the exponent affecting the units, for instance: if UNITAX = 'seconds' and EXPUNT = -6, we have microseconds;
- FACUNT: the multiplying factor affecting the units.

The received information is recorded in the SIMTMP files. In exchange, the procedure initializes the NUMAXE parameter (number of the axis) which identifies the axis in the SIMRES and DEPAXE (axis dependency) package which will mark the dependency of a sampling function with regards to an axis. It is important to note here that the value given to the DEPAXE parameter is in the power of two, thus the dependencies can be combined by addition. For example, the calls for SIMAXE will be the following:

```
SIMAXE ('x', 7, 'METERS', -2, 1.0, NUMAXX, DEPAXX)
SIMAXE ('y', 3, 'METERS', -2, 1.0, NUMAXY, DEPAXY)
```

The SIMECH declares to the SIMRES package the sampling function. The procedure takes in parameter:

- IDFECH : the identifier of the sampling function;
- NUMAXE : the number of the axis to which the function applies;
- DEPAXS : dependency in term of the axes of the sampling function, $DEPAXS = \sum_k DEPAXE_{k(i)}$ where k corresponds to the axes of which depends the function and {i} is the body of available dependencies for the axes.

In exchange, the procedure initializes the NUMFEC parameter (number of the sampling function) which identifies the sampling function when recording its values and the DEPFEC parameter (dependency of the sampling function) which will be used to mark the dependency of a results function as to a sampling function. In the example, the calls to SIMECH would be:

```
SIMECH ('XFC', NUMAXX, DEPAXX + DEPAXY, NUMFCX, DEPFECX)
SIMECH ('YFC', NUMAXY, DEPAXY, NUMFCY, DEPFECY)
```

The SIMFCT procedure defines a results function (as opposed to a sampling function). The procedure receives in parameter the identifier of the function (IDFCT) and its dependency in term of sampling functions (sum of the value type DEPFEC feedback by SIMECH). The NUMFCT parameter returns the number of the function: it is the number that must be used in the calls to SIMVAL to identify the values of a function. Thus, in the example used here, the three functions would be defined as follows:

```
SIMFCT ('ENER', DEPFECX + DEPFECY, NUMFEN)
SIMFCT ('PEAKX', DEPFECY, NUMFPX)
SIMFCT ('PEAKY', DEPFECX, NUMFPY)
```

The procedure SIMSEL changes the value of lack of selectors of an axis for one or several functions. By their absence, all the points of an axis are selected. The parameters of the SIMSEL procedure are the following (there is no exit parameters):

- TABFCT : vector containing the numbers of the functions;
- DIMTAB : give the number of elements in TABFCT;
- NUMAXE : number of the axis for which the selectors are to be changed;
- DESSEL : number of the first selected point;
- INCSSEL : increment for the selected points.

It must be noted that changing the selectors of an axis affects only those functions whose numbers have been received by SIMSEL. Thus, in our example, the following call:

```
SIMSEL (NUMFEN, 1, NUMAXY, 1, 2)
```

implies that the values of function ENER will be kept only for 1 of 2 points of the Y axis, but this does not touch the PEAKX function which also depends on the Y axis.

The SIMPAR procedure allows the addition to the SIMTMP file of the simulation parameters; in that way, the data needed to identify the simulation always comes with the results. The procedure receives the following information:

NAME : parameter identifier;
 TYPE : complete code giving the type of the parameter (0 for complete, 1 for real, ...);
 VALUE : list of values of the parameter (vectorial parameters are allowed);
 NBELEM : number of elements in VALUE array.

Thus, in our example, there will be the two following calls:

```
SIMPAR ('PHI', 1, 20.0, 1)
SIMPAR ('THETA', 1, 45.0, 1)
```

The SIMVAL procedure writes the values of the sampling functions or results functions. The SIMRES package awaits the values of the functions in an order which is induced by the axes declaration, the last declared axis varies first. As there is no order among the functions, and as each function can evolve at its own rhythm, it is expected that the values of a same function are dispersed in the SIMTMP file. It is thus necessary that the SIMVAL procedure precedes each block of values by a label identifying the function and the length of the block. It is also the SIMVAL procedure which controls the application of the selectors (thus it may happen that SIMVAL is called and that nothing is written on the SIMTMP file). The parameters of the procedure are the following ones:

- NOFCT : number of the sampling or result function;
- TABVAL: list of values;
- NBVAL : number of values in TABVAL.

Figure 4.6 gives a valid scenario for one example showing the use of the SIMVAL procedure.

The SIMAVC procedure was conceived to make pre-positioning and in that way contravene the order imposed by the writing of the values of the functions. The procedure changes the context of the required functions by replacing the numbers of the last points of the axes that have been recorded by numbers entered in parameters. This "skip" is noted in the SIMTMP file by a special label. Thus this procedure avoids loading the SIMTMP file with unusable values where it is impossible to correctly assess one or several functions. The parameters of this procedure are as follows:

- TABFCT : list of functions numbers for which the context is to be changed;
- NBFCT : number of functions;
- TABIND : list of the numbers of the points on the axes for each declared axis;
- NSIND : number of values in TABIND.

The SIMFIN procedure, which has no parameter, must be called on to terminate the generation of the SIMTMP file. This procedure adds an end of file mark to the SIMTMP file.

4.1.3 CONVERSION OF SIMTMP TO SIMRES

The SIMTMP file is a sequential file in which the position of the values associated to the different functions depends on the order in which they are written. The dispersion of the information in the SIMTMP file makes the search for the values of a function quite long and complex. The SIMNET program (SIM for simulation and NET for cleaning) has thus been created to convert a SIMTMP file to a direct access file in which the values of a same function will be in consecutive locations. This new file format is the SIMRES format.

Figure 4.7 shows the functioning of the SIMNET program. It is possible to create a file where the values of each function are pooled because the SIMRES program knows the number of values of each function and can thus assess the locations where the writing is to be made. For this, a memory zone is divided in as many buffers as there are functions on the SIMTMP file. The size of each buffer is determined in such a way as to minimize the number access to the disk. The program reads the SIMTMP file sequentially, pools the "bits" of functions in the appropriate buffer and, when the buffer is full, it is written at its place in the SIMRES file.

The size of the memory zone required for proper functioning has made it necessary to opt for a special conversion program rather than directly writing the results in the SIMRES format. It has thus been deemed preferable to have a program using a large working area during a short time spread, rather than adding this time to simulation programs already quite loaded and using already too much time.

4.2 THE XTRACT PACKAGE

The XTRACT package allows the extraction of information from the SIMRES file. The package procedure can be divided into three sub-groups. The first sub-group includes the EXTDEB procedure which initializes the XTRACT package. The second includes the procedures which extract the descriptive information, that is the information written by the SIMAXE, SIMTECH, SIMFCT and SIMPAR procedures. These are procedures that work more or less alone. Finally, the procedures of the last sub-group extract the values of the function of a SIMRES file, that is the information written by the SIMVAL procedure. These procedures are interdependent and they follow a rigorous sequence.

4.2.1 THE EXTDEB PROCEDURE

The EXTDEB procedure initializes the package and opens the SIMRES file on which the other procedures will work. It is thus essential to call the EXTDEB procedure before trying to extract any information from the SIMRES file. The procedure gets as parameter the name of the SIMRES file and the number of logical unit of E/S associated to the printing file. In exchange, the procedure gives the following information: the name of the program generating the SIMRES file, the version number of this program, the sequential number of the file and the computer on which this file has been generated.

4.2.2 PROCEDURE OF EXTRACTION OF THE DESCRIPTIVE INFORMATION

This sub-group is composed of the following procedures:

- EXTTIM : gives the date and the hour of the generation of the SIMRES file;
- EXTNUM : gives the axes identifiers, the sampling functions, the result functions or of the parameters;
- EXTAXE : gives the characteristics of an axis;
- EXTTECH : gives the characteristics of a sampling function;
- EXTFACT : gives the characteristics of a results function;
- EXTPAR : gives the characteristics of a parameter.

It is important to note here the particular role played by the EXTNUM procedure, which provides the identifiers of different objects (axes, functions, parameters). The characteristics of those objects could be later called up by the appropriate procedure.

The running of each procedure is relatively easy. The input parameters identify the needed information. This information is extracted from the SIMRES file and returned to the caller through the output parameters. Figure 4.8 gives a list of the parameters of each of procedures of this sub-group.

4.2.3 PROCEDURE FOR THE EXTRACTION OF THE RESULTS FUNCTIONS

The procedures which extract the values not only locate and retrieve the information on the SIMRES file but they also have a mechanism which splits the data to be extracted in sub-groups or pages. At this point, the extraction loop allows the routine to receive data page by page. This mechanism has three steps.

The first step consists in establishing the field of extraction, i.e. the set of evaluation points for which a value of a given function is needed. This specification is done by indicating the name of the function and by giving, for each of the axes on which the function depends, a list of selection intervals. Each selection interval is defined by the number of the first and the last point of the interval and by an increment. The special value, in this case 0, allows us to choose all the points of an axis. For instance, for function A which depends on axis X, we can choose the points 1 to 20 by sets of 5 and the points 22 to 30 by sets of 2. The order of the presentation of the axes is important because it induces the nesting order of the extraction loops. Moreover, the choice of the selection intervals must take into account the points for which the requested function has been assessed and written in the SIMRES files.

The second step establishes the segmentation of the extraction field and the specification of the tuples configuration needed. The segmentation of the extraction field is done

195

by giving the number of axes that must vary to form a page. These varying axes are always the last to be declared, and they are called the internal axes. It is thus the external axes, those left aside, which will define the loops extracting the different pages. Figure 4.9 gives an example showing the extraction field and the segmentation of a function.

The information feedback by an "elementary" extraction has a list of tuples of the form (<value of the results function>, <value of the sampling function 1>, ..., <value of the sampling function M>) and a list giving, for each non-identified axis in the tuple, the value of the point where the extraction has taken place. In the case of orthogonal grids, the tuples must be composed of the value of the function followed by the value of the internal axes points. The list of the axes points should give the value of the external axes points. Thus the varying data is separated from the fixed data, this avoids redundancies. However, this is not always the case. In fact, when the grids are not orthogonal, it is possible that even the internal axes may have different points for each of the values of the results function. In order to hold the possible different cases and to permit a maximum of flexibility, the XTRACT package works either by the explicit specification of the composition of a tuple or by a specification by default where all happens as if in an orthogonal grid. The explicit specification of a tuple is done by giving a list of the axes for which we need the values of the point in the tuple. In this case, the identification of the points of the other axes is done when possible in the list of the axes points (i.e. as this list gives only one point per axis, if 1 axis varies, the value is indicated as 1E300). Figure 4.10 shows the example of figure 4.9 and the organization of the tuples and the list of axes points.

The third and last step consists in calling the extraction procedure as many times as needed by the segmentation. The role of the package here is to control the evolution of the loops dealing with the external axes, to retrieve the data making up a page on the SIMRES file and to organize the tuples and the list of axes points according to the required configuration.

One option of the XTRACT package gives as an added information the minimums and the maximums of the functions and axes making up a tuple.

Indispensable for graphic applications, this piece of information can easily be obtained if the minimums and maximums can be assessed on one page. But this is not always the case. There may be a need for the minimums and maximums for a larger set of values: for example, for the field of extraction or even for all the SIMRES file. In these cases, the application program must make a special extraction run to assess the minimums and maximums. This task has therefore been given to the XTRACT package which will do it in the most efficient way.

In terms of application, by obtaining the minimums and maximums, it is possible to establish a scale to express the values obtained in the tuples. The XTRACT package can assess the minimums and maximums on three specific fields defining three types of scales: the global scale, the local scale and the standard scale. The global scale is defined by all the values whether selected or not from an axis or a function. The local scale is defined by the values of an extraction page. And finally, the standard scale is defined by the field of extraction either by taking the whole field or by taking a sub-set of this field. In this latter case, the sub-set is delimited by an axis, and each time the counter of the axis is incremented (i.e. there is a change of point), the minimums and maximums of the points covered by the interior axes must be reassessed. Figure 4.11 gives an example of the different scales.

The EXTRAC, EXTSEL, EXTDEF and EXTUP procedures show how the work described above can be processed.

The extraction process starts with the EXTRAC procedure. This procedure specifies the function from which we would like to extract the values. It gets in parameter the identifier of the function. It outputs NBAXES a complete parameter giving the number of axes on which depends the function and IERR indicating, and if it exists, the number of the detected error.

Second, the EXTSEL defines the field of extraction. A call on the EXTSEL procedure indicates for an axis on which the function depends, the number of the points for which we need the values of the function. This procedure must be called NBAXES times and the order in which the axes are presented is important for the definition of the extraction loops. The procedure receives the following parameters:

- NAME : the axis identifier;
- SELAXE : list of selection intervals, one selection interval is made up of either 3 values (the first selected point, the last selected point and an increment) or the value 0 (all points are selected);
- NBSEL : gives the number of intervals in SELAXE.

The procedure outputs the following data:

- NPTSEL : indicates the total number of points chosen on the axis;
- FIXE : the boolean value which is realized if the value of the points on the axis does not depend on other axes, i.e. if the grid is orthogonal in relation to that axis;
- IERR : in case of error, writes the number of the error.

Third, comes the EXTDEF procedure which defines the configuration of a page, the composition of a tuple and the type of scale needed. The procedure receives the following data:

- NBDIM : defines the cut by giving the number of axes that must be made to vary to obtain a tuple page (the innermost axes vary first);
- TABAXE : explicitly specifies the contents of a tuple by giving the list of axes which make up the tuple. This chart is only used if NBOXE > 0;
- NBOXE : if this parameter is less than 0, then the option by default is applied and the tuples are made up of the value of the function followed by the deepest NBDIM axes. If not, then the tuples are made up of the value of the function and of the NBOXES axes declared in TABAXE;
- TYSECH : is a chain of characters which gives the type of the requested scale. The possible values are: none, global, local, standard;
- AXECH : specifies, in the standard scale case, an axis which limits the scope of the scale: i.e., the field of the standard scale is then defined only on the axes deeper than that axis.

The procedure outputs NBEXT the number of pages necessary to cover all the field of extraction and IERR indicating if an error has been detected.

Finally, it is the EXTTUP which carries out the extraction of the information and the computations of the scales. Usually, this procedure should be called up NBEXT times so that all the field of extraction is covered. The parameters of this procedure are the following:

- TABVAL : the array containing the tuples. For a given extraction, the structure of the array is TABVAL (DINTUP, NPT₁, ..., NPT_M) where DINTUP is the number of the value making up the tuple, NPT₁ the number of points selected on the deepest axis, ..., NPT_M the number of points selected on the least deep axis making the page;
- DINTAB : input parameter giving the total dimension in number of TABVAL words;
- TABIND : gives the numbers which identify the non-varying axes;
- TABVAX : gives the value of the points on the non-varying axes;
- DIMIND : input parameter giving the dimension of the TABIND and TABVAX arrays;
- TABECH : array giving the minimums and maximums for the function and the axes making up the tuple;
- DIMECH : input parameter giving the number of TABECH columns (there is always 2 lines, one for the minimum and one for the maximum);
- IERR : indicates the presence of an error.

Figure 4.12 shows the call sequence of the EXTRAC, EXTSEL, EXTDEF and EXTTUP procedures. As can be seen, it is possible to define the cut of a field of extraction, the configuration of the tuples and the type of required scale and then to restart the extraction of the values.

4.3 THE DATSIM PACKAGE

When a group of entities (or objects) have the same information fields, the DATSIM package stores these fields, or a sub-set of these fields, in a same direct access file thus creating a kind of data bank. In this data bank, the model, that is: the necessary information needed to operate the file, specifically the description of the fields of information, is kept in the file heading. The recording of the data bank is made up of the information field of one entity. By giving a sequence number to the different entities and an identifier to the different information fields, it is possible to construct keys which will identify in a unique manner the different recordings.

In the DATSIM file, an entity can then have as many recording as there are information fields. When applicable however, the DATSIM package avoids an excessive proliferation of recordings by defining a value by default for an information field. At this moment, all the active entities (an entity may be non-active) of the data bank must have the same information fields. If the recording of an active entity does not show up in the data bank, then it has a value by default.

In the context of the laser modeling project, the DATSIM package keeps on disk a summary of the SIMRES files. It is thus possible to concentrate in one file, information which would have been otherwise dispersed in several files and only a small part of this information would have fit on disk (the major part of the SIMRES files would be filed away on magnetic tape).

The summaries of the SIMRES files produced by a laser simulation program are regrouped in a same DATSIM data bank. A simulation is an entity at the level of the data bank, and the simulation sequence number (which is also the SIMRES file number) identifies the recordings belonging to a same simulation. The information fields written in the DATSIM files are: some general information on the simulation, the parameters of the simulation and the values of the results functions usually implicated in a comparison.

The components of the DATSIM package can be divided into two sub-groups. The first is made up of programs which generate and modify a heading of a DATSIM file. The second sub-group is made up of the procedures that allow the running in reading and writing mode of a DATSIM file.

4.3.1 GENERATION AND MODIFICATION OF A DATSIM FILE

The generation phase of a DATSIM file is done in two steps. First, the generated file holds in its heading only the data needed for an empty DATSIM file. Next, the description of the data that can be recorded in the file is added to the heading. It is preferable to write from the beginning the description of all the information fields, however it is also possible to make additions to an already operational DATSIM file, that is: a file which contains other data than the descriptive ones.

The DATCRE generates the base of a DATSIM file. This program reads in the input file the generic name of the entities composing the data bank, namely the name of the simulation program producing the SIMRES files which feed the data bank. The base of a DATSIM file includes the identifier of the current version of the DATSIM package, the generic name of the entities, the sequence number of the last entity for which data has been recorded, that is 0, and the number of information fields described in the heading, which is also 0.

The DATEDI program adds to a DATSIM file heading the description of the information fields that can be recorded in the files. The input file of the DATEDI program include, in first line, the command ADD or MODIFY. This command indicates to the DATEDI program whether it is a first addition to the heading (command ADD) or of a subsequent addition (command MODIFY). The description of the different information fields is found later in free form in the input file. This description includes the field identifier, the field class, the type of values of the field (complete, real, boolean, chain of characters), the number of values by default that follow (possibly 0), and finally the list of values by default (possibly empty). The information field class is an identifier known by DATSIM (through an interchangeable table) which allows the pooling and the organization of the information.

For security reasons, the DATEDI program proceeds by two runs. In the first run, the data is validated. If no error is detected, then the program runs the data one more time and writes the data in the heading of the DATSIM file. This way, it is possible to avoid situations where an error invalidates work already done. Figure 4.13 gives an example of data for the DATEDI program. It is to be noted that the number of values by default in no way fixes the number of the values associated to a field: the same field could include a varying number of information from one entity to another.

4.3.2 OPERATION OF A DATSIM FILE

The procedures that run a DATSIM file are:

- DATDEB : starting of a DATSIM file;
- DATNCM : returns the list of identifier of the information fields;
- DATINF : returns the characteristics of an information field;
- DATLIR : reading of a recording;
- DATECR : writing of a recording;
- DATACT : activation or non-activation of an entity;

- DATFIN : closing of a DATSIM file.

The information and the space necessary for the manipulation of a DATSIM file are concentrated in a control block entered as a parameter at the different procedures of the package. This way, an application program can work on several DATSIM files at the same time on the condition of having a control block for each file.

Following is an overview of the operation of each of the package procedures.

The DATDEB procedure is called upon to start a DATSIM file and to initialize the control block associated to this file. Any attempt to work with a DATSIM file without starting first with DATDEB will be an error. The procedure will then receive as parameter the name of DATSIM file to be started, the control block, and the size in number of words of the control block (the suggested size is 2500 words). The procedure returns part of the information composing the base of the heading, in other words, the generic name of the entities making up the file, the sequence number of the last recorded entity and the number of fields described in the heading.

The DATNOM procedure obtains the list of the information fields identifiers. This list is taken from the DATSIM file heading. The parameters of the procedure follow:

- DATBLK (input) : control block of the DATSIM file;
- TABNOM (output): chart containing the information fields identifiers;
- DIMTAB (input) : size of TABNOM;
- NBNOMS (output): number of identifiers placed in TABNOM.

The DATINF procedure obtains the characteristics of an information field. The parameters of this procedure are:

- DATBLK (input) : control block of the DATSIM file;
- NOM (input) : identifier of field of which we need the characteristics;
- CLASSE (output): class of information;
- TYPE (output) : type of value of the information field;
- TABDEF (output): chart giving the values by default (if there are no values by default for the field, the chart will be empty);
- DIMTAB (input) : size of TABDEF;
- LGDEF (output) : number of elements placed in TABDEF;
- IERR (output) : gives 0 if there are no errors, if not, it gives the number of the error.

The DATLIR procedure reads the recording of a DATSIM file, that is, it gives access to the values contained in the information field of a given entity. If the entity exists (i.e. if its sequence number is smaller than the number of the last recorded entity in the file) and if it is active, the procedure assembles the key (entity number and field identifier) and orders the reading of the recording. If the recording exists, then all it does is to transfer it to the caller. If not, then the procedure verifies if there is a value by default for the field, and if it finds one, it returns it. In case the data required does not exist at all, an error number is returned to the application program. Figure 4.14 shows schematically the running just described. The parameters are as follows:

- DATBLK (input) : control block of the DATSIM file;
- NUMSIM (input) : entity number (in this case, it is a simulation number);
- NOM (input) : field of information identifier;
- TABVAL (output): field of information values;
- DIMTAB (input) : size of TABVAL;
- DIMVAL (output): number of values read and returned in TABVAL;
- IERR (output) : gives 0 if there is no error. If not, it gives the error number.

The DATECR procedure can add a recording to a DATSIM file. First, the procedure verifies if the entity at hand is new, in this case it must update the number of the last recorded entity in the file. If it is an already recorded entity, it must see if it is active, as there should be no access to the information field of a non-active entity. If all works well until this step, then the procedure checks to see if there is no values by default for the requested field. If none exists, then the recording is written in (in some cases, it will be a rewriting). If however there is a value by default, then there must be a comparison between the values by default and those received for the field. If they are equal, nothing is written in the file, and the previous recording is deleted. If they are not equal, then the recording is written into the file or the previous recording is replaced by the new one. Figure 4.15 shows schematically how this is done. The different parameters of the procedure are as follows:

- DATBLK (input) : control block of the DATSIM file;
- NUMSIM (input) : entity number for which an information field is to be written;
- NOM (input) : information field identifier;
- VALEUR (input) : chart containing the field values;
- DIMVAL (input) : number of values in the VALEUR chart;
- IERR (output) : gives 0 if there are no errors, if not, gives the number of the error.

The DATACT procedure specifies the state of an entity in the DATSIM file, in other words, an entity can be active or non-active. The recordings of a non-active entity cannot be retrieved but they are not destroyed. Thus by reactivating a non-active entity, we can have access to its recording. The parameters of this procedure are as follows:

- DATBLK (input) : control block of the DATSIM file;
- NUMSIM (input) : number of the entity that has to be modified;
- ACTIF (input) : boolean parameter with its true values if the entity is active, and its false value if it is non-active.
- IERR (output) : gives 0 if there are no errors, if not, gives the number of the error.

Finally, the DATFIN procedure terminates the operation of the DATSIM file. It is imperative to call the DATFIN procedure because the buffer associated to the DATSIM file must be cleared. The only parameter of this procedure is DATBLK, the control block of the DATSIM file that is to be closed.

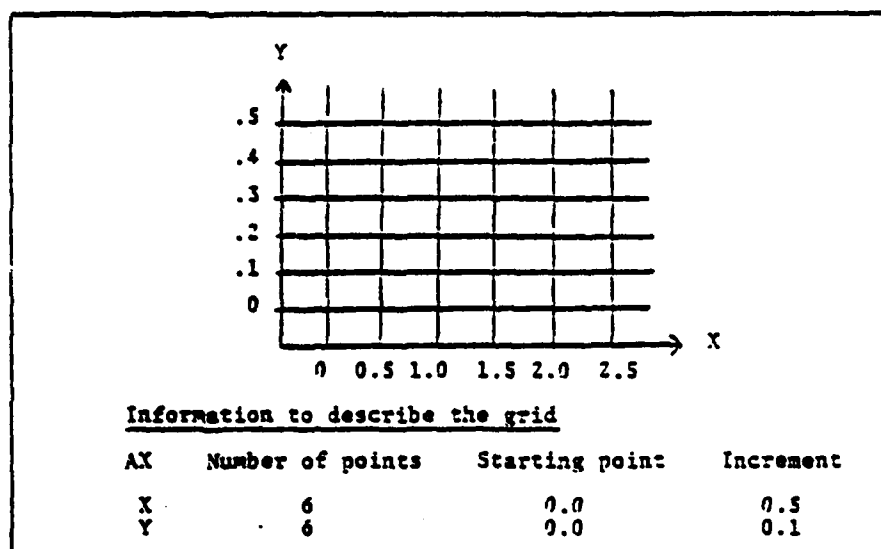


FIGURE 4.1 - LINEAR ORTHOGONAL GRID

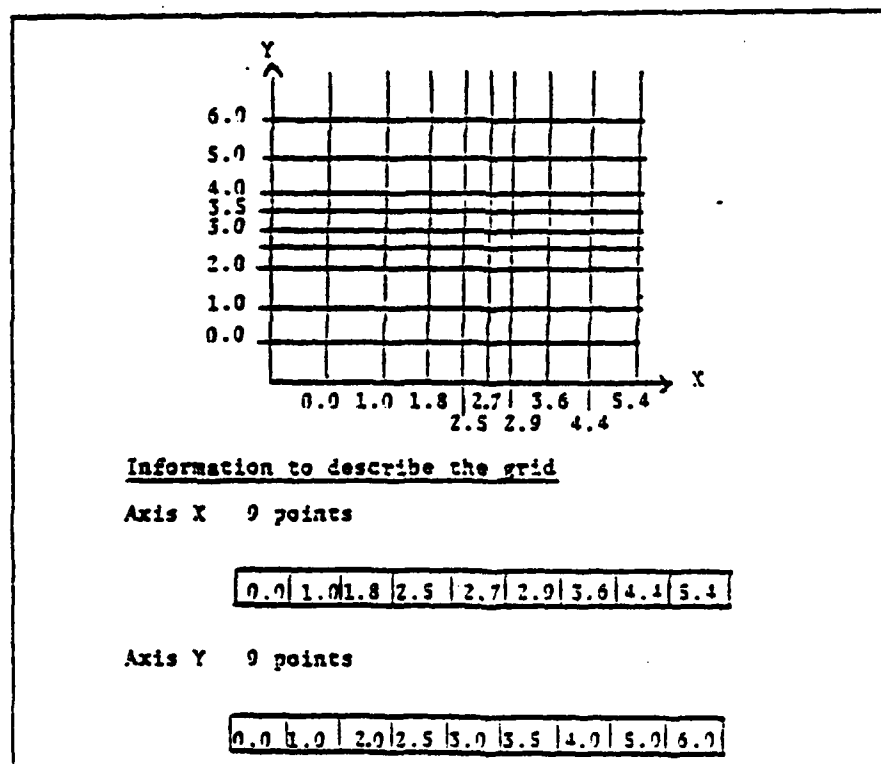


FIGURE 4.2 - NONLINEAR ORTHOGONAL GRID

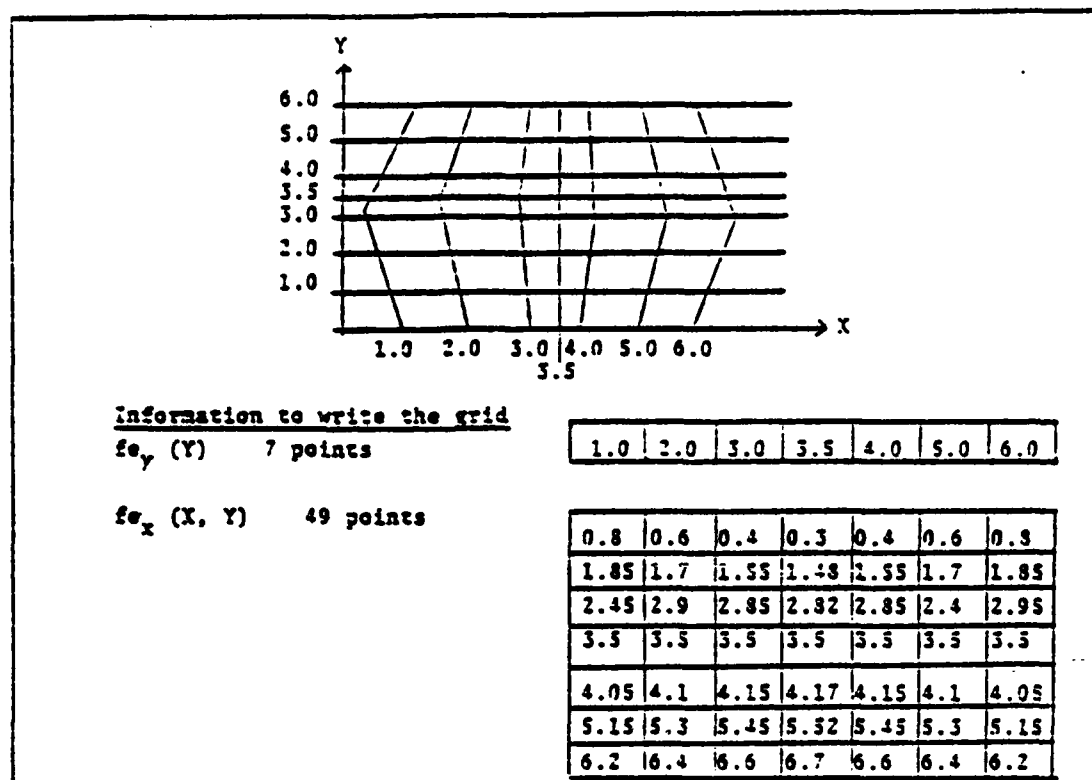


FIGURE 4.3 - NON ORTHOGONAL GRID

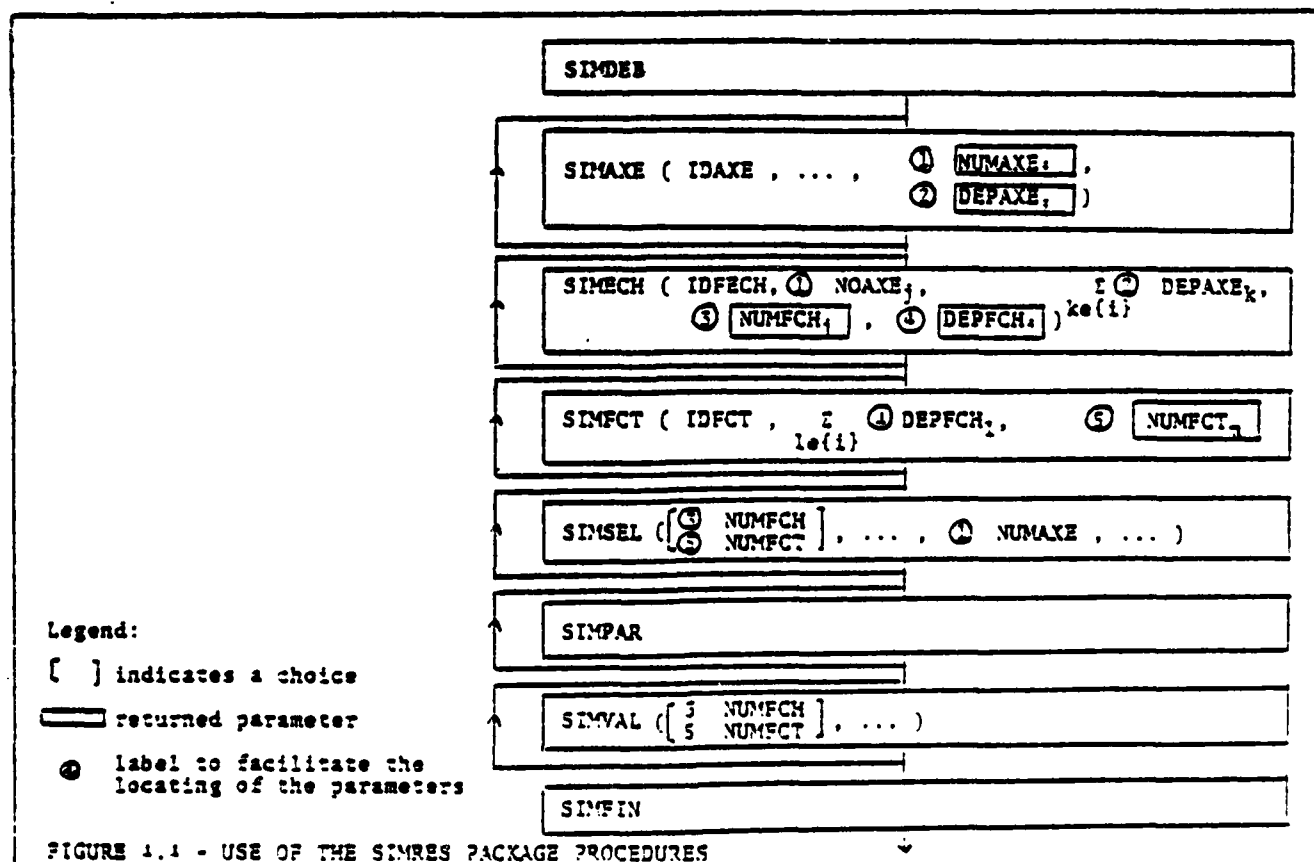


FIGURE 1.1 - USE OF THE SIMRES PACKAGE PROCEDURES

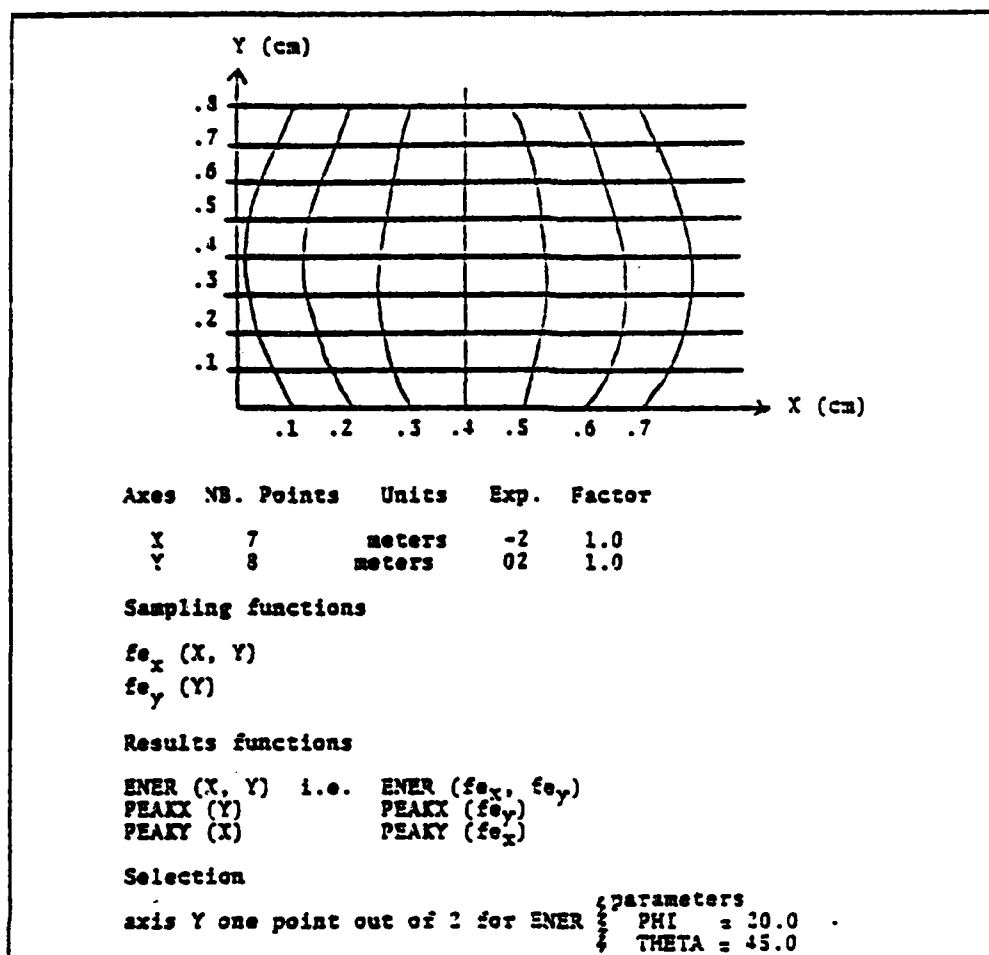


FIGURE 4.5 - CONTEXT DEFINITION TO ILLUSTRATE THE USE OF SIMRES PACKAGE PROCEDURES IN A PROGRAM

```

REAL ENERY (3),
    PEAKX,
    PEAKY (3),
    AXEY (3),
    AXEX (7),

:
<Establish axis Y>
call SIMVAL (NUMFCY, AXEY, 3)
DO 10 IX = 1,7

<Establish a column of axi X>
call SIMVAL (NUMFCX, AXEX, 3)
DO 20 IY = 1,8
ENERY (IY) = ...

20 continue
call SIMVAL (NUMFEN, ENERY, 3)
PEAKX = MAX (ENERY, 3)
call SIMVAL (NUMFPX, PEAKX, 1)

<asses partial PEAKY>

10 continue
call SIMVAL (NUMFPY, PEAKY, 1)

```

FIGURE 4.6 - USE OF SIMVAL PROCEDURE

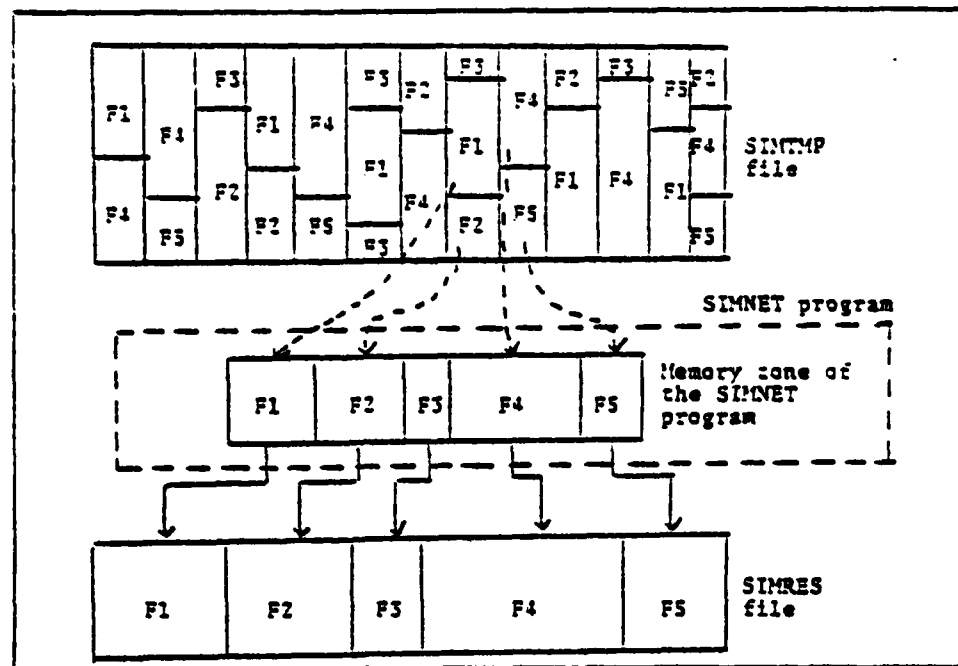


FIGURE 4.7 - CONVERSION OF A SIMTMP FILE INTO A SIMRES FILE

Procedure	Parameter	Description
EXTTIM	DATE (output)	Date of generation of the file
	HOURL (output)	Hour of generation of the file
EXTNOM	KIND (input)	Indicates which identifier is needed AXE - AXES ECH - sampling functions PCT - results functions PAR - parameters
	TABNOM (output)	List of identifiers
	DIMTAB (input)	Size of TABNOM
	NBNOMS (output)	Number of identifiers put in TABNOM
	NAME (input)	Axis identifier
EXTAXE	UNITS (output)	Type of units of the axis
	EXPO (output)	Exhibitor affecting the units
	FACT (output)	Factor affecting the units
	RESOL (output)	Number of resolution points on the axis (not to be mistaken with the number of selected points)
	NAME (input)	Identifier of the sampling function
EXTTECH	AXEREP (output)	Identifier of the axis associated to the function
	AXESEP (output)	Boolean array giving the dependencies of the function as to each of the axes (1)
	DIMSEP (input)	Dimension of AXESEP
EXTPCT	NAME (input)	Identifier of the results functions
	ECHSEP (output)	Boolean array in which the I element indicates whether the function depends on the Ith sampling function
	AXESEP (output)	Boolean array in which the I element indicates if the function depends on the Ith axis
	DIMSEP (input)	Dimension of ECHSEP and AXESEP
EXPAR	NAME (input)	Identifier of the parameter
	TYPE (OUTPUT)	Code indicating the type of parameter (0: complete, 1: actual, ...)
	TABVAL (output)	Value of the parameter (can be a vector)
	DIMTAB (input)	Dimension of TABVAL
	NBVAL (output)	Number of effective value in TABVAL

(1) The order of the elements is that in which they have been declared.

FIGURE 4.8 - PARAMETERS OF THE PROCEDURES EXTRACTING DESCRIPTIVE INFORMATIONS FROM A SIMRES FILE

ASD + JNR

28

**International Conference
on Excited states
and Multiresonant nonlinear
optical processes
in solids**

Digest of Technical Papers

**Aussois, French Alps
March 18-20, 1981**

LES ÉDITIONS DE PHYSIQUE

Avenue du Hoggar
Zone Industrielle de Courtabœuf

Swept-gain superradiance in two- and three-level systems with transverse effects and diffraction (*)

F. P. Mattar and C. M. Bowden (**)

Aerodynamics Laboratory, Polytechnic Institute of New York, Farmingdale, New York 11735, U.S.A.

(**) Research Directorate, US Army Missile Laboratory, US Army Missile Command, Redstone Arsenal, Alabama 35898, U.S.A.

Abstract. — Results of numerical calculations using computational methods developed earlier to efficiently treat transverse as well as longitudinal reshaping associated with single-stream and two-way pulse propagation and generation effects in cooperative light-matter interactions, using the semiclassical model, are presented. Specifically, the results are presented and discussed for the two- as well as three-level system for a traveling excitation for both Gaussian and uniform gain distributions. Conditions are established for lethargic and highly nonlinear soliton pulse evolution through the asymptotic large Z regime.

Summary. — Computational methods based upon the Bloch-Maxwell semiclassical model were developed earlier [1] to efficiently treat transverse as well as longitudinal reshaping and diffraction associated with single-stream and two-way pulse propagation and generation effects in cooperative interaction between the radiation field and a medium consisting of a collection of two-level atoms. Results of the calculation are presented for pulse evolution as a function of propagation distance Z in the two-level system for a traveling excitation with both Gaussian and uniform gain distributions with a classical initial tipping angle distribution. We present the conditions under which the system evolves from a superfluorescent condition [2], where the atoms are contained within a cooperation volume, to an asymptotic steady-state [3] or sufficiently large propagation distance Z where soliton behavior is exhibited. The steady-state condition is interpreted in terms of the asymptotic behavior of the principal mode pulse area and stabilization of the entire pulse shape. Pulse areas greater than π are shown to occur because of multiple pulse generation and self-focusing. Furthermore, it is shown that diffraction plays a much greater role in the results for the swept-gain superradiance regime [3] than for the conditions for which superfluorescence occurs [2]. The results of our numerical calculations for the asymptotic large Z regime are compared with the one-dimensional analytical results for swept-gain superradiance [3].

The numerical code was extended [1] to represent a collection of three-level atoms in the presence of two laser fields, consistent with the usual parity considerations [4, 5]. Results are presented for traveling excitation corresponding to optical pumping for both Gaussian and uniform radial gain distributions and several different temporal functions for the excitation. Superfluorescence is shown to occur for conditions analogous to those for the two-level case [1]; however, two-photon (coherent Raman) effects play a strong role in pulse delay and shape characteristics, as predicted from earlier analytical work [4, 5]. Pulse evolution characteristics are shown to depend upon the excitation temporal function dependence and radial function dependence as well as temporal duration and total area.

We show also in this case the conditions under which the system evolves to an asymptotic steady-state condition at sufficiently large Z in terms of the principal mode pulse area and total pulse shape stabilization. As in the case of two-level swept-gain superradiance, strong self-focusing and multiple pulse generation is indicated.

Finally, results for simulton [6] behavior in the three-level system is presented with two injection signals and also with one injection signal (the optical pump) and a uniform tipping angle (determined from a thermal population distribution) which allows the second pulse to evolve. The latter conditions correspond most realistically in the large [7] region with experimental conditions for swept-gain superradiance reported in the literature [7, 8]. Results of the calculation are presented and compared with the experimental data.

(*) Work jointly sponsored by the Research Corporation, the International Division of Mobil Corporation, the University of Montreal, the US Army Research Office, DAAG29-79-C-0148, the Office of Naval Research, N000-14-80-C-0174, and Battelle Columbus Laboratories contract DAAG29-76-D-0100.

References

- [1] MATTAR, F. P., *Effects of Propagation, Transverse Mode Coupling and Diffraction on Nonlinear Light Pulse Evolution*, in *Optical Bistability*, edited by C. M. Bowden, M. Cif-
tan and H. R. Robl (Plenum Press, NY, 1981), in press.
- [2] MATTAR, F. P., GIBBS, H. M., MCCALL, S. L. and FIELD, M. S., *Transverse Effects in Superradiance*, submitted for publication.
- [3] BONIFACIO, R., HOPP, F. A., MEYSTRE, P. and SCULLY, M. O., *Phys. Rev. A* 12 (1975) 2568.
- [4] BOWDEN, C. M. and SUNG, C. C., *Phys. Rev. A* 18 (1978) 1558.
- [5] BOWDEN, C. M. and SUNG, C. C., *Phys. Rev. A* 20 (1979) 2033.
- [6] KONOPNICKI, M. J., DRUMMOND, P. D. and EBERLY, J. H., *Theory of Lossless Propagation of Simultaneous, Different-Wavelength Optical Pulses*, private communication.
- [7] EHRLICH, J. J., BOWDEN, C. M., HOWGATE, D. W., LEHNIGR, S. H., ROSENBERGER, A. T. and DeTEMPLE, T. A., in *Coherence and Quantum Optics*, edited by L. Mandel and E. Wolf (Plenum Press, NY, 1978), Vol. 4, p. 555.
- [8] ROSENBERGER, A. T., DeTEMPLE, T. A., BOWDEN, C. M. and SUNG, C. C., *Superradiance and Swept-Gain Superradiance in CH₃F*, in *Proceedings of Tenth International Quantum Electronics Conference*, 1978.

TRANSIENT COUNTER-BEAM PROPAGATION IN A NONLINEAR FABRY-PEROT CAVITY *

F.P. MATTAR **, G. MORETTI

Aerodynamics Laboratory, Polytechnic Institute of New York, Brooklyn, NY 11201, USA

and R.E. FRANCEOUR

The International Division, Mobil, New York, NY 10017, USA

Received 10 December 1980

By adapting Moretti's self-consistent numerical approach to integrating the Euler equation of compressible flow, a unified complete temporal and spatial description of superfluorescence and optical bi-stability was undertaken. (The simulation includes material initialization as well as refractive transverse and longitudinal field boundary conditions appropriate to the cylindrical laser cavity). The respecting of physical causality in Moretti's method was maintained; but by using an improved derivative estimator at both the predictor and corrector levels, the overall accuracy was improved.

The physical model includes nonplanar two-way Maxwell-Bloch propagation with spontaneous sources. The problem of dynamic transverse effects as they relate to soliton collisions is addressed. The calculations are based upon an extension of Mattar's previous semi-classical model for diffraction and phase effects in self-induced transparency at thick optical absorptions.

The computational algorithm relies on the use of characteristics, but is strictly a finite-difference scheme. This explicit scheme involves the simultaneous integration along the time coordinate for both forward and backward wave. However, directional derivatives must be considered to appropriately take into account the mutual influence of the two light beams without violating the laws of forbidden signals. Particular case is exercised to maintain at least a second-order accuracy using one-sided approximations to spatial derivatives. Each forward/backward field derivative will be related to its respective directional history. A numerical approach in which the discretization is not consistent with these physical facts will inevitably fail. Thus the numerical algorithm must discriminate between different domains of dependence of different physical parameters.

The physical process can now be analyzed with a degree of realism not previously attainable. Significant agreement with experimental observations is reported from the planar or time-independent analysis counterpart confined to the central portion of the beam.

1. Introduction

The modelling of longitudinal and transverse coherent pulse reshaping that occurs when forward- and backward-travelling beams interact coherently with a medium resonant to the pulse-carrier frequency and with each other is presented. The physical system is characterized by a pulse duration much shorter than all the atomic relaxation lifetimes and dephasing times. In addition, the field is large enough so that significant exchange of energy between the light pulse and matter takes place in a time that is short compared to a relaxation time.

The response of the resonant medium is not instantaneous but cumulative (i.e., it is associated with the past history of the applied field). Hence, the inertial response of the medium is not describable in terms of an intensity-dependent susceptibility. Instead it necessitates a more general functional of the applied field. The treatment differs from earlier theoretical and experimental studies where a rate-equation approximation was considered. Consequently, a semiclassical formalism, similar to the one used by McCall and Hahn [1] in their analysis of self-induced transparency, must be adopted. The physical model is based on counter-propagating travelling-wave equations, derived from Maxwell's equations including transverse [2,3] and transient phase variation [4], and a two-model

* Work supported in part by the Research Corporation, the Army Research Office, the Office of Naval Research and the International Division of Mobil.

The concept of this analysis was proposed at ICO-11 Madrid (September 1978) ed. J. Buescos, Proc. distributed by the Spanish Optical Society, Madrid.

** Author is also presently with Lab. Laser Spectroscopy, MIT, Cambridge, MA 02139, USA.

[5,6] version of the Bloch's [7] equations describing a distribution of two-level homogeneously broadened atomic systems. Furthermore, the simplifying mean-field approximation is not considered; instead, an exact numerical approach that adapts computational methodologies gained in solving fluid dynamics problems is developed.

In the slowing-varying-envelope approximation, both the phase and amplitude variations of a linearly-polarized field in the transverse direction are described by two scalar wave equations, one for each mode: forward-travelling propagation. Each equation is driven by the appropriate polarization associated with the nonlinear inertial response of the active medium. The dynamic crosscoupling of the two waves appears explicitly in the two-mode analogue of the traditional single-mode Bloch's equations describing the material system. The presence of the longitudinal mirrors will further enhance the mutual influence of the two beams. Variations in polarization and population over wavelength distances are treated by means of expansions in spatial Fourier series. The Fourier series are truncated after the third or fifth harmonic. As McCall [6] and Fleck [5] outlined it, the number of terms needed is influenced by the relative strength of the two crossing beams and the importance of pumping and relaxation processes in restoring depleted population differences.

Counter-propagation studies have been previously considered for pulses with infinite transverse extent (i.e., uniform planes) by Marburger and Felber [8] in connection with nonresonant nonlinearities. Two-mode one-dimensional analysis involving resonant interactions have been tackled by McCall [5], Fleck [6], Saunderson and Bullough [9], and more recently by Eberly, Whitney and Konopnicki [10]. However, restrictive assumptions were made relating to the allowed form of the temporal field variations. Since the experimental arrangements often do not satisfy the uniform plane-wave condition, the detailed nature of transverse behavior (using rigorous Laplacian coupling) must be worked out. This present three-dimensional treatment assumes azimuthal cylindrical symmetry.

Furthermore, the interplay of diffraction coupling (through the Laplacian term), and the medium response will inevitably redistribute the beam energy spatially and temporally [11–14]. This transient two-stream beam reshaping profoundly affects a device that relies on this nonlinear light–matter interaction effect. Several physical effects such as strong self-phase modulation, spectral broadening, self-steepening and self-focusing that have been separately studied, combine here to affect the behavior diversely during different positions and times of the pulse evolution. Due to the essential complexity of the governing equations of motion, only effective numerical methods which are consistent with the physics can make attainable a heretofore unachievable solution.

An extension of an efficient numerical approach [15–17] was developed by Mattar to study the transverse energy flow associated with beam variations in the single mode SIT problem. The latter code, which simulates the rigorous interplay of diffraction (Laplacian term) and the inertial two-level atom (Bloch equation) response, had led to the discovery of a new transient on-resonance self-lensing phenomenon which was subsequently verified in sodium [18], neon [19] and more recently in iodine [20] vapour in laboratory experiments. Accurate comparison over a wide domain of physical dependencies was reported [21]. Consequently, the numerics of diffraction and Bloch equations will only be briefly outlined.

In the standing-wave problem, the two waves are integrated simultaneously along t the physical time: no retarded time [22] (or Galilean) transformation as in SIT will be introduced.

To ensure proper handling of the two-stream effect, special attention must be exercised. For causality reasons, as advanced by Moretti [23], only directional resolution for spatial derivatives of each stream (forward and backward field) must be sought. This is achieved by using one-sided discretization techniques. The forward field derivative will be approximated by a different set of points than those used for the backward field derivative. The spatial derivative of the forward field is discretized using points which lie to the left as all preceding forward waves have propagated in the same left–right direction. The backward field is approximated by points positioned to the right. As a result, each characteristic (information carrier) is related to its respective directive history. Thus, violation of the law of forbidden signals is prevented.

Once the basic effects are observed and assessed using straightforward orthogonal computational meshes, non-uniform grids which alleviate the calculational effort [24–28], will be implemented. (The nonuniform grid permits greater point concentrations in the temporal and spatial regions of main interest.)

The prime goals of this study are to achieve an understanding of beam effects in soliton collision [29], and to

relate this situation to the single stream SIT problem and to observations in super-fluorescence [30–33] and optical bi-stability [34,35] experiments. Furthermore, one readily investigates the dependence of the counter-propagation transmission characteristics on pulse and beam shape, on the relaxation times, the resonance frequency offset, the input pulse area(s) on-axis and, the Fresnel number, the mirror reflectivity, the initial tipping angle. The outline of this paper is as follows: in section 2 are the standing-wave Maxwell–Bloch equations and the initial and boundary condition. Section 3 presents the law of forbidden signals. The accuracy of the predictor/corrector scheme is presented in section 4. The effect of improving the derivative estimator on the overall numerical scheme is described in section 5, while section 6 presents the theory of approximating linear operators. In section 7, three-point estimator formulae for the first derivative of a function are derived. Section 8 describes the treatment of the longitudinal boundary condition. Section 9 presents the three-point estimate as an example for the four-point estimator for the Laplacian of a function. Section 10 concludes the paper.

2. Equation of motion

In the slowly-varying-envelope approximation, the dimensionless field–matter equations are:

$$-iF\nabla_T^2 e^+ + \frac{\partial e^+}{\partial \tau} + \frac{\partial e^+}{\partial z} = +g^+ \langle P \exp(-ikz) \rangle, \quad (2.1)$$

$$-iF\nabla_T^2 e^- + \frac{\partial e^-}{\partial \tau} - \frac{\partial e^-}{\partial z} = +g^- \langle P \exp(+ikz) \rangle, \quad (2.2)$$

with g^+ and g^- the nonuniform gain associated to the pump experienced by the forward (e^+) and backward (e^-) travelling wave. The quantities in the r.h.s. undergo rapid spatial variations; $\langle \rangle$ represents the spatial average of these quantities over a period of half a wavelength

$$\frac{\partial P}{\partial \tau} + (-i(\Delta\Omega) + \tau_2^{-2}) P = +\{W(e^+ + e^-)\}, \quad (2.3)$$

$$\frac{\partial W}{\partial \tau} + \tau_1^{-1}(W^* - W) = -\frac{1}{2}(P + P^*)(e^+ + e^-). \quad (2.4)$$

Equivalently

$$\frac{\partial P}{\partial \tau} + (-i(\Delta\Omega) + \tau_2^{-1}) P = W[e^+ \exp(-ikz) + e^- \exp(+ikz)], \quad (2.5)$$

$$\frac{\partial W}{\partial \tau} + \tau_1^{-1}(W^* - W) = -\frac{1}{2}(Pe^{+*} \exp(ikz) + Pe^{-*} \exp(-ikz) + \text{c.c.}), \quad (2.6)$$

with

$$e^\pm = (2\mu\tau_p/\mu) e^\pm, \quad (2.7)$$

$$P = (P'/2\mu), \quad (2.8)$$

$$E^\pm = \text{Re}\{e^\pm \exp[i(\omega t \mp kz)]\} \quad (2.9)$$

and

$$P = \text{Re}\{ip' \exp(i\omega t)\}. \quad (2.10)$$

The complex field amplitude e^\pm , the complex polarization density P' and the energy stored per atom are func-

tions of the transverse coordinate

$$\rho = r/r_p, \quad (2.11)$$

the longitudinal coordinate

$$z = \alpha_{\text{eff}} z \quad (2.12)$$

and the physical time

$$\tau = t/\tau_p. \quad (2.13)$$

The time scale is normalized to a characteristic time of the forward input pulse τ_p , and the transverse dimension scales to a characteristic spatial width r_p of the forward input transient beam. The longitudinal distance is normalized to the effective absorption length [37].

$$\alpha_{\text{eff}}^{-1} = 8\pi\omega\mu^2 N\tau_p/nhc. \quad (2.14)$$

In this expression ω is the angular carrier frequency of the optical pulse, μ is the dipole moment of the resonant transition, N is the number density of resonant molecules and can sustain radial variations, and n is the index of refraction of the background material. The dimensionless quantities

$$\Delta\Omega = (\omega - \omega_0)\tau_p, \quad (2.15)$$

$$\tau_1 = T_1/\tau_p, \quad (2.16)$$

$$\tau_2 = T_2/\tau_p, \quad (2.17)$$

measure the offset of the optical carrier frequency ω from the central frequency of the molecular resonance ω_0 , the thermal relaxation time T_1 , and the polarization dephasing relaxation time T_2 , respectively. The dimensionless parameter F (which is the gain to loss ratio) is given by

$$F = \lambda\alpha_{\text{eff}}^{-1}/4\pi r_p^2 \quad (2.18)$$

and is the reciprocal of the Fresnel number associated with an aperture of radius r_p and a propagation distance (α_{eff}^{-1}). The magnitude of F determines whether or not it is possible to divide up the transverse dependences of the fields into "pencils" (one pencil for each radius) which may be treated in the plane-wave approximation. The diffraction coupling term and the nonlinear interaction terms alternately dominate depending on whether $F < 1$ or $F > 1$.

The presence of opposing waves leads to a quasi-standing wave pattern in the field intensity over a half wavelength. To effectively deal with this numerical difficulty, one decouples the material variables using Fourier series [5,6] namely

$$P = \exp(-ikz) \sum_{p=0}^{\infty} P_{(2p+1)}^+ \exp(-i2pkz) + \exp(+ikz) \sum_{p=0}^{\infty} P_{(2p+1)}^- \exp(+i2pkz). \quad (2.19)$$

$$W = W_0 + \sum_{p=1}^{\infty} [W_{2p} \exp(-i2pkz) + \text{c.c.}] , \quad (2.20)$$

with W_0 a real number. By substituting in the travelling equation of motion one obtains

$$\partial_\tau P_1^+ + P_1^+/\tau_2 = W_0 e^+ + W_2 e^-, \quad (2.21)$$

$$\partial_\tau P_3^+ + P_3^+/\tau_2 = W_2 e^+ + W_4 e^-, \quad (2.22)$$

...

...

$$\partial_\tau P_{(2p+1)}^+ + P_{(2p+1)}^+/\tau_2 = W_{2p}e^+ + W_{2(p+1)}e^-, \text{ and} \quad (2.24)$$

$$\partial_\tau P_1^- + P_1^-/\tau_2 = W_0e^- + W_2^*e^+, \quad (2.25)$$

$$\partial_\tau P_3^- + P_3^-/\tau_2 = W_2e^- + W_4^*e^+, \quad (2.26)$$

...

...

$$\partial_\tau P_{(2p+1)}^- + P_{(2p+1)}^-/\tau_2 = W_{2p}^*e^- + W_{2(p+1)}^*e^+, \quad (2.27)$$

$$\partial_\tau W_0 + (W_0 - W_0^*)/\tau_1 = -\frac{1}{2}(e^-^*P_1^- + e^+^*P_1^+ + \text{c.c.}), \quad (2.28)$$

$$\partial_\tau W_2 + W_2/\tau_1 = -\frac{1}{2}(e^-^*P_1^+ + e^+^*P_3^- + e^+P_1^-^* + e^-P_3^-^*), \quad (2.29)$$

$$\partial_\tau W_{2p} + W_{2p}/\tau_1 = -\frac{1}{2}(e^-^*P_1^+ + e^+P_{2p+1}^+ + e^+P_{2p+1}^-^* + e^-^*P_{2p+1}^-^*). \quad (2.30)$$

The field propagation and atomic dynamic equation are subjected to the following initial and boundary conditions.

1. Initial

$$\text{For } \tau \geq 0, \quad (2.31)$$

$$e^\pm = 0, \quad (2.31)$$

$$W_0 = W_0^*, \quad (2.32)$$

a known function to take into account the pumping effects. For SIT soliton collision

$$P_{(2p+1)}^\pm = 0, \quad \text{for all } p, \quad (2.33)$$

while for the superfluorescence problem

$$P_{(2p+1)}^\pm \quad (2.34)$$

is defined in terms of a non-uniform initial tipping angle that reflects the radial variations of the atomic density – its value can either be deterministic or fluctuating.

2. Longitudinal

For $z = 0$ and $z = L$: e^+ and e^- are given in terms of a known incident function

$$e_{10} \quad (2.35)$$

and

$$e_{1L} \quad (2.36)$$

of τ and ρ . Should enclosing mirrors to delineate the cavity be considered in the analysis, one must deal with the following longitudinal boundary equations

$$e^+ = \sqrt{(1-R_1)} e_{10} + \sqrt{R_1} e^-, \quad \text{at } z = 0, \quad (2.37)$$

$$e^- = \sqrt{(1-R_2)} e_{1L} + \sqrt{R_2} e^+, \quad \text{at } z = L, \quad (2.38)$$

where R_1 , R_2 and $(1-R_1)$, $(1-R_2)$ are the respective reflectivity and transmitting factor associated with each left and right mirror.

3. Transverse

For all z and τ $[\partial e^\pm/\partial \rho]_{\rho=0}$ and $[\partial e^\pm/\partial \rho]_{\rho=\rho_{\max}}$ vanishes. ρ_{\max} defines the extent of the region over which the numerical solution is to be determined. To avoid unphysical reflection from the transverse boundary, one

must, for amplifier calculations, use stretched (nonuniform) radial grids (i.e., consider a quasi-infinite physical domain and map it on a finite computation region) and confine the pre-excited active medium by radially-dependent absorbing shells [17]. Note that this condition represents an actual experimental approach in which the laser amplifier is coated to circumvent any spurious reflections.

3. The law of forbidden signals

The concept of the physical law of forbidden signals and how it affects two-stream flow discretization problems was originally written by Moretti to handle the numerical integration of Euler equations. The method, referred to as the λ -scheme, was presented elsewhere [38]. However, since it represents the basis of our present algorithm, we felt useful to summarize here its salient features.

In any problem involving wave propagation, the equations describe the physical fact that any point at a given time is affected by signals sent to it by other points at previous times. Such signals travel along lines which are known as the 'characteristics' of the equations.

For example, a point such as A in fig. 1 is affected by signals emanating from B (forward wave) and from C (backward wave), while point A' will be the recipient of signals launched from A and D.

Similar wave trajectories appear in our present problem, but the slopes of the lines can change in space and time.

It is clear that the slopes of the two characteristics which carry the information necessary to define the forward and backward propagating variables at every point, are of different signs; they $\lambda_{1,2}$, are numerically equal to $\pm c/n$. For such a point, A (fig. 2), the domain of dependence is defined by point B and point C, the two characteristics being defined by AC and AB, respectively, to a first degree of accuracy. When discretizing the partial differential equations for computational purposes, point A must be made dependent on points distributed on a segment which brackets BC, for example on points D, E and F of fig. 2. Such a condition is necessary for stability but it must be loosely interpreted. Suppose, indeed, that one uses a scheme in which a point such as A is always made to depend on D, E and F, indiscriminately (this is what happens in most of the schemes currently used, including the MacCormack method). Suppose, now, that the physical domain of dependence of A is the segment BC of fig. 3. The information carried to A from F is not only unnecessary, it is also untrue. Consequently, the numerical scheme, while not violating the CFL stability rule, would violate the law of forbidden signals. Physically, it would be much better to use information from D and E to define A, even if this implied lowering the nominal degree of accuracy of the scheme. In other words, to say that a given scheme, using points D, E and F, has a second-order accuracy is meaningless since a wrong scheme has no accuracy whatsoever.

In two-wave propagation problems treated by relaxation methods, the need for a switching of the discretization scheme in passing from forward (advanced) to backward (retarded) points is evidently related to the law of forbidden signals.

The sensitivity of results to the numerical domain of dependence as related to the physical domain of dependence explains why computations which use integration schemes such as MacCormack's [40,41] show a progressive deterioration as the AC line of fig. 2 becomes parallel to the T -axis ($\lambda_1 \rightarrow 0$), even if λ_1 is still negative [38]. The information from F actually does not reach A; in a coarse mesh, such information may be drastically different from the actual values (from C) which affect A. On the other hand, since the CFL rules must be satisfied and

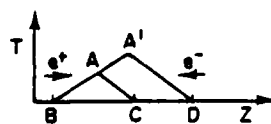


Fig. 1.

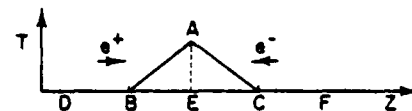


Fig. 2.

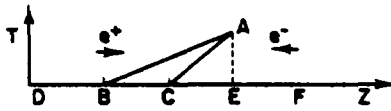


Fig. 3.

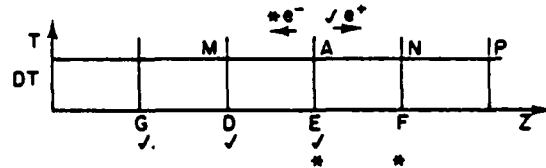


Fig. 4.

F is the nearest point to C on its right, the weight of such information should be minimized. Moretti's λ -scheme, relying simultaneously on the two field equations, provides us with such a possibility.

Every spatial derivative of the forward field is approximated by using points which lie on the same side of E as C, and every derivative of the backward scattered field is approximated by using points which lie on the same side of E as B. By doing so, not only is each characteristic related with information which is only found on the same side of A from which the characteristic proceeds, but such information is appropriately weighted with factors. These depend on the slopes of the characteristic so that the contribution of points located too far outside the physical domain of dependence is minimized. A one-level scheme which defines

$$\partial e^+ / \partial z = (e_E^+ - e_D^+) / \Delta z, \quad (\text{forward wave}), \quad (3.1)$$

$$\partial e^- / \partial z = (e_F^- - e_E^-) / \Delta z, \quad (\text{backward wave}), \quad (3.2)$$

is Gordon's scheme [42], accurate to first order. To obtain a scheme with second-order accuracy, Moretti considered two levels, in a manner very similar to MacCormack's [40]. More points, as in fig. 4, must be introduced. At the predictor level following Moretti's scheme one defines

$$\partial \tilde{e}^+ / \partial z = (2e_E^+ - 3e_D^+ + e_G^+) / \Delta z, \quad (\text{forward wave}), \quad (3.3)$$

$$\partial \tilde{e}^- / \partial z = (e_F^- - e_E^-) / \Delta z, \quad (\text{backward wave}). \quad (3.4)$$

At the corrector level, one defines

$$\partial \tilde{e}^+ / \partial z = (\tilde{e}_A^+ - \tilde{e}_M^+) / \Delta z, \quad (\text{forward wave}) \quad (3.5)$$

and

$$\partial \tilde{e}^- / \partial z = (-2\tilde{e}_A^- + 3\tilde{e}_N^- + \tilde{e}_P^-) / \Delta z. \quad (3.6)$$

It is easy to see that, if any function f is updated as

$$\tilde{f} = f + f_T \Delta T \quad (3.7)$$

at the predictor level, with the T -derivatives defined as in (2.21) and the z -derivatives defined as in (3.3), (3.4) and as

$$f(T + \Delta T) = \frac{1}{2}(f + \tilde{f} + f_T \Delta T) \quad (3.8)$$

at the corrector level, with the T -derivatives defined again as in (2.1), (2.2), and the z -derivatives defined as in (3.5), (3.6), the value of f at $T + \Delta T$ is obtained with second-order accuracy. The updating rule (3.7) and (3.8) are the same as in the MacCormack scheme.

At the risk of increasing the domain of dependence, but with the goal of modularising the algorithm, we have used three- and four-point estimators for each first and second derivative, respectively. We have also extended Moretti's algorithm to a nonuniform mesh to handle the longitudinal refractive (left and right) mirrors: the same one-sided differencing (to satisfy the law of causality) is used for both predictor and corrector steps. Nevertheless, we derived, using the theory of estimation, conveniently presented by Hamming [43], second order derivative estimators at both the predictor and corrector levels. As a result, the overall accuracy of Moretti's scheme was increased.

4. Order of error for straight-line predictor/corrector

We consider the following predictor/corrector scheme as suggested by MacCormack

$$\text{predict: } \tilde{f}_{n+1} = f_n + \delta \tilde{f}'_n, \quad (4.1)$$

$$\text{correct: } \hat{f}_{n+1} = \frac{1}{2}(\tilde{f}_{n+1} + f_n + \delta \tilde{f}'_{n+1}), \quad (4.2)$$

where \tilde{f} indicates predicted, \hat{f} corrected and f exact values. Assume that the derivative estimator for prediction has an error of order p and that for correction of order c , so that:

$$\tilde{f}'_n = f'_n + O(\delta^p) \quad (4.3)$$

$$\hat{f}'_{n+1} = f'_{n+1} + O(\delta^c) \quad (4.4)$$

where $O(\delta^i)$ is a sum involving terms in δ to the power i or higher. Combining (4.1) with (4.3) and (4.2) with (4.4) we get:

$$\text{predict: } \tilde{f}_{n+1} = f_n + \delta f'_n + O(\delta^{p+1}), \quad (4.5)$$

$$\text{correct: } \hat{f}_{n+1} = \frac{1}{2}[\tilde{f}_{n+1} + f_n + \delta \hat{f}'_{n+1} + O(\delta^{c+1})]. \quad (4.6)$$

The Taylor series expansion for f_{n+1} is:

$$f_{n+1} = f_n + \delta f'_n + \frac{\delta^2}{2} f''_n + O(\delta^3). \quad (4.7)$$

Combining (4.7) and (4.5) we get the predictor error \tilde{e}_{n+1} as follows:

$$\begin{aligned} \tilde{e}_{n+1} &= f_{n+1} - \tilde{f}_{n+1} = f_n + \delta f'_n + \frac{\delta^2}{2} f''_n + O(\delta^3) - f_n - \delta f'_n + O(\delta^{p+1}) \\ &= \left(\frac{f''_n}{2}\right) \delta^2 + O(\delta^{p+1}). \end{aligned} \quad (4.8)$$

Thus

$$\tilde{e}_{n+1} = O(\delta^2), \quad \text{for all } p \geq 1. \quad (4.9)$$

Consider now the corrector error:

$$\begin{aligned} \tilde{e}_{n+1} &= f_{n+1} - \hat{f}_{n+1} = f_n + \delta f'_n + \frac{\delta^2}{2} f''_n + O(\delta^3) - \frac{1}{2}\tilde{f}_{n+1} - \frac{1}{2}f_n - \frac{\delta}{2}f'_{n+1} + O(\delta^{c+1}) \\ &= \frac{1}{2}f_n + (f'_n - \frac{1}{2}f'_{n+1})\delta + \frac{f''_n}{2}\delta^2 - \frac{1}{2}[f_n + \delta f'_n + O(\delta^{p+1})] + O(\delta^{c+1}) \\ &= \left(\frac{f'_n - f'_{n+1}}{2}\right)\delta + \frac{f''_n}{2}\delta^2 + O(\delta^{c+1}) + O(\delta^{p+1}). \end{aligned} \quad (4.10)$$

But

$$f'_{n+1} = f'_n + \delta f''_n + O(\delta^2). \quad (4.11)$$

Thus

$$\left(\frac{f'_n - f'_{n+1}}{2}\right)\delta = -\frac{f''_n}{2}\delta^2 + O(\delta^3). \quad (4.12)$$

Whence

$$\tilde{e}_{n+1} = O(\delta^3) + O(\delta^{c+1}) + O(\delta^{p+1}) \quad (4.13)$$

or

$$\tilde{e}_{n+1} = O(\delta^{\min(3, c+1, p+1)}). \quad (4.14)$$

Thus the order of error for the predictor/corrector is the minimum of 3, $c + 1$ and $p + 1$. If $c = 2$ and $p = 2$, their

Table 1

Comparison table between weighting coefficients for derivative estimators using Hamming's estimation theory and Moretti's law of forbidden signals

Hamming: $\tilde{f}'_n = f'_n + O(\delta^2) \rightarrow \tilde{f}_n = f'_n + O(\delta^2)$

Moretti: $\tilde{f}'_n = f'_n + \frac{5f''_n}{2} \delta + O(\delta^2) \rightarrow f'_n = \tilde{f}'_n - \frac{5f''_n}{2} \delta + O(\delta^2)$

Moretti	Hamming
Predictor	
$f_{n+1} = f_n + \delta f'_n + \frac{f''_n}{2} \delta^2 + O(\delta^3)$	$\tilde{f}_{n+1} = f_n + \delta f'_n + O(\delta^3)$
$\tilde{f}_{n+1} = f_n + \delta f'_n + \frac{5f''_n}{2} \delta^2 + O(\delta^3)$	$\tilde{f}_{n+1} - f_{n+1} = -\frac{f''_n}{2} \delta^2 + O(\delta^3)$
$\tilde{f}_{n+1} - f_{n+1} = 2f''_n \delta^2 + O(\delta^3)$	
Corrector	
$\hat{f}_{n+1} = \frac{1}{2}(\tilde{f}_{n+1} + f_n + \tilde{f}'_{n+1})$	$\hat{f}_{n+1} - f_n = \frac{1}{2} f_n + \frac{\delta}{2} f'_n + O(\delta^3)$
$\tilde{f}_{n+1} - f_{n+1} = \frac{1}{2} f_n + \frac{\delta}{2} f'_n + \frac{5f''_n}{2} \delta^2 + O(\delta^3)$	$+ \frac{1}{2} f_n + \frac{\delta}{2} f'_{n+1} + O(\delta^3)$
$+ \frac{1}{2} f_n + \frac{\delta}{2} f'_{n+1} + \frac{f''_{n+1}}{4} \delta^2 + O(\delta^3)$	$- f_n - \delta f'_n - \frac{f''_n}{2} \delta^2 + O(\delta^2)$
$+ f_n - \delta f'_n - \frac{f''_n}{2} \delta^2 + O(\delta^3)$	$= \left(\frac{f'_{n+1} - f'_n}{2} \right) \delta - \frac{f''_n}{2} \delta^2 + O(\delta^3)$
$= \left(\frac{f'_{n+1} - f'_n}{2} \right) \delta + \left(\frac{5f''_{n+1} - 3f''_n}{4} \right) \delta^2 + O(\delta^3)$	$= \left(\frac{f''_n}{2} - \frac{f''_n}{2} \right) \delta^2 + O(\delta^3)$
but	
$f'_{n+1} = f'_n + f''_n \delta + \frac{\delta^2}{2} f'''_n + O(\delta^3)$	$= O(\delta^3)!$
$= \left(\frac{f''_n}{2} + \frac{5f''_{n+1} - 2f''_n}{4} \right) \delta^2 + O(\delta^3)$	
$= \left(\frac{5f''_{n+1} - f''_n}{4} \right) \delta^2 + O(\delta^3)$	

second-order errors effectively cancel out. From the above, it is clear that for maximum accuracy with the straight-line predictor/corrector, the derivative estimators for both prediction and correction should guarantee at least second-order accuracy. Anything above second-order accuracy, however, will not necessarily improve the results.

5. The effect of prediction error on correction error for a weighted formula estimator of the correction derivative

We investigate derivative estimator formulae of the type:

$$\hat{f}'_n = \sum_i \alpha_i f_n(s_i). \quad (5.1)$$

Let $\delta = \max_i (|x_{i+1} - x_i|)$ and assume

$$\hat{f}'_n = f'_n + O(\delta^c), \quad (5.2)$$

so that (5.1) has error c .

In applying a straight-line predictor/corrector with such an estimator for the corrector, we observe that the error in the estimated corrector derivative, since it based on predicted values, will also depend on the error of prediction. From (4.9) we know that the error in predicted values is $O(\delta^2)$ for any reasonable derivative estimator. Thus we may write:

$$\tilde{f}_{n+1}(x_i) = f_{n+1}(x_i) + O(\delta^2). \quad (5.3)$$

Applying formula (5.1) to (5.3) we get:

$$\tilde{f}'_{n+1} = \sum_i \alpha_i \tilde{f}_{n+1}(x_i) = \sum_i \alpha_i f_{n+1}(x_i) + O(\delta^2). \quad (5.4)$$

Thus, using (5.2):

$$\tilde{f}'_{n+1} = f'_{n+1} + O(\delta^c) + O(\delta^2) = \hat{f}'_{n+1} + O(\delta^{\min(c,2)}). \quad (5.5)$$

Therefore the effective error of the corrected derivative cannot be increased beyond 2 for a straight-line corrector. It makes no sense to use a formula of type (5.1) with $c > 2$. From the theory of estimation, conveniently presented by Hamming [43], this means that only three weighting factors $\alpha_1, \alpha_2, \alpha_3$ need be used. See table 1 for comparison between weighting coefficients.

6. Approximating linear operators

Let $\bar{x} = (x_1, x_2, x_3, \dots, x_m)$, $x_i < x_j$ for $i \neq j$. Consider the function f and let $f(\bar{x})$ and W be the column vectors

$$f(\bar{x}) = \begin{pmatrix} f(x_1) \\ f(x_2) \\ f(x_3) \\ \vdots \\ f(x_m) \end{pmatrix}, \quad W = \begin{pmatrix} w_1 \\ w_2 \\ w_3 \\ \vdots \\ w_m \end{pmatrix}. \quad (6.1)$$

Let L be a linear operator. We seek a vector W such that:

$$f = W \cdot f(\bar{x}) + O(\delta^m),$$

where $\delta = \max_i (|x_{i+1} - x_i|)$, $i = 1, \dots, m-1$. We approximate f by a polynomial P_f of order $m-1$ which agrees, exactly with f at points $x_1, x_2, x_3, \dots, x_m$:

$$P_x(x) = \sum_{j=1}^m L_{jm}(x) f(x_j), \quad (6.2)$$

where L_{jm} are the Lagrange polynomials for x . It can easily be shown that

$$f(x) = P_f(x) + R(f, \bar{x}; x), \quad (6.4)$$

where the remainder term $R(f, X; x)$ is

$$R(f, \bar{X}; x) = \frac{f^{(m)}(\theta)}{m!} \prod_{i=1}^m (x - x_i) \leq O(\delta^m), \quad (6.5)$$

for some $\theta: x_1 \leq \theta \leq x_m$. Let λ_{ij} be the coefficients of L_{jm} so that

$$L_{jm}(x) = \sum_{i=0}^{m-1} \lambda_{ij} x^i, \quad (6.6)$$

yielding

$$f(x) = \sum_{j=1}^m f(x_j) \sum_{i=0}^{m-1} \lambda_{ij} x^i + R(f, X; x). \quad (6.7)$$

Applying L to both sides of (3.7), we get

$$Lf(x) = \sum_{j=1}^m f(x_j) \sum_{i=0}^{m-1} \lambda_{ij} Lx^i + LR(f, X; x). \quad (6.8)$$

Define the column vector M_m as:

$$M_m(x) = \begin{pmatrix} 1 \\ x \\ x^2 \\ \vdots \\ x^{m-1} \end{pmatrix},$$

and let $\Lambda_m(\bar{X})$ be the matrix of coefficients of the Lagrange polynomials on \bar{X} . Then (6.8) may be rewritten as:

$$Lf(x) = (\Lambda_m(\bar{X}) \cdot LM_m(x))^T \cdot f(\bar{X}) + LR(f, \bar{X}; x), \quad (6.9)$$

where superscript T represents the matrix transpose operation. We propose the vector

$$W = \Lambda_m(\bar{X}) \cdot LM_m(x) \quad (6.10)$$

as our weighting vector. Note that this vector is independent of the function f .

Eq. (6.9) represents a formula for estimating a linear operation on a function given the function's values at a set of points. Unfortunately, little can be said at this point about the error term $LR(f, \bar{X}, x)$ for arbitrary L . Let us concentrate our attention now on derivative operators. In this case:

$$\frac{d}{dx} R(f, \bar{X}; x) = \frac{d}{dx} \left(\frac{f^{(m)}(\theta)}{m!} \prod_{i=1}^m (x - x_i) \right)$$

$$\begin{aligned}
&= \frac{1}{m!} \left[f^{(m+1)}(\theta) \frac{d\theta}{dx} \prod_{i=1}^m (x - x_i) + f^{(m)}(\theta) \frac{d}{dx} \prod_{i=1}^m (x - x_i) \right] \\
&= \frac{1}{m!} \left[f^{(m+1)}(\theta) \frac{d\theta}{dx} \prod_{i=1}^m (x - x_i) + f^{(m)}(\theta) \left(\prod_{i=2}^m (x - x_i) + \sum_{j=1}^{m-1} \prod_{i=1}^j (x - x_i) \right) \right],
\end{aligned} \quad (6.11)$$

since θ is in general a function of x . Let us further restrict ourselves to cases where $x = x_k$ for some k . If we assume that $f^{(m)}(\theta(x_k))$, $f^{(m+1)}(\theta(x_k))$ and $(d\theta/dx)|_{x=x_k}$ are defined, then the first term above cancels yielding

$$\frac{d}{dx} R(f, X; x)|_{x=x_k} = \frac{f^{(m)}(\theta(x_k))}{m!} \left[\prod_{i=2}^m (x_k - x_i) + \sum_{j=1}^{m-1} \prod_{i=1}^j (x_k - x_i) \right]. \quad (6.12)$$

If $k = 1$, then all the terms under the summation sign will vanish yielding:

$$\frac{d}{dx} R(f, X; x)|_{x=x_1} = \frac{f^{(m)}(\theta(x_1))}{m!} \prod_{i=2}^m (x_1 - x_i), \quad (6.13)$$

$$\frac{d}{dx} R(f, X; x)|_{x=x_1} = \frac{f^{(m)}(\theta(x_1))}{m!} \prod_{k \neq i=1}^m (x_1 - x_i). \quad (6.14)$$

The absolute value of this error term is clearly $\leq O(\delta^{m-1})$. Thus if m is the order of approximation of formula (5.7), then $m - 1$ is the order of approximation of formula (5.9) for the first derivative operator. Similarly, it can be shown under suitable conditions on $\theta(x)$ and $f^{(n)}(\theta(x))$ that

$$\left| \frac{d^n}{dx^n} R(f, X; x) \right|_{x=x_k} \leq O(\delta^{m-n}). \quad (6.15)$$

7. A three point estimator formula for the first derivative of a function

From the results of section 6, we know that a three point formula of type 6.9 should yield an error of order 2. To define the Lagrange coefficient matrix, define the fundamental polynomials as:

$$\pi_j(x) = \prod_{i \neq j}^3 (x - x_i). \quad (7.1)$$

Then the three point Lagrange coefficient matrix is

$$\Lambda_3 = \begin{pmatrix} \frac{x_2 x_3}{\pi_1(x_1)} & \frac{-x_2 - x_3}{\pi_1(x_1)} & \frac{1}{\pi_1(x_1)} \\ \frac{x_1 x_3}{\pi_2(x_2)} & \frac{-x_1 - x_3}{\pi_2(x_2)} & \frac{1}{\pi_2(x_2)} \\ \frac{x_1 x_2}{\pi_3(x_3)} & \frac{-x_1 - x_2}{\pi_3(x_3)} & \frac{1}{\pi_3(x_3)} \end{pmatrix}. \quad (7.2)$$

Let D_1 , D_2 and D_3 be the weighting vectors of formula (6.10) for the derivative at points x_1 , x_2 and x_3 , respectively. Since

$$\frac{d}{dx} M_3(x) = \begin{pmatrix} 0 \\ 1 \\ 2x \end{pmatrix}, \quad (7.3)$$

we have

$$\frac{d}{dx}f(x)|_{x=x_l} = \left(\Lambda_3 \cdot \begin{pmatrix} 0 \\ 1 \\ 2x_l \end{pmatrix} \right)^T f \begin{pmatrix} x_1 \\ x_2 \\ x_3 \end{pmatrix}, \quad (7.4)$$

or

$$D_l = \Lambda_3 \cdot \begin{pmatrix} 0 \\ 1 \\ 2x_l \end{pmatrix}, \quad (7.5)$$

which yields the forward, central and backward differencing estimators, respectively,

$$D_1 = \left(\frac{2x_1 - x_2 - x_3}{\pi_1(x_1)}, \quad \frac{x_1 - x_3}{\pi_2(x_2)}, \quad \frac{x_1 - x_2}{\pi_3(x_3)} \right), \quad (7.6)$$

$$D_2 = \left(\frac{x_2 - x_3}{\pi_1(x_1)}, \quad \frac{2x_2 - x_1 - x_3}{\pi_2(x_2)}, \quad \frac{x_2 - x_1}{\pi_3(x_3)} \right), \quad (7.7)$$

$$D_3 = \left(\frac{x_3 - x_2}{\pi_1(x_1)}, \quad \frac{x_3 - x_1}{\pi_2(x_2)}, \quad \frac{2x_3 - x_1 - x_2}{\pi_3(x_3)} \right). \quad (7.8)$$

To simplify the expressions, we introduce the following

$$\delta_1 = x_2 - x_1, \quad \delta_2 = x_3 - x_2, \quad \delta = \frac{1}{2}(x_3 - x_1) = \frac{1}{2}(\delta_1 + \delta_2), \quad (7.9)$$

$$p_1 = \frac{1}{2} \left(\frac{\delta_1}{\delta_2} - 1 \right) \rightarrow \frac{\delta_1}{\delta_2} = 2p_1 + 1, \quad p_2 = \frac{1}{2} \left(\frac{\delta_2}{\delta_1} - 1 \right) \rightarrow \frac{\delta_2}{\delta_1} = 2p_2 + 1.$$

The fundamental polynomials then become:

$$\begin{aligned} \pi_1(x_1) &= (x_1 - x_2)(x_1 - x_3) = \delta_1(\delta_1 + \delta_2), \quad \pi_2(x_2) = (x_2 - x_1)(x_2 - x_3) = -\delta_1\delta_2, \\ \pi_3(x_3) &= (x_3 - x_1)(x_3 - x_2) = (\delta_1 + \delta_2)\delta_2. \end{aligned} \quad (7.10)$$

The weight vectors for our estimation formulae then become:

$$D_1 = \left(\frac{-2\delta_1 - \delta_2}{\delta_1(\delta_1 + \delta_2)}, \quad \frac{\delta_1 + \delta_2}{\delta_1\delta_2}, \quad \frac{-\delta_1}{(\delta_1 + \delta_2)\delta_2} \right) = \frac{1}{\delta_1 + \delta_2} \left(-2 - \frac{\delta_2}{\delta_1}, \quad \frac{(\delta_1 + \delta_2)^2}{\delta_1\delta_2}, \quad -\frac{\delta_1}{\delta_2} \right) \quad (7.11)$$

$$= \frac{1}{\delta} \left(-(3 + 2p_2), 2p_1 + 1 + 2 + 2p_2 + 1, -(1 + 2p_1) \right) = \frac{1}{\delta} \left(-\left(\frac{3}{2} + p_2\right), 2 + (p_1 + p_2), -\left(\frac{1}{2} + p_1\right) \right),$$

$$\begin{aligned} D_2 &= \left(\frac{-\delta_2}{\delta_1(\delta_1 + \delta_2)}, \quad \frac{\delta_2 - \delta_1}{\delta_1\delta_2}, \quad \frac{\delta_1}{(\delta_1 + \delta_2)\delta_2} \right) \\ &= \frac{1}{\delta_1 + \delta_2} \left(-\frac{\delta_2}{\delta_1}, \quad \frac{\delta_2^2 - \delta_1^2}{\delta_1\delta_2}, \quad \frac{\delta_1}{\delta_2} \right) = \frac{1}{\delta} \left(-\left(\frac{1}{2} + p_2\right), p_2 - p_1, \frac{1}{2} + p_1 \right), \end{aligned} \quad (7.12)$$

$$\begin{aligned} D_3 &= \left(\frac{\delta_2}{\delta_1(\delta_1 + \delta_2)}, \quad \frac{\delta_1 + \delta_2}{-\delta_1\delta_2}, \quad \frac{\delta_1 + 2\delta_2}{(\delta_1 + \delta_2)\delta_2} \right) \\ &= \frac{1}{\delta_1 + \delta_2} \left(\frac{\delta_2}{\delta_1}, \quad \frac{-(\delta_1 + \delta_2)^2}{\delta_1\delta_2}, \quad 2 + \frac{\delta_1}{\delta_2} \right) = \frac{1}{\delta} \left(\left(\frac{1}{2} + p_2\right), -(2 + p_1 + p_2), \frac{3}{2} + p_1 \right). \end{aligned} \quad (7.13)$$

8. Treatment of longitudinal boundary

When treating any point within the cavity or at either longitudinal boundary (where a partially reflecting mirror is situated) there is no problem. But, for example, at $z = 0$, e^+ is determined by eq. (2.35) and not through previous predictor/corrector formulae (7.11)–(7.13) as only e^- is calculated at $z = 0$ in that manner. However, for a point one increment ($\delta = \Delta z$) from the left mirror, one encounters difficulties calculating the forward wave. The second needed point, which is vital to the formulae, would fall outside the cavity. An identical difficulty arises from the counterpart backward wave with respect to the right hand mirror. The field traveling from the right is defined at $z = L$ by eq. (2.36).

To deal with this situation one has to modify the predictor/corrector schemes so that an increment δ^2 is used instead of δ . The loss of that second point, which reduces the accuracy of the derivative estimator maintains near the mirror the same order accuracy. One must compensate this loss by locally reducing the mesh size.

9. A three point estimator formula for the Laplacian of a function

We seek a weighting vector $L = \begin{pmatrix} l_1 \\ l_2 \\ l_3 \end{pmatrix}$ such that

$$\nabla^2 f|_x = \left(\frac{\partial^2 f}{\partial x^2} + \frac{1}{x} \frac{\partial f}{\partial x} \right) \Big|_x = L \cdot f \begin{pmatrix} x_1 \\ x_2 \\ x_3 \end{pmatrix}. \quad (9.1)$$

Because of the linearity of all operations, this may be rewritten:

$$\nabla^2|_x = {}^2D \cdot f(\bar{x}) + \frac{1}{x} D \cdot f(\bar{x}), \quad (9.2)$$

where D is the weighting vector for the first derivative derived in the previous section, and 2D is the weighting vector for the second derivative. To find 2D , we note:

$${}^2D \begin{pmatrix} 1 \\ x_2 \\ x \end{pmatrix} = \begin{pmatrix} 0 \\ 0 \\ 2 \end{pmatrix}, \quad (9.3)$$

so that our equations become, using the notation of the previous sections:

$$\begin{aligned} \left(\Lambda_3 {}^2D \begin{pmatrix} 1 \\ x \\ x^2 \end{pmatrix} \right)^T &= \left(\frac{2}{\delta_1(\delta_1 + \delta_2)}, \frac{-2}{\delta_1 \delta_2}, \frac{2}{(\delta_1 + \delta_2)\delta_2} \right) \\ &= \frac{2}{\delta^2} \left(1 + \frac{\delta_2}{\delta_1}, -\left(2 + \frac{\delta_1 + \delta_2}{\delta_1} \right), \frac{\delta_1 + 1}{\delta_2} \right) = \frac{4}{\delta^2} \left(1 + \frac{\rho_2}{2}, \left(2 + \frac{\rho_1 + \rho_2}{2} \right), 1 + \frac{\rho_1}{2} \right). \end{aligned} \quad (9.4)$$

Note that this formula is independent of x . Combining (9.4) with previous results, we get the following weighting vectors for our Laplacian:

$$L_1 = \frac{4}{\delta^2} \left(1 - \frac{3}{2} \left(\frac{\delta}{2x_1} \right) + \frac{\rho_2}{2} \left(1 - \frac{\delta}{2x_1} \right) - \left(2 - 2 \left(\frac{\delta}{2x_1} \right) + \frac{(\rho_1 + \rho_2)}{2} \left(1 - \frac{\delta}{2x_1} \right) \right), 1 - \frac{1}{2} \left(\frac{\delta}{2x_1} \right) + \frac{\rho_1}{2} \left(1 - \frac{\delta}{2x_1} \right) \right), \quad (9.5)$$

$$L_2 = \frac{4}{\delta^2} \left(1 - \frac{1}{2} \left(\frac{\delta}{2x_2} \right) + \frac{\rho_2}{2} \left(1 - \frac{\delta}{2x_2} \right), -\left(2 + \frac{\rho_1}{2} \left(1 + \frac{\delta}{2x_2} \right) + \frac{\rho_2}{2} \left(1 - \frac{\delta}{2x_2} \right) \right), 1 + \frac{1}{2} \left(\frac{\delta}{2x_2} \right) + \frac{\rho_1}{2} \left(1 + \frac{\delta}{2x_2} \right) \right), \quad (9.6)$$

$$L_3 = \frac{4}{\delta^2} \left(1 + \frac{1}{2} \left(\frac{\delta}{2x_3} \right) + \frac{\rho_2}{2} \left(1 + \frac{\delta}{2x_3} \right), -\left(2 + 2 \left(\frac{\delta}{2x_3} \right) + \left(\frac{\rho_1 + \rho_2}{2} \right) \left(1 - \frac{\delta}{2x_3} \right) \right), \right.$$

$$1 + \frac{3}{2} \left(\frac{\delta}{2x_3} \right) + \frac{\rho_1}{2} \left(1 + \frac{\delta}{2x_3} \right). \quad (9.7)$$

If we introduce the variables

$$r_1 = \frac{\rho_1}{2} = \frac{1}{2} \left(\frac{\delta_1}{2} - 1 \right), \quad (9.8)$$

$$r_2 = \frac{\rho_2}{2} = \frac{1}{2} \left(\frac{\delta_2}{\delta_1} - 1 \right), \quad (9.9)$$

$$d = \frac{\delta}{2} = \frac{1}{2} (\delta_1 + \delta_2). \quad (9.10)$$

The formula simplifies to:

$$L_1 = \frac{1}{d^2} \left(1 - \frac{3}{2} \frac{d}{x_1} + r_2 \left(1 - \frac{d}{x_1} \right), - \left(2 - 2 \frac{d}{x_1} + (r_1 + r_2) \left(1 - \frac{d}{x_1} \right) \right), 1 - \frac{1}{2} \frac{d}{x_1} + r_1 \left(1 - \frac{d}{x_1} \right) \right), \quad (9.11)$$

$$L_2 = \frac{1}{d^2} \left(1 - \frac{1}{2} \frac{d}{x_1} + r_2 \left(1 - \frac{d}{x_2} \right), - \left(2 + r_1 \left(1 + \frac{d}{x_2} \right) + r_2 \left(1 - \frac{d}{x_2} \right) \right), 1 + \frac{1}{2} \frac{d}{x_2} + r_1 \left(1 + \frac{d}{x_2} \right) \right), \quad (9.12)$$

$$L_3 = \frac{1}{d^2} \left(1 + \frac{1}{2} \frac{d}{x_3} + r_2 \left(1 + \frac{d}{x_3} \right), - \left(2 + 2 \frac{d}{x_3} + (r_1 + r_2) \left(1 + \frac{d}{x_3} \right) \right), 1 + \frac{3}{2} \frac{d}{x_3} + r_1 \left(1 + \frac{d}{x_3} \right) \right). \quad (9.13)$$

It should be noted that, since the Laplacian involves a second derivative and only three points are used, the above formulae will lead to error term of first order in δ (or d).

This section can be readily extended to a four-point estimator. The details of the derivation can be found in ref. [44].

10. Concluding remarks

Most features of the numerical model used to study temporal and transverse reshaping effects of short optical pulses counter-propagating in a nonlinear Fabry–Perot entry have been presented. The derivation of the differencing formulae was summarized. The experiment strives to achieve a rigorous analysis of this nonlinear interaction with maximum accuracy and minimum computational effort. The applicability of Moretti λ -scheme developed in gas dynamics to this laser physics problem has been demonstrated. Extension of his method to nonuniform grids were carried out. To facilitate the legibility, maintainability and portability of the program, as well as the implementation of further extensions of the planar wave theory, structural modular programming techniques have been used. The resultant code is concise and easy to follow. Results of this algorithm will be presented elsewhere.

Acknowledgements

The authors wish to thank S. Chitlaru for helping deriving the tedious four-point Laplacian formulae. F.P. Mattar would like particularly to express his appreciation to Drs. H.M. Gibbs and S.L. McCall for their unselfish guidance and enlightening discussions in the physics of this work. The hospitality of Dr. T.C. Cattrall at Mobil which made the computations possible is gratefully acknowledged. Furthermore, F.P.M. would also like to

thank Dr. C. Hazzi and D.J. Steele for their extended patience, unselfish support and continuous encouragement during his convalescence. The skillful word processing effort of E. Cummings is joyfully appreciated.

References

- [1] S.L. McCall and E.L. Hahn, *Phys. Rev. Lett.* 18 (1967) 308; *Phys. Rev.* 183 (1969) 487, A2 (1970).
- [2] N. Wright and M.C. Newstein, *Opt. Commun.* 1 (1973) 8; *IEEE J. Quantum Elec.* QE-10, (1974) 743.
- [3] M.C. Newstein and F.P. Mattar, *J. Opt. Soc. Am.* 65 (1975) 1181; *Opt. Commun.* 18 (1976) 70; *Recent Advances in optical physics*, eds. B. Havelka and J. Blabla, (Soc. of Czechoslovak Math. and Phys., Prague, 1975) p. 299; *IEEE J. Quantum Elec.* QE-13 (1977) 507.
- [4] J.-C. Diels and E.L. Hahn, *Phys. Rev.* A8 (1973) 1084, A10 (1974) 2501.
- [5] S.L. McCall, *Phys. Rev.* A9 (1974) 1515.
- [6] J.A. Fleck, Jr., *Phys. Rev.* B1 (1970) 84.
- [7] R.P. Feynman, F.L. Vernon, Jr. and R.W. Hellwarth, *J. Appl. Phys.* 28 (1957) 43.
E.L. Hahn, *Heritage of the Bloch equations in quantum optics*, to appear in *The Felix Bloch Festschrift 75 Birthday*.
- [8] J.H. Marburger and F.S. Feiber, *Appl. Phys. Lett.* 28 (1976) 731; *Phys. Rev.* A17 (1978) 335.
- [9] R. Sanders and R.K. Bullough, in: *Cooperative effects in matter and radiation*, eds. C.M. Bowden, D.W. Howgate and H.R. Robl (Plenum, New York, 1977) p. 209.
- [10] J.H. Eberly, K.G. Whitney and M. Konopnicki, unpublished Final Research Report to Office of Naval Research (Fall 1977) for research conducted at University of Rochester, Rochester, NY.
- [11] H.M. Gibbs, B. Bölger, F.P. Mattar, M.C. Newstein, G. Forster and P.E. Toschek, *Phys. Rev. Lett.* 37 (1976) 1743.
- [12] F.P. Mattar, M.C. Newstein, P.E. Serafim, H.M. Gibbs, B. Bölger, G. Forster and P.E. Toschek, *Coherence and quantum optics IV*, eds. L. Mandel and E. Wolf (Plenum, New York, 1977) p. 143.
- [13] J.H. Marburger, *Progress in quantum electronics*, vol. 4, eds. J.H. Sanders and S. Stenholm (Pergamon Press, London, New York, 1975) p. 35.
- [14] J.H. Marburger, *Theory of self-focusing with counter-propagating beams (CW Theory in Kerr cubic nonlinearity medium)*, preprint.
- [15] M.C. Newstein and F.P. Mattar, *Proc. 7th Conf. Numerical simulation of plasmas (Courant Inst. of Mathematical Studies, New York, 1975)* p. 273.
- [16] F.P. Mattar, *Appl. Phys.* 17 (1978) 53.
- [17] F.P. Mattar and M.C. Newstein, *Comput. Phys. Commun.* 20 (1980) 139.
- [18] H.M. Gibbs, B. Bölger and L. Baade, *Opt. Commun.* 18 (1976) 199.
- [19] G. Forster and P.E. Toschek, *Spring Annual Meeting of the German Physical Society, Hanover, Fed. Rep. Germany (February 1976)*.
W. Krieger, G. Gaide and P.E. Toschek, *Z. Phys.* B25 (1976) 197.
- [20] J.J. Bannister, H.J. Baker, T.A. King and W.G. McNaught, *Phys. Rev. Lett.* 44 (1980) 1062; *XI Intern. Conf. of Quantum Electronics*, Boston (June 1980).
- [21] See refs. [11,12], as well as F.P. Mattar and M.C. Newstein, (ref. [9], p. 139).
F.P. Mattar, *Kvantovaya Elektronika* 4 (1977) 2520.
F.P. Mattar, G. Forster and P.E. Toschek, *Kvantovaya Elektronika* 5 (1978) 1819.
- [22] F.A. Hopf and M.O. Scully, *Phys. Rev.* 179 (1969) 399.
- [23] G. Moretti, *AIAA* 14 (1976) 894; *Poly-M/AE Tech. Rep.* 78-22 (1980), Polytechnic Institute of New York.
- [24] G. Moretti, *PIBAL Rep.* 70-20 (1970); *Proc. ASME Symp. numerical Lab computer methods in fluid mech.*, ASME (Dec. 1976), *Poly M/AE Tech. Rep.* 76-06 (1976), Polytechnic Institute of New York.
- [25] L. Bradley and J. Hermann, *MIT Lincoln Lab Rep.* LTP-10 (1971); and internal note *On Changes of reference wavefront in the MIT CW nonlinear optics propagation code* (1974) (private communication to F.P. Mattar).
- [26] P.B. Ulrich, *Naval Research Lab. NRL Rep.* 7706 (1974).
- [27] J.A. Fleck, Jr., J.R. Morris and H.D. Feit, *Appl. Phys.* 10 (1976) 129, 14 (1977) 99.
- [28] G.T. Moore and F.J. McCarthy, *J. Opt. Soc. Am.* 67 (1977) 221, 228.
- [29] D.W. Dolf and E.L. Hahn, *Phys. Rev. A* (1980), to appear.
- [30] H.M. Gibbs, see ref. [9], p. 61; and lecture on *Superfluorescence experiments*, 1977 NATO/ASI on Coherence in spectroscopy and modern physics.
Q.H.F. Vrehen, see ref. [9], p. 78; *Laser spectroscopy IV*, eds. H. Walther and I.W. Rothe.
H.M.J. Hikspoors and H.M. Gibbs, see ref. [12], p. 543.

- [31] Q.H.F. Vreken, H.M.J. Hikspoors and H.M. Gibbs, *Phys. Rev. Lett.* 38 (1977) 764, 39 (1977) 547; *Laser spectroscopy III*, eds. by J.I. Hall and J.I. Carlsen (Springer-Verlag, Berlin, 1977).
- [32] J.C. MacGillivray and M.S. Feld, *Phys. Rev. A* 14 (1974); ref. [9], p. 1.
M.S. Feld and J.C. MacGillivray, in: *Advances in coherent nonlinear optics*, eds. M.S. Feld and V.S. Letokhov (Springer-Verlag, Berlin, 1981).
- [33] F.P. Mattar, H.M. Gibbs, S.L. McCall and M.S. Feld, *Phys. Rev. Lett.* 46 (1981) 1123, and European Conf. on Atomic physics (April 1981) paper W10, eds. J. Kowalski, G. zu Putlitz and H.B. Weber, publ. European Phys. Soc.
- [34] T.N.C. Venkatesan, *Opt. News* 5 (1979) 6; *J. Opt. Soc. Am.* 65 (1975) 1184; *Phys. Rev. Lett.* 36 (1976) 1135; US patents no. 012 699 (1975) and no. 121 167 (1976), lecture on optical bistability and differential gains at 1977 NATO/ASI on Coherence in spectroscopy and modern physics (Plenum, New York, 1975).
- [35] T.N.C. Venkatesan and S.L. McCall, *Appl. Phys. Lett.* 30 (1977) 282.
H.M. Gibbs, S.L. McCall, T.N.C. Venkatesan, A.C. Gossard, A. Passner and W. Wiegmann, *IEEE J. Quantum Electron.* QE-15 (1979) 108D; *Appl. Phys. Lett.* 35 (1979) 451.
S.L. McCall and H.M. Gibbs, *Opt. Commun.* (1980).
H.M. Gibbs, S.L. McCall and T.N.C. Venkatesan, Special issue on Optical feedback in *Opt. Eng.*, to be published.
- [36] T. Bischofberger and Y.R. Shen, *Appl. Phys. Lett.* 32 (1978) 156; *Opt. Lett.* 4 (1979) 40, 175 *Phys. Rev. A* 19 (1979) 1169.
- [37] H.M. Gibbs and R.E. Slusher, *Appl. Phys. Lett.* 18 (1971) 505; *Phys. Rev. A* 5 (1972) 1634, *A* 6 (1972) 2326.
- [38] G. Moretti, *Comput. Fluids* 7 (1979) 191.
B. Gabutti, La stabilita de una schema all differenze finite per le equazioni della fluide dinamica, Politecnico di Milano, preprint.
- [39] G. Moretti, PIBAL Rep. 68-15 (1968), Polytechnic Institute of New York.
- [40] R.W. MacCormack, AIAA hypervelocity impact Conf. (1969) paper 69-554.
- [41] R.W. MacCormack, Lecture notes in physics (Springer-Verlag, Berlin, 1971) p. 151.
- [42] P. Gordon, General Electric Final Rep. NOL Contract #N60921-7164 (1968).
- [43] R.W. Hamming, Numerical methods for scientists and engineers (McGraw-Hill, New York, Maidenhead, 1962).
- [44] F.P. Mattar, G. Moretti and R.E. Franceour, POLY-M/AE ADL Technical Report 80-12 (1980).

FLUID FORMULATION OF HIGH INTENSITY LASER BEAM PROPAGATION USING LAGRANGIAN COORDINATES*

F.P. MATTAR**

*Aerodynamics Laboratory, Polytechnic Institute of New York,
and
Physics Department, University of Montreal, Montreal, Canada*

J. TEICHMANN

Physics Department, University of Montreal, Montreal, Canada

Received 28 June 1979; in revised form 6 October 1980

The complete mathematical modeling of nonlinear light-matter interaction is presented in a hydrodynamic context. The field intensity and the phase gradient are the dependent variables of interest. The resulting governing equations are a generalization of the Navier-Stokes equations. This fluid formulation allows the insights and the methodologies which have been gained in solving hydrodynamics problems to be extended to nonlinear optics problems. To insure effective numerical treatment of the anticipated nonlinear self-lensing phenomena, a self-adjusted nonuniform redistribution, along the direction of propagation, of the computation points according to the actual local requirements of the physics must be used. As an alternative to the application of adaptive rezoning techniques in conjunction with Eulerian coordinates, Lagrangian variables are used to provide automatically the desired nonlinear mapping from the physical plane into the mathematical frame. In this paper we propose a method suitable for the solution of the described problem in one-dimensional cases as well as in two-dimensional cases with cylindrical symmetry. To overcome the numerical difficulties related to the inversion of the Jacobian, an analytical algorithm based on the paraxial approximation was developed.

1. Introduction

When sufficiently strong optical beams propagate through nonlinear media, significant self-action phenomena [1] can occur and the propagation characteristics are significantly altered from the vacuum propagation [2]. In particular, self-lensing associated with the nonlinear index of refraction of the medium appears. The corresponding nonlinear beam distortion due to the nonlinear interaction can be rigorously solved only by using appropriate numerical methods since the equations are far too complicated to be handled by any known analytical techniques.

Should the beam focus along the direction of propagation, its transverse dimensions will drastically change at the focal point from what it was at the aperture. It becomes necessary that the transverse dimensions of the three-dimensional grids shrink/expand in size as the focal point is approached/passed [3-8,17].

For the nonlinear interaction, the actual desired shrinkage/expansion of the transverse mesh cannot be guessed a priori; it must be locally determined by the solution to the problem itself. It is therefore necessary to have the

* A numerical algorithm associated with the hydrodynamic analogy of quantum mechanics was previously developed by the same authors, using explicit finite differencing methods in Eulerian coordinates as well as splitting and self-adaptive rezoning. The paper was presented at the Second International Symposium on Gas Flow and Chemical Lasers, Western Hemisphere (1979) held on 11-15 September 1978, at the Von Karman Institute of Fluid Dynamics in Belgium.

** Partially supported by the Research Corporation, the Army Research Office, the Office of Naval Research and the International Division of Mobil. Present address: Laser Spectroscopy Laboratory, MIT, Cambridge, MA, USA.

three-dimensional space grid changing concomitantly with the actual beam shape and size and the local wave-front. To avoid oscillatory behavior associated with the decomposing of the electric field into its real and imaginary parts, it is necessary to describe the field using the modulus and the phase [9–12].

The present paper deals with the hydrodynamic analogy [11,12] of the problem of nonlinear propagation.

In this approach, the evolution of the beam is interpreted in terms of a flowing fluid whose density is proportional to the gradient of the phase. This description allows the treatment of more slowly varying dependent variables and yields equations of motion that are similar and equivalent to those obtained by the method of moments used for the average description of the beam propagation characteristics [1,13–15]. Furthermore, this scheme could allow even larger and coarser marching mesh sizes if it were used simultaneously with an automatically adaptive nonuniform rezoned coordinate system. The set of governing equations thus obtained is a generalization of the Navier–Stokes equations [16–18] that describe a compressible fluid subjected to an internal potential which depends solely and nonlinearly upon the fluid density and its derivatives. This internal potential is often referred to as the quantum mechanical potential.

A further transformation of the dependent variable, namely the use of the natural logarithm of the density, is also introduced [17] to simplify the numerics. To generate an effective and reliable computational code with modest storage requirements, one usually introduces mapping techniques which consist of various function and coordinate transformations. An alternative method to this systematic is the adoption of Lagrangian coordinates. The Lagrangian approach [19] operates with the displacement of a fluid element, following the temporal evolution of its trajectory. In this way, one easily finds the evolution of the phase and the energy in the plane transverse to the direction of the beam propagation. Hence, the system of Lagrangian trajectories corresponds to the automatic self-adaptive nonuniform rezoning and mapping techniques used in the usual Eulerian system; it should also ensure an optimum redistribution of the computational points during the calculation in the various regions of interest. Furthermore, the number of equations is reduced (in comparison to the Eulerian description), and the coupling between the different variables is strengthened, thus accelerating the rate of convergence of the algorithms.

The organization of this paper is as follows: section 2 presents the equations of motion. Section 3 is devoted to the energy conservation and the motivation for an identification of physical variables. Section 4 introduces the fluid description. Section 5 reviews the method of moments. Section 6 summarizes the proposed algorithm based on the Lagrangian formulation. Section 7 presents the conclusion.

2. Equations of motion

For the class of problems describing the propagation of optical signals, the slowly varying envelope approximation is usually adopted, namely [1]

$$E(r, t) = \text{Re} \left\{ e(r, t) \exp \left[i \left(\frac{\omega_0}{c} z - \omega_0 t \right) \right] \right\}, \quad (1)$$

where z designates the propagation direction. Assuming that the complex amplitude $e(r, t)$ changes by a small fractional amount, temporally in the optical period $2\pi/\omega_0$ and spatially in the optical wavelength $2\pi c/\omega_0$, the field equation becomes first order in z and t and reduces, for a linearly polarized light, to the quasi-optics equation

$$-\frac{i}{2\omega_0} \frac{c}{n_0} \nabla_T^2 e + \frac{\partial}{\partial z} e + \frac{n_0}{c} \frac{\partial}{\partial t} e = \gamma |e|^2 e. \quad (2)$$

Here, n_0 is the linear index of refraction of the background material, γ is proportional to the nonlinear part of the refractive index n_2 , $n = n_0 + n_2 |e|^2$. The differential operator ∇_T^2 is the transverse Laplacian in Cartesian coordinates. The time scale is normalized to a characteristic time τ_0 of the input pulse and the transverse dimen-

sion scales to a characteristic spatial width r_p of the input pulse. The input beam is supposed to have azimuthal symmetry. By introducing a moving frame of reference,

$$\eta = z, \quad \tau = t - (n_0/c)z \quad (3)$$

the quasi-optics equation (2) reduces to the nonlinear Schrödinger equation:

$$-\frac{i}{2\omega_0} \frac{c}{n_0} \nabla_T^2 e + \frac{\partial}{\partial \eta} e = \gamma |e|^2 e. \quad (4)$$

3. Energy relations

By multiplying eq. (4) by e^* and adding the complex conjugate, one obtains (with $\gamma = \gamma_1 + i\gamma_2$)

$$\frac{i}{2\omega_0} \frac{c}{n_0} (e \nabla_T^2 e^* - e^* \nabla_T^2 e) + \frac{\partial}{\partial \eta} |e|^2 = 2\gamma_1 |e|^4 \quad (5)$$

or equivalently

$$\nabla_T \cdot J_T + \partial J_z / \partial \eta = 2\gamma_1 |e|^4, \quad (6)$$

where $J_z = |e|^2 = A^2$,

$$J_T = (2\omega_0 n_0)^{-1} c \nabla_T \cdot (e \nabla_T e^* - e^* \nabla_T e) = (c/n_0 \omega_0) [A^2 (\nabla_T \phi)].$$

In the last relation, the polar representation of the complex envelope was used:

$$e = A \exp(i\phi), \quad (7)$$

where A and ϕ are the real functions of coordinates.

The components J_z and J_T represent the longitudinal and transverse energy density flow. Thus, the existence of the transverse energy density current is related to the transverse gradient of the phase ϕ of the complex field (7). When $J_T < 0$ (i.e., $\nabla_T \phi < 0$), self-induced focusing dominates the spreading due to diffraction [20]. The choice of the intensity A^2 and the gradient of the phase ϕ as new variable is physically enlightening and eliminates most of the oscillatory phase difficulties [2] associated with the use of real and imaginary parts of the electric field.

4. Fluid description

Let the nonlinear polarization on the r.h.s. of eq. (4) be written as

$$P^{NL} = (\chi_R + i\chi_I) e = \chi_{NL} e, \quad (8)$$

where χ_R and χ_I are real functions of A . Using eq. (7), one obtains from eq. (4) the transport the the eikonal equations ($n_0 = k_0 c / \omega_0$) [21]:

$$k_0 \frac{\partial}{\partial \eta} A^2 + \nabla_T \cdot [A^2 \nabla_T \phi] = - \frac{4\pi\omega_0^2}{c^2} \chi_I A^2, \quad (9)$$

$$2k_0 \frac{\partial}{\partial \eta} \phi + \left[(\nabla_T \phi)^2 - \frac{A \cdot \nabla_T^2 A}{A^2} \right] = \frac{4\pi\omega_0^2}{c^2} \chi_R. \quad (10)$$

The transport equation (9) expresses the conservation of beam energy over the transverse plane. When $\chi_I = 0$, the

total power is conserved along the direction of propagation. The eikonal equation (10) describes the evolution of the surface of constant phase. It has the form of the Hamilton–Jacobi equation for the two-dimensional motion of particles having unit mass and moving under the influence of potential [1] given by

$$V = -\frac{1}{2k_0^2}(\nabla_T^2 A)A^{-1} - \frac{2\pi}{n_0^2}\chi_R, \quad (11)$$

if $k_0 z$ is regarded as time coordinate and $k_0 x, k_0 y$ as spatial coordinates. Furthermore, if one adopts A^2 and $\nabla_T \phi$ as new dependent variables, the equations of motion become similar to the continuity and momentum transport equations of ordinary hydrodynamics.

By defining

$$\mathbf{v} = k_0^{-1} \nabla_T \phi, \quad \rho = A^2 \quad (12)$$

and supposing $\chi_I = 0$, eqs. (9) and (10) can be written as

$$\frac{\partial \mathbf{v}}{\partial \eta} + (\mathbf{v} \cdot \nabla_T) \mathbf{v} = \frac{1}{2k_0^2} \nabla_T [\rho^{-1/2} (\nabla^2 \sqrt{\rho})] + \frac{\gamma_2}{k_0} (\nabla_T \rho), \quad (13)$$

$$\frac{\partial \rho}{\partial \eta} + \nabla_T \cdot (\rho \mathbf{v}) = 0. \quad (14)$$

These equations are the momentum and continuity transport equations of a fluid with a pressure $P = (\nabla_T^2 \sqrt{\rho})/\sqrt{\rho}$. It should be emphasized that this pressure depends here solely on the “fluid density” and not on the “velocity”.

Eq. (13) can be rearranged into

$$\frac{\partial}{\partial \eta} (\rho \mathbf{v}) + \nabla_T \cdot (\rho \mathbf{v} \mathbf{v}) = \frac{1}{2k_0^2} \nabla_T \cdot \left[\frac{1}{2} (\nabla_T^2 \rho) \mathbf{I} - \frac{1}{2\rho} (\nabla_T \rho)(\nabla_T \rho) \right] + \frac{\gamma_2}{k_0} \rho (\nabla_T \rho), \quad (15)$$

where \mathbf{I} is the unit tensor.

5. The averaged description of wave beams in nonlinear media, the method of moments

The existence of constants of motion and conservation laws, even in a limited number, is very useful for obtaining insight into the dynamics of the self-action phenomena associated with the propagation process. To analyze the nonlinear quasi-optic propagation, Vlasov et al. [13] extended the method of moments, originally developed in connection with the transport theory. In this theory the problem of finding a certain distribution $f(\xi)$ is replaced by that of determining the moments $M_n = \int_{-\infty}^{\infty} \xi^n f(\xi) d\xi$ of this distribution, which are usually more easily calculated than the function $f(\xi)$ itself. Knowledge of all the moments allows the use of known methods to reconstruct the form of the function $f(\xi)$. A simple expression for estimating the width of the diffracted beam is derived in terms of the zero, first-order moment and second-order centrifugal moment integrals of the incident field. These moments are integrated over the full beam cross-section and are, therefore, functions of the propagation coordinate only. The theory of moments only holds when the susceptibility is a function of $|e|^2$, (i.e., when the nonlinear index of refraction is a cubic or fifth-order power in the field).

The starting point of the method of moments is the recognition that the existence of a hierarchy of conservation equations [13,15]

$$\frac{\partial w}{\partial t} = -\nabla \cdot \mathbf{J}, \quad \frac{\partial}{\partial t} \mathbf{J} = c^2 \nabla \cdot \mathbf{T}, \quad \frac{\partial}{\partial t} [\text{Tr}(\mathbf{T})] = -\nabla \cdot \mathbf{Q}, \quad (16)$$

implies a relation between the conserved quantities and the time derivatives of the moments of w . Here, w is scalar, \mathbf{J} and \mathbf{Q} are vectors and \mathbf{T} is a symmetric tensor of second rank having the trace $\text{Tr}(\mathbf{T})$. The first three

moments of w are defined as follows:

$$W = \int_V dV w, \quad S = \frac{1}{W} \int_V dV r w, \quad (Q_{\text{eff}})^2 = \frac{1}{W} \int_V dV r^2 w. \quad (17)$$

The integrals are taken over the volume in which the field quantities are defined, and r is the position vector. Using the Gauss theorem, it can readily be shown that

$$\frac{dW}{dt} = \frac{d^2 S}{dt^2} = \frac{d^3}{dt^3} (Q_{\text{eff}}^2) = 0.$$

In deriving these results, it was assumed that

$$\hat{n} \cdot J = \hat{n} \cdot Q = \hat{n} \cdot T = 0$$

on the closed boundary Σ with normal \hat{n} of the volume V . If Σ is at infinity, all integrals converge. It thus follows that

$$W = W_0, \quad S = S_0 + v \cdot t \quad \text{and} \quad (Q_{\text{eff}}^2) = Q_0^2 + 2c_1 t + c_2 t^2, \quad (18)$$

where $S_0 = S(t=0)$, $Q_0 = Q(t_0)$ and

$$v = \frac{1}{W_0} \int_V dV J|_{t=0}, \quad c_1 = \frac{1}{S_0} \int_V dV r \cdot J|_{t=0}, \quad c_2 = -\frac{1}{W_0} \int_V dV \text{Tr}(T)|_{t=0}.$$

The relations (18) have a simple physical meaning: the energy W of the field is conserved, the energy center S moves along a straight line with a constant speed v and the square of the effective radius of the bunch, Q_{eff}^2 , varies according to a parabolic law (for $t \rightarrow \infty$, $Q_{\text{eff}} \approx t$). It can readily be verified that the conserved quantities satisfy

$$v = \frac{\partial}{\partial t} \int_V dV r w \quad \text{and} \quad c_2 = \frac{\partial^2}{\partial t^2} \int_V dV r^2 w. \quad (19)$$

The hierarchy of conservation laws is satisfied by Maxwell's vacuum equation when W is the density of electromagnetic energy, J is the Poynting vector and T is the Maxwell stress tensor.

Using the transformation (7) and introducing the fluid quantities (12), one obtains for the quasi-optics equation (4) where $t \rightarrow \eta$, $\nabla \rightarrow \nabla_T$ and $\gamma_1 = 0$

$$w = \rho, \quad J = \rho v,$$

$$T_{\alpha\beta} = -\frac{1}{4k_0^2 \rho} \left[(\nabla_\alpha \rho)(\nabla_\beta \rho) - \rho v_\alpha v_\beta + \frac{1}{4k_0^2} \delta_{\alpha\beta} (\nabla_T^2 \rho) + \frac{\gamma_2}{2k_0} \delta_{\alpha\beta} \rho^2 \right], \quad \alpha, \beta = x, y,$$

$$\text{Tr}(T) = \frac{1}{2k_0^2} [(\nabla_T^2 \rho) - \frac{1}{2} \rho^{-1} (\nabla_T \rho)^2 - 2k_0^2 \rho (v \cdot v) + 2k_0 \gamma_2 \rho^2],$$

$$Q = \frac{1}{2k_0^2} \{ \nabla_T [\nabla_T \cdot (\rho v)] - (\nabla_T \rho)(\nabla_T \cdot v) + v [(\nabla_T^2 \rho) - \frac{1}{2} \rho^{-1} (\nabla_T \rho)^2 - 2k_0^2 \rho (v \cdot v)] \} + \frac{2}{k_0} \gamma_2 \rho^2. \quad (20)$$

The equation of the effective beam radius is now

$$Q_{\text{eff}}^2 = Q_0^2 + 2c_1 \eta + c_2 \eta^2 \quad (21)$$

with the following constants of motion:

$$W_0 = \int_\Sigma d\sigma \rho|_{\eta=0}$$

$$\begin{aligned}
Q_0^2 &= \frac{1}{W_0} \int_{\Sigma} d\sigma r^2 \rho|_{\eta=0} \\
c_1 &= \frac{1}{W_0} \int_{\Sigma} d\sigma r \cdot (\rho v)|_{\eta=0} \\
c_2 &= -\frac{1}{W_0} \frac{1}{2k_0^2} \int_{\Sigma} d\sigma \{ (\nabla_T^2 \rho) - \frac{1}{2} \rho^{-1} (\nabla_T \rho)^2 - 2k_0^2 \rho (v \cdot v) + 2\gamma_2 k_0 \rho^2 \} |_{\eta=0}.
\end{aligned} \tag{22}$$

The beam quantities (20) verify the conservation relations (16). The invariant c_1 is related to the transverse energy current. In terms of amplitude and phase, the integrand is $A^2(r \cdot \nabla_T \phi)$. This shows that when the transverse current of energy, which is proportional to the transverse gradient of the phase ϕ , is negative ($\nabla_T \phi < 0$), self-induced lensing dominates diffraction spreading. It should be pointed out that these results only are valid for a nonconfined beam of finite power. The integrals in the x, y plane around the outside boundary of the beam cross-section can only vanish if both e and $\nabla_T e$ vanish. This is not possible on a finite boundary unless e vanishes everywhere. For a finite beam the boundary should recede to infinite. In the numerical solution it is necessary to introduce a perfect conducting wall. The surface integrals remain finite, although small. For this reason numerical solution will disagree with the average mean square radius calculated from the method of moments by a small finite difference.

A similar hierarchy of moments was derived via the quasi-particle approach [22]. An alternative to the Schrödinger picture [13] discussed here is the Heisenberg picture proposed in ref. [23]. Although both methods give the same expectation values, the Heisenberg picture is believed to be simpler.

The method of moments as outlined here represents a local check to the numerical analysis giving the average estimate for quantities related to e^2 .

6. The Lagrangian formulation

Let us summarize the fluid equations taking the quasi-optics relation (4) with the nonlinear polarization term in the form (9). One has for $\chi_I \neq 0$ (nonzero gain or absorption)

$$\frac{\partial}{\partial \eta} \rho + \nabla_T \cdot (\rho v) = \frac{1}{k_0} \chi_I \rho, \quad \rho \left[\frac{\partial}{\partial \eta} v + (v \cdot \nabla_T) v \right] = \frac{1}{2k_0^2} \rho \nabla_T [\rho^{-1/2} \nabla_T^2 (\rho^{1/2}) + \chi_R]. \tag{23}$$

The second equation can be rewritten as

$$\rho \left[\frac{\partial}{\partial \eta} v + (v \cdot \nabla_T) v \right] = \frac{1}{4k_0^2} \nabla_T [\rho \nabla_T^2 (\ln \rho)] + \frac{\rho}{2k_0^2} \nabla_T \chi_R$$

or, by analogy with usual "fluid" equations, as

$$\rho \left[\frac{\partial}{\partial \eta} + (v \cdot \nabla_T) \right] v = \nabla_T P + \frac{\rho}{2k_0^2} \nabla_T \chi_R, \tag{24}$$

where the scalar function P is defined as

$$P = \frac{1}{4k_0^2} [\rho \nabla_T^2 (\ln \rho)]. \tag{25}$$

To elaborate the appropriate computational code, we transform eqs. (23) and (24) into the Lagrangian coordinates [19].

The two hydrodynamic equations (23) may be rewritten in the Eulerian coordinates ($\chi_1 = 0$) in the form

$$\frac{D}{D\eta} \rho + \rho \nabla_T \cdot \mathbf{v} = 0, \quad \rho \frac{D}{D\eta} \mathbf{v} = \nabla_T P,$$

where $D/D\eta = \partial/\partial\eta + \mathbf{v} \cdot \nabla_T$ is the Eulerian derivative describing the motion of the fluid element in a given point of the laboratory frame of reference. Let us transform eq. (23) into Lagrangian coordinates in which the observer moves with the fluid element. In this way, the local derivative $\partial/\partial\eta$ becomes equal to the total derivative $D/D\eta$ although the new coordinates will be related to the initial position of the fluid element [24].

6.1. The one-dimensional case

Let X, η be the Eulerian coordinates and $X = X_0$ ($\eta = 0$ define the Lagrangian coordinate X_0). The speed v is defined in the one-dimensional case as $v = \partial X/\partial\eta$.

The transformation relations are as follows:

$$X = X(X_0, \eta_L) = X_0 + \int_0^{\eta_L} d\eta'_L v(X_0, \eta'_L), \quad \eta = \eta_L. \quad (26)$$

It thus follows that

$$\frac{\partial}{\partial X} = \left(\frac{\partial X}{\partial X_0} \right)^{-1} \frac{\partial}{\partial X_0}, \quad \frac{\partial}{\partial \eta_L} = \frac{\partial}{\partial \eta} + \frac{\partial X}{\partial \eta} \frac{\partial}{\partial X}.$$

The first equation (23) gives for $\chi_1 = 0$

$$\frac{\partial \rho}{\partial \eta_L} + \rho \left(\frac{\partial X}{\partial X_0} \right)^{-1} \frac{\partial}{\partial X_0} \frac{\partial X}{\partial \eta_L} = 0,$$

which integrates to the mass conservation law

$$\rho = \rho_0 (\partial X / \partial X_0)^{-1}. \quad (27)$$

The second equation (24) transforms with the help of (27) into

$$\rho_0 \frac{\partial^2 X}{\partial \eta_L^2} = \frac{\partial}{\partial X_0} P + \frac{1}{2k_0^2} \rho_0 \left(\frac{\partial X}{\partial X_0} \right)^{-1} \frac{\partial}{\partial X_0} \chi_R. \quad (28)$$

Using eq. (27), the scalar function P reads in Lagrangian coordinates

$$P = \frac{1}{4k_0^2} \left\{ \rho \left[2 \left(\frac{\partial X}{\partial X_0} \right)^{-4} \left(\frac{\partial^2 X}{\partial X_0^2} \right)^2 - \left(\frac{\partial X}{\partial X_0} \right)^{-3} \left(\frac{\partial^3 X}{\partial X_0^3} \right) \right] \right\} \quad (29)$$

and eq. (28) gives, using eq. (29),

$$\begin{aligned} \frac{\partial^2 X}{\partial \eta_L^2} = \frac{1}{4k_0^2} & \left\{ - \left(\frac{\partial X}{\partial X_0} \right)^{-5} \left(\frac{\partial^2 X}{\partial X_0^2} \right) \left[2 \left(\frac{\partial X}{\partial X_0} \right)^{-1} \left(\frac{\partial^2 X}{\partial X_0^2} \right)^2 - \left(\frac{\partial^3 X}{\partial X_0^3} \right) \right] \right. \\ & \left. + \left(\frac{\partial X}{\partial X_0} \right)^{-4} \left[7 \left(\frac{\partial X}{\partial X_0} \right)^{-1} \left(\frac{\partial^2 X}{\partial X_0^2} \right) \left(\frac{\partial^3 X}{\partial X_0^3} \right) - 8 \left(\frac{\partial X}{\partial X_0} \right)^{-2} \left(\frac{\partial^2 X}{\partial X_0^2} \right)^3 - \left(\frac{\partial^4 X}{\partial X_0^4} \right) \right] + 2 \left(\frac{\partial X}{\partial X_0} \right)^{-1} \frac{\partial}{\partial X_0} \chi_R \right\}. \end{aligned} \quad (30)$$

The system of fluid equations (23) reduces to a single equation in X which has a second-order derivative in variable η and derivatives in X_0 up to fourth order.

For a nonlinear media with a nonvanishing χ_1 , the first equation (23)

$$\frac{\partial}{\partial \eta} \rho + v \frac{\partial \rho}{\partial X} + \rho \frac{\partial v}{\partial X} = \frac{1}{k_0} \chi_1 \rho$$

is transformed into

$$\frac{\partial}{\partial \eta_L} \left[\ln \left(\rho \frac{\partial X}{\partial X_0} \right) \right] = \frac{1}{k_0} \chi_I$$

which by integration gives

$$\rho \left(\frac{\partial X}{\partial X_0} \right) = \rho_0 \exp \left(\frac{1}{k_0} \int_0^{\eta_L} d\eta'_L \chi_I \right). \quad (31)$$

With this dependence of ρ on η_L , the second equation (24) reads

$$\rho_0 \exp \left(\frac{1}{k_0} \int_0^{\eta_L} d\eta'_L \chi_I \right) \frac{\partial^2 X}{\partial \eta_L^2} = \frac{\partial}{\partial X_0} P + \frac{1}{2k_0^2} \rho_0 \left(\frac{\partial X}{\partial X_0} \right)^{-1} \left(\frac{\partial}{\partial X_0} \chi_R \right) \exp \left(\frac{1}{k_0} \int_0^{\eta_L} d\eta'_L \chi_I \right). \quad (32)$$

6.2. Two-dimensional case in cylindrical geometry

In cylindrical coordinates, the system (23) reads

$$\begin{aligned} \frac{\partial}{\partial \eta} \rho + v_r \frac{\partial}{\partial r} \rho + \rho \frac{1}{r} \frac{\partial}{\partial r} (rv_r) &= \frac{1}{k_0} \rho \chi_I, \\ \rho \left(\frac{\partial}{\partial \eta} v_r + v_r \frac{\partial}{\partial r} v_r \right) &= \frac{1}{4k_0^2} \frac{\partial}{\partial r} \left\{ \rho \frac{1}{r} \frac{\partial}{\partial r} \left[r \frac{\partial}{\partial r} (\ln \rho) \right] \right\} + \frac{\rho}{2k_0^2} \frac{\partial}{\partial r} \chi_R. \end{aligned} \quad (33)$$

Introducing the Lagrangian variables r_{0L} , η_L

$$r_E = r_E(r_{0L}, \eta_L), \quad \eta_E = \eta_L,$$

we find the solution of the first relation (38) in the form (for $\chi_I = 0$)

$$\rho = \rho_0 \left(\frac{\partial r_E}{\partial r_{0L}} \right)^{-1} \frac{r_{0L}}{r_E}. \quad (34)$$

Let us define the fluid "pressure" by analogy with previous cases as

$$P = \frac{1}{4k_0^2} \left\{ \rho \frac{1}{r_E} \frac{\partial}{\partial r_E} \left[r_E \frac{\partial}{\partial r_E} (\ln \rho) \right] \right\}. \quad (36)$$

The scalar P is explicitly

$$P = \frac{1}{4k_0^2} \rho \left(\frac{\partial r_E}{\partial r_{0L}} \right)^{-2} \left[2 \left(\frac{\partial r_E}{\partial r_{0L}} \right)^{-2} \left(\frac{\partial^2 r_E}{\partial r_{0L}^2} \right)^2 - \left(\frac{\partial r_E}{\partial r_{0L}} \right)^{-1} \left(\frac{\partial^3 r_E}{\partial r_{0L}^3} \right) - \frac{1}{r_E} \left(\frac{\partial^2 r_E}{\partial r_{0L}^2} \right) \right]. \quad (37)$$

Finally, the eq. (36) becomes

$$\begin{aligned} \frac{\partial^2 r_E}{\partial \eta_L^2} &= \frac{1}{4k_0^2} \left\{ \left[- \left(\frac{\partial r_E}{\partial r_{0L}} \right)^{-2} \left(\frac{\partial^2 r_E}{\partial r_{0L}^2} \right) - \frac{1}{r_E} \right] \left[2 \left(\frac{\partial r_E}{\partial r_{0L}} \right)^{-4} \left(\frac{\partial^2 r_E}{\partial r_{0L}^2} \right)^2 - \left(\frac{\partial r_E}{\partial r_{0L}} \right)^{-3} \left(\frac{\partial^3 r_E}{\partial r_{0L}^3} \right) \right. \right. \\ &\quad \left. \left. - \frac{1}{r_E} \left(\frac{\partial r_E}{\partial r_{0L}} \right)^{-2} \left(\frac{\partial^2 r_E}{\partial r_{0L}^2} \right) \right] + \left(\frac{\partial r_E}{\partial r_{0L}} \right)^{-2} \left[7 \left(\frac{\partial r_E}{\partial r_{0L}} \right)^{-3} \left(\frac{\partial^3 r_E}{\partial r_{0L}^3} \right) \left(\frac{\partial^2 r_E}{\partial r_{0L}^2} \right) - 8 \left(\frac{\partial r_E}{\partial r_{0L}} \right)^{-4} \left(\frac{\partial^2 r_E}{\partial r_{0L}^2} \right)^3 \right. \right. \\ &\quad \left. \left. - \left(\frac{\partial r_E}{\partial r_{0L}} \right)^{-2} \left(\frac{\partial^4 r_E}{\partial r_{0L}^4} \right) + \frac{1}{r_E^2} \left(\frac{\partial^2 r_E}{\partial r_{0L}^2} \right) + \frac{2}{r_E} \left(\frac{\partial r_E}{\partial r_{0L}} \right)^2 - \frac{1}{r_E} \left(\frac{\partial r_E}{\partial r_{0L}} \right)^{-1} \left(\frac{\partial^3 r_E}{\partial r_{0L}^3} \right) \right] \right\} + \frac{1}{2k_0^2} \left(\frac{\partial r_E}{\partial r_{0L}} \right)^{-1} \frac{\partial}{\partial r_{0L}} \chi_R. \end{aligned} \quad (38)$$

In the case of the imaginary part of χ , $\chi_I \neq 0$ we have by analogy with eq. (32)

$$\frac{\partial^2 r_E}{\partial \eta_L^2} = \left(\rho_0 \frac{r_{0L}}{r_E} \right)^{-1} \exp \left\{ -\frac{1}{k_0} \int_0^{\eta_L} d\eta'_L \chi_I(\eta'_L) \right\} \frac{\partial}{\partial r_{0L}} P + \frac{1}{2k_0^2} \left(\frac{\partial r_E}{\partial r_{0L}} \right)^{-1} \frac{\partial}{\partial r_{0L}} \chi_R. \quad (39)$$

Details of the two-dimensional case in Cartesian coordinates can be found in ref. [25].

The evolutional equations (30) and (38) are rather complex due to the presence of the inverse displacement gradient Jacobian J_{ij} . In order to obtain the evolutional equation more accessible to numerical analysis, we limit ourselves to the paraxial approximation, assuming that the beam convergence or divergence, respectively, due to the nonlinear polarization remains small. Let us introduce the Lagrangian displacement ξ [26]

$$\mathbf{x} = \mathbf{x}_0 + \xi, \quad |\xi| \ll |\mathbf{x}_0|, \quad J_{ij} = \frac{\partial X_i}{\partial X_{0j}} = \delta_{ij} + \frac{\partial \xi_i}{\partial X_{0j}}. \quad (40)$$

The value of any function (field) defined on \mathbf{x} , resulting from the displacement ξ may be expanded in power series of ξ either in form of Eulerian expansions defined at $\mathbf{x}(\eta)$, either in form of Lagrangian expansions defined at $\mathbf{x}_0(\eta)$. Introducing the Eulerian expansions

$$\rho(\mathbf{x}) = \rho_0(\mathbf{x}) + \delta_1 \rho(\mathbf{x}) + \delta_2 \rho(\mathbf{x}) + \dots, \quad \mathbf{v}(\mathbf{x}) = \mathbf{v}_0(\mathbf{x}) + \delta_1 \mathbf{v}(\mathbf{x}) + \delta_2 \mathbf{v}(\mathbf{x}) + \dots$$

into the system (23) and expressing the first and second order changes δ as functions of the displacement ξ , we obtain the following hierarchy of evolutional equations [24]. (We assume $\partial/\partial \eta \mathbf{v}_0 = 0$, $\chi_I = \chi_R = 0$):

$$\text{0th order: } (\mathbf{v}_0 \cdot \nabla_T) \mathbf{v}_0 = \frac{1}{2k_0^2} \nabla_T \{ \rho_0^{-1/2} \nabla_T^2 \rho_0^{1/2} \}; \quad (41)$$

1st order:

$$\begin{aligned} \xi'' + 2(\mathbf{v}_0 \cdot \nabla_T) \xi' + (\mathbf{v}_0 \cdot \nabla_T) [(\mathbf{v}_0 \cdot \nabla_T) \xi - (\xi \cdot \nabla_T) \mathbf{v}_0] + \{[(\mathbf{v}_0 \cdot \nabla_T) \xi - (\xi \cdot \nabla_T) \mathbf{v}_0] \cdot \nabla_T\} \mathbf{v}_0 \\ = \frac{1}{4k_0^2} \nabla_T \{ \rho_0^{-3/2} [\nabla_T \cdot (\rho_0 \xi)] \nabla_T^2 \rho_0^{1/2} - \rho_0^{-1/2} \nabla_T^2 [\rho_0^{1/2} \nabla_T \cdot (\rho_0 \xi)] \}; \end{aligned} \quad (42)$$

2nd order:

$$\begin{aligned} (\xi \cdot \nabla_T) [\xi'' + (\mathbf{v}_0 \cdot \nabla_T) \xi' - (\xi \cdot \nabla_T) \mathbf{v}_0] + \xi_i \xi_j \frac{\partial^2 \mathbf{v}_0}{\partial X_{0i} \partial X_{0j}} \\ + \{[(\xi \cdot \nabla_T) \mathbf{v}_0] \cdot \nabla_T\} [\xi' + (\mathbf{v}_0 \cdot \nabla_T) \xi - (\xi \cdot \nabla_T) \mathbf{v}_0] + \{(\xi \cdot \nabla_T) [\xi' + (\mathbf{v}_0 \cdot \nabla_T) \xi - (\xi \cdot \nabla_T) \mathbf{v}_0] \cdot \nabla_T\} \mathbf{v}_0 \\ + \frac{1}{2} (\mathbf{v}_0 \cdot \nabla_T) \xi_i \xi_j \frac{\partial^2 \mathbf{v}_0}{\partial X_{0i} \partial X_{0j}} + \frac{1}{2} \left[\xi_i \xi_j \frac{\partial^2 \mathbf{v}_0}{\partial X_{0i} \partial X_{0j}} \right] \cdot \nabla_T \mathbf{v}_0 \\ = \frac{1}{8k_0^2} \nabla_T \left\{ \rho_0^{-3/2} \left[[\nabla_T \cdot (\rho_0 \xi)] \nabla_T^2 [\rho_0^{-1/2} \nabla_T \cdot (\rho_0 \xi)] + \rho_0 \left[\frac{\partial \xi_i}{\partial X_{0i}} \frac{\partial \xi_j}{\partial X_{0j}} + (\nabla_T \cdot \xi)^2 \right] \nabla_T^2 \rho_0 \right. \right. \\ \left. \left. + \left[2(\xi \cdot \nabla_T) [\nabla_T \cdot (\rho_0 \xi)] - \xi_i \xi_j \frac{\partial^2 \rho_0}{\partial X_{0i} \partial X_{0j}} - 2\rho_0 \det \frac{\partial \xi_i}{\partial X_{0j}} \right] \nabla_T^2 \rho_0 \right] + \rho_0^{-1/2} \nabla_T^2 \left[\rho_0^{1/2} \left[-(\nabla_T \cdot \xi)^2 \right. \right. \right. \\ \left. \left. \left. - \frac{\partial \xi_i}{\partial X_{0i}} \frac{\partial \xi_j}{\partial X_{0j}} \right] - 2\rho_0^{-1/2} (\xi \cdot \nabla_T) [\nabla_T \cdot (\rho_0 \xi)] + \rho_0^{-1/2} \xi_i \xi_j \frac{\partial^2 \rho_0}{\partial X_{0i} \partial X_{0j}} + 2\rho_0^{1/2} \det \left(\frac{\partial \xi_i}{\partial X_{0j}} \right) \right] \right\}; \end{aligned} \quad (43)$$

for dispersive media $\chi_I \neq 0$, $\chi_R \neq 0$ and the integration of the first equation (23) results in

$$\rho = \rho_0 (\det J_{ij})^{-1} \exp \left[(1/k_0) \int_0^\eta d\eta' \chi_I \right]. \quad (44)$$

The r.h.s. of the second evolution equation should then be completed by an additional term

$$\frac{1}{2k_0^2} \{ \nabla_T \chi_R - (\nabla_T \cdot \xi) \nabla_T \chi_R \}. \quad (45)$$

In case of an azimuthally symmetric beam we introduce cylindrical coordinates assuming that the azimuth ϕ is ignorable. Then

$$\det J = \frac{r}{r_0} \frac{\partial r}{\partial r_0}.$$

Under the assumption of the paraxial approximation, $r = r_0 + \xi$ the hierarchy of evolutionary relations reads ($\chi_I = \chi_R = 0$):

$$v_{0r} \frac{\partial}{\partial r_0} v_{0r} = \frac{1}{2k_0^2} \frac{\partial}{\partial r_0} \left\{ \rho_0^{-1/2} \frac{\partial^2}{\partial r_0^2} \rho_0^{1/2} \right\}, \quad (46)$$

$$\begin{aligned} \xi'' + 2v_{0r} \frac{\partial}{\partial r_0} \xi' + v_{0r}^2 \frac{\partial^2}{\partial r_0^2} \xi - v_{0r} \xi \frac{\partial^2}{\partial r_0^2} v_{0r} + v_{0r} \left(\frac{\partial}{\partial r_0} \xi \right) \left(\frac{\partial}{\partial r_0} v_{0r} \right) - \xi \left(\frac{\partial}{\partial r_0} v_{0r} \right)^2 \\ = \frac{1}{8k_0^2} \frac{\partial}{\partial r_0} \left\{ \rho_0^{-3/2} \left[-\frac{1}{2} \rho_0^{-1} \left(\frac{\partial \rho_0}{\partial r_0} \right)^2 + \left(\frac{\partial^2 \rho_0}{\partial r_0^2} \right) + 2 \frac{\partial \rho_0}{\partial r_0} \frac{\partial}{\partial r_0} - 2 \rho_0 \frac{\partial^2}{\partial r_0^2} \right] \text{div}(\rho_0 \xi) \right\}, \end{aligned} \quad (47)$$

$$\begin{aligned} \xi \frac{\partial}{\partial r_0} \left[\xi'' + v_{0r} \frac{\partial \xi'}{\partial r_0} - \xi \frac{\partial v_{0r}}{\partial r_0} \right] + \xi \xi' \frac{\partial^2 v_{0r}}{\partial r_0^2} + \frac{1}{2} v_{0r} \frac{\partial}{\partial r_0} \left(\xi^2 \frac{\partial^2 v_{0r}}{\partial r_0^2} \right) \\ + \left[\xi v_{0r} \frac{\partial^2}{\partial r_0^2} - 2 \xi \frac{\partial v_{0r}}{\partial r_0} \frac{\partial}{\partial r_0} \right] \left[\xi' + v_{0r} \frac{\partial \xi}{\partial r_0} - \xi \frac{\partial v_{0r}}{\partial r_0} \right] + \frac{1}{2} \xi^2 \frac{\partial v_{0r}}{\partial r_0} \frac{\partial^2 v_{0r}}{\partial r_0^2} \\ = \frac{1}{8k_0^2} \frac{\partial}{\partial r_0} \left\{ \rho_0^{-3/2} \left[\left[\text{div}(\rho_0 \xi) \right] \frac{\partial^2}{\partial r_0^2} \left[\rho_0^{-1/2} \text{div}(\rho_0 \xi) \right] - 2 \rho_0 \frac{\partial^2}{\partial r_0^2} \left[\rho_0^{-1/2} \frac{\partial}{\partial r_0} [\text{div}(\rho_0 \xi)] \right] \right. \right. \\ \left. \left. + \rho_0^{1/2} \frac{\xi}{r_0} \frac{\partial \xi}{\partial r_0} - \frac{1}{2} \rho_0^{-1/2} \xi^2 \frac{\partial^2 \rho_0}{\partial r_0^2} + \rho_0^{1/2} \frac{\xi^2}{r_0^2} + \rho_0^{1/2} \left(\frac{\partial \xi}{\partial r_0} \right)^2 \right] \right. \\ \left. + \left(\frac{\partial^2}{\partial r_0^2} \rho_0^{1/2} \right) \left[2 \xi \frac{\partial}{\partial r_0} [\text{div}(\rho_0 \xi)] + 2 \rho_0 \frac{\xi}{r_0} \frac{\partial \xi}{\partial r_0} - \xi^2 \frac{\partial^2 \rho_0}{\partial r_0^2} + 2 \rho_0 \left(\frac{\xi^2}{r_0^2} \right) + 2 \rho_0 \left(\frac{\partial \xi}{\partial r_0} \right)^2 \right] \right\}. \end{aligned} \quad (48)$$

A generalization of these equations for the dissipative case, $\chi_I \neq 0$, $\chi_R \neq 0$ is straightforward.

In the two methods presented, the set of starting transport equations is combined, via the Lagrangian displacement X on ξ in the case of paraxial approximation, into one equation for X or ξ , respectively. This equation [eqs. (30) or (38), eqs. (47), (43) or (47), (48)] is further elaborated using a suitable differencing scheme. The virtue of the present analysis consists in the fact, that only one variable has to be calculated. This differs our method from Lagrangian analysis, carried out in the past [24].

7. Conclusion

By writing the paraxial scalar wave equation in a conservation form, one finds that it has the structure of the hydrodynamics equation. On the basis of this analogy, the intensity of the laser beam, $|e|^2$, can be interpreted as the density ρ , while the phase, ϕ , as the velocity potential ($v = \text{grad } \phi$) of a hydrodynamic flow process subjected to a pressure, which – in contrast to classical hydrodynamics – depends on derivatives of the fluid density.

It is noteworthy that this hydrodynamic approach to intense laser propagation in nonlinear media removes the rapid numerical oscillations encountered when the field is described by its real and imaginary parts: the new independent variables change much more slowly.

During the nonlinear interaction, significant reshaping and beam distortion take place. To achieve accuracy and efficiency simultaneously, one must resort to nonuniform grids which self-adjust according to the local requirements of the physics. Thus, the Lagrangian description — as opposed to the Eulerian description, which would have required mapping and adaptive rezoning techniques — is adopted.

The continuity and velocity equations reduce to only one evolution equation for the Lagrangian displacement. The resulting governing equation involves derivatives $\partial r / \partial r_0$ up to the fourth order. To overcome the numerical difficulties associated to the inversion of the Jacobian, an analytical algorithm valid in the paraxial limit was further presented.

The object of this communication was to illustrate a novel transfer of effective computational techniques gained in fluid and aerodynamics to optical physics [8] by emphasizing the fluid equivalency. The main goals of this study were to (1) propose an algorithm which is totally consistent with the subtle physics requirements; and (2) to readily gain additional physical insights in this essential nonlinear light-matter interaction.

It is noteworthy that a recent independent research effort also dealt with the hydrodynamic analogy in a Lagrangian description for nonlinear propagation in the atmosphere. However, an explicit algorithm was adopted [26].

Acknowledgements

This work was partially supported by DREV under Contract No. 85076-00219, F.P. Mattar gratefully acknowledges useful discussions with Dr. B.R. Suydam, Professor G. Moretti and Professor Dr. J. Deletrez on the numerical aspect of the problem.

References

- [1] J.H. Marburger, *Progr. Quant. Electron.* 4 (1976) part I.
- [2] H. Kogelnik and T. Li, *Appl. Opt.* 5 (1966) 1550.
- [3] L. Bradley, J. Hermann, MIT Lincoln Lab. Techn. Rep. (1971).
- [4] P.B. Ulrich, Naval Res. Lab. Techn. Rep. NRL 7382 (1971).
- [5] H.J. Breaux, Ball. Res. Lab. BRL Rep. 1723 (1974).
- [6] J.A. Fleck, J.R. Morris and M.J. Feit, LLL Rep. UCRL-51372 (1975).
- [7] J.A. Fleck, J.R. Morris and M.J. Feit, LLL Rep. UCRL-52071 (1976).
- [8] F.P. Mattar, *Appl. Phys.* 17 (1978) 63.
- [9] A.J. Glass, LLL Annual Laser Fusion Rep., Basic Studies (1973-1974).
- [10] O. Rossignol, DREV Rep. R-4029 (1976).
- [11] E. Madelung, *Z. Phys.* 40 (1926) 322.
- [12] H.E. Wilhelm, *Phys. Rev. D* 1 (1970) 2278.
- [13] S.N. Vlasov, V.A. Petrishev and V.I. Talanov, *Izv. Vysshikh Uchebn. Zavedenii Radiofiz.* 14 (1971) 1353.
- [14] B.R. Suydam, *IEEE J. Quant. Electron.* 10 (1974) 837.
- [15] J.E. Lam, B. Lipman and F.D. Tappert, *Phys. Fluids* 20 (1977) 1179.
- [16] R.W. MacCormack, AIAA Hypervelocity Impact Conf., paper No. 69-354 (1969).
- [17] G. Moretti, PIBAL Reps. 69-25 (1969), 69-26 (1969), 70-20 (1970), 70-48 (1970), 72-37 (1972), 74-15 (1974), 76-06 (1976).
- [18] P.J. Roache, *Computational fluid dynamics* (Hermosa, New Mexico, 1972).
- [19] R. Courant and K.O. Friedrich, *Supersonic flow and shock waves* (Interscience, New York, 1948).
- [20] F.P. Mattar and M.C. Newstein, in: *Cooperative effects in matter and radiation*, eds. C.M. Bowden, D.W. Howgate and H. Robl (Plenum, New York, 1977) p. 139; *Comput. Phys. Commun.* 20 (1980) 139.
- [21] S.A. Akhmanov, R.V. Khokhlov and A.P. Sukhorukov, in: *Laser handbook*, eds. F.T. Arrechi and E.O. Schults-DuBois (North-Holland, Amsterdam, 1972) p. 1151.
- [22] N. Marcuvitz, *IEEE Trans. Electron. Dev.* ED-17 (1970) 252.
- [23] M.C. Newstein and D. Ramakrishnan, Rep. POLY-MRI-1394-78 (1978).
- [24] F.P. Mattar and J. Teichman, *IEEE Conf. Plasma Science*, Montreal (1979).
- [25] F.P. Mattar and J. Teichman, Physics Dept., University of Montreal, Techn. Rep. UDM-PL 79/1 (1979).
- [26] J. Teichmann and F. Mattar, *Proc. IXth Conf. Numer. Simulation in Plasmas*, Evanston, Illinois (1980).
- [27] M. Lax, J. Battch and G.P. Agrawal, *Channeling of Intense Electromagnetic Beams*, preprint, Physics Dept. at CCNY, New York (1980).

91

Transverse effects in swept-gain superradiance: evolution from the superradiant state

C. M. Bowden

U.S. Army Missile Laboratory

U.S. Army Missile Command, Redstone Arsenal, Alabama 35898

F. P. Matter*

Aerodynamics Laboratory, Polytechnic Institute of New York

Brooklyn, New York 11201

Laser Spectroscopy Laboratory, Massachusetts Institute of Technology

Cambridge, Massachusetts 02139

Abstract

Results of numerical calculations are presented and analyzed for pulse generation and subsequent stabilization in large propagation distance z , for a collection of two-level absorbers which are swept-excited by an impulse inversion along the z -direction at the speed of light in the medium. The calculation is performed using the coupled Maxwell-Bloch formalism and for the conditions that $T_2 = T_1$, $T_2 \gg \tau_c$, $g/k \gg 1$, where T_2 is macroscopic dipole moment dephasing time, T_1 is the longitudinal relaxation time for the absorber, τ_c is the characteristic superradiant cooperation time among the absorbers and g/k is the linear gain, g , to diffraction loss, k , ratio. Results of the calculation for nonlinear pulse evolution and propagation for one spacial dimension (planar case) is compared with the results for the comparable case where transverse mode coupling is included.

Introduction

In 1975, Bonifacio, Hopf, Meystre and Scully¹ (hereafter referred to as BHMS) predicted the conditions for which steady-state pulses having characteristics of superradiance (intensity $\sim \rho^2$, temporal width $\sim 1/\rho$, where ρ is the density of absorbers, and pulse envelope varying in time as hyperbolic secant with characteristic delay of the peak from the excitation) can be generated in swept-gain amplifiers. They obtained and analyzed steady-state solutions of the coupled Maxwell-Bloch equations in the retarded time frame in one spacial dimension z in the limit $z \rightarrow \infty$, for the initial condition that impulse inversion occurs at $\tau = 0$, where $\tau = t - z/c$, in the retarded time. Exact analytical results under these conditions were obtained by BHMS for homogeneously-broadened systems for two special cases, $T_2 < T_1$ and $T_1 = T_2$, where T_2 and T_1 are the transverse and longitudinal atomic relaxation times, respectively.

Subsequent theoretical work which followed the initial work of BHMS¹ addressed to the quantum mechanical aspects of pulse buildup from noise and the role of spontaneous emission in the small signal regime for a system with small Doppler width² and for a homogeneously-broadened system.³ Further theoretical work analyzed the effects of coherent pumping, for the excitation, on pulse buildup, both numerically⁴ and analytically^{5,6,7}. The first reported detailed experimental study of swept-gain superradiance⁸ was for CO_2 -pumped CH_3F .

Since Dicke's initial prediction⁹ for the circumstances under which a macroscopic volume of atoms can radiate collectively (collective, spontaneous relaxation), a large amount of theoretical and experimental effort has been devoted to the subject of superradiance.⁹ Experimental arrangements for the study of superradiance has been identical with that for swept-gain superradiance.^{9,10} Even though the two phenomena stem from entirely different physical processes, the same physical model should account for both, each being a limiting case essentially in terms of the length of the active volume of atoms. Indeed, the first reported experimental study of swept-gain superradiance⁸ also constituted a study of the evolution from superradiant response of the system through swept-gain superradiance as a function of the length of the active volume along the propagation axis.¹⁰ The experimental results indicate a continuous transition from conditions supportive of superradiance or superfluorescence through swept-gain superradiance in the asymptotic regime of large propagation length z .

In this paper we analyze numerically, and interpret analytically, the evolution of the response of a collection of two-level absorbers to swept impulse excitation, from the small volume, superradiant regime, through the asymptotic, steady-state propagation at sufficiently large propagation distances z . We also determine the effects of transverse mode coupling on the pulse generation^{11,12} and propagation.¹³

*Work partially supported by ARO, ONR, Battelle, University of Montreal, and Research Corporation.

The model is presented in the next section and the analytical results for swept-gain superradiance in the planar regime obtained previously by BHMS¹ are briefly reviewed. A comparison is made between conditions for the observation of single pulse superfluorescence¹⁴ and swept-gain superradiance.¹ Results of the numerical calculations are presented and discussed in Section III for the evolution of pulse area with propagation distance z for the single spacial dimension. The evolution from superradiance to steady-state swept-gain superradiance and their connection is explicitly analyzed and discussed. Results for a comparable case incorporating transverse mode coupling with a Gaussian gain profile are presented and compared with results for the planar, one spacial dimension calculation. It is shown that the effects of self-focusing can be much more important in the swept-gain, steady-state condition than for the particular corresponding conditions for superradiance. The results of our calculation are summarized in the last section and future work connected with these results is outlined.

II. Coupled Maxwell-Bloch model for swept-gain superradiance

BHMS showed¹ that if a volume of two-level absorbers is gain-swept at the speed of light in the active medium by a traveling impulse excitation, a solitary pulse is generated from noise amplification in the amplifying medium and reaches a steady-state at sufficiently large propagation distance z , provided the gain, g , to loss, κ , ratio satisfies the condition $g/\kappa > 1$. The solitary pulse is characterized by super-radiant-like features with respect to pulse shape, intensity, temporal width, and delay of the peak of the pulse envelope from the impulse excitation.

They considered the coupled Maxwell-Bloch equations in the retarded time frame, which is a frequently used model for pulse propagation and generation in nonlinear media,

$$\frac{\partial P}{\partial \tau} = \epsilon \Delta - \frac{P}{T_2} \quad (2-1)$$

$$\frac{\partial \Delta}{\partial \tau} = -\epsilon P - \frac{\Delta}{T_1} \quad (2-2)$$

$$\frac{\partial \epsilon}{\partial z} = \alpha P - \kappa \epsilon. \quad (2-3)$$

In the above equations, P is the dimensionless macroscopic transverse polarization per atom, Δ is the inversion for the two-level atom, T_2 and T_1 , are the dephasing and relaxation times for the polarization and atomic inversion, respectively. The third equation, (2-3), is the linearized Maxwell equation¹⁵ in the retarded time frame in the slowly varying envelope (SVEA) and rotating wave approximation for the pulse envelope E . Here, the electromagnetic field envelope, E , is normalized to give the Rabi frequency¹⁵ ϵ ,

$$\epsilon = \frac{\mu_0 E}{\hbar} \quad (2-4)$$

where μ_0 is the matrix element of the transition dipole moment between the pair of atomic energy levels and E is the electromagnetic field envelope which is a function of the propagation coordinate z and retarded time τ ,

$$\tau = t - z/c. \quad (2-5)$$

The other quantities involved in Eqs. (2-1) - (2-3) are

$$\alpha = \frac{g}{T_2} = \frac{3}{4\pi} \frac{\lambda^2 \rho}{\tau_0} \quad (2-6)$$

where g is the gain and λ is the wavelength of the carrier frequency of the single mode radiation field envelope, ρ is the atomic density and τ_0 is the spontaneous atomic relaxation time. The loss term in (2-3) defined by κ is the linear loss which arises because of diffraction as well as other dissipative processes.

BHMS considered the steady-state solutions of (2-1) - (2-3), i.e., the solutions under the condition

$$\epsilon(z \rightarrow \infty, \tau) = \lim_{z \rightarrow \infty} \left\{ \epsilon(0, \tau) e^{-\kappa z} + \alpha \int_0^z dz' e^{-\kappa(z-z')} P(z', \tau) \right\} \quad (2-7)$$

and the initial condition

$$\Delta(\tau = 0) = 1. \quad (2-8)$$

Equation (2-7) leads immediately to the adiabatic relation between the field and polarization,

$$\epsilon(z \rightarrow \infty, \tau) = \frac{\alpha}{\kappa} P(z \rightarrow \infty, \tau). \quad (2-9)$$

This last expression can be used to eliminate P from (2-1) and (2-2) and steady-state solutions are found by solving the resulting pair of nonlinear differential equations.

Exact analytical results were obtained by BHMS for two distinct cases, $T_2 < T_1$ and $T_2 = T_1$. For $T_2 < T_1$:

$$\epsilon(\tau) = \frac{1}{\tau_s} \operatorname{sech} \frac{\tau}{\tau_s} \quad (2-10)$$

where

$$\tau_s = T_2 \left[(g - \kappa) / \kappa \right]^{-1} \quad (2-11)$$

For $g \gg \kappa$, we see from (2-10), (2-11), and (2-6) that the intensity I of the steady-state pulse, $I \sim E^2$, varies as the density squared, $I \sim \rho^2$, whereas (2-10) and (2-11) indicate that the width τ_s varies inversely as the density $\tau_s \sim 1/\rho$. Also, from (2-11) the pulse width is always less than T_2 whenever $g > \kappa$. For $T_2 = T_1$:

The set of equations (2-1) - (2-3) reduces to the generalized sine-Gordon equation¹

$$\frac{\partial^2 \phi(\xi, z)}{\partial \xi \partial z} + \kappa \frac{\partial \phi(\xi, z)}{\partial \xi} = \alpha \sin \phi(\xi, z) \quad (2-12)$$

where

$$\xi = \frac{1}{\gamma} (1 - e^{-\gamma \tau}) \quad (2-13)$$

is the reduced time and

$$\gamma = \frac{1}{T_2} = \frac{1}{T_1}.$$

The angle ϕ is the Bloch angle,

$$\epsilon = \frac{\partial \phi}{\partial \tau} \quad (2-14)$$

In the asymptotic regime, the space derivative term in (2-12) vanishes and the resulting solution, using (2-14), is

$$\epsilon(\tau) = \frac{1}{\tau_s} e^{-\gamma \tau} \operatorname{sech} \left\{ \frac{1}{\tau_s} \left[\xi(\tau) - \xi_0 \right] \right\} \quad (2-15)$$

where

$$\tau_s = \frac{\kappa T_2}{g} \quad (2-16)$$

and the time delay between the impulse excitation and the peak of the steady-state pulse ξ_0 , is given by

$$\xi_0 = \tau_s \log \left[\cot \frac{1}{2} \phi_0 \right]. \quad (2-17)$$

Here, ϕ_0 is the initial Bloch-angle at $\tau = 0$ to account for quantum noise which drives the atomic excitation away from the completely inverted metastable state.

Again, from (2-15) it is seen that the intensity $I \sim \rho^2$ whereas the pulse width $\tau_w \sim 1/\rho$. It was shown¹ by BHMS that such pulses will evolve provided $g/\kappa > 1$. The area of the pulse θ is defined as the Bloch angle ϕ at infinite time τ , and is obtained by integrating (2-14). From (2-12) in the asymptotic regime, i.e., neglecting the first term on the left,

$$\tan \frac{1}{2} \theta = (\tan \frac{1}{2} \phi_0) e^{g/\kappa}. \quad (2-18)$$

Thus, given an initial Bloch angle ϕ_0 , for g/κ sufficiently large, the area θ approaches π , i.e., as large as it can be for a single pulse. The threshold for $\theta \rightarrow \pi$ was determined to be

$$\left[g/\kappa \right]_{\text{threshold}} = \log \left(\frac{1}{\tan \frac{1}{2} \phi_0} \right). \quad (2-19)$$

Any further increase in the gain-to-loss, g/κ , does not increase the pulse area since it is saturated above threshold. However, from (2-15) the intensity continues to vary as the square of the density and the pulse width as inverse density.

The criteria, therefore, for the generation of steady-state pulses is that the active medium be swept-excited at the speed of light in the medium and that $g/\kappa > 1$. The resulting pulses have characteristics of superfluorescence¹⁴, although for different physical reasons. The major difference in realizing the two phenomena is that to produce superfluorescence the medium responds as though it were uniformly excited, i.e., the atoms are contained within a certain cooperation volume, whereas for swept-gain superradiance, the medium "sees" an impulse excitation traveling at the velocity of light in the medium. Table 1 compares the conditions for single pulse superfluorescence in the mean field limit¹⁴, with the corresponding conditions for pulse generation in swept-gain superradiance in the asymptotic regime. It is to be pointed out that the essential physical difference between what has been called superfluorescence¹⁴ and what is termed swept-gain superradiance¹ is that the atomic relaxation for the former occurs by collective, spontaneous relaxation⁴, whereas for the latter, individual atomic relaxation occurs by stimulated relaxation due to pulse propagation in the medium.

Table 1. Comparison of Conditions for Superfluorescence in Mean Field Approximation with Swept-Gain Superradiance in Asymptotic Approximation

<u>Superfluorescence</u> <u>Mean-Field Approximation</u>	<u>Swept-Gain Superradiance</u> <u>Asymptotic Approximation</u>
$\frac{\partial \epsilon(t)}{\partial t} = \alpha p(t) - \kappa' \epsilon(t)$	$\frac{\partial \epsilon(z, \tau)}{\partial z} = \alpha p(z, \tau) - \kappa \epsilon(z, \tau)$
$\kappa' \epsilon > \frac{\partial \epsilon}{\partial t}$	$\kappa \epsilon > \frac{\partial \epsilon}{\partial z}$
$p = \frac{\kappa'}{\alpha} \epsilon$	$p = \frac{\kappa}{\alpha} \epsilon$
$\tau_E < \tau_C < \tau_R < \tau_D < T_1, T_2, T_2^*$	$g/\kappa > 1$
$\tau_E = L/C$	$\tau_E' = (c\kappa)^{-1}$
$\tau_R = \frac{8\pi\tau_0}{3\alpha\lambda^2 L}$	$\tau_s = \frac{\kappa T_2}{g}$
$\tau_D = \tau_R \log \left(\frac{1}{\theta_0^2} \right)$	$\epsilon_0 = \tau_s \log \left[\cot \frac{1}{2} \phi_0 \right]$
$\tau_C = (\tau_E \tau_R)^{1/2}$	$\tau_C = (\tau_E' \tau_s)^{1/2}$

Here, τ_R is the characteristic superradiance time¹⁴ for $z = L$, τ_D is the delay time¹⁴ of the pulse peak from the excitation, and τ_C is the cooperation time¹⁶ corresponding to the cooperation length l_c , $\tau_C = cl_c$. Note that for $L = l_c$, $\tau_R = \tau_C$. τ_D is the delay time of the peak of the superradiant pulse from the impulse excitation.

We have calculated the evolution of pulse area for swept-gain superradiance as a function of propagation distance z according to the relations (2-1) - (2-3) for the conditions $T_1 = T_2$, $g/\kappa > \log(1/\phi_0)$ and for $\tau_R \ll T_2$ where τ_R is the characteristic superfluorescence time. Thus, we have determined the evolution of pulse area from the superfluorescence regime (small z) through the asymptotic swept-gain regime (large z). These results we compare with corresponding calculations taking into account transverse mode coupling and diffraction for a Gaussian gain profile. In this case, the Maxwell equation (2-3) takes the three-dimensional form

$$-i\tau_2 g^{-1} \nabla_{\perp}^2 \epsilon + \frac{\partial \epsilon}{\partial \eta} = d p \quad (2-20)$$

where d = radial function describing nonuniformity of gain profile, $\eta = z/\alpha$, and

$$\mathcal{F} = \frac{4\pi r_p^2}{\lambda g^{-1}} \quad (2-21)$$

is the Beer's length dependent Fresnel number relevant to propagation effects. Here r_p is the Gaussian gain width at half maximum. The transverse effects arising from (2-20) are related to the planar case using (2-3) by taking the linear field loss κ in the latter to be entirely diffraction-loss, i.e.

$$\kappa = \frac{\lambda}{A} \quad (2-22)$$

where $A = \pi r_p^2$. Thus, the Fresnel number \mathcal{F} , (2-21), is

$$\mathcal{F} = \frac{g}{\kappa} \quad (2-23)$$

the gain-to-loss ratio. The results of the calculation and related discussions are presented in the next section.

III. Numerical results for propagation and transverse effects: Evolution from superfluorescence to swept-gain superradiance

First we present the results of numerical integration of (2-1) - (2-3) for the initial condition (2-8) and for $T_1 = T_2$. We have also chosen the values for the system parameters such that the superradiance cooperation time, τ_c , satisfies the condition $\tau_c < T_2$ (see Table 1), where $\ell_c = c\tau_c$ is the maximum length of the sample over which the atoms can cooperate to produce superradiant emission. Also, the gain, g , to loss, κ , ratio, $g/\kappa > \log(1/\phi_0)$, (see (2-19)), so that results of the last section predict steady-state pulses of area $\theta = \pi$, Eq. (2-18).

The absolute pulse area $|\theta|$,

$$|\theta| = \int_0^\infty |\epsilon| d\tau \quad (3-1)$$

is shown as a function of propagation length z in Figure 1. There are three distinct regimes evident in the pulse area, $|\theta|$, propagation evolution. These are determined by the characteristic times for the system T_1 (Table 1), and τ_s , (2-16).

The first regime, characterized by the smallest values of the propagation distance z , shows a rapid rise of the pulse area, (3-1), with propagation distance z . The area proceeds in z through $|\theta| = \pi$, corresponding to single pulse buildup, to values $|\theta| > \pi$, which eventually corresponds to subsequent ringing, and finally peaks out at $|\theta| = 3\pi$. This behavior is described by the sine-Gordon equation (2-12), with the values of the parameters used in the calculation (see Figure 1). We have, for this particular small z regime,

$$\kappa \frac{\partial \phi}{\partial \tau} < \alpha \sin \phi, \quad (3-2)$$

so (2-12) becomes

$$\frac{\partial^2 \phi}{\partial \tau \partial z} = \alpha \sin \phi, \quad (3-3)$$

where, from (2-13), $\xi = \tau$ since in this case $\tau/T_2 < 1$. This is just the Burnham-Chiao propagation equation¹⁷, which yields the well-known solution for pulse buildup from gain with subsequent undamped ringing.

From (2-6) and Table 1, we have

$$\alpha = \frac{1}{2c\tau_c^2} \quad (3-4)$$

where τ_c is the Arecchi-Courtens superradiant cooperation time¹⁶ which corresponds to the superradiant cooperation length $z = \ell_c$, $\ell_c = c\tau_c$, the maximum length over which the atoms can cooperate collectively to produce superradiant emission. Equation (3-3) yields

$$\frac{d\theta}{dz} = \frac{1}{2\ell_c} \int_0^{z/\ell_c} dv \sin \phi. \quad (3-5)$$

Here,

$v = \tau/\tau_c = z/\ell_c$ and θ , as in (3-1), is related to the Bloch angle ϕ , by $\theta = \phi(\tau = z/c)$. Thus, the initial pulse buildup in Figure 1 is governed by the superradiance time τ_R (Table 1) where $\tau_R \sim z^{-1}$ and $\tau_R = \tau_c$ when $z = \ell_c$, and in this particular case, $\ell_c = 2.68$ cm. The region corresponding to $0 < |\theta| < \pi$ we call the single pulse superradiant regime, $z < \ell_c$, which is subsequently followed by Burnham-Chiao ringing. This initial superradiant pulse buildup occurs in this case because $\tau_c < T_2$.

After several diffraction lengths κ^{-1} , the area (3-1) reaches a maximum and then decays as $e^{-\kappa z}$ to the asymptotic steady-state $\theta = \pi$ pulse predicted analytically in the last section, and shown in Figure 1. This regime is governed by the characteristic time τ_s , (2-16).

The results shown in Figure 1 exhibit the pulse area evolution from pure superradiance, $|\theta| < \pi$, through Burnham-Chiao ringing, each governed by τ_R , to pulse area instability which subsequently decays by linear field loss κ to the asymptotic steady-state π pulse. The necessary and sufficient conditions for evolution from superradiance to π -pulse swept-gain superradiance are that $g/\kappa > \log 1/\phi_0 > 1$, $\tau_c < T_2$.

The effects of changes in the value of the linear field loss κ , all other parameters remaining the same, are shown in Figure 2 for four other values of κ and, hence g/κ . It is seen that asymptotic stability in the pulse area is reached for lower z values the higher the value for the loss κ , as one would expect. Also, the higher loss and lower gain-to-loss reduce the amplitude of the pulse area instability peak, again as one would expect. This further suggests that the transition from superradiance to asymptotic swept-gain superradiance can occur without intermediate ringing if $(\kappa c)^{-1} < \tau_c$.

When transverse effects are taken into account in the calculation, Eq. (2-3) is replaced by (2-20). The transverse mode coupling is generated through the first term in (2-20), and its contribution is governed by the Fresnel number \mathcal{F} , (2-21) and (2-23). This is not the conventional Fresnel number used in discussions of superradiance and superfluorescence¹⁸, but it is the one which is meaningful¹³ throughout the entire propagation regime. Generally, the larger the Fresnel number \mathcal{F} , (2-21), the less the importance of contributions from transverse effects, (2-20), i.e., large \mathcal{F} means more nearly plane wave propagation behavior.

We use the values of the parameters and the conditions which gave rise to the one-dimensional results of Figure 1, but choose the cross-sectional area A for a Gaussian initial gain profile from (2-22) and the value of κ used to obtain the results of Figure 1, where r_p is the radial Gaussian width for the gain distribution, and obtain the calculational results shown in Figure 3. Here, we show the pulse area (3-1) as a function of propagation distance z and radial dimension ρ . Energy which intersects the boundary $\rho = \rho_{\max}$ is absorbed in the calculation; thus diffraction as well as transverse mode coupling is explicitly treated in the calculation consistent with the conditions imposed by (2-20), (2-21) - (2-23). Thus, the calculation giving the results shown in Figure 3 is the three-dimensional extension of the calculation which gave the results shown in Figure 1. The pulse area (3-1) as a function of z for the on-axis mode is displayed in Figure 4.

It is noted by comparing Figures 1, 3, and 4 that the transverse effects almost completely wash-out the instability in the pulse area buildup which occurs in the one-dimensional calculation, Figure 1. Furthermore, Figures 3 and 4 indicate a different kind of pulse area instability at higher z values which is due to self-focusing. The qualitative effects of self-focusing on pulse propagation can be seen in Figure 5. The results of the three-dimensional calculation indicate, therefore, that a true steady-state may not exist, at least in the sense of the analytical predictions of Section II.

Similar one-spacial dimension calculations for pulse area evolution in swept-gain superradiance, but under the influence of lethargic gain conditions, have been reported by BHMS¹⁹.

IV. Summary and conclusions

We have demonstrated the pulse evolution in one-dimensional propagation from superfluorescence to asymptotic swept-gain superradiance for ideal conditions supportive of superfluorescence^{14,18} and π -pulse swept-gain superradiance.¹ The results are shown in Figures 1 and 2. Transverse effects tend to wash-out the early pulse area instability which occurs for the one-dimensional case as seen by comparing Figures 1 and 2 with Figures 3 and 4. However, as noted in Figures 3 and 4, the pulse area shows an instability in the asymptotic region of large z when transverse effects are taken into account. This evidently arises from self-focusing, Figure 5. Thus, in this case, a true steady-state does not exist due to transverse mode coupling effects.

This work is in process of being extended^{20,21} to the calculation of the effects of coherent optical pumping and propagation as well as transverse effects for three-level systems^{5,7} for three-level superfluorescence and swept-gain superradiance and coherent pulse shaping due to specified pulse injection and propagation in three-level systems.

References

1. Bonifacio, R., Hopf, F. A., Meystre, P., and Scully, M. O., *Phys. Rev. A* **12**, 2563. 1975.
2. Hopf, F. A. and Meystre, P., *Phys. Rev. A* **12**, 2534. 1975.
3. Hopf, F. A., Meystre, P., and McLaughlin, D. W., *Phys. Rev. A* **13**, 777. 1976.

4. Ehrlich, J. J., Bowden, C. M., Howgate, D. W., Lehnigk, S. H., Rosenberger, A. T., and DeTemple, T. A., "Swept-gain Superradiance in CO₂-pumped CH₃F", in Coherence and Quantum Optics IV, edited by L. Mandel and E. Wolf (Plenum, New York), p. 923. 1978.
5. Rosenberger, A. T., DeTemple, T. A., Bowden, C. M., and Sung, C. C., J. Opt. Soc. Am. 68, 700. 1978.
6. Bowden, C. M. and Sung, C. C., Phys. Rev. A 18, 1558. 1978.
7. Bowden, C. M. and Sung, C. C., Phys. Rev. A 20, 2033. 1979.
8. Dicke, R. H., Phys. Rev. 93, 99. 1954.
9. Cooperative Effects in Matter and Radiation, edited by C. M. Bowden, D. W. Howgate and H. R. Robl, (Plenum, New York). 1977.
10. Vrehen, Q. H. F. and Gibbs, H. M., "Superfluorescence Experiments", in Topics in Current Physics, edited by R. Bonifacio (Springer-Verlag, New York), in press. 1981.
11. Mattar, F. P., "Effects of Propagation, Transverse Mode Coupling and Diffraction on Nonlinear Light Pulse Evolution", in Optical Bistability, edited by C. M. Bowden, M. Cifan and H. R. Robl (Plenum Press, New York), p. 503. 1981.
12. Mattar, F. P., Gibbs, H. M., McCall, S. L. and Feld, H. S., Phys. Rev. Lett. 46, 1123. 1981. Also, "Transverse Fluctuations in Superfluorescence", European Conference on Atomic Physics, Heidelberg, Germany, April 1981, Paper W10.
13. Mattar, F. P. and Newstein, M. C., "Beam-Profile Effects in Self-induced Transparency: On-resonance Self-focusing of Coherent Optical Pulses in Absorbing Media", in Cooperative Effects in Matter and Radiation, edited by C. M. Bowden, D. W. Howgate and H. R. Robl (Plenum Press, New York), p. 139. 1977.
14. Bonifacio, R. and Lugiato, L. A., Phys. Rev. A 11, 1507. 1975. A12, 587. 1975.
15. Optical Resonance and Two-level Atoms, L. Allen and J. H. Eberly (John Wiley, New York). 1975.
16. Arecchi, F. T. and Courtens, E., Phys. Rev. A 2, 1730. 1970.
17. Burnham, D. C. and Chiao, R. Y., Phys. Rev. 188, 667. 1969.
18. Vrehen, Q. H. F., reference 9, page 79.
19. Bonifacio, R., Hopf, F. A., Meystre, P. and Scully, M. O., "Theory of a Short Wavelength Swept-gain Amplifier", in Laser Induced Fusion and X-Ray Laser Studies, Physics of Quantum Electronics, VOL III, edited by S. F. Jacobs, M. O. Scully, M. Sargent III, and C. D. Cantrell, III. (Addison-Wesley, London, 1976). p. 487.
20. Mattar, F. P. and Bowden, C. M., "Swept-gain Superradiance in Two- and Three-level Systems With Transverse Effects and Diffraction", International Conference on Excited States and Multiresonant Nonlinear Optical Processes in Solids, Aussois, France, March 18-20, 1981.
21. Mattar, F. P. and Bowden, C. M., to be submitted for publication.

Figures

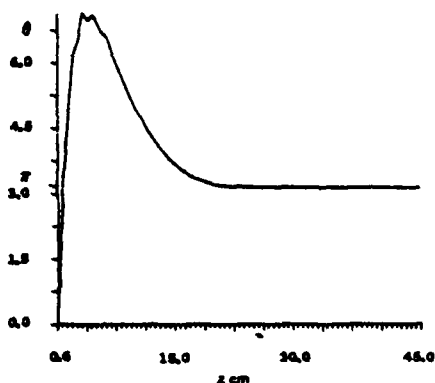


Figure 1. Pulse area $\theta = \int_0^\infty |E| dt$ vs. propagation distance z for numerical integration of Eqs. (2-1) - (2-3). Values of the parameters used in the calculation are: $g = 291.6 \text{ cm}^{-1}$, $\kappa = 2.60 \text{ cm}^{-1}$, $g/\kappa = 112.15$, $T_1 = T_2 = 70 \text{ nsec}$, $\phi_0 = 9.42 \times 10^{-4}$, $\tau_c = 89.4 \text{ psec}$.

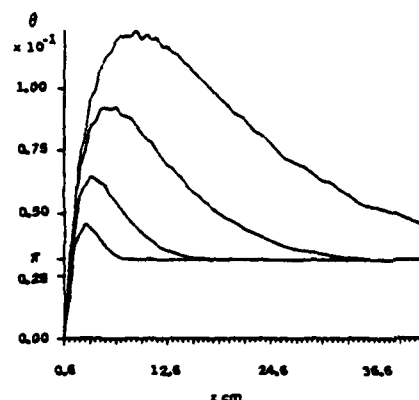


Figure 2. Pulse area $\theta = \int_0^\infty |E| dt$ vs. propagation distance z for numerical integration of Eqs. (2-1) - (2-3). Values of the parameters used are those of Figure 1 except for κ : 1) $\kappa = 5.2 \text{ cm}^{-1}$, $g/\kappa = 56.08$; 2) $\kappa = 10.4 \text{ cm}^{-1}$, $g/\kappa = 28.04$; 3) $\kappa = 20.8$, $g/\kappa = 14.02$; 4) $\kappa = 41.6 \text{ cm}^{-1}$, $g/\kappa = 7.01$.

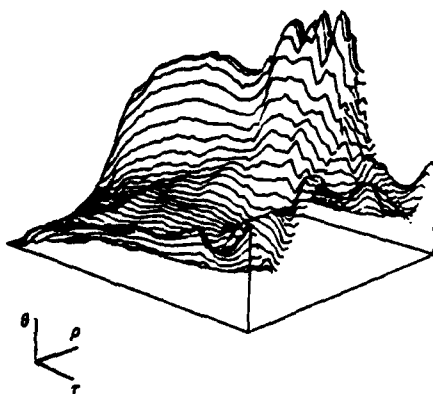


Figure 3. Pulse area θ vs. propagation distance z and radial dimension ρ for numerical integration of Eqs. (2-1), (2-2), and (2-20). Values of the parameters used are those of Figure 1, with the Fresnel number \mathcal{F} chosen according to (2-23) and a Gaussian initial gain profile determined from (2-21), (2-22).

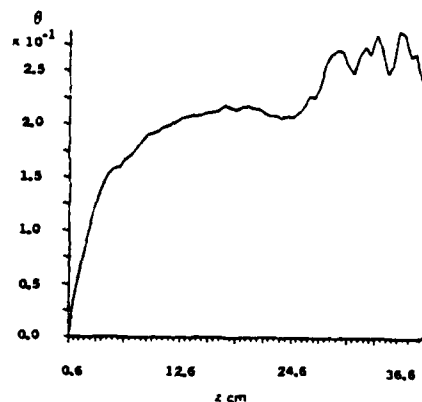


Figure 4. Pulse area θ vs. propagation distance z for the on-axis mode. Values of the parameters are those of Figure 3.

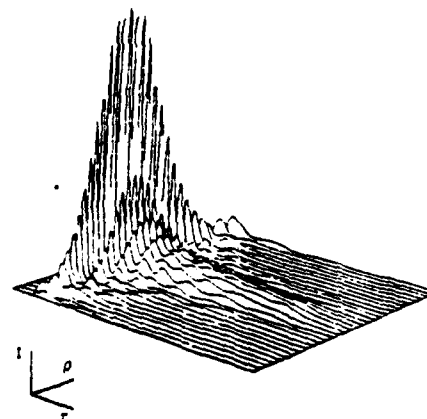


Figure 5. Temporal and radial dependence of pulse intensity at large z .

Reprinted from:
OPTICAL BISTABILITY (1981)
Edited by Charles M. Bowden, Mikael Ciftan
and Hermann R. Robl
Book available from: Plenum Publishing Corporation
233 Spring Street, New York, N.Y. 10013

EFFECTS OF PROPAGATION, TRANSVERSE MODE COUPLING AND DIFFRACTION ON
NONLINEAR LIGHT PULSE EVOLUTION

F.P. Mattar†

Aerodynamics Laboratory, Polytechnic Institute of
New York, Farmingdale, New York 11735

Abstract: The effective computational methods developed to efficiently tackle transverse and longitudinal reshaping associated with single-stream and two-way propagation effects in cooperative light-matter interactions, using the semi-classical model are described. The mathematical methods are justified on physical grounds. Typical illustrative results of propagation in resonant absorbers, amplifiers and superfluorescence systems are presented.

I. INTRODUCTION

This paper reviews the unified mathematical methods developed for three-dimensional simulation of several physical phenomena previously studied independently. The same basic algorithm with some alterations will simulate both superfluorescence^{1,2} and optical bistability^{3,4}. With extra modifications, it can also analyze four-wave mixing⁵ and phase conjugation⁶ systems. Further applications include two-way Self-Induced Transparency⁷ and Soliton Collision⁸ studies.

The proposed model evolved as a result of close collaboration with the experimentalists, H.M. Gibbs⁹⁻¹³, S.L. McCall¹¹⁻¹³ and recently, M.S. Feld¹³, enhancing the rate of progress in the re-

Work jointly sponsored by the Research Corporation, the International Division of Mobil Corporation, the University of Montreal, the U.S. Army Research Office, DAAG29-79-C-0148 and the Office of Naval Research, N000-14-80-C-0174.

search and leading to a better understanding of basic cooperative effects in light-matter interactions. Quantitative analyses in superfluorescence were obtained and are being developed in optical bistability.

The model encompasses propagation that includes rigorous diffraction^{16,15}, time-dependent phase variation, off-resonance¹⁶ as well as nonuniform excitation¹⁹ and transverse and longitudinal boundary conditions¹⁸. (An additional control probe-beam is being developed²¹.)

The adoption of proven computational techniques, developed by Moretti²²⁻²⁴ in aerodynamics, to solve problems in the laser field, is justified by the analogy between fluid and wave propagation problems described. The laser beam evolution can be interpreted in terms of an equivalent flowing fluid²⁵ whose density is proportional to the laser field intensity, and whose velocity is proportional to the gradient of the field phase. This description allows for the treatment of more slowly varying dependent variables and yields to governing equations of motion, which are a generalization of the Navier-Stokes equations²⁶. In the fluid formulation, the equivalent fluid is compressible and is subjected to an internal potential, depending solely and nonlinearly upon the fluid density and its derivatives; this is called the "quantum mechanical potential." Furthermore, the field scalar wave equation mathematically corresponds to a complex heat diffusion equation with a non-uniform functional source; while the Bloch equations, in a rotating frame, are structurally similar to the torque equation²⁷. For two-way problems, the simultaneous set of quasi-optic field equations (one for each traveling wave) play the same preponderant role as Euler equations in shock calculations for fluid dynamics problems.

Quite different effects, i.e., self-lensing²⁸, self-phase modulation²⁹, self-spectral broadening³⁰ and self-steepening³¹, previously studied separately, combine here to modify the pulse behavior diversely at different positions and times. For example, the interplay of diffraction coupling through the Laplacian term and the inertial response of the non-uniform pre-excited medium will inevitably redistribute the beam energy spatially and temporally³². This transient one- or multi-beam transverse reshaping will profoundly affect the performance of any device that relies upon it. Specifically, this pragmatic, three-dimensional analysis helps in the interpretation of recent experimental results in superradiance, superfluorescence, optical bistability and active-mirror amplifiers for laser-fusion. It also accounts for deviations and departures between recent experimental observations and predictions of planar wave theory (see Fig. (1)).

To circumvent excessive memory requirements while insuring adequate numerical resolution, one must resort to nonuniform

meshes. In this large computational problem, the calculational efficiency of the algorithm chosen is of crucial importance. A brute force, finite difference treatment of the governing equations is not feasible. Instead, by using the details of the physical processes to determine where to concentrate the computational effort, accuracy and economy are achieved. For example, if for self-focused beams, a fixed transverse mesh is used, a lack of resolution (see Fig. (2)) may result. A non-negligible loss of computational effort in the wings of the beam will also occur.

Coherent Pulse Propagation

I. Usual Theory

$$1 \text{ Dim. } \xi = \xi(\rho)$$

'Uniform Plane Wave'



II. Usual Experiment

$$\xi = \xi(\rho) e^{-\rho^2}$$

'Gaussian'



Fig. 1. The state of the art in coherent pulse propagation is displayed. The theoretical effort was restricted to a uniform plane wave prior to the work of Newstein et al; whereas the usual experiment was carried out using a Gaussian beam. To simulate a uniform plane wave, the smallest possible detector diameter was selected as compared to the Gaussian beam diameter (i.e., (i.e., $d_{\text{detector}} \ll d_{\text{beam}}$)).

In particular, evenly-spaced computational grid points are related to variable grids in a physical space by adaptive stretching (Fig. (3)) and rezoning (Fig. (4)) techniques. This mapping consists either of an a priori coordinate transformation or an adaptive transformation (Fig. (5)) based on the actual physical solution. Both stretching transformation in time and rezoning techniques in space are used to alleviate the computational effort. The propagation problem is thus reformulated in terms of appropriate coordinates that will automatically accommodate any change in the beam profile³⁴⁻⁴⁰.

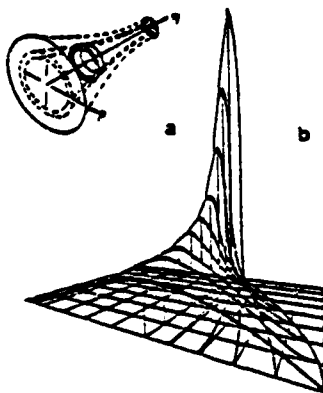


Fig. 2 (a) Isometric representation of the beam cross-section as it experiences self-focusing: The cross-section decreases as a function of the propagation distance; (b) An isometric display of the time integrated field energy as a function of ρ and η to illustrate the resolution limitation associated with uniform mesh.

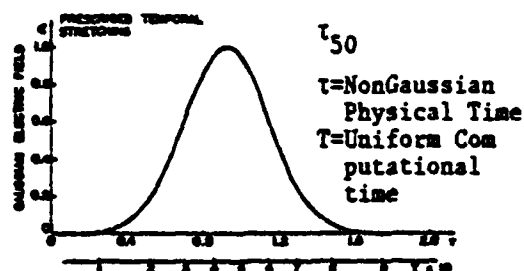


Fig. 3. Non-uniform prescribed temporal stretching.

The resultant dynamic grid removes the main disadvantage of insufficient resolution, where uniform Eulerian codes generally suffer. Furthermore, the advantages of grid sensitivity can be obtained by either using adequate rezoning and mapping in Eulerian coordinates or by simply using traditional Lagrangian methods^{41,42}. Thus, the convenience of moderate memory requirements can be combined with the desirable numerical resolution should one rezone the grids. The techniques due to Moretti³³ will economically generate precise results. Although this appears surprising because of the mesh coarseness, his technique succeeds because it discriminates intelligently between the different domains of the critical physical parameters.

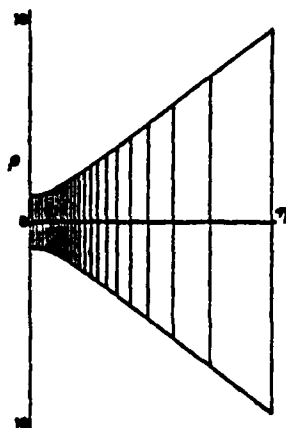


Figure 4. Two-dimensional prescribed rezoning for ρ and η . As the beam narrows the density of transverse points and the transmission planes increase simultaneously.

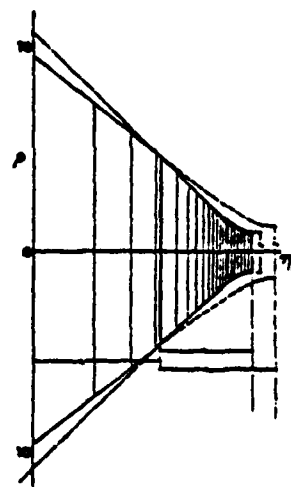


Fig. 5. Self-adjusted two-dimensional rezoning for ρ and η to follow more closely the actual beam characteristics. The (normalizing) Gaussian reference beam is redefined during the calculation.

For the two-beam analysis, our approach relies on one-way nonsymmetric discretizations of the longitudinal and transverse derivatives as well as nonuniform grids. Numerical instrumentation is unavoidable. The role of characteristics as information carriers is emphasized and therefore the law of forbidden signals cannot be violated⁴³. The physical subtleties of the nonlinear problem can be adequately implemented.

Interactive graphic software was developed to simplify the physics of extraction from these complex codes. Structural modular programming techniques are used, making the program easier to read, maintain and transport as well as for further extensions and generalizations of the planar wave theory. The resultant code is deceptively simple and easy to follow. This mathematical modeling, motivated by Gibbs' and McCall's experimental work, is engineering physics in its purest sense: its main goal is to obtain a numerical solution to and insight into a real physical problem, instead of reaching a neat analytical solution to an idealized problem of limited applications.

II. SIT/SUPERFLUORESCENCE EQUATIONS OF MOTION

In the slowly varying envelope approximation, the SIT dimensionless, semi-classical field-matter equations¹⁵ (which describe a system in a cylindrical geometry with azimuthal symmetry), are:

$$-iF \nabla_T^2 e + \frac{\partial e}{\partial \eta} = \rho \quad (1)$$

$$\partial \rho / \partial \tau = eW - (i\Delta\Omega + 1/\tau_2)\rho \quad (2)$$

and

$$\partial W / \partial \tau = -1/2(e^* \rho + e \rho^*) - (W - W^e)/\tau_1 \quad (3)$$

where

$$e = (2\mu/\hbar)\tau_p e', \text{ and } \rho = (2/\mu)\rho', \quad (4)$$

$$E = \text{Re}[e' \exp\{i(\kappa/c)z - \omega t\}]; \quad (5)$$

with W^e the equilibrium value of W , subjected to the initial and boundary conditions.

1. for $\tau \geq 0$: $e = 0$, $W = W_i$, $\rho = \rho_i$ known function to take into account the pumping effects or the initial tipping angle.

2. for $\eta = 0$: e is given as a known function of τ and ρ ;
3. for all η and τ : $[\partial e / \partial \rho]_{\rho=0}$ and $[\partial e / \partial \rho]_{\rho=\rho_{\max}}$ vanishes
(with ρ_{\max} defining the extent of the region over which the numerical solution is to be determined).

$$\text{with } k/c = w \quad (5)$$

$$\text{and } \nabla_T^2 e = \left[\frac{1}{\rho} \frac{\partial}{\partial \rho} \left(\rho \frac{\partial e}{\partial \rho} \right) \right]; \quad (7)$$

after applying l'Hopital's rule, the on-axis Laplacian reads:

$$\nabla_T^2 = 2 \frac{\partial^2 e}{\partial \rho^2} \quad (8)$$

$$P = i \operatorname{Re}[\rho' \exp\{i(\kappa/c)z - kt\}]. \quad (9)$$

The complex field amplitude e , the complex polarization density ρ , and the energy stored per atom W , are normalized functions of the transverse coordinate $\rho = r/r_p$, the longitudinal coordinate $\eta = z \times \alpha_{\text{eff}}$, and the retarded time $\tau = (t - zn/c)\tau_p$ (see Fig. (6)). The time scale is normalized to the full width half maximum (FWHM) input pulse length, τ_p and the transverse dimension scales to the input beam spatial width r_p . The longitudinal distance is normalized to the effective absorption length,⁴⁴ $(\alpha_{\text{eff}})^{-1}$ where

$$\alpha_{\text{eff}} = \left[\frac{\omega \mu^2 N}{n \hbar c} \right] \tau_p + [\alpha' \tau_p] \quad (10)$$

Here, ω is the angular carrier frequency of the optical pulse, μ is the dipole moment of the resonant transition, N is the number density of resonant molecules, and n is the index of refraction of the background material. The dimensionless quantities $\Delta\omega = (\omega - \omega_0)\tau_p$, $\tau_1 = T_1/\tau_p$, and $\tau_2 = T_2/\tau_p$ measure the offset of the optical carrier frequency ω from the central frequency of the molecular resonance ω_0 , the thermal relaxation time T_1 , and the polarization dephasing time T_2 , respectively.

Even in their dimensionless forms, the various quantities have a direct physical significance. Thus ρ is a measure of the component of the transverse oscillating dipole moment (ρ has the proper phase for energy exchange with the radiation field). In a two-level system, in the absence of relaxation phenomena, a resonant field cause each atom to oscillate between the two states,

$W=-1$ and $W=+1$, at a Rabi frequency $f_R = e/2\tau_p = (\mu/\hbar)e'$. Thus e measures how far this state-exchanging process proceeds in rp .

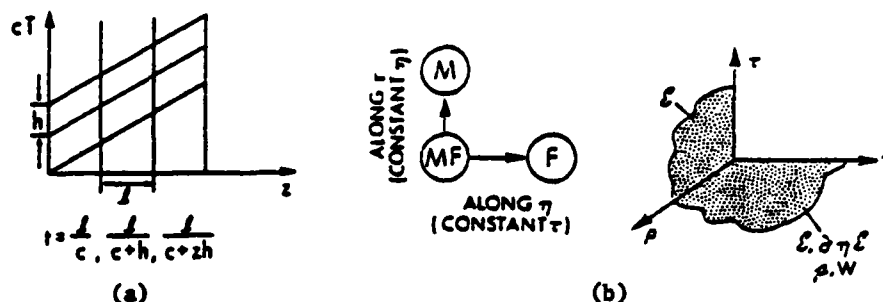


Fig. 6. Graph (a) displays the retarded time concept. Graph (b) outlines the numerical approach: a marching problem along η for the field simultaneously with a temporal upgrading of the material variables along τ .

The dimensionless parameter, F , is given by $F = \lambda(\alpha_{\text{eff}})^{-1} / (4\pi r_p^2)$. The reciprocal of F is the Fresnel number associated with an aperture radius r_p and a propagation distance $(\alpha_{\text{eff}})^{-1}$. The magnitude of F determines whether or not one can divide the transverse dependence of the field into "pencils" (one per radius ρ), to be treated in the plane-wave approximation.

As outlined by Haus et al.⁴⁵, the acceptance of equations (1-3) implies certain approximations: eq. (3) shows that the product ' $e\rho$ ' of the electric field e and the polarization ρ causes a time rate of change in the population difference leading to saturation effects. Inertial effects are considered.

III. IMPORTANCE OF BOUNDARY CONDITIONS

When the laser beam travels through an amplifier, the transverse boundary has an increasingly crucial effect compared to the absorber situation. The laser field which resonates with the pre-excited transition, experiences gain; the laser which encounters a transition initially at ground state, experiences resonant absorption and losses. A greater portion of the pulse energy is diffracted outwardly in the amplifier than in the absorber⁴⁶. Consequently, these boundary reflection conditions play a substantial role in the amplifier calculations and obscure the emergence of any new physical effects. Acceptable results are achieved only

by carefully coupling the internal points analyzed with the boundary points⁴⁷. Special care is required to reduce the boundary effect to a minimum such as using non-uniform grids and confining the active medium by an absorbing shell.

In practice, the transverse boundary is simulated by implementing an absorbing surface and mapping an infinite physical domain onto a finite computation region (see Fig. (7)). In Fig. (8), the first and second radial derivatives and the Laplacian term are drawn. Figure (9) contrasts in the stretched radial coordinate system, the transverse coupling and the electric field. The numerical domain sensitivity and the physical dependence on the boundary conditions can be readily assessed.

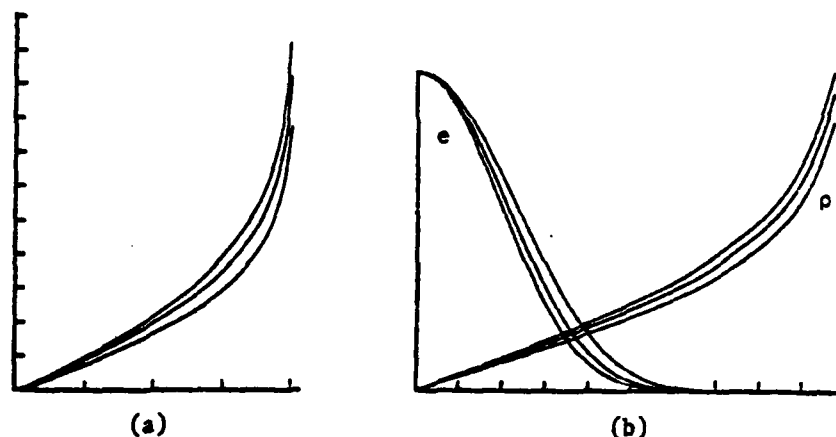


Fig. 7. Graph (a) shows non-uniform stretching of the transverse coordinate. Graph (b) contrasts the Gaussian beam e dependence with the nonuniform physical radius ρ . Both graphs are plotted versus the uniform mathematical radius R .

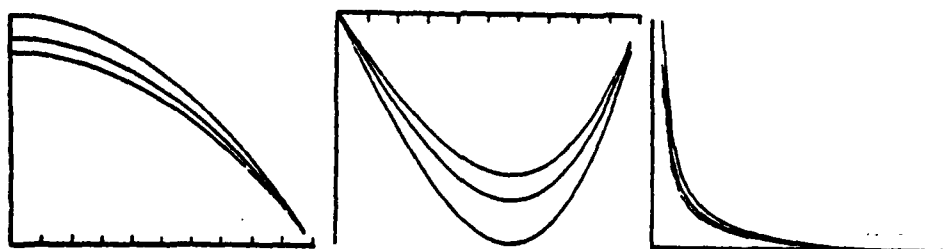


Fig. 8. This graph illustrates the dependence of the radial mapping and the derivatives on the different parameters versus the uniform mathematical radius: First weighting stretching factor $\partial R / \partial \rho$; 2nd weighting stretching factor, $\partial^2 R / \partial \rho^2$; weighted diffraction term, $\nabla_{Tp}^2 R$.

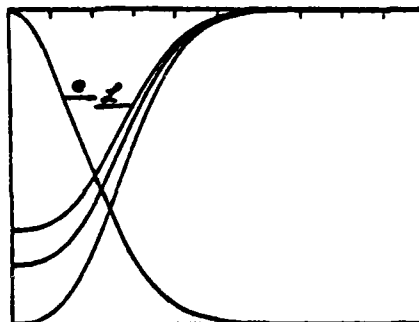


Fig. 9. This figure contrasts the Laplacian dependence 'f' for a given Gaussian profile 'e' for various non-uniform radial point densities.

IV. PRESCRIBED STRETCHING

The numerical grid is defined by widely-spaced computational nodes in the area most distant from the plane of interest and by densely clustered nodes in the critical region of rapid change; the latter being in the neighborhood of maxima and minima, or for multi-dimensional problems, in the vicinity of saddle points. Resolution is sought only where it is needed. The costs involving computer time and memory size dictate the maximum number of points that can be economically employed. In planning such a variable mesh size, the following must be kept in mind:

- (A) The stretching of the mesh should be defined analytically so that all additional weight coefficients appearing in the equations of motion in the computational space, and their derivatives, can be evaluated exactly at each node. This avoids the introduction of additional truncation errors in the computation.
- (B) To assure a maximum value of Δt , the mathematical grid step, the minimum value of Δt , the physical time increment, should be chosen at each step according to necessity. This means that the minimum value of Δt must be a function of the pulse function steepness.
- (C) The minimum value of Δt should occur inside the region of the highest gradient which occurs near the pulse peak.

For example, following Moretti's approach,³² if

$$T = \tanh(\alpha \tau) \quad (11)$$

and α the stretching factor must be larger than 1, the entire semi-axis τ greater than zero can be mapped on the interval $0 < T < 1$

with a clustering of points in the vicinity of $\tau_c = 0$, the center of gravity of the transformation for evenly-spaced nodes in t .

This mapping brings new coefficients into the equations of motion which are defined analytically and have no singularities. It avoids interpolation at the common border of differently spaced meshes. The computation is formally the same in the " T " space as it was in the " τ " space. Some additional coefficients, due to the stretching function, appear and are defined by coding the stretching function in the main program. A slightly modified stretching function is used in the laser problem. Figure (10) illustrates the transformation and its different dependencies on the particular choice of its parameters.

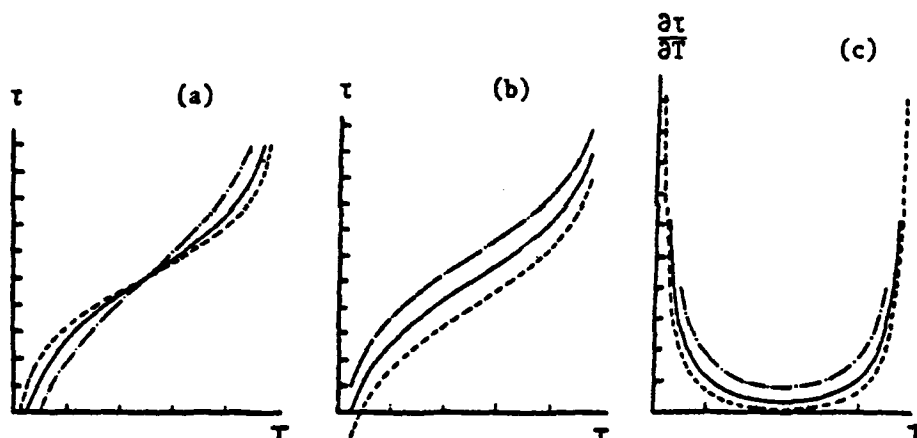


Fig. 10 Dependence of prescribed stretching τ and its derivatives $\partial\tau/\partial T$ on the point densities and the center of transformation versus the uniform computational T .

The derivative of the mapping function produced by the gradual variation along the " T " axis is also defined analytically. In response, the computational grid remains unchanged while the physical grid (and the associated weighting factors) can change a lot.

Should one need to study the laser field buildup due to initial random noise polarization (for superfluorescence), or an initial tipping angle (for superradiance), one must use a different stretching³². This stretching is like the one defined for treating radial boundary conditions. The mesh points are clustered near the beginning (small τ); their density decreases as τ increases.

V. ADAPTIVE STRETCHING IN TIME

As the energy continues to shift back and forth between the field and the medium, the pulse velocity is modified disproportionately across the beam cross-section. This retardation/advance phenomenon in absorber/amplifier can cause energy to fall outside the temporal window. Also, due to nonlinear dispersion, various portions of a pulse can propagate with different velocities, causing pulse compression. This temporal narrowing can lead to the formation of optical shock waves. To maintain computational accuracy, a more sophisticated stretching is needed. The accumulation center of the nonlinear transformation is made to vary along the direction of propagation. This adaptive stretching will insure that the redistribution of mesh points properly matches the shifted pulse, Figure (11).

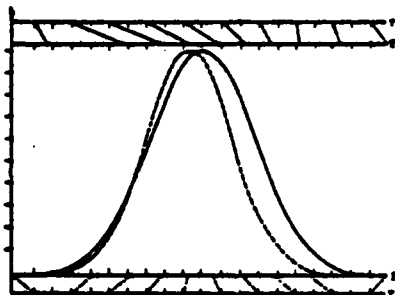


Fig. 11 Adaptive stretching with different centers of transformation.

Here, the transformation from τ to T is applied about a center τ_c which is a function of η . The stretching factor α could also be a function of η .

The field equation is similar to those of Section II, but contains an extra term:

$$-iF \nabla_{\rho}^2 e + \partial_{\eta} e + \frac{\partial e}{\partial T} \left[-\frac{\partial T}{\partial \tau} \right] \tau_c \frac{d\tau_c}{d\eta} = 0 \quad (12)$$

The role played by the time coordinate is different: an explicitly time-dependent term is now included.

VI. REZONING

The main difficulty in modeling laser propagation through inhomogeneous and nonlinear media stems from the difficulty of pre-assessing the mutual influence of the field on the atomic dynamics and vice versa. Strong beam distortions should occur based on a perturbational treatment of initial trends. One must

normalize out the critical oscillations to overcome the economical burden of an extremely fine mesh size. To insure accuracy and speed in the computation, a judicious choice of coordinate systems and appropriate changes in the dependent variables, which can either be chosen a priori or automatically redefined during the computation, must be considered (Figure (12))³³⁻⁴⁰.

This coordinate transformation alters the dependent variables and causes them to take a different functional form. The new dependent variables are numerically identical to the original physical amplitudes at equivalent points in space and time.

The requirements of spatial rezoning will be satisfied by simultaneously selecting a coordinate transformation (from the

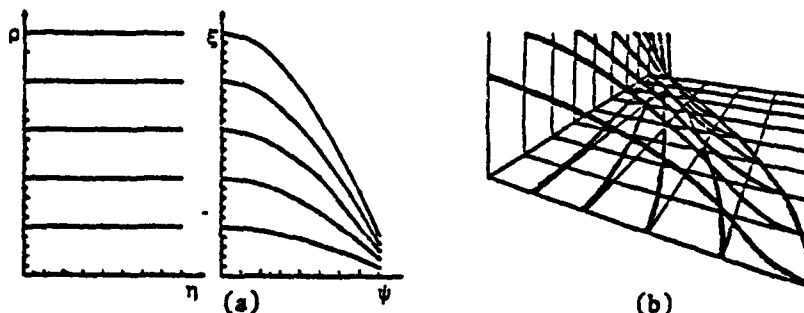


Fig. 12. The concepts of prescribed rezoning are shown in Graph (a); Graph (b) is a close-up of the nonuniform mapped grid of Fig. 2(b).

original coordinates ρ and η to new coordinates ξ and z) and an appropriate phase and amplitude transformation. The chosen function transformation will share the analytical properties of an ideal Gaussian beam propagating in a vacuum.

Since the parameter a , the measure of the transverse scale, shrinks or expands as the beam converges or diverges, it is logical to require the transverse mesh to vary as " a " varies. However, to assure stability and convergence, the ratio $[\Delta\eta/(\Delta\rho)^2]$ must be defined according to the chosen Fresnel number and it must be kept constant throughout the calculation. Accordingly, a new axial variable, z , must be introduced to keep this parameter constant as ρ varies. This should increase the density of η planes around the focus of the laser field where the irradiance sharply increases in magnitude causing a more extensive and severe field-material interaction to occur.

If the quadratic phase and amplitude variation are removed from the field and polarization envelopes, the new field equation

varies more slowly than its predecessor; thus, the numerical procedure allows one to march the solution forward more economically by using larger meshes.

VII. ADAPTIVE REZONING

The foregoing concepts may be generalized by repeating the simple coordinate and analytical function transformations along the direction of propagation at each integration step. Figure (5) and graphs (13a) and (13b) illustrate this self-adjusted mapping in planar and isometric graphs.

The feasibility of such automatic rezoning was demonstrated by Moretti in his conformal mapping of supersonic flow calculations³⁴, and by Hermann and Bradley in their CW analysis of thermal bloom-

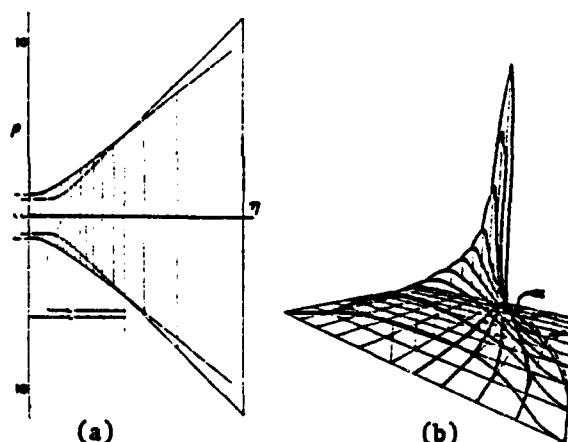


Fig. 13. Graph (a) illustrates the self-adjusted rezoned grid; Graph (b) shows the usefulness of adaptive two-dimensional mapping through isometric representation of the field fluency.

ing³⁵. In particular, the change of reference wavefront technique consists of tracking the actual beam features and then readjusting the coordinate system. The new axial coordinate z is defined as before. Previously, the center of the transformation where the radial mesh points were most tightly bunched was at the focus ($z = \eta = 0$). Now the transformation is defined in terms of an auxiliary axial variable z_ξ as a function of z , which is calculated adaptively, in a way that reflects and compensates the changing physical situation.

In this adaptive rezoning scheme, the physical solution near the current z plane is described better by a Gaussian beam of neck radius $a_{\xi 0}$ whose point is a distance z_ξ away than by an initially assumed Gaussian beam with parameters a_0 and z . In addition, to

remove the unwanted oscillations, new dependent variables are introduced without quadratic and quartic radial dependence in the phases of the pulse and polarization envelopes. By minimizing the local field phase gradient the relationship between the auxiliary z_c and z is obtained. Thus the rezoning parameters are determined appropriately from the local field variable at the preceding plane, so the new variable at this present point has no curvature. Note that the new equation varies less in its functional values than the original. The numerical computation is significantly improved. Notably, the instantaneous local rezoning parameters of the quadratic wavefront are determined by fitting the calculated phase of the local field to a quartic in the nonuniform radius. More specifically, the intensity-weighted square of the phase gradient integrated over the aperture is minimized. Consequently, the curvature at the highest intensity portion of the beam contributes the most. Various moment integrals of the local field variable and the local transverse energy current will be introduced, to specifically evaluate the adjustable rezoning parameters.

VIII. NUMERICAL RESULTS

This section outlines basic results in SIT, obtained with and without rezoning and stretching, and illustrates why the more sophisticated techniques required less computational efforts.

The first part of this investigation led to the discovery of new physical phenomena which promise to have significant applications for proposed optical communications systems. It had been shown that spontaneous focusing can occur in the absence of lenses, and that the focusing can be controlled by varying the medium parameters. The second part of this analysis dealt with amplifiers.

The dependence of the propagation characteristics on the Fresnel number F^{-1} associated with an effective medium length, on the on-axis input pulse "area," on the relaxation times and on the off-line center frequency shift, has been studied. Furthermore, particular care was exercised to ensure a perfectly smooth Gaussian beam (see Figure (10)) thereby eliminating any possibility of small-scale, self-focusing buildup⁴⁸.

The time-integrated pulse "energy" per unit area, $\int_0^T |e(\rho, \eta, t')|^2 dt'$, the fluency, is plotted for various values of the transverse coordinate, as a function of the propagation distance (see Fig. 14).

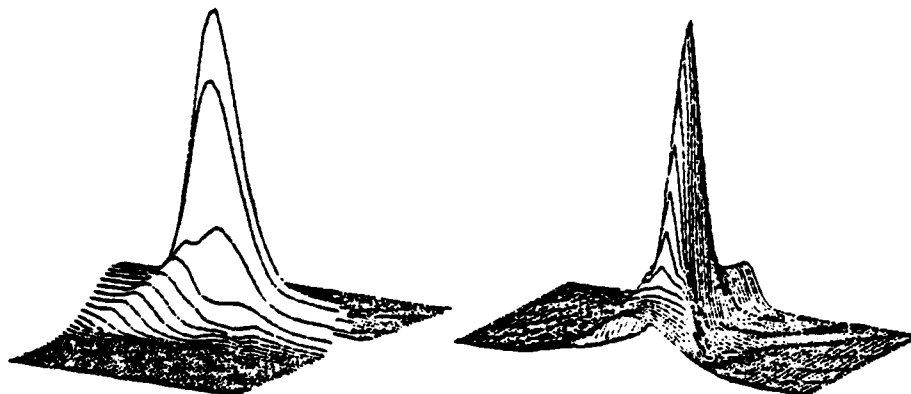


Fig. 14. The longitudinal orientation shown in the left-hand figure illustrates the gradual boosting mechanism that field energy experiences as it flows radially towards the beam axis (while η increases). The second orientation displays the severe beam distortion in its cross-section as a function of η .

The three-dimensional numerical calculations substantiate the physical picture based on a perturbational study of the phase evolution^{10,15}. It could be visualized using selected frames from a computer movie simulation of the numerical model output data. In the left-hand curves of Figure (15) the transverse energy current is isometrically plotted against the retarded time for various transverse coordinates at four specific regions of the propagation process: (a) the reshaping region where the perturbation treatment holds; (b) the buildup regions; (c) the focal region; and (d) the post-focal region. The field energy is displayed for the specific regions in the right-most curves of Fig. (15). A rotation of the isometric plots is displayed in Figure (16), to emphasize the radially dependent delay resulting from the coherent interaction. Positive values of the transverse energy current correspond to outward flow, and negative values to inward flow. The results of the reshaping and buildup regions in Figures (15) and (16) agree with the physical picture related to the analytic perturbation discussed elsewhere.

The burn pattern, iso-irradiance level contours (against r and ρ) for different propagation distances are shown in Figure (17). Severe changes in the beam cross-section are taking place as a function of the propagating distance. At the launching front, the beam is smooth and symmetrical; as the beam propagates into the nonlinear resonant medium, the effect of the nonlinear inertia takes place.

The general format for presenting three-dimensional coherent pulse propagation in amplifying medium will be the same as for the absorber (see Figs. (18) to (21)).

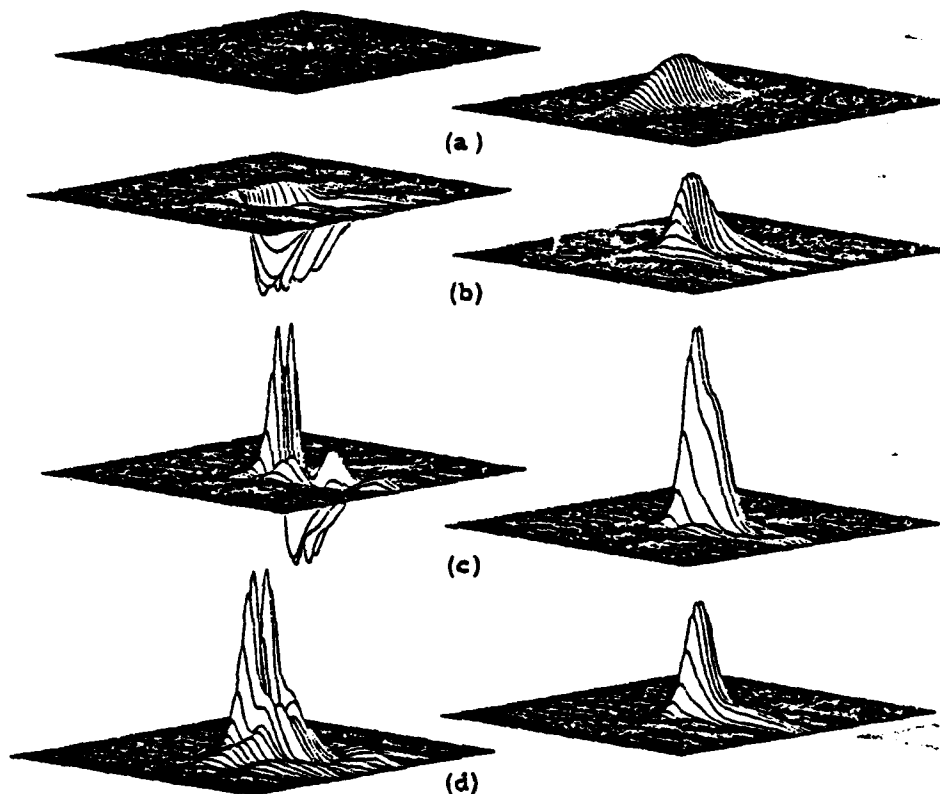


Fig. 15. Isometric plots of the absorber field energy and transverse energy flow, against the retarded time for various transverse coordinates at the four regions of interest.

IX. TRANSVERSE EFFECTS IN SUPERFLUORESCENCE

With the help of Gibbs, the outstanding question dealing with the strong reduction (and elimination) of ringing observed in the low-density Cs [2] experiment from the amount predicted in the one-dimensional calculations [1(b)] was resolved. This was accomplished by developing a rigorous two-dimensional theory of Burnham-Chiao ringing [1b] and superradiance and superfluorescence (SF) in a pre-excited thick medium using a semi-classical formulation [1e] which includes one-way propagation effects as in SIT. The initia-

tion of the SF emission process is characterized by a tipping angle θ_R . When the small signal field gain $\alpha_{\text{eff}} L/2$ (or equivalently, the characteristic radiation damping time τ_R of the collective atomic system) is sufficiently large, θ_R , the ratio of the length L to the coherence length L_c , and the Fresnel number \mathcal{F} (equal to $\text{area}/\lambda L$) completely characterize the system behavior. However, L/L_c is not a critical parameter as predicted by the mean field theory.^c

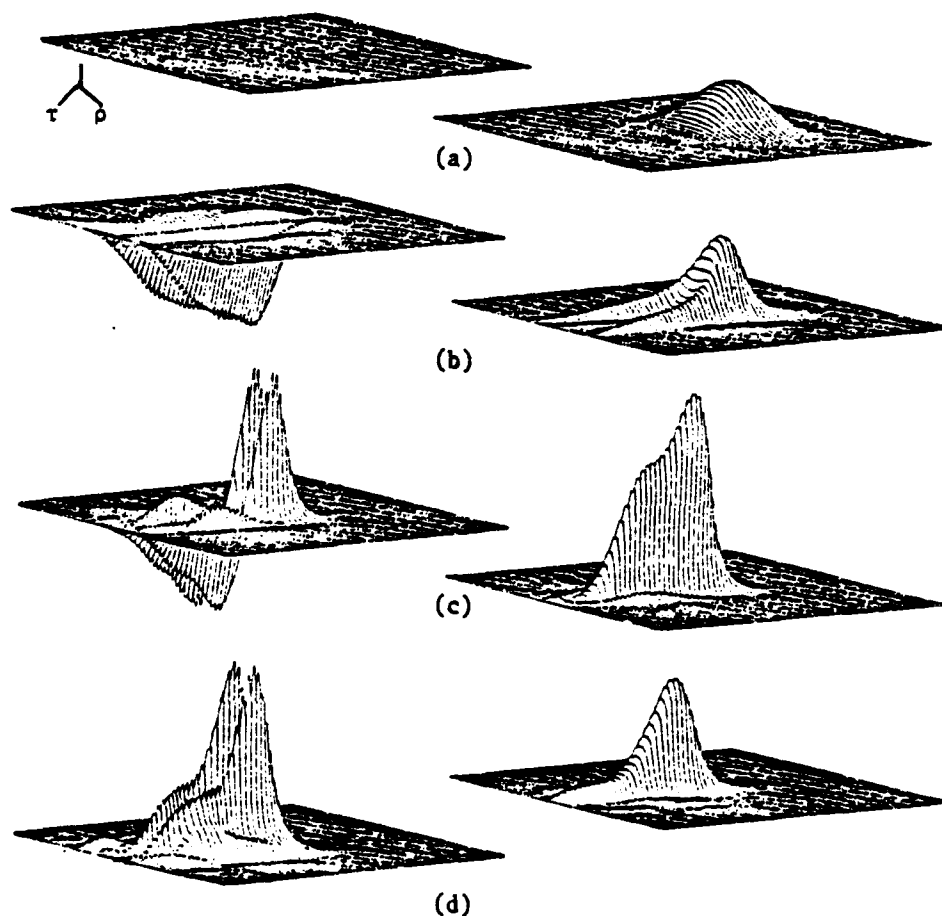


Fig. 16 Isometric plots of the absorber field energy and transverse energy flow profile for various time slices at the four regions of interest.

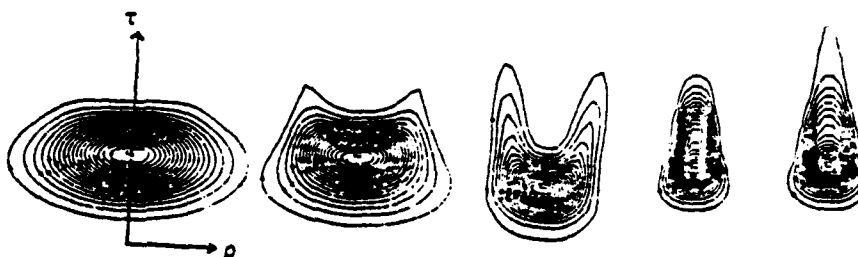


Fig. 17. Absorber field energy contour plots for the four propagation distances. Notice the temporal delay associated with the coherent exchange of energy between light and matter, as well as the beam cross-section narrowing.

Neither the mean-field approximations^{1d}, nor the substitution of a loss term to account for diffraction coupling^{1c, 20d}, are considered; instead self-consistent methods similar to those developed for SIT studies are adopted^{39, 46}. The numerical simulation takes fully into account both propagation and transverse (spatial profile and Laplacian coupling) effects.

The previously reported pronounced SF ringing for plane-wave simulation is reproduced for uniform input profile. The reduction of ringing is studied for various radial profiles for the gain $g_R = \alpha_{\text{eff}}[c\tau_R]$ (equivalently, the population inversion) and the small input pulse area θ_R ¹¹⁻¹³.

The ringing reduction can be explained by two physical mechanisms: (a) a shell (ring) model^{32(d)}: spatial averaging of uncoupled planar modes, each associated with a particular shell and subjected to both a distinct θ_R and a radiation time. Radial averaging by a Gaussian gain profile of very large \mathcal{T} eliminates most of the ringing, resulting in an asymmetric pulse with a long tail; and (b) a rigorous diffraction coupling: through the Laplacian term, the adjacent shells interact, causing the field energy to flow transversely across the beam from one region to another.

When diffraction coupling is considered concomitantly with radial variations of θ_R and g_R (i.e., of τ_R), the ringing is more subdued (see Fig. (23)). In other words, reducing \mathcal{T} of a Gaussian profile does reduce the asymmetry (in better agreement with the Cs data) since the outer beam portions are stimulated to emit earlier

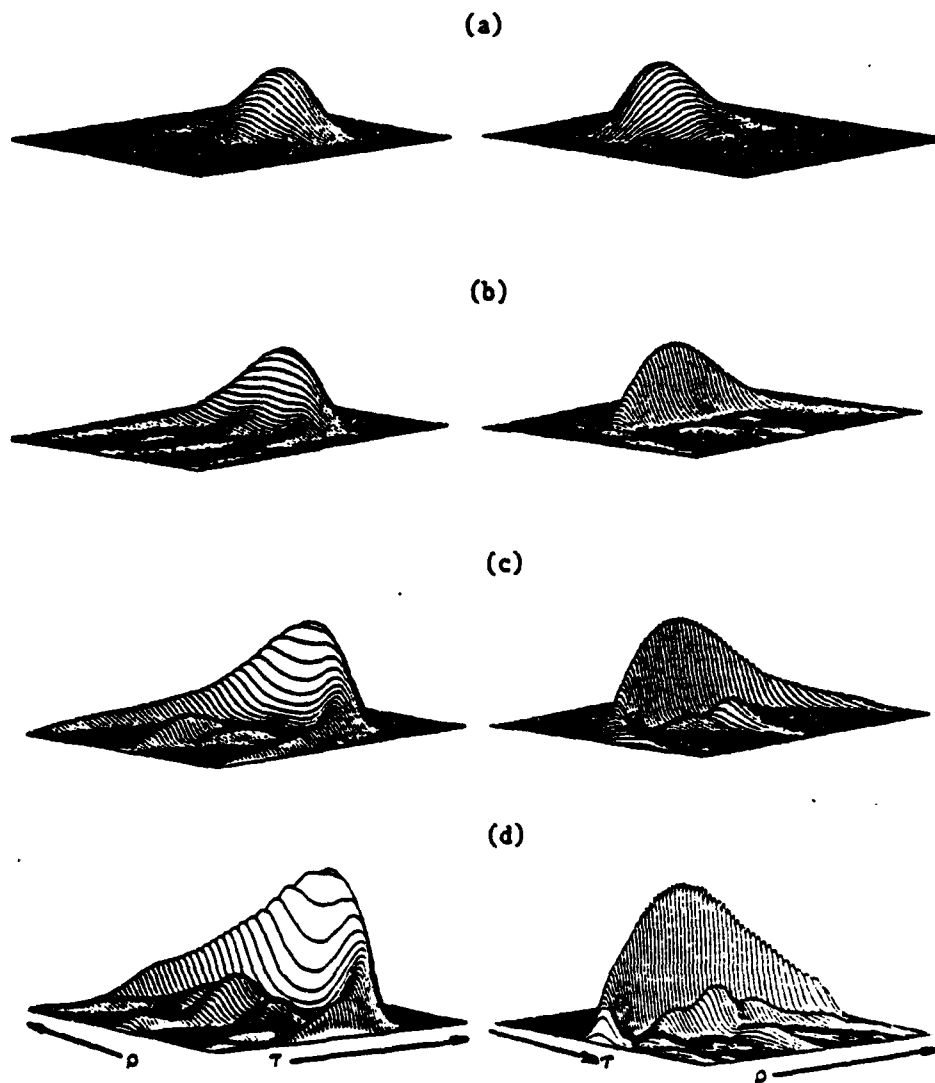


Fig. 18. Isometric plots of the amplifier field energy as a function of τ and ρ for two orientations $\pi/2$ apart at four locations along the propagation direction.

by diffraction from the inner portion. Thus, the effect of the Laplacian coupling is small for large \mathcal{F} but becomes progressively greater at about $\mathcal{F} \leq 1$.



Fig. 19. Amplifier field energy contour plots for the four propagation regions of interest. Note the temporal advance associated with coherent exchange of energy between light and matter (the smaller area propagates more slowly than the larger one), as well as beam cross-section expansion.

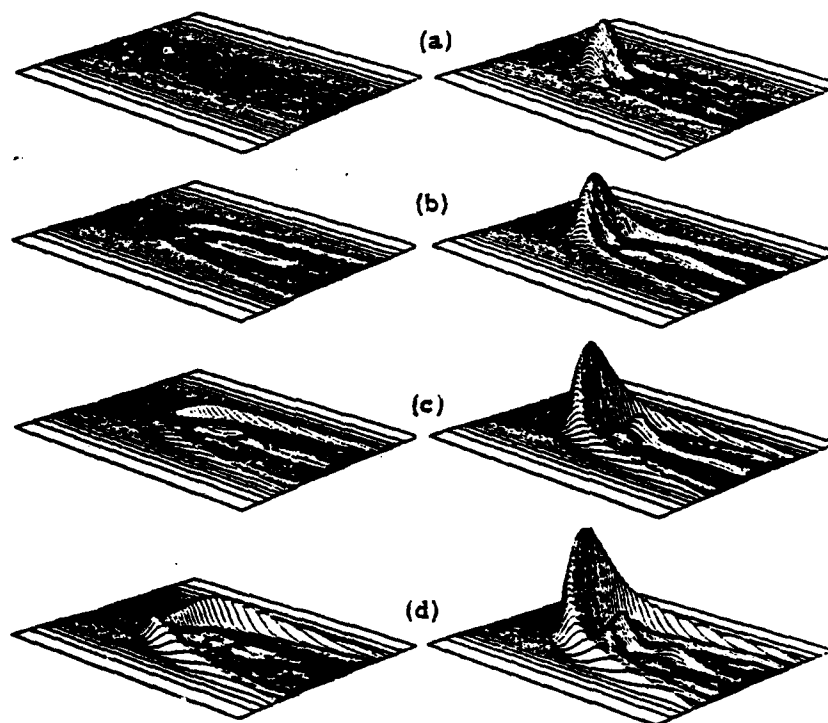


Fig. 20. Isometric plots of amplifier field energy and transverse energy flow against retarded time for various transverse coordinates at four propagation regions studied for absorbers. Stretched radial coordinate was adopted for proper accounting of transverse boundary condition. When these results are compared with those for an absorber, it is evident that a focusing phase is not restricted to the absorber, but develops also for the secondary pulses in amplifying media.

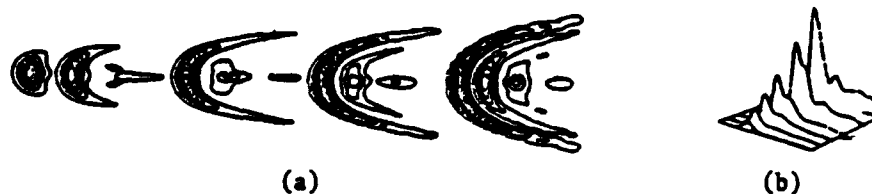


Fig. 21. Amplifier field energy contour plots for four propagation regions of interest with stretched radial coordinates. No severe reflection or abrupt variation in the field energy, at the wall boundary, is observed. The enhancement of diffraction by pre-excited two-level medium is clearly evident.

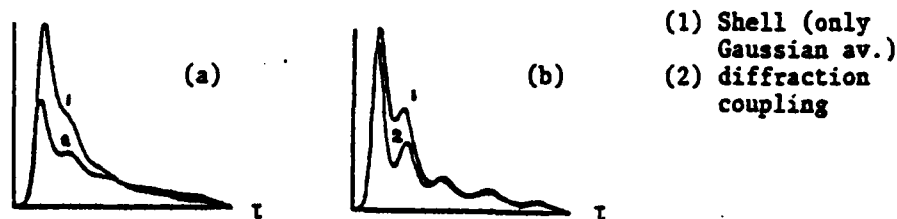


Fig. 22 Contrast the time dependence of the energy after integrating over ρ for the shell model (where θ_R and τ_R are both radially dependent) and the diffraction model (where the Laplacian coupling is rigorously present) for two population inversions: (a) Gaussian $g = g_0 \exp[-\rho^2]$, and (b) saturable inversion $g = g_0$ for $\rho < \rho_0$; $g = g_0 \exp[-\rho^2]$ for $\rho_0 < \rho < \rho_{\max}$.



Fig. 23. Total energy per atom as a function of time with J as the labeling parameter. $\tau_R = 0.046$ ns and $L/L_c = 1.95$. $\theta_R = 3 \times 10^{-3}$ for all radii. (a) Superfluorescence of uniform cylinder or small-area pulse propagation through uniform gain cylinder; (b) Uniform small-area pulse propagation through Gaussian gain medium.

Computer results representing the SF of uniform and nonuniform cylinders (i.e., small-area pulse propagating through a uniform Gaussian gain cylinder) are respectively displayed in Figure (24a) and Figure (24b) for different \mathcal{F} . In Figures (25a) and (25b), this initial small-area θ_R is now radially dependent. Figures (26a) and (26b) duplicate the physical situation in Figures (24a) and (24b), but for a smaller initial polarization. The universal superfluorescence scaling law is seen not to hold; the calculated pulse length is much more sensitive to the magnitude of θ_R in the transverse case than it is in the planar case.

The ringing predicted by this two-spatial-dimensional theory agrees more with experimental observations than that predicted by the uniform plane-wave counterpart. Detailed isometric graphs of the field energy buildup show, in Figures (27a), (27b) and (27c) qualitative agreement in peak intensity and peak delay with the ring (shell) model [1c]. Figure (28) illustrates the elimination of ringing under conditions similar to the low-density Cs data for different radial density distributions. Figure (29) contrasts the dependence of the radial gain on a typical \mathcal{F} by various θ_R ; Figure (30) illustrates the dependence of the radial gain on a typical θ_R by different \mathcal{F} . Figure (31) shows the effect of varying τ_R on this output intensity. Various small-scale ripples were introduced in the gain profile (see Fig. 31).

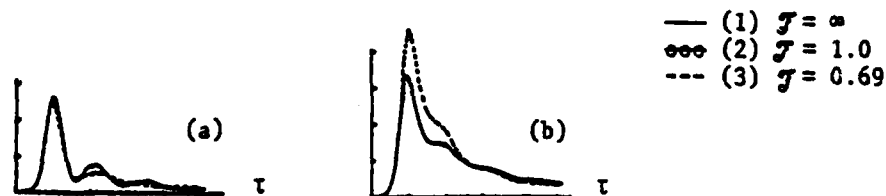


Fig. 24. (a) Propagation of small-area Gaussian profile pulse through uniform cylinders ($\tau_R = 0.046$ ns, $L/L_c = 1.35$ and $\theta_R = 3 \times 10^{-3}$ on-axis). (b) Superfluorescence with Gaussian radial gain ($\tau_R = 0.046$ ns, $L/L_c = 1.35$ and $\theta_R = 3 \times 10^{-3}$ on-axis).

Ringing is largely removed by a gain medium of $\mathcal{F} = 1$, resulting in an asymmetric output pulse with a long tail. It now seems that a larger θ_R , see Fig. (33a) (unlikely, according to measurement of feedback effects and estimates of Raman effects during the excitation pulse^{2d}), or smaller \mathcal{F} (perhaps 0.4 consistent with the range $0.35 < \mathcal{F} < 1.39$ of ref. 1(a) which used a $1/e$ rather than a half width half maximum (HWHM) definition of r_p), see Fig. (33b),

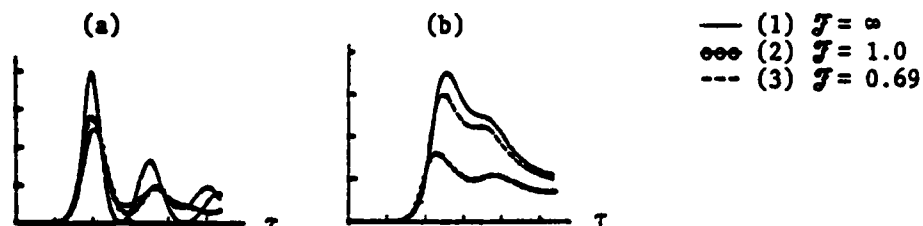


Fig. 25. Same parameters as in Fig. 23 but with a smaller $\theta_R = 10^{-4}$:

(a) Small area propagation in a uniformly inverted cylinder. (b) Small-area propagation in a Gaussian inversion cylinder.

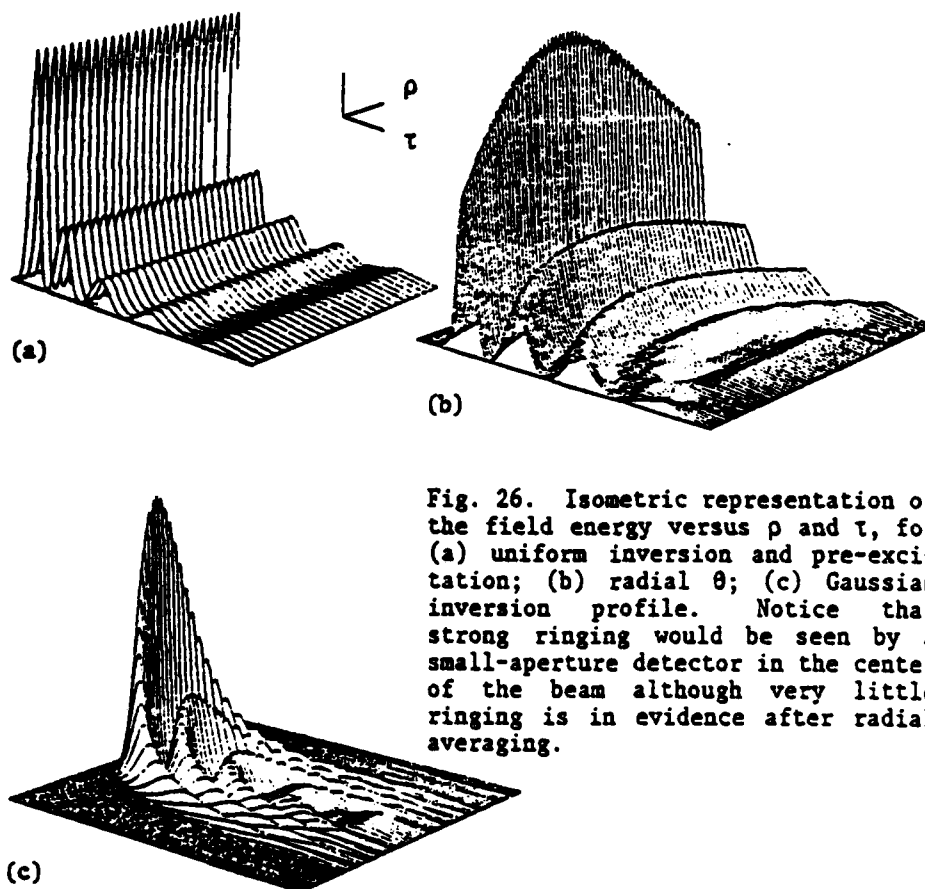


Fig. 26. Isometric representation of the field energy versus ρ and τ , for (a) uniform inversion and pre-excitation; (b) radial θ ; (c) Gaussian inversion profile. Notice that strong ringing would be seen by a small-aperture detector in the center of the beam although very little ringing is in evidence after radial averaging.

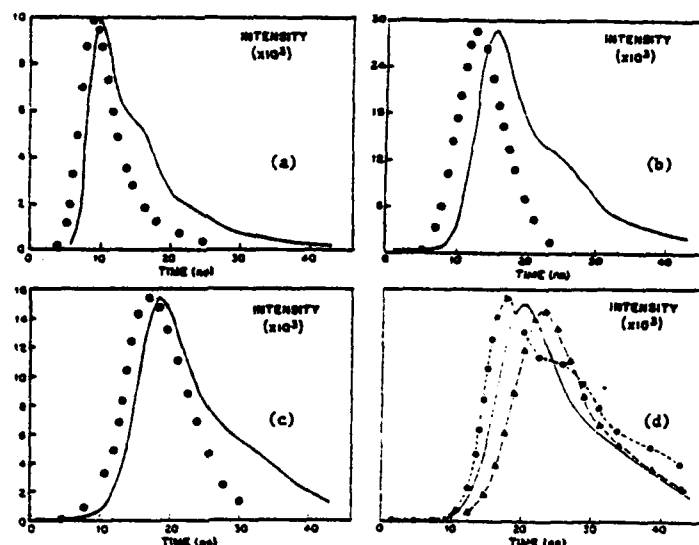


Fig. 27. Comparison of pulse shapes for situations where L/L_c is similar to the low density Cs. Relaxation terms were not included in this analysis. Note the asymmetry associated with an atomic beam of $\mathcal{T} = 1$. (a) $n = 1.9 \times 10^{11} \text{ cm}^{-3}$; $\theta_0 = 2.64 \times 10^{-4}$; (b) $n = 18.24 \times 10^{10} \text{ cm}^{-3}$; $\theta_0 = 1.37 \times 10^{-4}$; (c) $n = 11.9 \times 10^{10}$; $\theta_0 = 1.69 \times 10^{-4}$; (d) $n = 8.75 \times 10^{10}$; $\theta_0 = 1.96 \times 10^{-4}$. Time is measured in nsec.

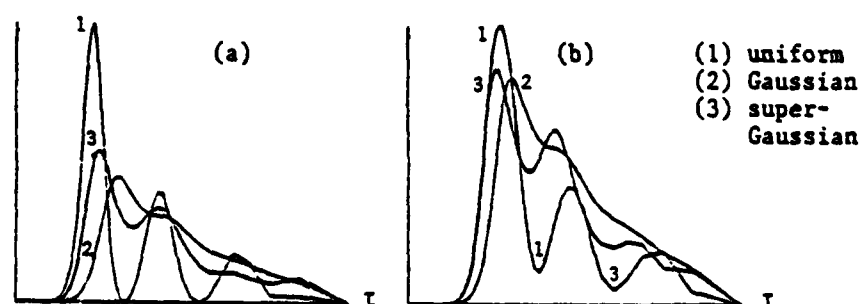


Fig. 28. Contrast of the total energy per unit atom (versus time) for different radiation damping time τ_R for a chosen $\mathcal{T} = 0.7$ and a uniform $\theta_R = 3 \times 10^{-3}$ (for different inversion profiles).

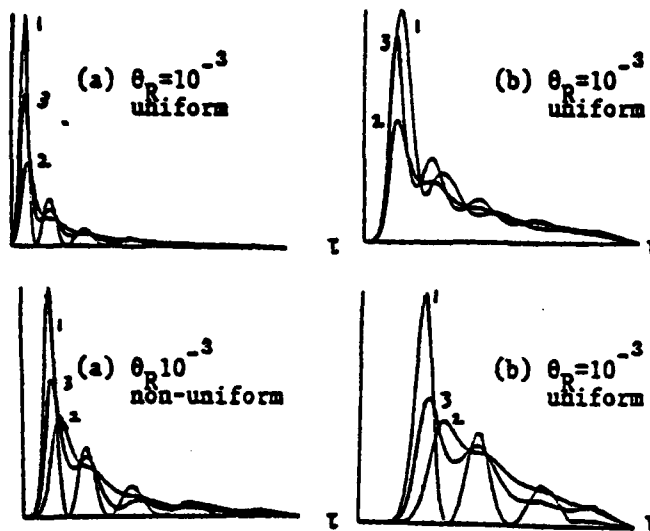


Fig. 29. Contrast of the total energy per unit atoms (versus time) for different inversions (1) uniform, (2) Gaussian (3) saturable Gaussian, and for particular tipping angle profiles. $\theta_R = 10^{-3}$ non-uniform $\tau_R = 0.46$ ns and $L/L_c = 1.95$. $\mathcal{T} = 6$.

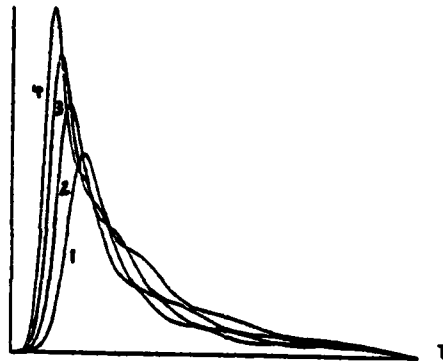


Fig. 30. Contrast of the total energy per unit atom (versus time) for different radiation damping time τ_R for a chosen $\mathcal{T} = 0.7$, and a fixed tipping angle $\theta_R = 3 \times 10^{-3}$. $g_R = 100$, 125, 150, 175.

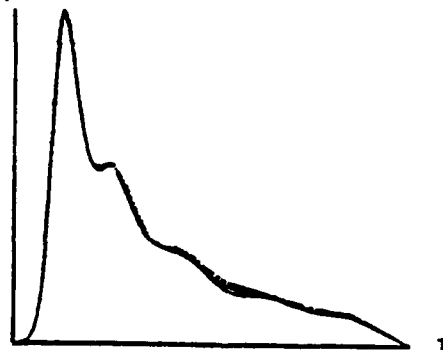
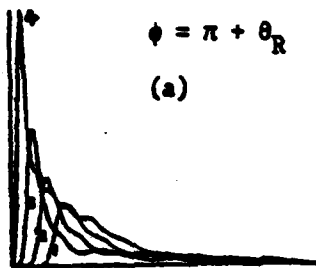


Fig. 31. Display of small-ripple effects in the Gaussian inversion of the cylinder on the total energy per unit atom (versus time) for $\mathcal{T} = 0.7$, $\tau_R = 0.46$ ns, and $L/L_c = 1.95$.

1. 3.1416986E+01
2. 3.142535E+01
3. 3.1510173E+01
4. 3.2358377E+01

$$\phi = \pi + \theta_R$$

(a)



(b)

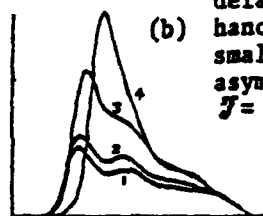


Fig. 32. (a) Emphasizes the effect of large θ_R versus small θ_R on the pulse shape asymmetry and the ratio of the calculated pulse length to the delay of the peak. (b) Enhancement of the effect of small θ_R on the pulse shape asymmetry.
 $\mathcal{J} = \infty, 2.76, 0.7, 0.4$.

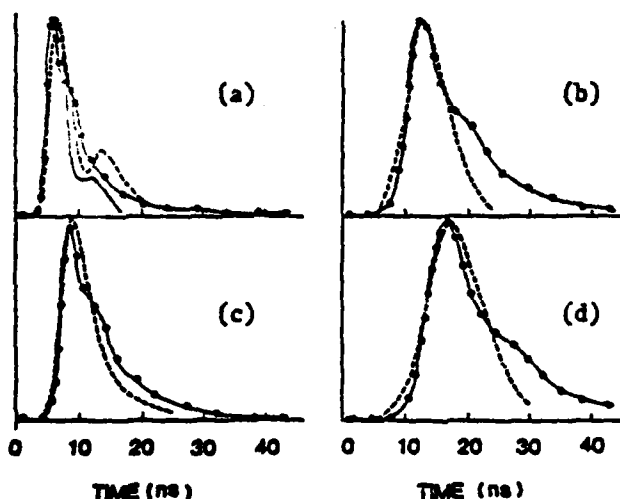


Fig. 33. Comparison of experimental and three-dimensional theoretical superfluorescence pulse shape for several densities N in an atomic beam of 2.0 cm length. The model encompasses rigorous radial dependence of N , τ_R and θ_R , diffraction (through the Laplacian) and relaxation times. $\mathcal{J} = 1$, $L = 2$ cm, $T_1 = 70$ ns, $T_2 = 30$ ns, $\lambda = 2.931\mu$, $\tau(0) = 551$ nsec, Gaussian and inversion; in the following columns are the on-axis inversion density n in units of 10^{11} cm $^{-3}$, n of the experiment in the same units and θ_0 in 10^{-4} radians: (a) 3.1, 1.9, 1.07; (b) 3.1, 7.6, 1.37; (c) 1.2, 3.8, 1.69; (d) 0.885, 3.1, 1.96.

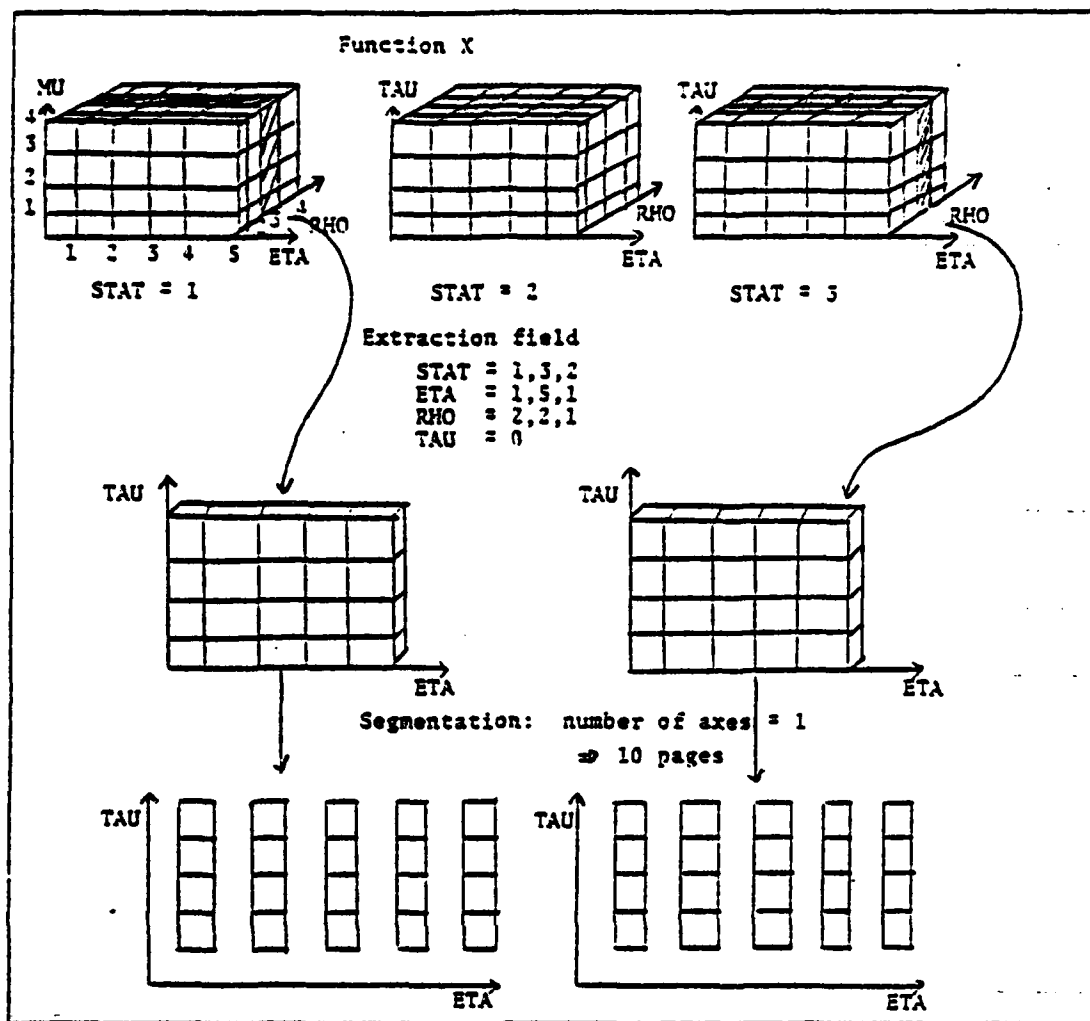


FIGURE 4.9 - EXTRACTION FIELD AND SEGMENTATION OF A FUNCTION

Function A depending on axes STAT, ETA, RHO, TAU

Extraction field: STAT = 1,3,2
 ETA = 1,5,1
 RHO = 2,2,1
 TAU = 0

A) Option by default

Tuples

Number of axes on a page: 1

List of axes points

1 page

Value A	point 1 TAU
"	" 2 "
"	" 3 "
"	" 4 "

point 1 STAT
 point 1 ETA
 point 2 RHO

B) Specification of Tuple = (TAU, ETA, STAT)

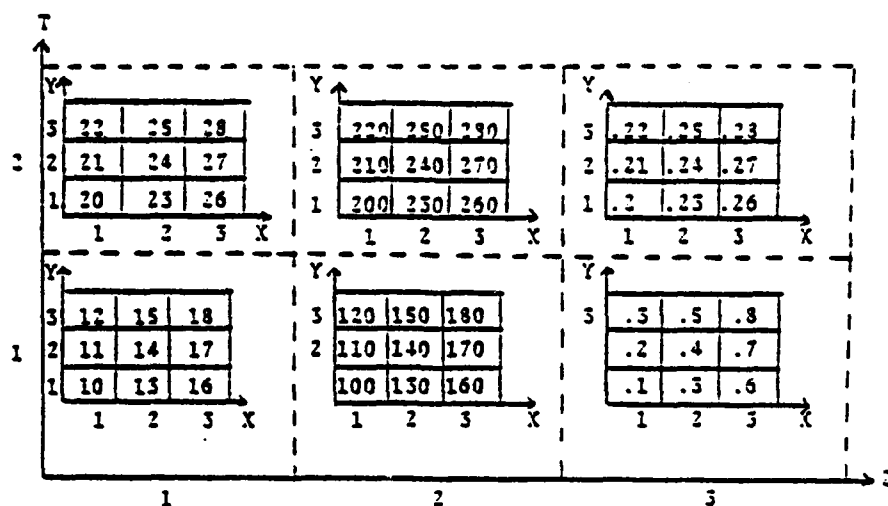
Tuples

List of axes points

Value A	Point 1 TAU	Point 1 ETA	Point 1 RHO
"	" 2 "	" 1 "	" 1 "
"	" 3 "	" 1 "	" 1 "
"	" 4 "	" 1 "	" 1 "

Point 2 RHO

FIGURE 4.10 - TUPLE COMPOSITION AND LIST OF AXES POINTS



Function A depends on axes Z, T, X and Y

Field of Extraction: Z = 1,3,2

T = 0

X = 1,3,2

Y = 0

Page comprises 1 axis

Global scale

	Fct A	Y
min	.1	1
max	230	3

Local scale: will change at each page extraction

ex. page 1 Z = 1, T = 1, X = 1

	Fct A	Y
min	10	1
max	12	3

page 2 Z = 1, T = 1, X = 3

	Fct A	Y
min	16	1
max	18	3

etc. ...

Standard scale

	Fct A	Y
min	.1	1
max	.22	3

Standard scale: with Z as axis implying a reevaluation of the minimums and maximums

Z = 1

	Fct A	Y
min	10	1
max	23	3

Z = 2

	Fct A	Y
min	.1	1
max	.2	3

FIGURE 4.11 - EXAMPLE SHOWING THE DIFFERENT SCALES

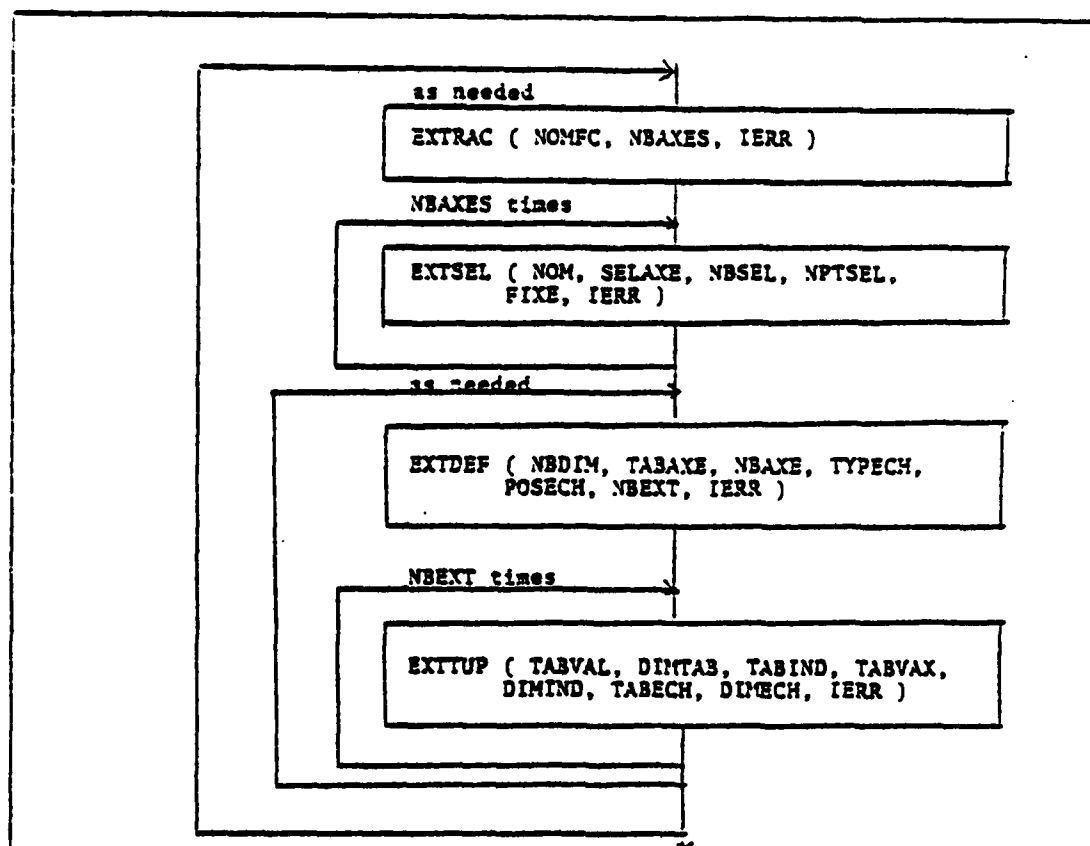


FIGURE 4.12 - CALL SEQUENCE OF THE PROCEDURES PRODUCING THE RESULTS FUNCTIONS EXTRACTION

ADD					
NBRUNS	BASE	COMPLETE	1	1	
JSAVE	BASE	COMPLETE	1	300	
MSAVE	BASE	COMPLETE	1	32	
KSAVE	BASE	COMPLETE	1	64	
CI	BASE	REAL	1	0.08	
TBRHO	BASE	REAL	1	4.236669	
IGV	BASE	COMPLETE	1	1	
PHIO	BASE	REAL	1	3.1417817	
AKAP	PHYSIQUE	REAL	0		
PSKA	PHYSIQUE	REAL	0		
DATE	TEMPS	CHAIN	0		
ETAPTS	AXE	REAL	5	1.0	2.0 3.0 4.0 5.0
RHOPTS	AXE	REAL	4	0.0	0.1 0.2 0.3
DUREZ	SYNTH	REAL	0		
ENER	SYNTH	REAL	0		

FIGURE 4.13 - EXAMPLE OF DATA FOR A DATEDI PROGRAM

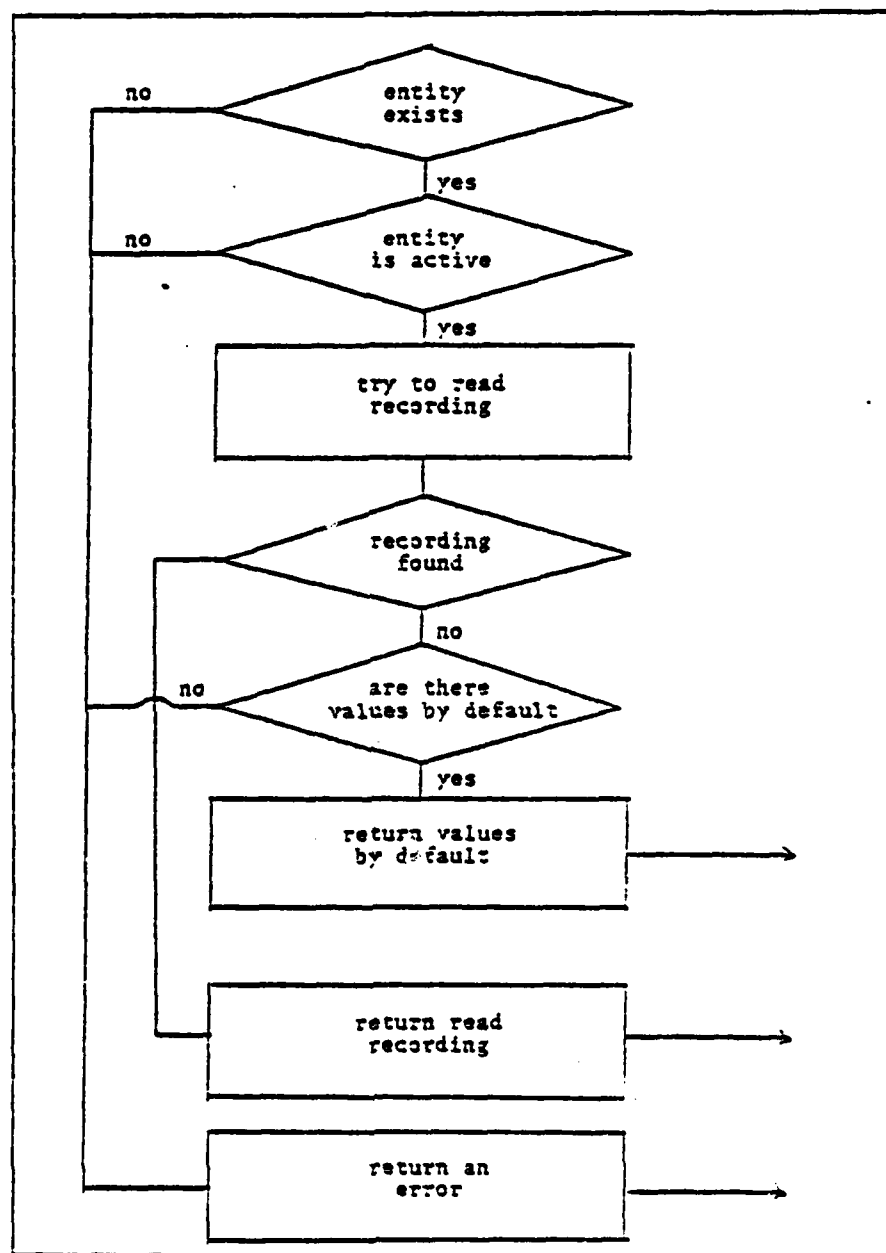


FIGURE 4.14 - RUNNING OF THE DATLIR PROCEDURE

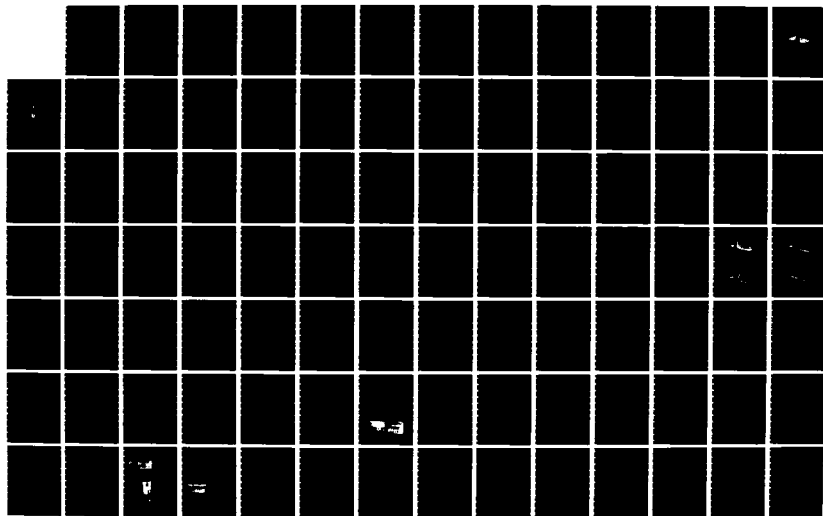
AD-A136 986

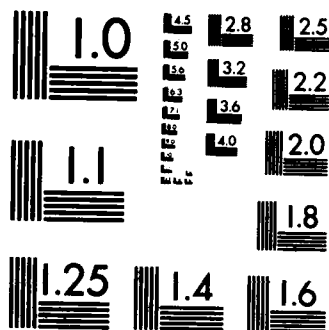
TRANSVERSE AND QUANTUM EFFECTS IN LIGHT CONTROL BY
LIGHT; (A) PARALLEL BE. (U) POLYTECHNIC INST OF NEW
YORK BROOKLYN DEPT OF MECHANICAL AND A. F P MATTAR
1983 POLY-M/AE-83-4 N00014-80-C-0174 F/G 20/6

4/6

UNCLASSIFIED

NL





MICROCOPY RESOLUTION TEST CHART
NATIONAL BUREAU OF STANDARDS-1963-A

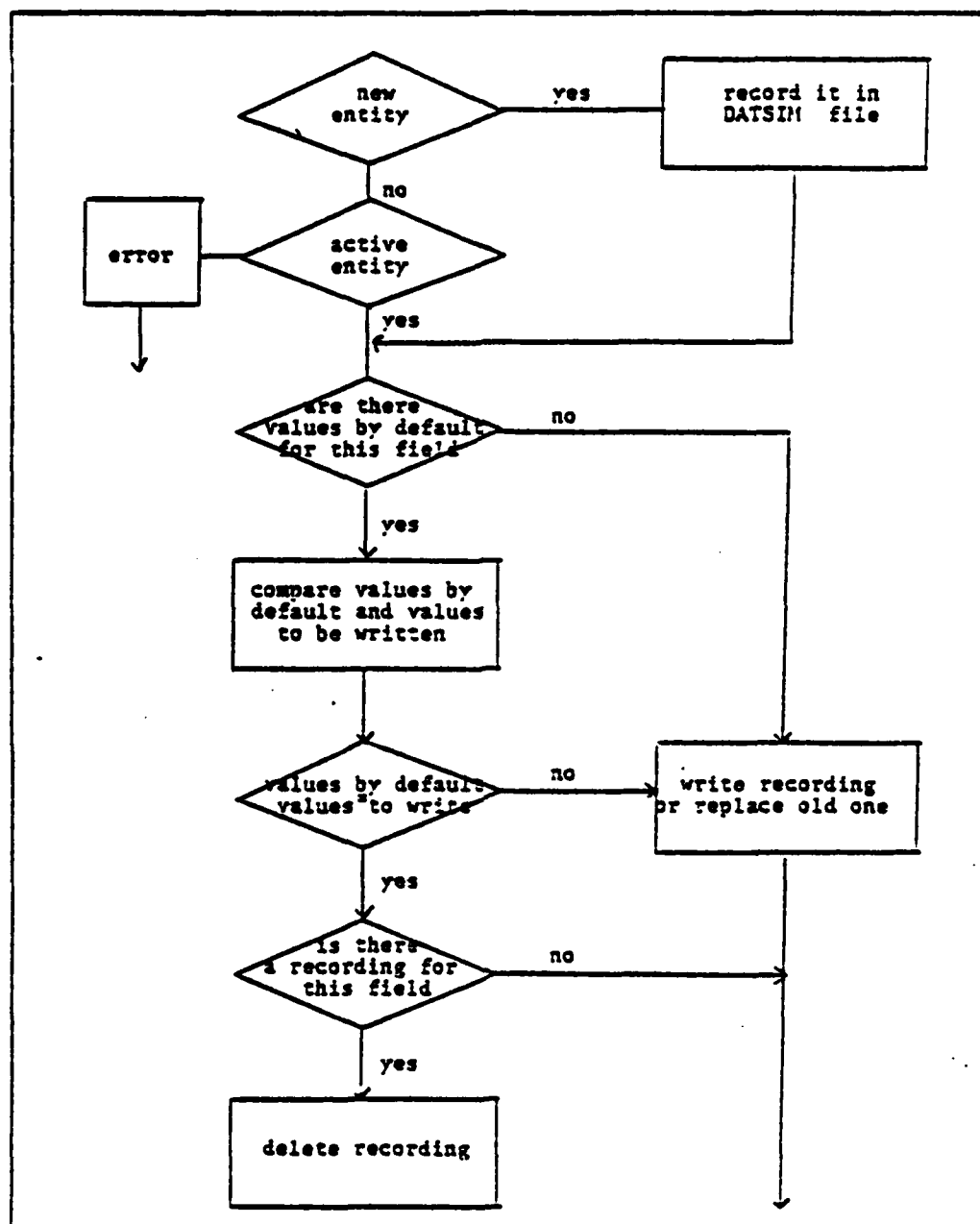


FIGURE 4.15 - RUNNING OF DATECR PROCEDURE

V - APPLICATION PROGRAMS

This section deals with the programs in the system that go beyond the frame of application in the laser model building project. These are the DEFPARM, DESRES and SYNTH programs created to treat in a general way a specific application. These also use the SIMRES, XTRACT and DATSIM software. All the examples in this chapter derive from the only source we have: the laser model building project.

5.1 THE DEFPARM PROGRAM

The DEFPARM program is an interactive tool which defines the FORTRAN NAMELISTs. A program generation of the NAMELISTs is a good way to validate them (syntactically) and to avoid certain trivial errors. DEFPARM is a program of general application but by referring to the laser model building project to describe its operation, the explanations will be more concrete.

In the DEFPARM program, the NAMELISTs are defined by statements that follow a specific syntax. A set of statements establishes the parameters of a group of simulations dealing with a particular phenomenon. These simulations differ only by the value of a limited number of parameters, all the other parameters being fixed. It is because of these fixed parameters that the information can be condensed and the syntax made more concise.

A statement specifies the value or values associated to a block of parameters. A block of parameters is made of one parameter or a group of interdependent parameters (varying conjointly). For example, $A = 0$ shows that a parameter has a given value. If the parameter is to be given several values or that there be a simulation for each of these values, the values are separated by a comma, $A = 0,1,2$. To specify that a group of parameters are interdependent, forming one whole, parenthesis are used. The values associated to the parameters are also put between parenthesis. The order of the elements in such a group is of major importance, and the order of the parameters induces the order of the values. Moreover, there must be as many values in each group of values as there are parameters in the reference group. Thus the following group of parameters can be defined as: $(A,3) = (0,1), (1,1)$.

Vectorial parameters are put between brackets and the different values are separated by a comma: thus $A = [0,1,2]$ or $B = [1]$. The specific values of the parameters need not have the same number of elements; thus: $A = [1,2], [1,2,3], [1,2,3,4]$. But the order of the values is important as it corresponds to the order of the elements in the vector.

The statements are separated by semi-colons and an empty statement ends the specification of a group of simulations. The following specifications can be written as: $A = 1;$
 $B = 1,2; C = 0,1;;$

The syntactic cards corresponding to the above mentioned syntax are shown in figure 5.1. It is possible to go from the specification of a family of simulations to the exhaustive lists of parameters of each simulation forming this family by making a Cartesian product between the values given to the parameters, or a group of parameters, by the different statements. Thus, the specification:

```
A = 1,2;
(B,C) = (0,0), (1,1);
D = -1,1;;
```

can create eight simulations (only the changes in the values of a parameter are noted in the following list).

Number	A	B	C	D
1	1	0	0	-1
2				1
3		1	1	-1
4				1
5	2	0	0	-1
6				1
7		1	1	-1
8				1

There are four principal steps to the execution of the DEFPARM program. The first step is initialization. The user indicates for which simulation program he needs the NAMELISTs. The DEFPARM program will find in the corresponding DATSIM file the number of the last encoded simulation and of the possible parameters for the simulation. The DEFPARM program will thus know which number to give to the new simulation and can verify the parameter identifiers that the user could eventually give it.

For the drawings, the user must indicate the scale and kind of drawing needed. The scale is specified by indicating one of the following identifiers: GLOBALE (the scale is for the whole file), LOCALE (the scale is for a given drawing), STANDARD (the scale is for the extraction field). If the chosen scale is the STANDARD scale, the user can also add, between parenthesis, the name of an axis to limit the scope of the scale to the axes within this axis. For instance, if a function depends on the STAT, ETA, RHO and TAU axes, and if the scale is limited to the standard scale on the ETA axis, this scale will be evaluated for the ETA, RHO and TAU axes only and there would be as many standard scales as there are points on the STAT axis. Section 4.2 gives more details on the nature of the different scales. The kind of drawing is indicated by the following identifier: PLOT 3D (surface drawings), PLOT 2D (curve drawings), CONTOUR (level curves) and PROJEC (2 dimension projection of a sub-array of curves describing the surface of a 2 variable function). The kind of drawing requested will induce a segmentation on the extraction field. Thus, one action can produce several plots; that is as many plots to empty the extraction field. An example of scale specification and type of drawing follows:

SCALE: STANDARD
DRAWING: PLOT 3D

The DESPES program will loop at the deepest level, that of drawing, then ask the user to specify a scale and a type of drawing. To get out of a level: enter an empty line or write the key word FIN (END). The user goes to the other level and here, it is possible to define this level or getting out of it. Figure 5.5 shows a complete example of a specification for the DESRES program.

In the interactive mode, the DESRES program analyzes the user's request and indicates as soon as possible the syntactical errors (data in the wrong format) and the invalid specifications (the requested function does not exist ...). The program then asks the user to hold some specification in order to continue its execution. When it is a submission by batch mode, when an error is detected, the running is stopped but the syntactical analysis can continue.

To execute a drawing specification, the SIMRES program must first localize the SIMRES files to be treated. These files are opened one at a time and the information showing the function to be plotted, the field of extraction, the composition of the tuples and the type of scales is given to the XTACT software. This information recovered by the EXTUP procedure is processed by the appropriate plotting procedure (PLOT 3D, PLOT 2D, CONTOUR, PROJEC). The program repeats this operation until all the requests have been fulfilled or until a non-retrievable error occurs.

Figures 5.7 to 5.11 show the different graphic output of the DESRES program. Figure 5.7 shows the list of parameters identifying the plotted simulation. Figure 5.8 shows the plot drawn by PLOT 3D for a 2 variable function. Figure 5.9 shows the curves set by the CONTOUR procedure for the same function. Figure 5.10 shows a projection of this function as produced by PROJEC. And finally, figure 5.11 shows the plot produced by PLOT 2D for a function which varies as to one axis.

5.5 THE SYNTH PROGRAM

The SYNTH program permits the synthesis of the information of many distinctive simulations in order to study a specific phenomenon. This synthesis is done by selecting the pertinent simulations necessary to draw out a specific phenomenon and by comparing one or several functions of these simulations. In its final version, the SYNTH program should allow the user to specify the phenomenon to be studied with the help of a predicate (studying the effect of a parameter in function of another, or studying the effect of such or such a model). The SYNTH program would find which simulations will satisfy the predicate. However, for a first version (still being developed), it is better to ask the user to identify the simulation to be compared. The SYNTH program thus verifies the validity of the comparison, makes up the headings identifying the work done and makes the comparisons.

There are three possible fields for comparisons:

- inside one simulation,
- between specific simulation produced by a same model (same simulation program),
- between simulation produced by different models.

With comparisons done inside the same simulation, it is the variation of an axis which will provide the criterion for a comparison: it is the position on the axis which is studied. Often, the comparison will deal with the repetitive axis, in other words, an axis which does not define the space of the simulation but which induces repetition of the stored information: this is specifically the case with the models with several lasers (where a "laser" axis will store information on the different lasers) and the model including statistics (where a "statistic" axis will store the different repetitions of the simulation).

The comparisons of simulations produced by the same model permits the study of the effect of parameter variation on a given model. For instance, it is possible to study the effect of a parameter by choosing simulations that are distinguished from each other only by the different values given to this parameter.

The comparison of simulations produced by different simulations brings out the impact of the models. This type of comparison is very complex as the different models do not necessarily use the same parameters. The SYNTH program must thus use equivalence tables between the parameters of the different model to judge the validity of a comparison and to make up a valid heading.

The functions to be compared can either be vectorial (a simulation produces a curve) or scalar (a simulation produces a point on a curve). The vectorial function can be used with the three types of comparison. According to the case, the curves of the comparisons are thus identified by the varying axis, by the distinguishing parameters, by the changing model. The scalar function can be used only in comparisons with simulations produced by a same model. Thus, the effect of a group of parameters can be studied in terms of another. In this case, the simulations providing the points of a curve are distinguished from one another by a group of parameters A defining the horizontal axis of the comparison. The comparison thus involves several curves distinguished from one another by a group of parameters B, group B does not include any of the parameters of A.

The specification of the required type of comparison is done in two steps: first, by indicating which function is to be compared and which are its selectors, second, by indicating the simulations involved in each comparison making up the series. A series is a group of comparisons which have logical bonds and which make up a more or less exhaustive study of a given phenomenon.

In the first step of the specification of a series of comparisons, the user must indicate the identifier of the required function. Next, the user must indicate the name of the axis, its type and the specification of the selected points for each of the axes on which the function depends. There are four possible types to characterize an axis and each type is shown by a letter (S, G, C or M). The specification of the selected points is done by a list of point numbers, and a set of selection separated by commas (in fact, it is the same syntax of the DESRES program, cf. section 5.2). This first step is ended when the user writes a semi-colon instead of a name of axis. For instance:

The S type indicates an axis used to select points of evaluation of the function to be compared. This is the "by default" type, and the symbol S can be omitted. Thus, the function O POWER is selected for all the points on the TAU axis evaluated at point 1 of axis STAT and at point 71 of axis ETA (what the SYNTH program writes is underlined):

```
FUNCTION  O POWER
STAT = S,1
ETA = S,71
TAU = .
;
```

The G type corresponds of an axis giving many comparisons, that is providing comparisons for each of the points selected on the axis. Thus, the following specification:

```
FUNCTION  O POWER
STAT = 1
ETA = G,61,71
TAU = .
;
```

indicates that 2 comparisons of the function O POWER are needed, one for point 61 on the ETA axis and another for point 71.

Type C corresponds to a comparison axis, that is, the impact of this axis on the function to be compared. There can be only one comparison axis for a given function. For instance, the specification:

```
FUNCTION  O POWER
STAT = C (1,7,1)
ETA = 71
TAU = .
;
```

indicates that the comparison contains the function O POWER seven times, once for each of the points selected on the STAT axis.

Finally, type M shows that the user would like to compare the arithmetic mean of the function rather than the function itself. When M qualifies an axis, it means that the arithmetic mean of the function for the points selected on the axis must be evaluated. Thus, in the case of

215

```

FUNCTION  O POWER
STAT = M,(1,7)
ETA = 71
TAU = .
;

```

the user must compare the average of the seven function O POWER selected on the STAT axis.

By analyzing the specification of the first step, the SYNTH program is already able to know some of the user's intentions and thus to determine which informations must be provided at the second step. In other words, if a type C axis is already known, the SYNTH program will automatically know that the comparison is done inside the same simulation and will expect only one simulation number per comparison. Moreover, if the specification of the points selected determine a scalar function (i.e. FUNCTION WIDTH STAT = M,(1,7) ETA = 71), the SYNTH program will conclude that the user wants to study the impact of a group of parameters on another group of parameters. In this case, the SYNTH program must ask the user to specify a list of parameters. Each of the parameters on this list will be used one after the other to define the points of the horizontal axis (axis x) which corresponds to the different simulations that make up the curves to be compared. For instance, in the following case:

PARAMETERS FOR AXIS X: TBRHO, FARUSKA, INVRNL

The program will produce three series of comparisons, one using the values of the TBRHO parameter to form axis x, another using the FARUSKA parameter and finally one using the INVRNL parameter.

The second major step for the definition of the work to be done comes when the series of comparisons are specified. A series includes one or several comparisons making up a logical whole, that is studying the same phenomenon. The SYNTH program produces a heading for each series of comparisons, showing the changes of parameters, of models, or of points on the axes for each of the involved simulations.

Depending on the kind of study, a comparison is made up of one or many simulations, and each simulation is identified by a model and a simulation number (one or several blank spaces separate the two elements). In order to avoid a repetition of the name of the model, the SYNTH program lets the user define, at the beginning of a series of simulation, a model by default.

To end a series of comparisons, the symbol period is used. At this moment, it is possible to redefine another series using the same function specification, or even to return with another point at the level of function specification.

What happens after this identification by "model by default" depends on the type of comparison that the user requires.

If the comparison deals with the same simulation, the program asks the user to indicate the simulation used for each comparison. The following example illustrates a series of these comparisons showing the variations produced by the STAT axis.

```

FUNCTION  O POWER
STAT = C,(1,7)
ETA = 71
TAU = .
MODEL BY DEFAULT: LR1CFS
SIMULATION: 100
SIMULATION: 101
SIMULATION: 102
SIMULATION: .
MODEL BY DEFAULT: .
FUNCTION: .

```

When the comparison studies the impact of certain parameters or of the model on a vectorial function, the SYNTH program will ask the user to give the numbers (at least two) of the simulations making up each comparison in the series. In the following example is defined a series of two comparisons involving three simulations, then a series of one comparison involving three simulations of different models.

```

FUNCTION  O POWER
STAT = M,(1,7)
ETA = 7
TAU = .
;
MODEL BY DEFAULT: LR1CFS
SIMULATIONS: 100,101,102
SIMULATIONS: 110,111,112
SIMULATIONS: .

```

216

```

MODEL BY DEFAULT: LR1CFS
SIMULATIONS: 100,LR1PS 5,LR1P4S 2
SIMULATIONS: .
MODEL BY DEFAULT: .
FUNCTION: .

```

Finally, when the comparison involves a scalar function, the SYNTH program asks the user, first, to indicate the simulations making up the curves, then to indicate which curves make up the comparison (it is possible to define one curve only). The following example shows a series of two comparisons involving three and two curves respectively.

```

FUNCTION: WIDTH (pulse width)
STAT = M,(1,7)
ETA = 71
MODEL BY DEFAULT: LR1CFS
SIMULATIONS MAKING UP THE CURVE
F1: 100,101,102
F2: 103,104,105
F3: 106,107,108
F4: 109,110
F5: 111,112
F6: .
CURVES MAKING UP THE COMPARISON
F1: 1,2,3
F2: 4,5
F3: .
MODEL BY DEFAULT: .
FUNCTION: .

```

By and large, the SYNTH program functions by processing the series of comparisons one by one. Syntactical verifications are done as the specifications are entered. When the definition of a series of comparison is completed, the program verifies the validity of what is requested. If there are no errors at this level, the program makes up the heading of the series. The data needed for this operation comes on the one hand from the series specification that defines the type of comparison requested and, on the other, from the DATSIM files which provide the values of the simulations parameters to be compared. A specific heading is given to each comparison in order to identify each plot. Finally, the comparisons are generated, and the value of the functions to be compared comes either from the DATSIM files (if it contains the needed information) or from the SIMRES files.

Figure 5.12 shows the heading of a series of comparisons, in which the impact of parameters IGVA, IGVB and IGVN on the vectorial function E-R-DR are studied. Figure 5.13 shows a comparison of this series. Figure 5.14 shows the heading of a series of comparisons showing the impact of parameter GLAO in terms of parameter SB on a scalar function. Figure 5.15 shows a comparison of this series.

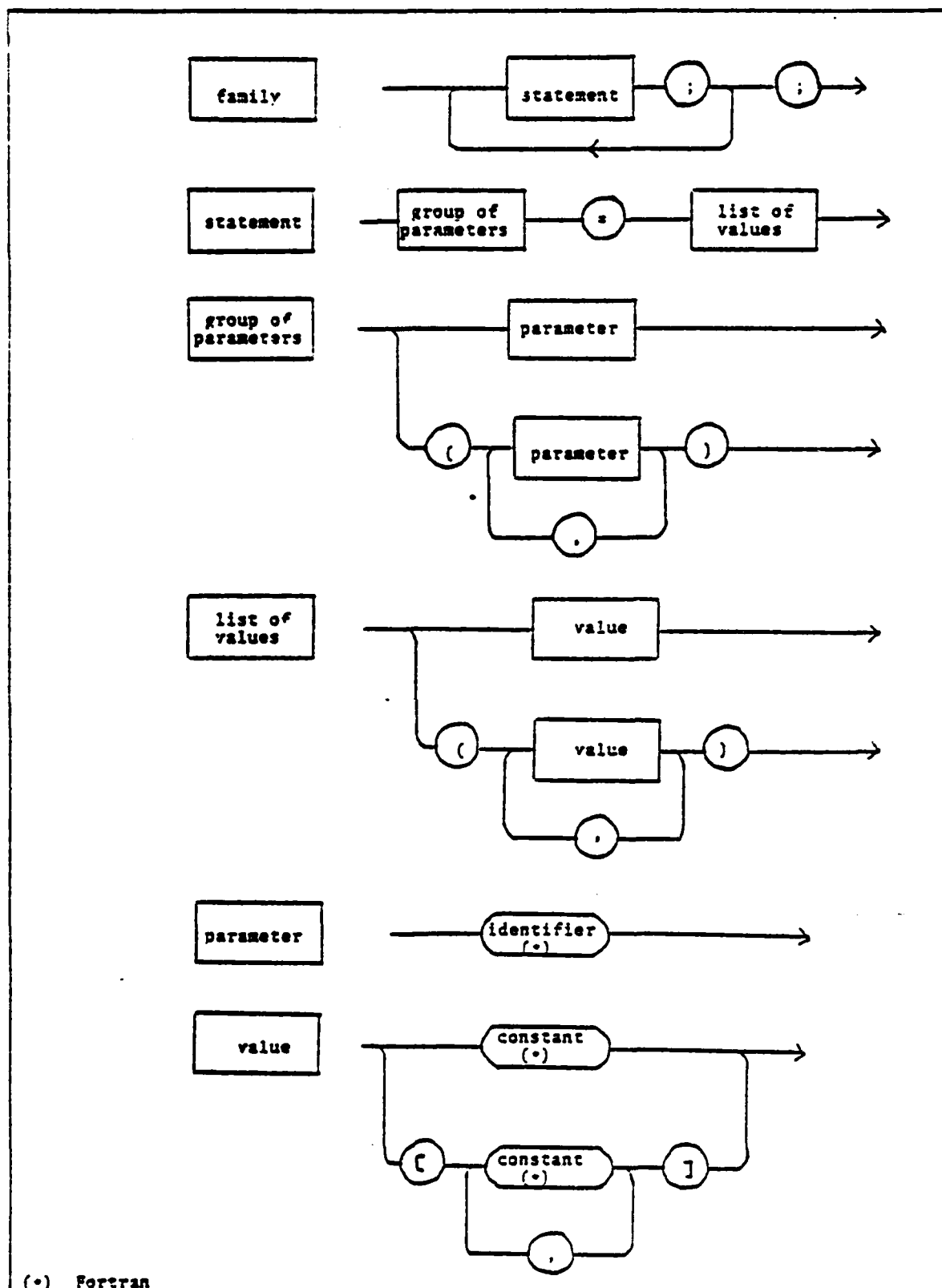


FIGURE 5.1 - SYNTACTICAL CARDS FOR THE SPECIFICATION LANGUAGE FOR THE SIMULATION FAMILIES

```

-PROGRAM DEFPARM 1.0
-HAPPY TO HELP YOU!
-LOAD THE PARAMETERS OF A PREVIOUS SIMULATION ? (YES/NO)
>yes
-GIVE THE NUMBER OF THIS SIMULATION
>312
-LOOKING FOR SIMULATION 312 WAIT A MOMENT PLEASE
-BE PATIENT I'M DOING MY BEST!
-ENTER PARAMETERS AND THEIR VALUES
>;

  - Program output
  > User's input

```

FIGURE 5.2 - CREATION OF A BASE FROM PARAMETER VALUES OF A PREVIOUS SIMULATION

```

-PROGRAM DEFPARM 1.0
-HAPPY TO HELP YOU!
-LOAD THE PARAMETERS OF A PREVIOUS SIMULATION ? (YES/NO)
>no
-LOOKING FOR THE NUMBER OF THE NEXT SIMULATION
-WAIT A MOMENT PLEASE
-ENTER PARAMETERS AND THEIR VALUES
>idimen= 1;
>( ideltas , ideltab. ) =
>( 1, 1 ) ;
>( 0, 0 ) ;
>toto = ab
-TOTO = AB
-*****
-ERROR NUMBER: 12
-THE GIVEN PARAMETER IS UNKNOWN
I.E. WAS NOT FOUND IN THE LIST OF PARAMETERS USED IN PREVIOUS SIMULATION)
-PLEASE RETYPE LINE FROM THE BEGINNING
>sla0 = 125.0 , 250.0, 375.0 ;
>ctsrhoa = 4.236669, 8.7;;

  - Program output
  > User's input

```

FIGURE 5.3 - USER'S SPECIFICATION OF A FAMILY OF SIMULATIONS

SIM#	IDIMEN	IDELTAA	IDELTAB	GLAO	TERHOA
649	1	1	1	125.0	4.236669
650					8.7
651				250.0	4.236669
652					8.7
653				375.0	4.236669
654					8.7
655		0	0	125.0	4.236669
656					8.7
657				250.0	4.236669
658					8.7
659				375.0	4.236669
660					8.7

>CORRECTIONS (YES/NO) ?

-yes

-FOR MODIFICATION ENTER NEW VALUE(S) OF PARAMETER(S) LISTED

-"." MEANS NO MODIFICATION

-"." MEANS END OF MODIFICATION

-NUMBER OF THE FIRST SIMULATION

>:

-IDIMEN =

>:

-(IDELTAA,IDELTAB) =

>(1,1),(2,2);

-GLAO =

>:

SIM#	IDIMEN	IDELTAA	IDELTAB	GLAO	TERHOA
649	1	1	1	125.0	4.236669
650					8.7
651				250.0	4.236669
652					8.7
653				375.0	4.236669
654					8.7
655		2	2	125.0	4.236669
656					8.7
657				250.0	4.236669
658					8.7
659				375.0	4.236669
660					8.7

>CORRECTIONS (YES/NO) ?

-no

FIGURE 5.4 - CORRECTION PHASE OF THE DEFPARM PROGRAM

```

SDATA NUMBER=649,
IDIMEN=1, IDeltaA=1, IDeltaB=1, GLAO=125.0,
TSRHOA=4.236669,
$
SDATA NUMBER=650,
IDIMEN=1, IDeltaA=1, IDeltaB=1, GLAO=125.0,
TSRHOA=8.7,
$
SDATA NUMBER=651,
IDIMEN=1, IDeltaA=1, IDeltaB=1, GLAO=250.0,
TSRHOA=4.236669,
$
SDATA NUMBER=652,
IDIMEN=1, IDeltaA=1, IDeltaB=1, GLAO=250.0,
TSRHOA=8.7,
$
SDATA NUMBER=653,
IDIMEN=1, IDeltaA=1, IDeltaB=1, GLAO=375.0,
TSRHOA=4.236669,
$
SDATA NUMBER=654,
IDIMEN=1, IDeltaA=1, IDeltaB=1, GLAO=375.0,
TSRHOA=8.7,
$
SDATA NUMBER=655,
IDIMEN=1, IDeltaA=2, IDeltaB=2, GLAO=125.0,
TSRHOA=4.236669,
$
SDATA NUMBER=656,
IDIMEN=1, IDeltaA=2, IDeltaB=2, GLAO=125.0,
TSRHOA=8.7,
$
SDATA NUMBER=657,
IDIMEN=1, IDeltaA=2, IDeltaB=2, GLAO=250.0,
TSRHOA=4.236669,
$
SDATA NUMBER=658,
IDIMEN=1, IDeltaA=2, IDeltaB=2, GLAO=250.0,
TSRHOA=8.7,
$
SDATA NUMBER=659,
IDIMEN=1, IDeltaA=2, IDeltaB=2, GLAO=375.0,
TSRHOA=4.236669,
$
SDATA NUMBER=660,
IDIMEN=1, IDeltaA=2, IDeltaB=2, GLAO=375.0,
TSRHOA=8.7,
$
..

```

FIGURE 5.5 - NAMELISTS PRODUCTS OF THE DEFARM PROGRAM

```

PROGRAM: LRICPS
SIMULATIONS: 1-5, 7, 12
FUNCTION: Energy
select STAT = TOUS (ALL)
select EIA = (1, 71, 10)
select RHO = (1, ., 2)
select TAU = (3, .)
SCALE : STANDARD
PLOT : PLOT 3D
SCALE : STANDARD
PLOT : CONTOUR
SCALE : FIN (END)
FUNCTION: 0 POWER
select STAT = TOUS
select EIA = (1, 71, 10)
select TAU = (3, .)
SCALE : STANDARD (STAT)
PLOT : PLOT 2D
SCALE : FIN (END)
FUNCTION: FIN
SIMULATIONS: FIN
PROGRAM: FIN

```

FIGURE 5.6 - PLOT SPECIFICATION FOR THE DESPES PROGRAM

DOUBLE LASER SIMULATION

NUMERO = 626.

LASER: A

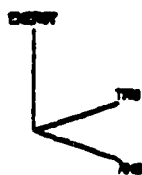
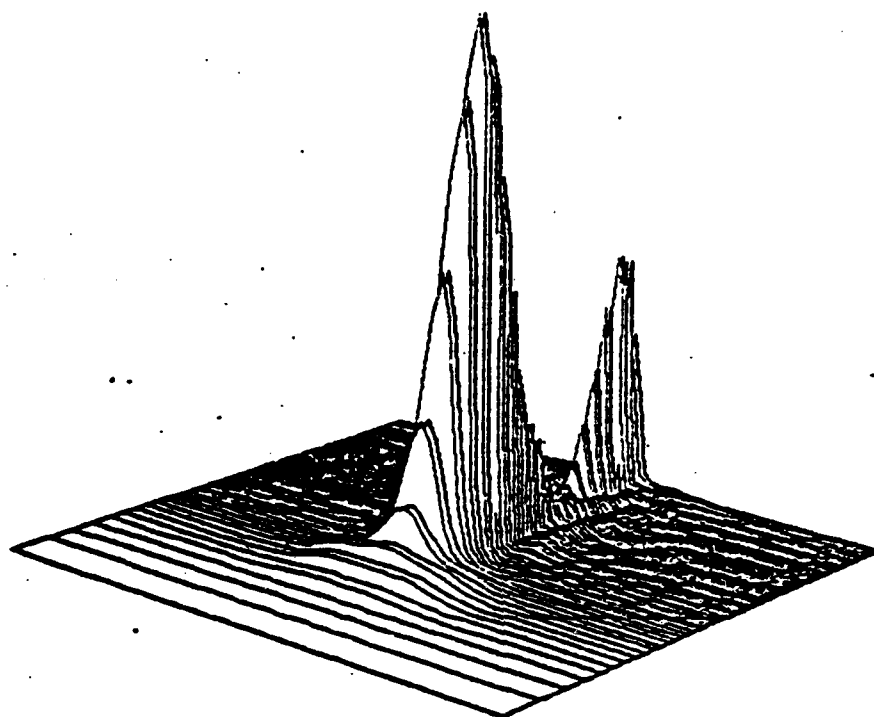
PARAMETERS

LASERA	= 1.	LASERB	= 1.
PHICR	= .31417817E+01.	PHICB	= .31417817E+01.
PHICR	= 0.0.	PHICB	= 0.0.
IBCR	= 1.	IBCB	= 1.
IBCR2	= 0.	IBCB2	= 0.
CIR	= .832E-03.	CIB	= .8E-01.
IGVA	= 1.	IGVB	= 1.
QIR	= .78E+01.	QIB	= .225E-03.
QIRFCT	= .1E+01.	QIBFCT	= .1E+01.
IGVFCTA	= 0.	IGVFCTB	= 0.
TERHOB	= .4236669E+01.	TERHOB	= .4236669E+01.
IRHOB	= 0.	IRHOB	= 0.
SIGMA	= -.99E+00.	SIGMB	= -.1E-03.
IDELTA	= 0.	IDELTAB	= 1.
OLNB	= 0.0.	OLNB	= 0.0.
OPHAB	= .1E+01.	OPHAB	= .1E+01.
SA	= .1E+01.	SB	= 0.0.
TBMA	= .5E+00.	TBMB	= .5E+00.
RKAPPA	= 0.0.	RKAPPA	= 0.0.
TAUC	= .7E+01.	TAUC	= .7E+01.
TININVA	= .125E-01.	TININVB	= .125E-01.
TZINVA	= .142857E-01.	TZINVB	= .142857E-01.
PHISTOA	= 0.0.	PHISTOB	= 0.0.
ISTPHIA	= 0.	ISTPHIB	= 0.
CLVA	= 0.0.	CLVB	= 0.0.
RKPLNA	= 0.0.	RKPLNB	= 0.0.
IDISTRA	= 0.	IDISTRB	= 0.
EPSILNA	= .1E+01.	EPSILNB	= .7E-03.
TZINVC	= .142857E-01.	LOCN	= 0.
TAUCF	= .4E+01.	TAUCF	= .5E+01.
WINCON	= .21E+02.	IDIMEN	= 3.
KSAVE	= 34.	MORVE	= 32.
JSAVE	= 300.	JSTEP	= 4.
HR	= .17867142867143E-01	HS	= .625E-03.
NR	= 32.	NAT	= 97.
INLR	= 1.	NERUNS	= 1.
IST	= 2.	ISR	= 2.
LUPPBN	= 0.	LEVEL	= 1.

FIGURE 3.7 - LIST OF PARAMETERS IDENTIFYING THE PLOTTED SIMULATION

LASERX VERSION 1.7 - LASERA

GRAF30 PAGE 2

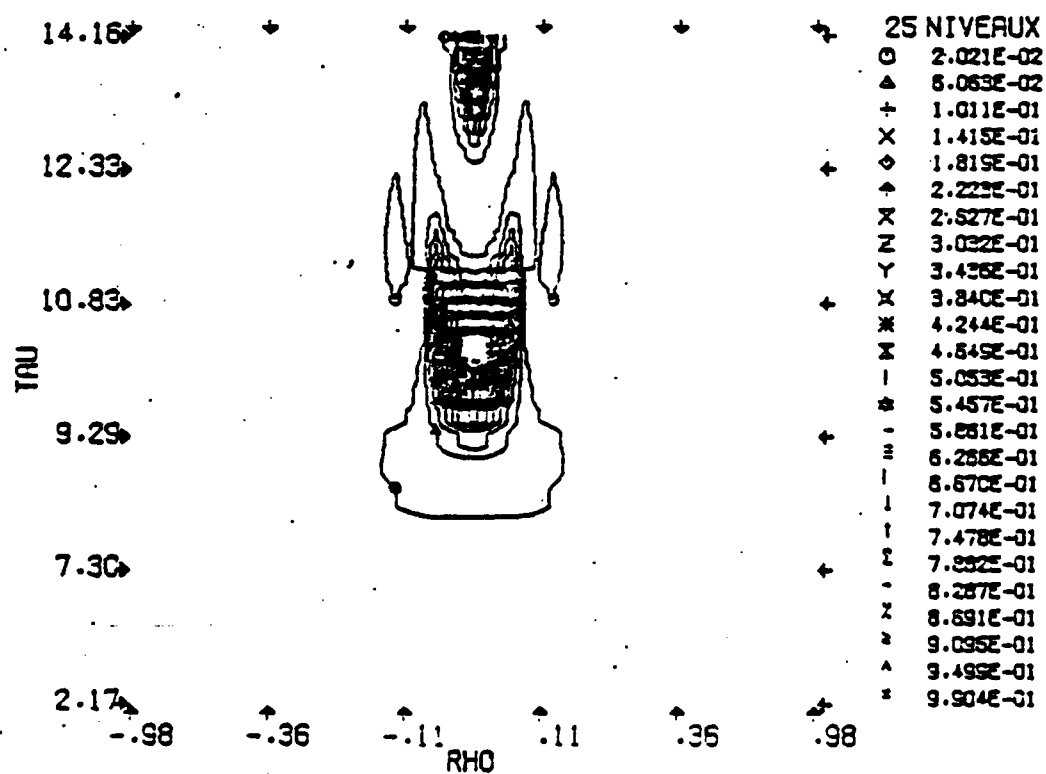


YMAX 1.0106
YMIN 0.0000

ENERGY

IG 71 / 75 NO 626
ETA 35.5000 PARTIEL

FIGURE 5.8 - PLOT DRAWN BY PLOT 3D FOR A 3 VARIABLE FUNCTION



YMAX 1.0106
YMIN 0.0000

ENERGY

IG 71 / 75 NO 626
ETA 35.5000 PARTIEL

FIGURE 5.9 - CURVES SET BY THE CONTOUR PROCEDURE FOR A 2 VARIABLE FUNCTION

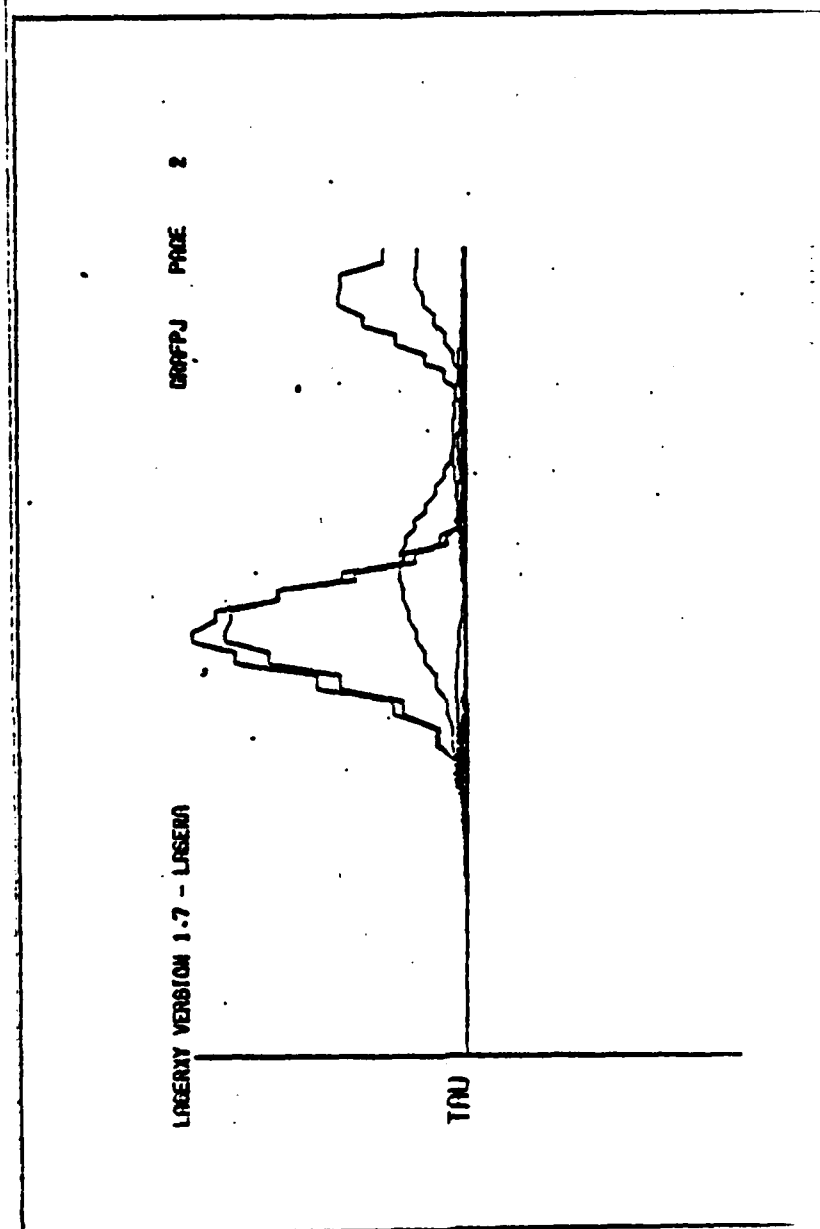


FIGURE 5.10 - PROJECTION OF A 2 VARIABLE FUNCTION
BY PROJEC

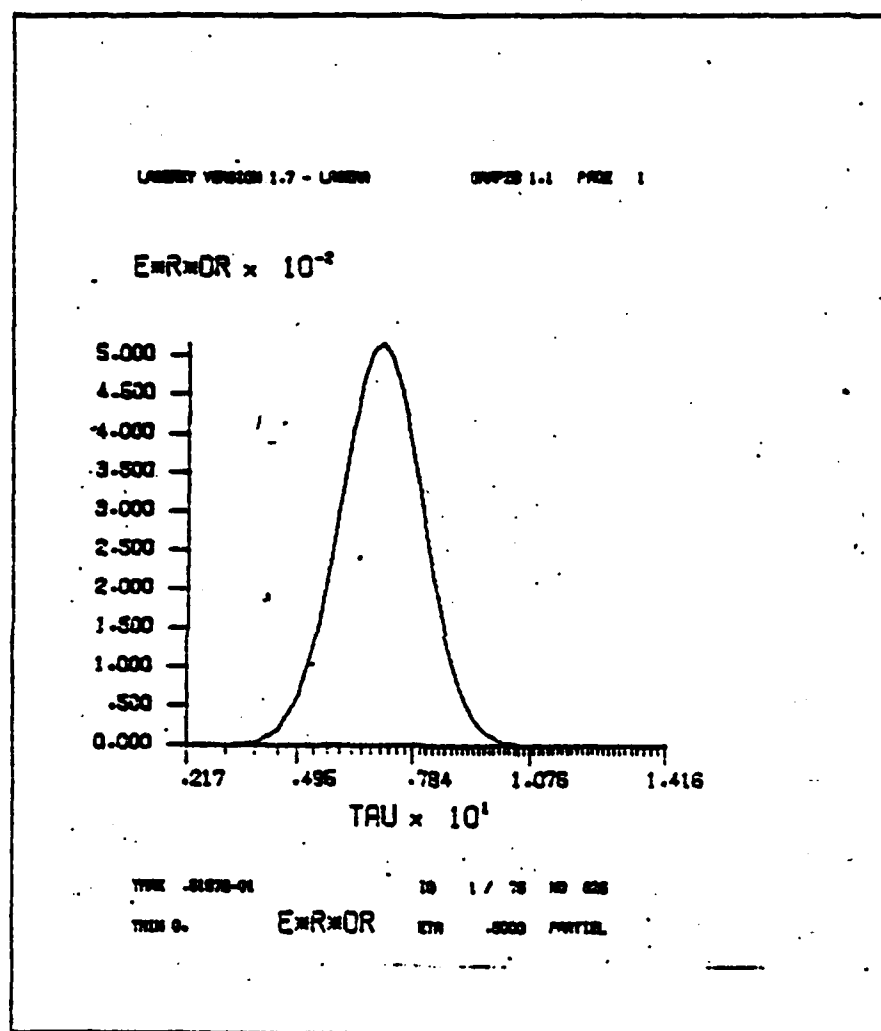


FIGURE 5.11 - PLOT PRODUCED BY PLOT 2D FOR A FUNCTION WHICH VARIES AS TO ONE AXIS

COMPARISON

SERIE 95 (NUMBER 1)
WITH NORMALIZATION

NUMBER	IGVA	IGVB	IDGN		
410.	1.	1.	0.		
580.	0.	0.	0.		
584.	0.	0.	1.		
LASERA	= 1,			LASERB	= 1,
PHIOA	= .3141782E-01,			PHIOB	= .3141782E-01,
PHI2A	= 0.0,			PHI2B	= 0.0,
IBCA	= 1,			IBCB	= 1,
IBCA2	= 0,			IBCB2	= 0,
CLA	= .632E-03,			CIB	= .8E-01,
GLAO	= .75E+01,			GLBO	= .275E+03,
GLAFCT	= .1E-01,			GLBFCT	= .1E+01,
IGVFCTA	= 0,			IGVFCTB	= 0,
TBRHOA	= .4236669E+01,			TBRHOB	= .4236669E+01,
IRANDA	= 0,			IRANDB	= 0,
SIGNA	= -.99E+00,			SIGNB	= -.1E-03,
IDELTAA	= 1,			IDELTAB	= 1,
DNNA	= 0.0,			DNNB	= 0.0,
GAMMAA	= .1E-01,			GAMMAB	= .1E-01,
SA	= .1E+01,			SB	= 0.0,
TBNA	= .5E+00,			TBNB	= .5E+00,
RKAPPAA	= 0.0,			RKAPPAB	= 0.0,
TAUCA	= .7E+01,			TAUOB	= .7E+01,
TININVA	= .125E-01,			TININVB	= .125E-01,
T2NINVA	= .14236E-01,			T2NINVB	= .14286E-01,
PHISTDA	= 0.0,			PHISTDB	= 0.0,
ISTPHIA	= 0,			ISTPHIB	= 0,
CURVA	= 0.0,			CURVB	= 0.0,
RKPLONA	= 0.0,			RKPLONB	= 0.0,
IDISTRA	= 0,			IDISTRB	= 0,
EPSILNA	= .1E-01,			EPSILNB	= .1E-02,
T2NINVC	= .14236E-01,			TAUSF	= .4E-01,
TAUOCT	= .9E+01,			WINDOW	= .21E+02,
IDIMEN	= 3,			KSAVE	= 64,
MSAVE	= 32,			JSAVE	= 300,
JSTEP	= 4,			HR	= .17857E-01,
HS	= .625E-03,			NA	= 32,
NAT	= 57,			INLR	= 1,
NBRUNS	= 1,			IST	= 2,
ISR	= 2,			IPUMPSH	= 0,
ILEVEL	= 1,			BETAA	= .474E-02,
BETAS	= .22E+02,			FARUSKA	= .8608E-01,
FARUSKB	= .394886013E+03,			INFRNLA	= .11344E-01,
INFRNLB	= .1435949E+01,			LGPHIOA	= .3723432E+01,
LGPHIOB	= -.3723432E+01,			IGVNEGA	= 0.0,
IGVNEGB	= 0.0,			IGVPOSA	= -1,
IGVPOSB	= -1,			LGPHSOA	= .13863943E+02,
LGPHSQB	= .13863943E+02,			INGIASQ	= .17779E-01,
INGIBSQ	= .13E-04,			INVGLAO	= .133333E+00,
INVGLBO	= .3636E-02,			GLAOSQ	= .5625E+02,
GLBOSO	= .75625E+05,			INVCIA	= .1562278481E+04,
INVCIB	= .125E+02,			RCGLAO	= .2738613E+01,
RCGLBO	= .18583124E+02,			AKAPPAA	= .6170670064E+04,
AKAPPAB	= .48748294E+02,			TAURA	= .713489E+00,
TAURB	= .19459E-01,			TAUSA	= .322756009E+03,
TAUSB	= .177267E+00,			GLRA	= .3508E-01,
GLRB	= .384886013E+03,			ALPHA	= .25E+00,
ALPHAB	= .9156667E+01,				

FIGURE 5.12 - HEADING OF A SERIES OF COMPARISONS IN WHICH THE IMPACT OF PARAMETERS IGVA, IGVB AND IDGN ON THE VECTORIAL FUNCTION E-R-DR ARE STUDIED

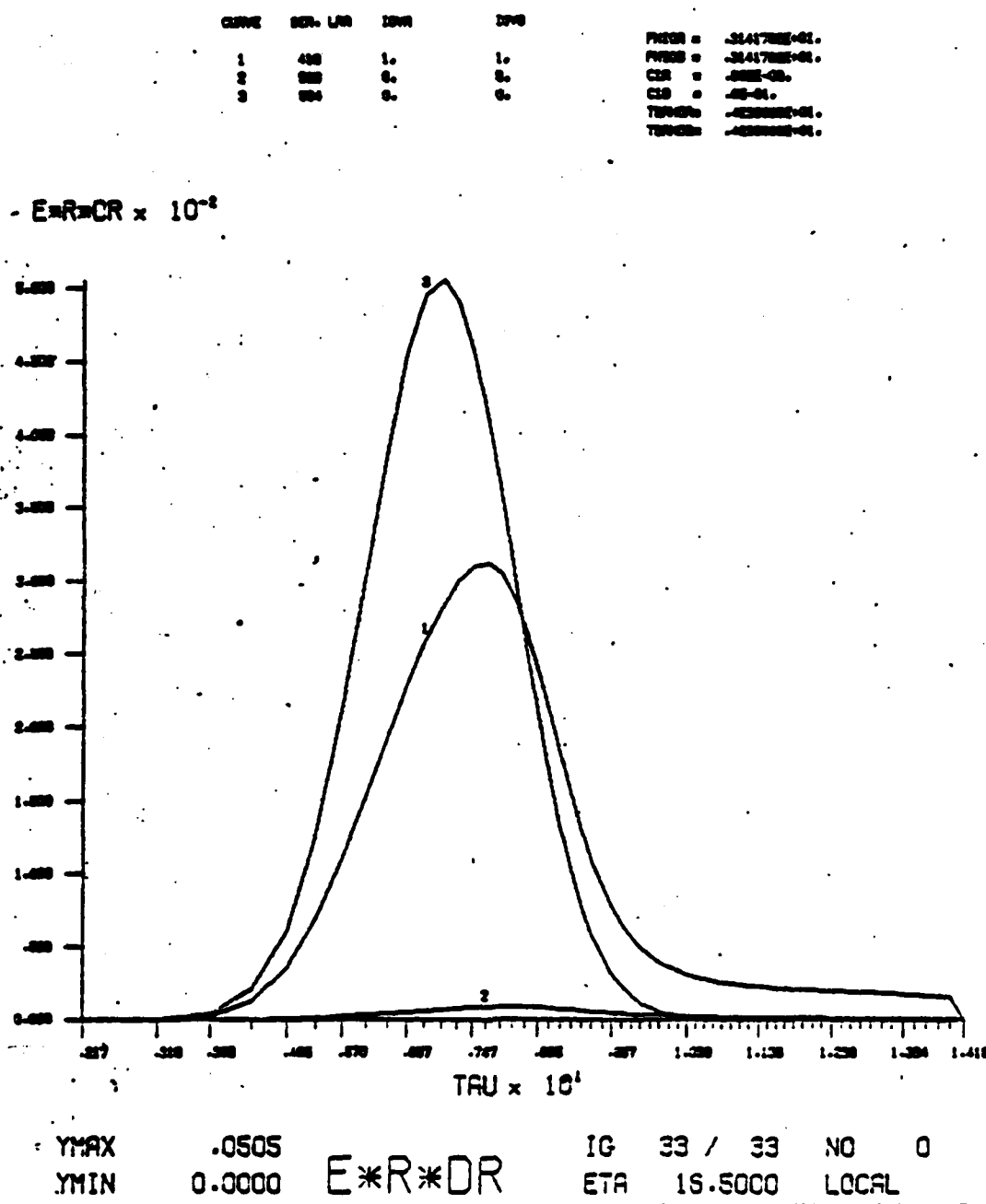


FIGURE 5.13 - COMPARISON OF A SERIES OF COMPARISONS IN WHICH THE IMPACT OF PARAMETERS IGVA, IGVB AND IGVN ON THE VECTORIAL FUNCTION $E \cdot R \cdot DR$ ARE STUDIED

COMPARISON

7. GLAO VS SB (CF. COMPARISON 27)

A) CONSTANT PARAMETERS

PARAMETER	VALUE	PARAMETER	VALUE
LASERA	= 1	LASERB	= 1
PHIOA	= 3.1417817	PHIOB	= 3.1417817
PHI2A	= 0.0	PHI2B	= 0.0
IBCA	= 0	IBCB	= 0
IBCA2	= 0	IBCB2	= 0
CIA	= .08	CIB	= .000632
IGVA	= 1	IGVB	= 1
GIBO	= 6.25	GLAFCT	= 1.0
GLBFCT	= 1.0	IGVFCTA	= 0
IGVFCTB	= 0	TBRHOA	= 4.236669
TBRHOB	= 4.236669	IRANDA	= 0
IRANDB	= 0	SIGNA	= -1.0
SIGNB	= -1.0	DWNA	= 0.0
DWNB	= 0.0	GAHAA	= 1.0
GAMBAB	= 1.0	SA	= 0.0
TBWA	= .5	TBWB	= .5
RKAPPAA	= 0.0	RKAPPAB	= 0.0
TAUOA	= 7.0	TAUOB	= 7.0
TININVA	= .0125	TININVB	= .0125
T2NINVA	= .0142857	T2NINVB	= .0142857
PHISTDA	= 0.0	PHISTDB	= 0.0
ISTPHIA	= 0	ISTPHIB	= 0
CURVA	= 0.0	CURVB	= 0.0
RKPLONA	= 0.0	RKPLONB	= 0.0
IDISTRA	= 0	IDISTRB	= 0
EPSILNA	= .001	EPSILNB	= 1.0
T2NINVC	= .0142857	IDGN	= 0
TAUSE	= 4.0	TAUOCT	= 9.0
WINDOW	= 21.0	IDIMEN	= 3
XSAVE	= 64	MSAVE	= 32
JSAVE	= 300	JSTEP	= 4
HR	= .017857142857	HS	= .000625
NA	= 32	NAT	= 57
INLR	= 1	NBRUNS	= 1
IST	= 4	ISR	= 2
IADRHQ	= 0	IPURPSH	= 0
ILEVEL	= 1		

B) PARAMETERS VARYING ON A CURVE

	GLAO
1.	225.0
2.	275.0
3.	325.0

C) PARAMETERS VARYING BETWEEN CURVES

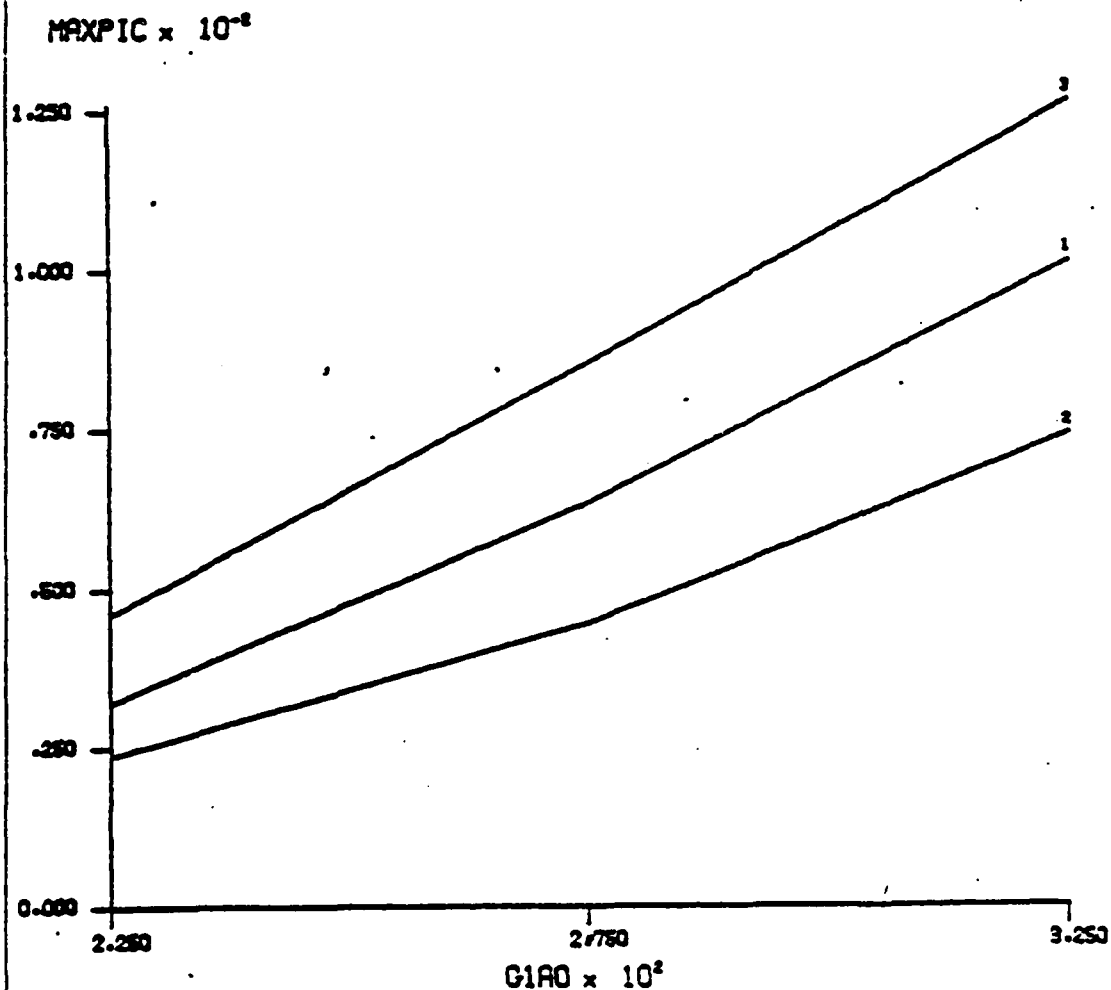
CURVE	SB
1	1.0
2	2.0
3	3.0

D) SIMULATIONS USED IN CURVES

CURVE	SIMULATIONS
1	498 501 504
2	345 351 357
3	348 354 360

FIGURE 5.14 -
HEADING OF A SERIES OF
COMPARISONS SHOWING THE
IMPACT OF PARAMETER
GLAO IN TERMS OF PARA-
METER SB ON A SCALAR
FUNCTION.

ORIG. LAYER. LAYER 1	ORIG. COORDINATES	SB	FLUX
1	400. 000. 304	1.0	00
2	300. 300. 307	2.0	00
3	300. 304. 300	3.0	01



YMAX	.0125	MAXPIC	IG	61 / 65	NO	0
YMAX	.0024		ETA	30.5000	LOCAL	

FIGURE 3.15 - COMPARISON OF A SERIES OF COMPARISONS SHOWING THE IMPACT OF PARAMETER G1A0 IN TERMS OF PARAMETER SB ON A SCALAR FUNCTION

VI - THE LASER PROGRAMS

Even though the laser simulation programs do not in themselves form the core or the basis of the system presented here, they remain nevertheless its fundamental motivation. It should be noted that the different softwares and programs making up the system are general enough to process several different problems. The SIMRES for instance can process any program using numerical integration for result calculations. Therefore, it seemed necessary to devote a whole chapter to discuss the production and resolution problems faced in the laser simulation programs.

It will not be possible to give here a detailed explanation of the physics and the numerical techniques used to solve the diverse differential equations in these programs. These two aspects will only be touched up descriptively in order to place the programs in their proper context.

This chapter is divided in four parts:

- 1 - the first part is a summary description of the programs with an overview of their particular techniques,
- 2 - the second part deals with the general characteristics of the programs: documentation, modularity, etc.,
- 3 - the third discusses the problems of validity and reliability of the programs,
- 4 - the last part shows how the problems created by the constraints of memory were resolved and how the performance of the programs was increased.

6.1 DESCRIPTION OF THE LASER SIMULATION PROGRAMS

Even though each program is essentially different from the other, all the programs use similar numerical techniques to solve the nonlinear propagation equations (Maxwell) and the atomic equations (Bloch). These equations are solved simultaneously by a dynamic predictor/corrector algorithm: the predictor used generally is the explicit method of the middle point (Euler's modified formula), the corrector used is the trapezoid.

Moreover, nonlinearly defined axes (transverse axes, temporal axes) are used in order to increase the efficiency of the predictor/corrector algorithm. These axes determine a non-uniform multi-dimensional meshing that show, around the focal point along the propagation axis, the interesting phenomena of the beam. Depending on the choice and the nature of the phenomena studied, this non-uniform meshing can be calculated statistically either at the beginning of the simulation or redefined locally as the simulation is in progress (dynamic adaptation) to check the rapid changes in self-focusing.

The names of the laser simulation programs follow these conventions:

- a - the prefix LR means Laser R;
- b - the number following the prefix indicates the number of lasers used in the simulation;
- c - the letter immediately following this number shows the implication of radial symmetry (C for Cylinder, thus one transverse axis) or its absence (P for Parallelepiped, thus two transverse axes, x and y);
- d - the letters or numbers that follow denote the principal characteristics of the program.

Also, the axes used in the different programs are designated as follows:

- longitudinal axis of the cylinder or parallelepiped: axis z;
- radial symmetry axis of the cylinder: axis r;
- Cartesian transverse axes of the parallelepiped: axis x and axis y;
- temporal axis: axis t;
- axis of frequencies: axis ω .

Following is the description of the laser simulation programs already integrated in the system and using the SIMRES software to produce the simulation results.

1) The LR1CFS program (P for frequency and S for statistics): the simulation is defined by the z, r, t, ω axes. The model is based on the scalar wave equation coupled to the two-level resonant atomic system without degeneracy. This program offers the following options:

- the possibility of inclusion of the transverse effects (activation of the r axis of the cylinder): this shows the increase in the inhomogeneities and the importance of the nonlinear dispersion and the nonlinear absorption;
- the possibility of inclusion of the quantum fluctuations in the medium initiation for superfluorescence evolution (activation of statistics calculations);
- possibility of inclusion of the "extended" Doppler effects (activation of the u axis associated with the atomic system).

It is also possible to include in this simulation all these possibilities at the same time.

2) The LR1PS program (S for statistics): the simulation is defined by the z , x , y , t axes. This model is essentially the same as the one used in LR1CFS without the inclusion of the extended Doppler effects into the program. The following characteristics should be noted however:

- the transverse axes x and y are only defined for the positive quadrant: i.e., the x axis is defined from 0.0 to x_{\max} and the y axis is defined from 0.0 to y_{\max} ;
- the transverse effects on one axis can be activated without necessarily activating the transverse effects on the other axis;
- the maximal delimiter chosen on the x axis (x_{\max}) can be different from the maximal delimiter (y_{\max}) on the y axis: this allows for a larger choice of situations.

3) The LR1P4S program (S for statistics and 4 to indicate that the transverse axes cover the four quadrants): the simulation is defined by the z , x , y and t axes. This model is identical to the one used in the LR1PS program except for the two following points:

- the transverse effects cannot be removed: i.e., the x axis is necessarily defined from $-x_{\max}$ to x_{\max} and the y axis is defined from $-y_{\max}$ to y_{\max} ;
- the minimal and maximal delimiters of the two axes are equal to one another, i.e., $-x_{\max} = -y_{\max}$ and $x_{\max} = y_{\max}$.

4) In the LR12C program, the simulation is defined by the z , r , t axes. This model is based on two scalar equations of the propagation movement defined by 2 intense ultra-wave laser beams propagating simultaneously through a gas of three-level atoms. This model shows the interaction between the two beams and how they influence each other. This program allows for the possibility of inclusion of the transverse effects on the simulation.

The following programs are not yet integrated to the system but will soon be added to the four programs described above.

5) The LR2CFS program (F for frequency and S for statistics): the simulation is defined by the z , r , t , u axes. The model used here is essentially the same as the one described in LR2C except that, as in the LR1CFS program, it offers the following options:

- the possibility of including transverse effects;
- the possibility of including statistical calculation (quantum fluctuations);
- the possibility of including the extended Doppler effects.

When this program will be integrated to the rest of the system, it will completely replace the LR2C program.

6) The LR1CC program (C for chemistry): this simulation is defined by the z , r , t axes. The model is similar to that used in the LR1CFS program but with a more refined atomic configuration system to allow for a six of ten levels of absorption. This model thus permits the study of the effects of coherent propagation in the multi-level atomic configuration such as Europium.

7) The LR1PH program (H for hydrodynamic): the simulation is defined by the z , x , y axes. This model is based on a hydrodynamic formulation. In order to avoid the oscillatory behavior resulting from the decomposition of the electrical field into its real and imaginary parts, it is necessary to describe the field by using the modulus and the phase, or equivalently, by using the field energy and the transverse gradient of its phase. The evolution of the beam can thus be seen as a flowing fluid whose density is proportional to the field energy and whose velocity is proportional to the gradient of the phase. This description leads to a generalized Navier-Stokes equation of motion for a compressible fluid subjected to an internal potential which depends solely and nonlinearly on fluid density and its derivatives.

8) The LRICP program (P for plasma): the simulation is defined by the z , r axes. This is based on a simplified LRICFS program: the transient effect is eliminated and the temporal variation is disregarded, what is calculated here is the asymptotic effects and adiabatic approximation response of the atomic field (off-resonance). The nonlinear field is characterized by an analytical susceptibility where the light-matter interaction is instantaneous (unlike the model used by the LRICFS program). This nonlinearity is cubic in nature: thus the Kerr effect. However, this effect can be corrected and limited by a saturation or even by a nonlinear exponentiality. The laser can therefore describe the evolution of the electromagnetic field in a plasma medium governed by these kinds of nonlinearities.

9) The LRIPP program (P for plasma): the simulation is defined by the z , x and y axes. It is essentially the same model as the one described in 8) but without the radial symmetry.

10) The LRICT program (T for transistor): the simulation is defined by the z , r and t axes. The model used here is based on the following approach: when two waves going in opposite directions (a forward wave and a backward wave) interact coherently with each other and with a medium resonant to the pulse frequency, this pulse adapts itself longitudinally and transversely during the simulation. The dynamic cross-coupling of these two waves appears explicitly in a two-mode equation analogous to the traditional one-mode Bloch equation describing the two-level absorption system. The variation of phase and the amplitude of the linear field polarized in the transverse direction are described by two wave equations, one for each mode: forward travelling propagation and backward travelling propagation. The equations derive from the Maxwell equation comprising the transverse and transient phase variations. ω denotes the spatial frequency harmonics associated with the standing wave nature of the field.

The algorithm used to solve these equations is a generalization of Moretti's scheme for the integration of the Euler equation of compressible flow. It is an explicit algorithm which demands a simultaneous integration along the t axis for both waves and which also takes into consideration the directional derivations to check the mutual influence of the two waves while respecting the law of forbidden signals. The program thus allows a unified simulation of the soliton collision, of the two-wave superfluorescence and of the optical instability phenomena in a nonlinear Fabry Perot cavity.

11) The LRICI program (I for implicit): the simulation is defined by the z , r and t axes. The model used here is similar to those used for the LRICFS and the LRICC programs, however this model uses an implicit efficient algorithm with dynamically adapting grids: to achieve a greater stability and a greater exactitude, in many cases, the algorithm is obtained by expressing the variable on the left side of a given equation in terms of an integral on the variables on the right side of that equation. The field equation solution is determined in terms of average quantities that varies less rapidly than the original variables. Every mesh point is determined with the associate neighboring points: the resulting triadiagonal Bloch matrix is solved by recurrence method.

The program offers the possibility of studying the influence of diffraction, of density variation and of the inertial response in a multi-level system for a large number of experimental parameters.

6.2 GENERAL CHARACTERISTICS OF THE LASER SIMULATION PROGRAMS

Several problems arise from the frequent modifications, from the handling by different users and from the transportation and implantation of these programs into other computers. These problems can be summarized as follows:

- general comprehension of the programs;
- detailed comprehension of the code;
- ease of program modification;
- transportability of the programs.

In order to answer all these requirements, the programs must adhere to certain basic criteria which make their manipulation and maintenance easier; these are:

- the documentation of the programs;
- the use of standard FORTRAN;
- the modularity of the programs.

It is important to point out here that all the laser simulation programs as well as the softwares presented here adhere to these requirements.

6.2.1 DOCUMENTATION

Following is presented the complete description of these programs when dealing with the above mentioned requirements of general comprehension.

- the principal program includes a summary description of the model used and a complete description of its algorithm;
- all the physical parameters (program data) are adequately reported;
- each subroutine of the program has a detailed description of its role in the program and, if need be, of its algorithm;
- the code of the principal program is reported in its smallest detail;
- all the global variables of the program (i.e. variables in the commons) and specific to the subroutines, as well as their parameters, are explicitly described as per their usage.

Not only is a proper and extensive documentation a time-saving device but it also allows a more detailed analysis of the program at hand.

6.2.2 TRANSPORTABILITY

The laser simulation programs can be installed on different kinds of computers, therefore they must be easily transportable. As a general rule, and whenever possible and feasible, these programs are coded in standard Fortran (ANSI).

Thus all the programs use identifiers (i.e. names of subroutines, variables, parameters, etc.) with at the most six alphanumeric characters: in fact, most Fortran programs installed in computers other than CDC or CRAY do not permit more than the maximum six characters allowed by the standard Fortran. Nevertheless, some non-standard statements, such as GOTO, the PROGRAM declaration, the indices in form of expression, etc., can also be used because most Fortran language processor accept these statements.

It is worth noting that the use of standard statements was promoted by the criterion of majority. The only exception to this is the BUFFER IN and BUFFER OUT used for pagination done for efficiency. More information about this will be given in section 5.4.

6.2.3 MODULARITY

The first advantage of modularity is the simplicity and clarity it brings to the program; that is: in the laser simulation programs, a subroutine performs only one precise task. For example: the C1DTAU subroutine of the LRICFS program deals with the calculations of the temporal axis and of its derivatives. The second advantage of modularity resides in the ease of introducing additions, modification or corrections to the program. In fact, when a program has been cut into simple functional and independent modules, its model can be refined (thus a new code) without upsetting all its structure. Moreover, any modification to the program will remain localized (i.e. modifying a numerical integration algorithm for a function) and its effects will be better understood; in other words, the risks of unexpected errors, produced by these modifications, will be considerably diminished.

Following is the general diagram of the LRICFS program (figures 6.2.1, 6.2.2 and 6.2.3).

6.3 MANAGEMENT CONTROL AND VALIDITY OF THE RESULTS

Two interdependent problems result from the relatively frequent modification to the laser simulation programs, whether these modifications are for the improvement of the performance or for refining the models at hand. These problems are:

- the minimization of errors due to modifications to the program;
- verification of the validity of the results.

6.3.1 HANDLING AND MANAGING THE PROGRAMS

All the laser simulation programs are controlled by the CDC UPDATE program which produces program libraries. Thus it is possible to keep a complete inventory of the programs and to retrieve anterior versions as each new modification to the programs generates a new version.

This method offers the advantage of:

- controlling the results: one is certain that a specific result was produced by a precise version of the program and the relevance of this result is verified in its production context;
- controlling all the modifications effected to the program over a period of time. It is thus possible to have a detailed verification of the code if there is a need to check the compatibility of certain results with others, previously produced.

Another advantage resides in the fact that all the laser simulation programs are centralized on the same file. Moreover, because it is necessary to use the UPDATE program to make any modification or addition to these programs, their manipulation must be very precise. It follows that the errors (accidental destruction of files, presentation of a wrong program), and the proliferation of more or less similar programs (i.e. different versions) stored on several different files are kept to a minimum, this in spite of the fact that a programmer always tends to create working space by using several files.

Given its facility and its great security, this practice has encompassed all the programs and software presented in this paper.

6.3.2 RELIABILITY OF THE PROGRAMS AND VALIDITY OF THE RESULTS

Validity of the results is one of the trickiest problems to deal with. Usually, a semantically faulty program will blow up, sometimes however the program will run till the end and produces completely wrong results. A program using integration techniques with slow evolving numerical values may be quite resistant to such minor errors as the use of a wrong constant in an equation or a wrong sign. The problem is then to recognize the wrong results.

The surest way of verifying the validity of the results is to test the program with previously obtained results known as valid. There is the possibility that the results obtained in the new version may not be strictly identical to the previous results (results are said to be identical when, for a given function and a given point, all the significant numbers are identical) however these may not be necessarily wrong. Indeed, if any modification to the program dealt with the numerical algorithm, or even with the order of certain calculations, the results will be slightly different (for example, only the first significant n numbers in the two versions agree). It is thus necessary to establish a percentage below which the results may be considered as valid and above which these can be seen as doubtful.

Moreover, one test only may be quite inadequate when dealing specifically with the reliability of the programs. With the introduction of modifications to the statistics of the LR1CFS program for instance, it will be necessary to determine whether the new version will function with or without the transverse effects, with or without frequencies. A minimum of four tests will be necessary in order to ascertain the proper running of the program. According to the importance of the modifications carried out, it is important to choose the most exhaustive set of tests to cover all the possible effects of the modifications on the model used in the program. The validity of the results will thus be verified in all cases (i.e. for any set of parameters).

This testing procedure with the mechanism of using other versions in program libraries establishes a consistency between the results of the different versions of the same program.

6.4 CONSTRAINTS OF THE LASER SIMULATION PROGRAMS

Like many other programs, those of laser simulation fall under two major constraints:

- the memory available on a computer, and
- the efficiency of the programs.

6.4.1 MEMORY

Two main factors must be dealt with, first:

- the rather small memory of the computer these programs run on: for example, depending on the equipment, the memory of the CYBER computers series 170 may vary between 300K₂ and 400K₂ words;
- the variable size of the programs are determined by the number of words sampled on the axes that define the simulation.

One of the smallest programs, the LR1CF3, will be used to show the importance of these two factors. This program depends on the following four axes:

- the z axis: longitudinal axis of the cylinder
- the r axis: radial axis (of symmetry) of the cylinder
- the t axis: temporal axis
- the ω axis: frequency axis.

Let us call E the electromagnetic field and DE the field derivative in connection to z: these two quantities depend explicitly on the z, r and t axes. For the purpose of this discussion, the ω axis will not be used. Moreover, if L is the current plane associated with the z axis and i is that associated with the r axis, and if k is the current point associated with the t axis; when the used predictor is considered (modified mid-point method) then: $E(L,i,k) = E(L-2,i,k) + (\Delta z/2) \times (DE(L-1,i,k) + DE(L,i,k))$; as can be seen, the three planes L-2, L-1, L of E and the two planes L-1 and L of DE must be kept. It should be noted that the quantities of E and DE are complex (i.e. one word must be counted for the real part and one word for the imaginary part).

With these informations, the size of the program can be assessed. Let us consider the following three cases:

- a) 32 points on the r axis and 64 points on the t axis;
- b) 64 points on the r axis and 128 points on the t axis;
- c) 64 points on the r axis and 192 points on the t axis.

The code and other variable will occupy a total of 50K_g words.

Following are the calculations to find out the size of the programs:

- a) required memory for E and DE: $(3-2) \times 2 \times 32 \times 64 = 50K_g$ words; total memory required: $50K_g + 50K_g = 120K_g$ words;
- b) required memory for E and DE: $(3-2) \times 2 \times 64 \times 128 = 240K_g$ words; total memory required: $50K_g + 240K_g = 310K_g$ words;
- c) required memory for E and DE: $(3-2) \times 2 \times 64 \times 192 = 360K_g$ words; total memory required: $50K_g + 360K_g = 430K_g$ words.

Depending on the number of points on the axes, it can be noted that the size of the very same program may fluctuate surprisingly. With facilities that can deal only with 300K_g to 400K_g words, like in cases b and c, there will be serious problems to face. Moreover, certain programs without the radial symmetry hypothesis, like the LR1PS, require a far greater memory. In the LR1PS program, where the quantities of E and DE depend explicitly on the z, x, y and the t axes, with 32 points on each of the transverse axes (x and y) and 64 points on the t axis, there is a need for 2400K_g words (i.e. $(3-2) \times 2 \times 32 \times 32 \times 64$). This is indeed a major problem for most installations.

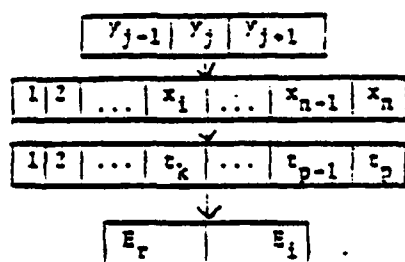
Nevertheless, the laser simulation programs have some common characteristics:

- the size of the programs in a function of the quantities of E and DE;
- the size needed by the programs is concentrated in two quantities E and DE (from 50% to 98% of the total size, depending on the program);
- the numerical integration uses a purely sequential algorithm in all the programs (i.e. inner loops structures).

One simple and direct way of solving the problem of memory is to use the computer disks to compensate the central memory; these disks have a great capacity to store information. Thus, as the calculations of the E and DE quantities proceed by successive iterations on the planes (z axis), the values of the quantities of E and DE, for a given plane are stored on a disk (writing operation), when these values are needed for prediction or corrections calculations of a given point of the r axis at given point on the t axis, all that is needed is to retrieve them from the disk (reading operation): this procedure is called pagination.

More precisely, the planes L-2, L-1 and L of E and the planes L-1 and L of DE will be associated to five binary files sequentially manipulated by the Fortran statements BUFFER IN and BUFFER OUT (writing and reading). What remains now is to define the buffers associated to the five files and to manipulate the values these deal with.

At this point, there is a need to distinguish two categories of programs:



where y_j : j th line on the matrix
 n : total number of points on x axis
 p : total number of points on t axis
 x_i : i th point on x axis
 t_k : k th point on t axis
 E_r : real part of E
 E_i : imaginary part of E

The control of this buffer is similar to the one described in 1) but there is no need here to manipulate the sections of the x axis as all the line fits in the buffer. However, to control the three lines of the buffer, it is necessary to define the supplementary pointers. For the same reasons, the buffer associated to the files holding the values of DE on the $L-1$ plane will have a similar structure but it will have only the two lines y_{j-1} and y_j . All the other buffers for E and DE will control only one y_j line at a time.

As in 1), the pointers on the files are used to go from plane to plane, yet the solution here is not as versatile. The main problem here is the great size of the buffers. In fact, for 32 points on the x axis and 64 points on the t axis, the size of the buffer controlling the three lines will be of $3 \times 2 \times 32 \times 64 = 30K_2$ words. Keeping in mind the fact that there are several buffers, and considering the memory needed by the code and the other variables (nearly $70K_2$ words for the LRIPS program), there will be $160K_2$ words for LRIPS. By changing the number of points on the axis, it will be easy to reach the $300K_2$ words of the computers used here.

Finally, it is necessary to note that in the two solutions presented here, only four buffers are needed instead of five, even though there are five files to control. In fact, as there is never any need for the values of E on the $L-2$ plane and for the $L-1$ plane simultaneously (the $L-2$ plane is used for prediction and the $L-1$ for correction). It is possible to use the same buffer to control the two files associated to these planes for the values of E .

6.4.2 EFFICIENCY

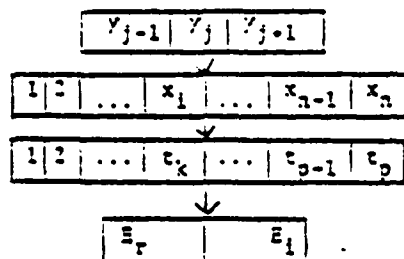
The pagination of the laser simulation programs may be the first source of inefficiency. In fact, it is slower to read or write a word on a disk than to accede to an address in core memory (primary storage). In order for the pagination not to affect the performance of the program to a great extent, the following rules have been adopted:

- using buffers large enough to minimize the access to the disk;
- using the statements BUFFER IN and BUFFER OUT to read and write the buffers on file, these statements are three times faster than equivalent binary statements READ and WRITE;
- using pointers for the control of files and buffers in order to avoid unnecessary manipulations (displacements of the values in the buffers, transfer of values from one file to another, etc.);
- non-usage of auxiliary panels for calculations (these will be done directly in the buffers) in order to avoid supplementary transfers.

Beside pagination, other points dealing with the efficiency of the programs must be checked:

- given the inner loops structure of this kind of programs, it is necessary to avoid the transfer of variables as parameters in the subroutines called for by the inner loops. For example, each variable transferred in parameter in the C1DRVE (or C1DRVP) subroutine of the LRIPS program will increase the total running time of the program by 0.5%, and if this subroutine has 10 variables transferred in parameters, the running time of the program will be increased by 5%: this is quite significant.
- It is necessary to minimize the number of divisions and multiplications in the equation used in the subroutines of the inner loops. This can be done, when possible, by linking all the constant terms for each point of the same axis and by storing the result in a panel subject to this axis. In that way, it will be possible to replace many multiplications and divisions by one multiplication and one address calculation (access to the element in the panel).

For example, the running time of the LRIPS program without storing the pagination mechanism goes from 500 seconds (on a CYBER 173) to 550 seconds but with the storing of the pagination mechanism, the gain is of 50%.



where y_j : j th line on the matrix
 n : total number of points on x axis
 p : total number of points on t axis
 x_i : i th point on x axis
 t_k : k th point on t axis
 E_r : real part of E
 E_i : imaginary part of E

The control of this buffer is similar to the one described in 1) but there is no need here to manipulate the sections of the x axis as all the line fits in the buffer. However, to control the three lines of the buffer, it is necessary to define the supplementary pointers. For the same reasons, the buffer associated to the files holding the values of DE on the $L-1$ plane will have a similar structure but it will have only the two lines y_{j-1} and y_j . All the other buffers for E and DE will control only one y_j line at a time.

As in 1), the pointers on the files are used to go from plane to plane, yet the solution here is not as versatile. The main problem here is the great size of the buffers. In fact, for 32 points on the x axis and 64 points on the t axis, the size of the buffer controlling the three lines will be of $3 \times 2 \times 32 \times 64 = 30K_g$ words. Keeping in mind the fact that there are several buffers, and considering the memory needed by the code and the other variables (nearly $70K_g$ words for the LRIPS program), there will be $160K_g$ words for LRIPS. By changing the number of points on the axis, it will be easy to reach the $300K_g$ words of the computers used here.

Finally, it is necessary to note that in the two solutions presented here, only four buffers are needed instead of five, even though there are five files to control. In fact, as there is never any need for the values of E on the $L-2$ plane and for the $L-1$ plane simultaneously (the $L-2$ plane is used for prediction and the $L-1$ for correction). It is possible to use the same buffer to control the two files associated to these planes for the values of E .

6.4.2 EFFICIENCY

The pagination of the laser simulation programs may be the first source of inefficiency. In fact, it is slower to read or write a word on a disk than to accede to an address in core memory (primary storage). In order for the pagination not to affect the performance of the program to a great extent, the following rules have been adopted:

- using buffers large enough to minimize the access to the disk;
- using the statements BUFFER IN and BUFFER OUT to read and write the buffers on file, these statements are three times faster than equivalent binary statements READ and WRITE;
- using pointers for the control of files and buffers in order to avoid unnecessary manipulations (displacements of the values in the buffers, transfer of values from one file to another, etc.);
- non-usage of auxiliary panels for calculations (these will be done directly in the buffers) in order to avoid supplementary transfers.

Beside pagination, other points dealing with the efficiency of the programs must be checked:

- given the inner loops structure of this kind of programs, it is necessary to avoid the transfer of variables as parameters in the subroutines called by the inner loops. For example, each variable transferred in parameter in the C1DRVE (or C1DRVP) subroutine of the LRIPS program will increase the total running time of the program by 0.5%, and if this subroutine has 10 variables transferred in parameters, the running time of the program will be increased by 5%: this is quite significant.
- It is necessary to minimize the number of divisions and multiplications in the equation used in the subroutines of the inner loops. This can be done, when possible, by linking all the constant terms for each point of the same axis and by storing the result in a panel subject to this axis. In that way, it will be possible to replace many multiplications and divisions by one multiplication and one address calculation (access to the element in the panel).

For example, the running time of the LRIPS program without storing the pagination mechanism goes from 500 seconds (on a CYBER 173) to 550 seconds but with the storing of the pagination mechanism, the gain is of 50%.

Terms used in the diagrams

eta: longitudinal axis of the cylinder
rho: transverse axis of the cylinder (symmetry axis)
tau: temporal axis t
dwn: frequency axis ω (associated to the material)
material: polarization P (complex quantity) and energy W
E : electromagnetic field (complex quantity)
DE : field derivation in terms of eta (complex quantity)
L : Lth plane on the eta axis
i : ith point on the rho axis
k : kth point on the tau axis
Euler formula: $E(L,i,k) E(L-1,i,k) zXDE(L-1,i,k)$
Modified Euler formula: $E(L,i,k) E(L-2,i,k) (zX2)XDE(L-1,i,k)$
Trapezoid method: $E(L,i,k) E(L-1,i,k) (z/s)X(DE(L,i,k)DE(L-1,i,k))$
PHI0, PHI2: initial tilting angles used in material calculation
Statistics: indicate that depending on certain distributions, the PHI0 and PHI2 angles will be randomly generated

Key to figures

.....: sub-routine contents
=====: loop on the number of laser simulations; (sta)
-----: loop on the eta axis
-----: loop on the rho axis
-----: loop on the tau axis
.....: loop on the dwn axis

The loops on the sta, rho and dwn axes are optional, i.e. it depends on the activation of certain effects in the simulation.

FIGURE 6.2.1 - GENERAL DIAGRAM OF THE CIIUVW SUB-ROUTINE

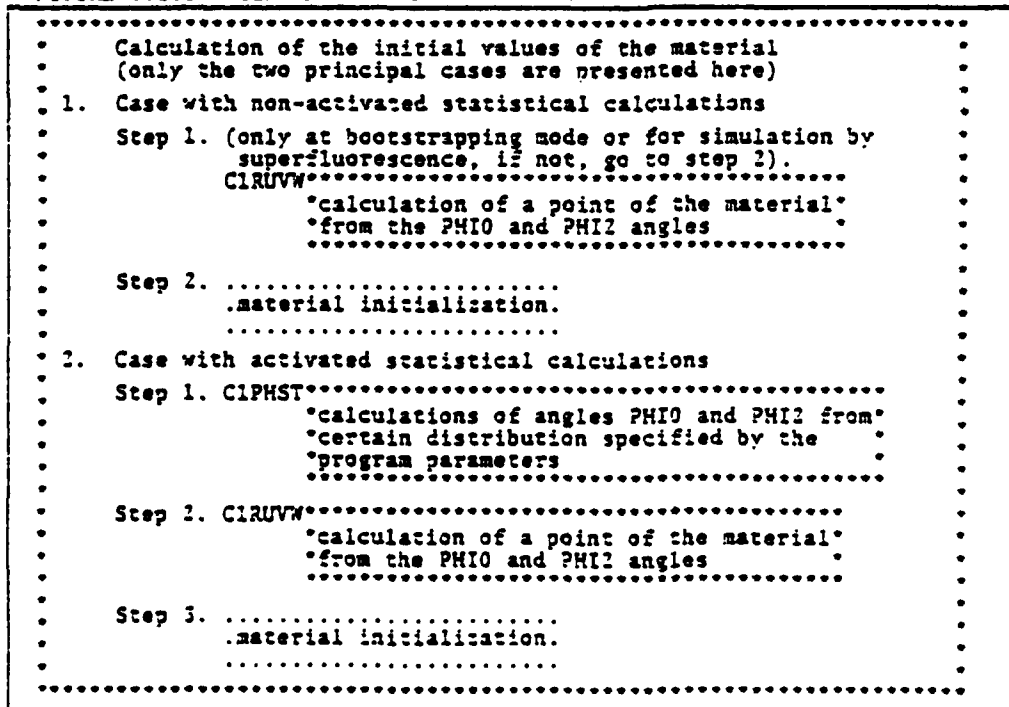


FIGURE 6.2.2 - GENERAL DIAGRAM OF THE C1INTG SUB-ROUTINE

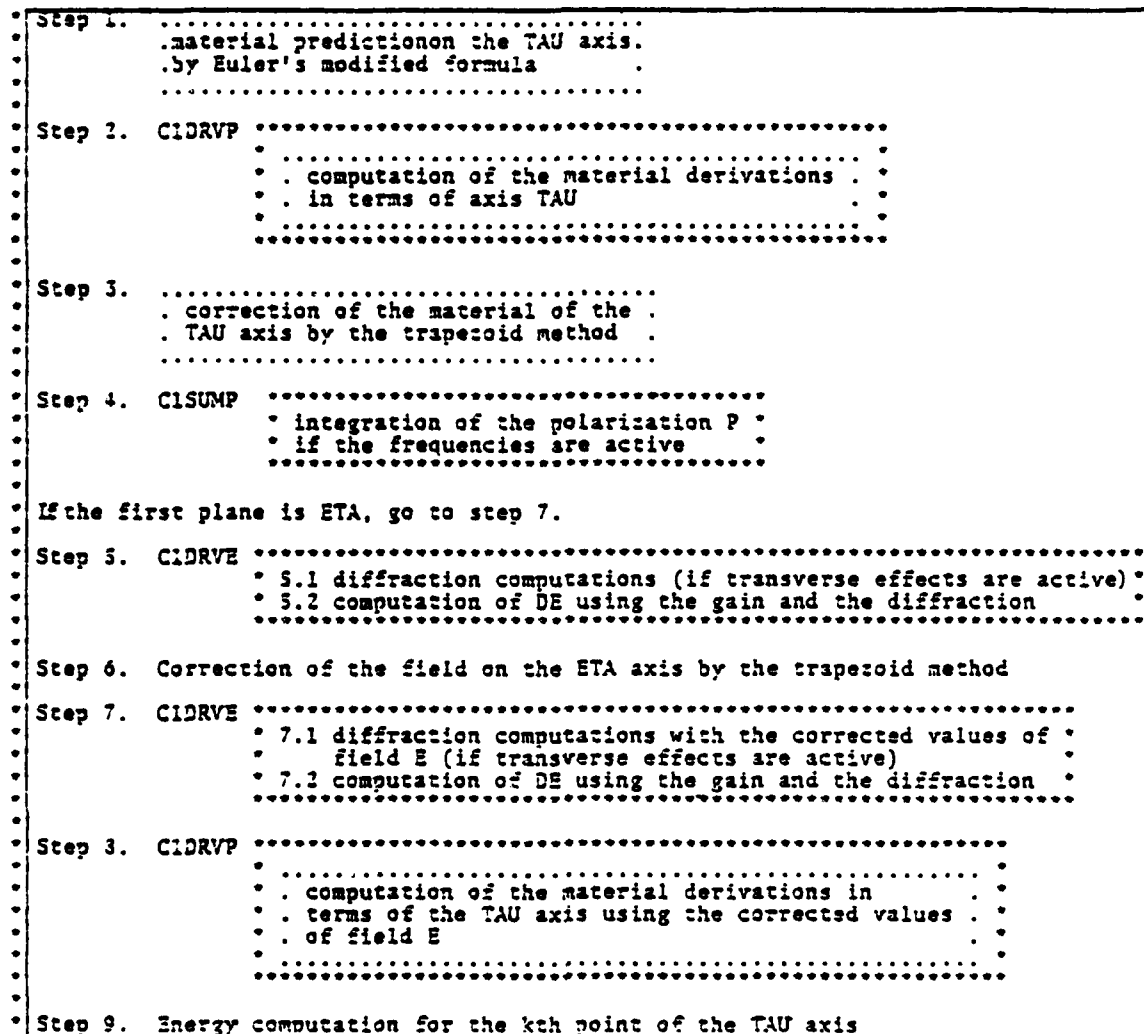


FIGURE 5.2.3 (cont'd)

Step 10. C1CPL1

this sub-routine deals with the initialization of field E and of its derivative DE on the first ETA plane.

10.1

initialization of field E; if in propagation mode, can depend on a series of Gaussian pulses.

10.2

10.2.1 C1IUVW (see figure 6.2.1)

10.2.2 C1INTG (calculation of DE for the first ETA plane: see figure 6.2.2)

Step 11. C1CPL2

this sub-routine deals with the calculations of field E and its derivation DE on the second ETA plane.

11.1

prediction of field E by Euler's formula.

11.2

11.2.1 C1IUVW (see figure 6.2.2)

11.2.2 C1INTG (computation of DE for the second ETA plane and correction of E for that plane: see figure 6.2.2)

Step 12. C1CPLJ

this sub-routine calculates the evolution of field E and of the material along the propagation axis of the cylinder.

12.1 C1PRDF

prediction of field E by the modified Euler's formula.

12.2 C1IUVW (see figure 6.2.1)

12.3 C1INTG (computation of DE and of the material, correction of E and of the material: see figure 6.2.2)

12.4 Production of the results (if the ETA plane has been selected by the program)

12.4.1 C1IET

calculation of the energy integrals on the TAU axis

12.4.2 C1FETR

calculation of the transverse flux

12.4.3 C1OPWR

calculation of the output pulse

FIGURE 6.2.3 - GENERAL DIAGRAM OF THE LRICFS PROGRAM

```

=====
Step 1. Reading of datas (i.e. number of the simulation, optional selectors on the
functions, simulation parameters).

Step 2. Parameters verification (markers and compatibility).

Step 3. Simulation definition at the SIMRES package (i.e. declaration of axes,
functions, selectors, parameters, etc.).

Step 4. Axes calculations.
    4.1 CIDETA .....
        * calculation of the ETA axis and its dependencies *
    4.2 CIRHO .....
        * calculation of the RHO axis and its dependencies; *
        * can be defined in linear or nonlinear mode
    4.3 CIDTAU .....
        * calculation of the TAU axis and its dependencies; *
        * can be defined in propagation or superfluorescence mode *
    4.4 CIDDWN .....
        * calculations of the DWN axis and its dependencies; *
        * can be defined symmetrically or asymmetrically and *
        * can define a Gaussian or a Lorentzian curve

Step 5. Calculation of the physical quantities used by the simulation.
    5.1 CIGAIN .....
        * computation of the gain in terms of the RHO axis; *
        * can be defined constant or Gaussian; can introduce *
        * disruptions
    If the statistics calculations are non-activated, go to step 5.3
    5.2 CIDPHN .....
        * density calculations in terms of RHO
        * used for the normalization of angle PHI0
    5.3 CIEVBX .....
        * outline calculations of angles PHI0 AND PHI2

Step 6. Initializations dealing with pagination.

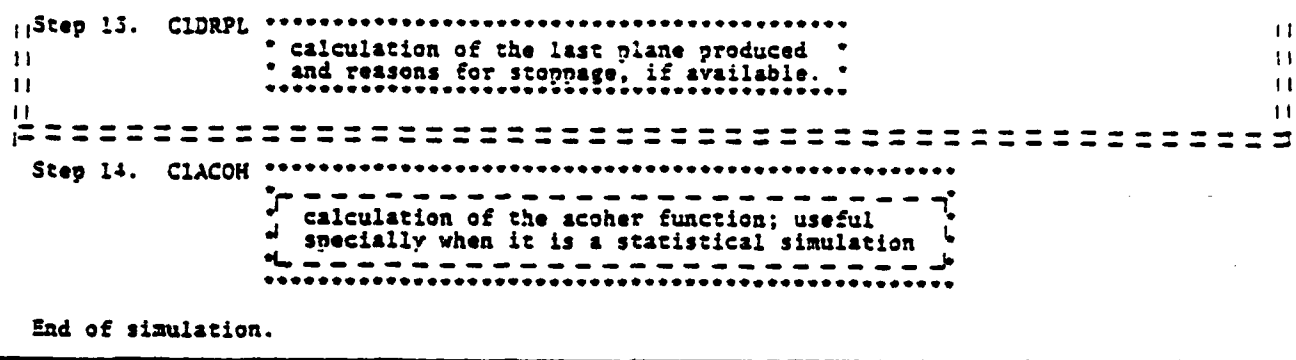
Step 7. Initialization of angles PHI0 and PHI2, this initialization follows certain
laws if the statistical calculation has been activated and can be done through
the CIPHST sub-routine (see figure 6.2.1).

Step 8. Initialization and adjustment of vector EO used for the initialization of
field E in the first ETA plane (only if the laser is defined in propagation mode).

Step 9. Initialization of the principal variables of the program.

```

FIGURE 6.2.3 (cont'd)



VII - CONCLUSION

It is noteworthy to state at this point that the functioning part of the system corresponds to the packages in section IV and to an appreciable part of the laser simulation programs presented in section VI (LR1CFS, LR2CFS, LR1PS, LR1P4S, LR1CP, LR1PP). The programs of application DEFPARM, DESRES and SYNTH are still being developed, however DEFPARM and DESRES are already in use.

In conclusion, it would be of value to review our objectives and to examine how the software developed for the laser model building project answered our expectations.

With respect to modularity, it is evident at this stage that a considerable effort has been extended to divide the work into concrete jobs and to limit these different jobs into procedures or groups of procedures. By their very definition and by their conception, these packages constitute evident examples of modularity. This modularity can be also found in the step by step division of the programs of application.

As to flexibility, there was an effort, all along the conception of the new system, to identify the problems of general concern by liberating us of the specific constraints of the laser project in order to concentrate on the fundamental aspects of the tasks at hand. It follows that the softwares thus developed have enough flexibility to be adapted to the different situations arising within the same laser model building project or even to be adapted to other projects where to results are functions and where there is a sufficient quantity of results to justify a data bank.

The question of security is more difficult to evaluate. Nevertheless, the use of techniques such as data validation, exhaustive tests during the set up period, etc., increase the security aspects of the programs. Moreover, splitting up the work into modules facilitates the inception and set up of the programs and contributes to their strength. Finally, the fact of using these programs in the context of production makes it easier to test them and to find their loopholes.

As to efficiency, it is clear that the development of more complex laser models has forced us to take into consideration of execution time and memory requirements. For instance, the direct access to the SIMRES and DATSIM files has increased the efficiency of the application programs and made them more amenable to use in the interactive. Moreover, the use of pagination in the laser modeling programs has cut down the size of the programs, and facilitates their use on computer with limited memory.

Much attention was given to transportability in order, on the one hand, to execute certain laser programs on computers more powerful than those at our disposal, and on other, to use our auxiliary software in other projects. To make the software more transportable, we have chosen to write it FORTRAN IV and to respect the ANSI standard. Moreover, we have isolated in procedures the instructions or portions of code that are particular to a given environment (like the files direct access subroutines) thus making it easy to locate what is to be modified in order to transfer the software to another system.

With respect to documentation finally, we have established and tried to follow a strict standard for the programs comments. We expect to publish (internal publication) a technical report and a user's manual for the different packages and the programs dealt with in this document.

ACKNOWLEDGEMENTS

This work would not have been possible without the help of several people who have given us technical help and who have stimulated and enlightened us with their invaluable advice. Not least among them are Dr. J. Teichman, Dr. R. Zahar and Dr. W. Armstrong. By their hospitality, they have made this project possible at the Université de Montréal.

As to the Physics, Dr. Farres P. Mattar wishes to acknowledge the extensive discussions with Prof. G. Moretti, Dr. J. Herrman, Dr. B.R. Suydam, Dr. J. Fleck and Dr. R.E. Francoeur who have helped in the development of the computational algorithms used in the laser programs.

The collaboration of C. Goutier, M. Béliveau and M. Lavoie with regards to the development of the productions system is greatly appreciated.

We also wish to thank Miss D. Reid for the translation of the first three sections and Miss W. Bashour for the translation of the last three sections of this document originally written in French. The skilful typing of Miss L. Leclair is commended with pleasure.

BIBLIOGRAPHY

Software for the Laser Project

1. P. CADIEUX, M. CORMIER, Y. CLAUDE, C. GOUTIER and F.P. MATTAR, Proc. of The Twelfth Annual Pittsburgh Conference of Modeling and Simulation, Ed. W.G. Vogt and H.H. Wickle, published by Instrument Society of America (May 1981), p. 1527.

Cylindrical Laser

2. F.P. Mattar and M.C. NEWSTEIN, Proc. Seventh Conf. on Numerical Simulation of Plasma, Courant Inst., New York Univ. (June 1975), p. 223.
3. F.P. MATTAR, Adaptive Stretching & Rezoning as Effective Computational Techniques for Two Level Paraxial Maxwell-Bloch Simulation, Tech. note 83, Laboratory for Laser Energetics, University of Rochester, Rochester, N.Y.

Adaptive Rezoning

4. F.P. MATTAR, Appl. Phys. 17, 55 (1978).
5. F.P. MATTAR and M.C. NEWSTEIN, Comp. Phys. Comm. 20, 139 (1980).

Implicit Laser

6. F.P. MATTAR, Proc. of Ninth Conf. of Numerical Methods in Plasma, Monterey, Calif. (June 1973), Lawrence Livermore Lab. Tech. Rep. LLL 73-004.

Hydrodynamic Laser

7. F.P. MATTAR, J. TEICHMAN, L. BISSONNETTE and R.W. MacCORMACK, Proc. of Second Int'l Symp. on Gas Flow and Chemical Lasers, Ed. by J. Wendt, Western Hemisphere Pub. (1979).
8. F.P. MATTAR and J. TEICHMAN, Comp. Phys. Comm. 22, 1 (1981).

Transistor Laser

9. F.P. MATTAR, Proc. of Eleventh Congress for the International Commission for Optics, Ed. J. Besca, Madrid (1979).
10. F.P. MATTAR, G. MORETTI and R.E. FRANCOEUR, Comp. Phys. Comm. 23, 1 (1981).

Double Laser

11. F.P. MATTAR and J.M. EBERLY, Proc. of the Physics and Chemistry of Laser-Induced Processes in Molecules, Edinburgh (1978), Ed. A.L. Kompa and S.C. Smith, 61, Springer-Verlag.

Others

12. F.P. MATTAR and B.R. SUYDAM, A Novel Resonant Implicit Algorithm for Coherent Propagation in Multi-Level System, Polytechnic Institute of New-York Aerodynamics Lab., Tech. Report (1981).
13. F.P. MATTAR, in Optical Bistability, Ed. C.M. Bowden, M. Cifan and H.R. Robl, Plenum Press, New York (1981), p. 503.

LIGHT CONTROL BY LIGHT
WITH AN EXAMPLE IN COHERENT PUMP DYNAMICS,
PROPAGATION, TRANSVERSE & DIFFRACTION EFFECTS
IN THREE-LEVEL SUPERFLUORESCENCE

FARRES P. MATTAR*

Mechanical and Aerospace Engineering Department
Polytechnic Institute of New York, Brooklyn, NY 11201, USA, and
Spectroscopy Laboratory, Massachusetts Institute of Technology
Cambridge, MA 02139, USA, Telephone: (617) 253-7700

and

C. M. BOWDEN

Research Directorate, US Army Missile Laboratory, US Army
Missile Command, Redstone Arsenal, AL 35898, USA
Telephone: (205) 876-3342

ABSTRACT

A model and results are presented which describe copropagational coherent pump dynamics and evolving superfluorescence (SF). Specification of certain pump pulse initial conditions results in specific SF characteristics, as recently observed in CH_3F and Ba.

* Partially supported by the U. S. Army Research Office, the U. S. Office of Naval Research, the U. S. Science Foundation and Battelle Columbus Laboratories.

247

LIGHT CONTROL BY LIGHT
WITH AN EXAMPLE IN COHERENT PUMP DYNAMICS,
PROPAGATION, TRANSVERSE & DIFFRACTION EFFECTS
IN THREE-LEVEL SUPERFLUORESCENCE

FARRES P. MATTAR*

Mechanical and Aerospace Engineering Department
Polytechnic Institute of New York, Brooklyn, NY 11201, USA
and Spectroscopy Laboratory, Massachusetts Institute of Technology
Cambridge, MA 02139, USA, Telephone: (617) 253-7700

and

C. M. BOWDEN

Research Directorate, U.S. Army Missile Laboratory, U.S. Army
Missile Command, Redstone Arsenal, AL 35898, USA
Telephone: (205) 876-3342

SUMMARY

Recently developed computational methods, are used to evaluate for the first time the dynamic longitudinal and transverse reshaping associated with the concomitant propagation of two light beams in a three-level medium. Neither the mean field theory [1] nor the adiabatic following [2] or even the rate equation [3] approximations have simplified this analysis. Instead, the full Maxwell-Bloch [4,5] equations with phase and diffraction effects [6] included are solved rigorously, using self-consistent numerical methods [7].

A new concept in nonlinear light matter interactions is introduced: The results obtained for the first time display the conditions under which an injected light pulse of a given frequency can be used to shape and control a second light pulse of a different frequency coupled through the nonlinear three-level medium. Thus, a specific aspect of the phenomenon of light control by light is demonstrated [8].

The model has been applied to double coherent transients (i.e., double self-induced transparency) and to the pump dynamics effects in super-fluorescence (SF).

The goal of this paper is to illustrate how the output characteristics of the collective spontaneous emission of the SF pulse [9] (such as delay time, pulse width, peak intensity, shape, etc.) can be controlled, deterministically, by appropriately selecting certain initial and boundary conditions for the injected pump pulse.

* Partially supported by the U.S. Army Research Office, the U. S. Office of Naval Research, the U.S. Science Foundation and Battelle Columbus Laboratories.

With the exception of Bowden and Sung [10], all theoretical work has dealt exclusively with the relaxation process from a prepared state of complete inversion in a two-level manifold of atomic energy levels, and thus do not consider the dynamic effects of the pumping process. Yet, all reported experimental work has utilized optical pumping on a minimum manifold of three atomic [11-13] or molecular [14-15] energy levels by laser pulse injection into the nonlinear medium, which subsequently superfluoresces. (Note that the two-level analysis is only valid for $\tau_R \gg \tau_p$, where τ_R is the characteristic SF time and τ_p is the pump pulse temporal width, and has not been realized over the full range of reported data).

Our analysis extends

~~Contrary to~~ Bowden and Sung's analytical treatment, we do not confine our solution to the mean field regime and the linearized short time regime but have adopted the semiclassical model advanced by Feld and co-authors [16] where both transients and propagation effects are rigorously studied. Quantum fluctuations [17-19] are not discussed in the treatment; instead, a classical uniform (not random) tipping angle concept is used for initiating the polarization to simulate the fluorescence initiation. The latter method is well-established for both two- and three-level [20-21] propagation calculations. Since transverse effects are also considered, the obtained results also extend the pumpless analysis that previously modelled the Cs experiment [22].

In particular, it is shown that the injected coherent pump initial characteristics, such as on-axis area, temporal and radial width (and associated gain-length-Fresnel number), and shape alter the SF pulse characteristics. The effects of changing the effective gain [23] of either the SF or the pump transition and the density of active atoms are also studied.

For sufficiently large effective gain and/or large input pump area, the two light pulses overlap and the two-photon processes (RCR-resonant coherent Raman) make strong contributions to the mutual pulse development. ←

Dependencies of this type have been recently observed in methyl fluoride [24] and in barium [25]. Furthermore, under other conditions, we obtained a SF pulse of temporal width much less than that of the pump even though the two pulses temporally overlap. This calculation agrees qualitatively with the results of recent experiments in mode locked CO_2 pumped CH_3F [26].

REFERENCES

- [1] R. Bonifacio and L.A. Lugiato, Phys. Rev. A11, 1507 (1975); and A12, 587 (1975).
- [2] D. Grischkowsky, M.M.T. Loy and P.F. Liao, Phys. Rev. A12, 2514 (1975).
- [3] A. Javan, Phys. Rev. 107, 1579 (1957).
A.M. Clogstar, J. Phys. Chem. Solids 4, 271 (1958).
R.L. Panock and R.J. Temkin, QE 13, 425 (1977).
- [4] S.L. McCall and E.L. Hahn, Phys. Rev. 183, 457 (1967).
- [5] R.G. Brewer and E.L. Hahn, Phys. Rev. A11, 1641 (1975).
- [6] F.P. Mattar and M.C. Newstein, IEEE J. Quantum Electron 13, 507 (1977).
- [7] F.P. Mattar, Appl. Phys. 17, 53 (1978); F.P. Mattar and M.C. Newstein, Comput. Phys. Commun. 20, 139 (1980).
- [8] F.P. Matter and C.M. Bowden, Topics of Current Physics: Multiple Photon Dissociation of Polyatomic Molecules, ed. C.D. Cantrell, Springer Verlag, 1982.
- [9] R.H. Dicke, Phys. Rev. 93, 99 (1954).
- [10] C.M. Bowden and C.C. Sung, Phys. Rev. A18, 1558 (1978); and A20, 2033 (1979).
- [11] M. Gross, C. Fabre, P. Pillet and S. Haroche, Phys. Rev. Lett. 36, 1035 (1976).
- [12] A. Flusberg, F. Mossberg and S.R. Hartmann, Cooperative Effects in Matter and Radiation, ed. C.M. Bowden, D.W. Howgate and H.R. Robl (Plenum Press, 1977) p. 139.
- [13] H. M. Gibbs, Q.H.R. Vrehen and H.M.J. Hicks-pooes, Phys. Rev. Lett. 39, 547 (1977).
- [14] N. Skribanowitz, I.P. Herman, J.C. MacGillivray and M.S. Feld, Phys. Rev. Lett. 30, 309 (1973).
- [15] J.J. Ehrlich, C.M. Bowden, D.W. Howgate, S.H. Lehnigk and T.A. DeTemple, Coherence and Quantum Optics IV, ed L. Mandel and E. Wolf (Plenum Press), 1978, p. 923.
- [16] J.C. MacGillivray and M.S. Feld, Phys. Rev. A14, 1169 (1976).
- [17] F. Haake, J. Haus, H. King, G. Schroder and R. Glauber, Phys. Rev. Lett. 45, 558 (1980).

- 276
- [18] D. Polder, M.F.H. Schuurmans and Q.H.F. Vreken, Phys. Rev. A19, 1192 (1979).
 - [19] F. Hopf, Phys. Rev. A20, 2064 (1979).
 - [20] M.S. Feld and J.C. MacGillivray, Coherent Nonlinear Optics, ed. M.S. Feld and V.S. Letokhov (Springer Verlag, 1980).
 - [21] J.R.R. Leite, R.S. Scheffield, M. Ducloy, R.D. Sharma and M.S. Feld, Phys. Rev. A14, 1151 (1976).
 - [22] F.P. Mattar, H.M. Gibbs, S.L. McCall and M.S. Feld, Phys. Rev. Lett. 46, 1123 (1981).
 - [23] F.P. Mattar and M.C. Newstein, Cooperative Effects in Matter and Radiation, ed. C.M. Bowden, D.W. Howgate and H.R. Robl (Plenum Press, 1977) p. 139.
 - [24] A.T. Rosenberger and T.A. DeTemple, Phys. Rev. A24, 868 (1981).
 - [25] A. Crubellier, S. Liberman, D. Mayou, P. Pillet and M.G. Schweighofer, Optics Lett. 7, 16 (1982).
 - [26] T.A. DeTemple, Private Communication.

251

Coherent pump dynamics, propagation, transverse, and diffraction effects in three-level superfluorescence and control of light by light

F. P. Mattar

*Aerodynamics Laboratory, Mechanical and Aerospace Engineering Department,
Polytechnic Institute of New York, Brooklyn, New York 11201 and Laser Spectroscopy Laboratory,
Massachusetts Institute of Technology, Cambridge, Massachusetts 02139*

C. M. Bowden

*Research Directorate, United States Army Missile Laboratory, United States Army Missile Command,
Redstone Arsenal, Alabama 35898*

(Received 1 June 1982)

A model is presented for the dynamical evolution of superfluorescence from an optically pumped three-level system. The full propagation, transverse, and diffraction effects are taken into account. With the use of a previously developed algorithm, a computational simulation was constructed from this model and results are presented and discussed. In particular, it is shown that the injected coherent pump-pulse initial characteristics, such as on-axis area, temporal and radial width and shape, can have significant deterministic effects on the superfluorescent pulse delay time, peak intensity, temporal width, and shape. Thus, by specifying certain initial properties of the injected pump pulse, the superfluorescent pulse can be shaped and altered. The results predict the conditions under which an injected light pulse of a given frequency can be used to generate, shape, and control a second light pulse of a different frequency via a nonlinear medium, thus demonstrating a new aspect of the phenomenon of light control by light.

I. INTRODUCTION

Superfluorescence¹ is the phenomenon whereby a collection of atoms or molecules is prepared initially in a state of complete inversion and then allowed to undergo relaxation by collective, spontaneous decay. Since Dicke's initial work,² there has been a preponderance of theoretical and experimental work dealing with this process.³

With the exception of the more recent work of Bowden and Sung,⁴ all theoretical treatments have dealt exclusively with the relaxation process from a prepared state of complete inversion in a two-level manifold of atomic energy levels and thus do not consider the dynamical effects of the pumping process. Yet, all reported experimental work⁵⁻¹⁰ has utilized optical pumping on a minimum manifold of three atomic or molecular energy levels by laser pulse injection into the nonlinear medium, which subsequently superfluoresces.

It was pointed out by Bowden and Sung⁴ that for a system otherwise satisfying the conditions for superfluorescent (SF) emission, unless the characteristic super-radiance time¹ τ_R is much greater than the pump-pulse temporal duration τ_p , i.e., $\tau_R \gg \tau_p$, the process of coherent optical pumping on a three-level system can have dramatic effects on the SF. This is a condition which has not been realized over the full

range of reported data.³

In this paper, we present calculational results and analysis for the effects of coherent pump dynamics, propagation, transverse, and diffraction effects on SF emission from an optically pumped three-level system. The full, nonlinear, copropagational aspects of the injected pump pulse, together with the SF which evolves, are explicitly treated in the calculation. Not only do our results relate strongly to previous calculations and experimental results in SF, but we introduce and demonstrate a new concept in nonlinear light-matter interactions, which we call light control by light. We show how characteristics of the SF can be controlled by specifying certain characteristics of the injection pulse in the regime $\tau_p > \tau_R$.

In Sec. II, the model upon which the calculation is based is presented, and the algorithm used in the simulation is outlined. Results of the calculation are presented and discussed in Sec. III. Section IV is used to summarize the results and cite implications and to discuss future work.

II. MODEL FOR THREE-LEVEL SUPERFLUORESCENCE

The model upon which the calculation is based is composed of a collection of identical three-level

atoms, each having the energy-level scheme shown in Fig. 1. The $1 \rightarrow 3$ transition is induced by a coherent electromagnetic field injection pulse of frequency ω_0 nearly tuned to the indicated transition. The properties of this pumping pulse are specified initially in terms of the initial and boundary conditions. The transition $3 \rightarrow 2$ evolves by spontaneous emission at frequency ω . It is assumed that the energy-level spacing is such that $\epsilon_3 > \epsilon_2 \gg \epsilon_1$ so that the fields at frequencies ω_0 and ω can be treated by separate wave equations. The energy levels $2 \rightarrow 1$ are not coupled radiatively due to parity considerations.

Further, we neglect spontaneous relaxation in the $3 \rightarrow 1$ transition, and spontaneous relaxation in the $3 \rightarrow 2$ transition is simulated by the choice of a small, but nonzero, initial transverse polarization¹¹ characterized by the parameter $\phi_0 \sim 10^{-3}$. Our results do not depend upon nominal variations of this parameter.

$$\begin{aligned} \mathcal{H} = & \hbar \sum_{r=1}^3 \sum_{j=1}^N \epsilon_r R_r^{(j)} - \frac{i\hbar}{2} \sum_{j=1}^N \{ \Omega^{(j)} R_{32}^{(j)} \exp[-i(\omega t - \vec{k} \cdot \vec{r}_j)] - \Omega^{(j)*} R_{23}^{(j)} \exp[i(\omega t - \vec{k} \cdot \vec{r}_j)] \} \\ & - \frac{i\hbar}{2} \sum_{j=1}^N \{ \omega_k^{(j)} R_{31}^{(j)} \exp[-i(\omega_k t - \vec{k}_0 \cdot \vec{r}_j)] - \omega_k^{(j)*} R_{13}^{(j)} \exp[i(\omega_k t - \vec{k}_0 \cdot \vec{r}_j)] \}. \end{aligned} \quad (2.1)$$

The first term on the right-hand side (rhs) of Eq. (2.1) is the free atomic system Hamiltonian with atomic level spacings ϵ_r , $r=1,2,3$; $j=1,2,\dots,N$. The second term on the rhs describes the interaction of the atomic system with the fluorescence field associated with the $3 \rightarrow 2$ transition, whereas the last term on the right in (2.1) describes the interaction between the atomic system and the coherent pumping field. The fluorescence field and the pumping field have amplitudes $\Omega^{(j)}$ and $\omega_k^{(j)}$, respectively, in terms of Rabi frequency, at the position of the j th atom, \vec{r}_j . The respective wave vectors of the two fields are \vec{k} and \vec{k}_0 and the carrier frequencies are ω

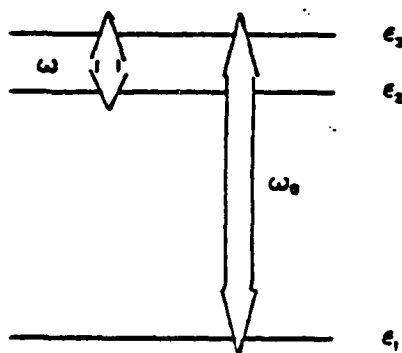


FIG. 1. Model three-level atomic system and electric field tunings under consideration. For the results reported here, the injected pulse is tuned to the $1 \rightarrow 3$ transition.

and ω_0 . The initial condition is chosen consistent with the particular choice of ϕ_0 (see the Appendix) with nearly all the population in the ground state and the initial values of the other atomic variables chosen consistently^{4,12} according to the initial equilibrium properties of the system.¹³ The full statistical treatment of the quantum initiation process with resulting temporal fluctuations will be presented in a future development. Thus, the results presented here are to be regarded as expectation values or ensemble averages.

We use the electric-dipole and rotating-wave approximations and couple the atomic dipole moments to classical field amplitudes which are determined from Maxwell's equations. The Hamiltonian which describes the field-matter interaction for this system comprising N atoms⁴ is

and ω_0 . It is assumed that the electromagnetic field amplitudes vary insignificantly over the atomic dimensions and that all of the atoms remain fixed during the time frame of the dynamical evolution of the system.

The atomic variables in (2.1) are the canonical operators⁴ $R_{ij}^{(j)}$ which obey the Lie algebra defined by the commutation rules¹⁴⁻¹⁶

$$[R_{ij}^{(m)}, R_{lk}^{(n)}] = R_{ik}^{(m)} \delta_{jn} - R_{jl}^{(m)} \delta_{in} \delta_{mn}, \quad (2.2)$$

where $i, j=1,2,3$; $m, n=1,2,\dots,N$. The Rabi rates $\Omega^{(j)}$ and $\omega_k^{(j)}$ are given in terms of the electric field amplitudes $E^{(j)}$ and $E_0^{(j)}$, respectively, and the matrix elements of the transition dipole moments $u_{32}^{(j)}$ and $u_{31}^{(j)}$ by

$$\Omega^{(j)} = \frac{E^{(j)} u_{32}^{(j)}}{\hbar}, \quad (2.3a)$$

$$\omega_k^{(j)} = \frac{E_0^{(j)} u_{31}^{(j)}}{\hbar}, \quad (2.3b)$$

where we have considered only one linear polarization for the two fields and propagation in the positive z direction.

It is convenient to canonically transform (2.1) to remove the rapid time variations at the carrier frequencies ω and ω_0 and the rapid spatial variations due to the wave vectors \vec{k} and \vec{k}_0 . We assume that the field envelopes $\Omega^{(j)}$ and $\omega_k^{(j)}$ vary much more slowly than the periods ω^{-1} and ω_0^{-1} , respectively. In the transformed representation, we are thus deal-

ing with slowly varying field amplitudes and atomic operators. The desired unitary transformation U , such that

$$\tilde{\mathcal{H}}_T = U \mathcal{H} U^{-1}, \quad (2.4)$$

is given by

$$U(t) = \prod_{j=1}^N \exp[i\lambda_j^{(j)}(t)R_{11}^{(j)}] \exp[i\lambda_j^{(j)}(t)R_{22}^{(j)}], \quad (2.5)$$

where

$$\lambda_j^{(j)}(t) = \omega_0 t - \vec{k}_0 \cdot \vec{r}_j, \quad (2.6a)$$

$$\lambda_j^{(j)}(t) = [(\omega_0 - \omega)t - (\vec{k}_0 - \vec{k}) \cdot \vec{r}_j]. \quad (2.6b)$$

If (2.5) is applied to (2.1) and the commutation rules (2.2) are used, we get for the canonically transformed Hamiltonian $\tilde{\mathcal{H}}_T$,

$$\tilde{\mathcal{H}}_T = \hbar \sum_{j=1}^N \Delta^{(j)} R_{11}^{(j)} + \hbar \sum_{j=1}^N \delta^{(j)} R_{22}^{(j)} - \frac{i\hbar}{2} \sum_{j=1}^N (\Omega^{(j)} R_{12}^{(j)} - \Omega^{*(j)} R_{21}^{(j)}) - \frac{i\hbar}{2} \sum_{j=1}^N (\omega_k^{(j)} R_{11}^{(j)} - \omega_k^{*(j)} R_{22}^{(j)}), \quad (2.7)$$

where

$$\Delta^{(j)} = \epsilon_{11}^{(j)} - \omega_0, \quad \delta^{(j)} = \epsilon_{22}^{(j)} + \omega - \omega_0, \quad \epsilon_{11} = 0. \quad (2.8)$$

The equations of motion for the atomic variables are calculated from (2.7) according to

$$\dot{R}_M^{(j)} = \frac{i}{\hbar} [\tilde{\mathcal{H}}_T, R_M^{(j)}]. \quad (2.9)$$

By imposing the canonical transformation defined by (2.5) we, in fact, transformed to a slowly varying operator representation which is consistent with the slowly varying envelope approximation to be imposed later on in the Maxwell's equations coupled to the hierarchy of first-order equations (2.9).

If (2.7) is used in (2.9), the following hierarchy of coupled nonlinear equations of motion is obtained for the atomic variables:

$$\dot{R}_{11}^{(j)} = -\frac{1}{2}(\Omega^{(j)} R_{12}^{(j)} + \Omega^{*(j)} R_{21}^{(j)}) - \frac{1}{2}(\omega_k^{(j)} R_{11}^{(j)} + \omega_k^{*(j)} R_{22}^{(j)}) - \gamma_{11}(R_{11}^{(j)} - R_{11}^{(e)}), \quad (2.10a)$$

$$\dot{R}_{22}^{(j)} = +\frac{1}{2}(\Omega^{(j)} R_{12}^{(j)} + \Omega^{*(j)} R_{21}^{(j)}) - \gamma_{11}(R_{22}^{(j)} - R_{22}^{(e)}), \quad (2.10b)$$

$$\dot{R}_{11}^{(j)} = +\frac{1}{2}(\omega_k^{(j)} R_{11}^{(j)} + \omega_k^{*(j)} R_{22}^{(j)}) - \gamma_{11}(R_{11}^{(j)} - R_{11}^{(e)}), \quad (2.10c)$$

$$\dot{R}_{12}^{(j)} = -i\delta^{(j)} R_{12}^{(j)} - \frac{1}{2}\Omega^{*(j)}(R_{22}^{(j)} - R_{11}^{(j)}) - \frac{1}{2}\omega_k^{*(j)} R_{12}^{(j)} - \gamma_1 R_{12}^{(j)}, \quad (2.10d)$$

$$\dot{R}_{12}^{(j)} = -i\delta^{(j)} R_{12}^{(j)} + \frac{1}{2}(\Omega^{*(j)} R_{13}^{(j)} + \omega_k^{(j)} R_{32}^{(j)}) - \gamma_1 R_{12}^{(j)}, \quad (2.10e)$$

$$\dot{R}_{13}^{(j)} = -i\Delta^{(j)} R_{13}^{(j)} - \frac{1}{2}\Omega^{(j)} R_{12}^{(j)} + \frac{1}{2}\omega_k^{(j)}(R_{13}^{(j)} - R_{11}^{(j)}) - \gamma_1 R_{13}^{(j)}. \quad (2.10f)$$

In Eqs. (2.10), we have added phenomenological relaxation γ_{11} and dephasing γ_1 and taken these to be uniform, i.e., the same parameters for each transition. For the diagonal terms $R_{kk}^{(j)}$ the equilibrium values are designed as $R_{kk}^{(e)}$, the same for all atoms.

We shall treat the Eqs. (2.10) from this point as c-number equations, i.e., expectation values. Further, we assume that all the atoms have identical energy-level structure and also, we drop the atomic labels j , so it is taken implicitly that the atomic and field variables depend upon the spacial coordinates x, y , and z , as well as the time t .

It is convenient to introduce a new set of real variables in terms of the old ones. We let

$$W_k = R_{kk} - R_{11}, \quad k > 1 \quad (2.11a)$$

$$R_k = \frac{1}{2}(U_k + iV_k), \quad k > 1 \quad (2.11b)$$

where U_k , V_k , and W_k are real variables, and $U_k = U_k$, $V_k = V_k$.

$$\Omega = X + iY, \quad (2.11c)$$

$$\omega_k = X_0 + iY_0, \quad (2.11d)$$

where X , Y , X_0 , and Y_0 are real variables.

If the transformation (2.11) is applied to (2.10), the resulting equations of motion for the real variables $\{W_k, U_k, V_k\}$ are

$$\begin{aligned} \dot{W}_{11} = & -\frac{1}{2}[XU_{12} - YV_{12}] - [X_0U_{11} - Y_0V_{11}] \\ & - \gamma_{11}(W_{11} - W_{11}^{(e)}), \end{aligned} \quad (2.12a)$$

$$\begin{aligned} \dot{W}_{12} = & -[XU_{12} - YV_{12}] - \frac{1}{2}[X_0U_{11} - Y_0V_{11}] \\ & - \gamma_{11}(W_{12} - W_{12}^{(e)}), \end{aligned} \quad (2.12b)$$

with
with
d the
boson
rium
treat-
result-
a fu-
here
mble

e ap-
sents
ined
which
stem

(2.1)

field
c di-
dur-
d the

nical
fined

(2.2)
rates
field
ma-
u₁₂

2.3a)

2.3b)

riza-
posi-

1) to
fre-
quon-
that
more
vely.
leat-

$$\dot{U}_{12} = +\delta V_{12} + XW_{12} - \frac{1}{2}(X_0 U_{12} - Y_0 V_{12}) - \gamma_1 U_{12}, \quad (2.12c)$$

$$\dot{V}_{12} = -\delta U_{12} - YW_{12} + \frac{1}{2}(X_0 V_{12} + Y_0 U_{12}) - \gamma_1 V_{12}, \quad (2.12d)$$

$$\dot{U}_{31} = -\delta V_{31} - \frac{1}{2}(XU_{21} + YV_{21}) + X_0 W_{31} - \gamma_1 U_{31}, \quad (2.12e)$$

$$\dot{V}_{31} = +\delta U_{31} - \frac{1}{2}(XV_{21} - YU_{21}) - Y_0 W_{31} - \gamma_1 V_{31}, \quad (2.12f)$$

$$\dot{U}_{21} = -\delta V_{21} + \frac{1}{2}(XU_{31} - YV_{31}) + \frac{1}{2}(X_0 U_{12} - Y_0 V_{12}) - \gamma_1 U_{21}, \quad (2.12g)$$

$$\dot{V}_{21} = +\delta U_{21} + \frac{1}{2}(XV_{31} + YU_{31}) - \frac{1}{2}(X_0 V_{12} + Y_0 U_{12}) - \gamma_1 V_{21}. \quad (2.12h)$$

In obtaining Eqs. (2.12), we have made use of the invariant $\text{tr}R = I$

$$I = R_{11}^{(0)} + R_{22}^{(0)} + R_{33}^{(0)}. \quad (2.13)$$

It is noted that $\dot{I} = 0$ is satisfied identically in (2.10a)–(2.10c) for $\gamma_{11} \rightarrow 0$. For $\gamma_{11} \neq 0$, the condition (2.13) together with (2.10a)–(2.10c) constitutes the statement of conservation of atomic density, i.e., particle number.

Equations (2.12) are coupled to Maxwell's equations through the polarizations associated with each transition field. It is easily determined that the Maxwell's equations in dimensionless form in the rotating-wave and slowly varying envelope approximations can be written in the following form:

$$\mathcal{F}_1^{-1} \nabla_\rho^2 \begin{bmatrix} -\bar{X}_0 \\ \bar{Y}_0 \end{bmatrix} + \frac{\partial}{\partial \eta_\rho} \begin{bmatrix} \bar{Y}_0 \\ \bar{X}_0 \end{bmatrix} = d \begin{bmatrix} -U_{31} \\ V_{31} \end{bmatrix}, \quad (2.14a)$$

$$\mathcal{F}_2^{-1} \nabla_\rho^2 \begin{bmatrix} -\bar{X} \\ \bar{Y} \end{bmatrix} + \frac{\partial}{\partial \eta_\rho} \begin{bmatrix} \bar{Y} \\ \bar{X} \end{bmatrix} = d \begin{bmatrix} -U_{12} \\ V_{12} \end{bmatrix}, \quad (2.14b)$$

where the variables \bar{X} , \bar{Y} , \bar{X}_0 , \bar{Y}_0 are the same as those defined in (2.11c) and (2.11d), but in units of γ_1 . In the above equations, we have assumed cylindrical symmetry, thus

$$\nabla_\rho^2 = \frac{1}{\rho} \frac{\partial}{\partial \rho} \left[\rho \frac{\partial}{\partial \rho} \right].$$

The first term on the left-hand side in (2.14a) and (2.14b) accounts for transverse effects with normal-

ized radial coordinate $\rho = r/r_p$, where r is the radial distance and r_p is a characteristic spatial width. In (2.14), $\eta_\rho = z g_{\text{eff}, \rho}$, where $g_{\text{eff}, \rho}$ is the on-axis effective gain

$$g_{\text{eff}, \rho} = \frac{\left[\frac{\omega_0}{\omega} \right] \left[\frac{\mu_{32}}{\mu_{31}} \right]^2 N}{n k c} T_2, \quad (2.15)$$

where N is the atomic number density (assumed longitudinally homogeneous), and n is the index of refraction assumed identical for each transition wavelength. The quantity

$$d = \frac{N(r)}{N_0} \quad (2.16)$$

governs the relative radial population density distribution for active atoms. This could have variation, say, for an atomic beam. Equations (2.14) are written in the retarded time τ frame where

$$\tau = t - n z / c.$$

From this point on, the dot in Eqs. (2.12) is taken to be $\partial/\partial \tau$. Finally, the first factors on the first terms on the lhs in (2.14) are the reciprocals of the "gain-length" Fresnel numbers defined by

$$\mathcal{F}_i = \frac{2\pi r_p^2}{\lambda_i g_{\text{eff}, i}}. \quad (2.17)$$

It is seen from (2.14) that for sufficiently large Fresnel number \mathcal{F} the corrections due to transverse effects become negligible. The gain-length Fresnel numbers \mathcal{F} are related to the usual Fresnel numbers $F = 2\pi r_p^2 / \lambda L$, where L is the length of the medium, by

$$\mathcal{F}/F = g_{\text{eff}} L, \quad (2.18)$$

i.e., the total gains of the medium. In the computations, diffraction is explicitly taken into account by the boundary condition that $\rho = \rho_{\text{max}}$ corresponds to completely absorbing walls.

The initial conditions are chosen to establish a small, but nonzero transverse polarization for the $3 \rightarrow 2$ transition with almost the entire population in the ground state. This requires the specification of two small dimensionless parameters $\epsilon \sim 10^{-3}$ for the ground-state initial population deficit, and $\delta \sim 10^{-1}$ for the tipping angle for the initial transverse polarization for the $3 \rightarrow 2$ transition. The derivation for the initial values for the various matrix elements is presented in the Appendix, and the results are given by (A22), (A23), and (A28)–(A33).

III. CALCULATION RESULTS AND ANALYSIS

Calculational methods developed earlier¹⁷ and discussed elsewhere^{18,19} were applied to the model presented in Sec. II to compute the effects on SF pulse evolution for various initial conditions for the injected (pump) pulse. The results presented here demonstrate many facets of the control and shaping of the SF signal by control of the input signal initial characteristics. The material parameters chosen for these calculations are arbitrary, but correspond roughly to those for optically pumped metal vapors in the regime $\tau_p > \tau_R$.

Thus, although the simulation inherently yields numerically accurate results for particular experimental design, the results reported here must be taken as qualitative. Our main purpose here is to demonstrate and analyze specific correlations between the initial and boundary conditions associated with the injected pump pulse and characteristics of the SF pulse which evolve. In many of the cases which follow, rules are established through the analysis which can be used to predict quantitative results for any particular experimental conditions. Our choice of particular initial and boundary conditions has been motivated in part by processes which may have been operative in experiments which have been reported⁵⁻¹⁰ and in part by the feasibility of experimental selection or specification. In connection with the latter, we demonstrate the control of one light signal by another via a nonlinear medium, thus imparting nonlinear information transfer and pulse shaping of the SF from specific initial and boundary conditions associated with the pump injection signal.

Figure 2 shows results of the numerical calculation for the transverse integrated intensity profiles for the copropagating SF and injected pulses at a penetration depth of $z=5.3$ cm in the nonlinear medium. These profiles correspond to what would be observed with a wide aperture, fast, energy detector. The pumping pulses are labeled by capital letters, and the corresponding SF pulses are labeled by the corresponding lower case letters. Each set of curves represents a different initial on-axis area for the pump pulse, i.e., curve A is the reshaped pump pulse at $z=5.3$ cm which had its initial on-axis area specified as $\theta_p=\pi$, and curve a is the resulting SF pulse which has evolved. All other parameters are identical for each set of pulses. The initial conditions for the atomic medium is that nearly all the population is in the ground state e_1 at $t=0$, and a small, but nonzero macroscopic polarization exists between levels e_1 and e_2 . These two conditions are specified by two parameters ϵ and δ , respectively, and we have chosen $\delta=\epsilon=10^{-3}$ self-consistently as

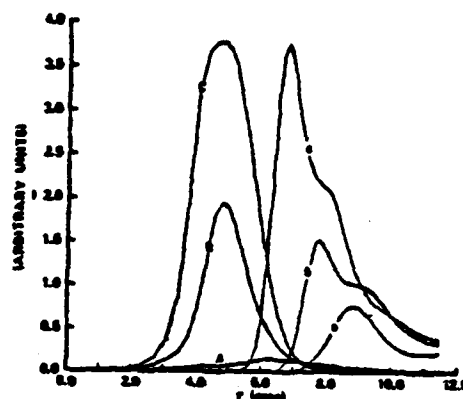


FIG. 2. Radially integrated normalized intensity profiles for the SF and injected pulse at $z=5.3$ -cm penetration depth for three different values for the initial on-axis injection pulse area θ_p . The SF pulses are indicated by a, b, and c, whereas the corresponding injected pump pulses are labeled A, B, and C. The injected pulses are initially Gaussian in r and t with widths (FWHM) $r_0=0.24$ cm and $\tau_p=4$ nsec, respectively. The level spacings are such that $(e_3-e_1)/(e_3-e_2)=126.6$. The effective gain for the pump transition $g_p=17$ cm⁻¹ and that for the SF transition $g_s=291.7$ cm⁻¹. The gain-length Fresnel numbers for the two transitions are $\mathcal{F}_p=16800$ and $\mathcal{F}_s=2278$. The relaxation and dephasing times are taken as identical for all transitions and are given as $T_1=80$ nsec and $T_2=70$ nsec, respectively. The injected pulse initial on-axis areas are (A) $\theta_p=\pi$, (B) $\theta_p=2\pi$, and (C) $\theta_p=3\pi$.

specified in the Appendix. These initial conditions are uniform for the atomic medium and are the same for all results reported here. Notice that we have neglected spontaneous relaxation in the pump transition $1\leftrightarrow 3$ relative to the SF transition $3\leftrightarrow 2$. This is justified owing to our choice of relative oscillator strengths (see Fig. 2 caption).

These results clearly indicate the coherence effect of the initial pump-pulse area on the SF signal which evolves. Notice that the peak intensity of the SF pulses increases monotonically with initial on-axis area for the pump pulse. This is caused by self-focusing due to transverse coupling and propagation. For instance, a 2π -injection pulse would generate a very small SF response compared to an initial π -injection pulse for these conditions at relatively small penetration z , or for the corresponding case in one spatial dimension. Even so, the peak SF intensity is approximately proportional to the square of the pump-pulse initial on-axis area, whereas the delay time τ_d between the pump-pulse peak and the corresponding SF pulse peak is very nearly inversely proportional to the input pulse area. The temporal SF pulse width at full width at half maximum (FWHM) τ_s is approximately invariant with respect

to the injection pulse area.

Since the average values of τ_D and the peak SF intensity are important quantities for interpreting experimental results with theories of SF^{1,2,11}, the manner in which the pump-pulse coherence and initial on-axis area affects these quantities is seen to be of extreme importance in any analysis.

Figure 3 shows the effect upon the SF pulse of variation in the initial temporal width at half maximum intensity for the pumping pulse. As the initial temporal width of the injected pulse τ_p becomes smaller, the SF delay time τ_D increases, whereas the peak SF intensity decreases, and the SF temporal width τ_s remains very closely fixed.

It is clear from these results that there exists an approximate linear relationship between the time delay τ_D , between the peak SF intensity and the corresponding pump-pulse intensity, and the initial temporal width τ_p of the pump pulse.

This linear relationship is shown in Fig. 4, where the time delay τ_D is plotted versus the corresponding pump-pulse initial temporal width, from Fig. 3. These results generate the following empirical formula for τ_D as a function of τ_p :

$$\tau_D = 0.375\tau_R [\ln(4\pi/\phi_0)]^2 - 4\tau_R\gamma_1(\gamma_R/4\gamma_1 - 1)\tau_p, \quad (3.1)$$

where²⁰

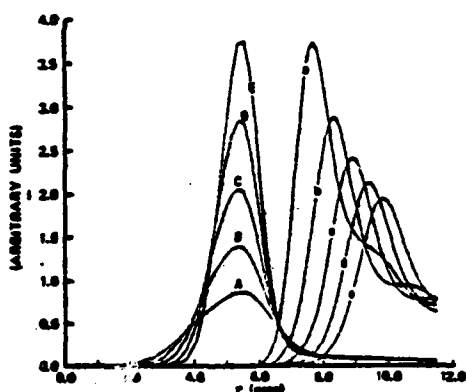


FIG. 3. Radially integrated normalized intensity profiles for the SF and injected pulses at $x=5.3$ -cm penetration depth for five different values for the initial temporal width of the injected pulse. The initial on-axis area of the injected pulse is $\theta_p = \pi$, and the pump transition and SF effective gains are $g_p = 17.5 \text{ cm}^{-1}$ and $g_s = 641.7 \text{ cm}^{-1}$, respectively. All other parameters except for the Fresnel numbers are the same as those for Fig. 2. The injected pulse initial temporal widths at half maximum are (A) $\tau_p = 4 \text{ nsec}$, (B) $\tau_p = 3.3 \text{ nsec}$, (C) $\tau_p = 2.9 \text{ nsec}$, (D) $\tau_p = 2.5 \text{ nsec}$, and (E) $\tau_p = 2.2 \text{ nsec}$.

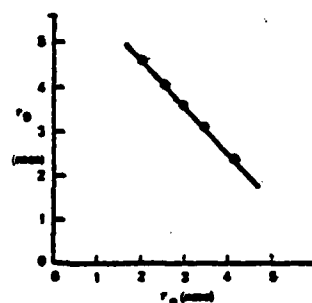


FIG. 4. Delay time τ_D of the SF peak intensity from the corresponding pump-pulse peak intensity vs the pump-pulse initial full temporal width at half maximum intensity τ_p , according to Fig. 3.

$$\tau_R = \frac{2T_2}{g_s z} \quad (3.2)$$

is the characteristic superfluorescence time,^{1,3} and ϕ_0 is a parameter adjusted to give a best fit to the calculational results. For the case treated here, $\tau_R = 41 \text{ psec}$, $T_2 = 70 \text{ nsec}$, and $\phi_0 = 10^{-8}$, and the Fresnel number $F = 1.47$.

The relation (3.1) is at least in qualitative agreement with the analytical prediction made in Ref. 4(b), Eq. (5.1), based upon mean-field theory. The first term in (3.1) was chosen to conform with the quantum-mechanical SF initiation result.²¹ The quantity ϕ_0 can be interpreted as the "effective tipping angle" for an equivalent π -initial impulse excitation, i.e., for $\tau_p \rightarrow 0$, which initiates subsequent superfluorescence. It is to be noted that the value for ϕ_0 is dependent upon our choice of δ (see the Appendix); however, τ_D varies less than 25% for order-of-magnitude changes in δ for $|\delta| < 10^{-2}$. The choice of δ is simply an artificial way of instigating the semiclassical numerical calculation, and reasonable variations in its value do not strongly affect the results. The physical parameter is, then, ϕ_0 , which, interpreted on the basis of (3.1), is generated through the dynamics caused by the pumping process and represents quantum SF initiation. The full statistical treatment for three-level superfluorescence with pump dynamics included will be presented in another publication.²²

These results emphasize the importance of the initiating pulse characteristics in SF pulse evolution, and the effect of SF pulse narrowing with approximate pulse shape invariance by increasing the initial temporal width of the injected pulse. It is emphasized that all other parameters, including the initial value for the injected pulse on-axis area, are identical among these sets of curves.

The initial radial width r_0 of the injected pulse

was varied and the effect upon the SF pulse evolution is shown in Fig. 5. There is clearly indicated an optimum value for r_0 for which the SF peak intensity is a maximum and the SF temporal width τ_s is a minimum. If the relation (2.18) is used in conjunction with the values of the parameters given in Fig. 5 and its caption, it is seen that optimization occurs for a value for the conventional Fresnel number F_s for the SF transition $F_s = 1$. Thus from (2.18) and $F_s = 1$, we have

$$\mathcal{F}_s = 2z_{\text{max}} \quad (3.3)$$

for the gain-length Fresnel number. Since $F_s \sim 1/z$, the implication is that Eq. (3.3) gives the penetration depth z_{max} at which the SF peak intensity reaches a maximum in terms of the ratio \mathcal{F}_s/g_s . Since this takes both transverse and diffraction explicitly into account as well as propagation, this is indeed a profound statement.

Further insight into the implication of (3.3) can be obtained by considering a one-spatial dimension analogy. If the linear field loss is taken to be entirely due to diffraction, then the one-dimensional linear loss κ corresponding to the two-dimensional case

specified by \mathcal{F}_s is given by

$$\kappa_s = -\frac{1}{r_0^2} \quad (3.4)$$

Then, from (2.17),

$$\mathcal{F}_s = \frac{2}{\kappa_s} \quad (3.5)$$

is the effective gain g_s to loss κ_s ratio. From the condition (3.3),

$$z_{\text{max}} = \kappa_s^{-1}, \quad (3.6)$$

i.e., z_{max} is the penetration depth at which the SF peak intensity is a maximum and corresponds to one effective diffraction length, as defined by (3.4). Carrying the one-dimensional analogy one step further, (3.5) used in (2.18) gives

$$F = (\kappa_s)^{-1} \quad (3.7)$$

From (3.4) and (3.7) we have exhibited the significance of the Fresnel numbers \mathcal{F} and F in terms of diffraction loss, i.e., \mathcal{F} can be thought of as gain to loss ratio, Eq. (3.5), whereas F can correspondingly be thought of as the reciprocal of the strength of the diffraction loss, Eq. (3.7).

The effect on SF pulse evolution of variation of the initial radial shape of the initiating pulse is shown in Fig. 6. The shape parameter ν is defined in terms of the initial condition for the pump transition field amplitude $\omega_R(r)$:

$$\omega_R(r) = \omega_R(0) \exp[-(r/r_0)^\nu] \quad (3.8)$$

Thus for $\nu=2$, the initial amplitude of the injected pulse is radially Gaussian, whereas for $\nu=4$, it is radially super-Gaussian. We see from the results presented in Fig. 6 that as the initial radial shape of the injected pulse becomes broader, i.e., larger values for ν , the peak intensity of the SF pulse generated becomes larger, and the width τ_s and delay time τ_D diminish. It is emphasized that all other parameters, including the initial values for the radial and temporal widths are invariant among these sets of curves.

Thus if the initial radial shape of the injected pulse is modulated from one injection to the next, the SF temporal width and delay time τ_D are correspondingly modulated as well as the SF peak intensity. Correspondingly, the coherence and initial radial shape of the pump pulse cannot, with validity, be ignored in interpretation of SF experiments in terms of τ_s and τ_D .

Whereas the initial on-axis area for the pumping pulse was $\theta_0 = 2\pi$ for the results shown in Fig. 6, the identical conditions and parameters were imposed, but the initial on-axis pump-pulse area was changed

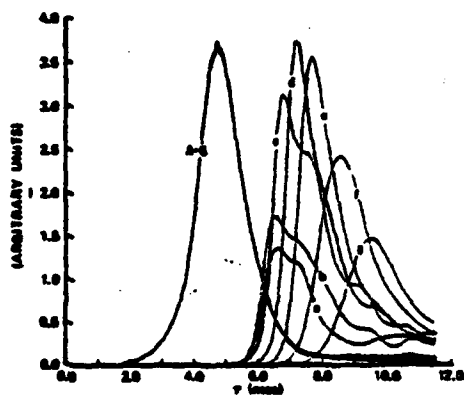


FIG. 5. Radially integrated normalized intensity profiles for the SF and injected pulses at $z=5.3$ -cm penetration depth for seven different values for the injected pulse initial radial width at half maximum r_0 . The initial on-axis area θ_0 of the injection pulse is $\theta_0 = 2\pi$; the SF effective gain $g_s = 758.3 \text{ cm}^{-1}$, and the pump transition effective gain $g_p = 14.6 \text{ cm}^{-1}$. All other parameters are the same as for Fig. 2. The initial radial widths at half maximum for the injected pulses are (a) $r_0 = 0.57 \text{ cm}$, (b) $r_0 = 0.43 \text{ cm}$, (c) $r_0 = 0.24 \text{ cm}$, (d) $r_0 = 0.18 \text{ cm}$, (e) $r_0 = 0.15 \text{ cm}$, (f) $r_0 = 0.11 \text{ cm}$, and (g) $r_0 = 0.09 \text{ cm}$. The corresponding geometrical Fresnel numbers are (a) $F_s = 8.46$, (b) $F_s = 4.79$, (c) $F_s = 1.47$, (d) $F_s = 0.85$, (e) $F_s = 0.57$, (f) $F_s = 0.35$, and (g) $F_s = 0.21$.

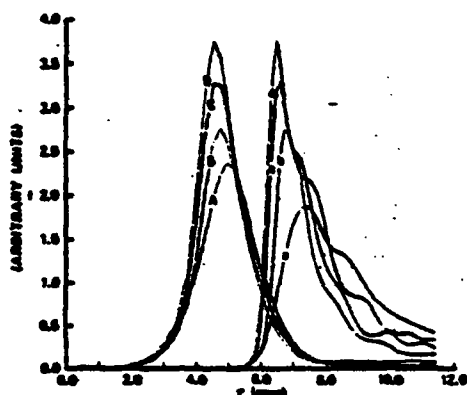


FIG. 6. Radially integrated normalized intensity profiles for the SF and injected pulses at $z=5.3$ -cm penetration depth for four different values for the injected pulse initial radial shape parameter v (see text). The initial on-axis area θ_p of the injected pulse is $\theta_p=2\pi$, and the SF effective gain $g_s=738.3 \text{ cm}^{-1}$, whereas the effective gain for the pump transition $g_p=14.6 \text{ cm}^{-1}$. All other parameters are the same as for Fig. 2. The initial radial shape parameters for the injected pulses are (A) $v=1$, (B) $v=2$, (C) $v=3$, and (D) $v=4$.

to $\theta_p=3\pi$, and the results are shown in Fig. 7. It is seen that the major effect of changing the initial on-axis area from 2π to 3π is to cause more ringing in the SF pulses and to modify the pump-pulse temporal reshaping as is noted by comparing Fig. 7 with Fig. 6.

The response of SF pulse evolution to changes in the initial temporal shape of the injection pulse is shown in Fig. 8, which compares the effect of a

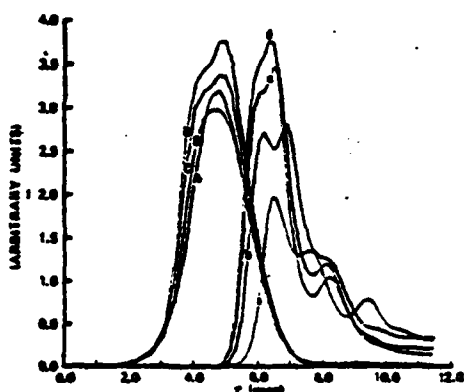


FIG. 7. Radially integrated normalized intensity profiles for the SF and injected pulses at $z=5.3$ -cm penetration depth for four different values for the injected pulse initial radial shape parameter v (see text). The initial on-axis area θ_p of the injected pulse is $\theta_p=3\pi$. All other parameters are the same as for Fig. 6.

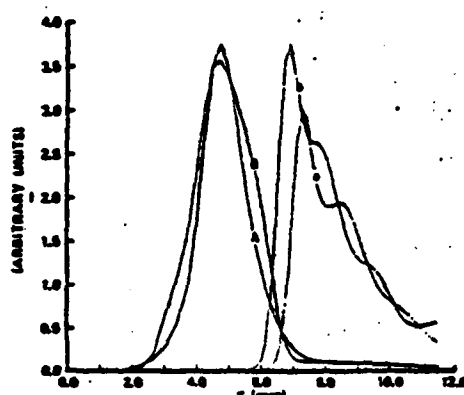


FIG. 8. Radially integrated normalized intensity profiles for the SF and injected pulses at $z=5.3$ -cm penetration depth for two different values for the injected pulse initial temporal shape parameter σ (see text). The initial on-axis area θ_p of the injected pulse is $\theta_p=2\pi$, and the SF effective gain $g_s=641.7 \text{ cm}^{-1}$. All other parameters are the same as for Fig. 3(c). The initial radial shape parameters for the injected pulses are (A) $\sigma=2$ and (B) $\sigma=4$.

Gaussian initial temporal shape for the pump pulse, identified by the temporal shape parameter $\sigma=2$ with that of a super-Gaussian identified by $\sigma=4$. As for the radial distribution discussed previously, the temporal shape parameter σ is defined in terms of the initial condition for the pump transition field amplitude $\omega_R(\tau)$,

$$\omega_R(\tau) = \omega_R(0) \exp[-(\tau/\tau_p)^\sigma]. \quad (3.9)$$

Again, it is seen that the broader initial pump pulse causes an increase in the peak SF intensity and a reduction in the delay time τ_D and SF pulse width τ_s .

Whereas the results of Fig. 8 correspond to an initial on-axis area $\theta_p=2\pi$ for the pump pulse, the results of Fig. 9 correspond to identical conditions and values for the parameters as those for Fig. 8, except that the initial on-axis area for the injection pulse is $\theta_p=3\pi$.

The effect of changing the effective gain for the SF transition g_s and hence the relative oscillator strength between the SF transition and the pump transition is demonstrated in the results of Figs. 10–13. Each of these figures corresponds to a different on-axis initial area θ_p for the injection pulse. Consistent among the entire set of results is that increasing the effective gain g_s results in a nearly linear increase in the SF peak intensity as well as decrease in the delay time τ_D . Also, the smaller area initiating pulse causes a narrower SF pulse to evolve and with apparently less ringing.

fil-
tic,
in-
on-
pa-
sh-
(B)

sir-
are-
sit-
 I_c /
the
(ρ_c
fro

F
files
tion
effec-
ed p-
those
 $g_s =$
cm⁻¹

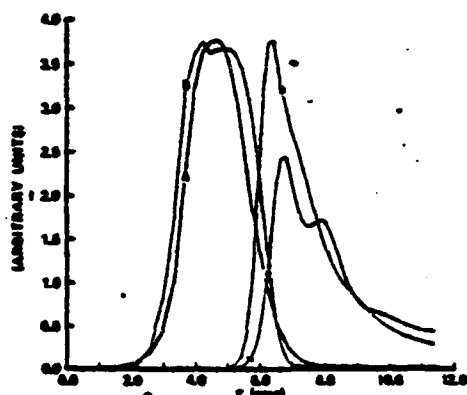


FIG. 9. Radially integrated normalized intensity profiles for the SF and injected pulses at $z=5.3$ -cm penetration depth for two different values for the injected pulse initial temporal shape parameter σ (see text). The initial on-axis area θ_0 of the injected pulse is $\theta_0=3\pi$. All other parameters are the same as for Fig. 8. The initial radial shape parameters for the injected pulses are (A) $\sigma=2$ and (B) $\sigma=4$.

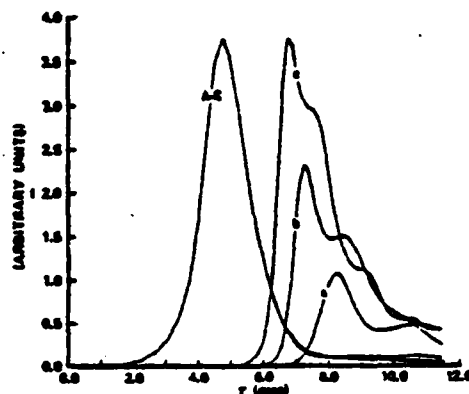


FIG. 11. Radially integrated normalized intensity profiles for the SF and injected pulses at $z=5.3$ -cm penetration depth for three different values for the SF transition effective gain g_s . The on-axis initial area θ_0 for the injected pulse is $\theta_0=2\pi$. All other parameters are the same as for Fig. 10.

Figure 14 shows the effect of variation of the density ρ of active atoms. The effective gains g_s and g_i are changed proportionally, corresponding to a density variation ρ . The ratio of the SF intensities is $I_s/I_b=1.76$ and $I_s/I_a=2.06$; these ratios are larger than the corresponding density ratios squared, $(\rho_s/\rho_b)^2=1.40$ and $(\rho_s/\rho_a)^2=1.49$. This difference from the predictions from previous theories of

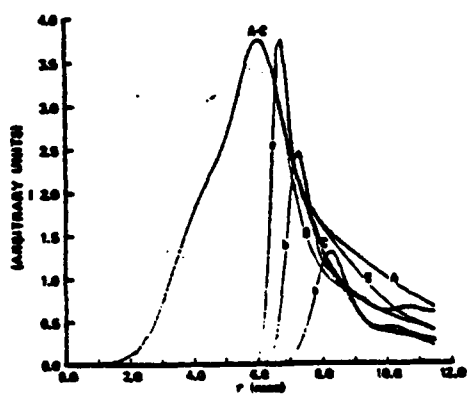


FIG. 10. Radially integrated normalized intensity profiles for the SF and injected pulses at $z=5.3$ -cm penetration depth for three different values for the SF transition effective gain g_s . The on-axis initial area θ_0 for the injected pulse is $\theta_0=\pi$. All other parameters are the same as those for Fig. 9(c). The SF transition effective gain is (a) $g_s=525.0 \text{ cm}^{-1}$, (b) $g_s=641.7 \text{ cm}^{-1}$, and (c) $g_s=758.3 \text{ cm}^{-1}$.

SF¹⁻³ may be due to self-focusing, especially since the values of the effective gains used in this case are quite high. However, the ratio of the temporal widths τ_s , FWHM, are within 15% of the corresponding inverse ratios of the densities; the same is true for the delay time τ_D of the SF intensity peak with respect to the pump intensity peak. These results compare qualitatively reasonably well with the mean-field predictions for SF in two-level systems initially prepared in a state of complete inversion.¹

A comparison of the effects upon the injection pulse of variation in oscillator strengths between the

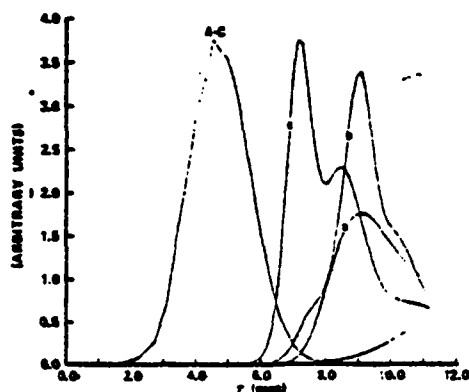


FIG. 12. Radially integrated normalized intensity profiles for the SF and injected pulses at $z=5.3$ -cm penetration depth for three different values for the SF transition effective gain g_s . The on-axis initial area θ_0 for the injected pulse is $\theta_0=3\pi$. All other parameters are the same as for Fig. 10.

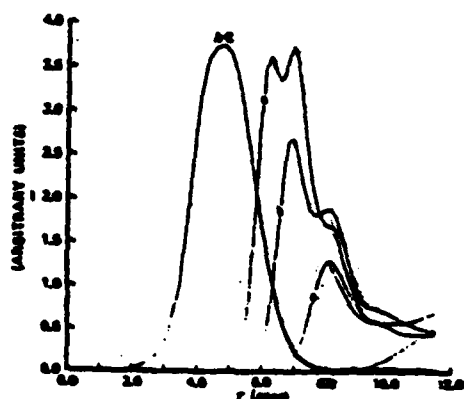


FIG. 13. Radially integrated normalized intensity profiles for the SF and injected pulses at $z=5.3$ -cm penetration depth for three different values for the SF transition effective gain g_s . The on-axis initial area θ_0 for the injected pulse is $\theta_0 = 4\pi$. All other parameters are the same as for Fig. 10.

SF and pump transition (variation of g_s) as contrasted to effects upon the pump pulse of a density variation (variation of both g_p and g_s proportionally) is given in Figs. 15 and 16, respectively. It is seen that the respective effects in the pump-pulse reshaping are quite distinct. The variation in oscillator strengths, Fig. 15, essentially causes "hole burning"

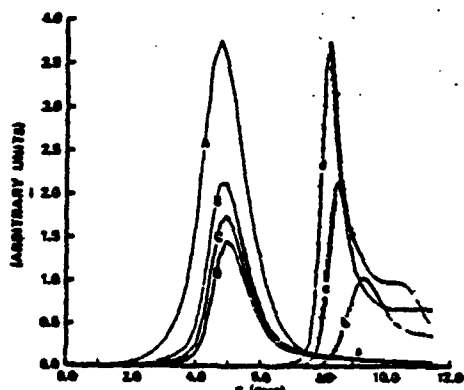


FIG. 14. Radially integrated normalized intensity profiles for the SF and injected pulses at $z=5.3$ -cm penetration depth for three different values for the density ρ of atoms. The on-axis initial area θ_0 for the injected pulse is $\theta_0 = 2\pi$. Except for the effective gains and Fresnel numbers, the values for all other parameters are the same as for Fig. 5(c). For each set of curves, the gain values are (b) $g_s = 525.0 \text{ cm}^{-1}$, $g_p = 26.3 \text{ cm}^{-1}$; (c) $g_s = 641.7 \text{ cm}^{-1}$, $g_p = 32.1 \text{ cm}^{-1}$; and (d) $g_s = 758.3 \text{ cm}^{-1}$, $g_p = 37.9 \text{ cm}^{-1}$. The corresponding Fresnel numbers are (b) $\mathcal{F}_p = 25\,992$, $\mathcal{F}_s = 4100$; (c) $\mathcal{F}_p = 31\,724$, $\mathcal{F}_s = 5010$; and (d) $\mathcal{F}_p = 37\,456$, $\mathcal{F}_s = 5922$.

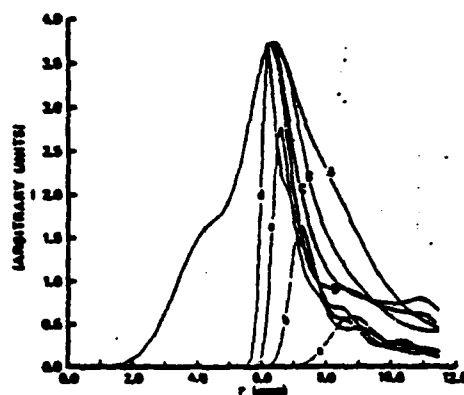


FIG. 15. Radially integrated normalized intensity profiles for the SF and injected pulses at $z=5.3$ -cm penetration depth for four different values for the SF transition effective gain g_s . The initial on-axis area for the injected pulse is $\theta_0 = \pi$, and the effective gain for the pump transition $g_p = 17.5 \text{ cm}^{-1}$. Except for the effective gain g_s , all other parameters are the same as those for Fig. 5(c). The SF transition effective gain g_s for each set of curves is (a) $g_s = 291.7 \text{ cm}^{-1}$, (b) $g_s = 408.3 \text{ cm}^{-1}$, (c) $g_s = 525.0 \text{ cm}^{-1}$, and (d) $g_s = 641.7 \text{ cm}^{-1}$.

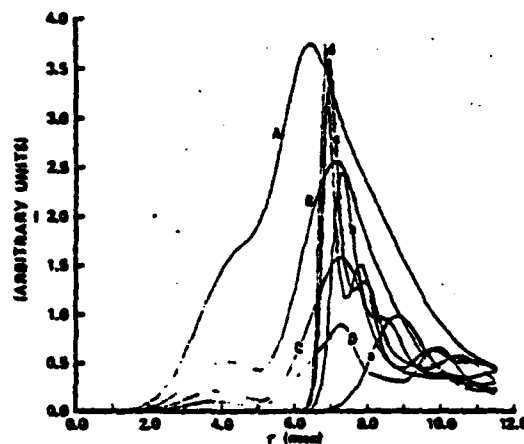


FIG. 16. Radially integrated normalized intensity profiles for the SF and injected pulse at $z=5.3$ -cm penetration depth for four different values for the density ρ of atoms. The on-axis initial area θ_0 for the injected pulse is $\theta_0 = \pi$. Except for the effective gains and Fresnel numbers, the values for all other parameters are the same as for Fig. 5(c). For each set of curves, the gain values are (a) $g_s = 291.7 \text{ cm}^{-1}$, $g_p = 17.5 \text{ cm}^{-1}$; (b) $g_s = 408.3 \text{ cm}^{-1}$, $g_p = 24.5 \text{ cm}^{-1}$; (c) $g_s = 525.0 \text{ cm}^{-1}$, $g_p = 31.5 \text{ cm}^{-1}$; and (d) $g_s = 641.7 \text{ cm}^{-1}$, $g_p = 38.5 \text{ cm}^{-1}$. The corresponding Fresnel numbers are (a) $\mathcal{F}_p = 17\,296$, $\mathcal{F}_s = 2278$; (b) $\mathcal{F}_p = 24\,212$, $\mathcal{F}_s = 3188$; (c) $\mathcal{F}_p = 31\,130$, $\mathcal{F}_s = 4100$; and (d) $\mathcal{F}_p = 38\,048$, $\mathcal{F}_s = 5010$.

in the following edge of the pump pulse, whereas the variation in density, Fig. 16, affects the whole pump pulse. This contrast has an analogy as an inhomogeneous, Fig. 15, as opposed to a homogeneous, Fig. 16, effect on the pump pulse. This effect might be used for the purposes of pulse shaping under suitable conditions.

Shown in Fig. 17 is the transverse integrated SF pulse intensity versus retarded time τ (curve 2) together with the transverse integrated pump-pulse intensity versus τ (curve 1) for a gain and propagation depth chosen so that the pulses temporally overlap. Under these conditions the two pulses strongly interact with each other via the nonlinear medium, and the two-photon processes (resonant, coherent Raman—RCR), which transfer populations directly between levels e_2 and e_1 , make strong contributions to the mutual pulse development.⁴ The importance of the RCR in SF dynamical evolution in an optically pumped three-level system was pointed out for the first time in Ref. 4. Indeed, the SF pulse evolution demonstrated here has greater nonlinearity than SF in a two-level system which has been prepared initially by an impulse excitation. What is remarkable is that this is an example where the SF pulse temporal width τ_s is much less than the pump width τ_p , even though the two pulses temporally overlap, i.e., the SF process gets started late and terminates early with respect to the pump time duration. Pulses of this type have been observed²³ in CO_2 -pumped CH_3F .

The remaining figures are isometric representa-

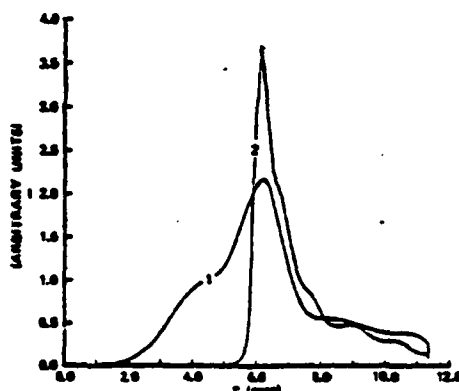


FIG. 17. Radially integrated intensity profiles, in units of Rabi frequency, for the SF (2) and injected pulse (1) at a penetration depth of $z=5.3$ cm. The effective gain for the pump transition and the SF transition are $g_p=17$ cm^{-1} and $g_s=641.7$ cm^{-1} , respectively. The initial on-axis area for the injected pulse is $\theta_s=\pi$. All other parameters are the same as for Fig. 2.

tions of pump-pulse and SF pulse copropagation and interaction via the nonlinear medium. These figures exhibit details of the dynamic mutual pulse reshaping, self-focusing and defocusing during SF buildup.

The pulse intensities as functions of the radial coordinate ρ and retarded time τ are presented in Figs. 18 and 19 for two different penetrations $z=4.4$ cm and $z=5.3$ cm, respectively, into the high gain medium. The injected pulse is initially radially and temporally Gaussian. Both the pump pulse and the SF pulse are seen to exhibit considerable self-defocusing with ringing following the main SF peak. At the larger penetration, Fig. 19, a large postpulse appears in both the pump and SF pulse propagation. This is due to energy feedback from the SF to the pump transition. The postpulses overlap, and so the two-photon RCR effects are active and quite significant in the dynamic evolution and coupling between the pump and SF pulses. This effect is due entirely to the coherence in the dynamical evolution of the system.

Portrayed in Figs. 20 and 21 are isometric representations for the radial and temporal dependence of the copropagating injected and SF pulses for two different initial shape distributions for the pump pulse. In the first case, Fig. 20, the initial temporal distribution of the injected pulse is Gaussian, whereas the initial radial distribution is characterized by the parameter $\nu=3$, Eq. (3.8). It is observed that the injected pulse has undergone considerable reshaping, due to propagation, to a more Gaussian radial distribution, and the SF pulse exhibits strong self-defocusing in the wings of the tail region. In the second case, Fig. 21, the initial radial distribution of the injected pulse is Gaussian, whereas the initial temporal distribution is half-Gaussian, with the sharp temporal cutoff on the following temporal half-section of the pulse. The SF pulse rises extremely sharply, in comparison to the other cases analyzed, and tapers off with strong self-defocusing indicated in the wings of the pulse tail. Pump pulses of this type are generated using a plasma switch¹⁰ and the corresponding SF pulses with steep rise have been observed.

IV. CONCLUSIONS

The effects presented here clearly demonstrate the coherence and deterministic effects on SF pulse evolution of injection pump-pulse characteristics and conditions in the regime $\tau_p < \tau_R$. It is suggested that effects of the type discussed here may have in fact been operative in SF experiments and their results which were published earlier.⁵⁻¹⁰ The pump pulse was taken as purely coherent in these calculations. To determine whether or not effects of the nature

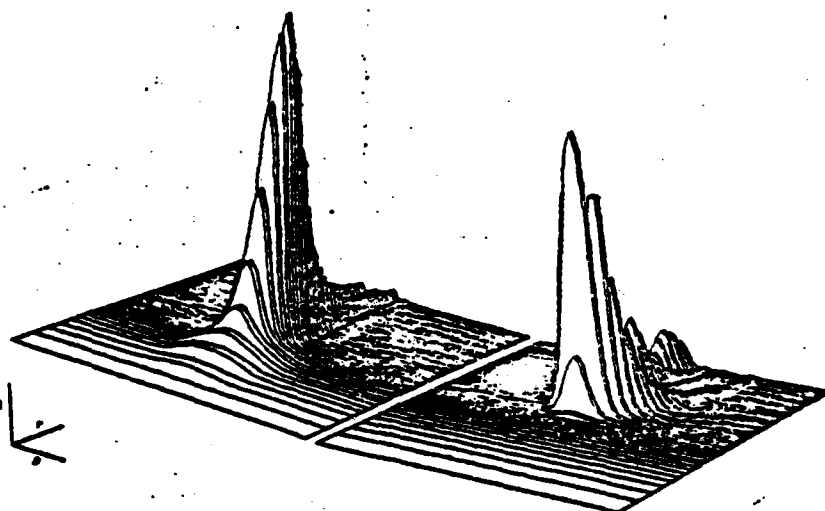


FIG. 18. Pulse intensity I as a function of the radial coordinate ρ and retarded time τ at penetration $z=4.4$ cm. The injected pump pulse is in the upper left, and the SF pulse, which is generated, is in the lower right. The parameters are the same as for Fig. 3(A).

reported here are indeed operative in a given experiment, it is crucial to determine the degree of coherence of the pumping process as well as its temporal duration.⁴

Furthermore, and perhaps of greater importance, we have demonstrated the control and shaping of the SF pulse which evolves by specification of par-

ticular initial characteristics and conditions for the pumping pulse which is injected into the nonlinear medium to initiate SF emission. These manifestations and others of the same class we call the control of light by light via a nonlinear medium. This phenomenon constitutes a method for nonlinear information encoding, or information transfer, from

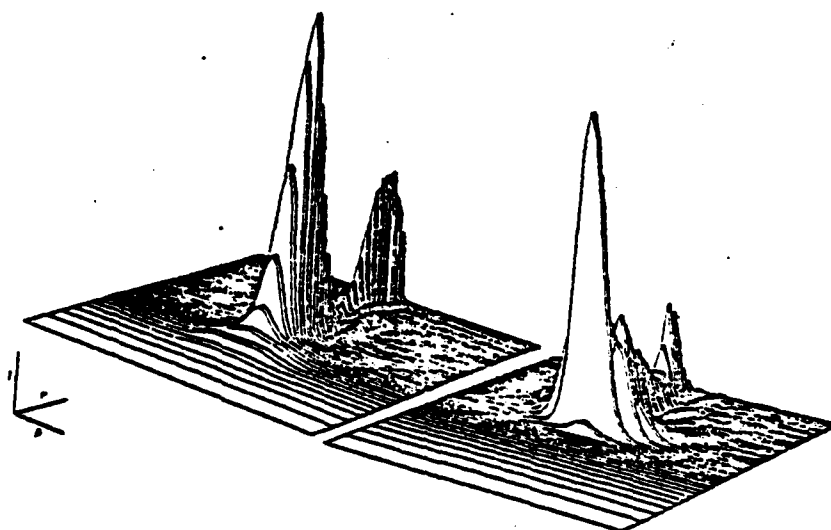


FIG. 19. Pulse intensity I as a function of the radial coordinate ρ and retarded time τ at penetration $z=5.3$ cm. The injected pump pulse is in the upper left, and the SF pulse, which is generated, is in the lower right. The parameters are the same as for Fig. 18.

ject
sar
pa:

th:
sp:
to
me

F
ject
sar
the
pul

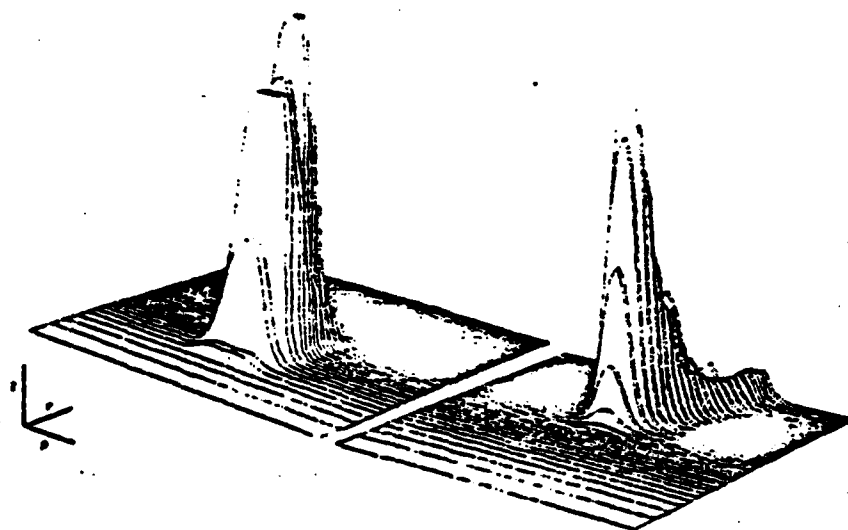


FIG. 20. Pulse intensity I as a function of the radial coordinate ρ and retarded time τ at penetration $z=5.3$ cm. The injected pump pulse is in the upper left, and the SF pulse, which is generated, is in the lower right. The parameters are the same as for Fig. 14(b) except that the initial on-axis area for the injected pump pulse is $\theta_p=3\pi$ and the initial radial shape parameter is $v=3$ (see text).

the injection pulse initial characteristics to corresponding SF pulse characteristics which evolve due to the interaction and interaction in the nonlinear medium.

Work is now in progress to incorporate the effects of quantum statistics of the SF spontaneous relaxation process.²² We are in the process of further determination and analysis of the nonlinear interac-

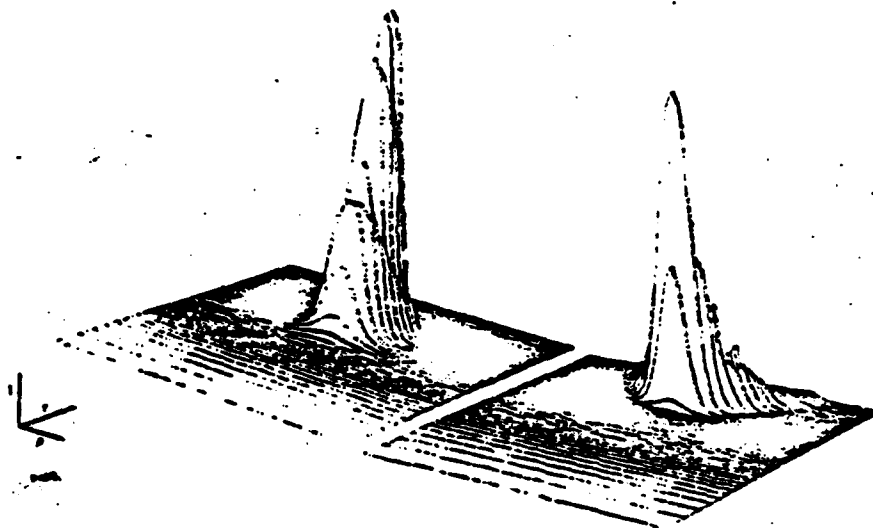


FIG. 21. Pulse intensity I as a function of the radial coordinate ρ and retarded time τ at penetration $z=5.3$ cm. The injected pump pulse is in the upper left, and the SF pulse, which is generated, is in the lower right. The parameters are the same as for Fig. 6(B) except that the initial on-axis area for the injected pulse is $\theta_p=3\pi$, and the initial temporal shape of the injected pulse is half-Gaussian with the sharp temporal cutoff on the following, i.e., increasing τ , side of the pumping pulse.

tion between two copropagating pulses resonantly, as well as nonresonantly, interacting by a nonlinear medium.

ACKNOWLEDGMENTS

The programming assistance of Y. Claude and M. Cormier is gratefully acknowledged. The work of F. P. M. was partially supported by the U. S. Army Research Office, Battelle Columbus Laboratories, and the Office of Naval Research.

APPENDIX

We must choose the initial conditions self-consistently. We wish to establish a small, but nonzero, uniform initial transverse polarization δ for the $3 \rightarrow 2$ transition. For self-consistency, this corresponds to initial population depletion ϵ of the ground-state population, consistent with (2.13) and Eqs. (2.10).

In terms of initial population numbers N_k ,

$$W_{32} = N_3 - N_2, \quad (A1)$$

$$W_{31} = N_3 - N_1. \quad (A2)$$

We choose

$$N_1 = 1 - \epsilon, \quad (A3)$$

ϵ small and positive and impose the ansatz

$$U_{32} = p \sin \delta \sin \phi, \quad (A4)$$

$$V_{32} = p \sin \delta \cos \phi, \quad (A5)$$

and let

$$p = \epsilon, \quad N_2/N_3 \ll 1. \quad (A6)$$

The condition (A6) means essentially that $N_3 \approx \epsilon$ and $N_2 \approx 0$. Equations (A1), (A4), and (A5) under condition (A6) become

$$U_{32} \approx \epsilon \delta \sin \phi, \quad (A7)$$

$$V_{32} \approx \epsilon \delta \cos \phi, \quad (A8)$$

$$W_{32} \approx \epsilon \cos \delta. \quad (A9)$$

Our uniform initial conditions are just the conditions which led to the linearized mean-field equations in the small fluorescence signal regime of Ref. 4, Eqs. (4.14c)–(4.14f). Initially, the pump field amplitude $\omega_R = 0$, and these equations of motion become

$$\dot{R}_{13} = -i\alpha/2A_T R_{12}, \quad (A10)$$

$$\dot{R}_{32} = -2i\alpha A_T^\dagger R_1, \quad (A11)$$

$$\dot{R}_{12} = -2i\alpha A_T^\dagger R_1, \quad (A12)$$

$$\dot{A}_T = -i\alpha R_{23} - \kappa A_T, \quad (A13)$$

and A_T is the initial fluorescence field amplitude, $\alpha = g_{eff}\gamma_L$, and κ is the linear fluorescence field loss. We let

$$R_3 \equiv \frac{1}{2} W_{32},$$

and initially,

$$\kappa A_T \gg \frac{\partial A_T}{\partial t}. \quad (A14)$$

The condition (A14) in (A13) gives

$$A_T = -\frac{i\alpha}{\kappa} R_{23}. \quad (A15)$$

Using (A15) and (A14) to eliminate the field amplitude A_T from Eqs. (A10)–(A13), we get

$$\dot{R}_{31} = -\frac{\alpha^2}{2\kappa} R_{21} R_{32}, \quad (A16)$$

$$\dot{R}_{12} = \frac{2\alpha^2}{\kappa} R_{13} R_{32}, \quad (A17)$$

$$\dot{R}_{32} = \frac{\alpha^2}{\kappa} W_{32} R_{32}. \quad (A18)$$

Dividing (A17) by (A16),

$$\frac{dR_{12}}{dR_{31}} = -4 \frac{R_{13}}{R_{21}}. \quad (A19)$$

Integrating (A19),

$$R_{13}^2 = -\frac{1}{4} R_{12}^2, \quad (A20)$$

where the constant of integration has been set equal to zero. Thus

$$R_{13} = \frac{i}{2} R_{12}. \quad (A21)$$

In terms of the real variables defined by (2.11b), and using (A21), we get

$$U_{21} = -2V_{32}, \quad (A22)$$

$$V_{21} = 2U_{32}. \quad (A23)$$

From the initial conditions (A1)–(A6),

$$W_{32} \equiv \cos \eta = -1 + 2\epsilon. \quad (A24)$$

Thus

$$\eta = \cos^{-1}(2\epsilon - 1), \quad (A25)$$

and

$$U_{31} = \sin \eta \sin \phi, \approx \eta \sin \phi, \quad (A26)$$

$$V_{31} = \sin \eta \cos \phi, \approx \eta \cos \phi. \quad (A27)$$

We have, therefore, using (A9),

27

27

(A13)
splitting,
field loss.

$W_{12} = \epsilon$, (A28)

since we must choose the phase ϕ_2 such that $\sin \phi_2 = 0$. We have

$W_{11} = 2\epsilon - 1$, (A29)

$U_{31} = \eta \sin \phi_p$, (A32)

$U_{22} = \epsilon \delta \sin \phi_p = 0$, (A30)

$V_{31} = \eta \cos \phi_p$, (A33)

$V_{22} = \epsilon \delta \cos \phi_p = \epsilon \delta$, (A31)

with η given by (A25) and ϕ_p chosen arbitrarily.

(A14)

¹R. Bonifacio and L. A. Lugiato, *Phys. Rev. A* **11**, 1507 (1975); **12**, 587 (1975).

²R. H. Dicke, *Phys. Rev.* **91**, 99 (1954).

³See papers and references in *Cooperative Effects in Matter and Radiation*, edited by C. M. Bowden, D. W. Howgate, and H. R. Robl (Plenum, New York, 1977).

⁴(a) C. M. Bowden and C. C. Seng, *Phys. Rev. A* **18**, 1558 (1978); (b) **20**, 2033 (1979).

⁵N. Skirbanowitz, J. P. Herman, J. C. MacGillivray, and M. S. Feld, *Phys. Rev. Lett.* **30**, 309 (1973).

⁶H. M. Gibbs, Q. H. F. Vrehan, and H. M. J. Hicksports, *Phys. Rev. Lett.* **39**, 547 (1977).

⁷Q. H. F. Vrehan, *Ref. 3*, p. 79.

⁸M. Gross, C. Fabre, P. Fillet, and S. Haroche, *Phys. Rev. Lett.* **36**, 1035 (1976).

⁹A. Flusberg, F. Mossberg, and S. R. Hartmann, *Ref. 3*, p. 37.

¹⁰A. T. Rosenberger and T. A. DeTemple, *Phys. Rev. A* **24**, 868 (1981).

¹¹N. E. Rehler and J. H. Eberly, *Phys. Rev. A* **3**, 1735 (1971).

¹²F. T. Hies and J. H. Eberly, *Phys. Rev. Lett.* **47**, 838 (1981).

¹³J. R. R. Leite, R. S. Sheffield, M. Ducloy, R. D. Sharma, and M. S. Feld, *Phys. Rev. A* **14**, 1151 (1976).

¹⁴R. Gilmore, *Lie Groups, Lie Algebras, and Some of*

Their Applications (Wiley, New York, 1974), Chap. 6, Sec. 2.

¹⁵R. Gilmore, C. M. Bowden, and L. M. Narducci, *Phys. Rev. A* **12**, 1019 (1975).

¹⁶R. Gilmore, C. M. Bowden, and L. M. Narducci, in *Quantum Statistics and the Many-Body Problem*, edited by S. B. Trickey, W. R. Kirk and J. W. Dufty (Plenum, New York, 1975).

¹⁷F. P. Mattar and M. C. Newstein, *Ref. 3*, p. 139.

¹⁸F. P. Mattar, in *Optical Bistability*, edited by C. M. Bowden, M. Cifan, and H. R. Robl (Plenum, New York, 1981), p. 503; in *Proceedings, Tenth Simulation and Modeling Conference, Pittsburgh, 1978*, edited by W. Vogt and M. Mickle (Instrument Society of America, Pittsburgh, 1979).

¹⁹F. P. Mattar, H. M. Gibbs, S. L. McCall, and M. S. Feld, *Phys. Rev. Lett.* **46**, 1123 (1981).

²⁰R. Friedberg and S. R. Hartmann, *Phys. Rev. A* **13**, 495 (1976).

²¹F. Haake, J. Haus, H. King, G. Schroder, and R. Glauber, *Phys. Rev. Lett.* **45**, 558 (1980); D. Forder, M. F. H. Schuurmans, and Q. H. F. Vrehan, *Phys. Rev. A* **19**, 1192 (1979).

²²C. M. Bowden and F. P. Mattar (unpublished).

²³T. A. DeTemple (private communication).

(A15)

3d am-

(A16)

(A17)

(A18)

(A19)

A20)

qual

A21)

and

22)

23)

24)

15)

6)

7)

273

*presented at Laser '82 Workshop
(Dec 82) submitted to Physica*

FRESNEL DEPENDENCE OF QUANTUM FLUCTUATION IN TWO-COLOR SF FROM THREE-LEVEL SYSTEMS†,††

Farres P. Mattar†††

Fachbereich Physik
Universität Essen-Gesamthochschule, Essen F. R. Germany

and

Spectroscopy Laboratory
Massachusetts Institute of Technology, Cambridge, MA 02139, USA

ABSTRACT

The concomitant effect of dynamic diffraction coupling and quantum initiation are examined in two-color superfluorescence SF with use of a semi-classical model in which diffraction and transverse density variations are rigorously included. The model consists of two scalar field equations closely intertwined in the generalized Bloch equations of a three-level atomic system of a lambda configuration. The medium is completely inverted. The planar regime data accurately reproduces Haake and Reibold results [1] and are in qualitative agreement with Florian, Schwan and Schmid [2] measurements. Feld's [3] propagational model is also shown to be relevant to the physical interpretation and modeling as it was for the two-level [4] case studied by Mattar, Gibbs, McCall and Feld. A synchronization of the delays associated with the two-color SF pulses is always achieved in the plane wave, thus confirming Eberly et al.'s simulation [5] predictions. Moreover, when you refine the model to include phase and transverse variation the synchronization is reduced from 95% to 65% of the number of shots depending on the value of the Fresnel number per gain length F. The variance of delay difference has been calculated as a function of F [6]. The computational model combines the implicit features of the double coherent transient analysis of Mattar and Eberly [7] and the pump dynamic reshaping on SF evolution of Mattar and Bowden [8]. The Fresnel dependencies results of the fluctuations are consistent with those of the two-level counterpart [9].

Classical Equations of Motion and Computational Method

The calculation of SF pulse evolution in the nonlinear regime is necessarily a calculational problem if propagation is explicitly included. We use an algorithm presented elsewhere [10-12] and the model defined by the equations of motion to analyze the effects of coherent pump dynamics, propagation, transverse and diffraction effects on SF emission. To facilitate numerical calculation, the equations of motion are taken in their factorized, semiclassical form with the field operator replaced by its classical representation which is described by Maxwell's equation. The two fluorescence field operator are determined dynamically and spatially in retarded time, by initial and boundary conditions and the equations (The variables transformations and normalization are identical to those for the two-level SF study)

$$\epsilon_{a,b} = \text{Re} \{ \tilde{E}_{a,b} \exp [i (\omega_{a,b} t - K_{a,b} z)] \} \quad (2)$$

$$P_{a,b} = \text{Re} \{ i \tilde{P}_{a,b} \exp [i (\omega_{a,b} t - K_{a,b} z)] \} \quad (3)$$

$$E_{a,b} = (2\mu\tilde{E}/M)\tau_{Ra,b} \quad (4), \quad P_{a,b} = \tilde{P}_{a,b}/\mu_{a,b} \quad (5)$$

$$\tau = 2(z - z/c)/(\tau_{Ra} + \tau_{Rb}) \quad (6)$$

$$\eta_{a,b} = z/\lambda^{\dagger\dagger\dagger} \quad (7)$$

where $E_{a,b}$ and $P_{a,b}$ are the slowly varying complex amplitudes of the electric field and polarization, respectively; W is the population difference; τ is the retarded time; $\eta_{a,b}$ or $\zeta_{a,b}$ the normalized axial coordinate;

† The development -of the numerical program applied to this study was sponsored by the U.S. Army Research office (DAAG23-79-C-0148) and the U.S. office of Naval Research (N00-14-80-C-0175)

†† Stipend was supported by DAAD (F.R. Germany Academic Exchange Service), whereas calculations were supported by KFA-IFF (Kern Forschungs Anlage, Institut für Festkörper Forschung) Jülich, GmbH F.R. Germany

††† On extended leave of absence from the Polytechnic Institute of New York, Brooklyn, New York 11201

†††† If one select λ in terms of the unit nanosecond pulse duration $\lambda = c\tau_p$, one recuperates the SIF normalisation [10,11]; whereas if one select $\lambda = c\tau_R$, the two normalisations given by equation (7) and (9) become equivalent.

$\mu_{a,b}$ is the transition dipole moment matrix element; and $T_1^{a,b}$ the population relaxation and $T_2^{a,b}$ is the polarization dephasing times; T_D the Doppler Broadening time and $\tau_{Ra,b}$ the radiation time for transition a and transition b respectively

$$-\frac{i}{4F_{a,b}} \nabla_T^2 E_{a,b} + \frac{\partial E_{a,b}}{\partial \eta} = (\alpha_{Ra,b} - 2) d \int P_{a,b}(\Delta\Omega) g(\Delta\Omega) d(\Delta\Omega) \quad (8)$$

$$\text{if } \zeta_{a,b} = \alpha_{Ra,b} \quad (9)$$

instead, one obtains

$$-\frac{i}{4F_{ga,b}} \nabla_T^2 E_{a,b} + \frac{\partial E_{a,b}}{\partial \zeta_{a,b}} = d \int P_{a,b}(\Delta\Omega) g(\Delta\Omega) d(\Delta\Omega) \quad (10)$$

$$\text{with } \alpha_{Ra,b} = \frac{\{ \omega_{0a} \mu_a^2 \}}{\omega_{ab} \mu_b^2} N \tau_{Ra,b}; \quad (11) \quad \text{and} \quad \zeta_{a,b} = \frac{\alpha_{Ra,b} T_2}{\tau_{Ra,b}} \quad (\text{see ref [8]}) \quad (12)$$

Equivalently, one solves numerically

$$-i F_{ga}^{-1} \nabla_T^2 E_a + \partial_{\zeta_a} E_a = d P_a \quad (13)$$

$$-i \left(\frac{\alpha_{Rb}}{\alpha_{Ra}} \right) F_{gb}^{-1} \nabla_T^2 E_b + \partial_{\zeta_b} E_b = d \left(\frac{\alpha_{Rb}}{\alpha_{Ra}} \right) P_b \quad (14)$$

Diffraction is taken into account by the transverse Laplacian ∇_T^2

$$= \frac{1}{\rho} \frac{\partial}{\partial \rho} \left(\rho \frac{\partial}{\partial \rho} \right) \text{ with } \rho = r/r_p \text{ for cylindrical geometry} \quad (15)$$

$$= \frac{\partial^2}{\partial \xi^2} + \frac{\partial^2}{\partial \zeta^2} \text{ with } \xi = X/r_p \text{ and } \zeta = Y/r_p \text{ for cartesian geometry} \quad (16)$$

Furthermore, diffraction is also explicitly taken into account by the boundary condition that $\rho = \rho_{\max}$ (or, $\xi = \xi_{\max}$ and $\zeta = \zeta_{\max}$) corresponds to completely absorbing walls (i.e., $\partial_\rho E_{a,b} = 0$ or $\partial_X E_{a,b} = \partial_Y E_{a,b} = 0$). To insure that (1) the entire field is accurately simulated, (2) no artificial reflections are introduced at the numerical boundary $\rho_{\max} \gg r_p$, and (3) fine diffraction variations near the axis are resolved; the sample cross-section is divided into non-uniform stretching cells.^{47,50}

$F_{a,b} = \pi r_p^2 / \lambda_{a,b} L$ (17), the geometric Fresnel number;

if $\alpha_R \equiv \frac{\omega_{0a,b}}{n h c} N \tau_R$ (18) the on-axis effective gain then $F_{ga,b} = \frac{\pi r_p^2}{\lambda_{a,b} \alpha_{Ra,b}^{-1}}$ (19) is the gain length Fresnel number, $F_{ga,b}$ is related to the usual Fresnel number $F_{ga,b}/F_{a,b} = \alpha_{Ra,b} L$ (30) (i.e. the total gain of the medium); one can think of $F_{ga,b}$ as effective gain $\alpha_{Ra,b}^{-1}$ to diffraction loss ratio, $\kappa_{a,b}^{-1}$; whereas $F_{a,b}$ can correspondingly be thought of as the reciprocal of the strength of the diffraction loss $\kappa_{a,b}$ for a length L ,^{34,37} $\kappa_{a,b} = \lambda_{a,b} / \pi r_p^2$

$$F_{ga,b} = \alpha_{Ra,b} / \kappa_{a,b} \quad (22) \quad \text{and} \quad F_{a,b} = (\kappa_{a,b} L)^{-1} \quad (23)$$

α_R^{-1} is the effective Beer length as defined by Gibbs and Slusher⁴⁶ in SIT for sharp line atomic system at with T_2 replaced by τ_R i.e. $\alpha_R = \frac{2\pi\mu^2\omega_0 N}{hc} \tau_R$

Transverse effects influence the SF pulse evolution process in two major ways, (as included in the equation of motion), one of which is spatial averaging. If SF experiments the initial inversion density is radially dependent (see d in the RHS of the field equations), since the pump the light pulse which inverts the sample has typically a Gaussian-like profile. In the absence of diffraction the resulting cylinder of inverted atoms can be thought of as a set of concentric cylindrical shells, each with its own density, initial conditions and delay time. The radiation is a sum of plane-wave intensities; when the entire output signal is viewed the ringing averages out, resulting in an asymmetric pulse with a long tail.¹⁵

A second transverse effect, diffraction, becomes important in samples with small Fresnel number $F = A/\lambda L$, with L the cylinder length and A the cross-section. This effect causes light emitted by one shell to affect the emission from adjacent shells. The Laplacian term ∇_{\perp}^2 , couples together atoms in various parts of the cylindrical cross-section, so that they tend to emit at the same time. This coupling mechanism causes transverse energy flow. Furthermore, this effect slightly increases the delay and reduces the tail and asymmetry.

SF is thus an inherent transverse effect problem even for large F samples since the off-axis modes are not discriminated against. This work is a collaboration with Gibbs, McCall and Feld [4] and was the first one to correctly include this crucial element long sought for [29].

The Mattar model automatically includes the effects of both spatial averaging and diffraction coupling. The first calculations described a geometry with cylindrical symmetry (two spatial dimensions). Subsequent calculations for the two level case have been extended to the more complex case where azimuthal symmetry is absent and two transverse dimensions are required [3]. The latter model is needed to describe short-scale-length phase and amplitude fluctuations which result in multiple transverse mode initiation and lead to multi-directional output with hot spots. This effect is only important in samples with large Fresnel numbers, since diffraction singles out a smooth phase front in small F samples.

However, for the three level case we have for the moment limited our analysis to cylindrical geometry and left cartesian calculation for future work.

$$\tau_{R,a,b} = \lambda \lambda_{a,b} / 4\pi^2 \mu_{a,b}^2 \eta_0^2 L = 8\pi\tau_0 / 3\eta_0^2 \lambda_{a,b}^2 L \quad (24)$$

$$\tau_1^{a,b,c} = 2T_1 / (\tau_{Ra} + \tau_{Rb}) \quad (\text{i.e., the normalisation time } \tau_1 = \frac{1}{2} (\tau_{Ra} + \tau_{Rb})) \quad (25)$$

$$\tau_2^{a,b} = 2T_2 / (\tau_{Ra} + \tau_{Rb}) \quad (26)$$

$$\tau_2^{\frac{1}{2}} = 2T_2^{\frac{1}{2}} / (\tau_{Ra} + \tau_{Rb}) \quad (27)$$

$$\Delta\Omega_{a,b} = 1/2 (\omega_{0,a,b} - \omega_{a,b}) / (\tau_{Ra} + \tau_{Rb}) \quad (28)$$

$$\int_{-\infty}^{\infty} g(\Delta\Omega) d(\Delta\Omega) = \sqrt{\pi} / \tau_2^{\frac{1}{2}} \int_{-\infty}^{\infty} \exp \{ - [(\Delta\Omega)\tau_2^{\frac{1}{2}}]^2 \} d(\Delta\Omega) = 1 \quad (29)$$

$$d = \exp \{ - (\rho/\rho_N)^m \} = \frac{N(\rho)}{N(0)} \quad (30)$$

$d = 1$, uniform density

for $m > 0$ the radial population density distribution for active atoms is variable, say, for an atomic beam

$m = 2$, gaussian density profile

$m = 4$, super-gaussian density profile

$m = 6$, hyper-gaussian density profile

ρ_N is $(1/e)$ radius of the atomic density N distribution

The relationships of α_R and τ_R leads directly to

$$\alpha_R L = 1 \quad (31)$$

As noted previously in the plane wave regime, a universal scaling of the equation exists. The gain length Fresnel number F_g qualifies the competition between diffraction (i.e., transverse effects) and the nonlinear gain of the SF system as it did in SIT²⁵. Drummond and Eberly²¹ also recently recognized this scaling.

- Energy consideration for sharp line $g(\Delta\Omega) = \delta(\Delta\omega)$

$$-iF_{ga}^{-1} \nabla_T (E_a \nabla_T E_a^* - E_a^* \nabla_T E_a) + \partial_{\zeta_a} |E_a|^2 = d(E_a^* P_a + E_a P_a^*) \quad (32)$$

$$-i \left(\frac{\alpha_{Rb}}{\alpha_{Ra}} \right) F_{gb}^{-1} \nabla_{Tb} (E_b \nabla_{Tb} E_b^* - E_b^* \nabla_{Tb} E_b) + \partial_{\zeta_b} |E_b|^2 = d \left(\frac{\alpha_{Rb}}{\alpha_{Ra}} \right) (E_b^* P_b + E_b P_b^*) \quad (33)$$

Summing up for $\alpha_{Rb} = \alpha_{Ra}$

$$\nabla \cdot J_{Tot} = -2d [\partial_{\tau} W_a + (W_a - 1)/\tau_1^a + \partial_{\tau} W_b + (W_b - 1)/\tau_1^b] \quad (34)$$

with J_{Tot} having both longitudinal $J_z^{a,b}$ and transverse ($J_T^{a,b}$ (or, equivalently $J_x^{a,b}$ and $J_y^{a,b}$)) components; when using the polar representation of the complex envelope, we have

$$E_{a,b} = A_{a,b} \exp(i\phi_{a,b}) \quad (35)$$

$$J_z^{a,b} = A_{a,b}^2 \quad \text{and} \quad J_T^{a,b} = 2iF_{ga,b}^{-1} A_{a,b}^2 \nabla_T \phi_{a,b} \quad (36)$$

for cylindrical geometry $J_T^{a,b} = 2iF_{ga,b}^{-1} A_{a,b}^2 \partial_{\phi_{a,b}}/\partial\rho$ (37) whereas for Cartesian geometry

$$J_x^{a,b} = 2F_{ga,b} A_{a,b}^2 \partial_x \phi_{a,b} \quad \text{and} \quad J_y^{a,b} = 2F_{ga,b} A_{a,b}^2 \partial_y \phi_{a,b} \quad (38)$$

The components $J_z^{a,b}$ and $J_T^{a,b}$ represents the longitudinal and transverse energy current flow. Thus, the existence of transverse energy flow is clearly associated with the radial variation of the phase $\phi_{a,b}$ of the complex field amplitude. When $J_T^{a,b}$ is negative [i.e., $\nabla_T \phi_{a,b} > 0$], self-induced focusing dominates diffraction spreading.

One may rewrite the energy continuity equation, Eq. (20) in the laboratory frame to recover its familiar form:

$$\nabla \cdot J_{Tot} = -d \left\{ \frac{\partial}{\partial \tau} [2(W_a + W_b)] + \frac{1}{c\tau_{Ra}\alpha_{Ra}} A_a^2 + \frac{1}{c\tau_{Rb}\alpha_{Rb}} A_b^2 \right\} - (W_a - 1)/\tau_1^a - (W_b - 1)/\tau_1^b \quad (39)$$

It is noteworthy that the two scalar field equations appear to be uncoupled. Nevertheless, the two fields are coupled through the material equations [1,7,8] where the cross-coupling appears explicitly. The inertial response of the resonant three-level atoms closely and tightly interweaves the two waves through the parametric terms.

Following [17-19], we interpret the material equations of motion as c-number representation of the corresponding operator equations.

$$\frac{\partial P_a}{\partial \tau} + \beta_a P_a = E_a W_a - \frac{1}{2} E_b Q \quad \beta_a = \frac{1}{\tau_2^a} + i\Delta\omega_a$$

$$\frac{\partial P_b}{\partial \tau} + \beta_b P_b = E_b W_b - \frac{1}{2} E_a Q^* \quad \beta_b = \frac{1}{\tau_2^b} + i\Delta\omega_b$$

$$\frac{\partial Q}{\partial \tau} + \beta_c Q = \frac{1}{2} (E_a P_b^* + E_b^* P_a)$$

$$\beta_c = \frac{1}{\tau_c} + i\Delta\omega_c$$

$$\frac{\partial W_a}{\partial \tau} + \gamma_a (W_a - W_a^0) = -\frac{1}{2} (E_a^* P_a + E_a P_a^*) - \frac{1}{4} (E_b^* P_b + E_b P_b^*) \quad \gamma_a = \frac{1}{\tau_1}, \quad \gamma_b = \frac{1}{\tau_1} \quad \text{Real}$$

$$\frac{\partial W_b}{\partial \tau} + \gamma_b (W_b - W_b^0) = -\frac{1}{2} (E_b^* P_b + E_b P_b^*) - \frac{1}{4} (E_a^* P_a + E_a P_a^*) \quad (40)$$

$$\text{we introduce the following transformation: } f = e^{-Y\tau} f^s, \text{ thus } \frac{\partial f}{\partial \tau} = e^{-Y\tau} \left(\frac{\partial f^s}{\partial \tau} - Y f^s \right) \quad (41)$$

$$\text{at } \frac{\partial f}{\partial \tau} = e^{Y\tau} \frac{\partial f^s}{\partial \tau} - Y f^s \quad (42)$$

$$(\gamma = \beta_a, \beta_b, \beta_c, \gamma_a, \gamma_b)$$

Thus we obtain:

$$\frac{\partial P_a^s}{\partial \tau} = e^{(\beta_a - \gamma_a)\tau} E_a W_a^s - \frac{1}{2} e^{(\beta_a - \beta_a)\tau} E_b Q^s$$

$$\frac{\partial P_b^s}{\partial \tau} = e^{(\beta_b - \gamma_b)\tau} E_b W_b^s - \frac{1}{2} e^{(\beta_b - \beta_c)\tau} E_a Q^{s*}$$

$$\frac{\partial Q^s}{\partial \tau} = \frac{1}{2} e^{(-\beta_c - \beta_b)\tau} E_a P_b^{s*} + \frac{1}{2} e^{(-\beta_c - \beta_a)\tau} E_b^* P_a^s$$

$$\frac{\partial W_a^s}{\partial \tau} = e^{Y_a \tau} [Y_a^0 W_a^s - \text{Re} (e^{-\beta_a \tau} E_a^* P_a^s) - \frac{1}{2} \text{Re} (e^{-\beta_b \tau} E_b^* P_b^s)]$$

$$\frac{\partial W_b^s}{\partial \tau} = e^{Y_b \tau} [Y_b^0 W_b^s - \text{Re} (e^{-\beta_b \tau} E_b^* P_b^s) - \frac{1}{2} \text{Re} (e^{-\beta_a \tau} E_a^* P_a^s)] \quad (43)$$

$$\text{Introducing the notation } \Gamma(\tau) = e^{Y\tau}, \text{ we get:} \quad (44)$$

$$\frac{\partial P_a^s}{\partial \tau} = \Gamma_{\gamma_a} \frac{\Gamma_{\beta_a}}{\Gamma_{\gamma_a}} E_a W_a^s - \frac{1}{2} \Gamma_{\beta_c} \frac{\Gamma_{\beta_a}}{\Gamma_{\gamma_a}} E_b Q^s \quad \text{with } f = \frac{f^s(\tau)}{\Gamma(\tau)}$$

$$\frac{\partial P_b^s}{\partial \tau} = \Gamma_{\gamma_b} \frac{\Gamma_{\beta_b}}{\Gamma_{\gamma_b}} E_b W_b^s - \frac{1}{2} \Gamma_{\gamma_c} \frac{\Gamma_{\beta_b}}{\Gamma_{\gamma_b}} E_a Q^{s*}$$

$$\frac{1}{2} \Gamma_{\gamma_b} \frac{\Gamma_{\beta_c}}{\Gamma_{\gamma_b}} E_a P_b^{s*} + \frac{1}{2} \Gamma_{\beta_a} \frac{\Gamma_{\beta_c}}{\Gamma_{\gamma_b}} E_b^* P_a^s$$

$$\frac{\partial W_a^s}{\partial \tau} = \Gamma_{\gamma_a} [Y_a^0 W_a^s - \text{Re} \left(\frac{1}{\Gamma_{\beta_a}} E_a^* P_a^s \right) - \frac{1}{2} \text{Re} \left(\frac{E_b^* P_b^s}{\Gamma_{\beta_b}} \right)]$$

$$\frac{\partial w_b^2}{\partial t} = \Gamma_{yb} [\gamma_b w_b^0 - \text{Re} \left(\frac{E_b^* P_b^2}{\Gamma_{yb}} \right) - \frac{1}{2} \text{Re} \left(\frac{E_b^* P_b^2}{\Gamma_{ba}} \right)] \quad (46)$$

It is important to realize, that the yellow polarization P_a is driven not only by the yellow field component E_a but also by the red one, E_b since the product $E_b Q$ corresponds to an oscillation at the yellow frequency, too. Similarly, the product $E_a Q^*$ contributes to the time rate of change of the red P_b polarization.

The nonlinear coupling of the yellow E_a and the red E_b field components just described involves the polarization component Q . Note that, due to the absence of a corresponding dipole moment, Q does not give rise to an electric field component E_c radiating at the difference of the two colour.

The material equations are subjected to the following initial conditions

$$\begin{aligned} P_{a,b} &= w_{a,b}^0 \sin \theta_0 \exp(i\phi_{a,b}) \\ w_{a,b} &= w_{a,b}^0 \cos \theta_0 \end{aligned} \quad (47)$$

for an initially inverted medium $w_{a,b}^0 = +1.0$

$$\theta_0 = 2/\sqrt{N} = 2/\sqrt{n_0 \pi r_p^2 L} \quad (48)$$

$$0 \leq \phi_{a,b} \leq 2\pi \quad (49)$$

θ_0 and $\phi_{a,b}$ are the amplitude and phase of the average (i.e., deterministic) uniform along the cell axis initiating tipping angle.

$n_0(r) = n_0 \exp[-2n_2(r^2/r_p^2)]$ (50) the inversion density with r_p the HWHM radius; L the sample length, $r^2 = x^2 + y^2$ (51);

(ii) Quantum fluctuations. The initiation process is treated rigorously. The emission begins by incoherent spontaneous emission; only the geometry of the inverted medium leads to directed emission. Quantum effects occur during the very beginning of the pulse evolution when the problem is still linear i.e., with coupled Maxwell-Bloch solutions. The quantum initiation is then described by a statistical ensemble of initial conditions for Maxwell-Bloch solutions. One can adopt an initial polarization source at each z position with random phase ϕ (relative to the coherent emission electric field which eventually develops) and with tipping angle θ which is a bivariate Gaussian with RMS value $2/\sqrt{N}$ where N is the number of atoms in each step in z . There are two experiments by Vreken et al. and Carlson et al., that indicate that θ_0 is about this size; they show that injected pulses must have input pulse areas larger than θ_0 in order to shorten the SF delay time.

In particular the polarization magnitude for each transition a and b is determined by a Gaussian distribution as outlined by Haake et al [13,15] and Polder et al [16] for the two-level system

$$P(u,v) du dv = \frac{1}{\pi \sigma^2} \exp[-(u^2+v^2)/\sigma^2] du dv \quad (52)$$

Where u and v are the transverse components of the Bloch vector (i.e., the real and imaginary part of the polarization P_a or P_b) and

$$\sigma = \langle \theta^2 \rangle^{1/2} = 2/\sqrt{N} \quad (53)$$

to represent the quantum initiation properly (following Glauber & Haake;¹⁷ Polder, Vreken Shuurmans¹⁸ and Hopf).¹⁹ The angular brackets denote an ensemble average. Equation (2) is easily checked using

$$u^2 + v^2 = 1 - w^2 = \sin^2 \theta \approx \theta^2 \quad (54)$$

For small θ as assumed here; then

$$P(\theta^2)d\theta^2 = \frac{1}{\sigma^2} \exp [-\theta^2/\sigma^2] d\theta^2 \quad (55)$$

the probability that θ^2 is less than θ_0^2 is

$$\int_0^{\theta_0^2} P(\theta^2)d\theta^2 = 1 - \exp [-\theta_0^2/\sigma^2] \quad (56)$$

So that Eq. (5) can be set equal to $1 - R$, when R is a random number R between 0 and 1, or alternatively $\exp [-\theta_0^2/\sigma^2]$ can be set equal to R . This leads to

$$\theta_0 = \frac{2}{\sqrt{N}} \left(\ln \frac{1}{R} \right)^{1/2}. \quad (57)$$

When the population inverted medium is divided into smaller volume elements, N is replaced by the number of atoms in each volume element, i.e.,

$$\theta_0^i = \frac{2}{\sqrt{N_i}} \left[\ln \left(\frac{1}{R} \right) \right]^{1/2} \quad (58)$$

is the initial tipping angle for the i th volume element containing N_i atoms. The smaller the volume element the larger the initial tipping angle and the fluctuations for that element, but also the smaller their effect.

$$N_i = N(\rho_i) = \frac{\exp [-(\rho_i/\rho_N)^m] \{ \pi(\rho_{i+1/2}^2 - \rho_{i-1/2}^2) \}}{\pi\rho_{i/2}^2 + \sum_{i=2}^{Np-1} \exp [-(\rho_i/\rho_N)^m] \{ \pi(\rho_{i+1/2}^2 - \rho_{i-1/2}^2) \} + \{ \exp [-(\rho_{Np}/\rho_N)^m] \pi(\rho_{Np}^2 - \rho_{Np-1/2}^2) \}} \quad (59)$$

With m the index of the exponential density distribution (for a gaussian profile $m = 2$; for a super-gaussian, $m = 4$; and for a hyper-gaussian $m = 6$) and Np the number of radial shell. If we study large Fresnel numbers the geometry changes from cylinder to Cartesian parallelepiped. The localized area of the computational cell becomes $4(x_{i+1/2} y_{i+1/2} - x_{i-1/2} y_{i-1/2})$ (60). The smaller the volume element the larger the initial tipping angle and the fluctuations for that element, but also the smaller their effect.

The random numbers R used in Eq. (58) and the one used in defining $\phi_{a,b}$ between 0 and 2π are uniform; they are obtained from a table of random numbers. The starting address in the table is changed at the beginning of each run to simulate the variation from shot-to-shot.

B. Delay Time Fluctuations

For each colour, one can construct a histogram showing the fluctuations in delay time τ_D when quantum fluctuations are included in the plane-wave approximation. The associated standard deviation is given by

$$\frac{\sigma(\tau_D)}{\bar{\tau}_D} = \frac{\sum_{i=1}^{NR} (\tau_D^i - \bar{\tau}_D)^2 / NR}{\bar{\tau}_D} \left\{ 1 \pm \frac{1}{\sqrt{NR-1}} \right\} \quad \text{with } NR \text{ the number of runs with } \tau_{Da,b} = \langle \tau_{Da,b} \rangle \quad (61)$$

The synchronisation of the two pulse is measured in term of the fluctuation of the delay difference; it is given as

$$\sigma(\tau_{Da} - \tau_{Db}) = \sigma(\Delta\tau_D) \quad (62),$$

$$\text{with } \Delta\tau_D = \tau_{Da} - \tau_{Db} \quad \text{and} \quad \Delta\tau_D^i = \tau_{Da}^i - \tau_{Db}^i \quad \text{and} \quad \Delta\tau_D = \sum_{i=1}^{NR} \Delta\tau_D^i / NR = \langle \Delta\tau_D \rangle \quad (63)$$

the normalisation can be done with respect to $\langle \Delta \tau_D \rangle$ the average delay difference

$$\frac{\sigma(\Delta \tau_D)}{\langle \Delta \tau_D \rangle} = \frac{\sum_{i=1}^{NR} (\Delta \tau_D^i - \overline{\Delta \tau_D})^2 / NR}{\langle \Delta \tau_D \rangle} \left(1 \pm \frac{1}{\sqrt{NR-1}} \right) \quad (64)$$

or the normalisation can be constructed versus the arithmetic mean of the two average SF delay time

$$\frac{\sigma(\Delta \tau_D)}{1/2(\overline{\tau_{Da}} + \overline{\tau_{Db}})} = \frac{\sum_{i=1}^{NR} (\Delta \tau_D^i - \overline{\Delta \tau_D})^2 / NR}{1/2(\overline{\tau_{Da}} + \overline{\tau_{Db}})} \left(1 \pm \frac{1}{\sqrt{NR-1}} \right) \quad (65)$$

Equivalently the synchronisation can be measured by the introduction of an auxiliary variable *a la* Haake and Reibold [1]

$$T_H = 1/2 (\tau_{Da} + \tau_{Db}) - 1/2 \langle \tau_{Da} + \tau_{Db} \rangle$$

$\langle \dots \rangle$ denotes the average over all the NR trajectories. Two new curves from the two-level SF counterpart can be drawn to summarize the statistical results. The vertical axis represents $\Delta \tau_D^i$ the difference of delay, while the horizontal axis is the new variable T_H . Each cross corresponds to a particular pulse pair and gives the difference and the sum of the delay times of the SF_a (e.g., red) and the SF_b (e.g., yellow) components. The cloud formed by the NR crosses indeed is a good measurement of synchronisation of the two SF pulse as it can be seen in Fig. 7. The variance of $\Delta \tau_D$ and T_H turn out in agreement to Haake et al [1] 0.96% and 5.3% of the mean common delay, respectively. This variance of T_H is significantly smaller than the one relevant to the Cs experiment of Vreken et al [17-19]. This difference is due to the larger number of atoms (i.e., the larger gain *g* and the smaller Beer's length α_R) used in one present calculation and to the coupling of the two pulses.

A second diagram summarising the statistics, also suggested by Haake et al, displays the ratio of the maximum intensities and the ratio $\{2(\Delta \tau_D)/(\tau_{Da} + \tau_{Db})\}$ for a pulse pair. The cloud as shown in Fig. 8 suggests (i) that an order-of-magnitude difference of the two SF intensity maximal is not untypical and (ii) that within a pulse pair the earlier pulse tends to be more intense than the subsequent one.

Figure 1 represents the three-level λ atomic configuration which strongly intertwines the two evolving light beams each at a different frequency.

Figure 2 illustrates in the plane wave regime when no quantum fluctuations are considered of the initial stage, how the two SF pulses coincide in time (their delays are equal). Following Feld et al's [3] propagation theory one notices a new manifestation of simultaneous solitons propagation (or simultons, as named by Eberly et al [5])

Figure 3 illustrates how the pulse synchronisation still holds for uniform tipping angle even when diffraction is considered

Figure 4 illustrates the standard deviation of the delay difference $\sigma(\Delta \tau_D)$ either the delay difference (4a) or the arithmetic mean of the average delay for each SF for plane wave calculation with various ohmic loss κ . Even though quantum fluctuations were allowed in the initial process, which gave rise to corresponding fluctuations as the output characteristic of the SF pulse, synchronisation was still achieved for certain gain to loss ratio

$\kappa_{a,b}$	$\sigma(\tau_{Da})/\langle \tau_{Da} \rangle$	$\sigma(\tau_{Db})/\langle \tau_{Db} \rangle$	$\sigma(\text{difdel})/\langle \text{difdel} \rangle$	$\sigma(\text{difdel})/1/2\{\langle \tau_{Da} \rangle + \langle \tau_{Db} \rangle\}$
0	8.47 ± 1.128	8.94 ± 1.128	63.86 ± 9.12	2.61 ± 0.373
4.022	9.04 ± 1.30	16.22 ± 2.32	257.1 ± 37.1	13.27 ± 1.895
8.0434	27.1 ± 3.87	22.15 ± 3.16	211.96 ± 30.28	32.72 ± 4.67
10.657	33.31 ± 4.83	24.33 ± 3.47	195.55 ± 28.22	34.46 ± 4.32

Figure 5 illustrates $\sigma(\Delta\tau_D)/\langle\Delta\tau_D\rangle$ and $\sigma(\Delta\tau_D)/1/2\{\langle\tau_{Da}\rangle + \langle\tau_{Db}\rangle\}$ for a cylindrical geometry configuration where both diffraction and gaussian radial variation of the atomic density are included. The smaller the Fresnel number, the more unified the difference portions of the beam act together and super-fluoresce together (i.e., the standard deviation is minimum). However, for large Fresnel number the various concentric shells act more independently from each other leading to a larger normalized standard deviation. For simplicity, the gain-length Fresnel number for both colour was chosen to be equal (i.e., the value of the dipole moment $\mu_{a,b}$ entering in the calculation of $\alpha_{Ra,b}$ was such that the product $\lambda_{a,b} \alpha_{Ra,b}$ was the same for both colours). This set of calculations was set up to compare with Haake et al [1]. Synchronisation resulted for small gain length Fresnel number. The arithmetic average of the output power is displayed in Fig. 5b to show that the d-synchronisation in general is not large.

$1/\tau_{pa,b}$	$F_{ga,b}$	$\sigma(\tau_{Da})/\langle\tau_{Da}\rangle$	$\sigma(\tau_{Db})/\langle\tau_{Db}\rangle$	$\sigma(\text{difdel})/\langle\text{difdel}\rangle$	$\sigma(\text{difdel})/1/2\{\langle\tau_{Da}\rangle + \langle\tau_{Db}\rangle\}$
3.9	226.05	23.60 ± 7.866	44.73 ± 1.69	133.18 ± 44.39	32.25 ± 10.75
4.23	192.225	18.80 ± 3.49	14.42 ± 2.67	146.11 ± 27.13	26.7 ± 4.9
5.5771	110.55	4.487 ± 1.495	6.078 ± 2.026	121.85 ± 40.62	7.58 ± 2.53
8.7	45.375	8.60 ± 1.60	6.07 ± 1.13	138.78 ± 26.7	4.28 ± 0.4
11.54	25.81	4.104 ± 1.37	5.107 ± 1.702	118.44 ± 44.766	3.83 ± 1.28

Figure 6 illustrates a generalisation of Fig. 5, where no restriction were put on the value of the dipole moments (i.e., where each colour will have its own, geometric Fresnel number). The effective gain lengths $F_{a,b}$ are also different.

$1/\tau_p$	F_a	F_b	$\sigma(\tau_{Da})/\langle\tau_{Da}\rangle$	$\sigma(\tau_{Db})/\langle\tau_{Db}\rangle$	$\sigma(\text{Difdel})/\langle\text{difdel}\rangle$	$\sigma(\text{difdel})/1/2\{\langle\tau_{Da}\rangle + \langle\tau_{Db}\rangle\}$
3.9	0.82	103.79	7.80 ± 1.56	22.6 ± 4.5	50.9 ± 10.18	30.66 ± 6.133
4.23	0.698	88.35	8.92 ± 1.78	22.5 ± 4.5	47.4 ± 9.47	30.76 ± 6.152
5.577	0.402	50.885	9.48 ± 1.896	23.35 ± 4.67	45.9 ± 9.19	32.72 ± 6.543
6.251	0.320	40.505	11.02 ± 2.204	21.5 ± 4.31	41.70 ± 8.34	30.61 ± 6.121
8.7	0.165	20.886	11.38 ± 2.277	17.8 ± 3.56	33.93 ± 6.78	27.91 ± 5.542
11.542	0.100	12.658	11.49 ± 2.298	29.1 ± 5.8	43.31 ± 8.66	43.501 ± 8.70

Fig. 6b enhances the fact that in this physical situation, where both geometric and gain length Fresnel numbers are different for each column, the de-synchronisation is more important than in the physical situation of Fig. 5.

Figure 7 illustrates the delay statistics for SF_a , SF_b and the delay difference $\Delta\tau_D$ and common delays T_H as well as the peak ratio for 50 pulse pairs. Each cross represents a pulse pair in a uniform plane wave regime (#660).

Delay A		Delay B	
delay SF_a		delay SF_b	
Arithmetic average	.74117752E + 00	Arithmetic Average	.77272872E + 00
Variance	.40352590E - 01	Variance	.29290073E - 01
Standard deviation I.E. SQRT (VAR X)	.20087954E + 00	Standard deviation I.E. SORT (VAR X)	.17114343E + 00
Total number of Shots	50	Total number of Shots	50
Maximum value	.14911260E + 01	Maximum value	.14911260E + 01
Minimum value	.23079303E + 00	Minimum value	.5795326 E + 00
Standard deviation/ Arithmetic Ave.	(27 \pm 3.87)%	Standard deviation/ Arithmetic Ave.	(22.15 \pm 3.16)%

<u>Difdel</u>		<u>Dtpndt</u>	
delay difference		$DTPNDT = 2 \text{ DIFDEL} / \{(\tau_{Da} + \tau_{Db}) - (\langle \tau_{Da} \rangle + \langle \tau_{Db} \rangle)\}$	
Arithmetic average	-.31551206E - 01	Arithmetic Average	-.14368178E + 00
Variance	.61325926E - 01	Variance	.209100071E + 01
Standard deviation I.E. SQRT (VAR X)	.24764072E + 00	Standard deviation I.E. SQRT (VAR X)	.14460291E + 00
Total number of Shots	50	Total number of Shots	49
Maximum value	.79914208E + 00	Maximum value	.20552767E + 01
Minimum value	-.85293195E + 00	Minimum value	-.5795011 E + 01
Standard deviation/ Arithmetic Ave.	(7.85 ± 1.12)%	Standard deviation/ Arithmetic Ave.	(10.06 ± 1.453)%
Arithmetic average	-.31551206E - 01	Arithmetic Average	-.14368178E + 00

Rappk

Peak ratio	SF_a / SF_b
Moyenne Arithmetic Average	-.20686434E + 00
Variance	.15611884E + 01
Standard deviation I.E. SQRT(VAR X)	.12494753E + 01
Total number of Shots	50
Maximum value	.16816556E + 01
Minimum value	-.5790247E + 01
Standard deviation/Arithmetic over	(6.04 ± 0.863)%

Figure 8 illustrates the effect of transverse variations on the statistics of SF delay, SF delay difference and the ratio of the maximum intensities of a (for yellow) and b (for red) respectively as well as the relative delay time differences for the generalised three-dimensional (#760) version of the pulse ensemble referred to in Fig. 7.

Simulation No. 760 <u>Delay A</u>		Simulation No. 760 <u>Delay B</u>	
delay SF_a			
Arithmetic average	.82498162E + 00	Arithmetic Average	.24900598E + 01
Variance	.89926436E - 02	Variance	.52384771E + 00
Standard deviation I.E. SQRT (VAR X)	.94829550E - 01	Standard deviation I.E. SORT (VAR X)	.72377324E + 00
Total number of Shots	26	Total number of Shots	26
Maximum value	.99521732E + 00	Maximum value	.47629518E - 01
Minimum value	.63819401E + 00	Minimum value	.13018090E + 01
Standard deviation/ Arithmetic Ave.	.11494747E + 02	Standard deviation/ Arithmetic Ave.	.29066501E + 02
Error Barr of (1)	.22989494E + 01	Error Barr of (1)	.58133001E + 01

Simulation No. 760
Difdel

Arithmetic average	-.16650782E + 01
Variance	.52015767E + 00
Standard deviation I.E. SQRT (VAR X)	.72121957E + 00
Total number of Shots	26
Maximum value	-.54565383E + 00
Minimum value	-.39474558E + 01
Standard deviation/ Arithmetic Ave.	-.43314457E + 02
Error Barr of (1)	-.86628914E + 01
Absolute Arithmetic average	.16650782E + 01
Standard deviation/ Abs. Arith. Aver.	.43314457E + 02
Error Barr of (2)	.86628914E + 01

Simulation No. 760
Rappk

Arithmetic average	.29367574E + 00
Variance	.68020016E - 01
Standard deviation I.E. SQRT (VAR X)	.26080647E + 00
Total number of Shots	25
Maximum value	.68407412E + 00
Minimum value	-.35780137E + 00
Standard deviation/ Arithmetic Ave.	.88807632E + 02
Error Barr of (1)	.18127782E + 02
Absolute Arithmetic average	.34439806E + 00
Standard deviation/ Abs. Arith. Aver.	.75728206E + 02
Error Barr of (2)	.15457955E + 02

Conclusion

The effect of transverse variations in the concomitant evolution of two superfluorescent (SF) emission, (each of a different colour), is shown to be important. In the general case, the conclusions reached in the uniform plane wave regime, namely the exact time coincidence of the two SF pulses, does not hold. However, the de-synchronisation is still smaller than any of the SF output power pulse HMMW half maximum half width as shown in Fig. 5b and 6b.

Simulation No. 760
Dtpndt

$$DTPNDT = 2 \text{ DIFDEL} / \{ (\tau_{Da} + \tau_{Db}) - (\langle \tau_{Da} \rangle + \langle \tau_{Db} \rangle) \}$$

Arithmetic Average	.20397345E + 01
Variance	.25832079E + 03
Standard deviation I.E. SQRT (VAR X)	.16072361E + 02
Total number of Shots	26
Maximum value	.38259894E + 02
Minimum value	-.39469464E + 02
Standard deviation/ Arithmetic Ave.	.78796339E + 03
Error Barr of (1)	.16084235E + 03
Absolute Arithmetic Average	.12175411E + 02
Standard deviation/ Abs. Arith. Aver.	.13200672E + 03
Error Barr of (2)	.26945760E + 02

Acknowledgement

The author gratefully acknowledges the hospitality as well the Technical guidance of Prof. F. Haake. The sponsorship and DAAD and KFA-IFF is joyfully acknowledged. Numerous discussion with Dr. R. Reibold have simplified the visualization of the physics. Without the hospitality of Prof. H. Müller-Krumbhaar and Prof. G. Ellenberger at KFA-IFF, these calculations could not have been carried out. The author thank Ms. Fatmatta Kay-Kamara for her diligent Word Processing effort.

Reference

1. F. Haake and R. Reibold, *Physics Letters* 92A, 29 (1972).
2. R. Florian, L.O. Schwan and D. Schmid, *Solid State Commun.* 42, 55 (1982).
3. J.C. MacGillivray and M.S. Feld, *Physics Rev.* A14, 1169 (1976).
4. F.P. Mattar, H.M. Gibbs, S.L. McCall and M.S. Feld, *Phys. Rev. Lett.* 46, 1123 (1981).
5. M. Konopnicki and J.H. Eberly, *Physics Rev. A* (Nov. 81).
6. F.P. Mattar and F. Haake (unpublished).
7. F.P. Mattar and J.H. Eberly, *Physics and Chemistry of Laser and Induced Processes*, edited by R.L. Kompa and B.D. Smith. Springer-Verlag 1979; and F.P. Mattar, *Proceedings of the Tenth Simulation and Modeling Conference*, Pittsburgh 1978, edited by W. Vogt (ISA Pittsburgh 1979).
8. F.P. Mattar and C.M. Bowden, *Phys. Rev.* A27, 345 (1983).
9. E. Watson, H.M. Gibbs, F.P. Mattar, Y. Claude, M. Cormier, S.R. McCall and M. Feld, *Phys. Rev.* A27 (March 1983).
10. F.P. Mattar, *Appl. Phys.* 17, 53 (1978); and F.P. Mattar and M.C. Newstein, *comp. Phys. Comm.* 20, 139 (1980).
11. F.P. Mattar, in *Optical Bistability*, ed. by C.M. Bowden, M. Ciftan and H.R. Robl (Plenum Press, 1981) p. 503, in *Proceedings Tenth Simulation and Modeling Conference*, Pittsburgh 1978, ed. by W. Vogt and M. Mickle (Instrument Society of America, Pittsburgh, 1979).
12. M. Cormier, Y. Claude, P. Cadieux and F.P. Mattar, *Proceedings of the International Conference on Laser 1981*, ed. by C-B. Collins (STS, MacLean, Virginia) pp. 1085-1115.
13. R. Glauber and F. Haake, *Physics Lett.* 68A, 29 (1978).
14. F. Haake, J. Haus, H. King, G. Schröder and R. Glauber, *Phys. Rev.* A20, 2047 (1979); and *ibid* A23, 1322 (1981).
15. F. Haake *Laser Spectroscopy IV* ed. by Walther and K.W. Rothe p. 451 Springer Verlag (1979).
16. D. Polder, M.F.H. Schuurmans and Q.H.F. Vrehen, *J. Opt. Soc. Am.* 68, 699 (1978); and *Phys. Rev.* A19, 1192 (1979).
17. Q.H.F. Vrehen, *Laser Spectroscopy IV*, ed. by H. Wlather and K.W. Rothe (Springer Verlag 1979).
18. Q.H.F. Vrehen and M.F. Schuurmans, *Phys. Rev. Lett.* 42, 224 (1979).
19. H.M. Gibbs Nato Advanced Study Institute, *Coherence in Spectroscopy and Modern Physics*, ed. by F.T. Arechi, R. Bonifacio, M.O. Scully, Plenum Press (1978) p. 121.
20. N.W. Carlson, D.J. Jackson, A.L. Schawlow, M. Gross and S. Haroche, *Opt. Commun* 32, 35 (1980).
21. A. Javan *Phys. Rev.* 107, 1579 (1957).
22. R. L. Panock and R.J. Temkin, *IEEE J. Quantum Electron.* 13, 425 (1977).
23. R. J. Temkin, *IEEE J. Quantum Electron* 13, 450 (1977).
24. M. Takami, *Japan J. Appl. Phys.* 15, 1063 (1976); *ibid* 15, 1889 (1976).
25. T. Tsai and T.F. Morse, *IEEE J. Quantum Electron.* 15, 1334 (1979); *ibid* 18, 1119 (1982).
26. A.T. Rosenberger and T.A. DeTemple, *Phys. Rev.* A24, 868 (1981).
27. S.H. Lee, S.J. Petuchowski, A.T. Rosenberger and T.A. DeTemple, *Opt. Lett* 4, 6 (1979).
28. H.K. Chung, J.B. Lee and T.A. DeTemple, *Opt. Comm.* 39, 105 (1981).
29. T.A. DeTemple, *"Nanosecond Near Millimeter Waves"*, Tech. Rep. RH-CR-82-1, US Army Missile Command, Redstone Arsenal, AL, (1981).

30. R.T.V. Kung, IEEE J. Quantum Electron. 18, 2056 (1982).
31. G.-D. Willenberg, J. Heppner and F.B. Foote, IEEE J. Quantum Electron. 18, 2060 (1982).
32. J.R. Murray, J. Goldhar, D. Elmerl and A. Szöke, IEEE J. Quantum Electron 15, 342 (1982).
33. K.I. Keda, J. Okada and M. Matsuoka, J. Phys. Soc. Japan 5, 1636 (1980); *ibid* 5, 1646 (1980).
34. V.B. Gerasimov, S.A. Gerasimova, E.M. Zenskov and V.K. Orlov, Sov. J. Quantum Electron 6, 96 (1976).

Figures Caption

- Fig. 1. The atomic configuration of the three level system initially inverted is shown. The pump dynamics effects are neglected in this calculation.
- Fig. 2. (a) a plane wave superradiance (average superfluorescence) simulation displaying the coincidence of the two output power as for simulton (simultaneously propagating solitons); (b) The coincidence remains for different linear losses. The two pulses (a and b) can not be distinguished from each other.
- Fig. 3. (a) a two-space (r,z) superradiance calculation (with a uniform tipping angle ala to Feld) is shown ascertaining the output pulse delay synchronisation even when transverse effects are considered (both radial atomic density variations and Laplacian coupling between the different concentric shells) for different Fresnel numbers; (b) the arithmetic average of the two colour superfluorescence output powers evolving from a quantum initiation are contrasted for a unity geometric Fresnel number: the peak delays are identical.
- Fig. 4. The standard deviation of the two colors superfluorescence output power peak delay difference is shown as a function of linear loss corresponding to different Fresnel numbers. The stronger, the loss thus the weaker is the peak coincidence.
- Fig. 5. The standard deviation of the delay difference normalised to either the arithmetic average difference of delays (graph a) or the arithmetic mean of the two superfluorescence delays (graph b) for plotted as a function of the gain Fresnel number for the particular case where the product $\lambda_{a,b} \sigma_{a,b}$ is the same for both colors.
- Fig. 6. The standard deviation of the delay difference normalised to the average delay difference and to the arithmetic mean of the average delay for each colour is now plotted for general transverse effects in graph a and graph b respectively.
- Fig. 7. In this figure, the various histograms s corresponding to the plane wave situation namely the time delay statistics for each SF (graphs a & b), their delay difference (graph c), their weighted delay difference (graph d) and the ratio of the two output power peaks (graph e) are shown. Graph f and g illustrates a la Haake the difference of delays and the logarithmic ratio of the peaks.
- Fig. 8. In this figure the statistics corresponding to the physical situation studied with transverse effects considered as in Fig. 6 are displayed. In particular, graph a and b illustrate the histograms for the delay statistics for each SF, graph c and d represents the histograms of the delay difference; whereas graph e shows the statistics of the ratio of the two output power peaks. Graph f and g display a la Haake the delay difference versus T and 'DTPNDT', whereas graph h illustrate the logarithm of the peak ratio versus 'DT2DST'.

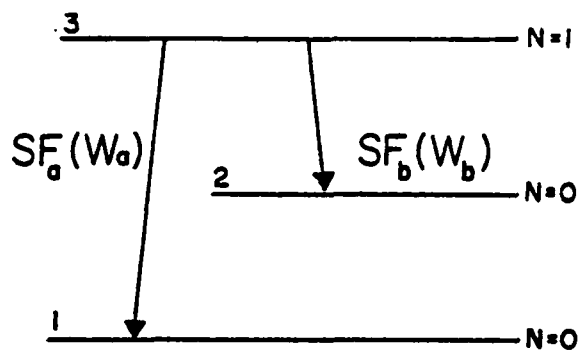


Figure 1

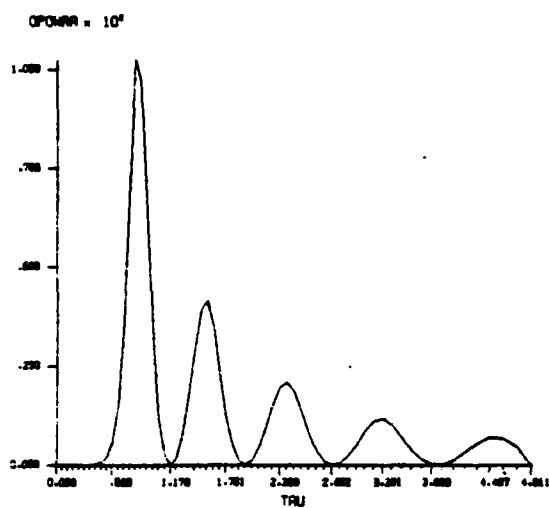


Figure 2a

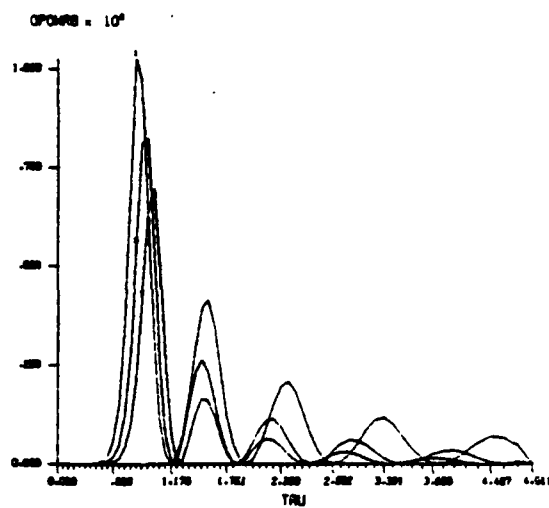


Figure 2b

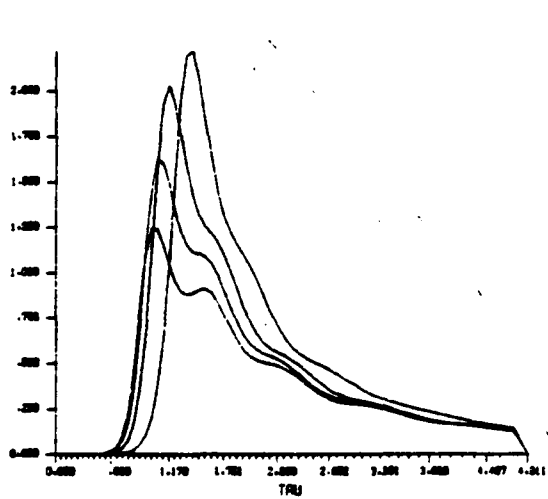


Figure 3a

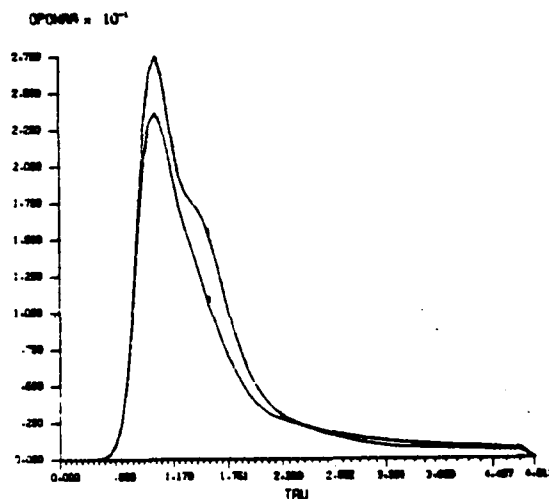


Figure 3b

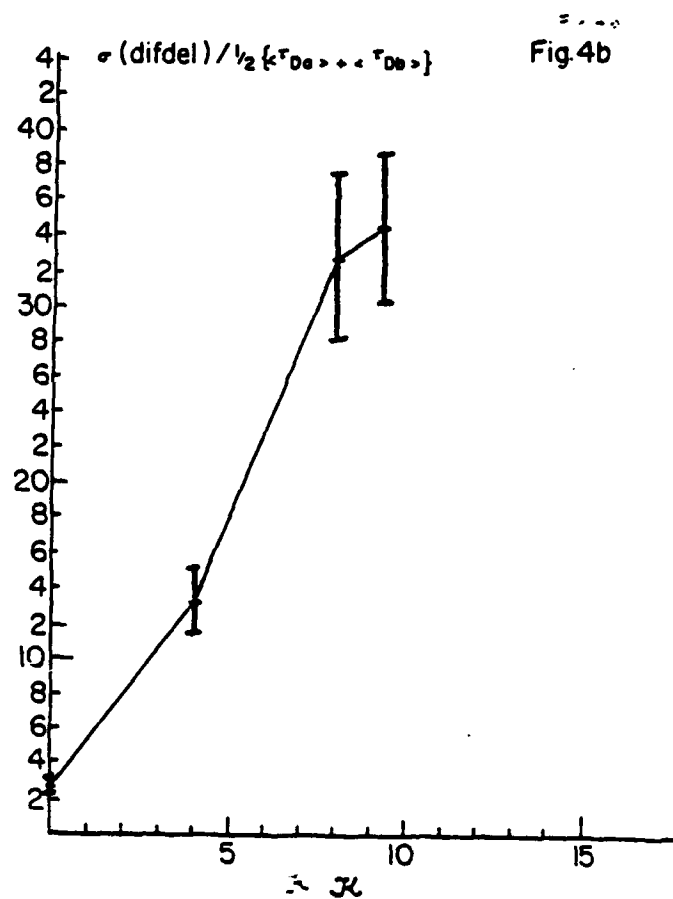
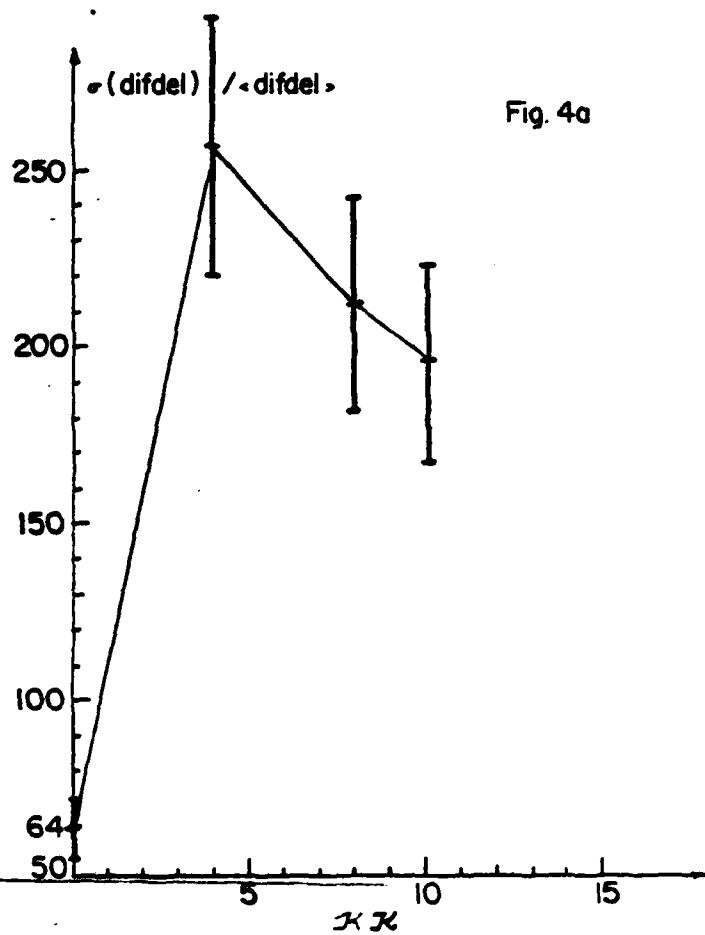


Figure 4a

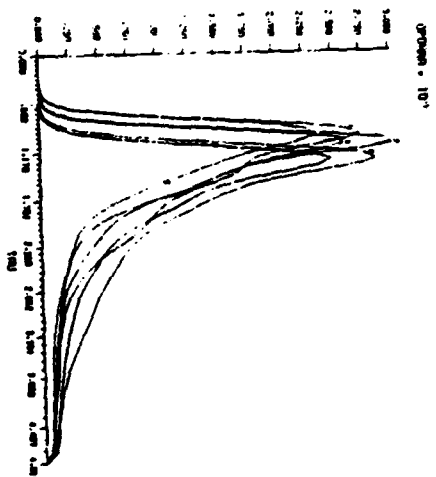


Figure 4b

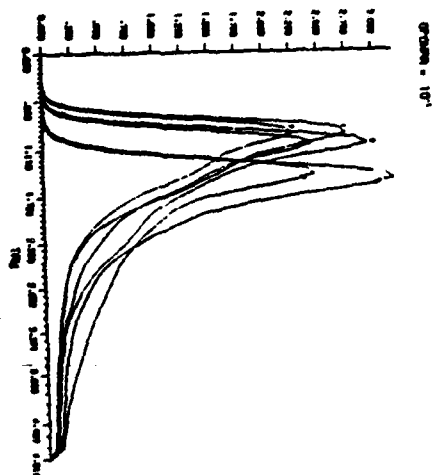


Figure 5a

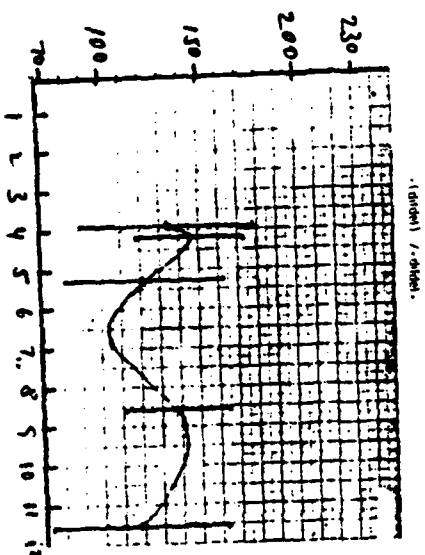


Figure 5b

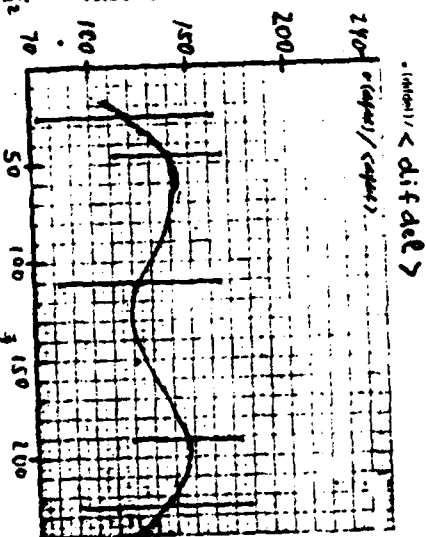


Figure 5a I

Figure 5a II

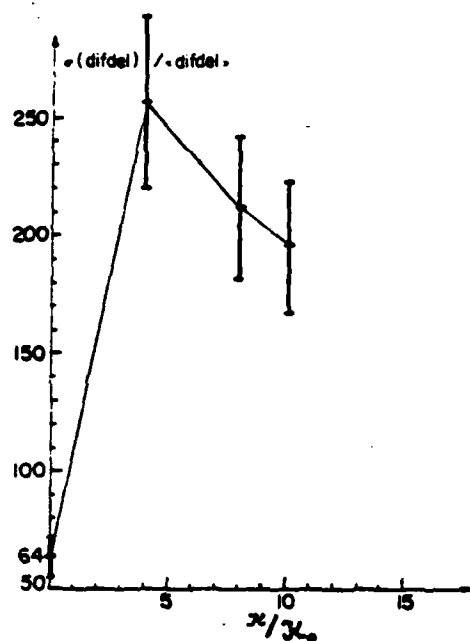


Figure 4a

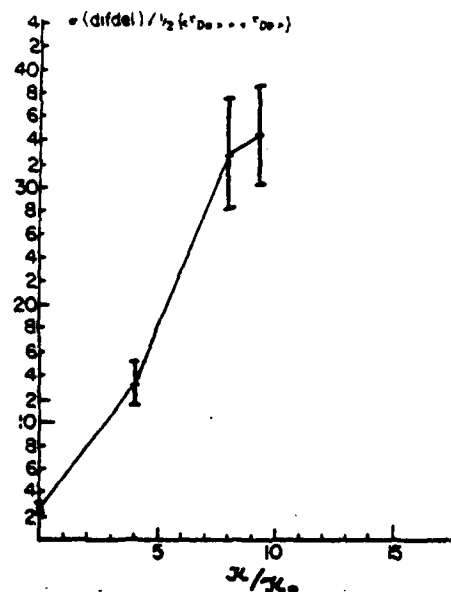


Figure 4b

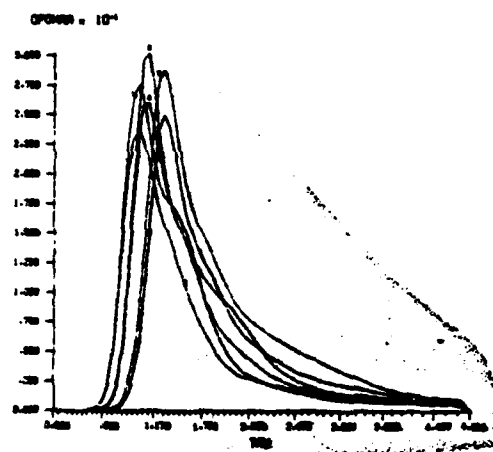


Figure 5a

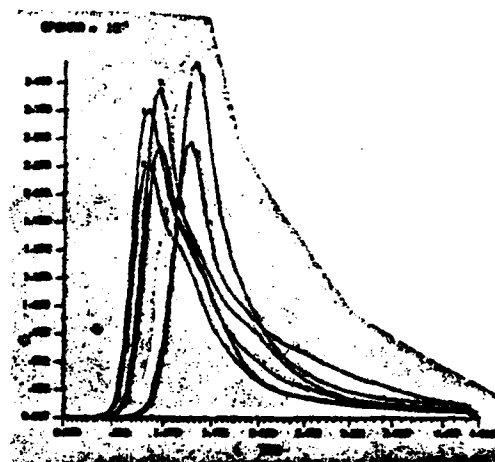


Figure 5b

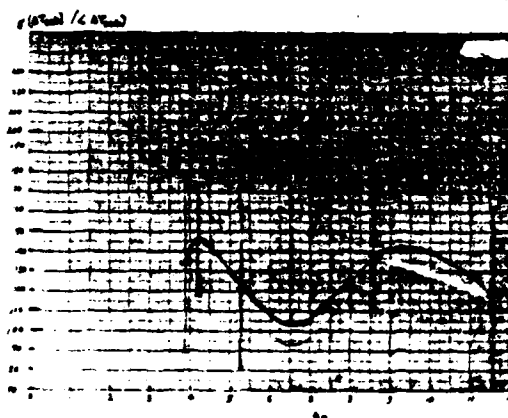


Figure 5a I

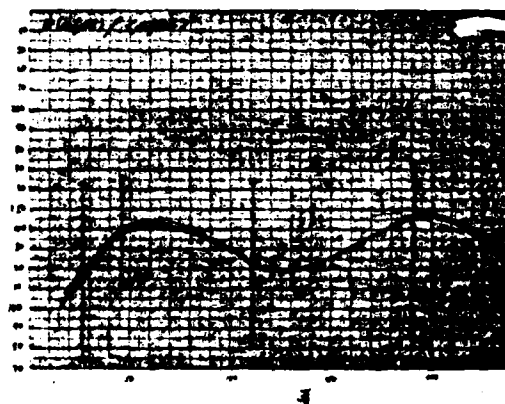


Figure 5a II

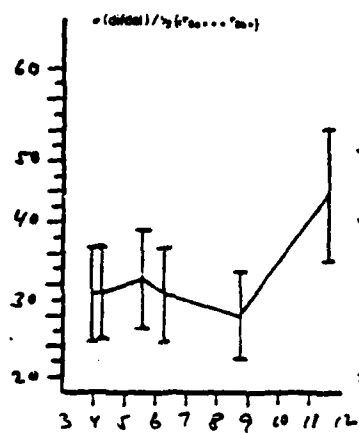
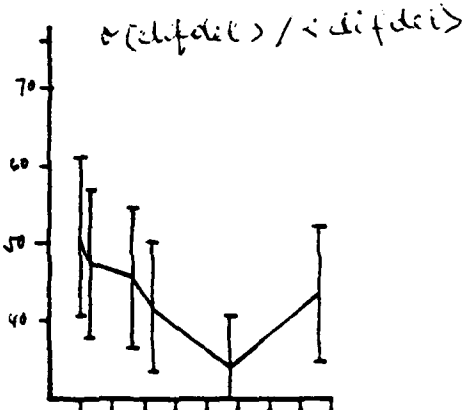
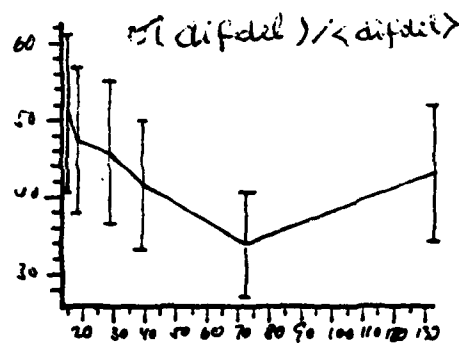
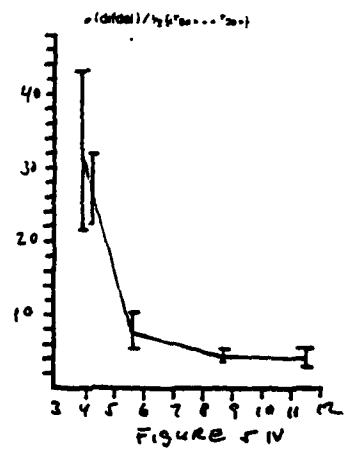
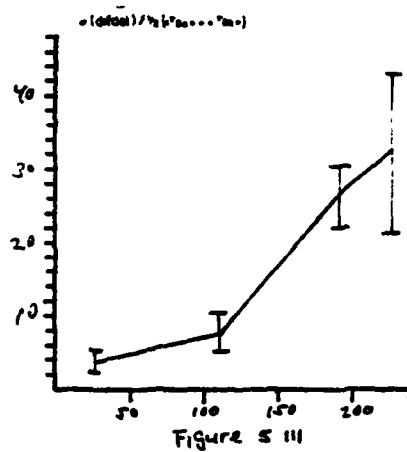
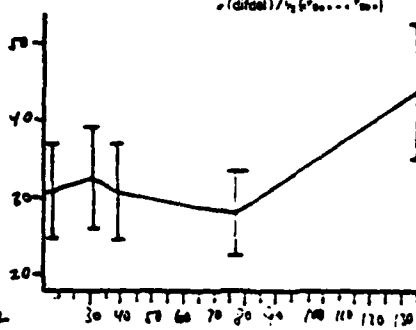
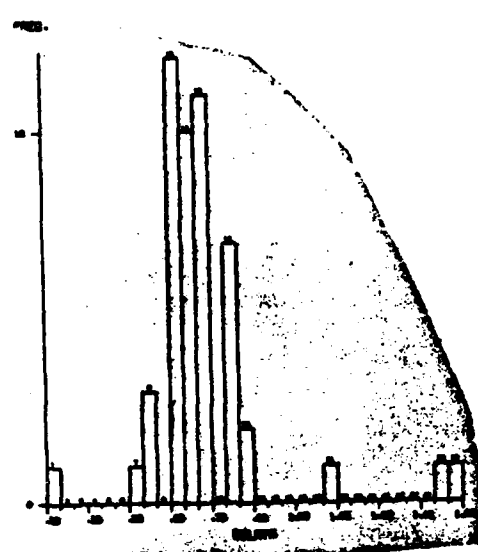
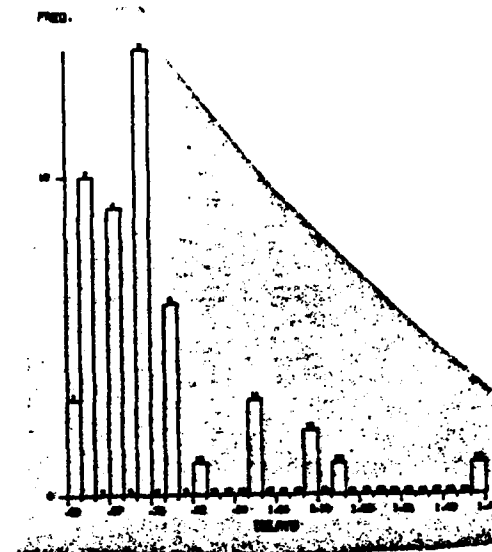


FIGURE 6

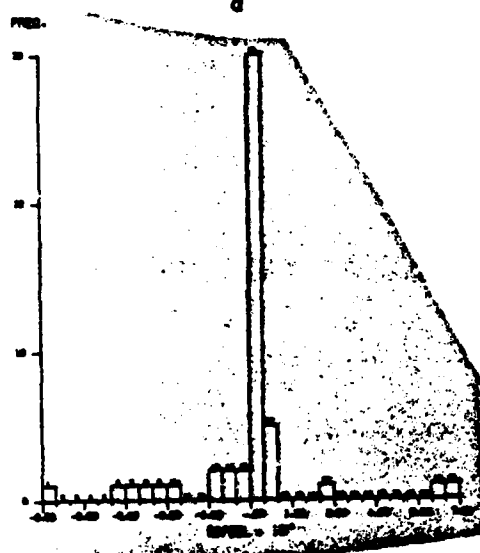




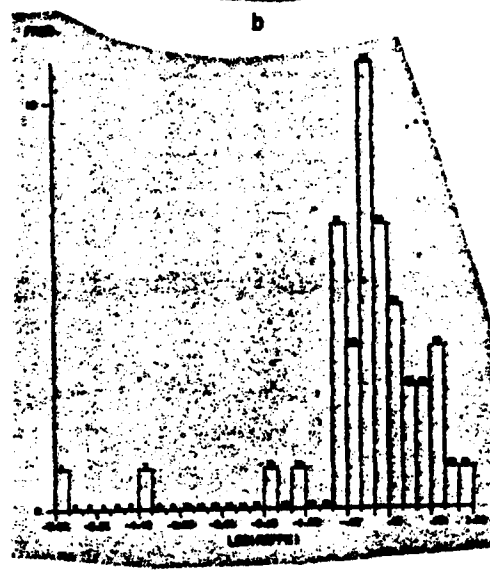
a



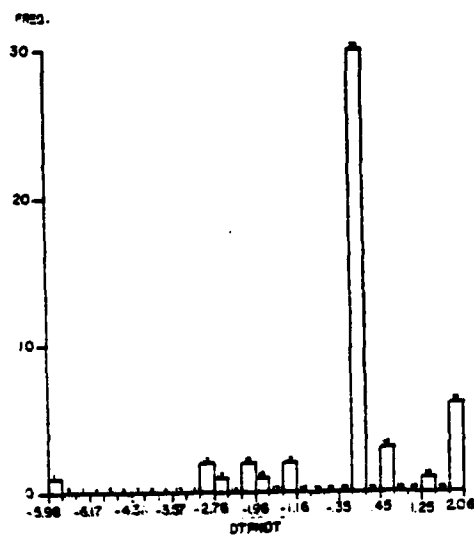
b



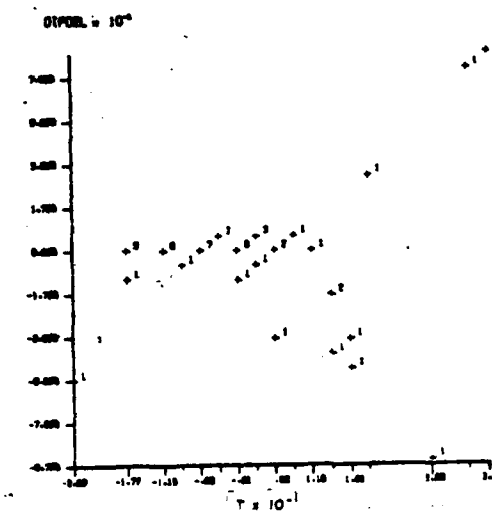
c



d

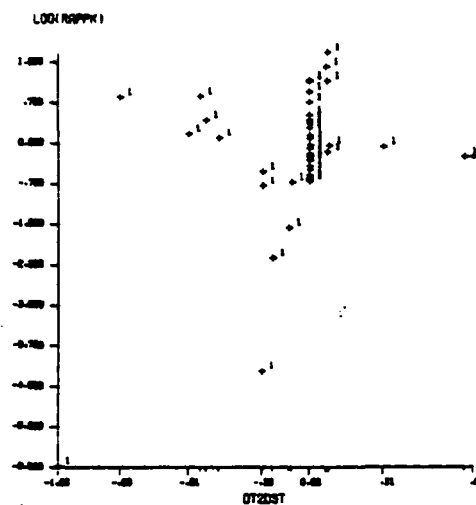
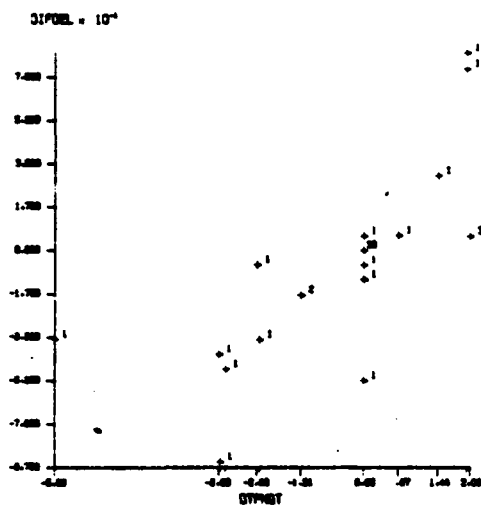


e



f

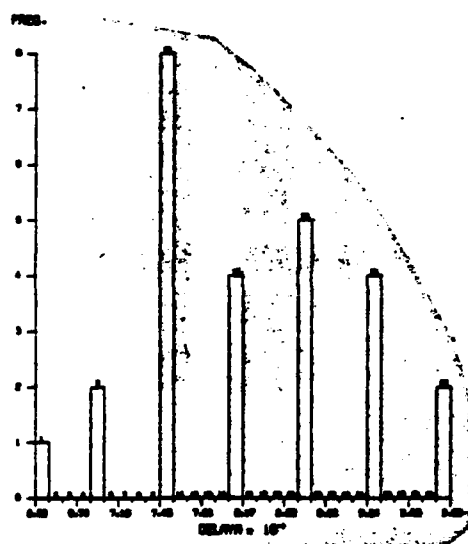
Figure 7



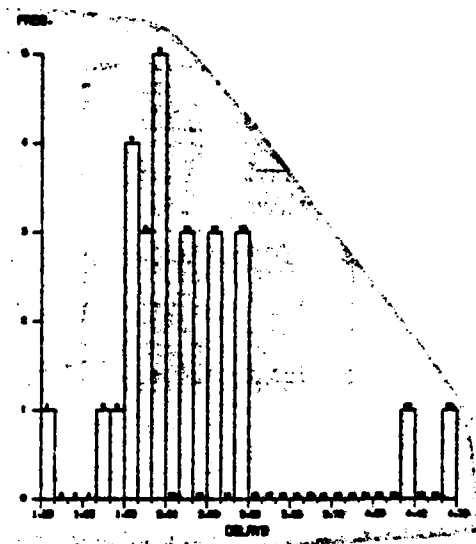
g

Figure 7

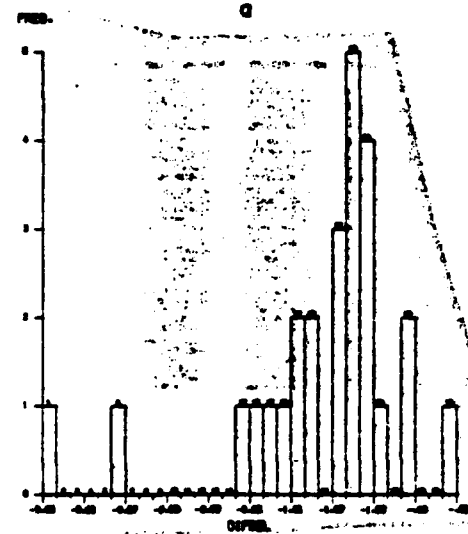
h



a

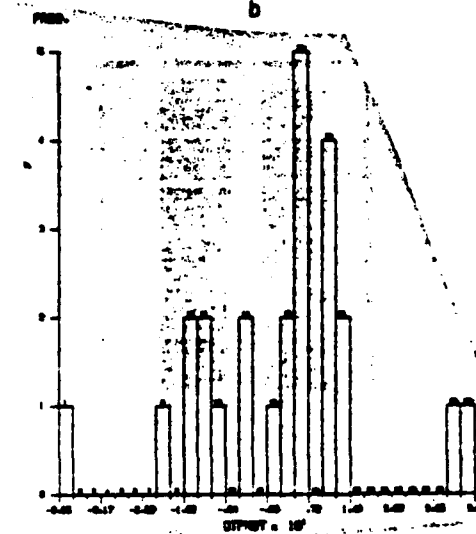


b

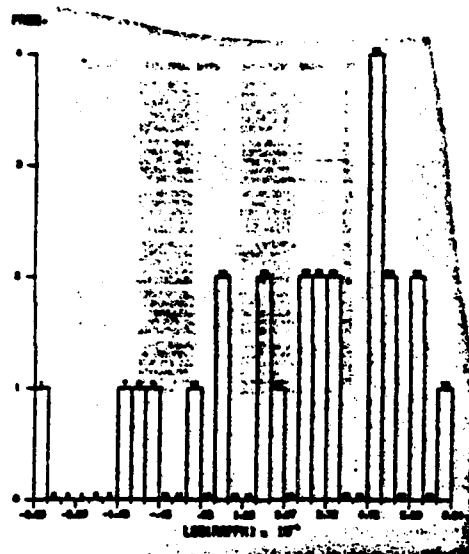


c

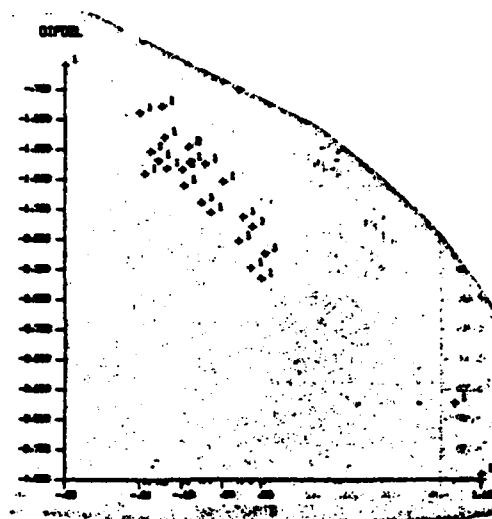
Figure 8



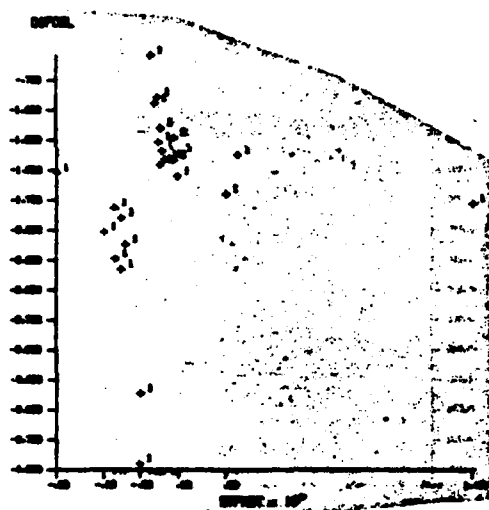
d



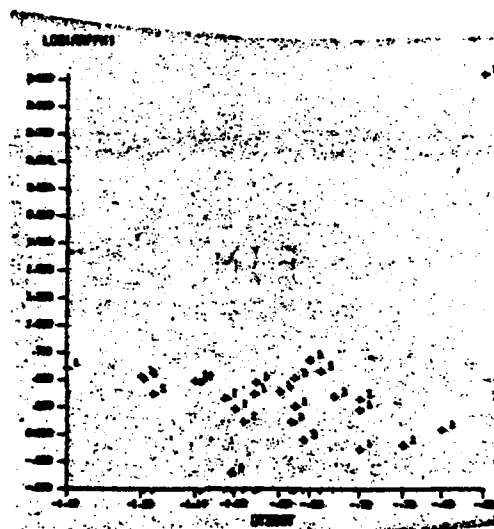
e



f

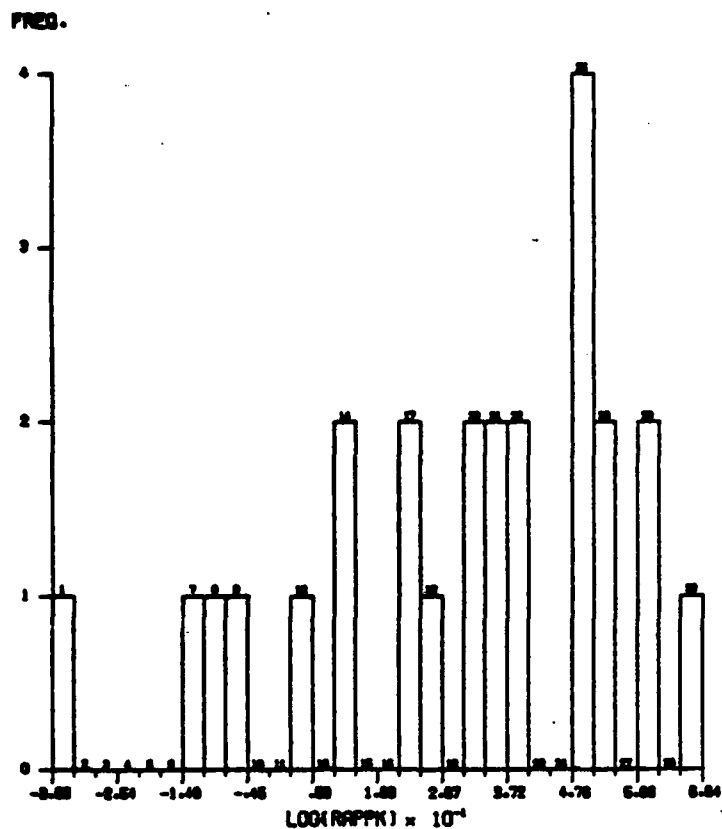


g

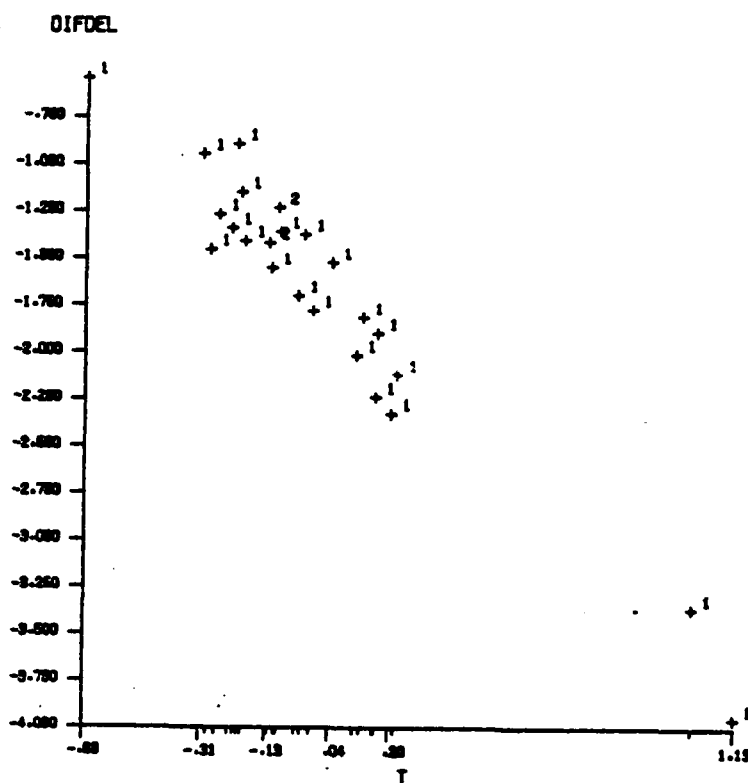


h

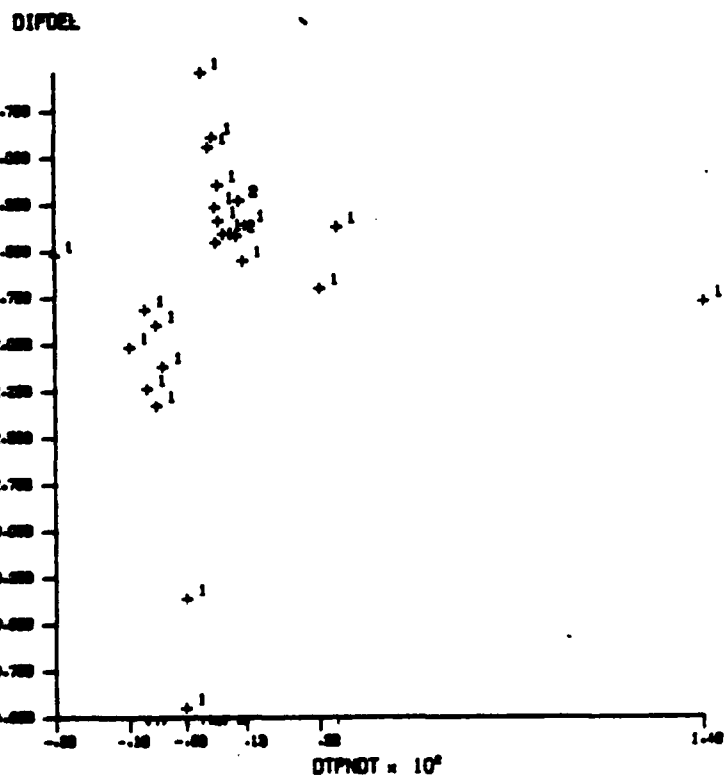
Figure 8



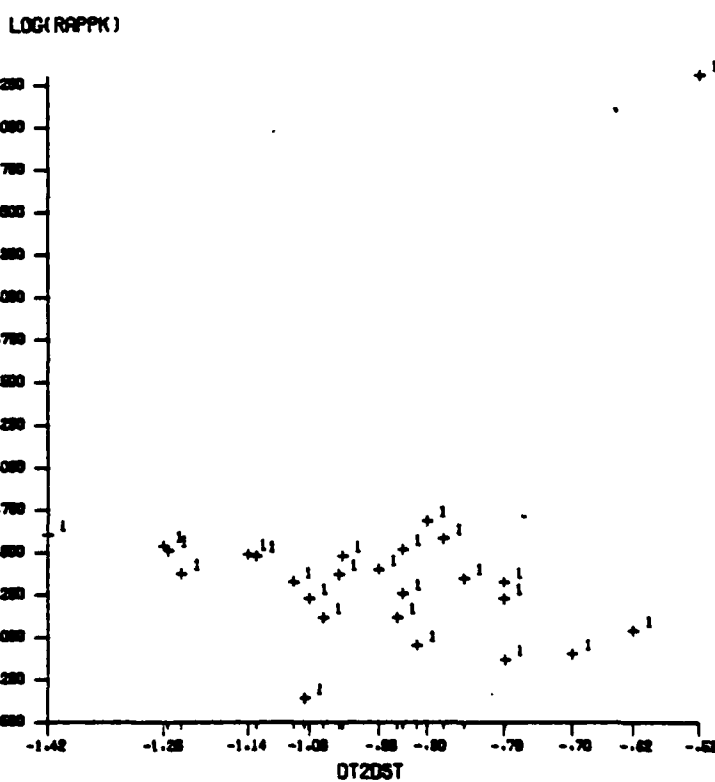
e



f

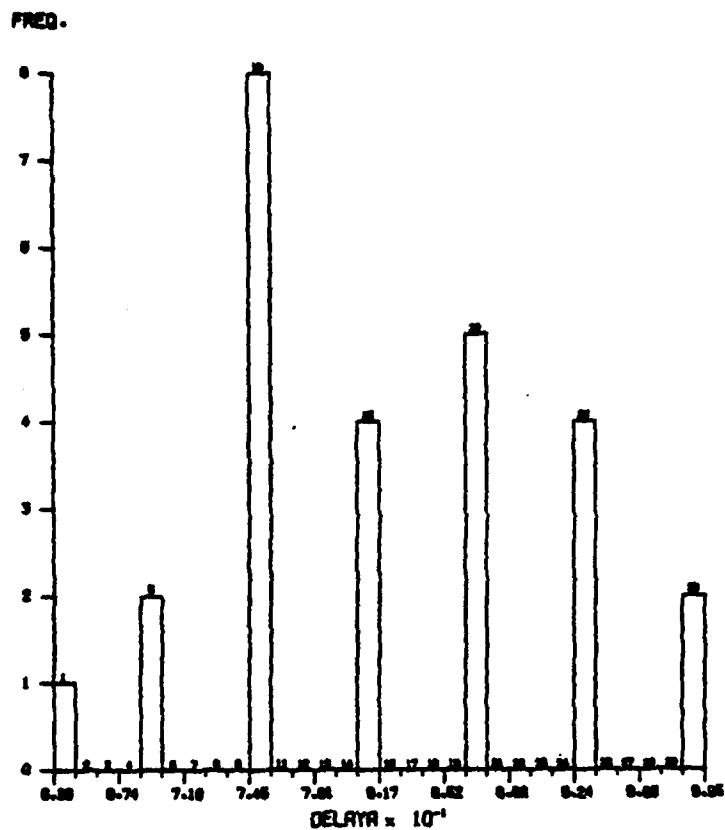


g

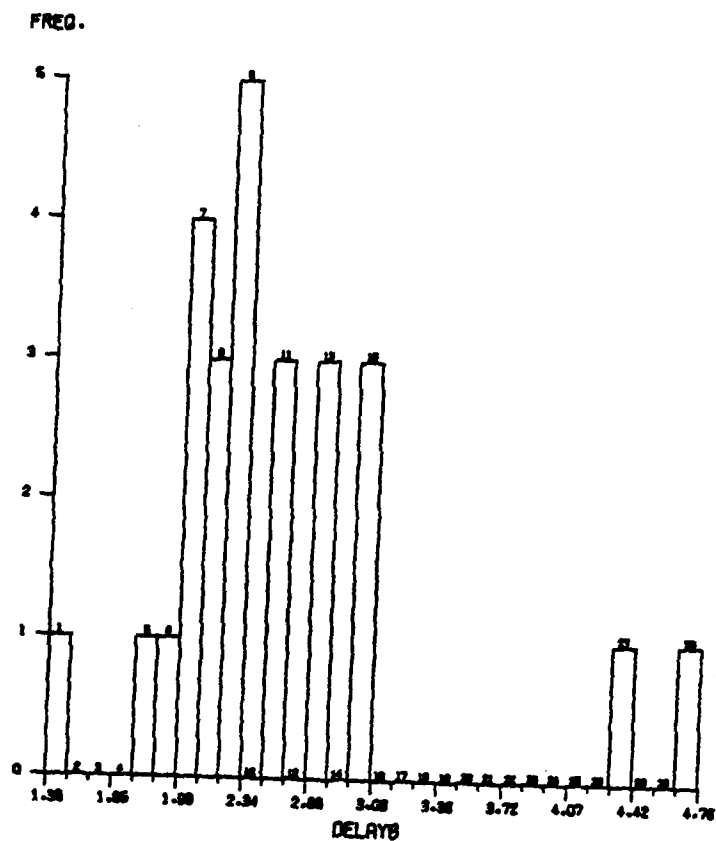


h

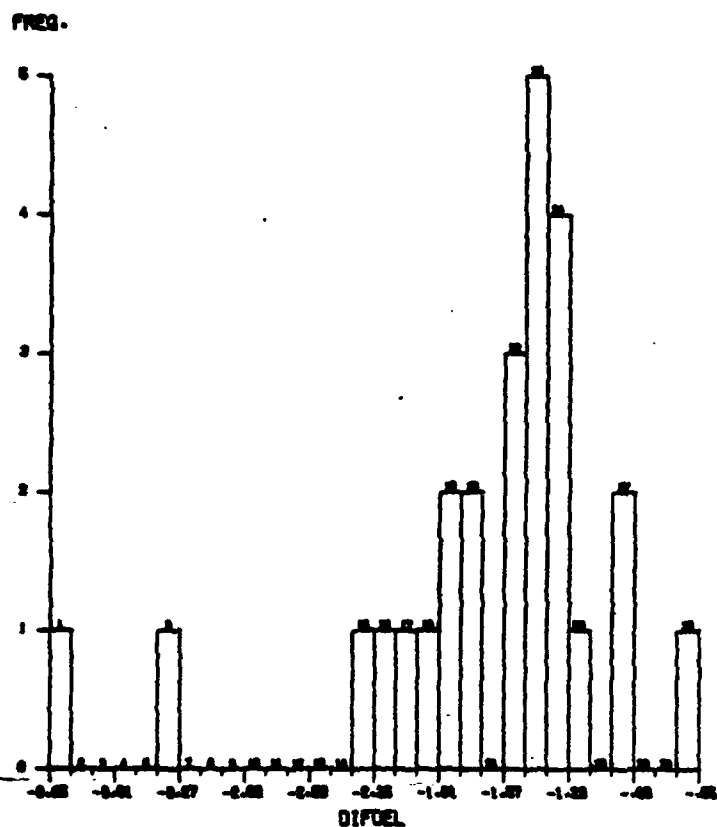
Figure 8



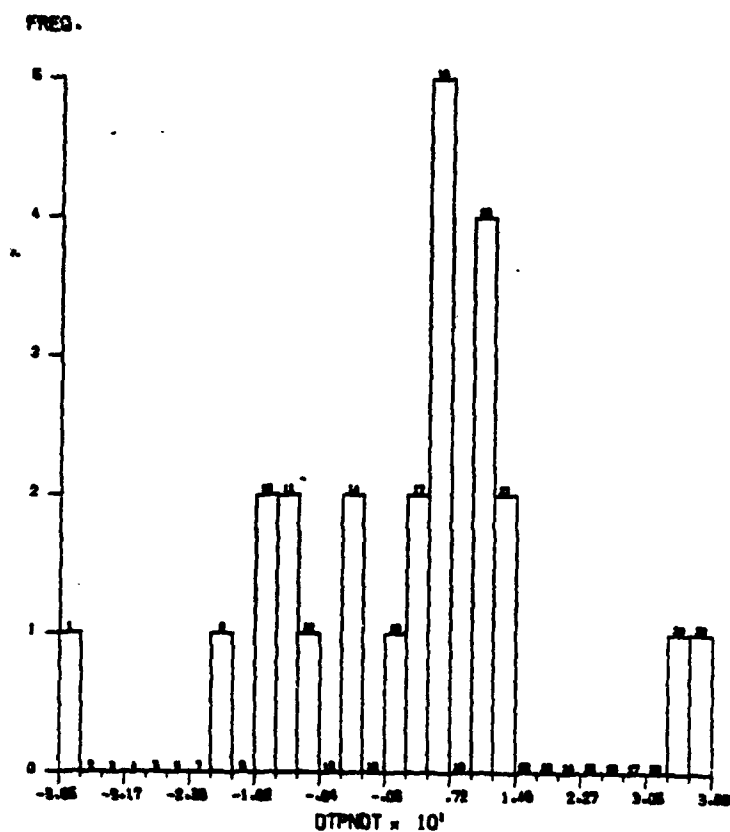
a



b

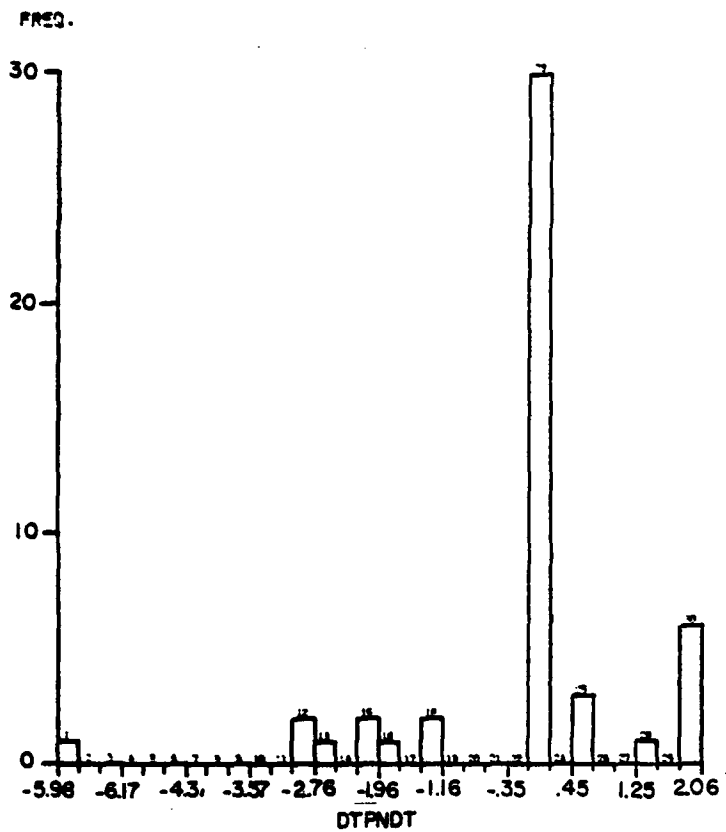


c

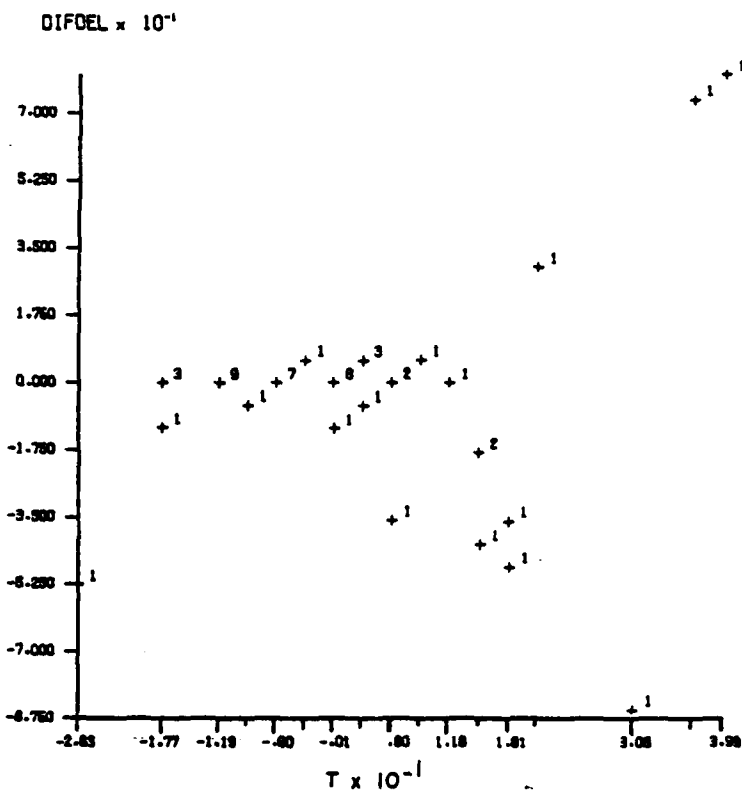


d

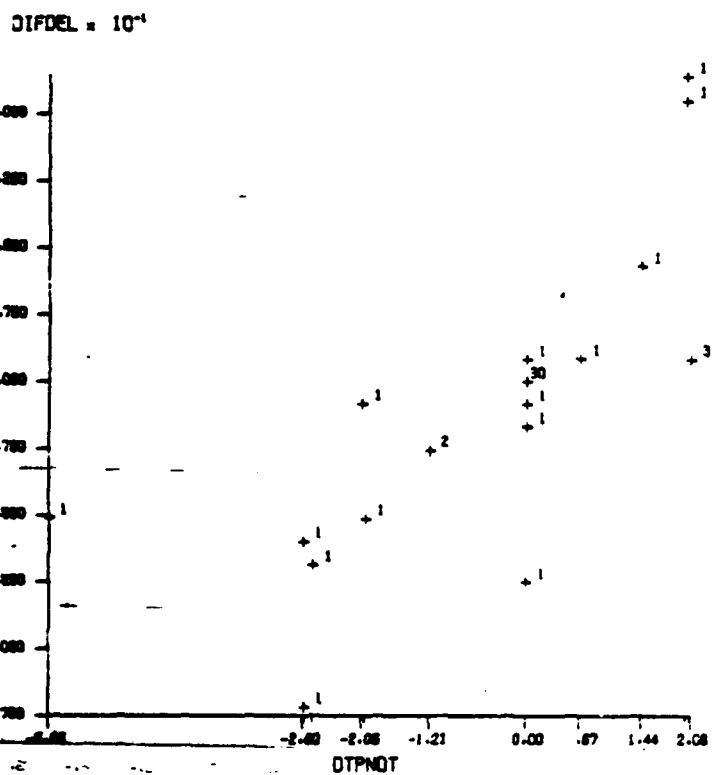
Figure 8



e

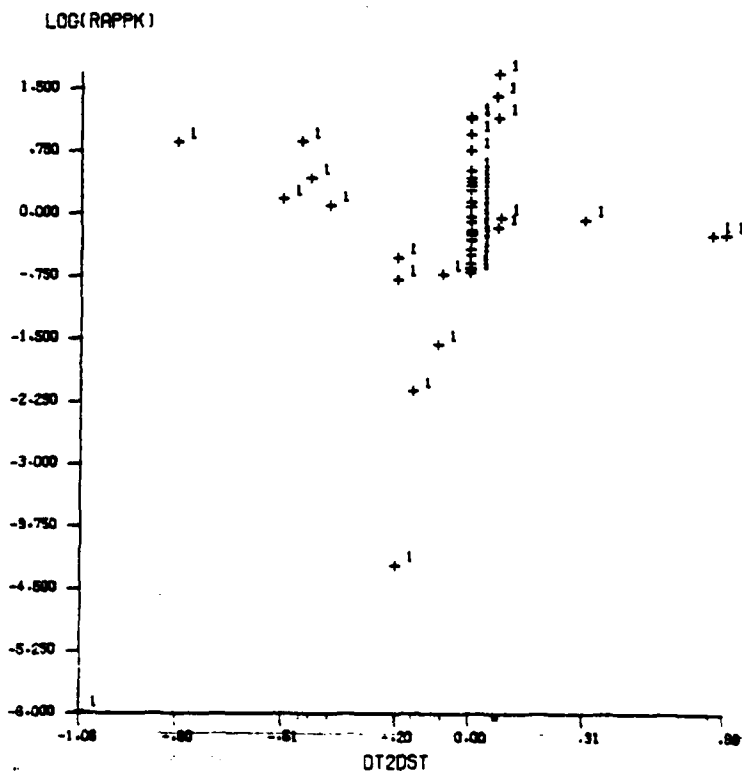


f

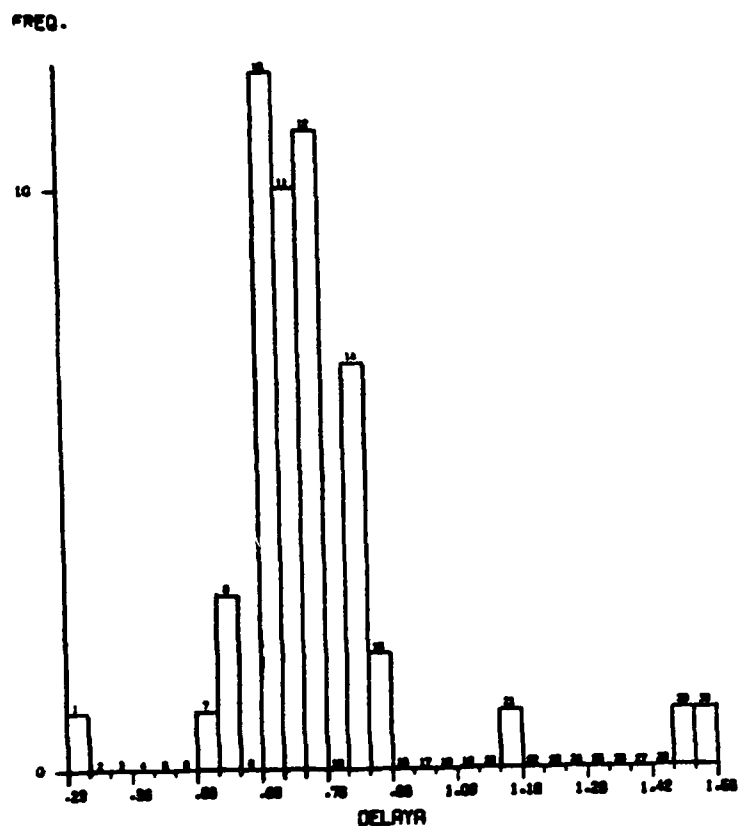


g

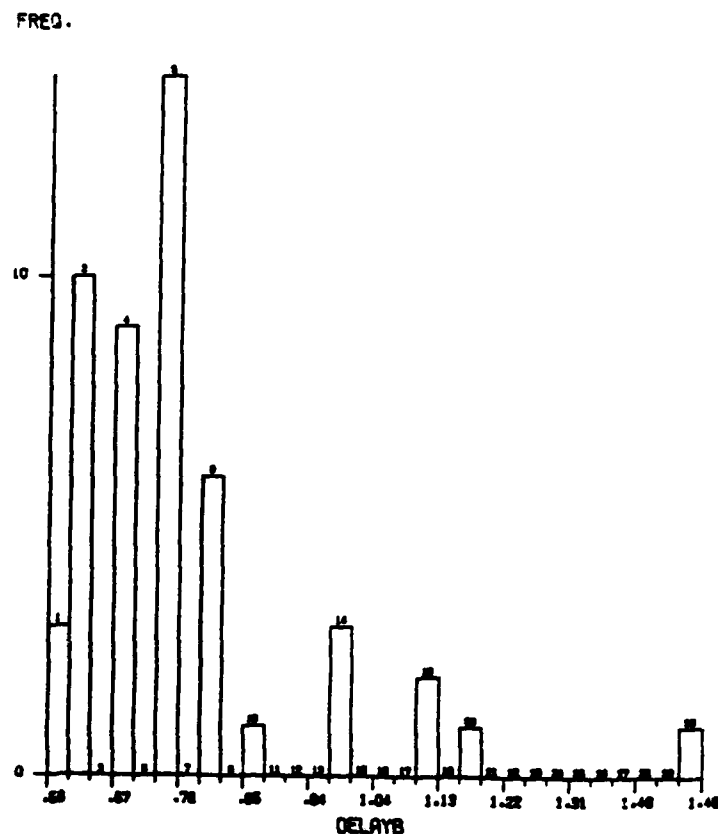
Figure 7



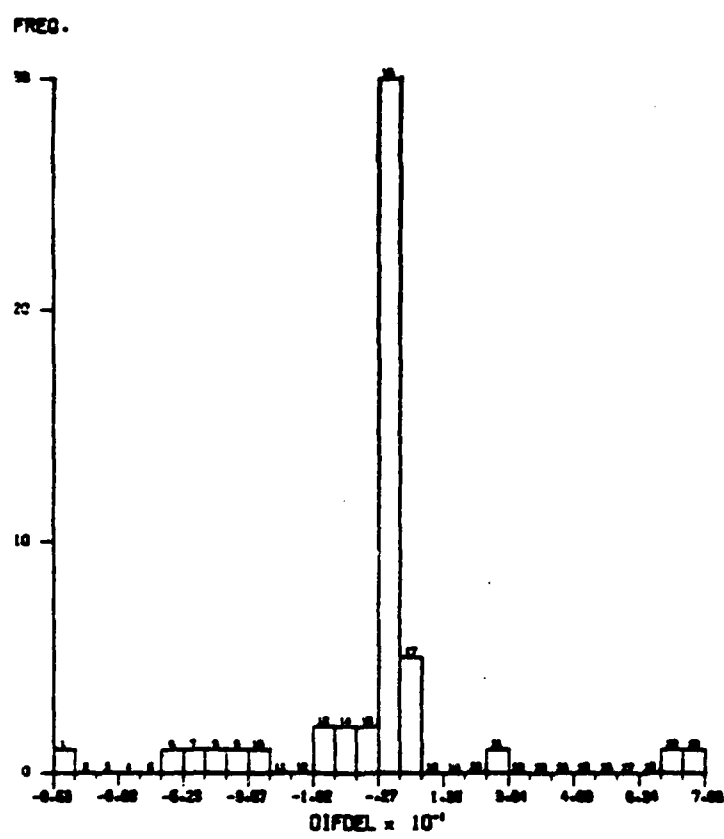
h



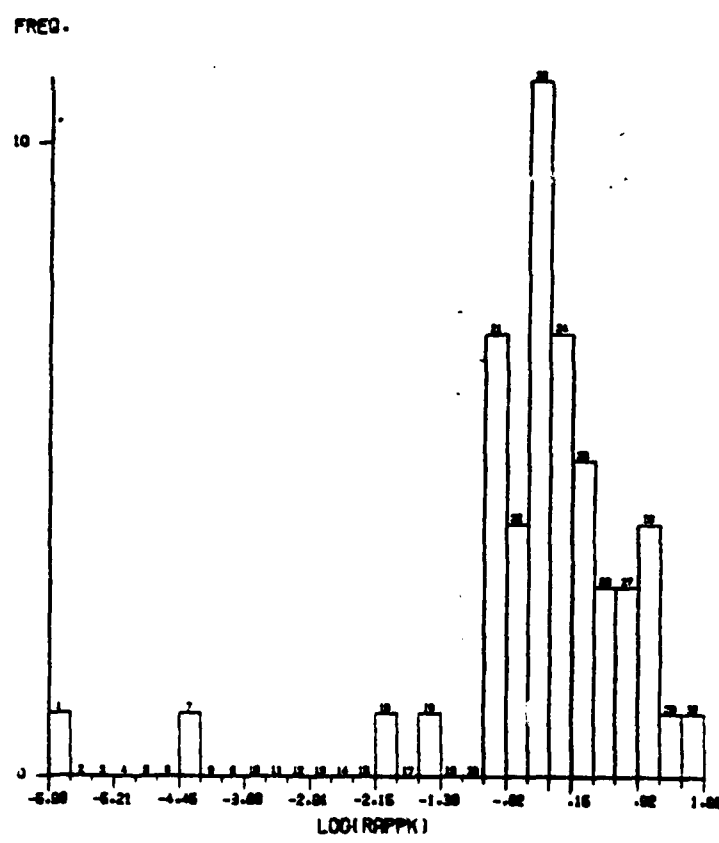
a



b



c



d

Figure 7

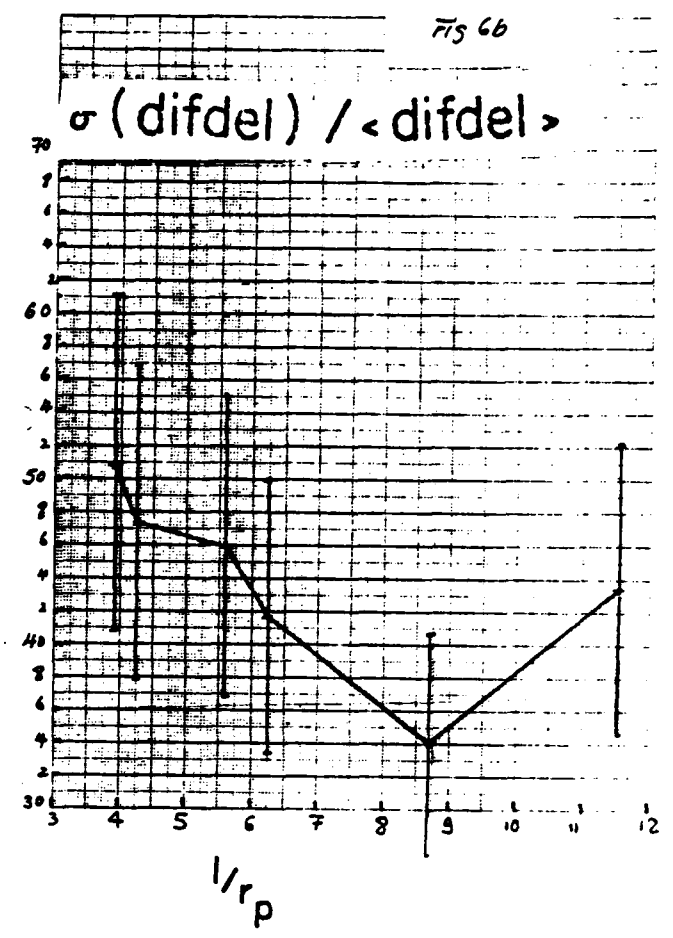
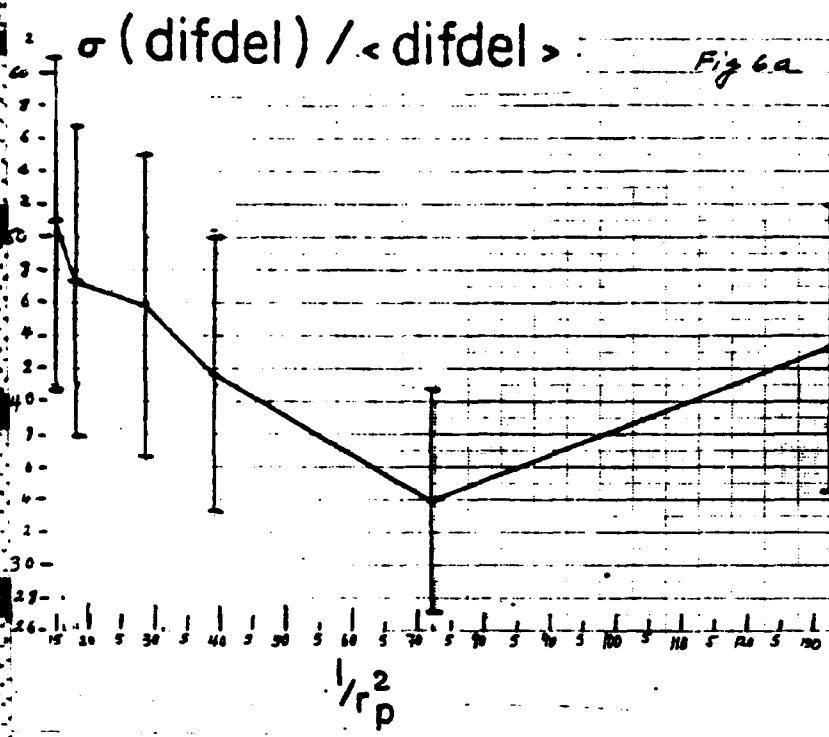
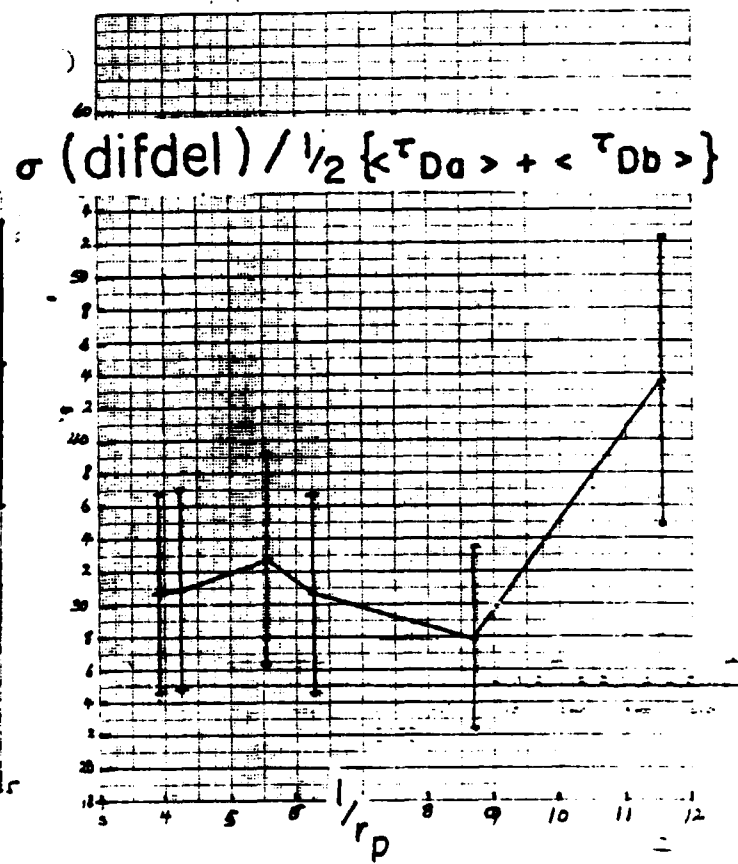
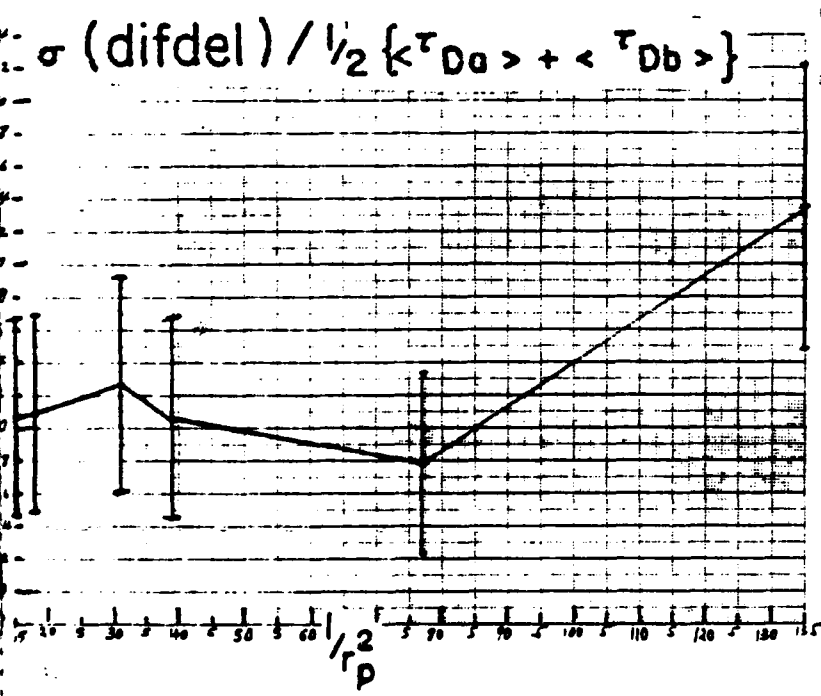


Figure 6



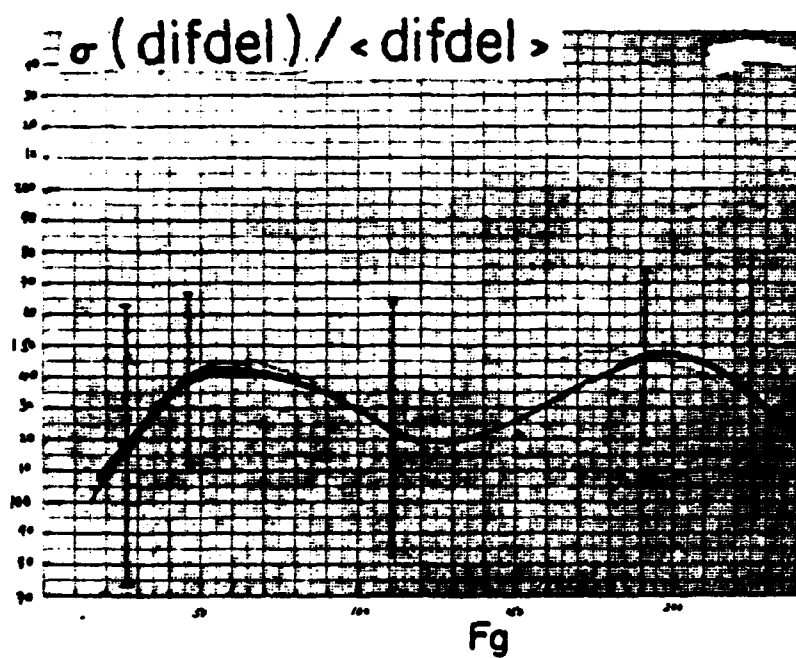


Figure 5a II

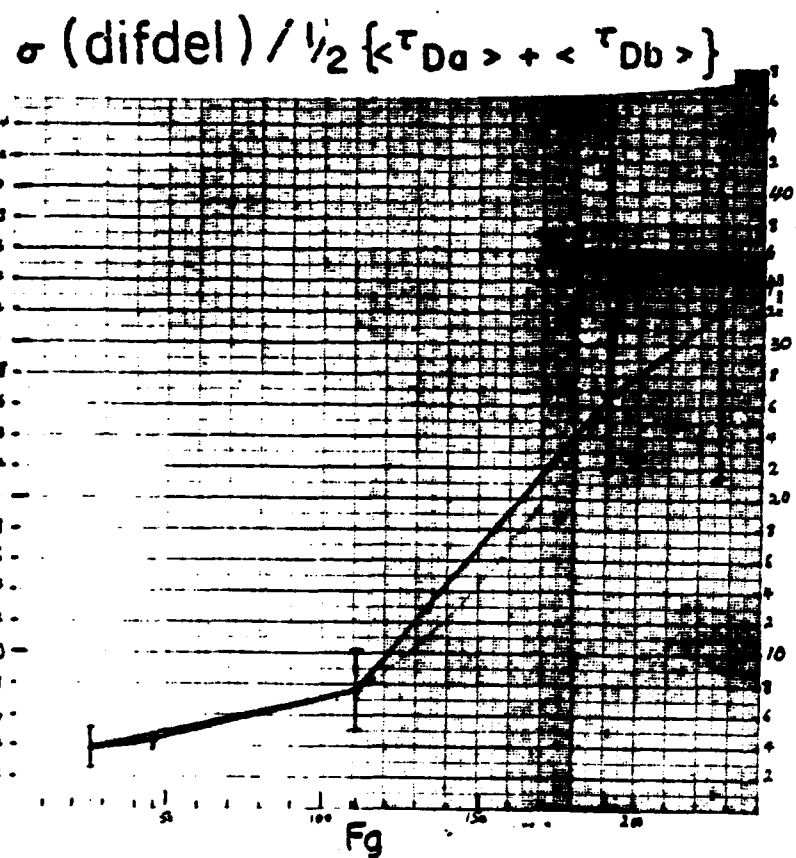
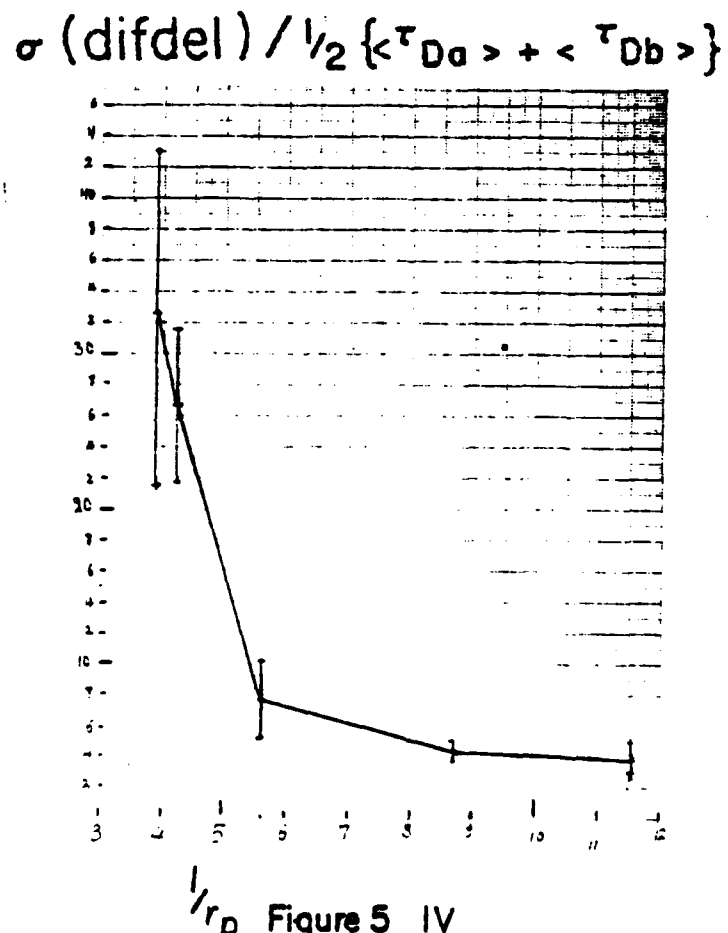


Figure 5 III



$1/r_p$ Figure 5 IV

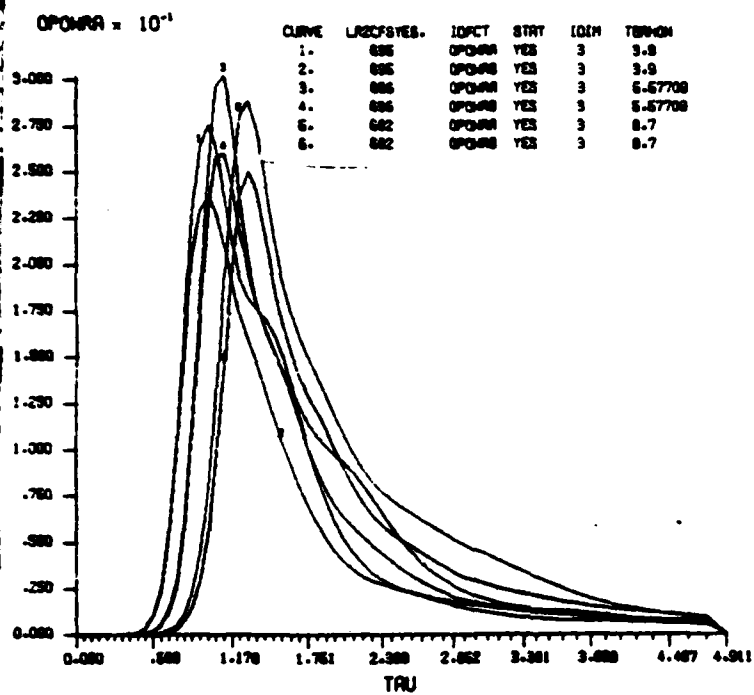


Figure 5a

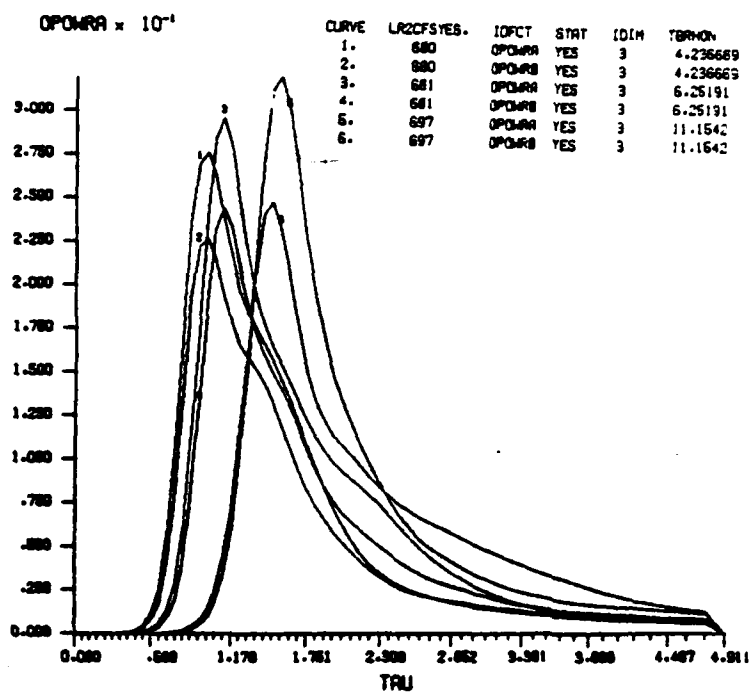
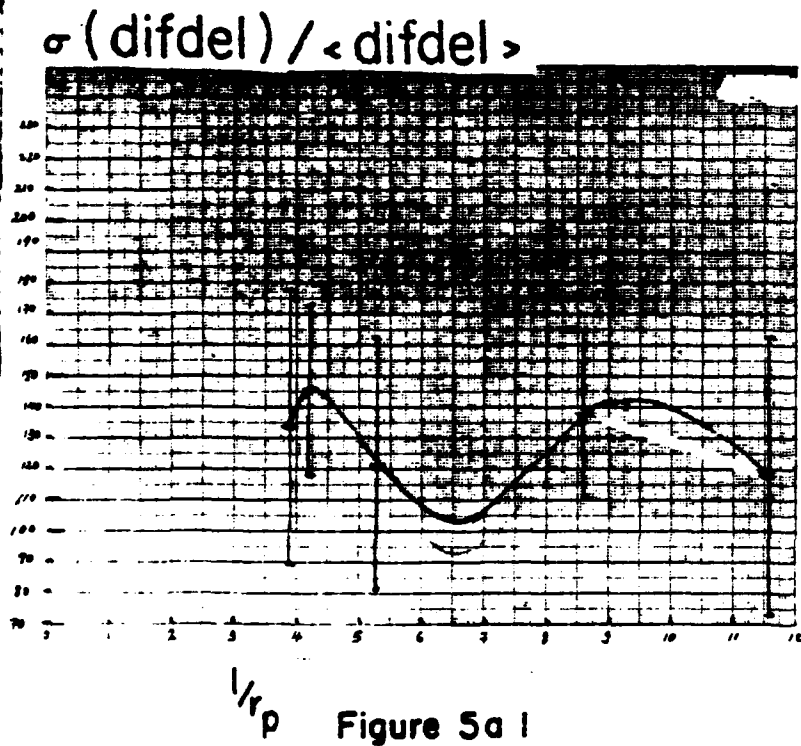


Figure 5b



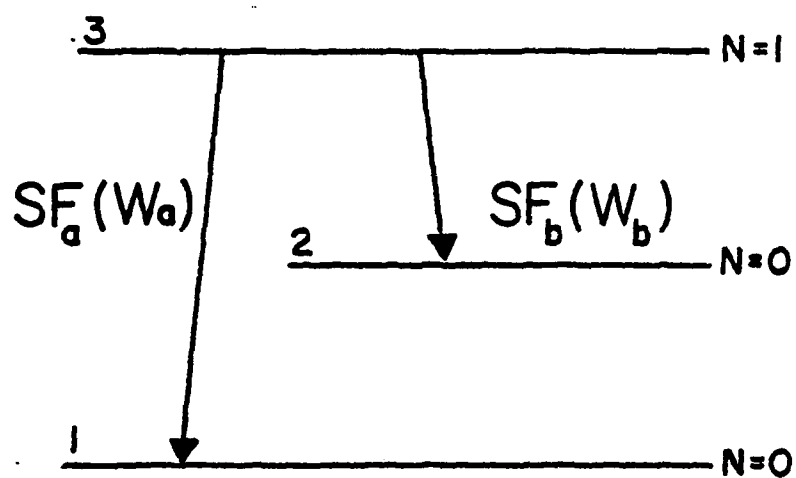


Figure 1

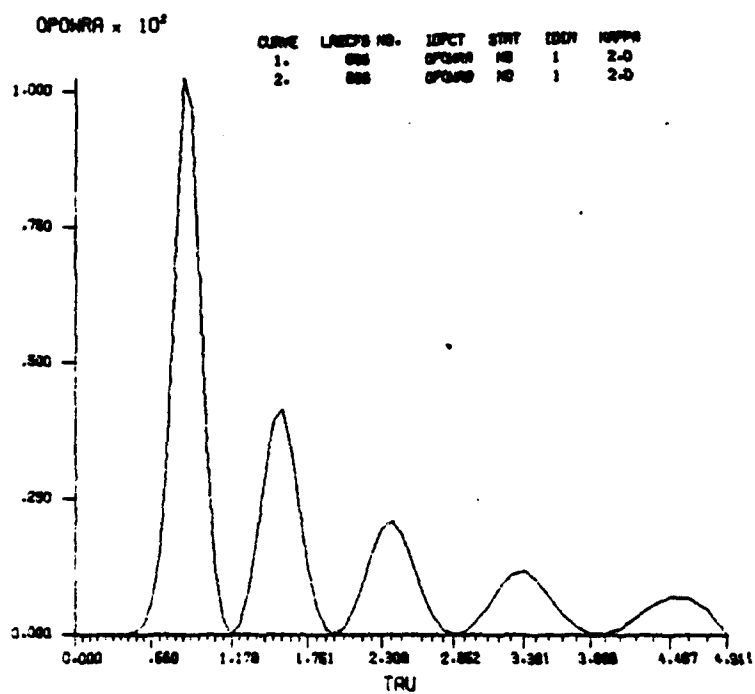


Figure 2a

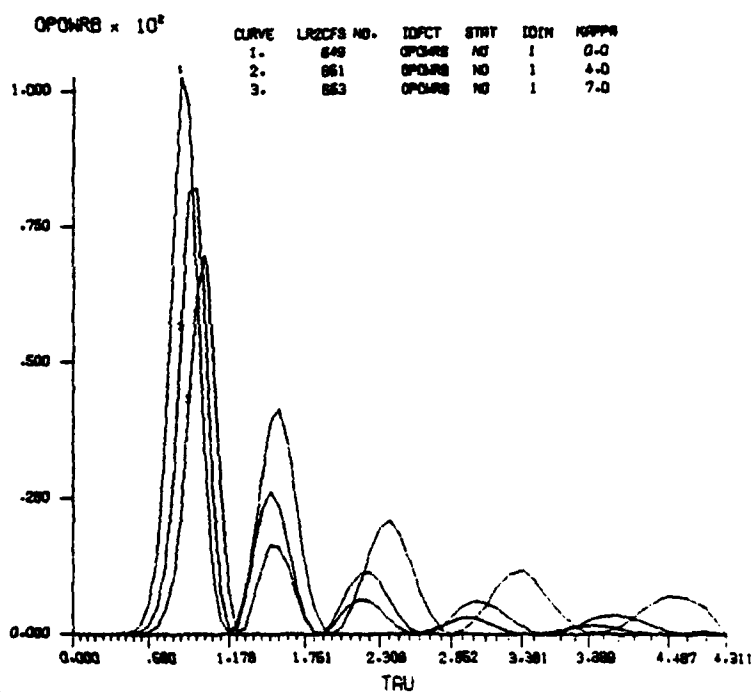


Figure 2b

Fresnel variation of deterministic and quantum initiation in two and three level superfluorescence†

Farres P. Mattar††

Division de Physico-chimie, Commission de l'énergie atomique
Centre d'Etudes Nucleaires de Saclay, Gif-sur-Yvette, France
and

Spectroscopy Laboratory, Massachusetts Institute of Technology
Cambridge, Massachusetts 02139, USA

Abstract

Recent work is reviewed where dynamic diffraction coupling is examined in Superfluorescence SF with use of a one-way semiclassical model in which diffraction and transverse density variations are rigorously included. The Cs data are correctly simulated for the first time in conjunction with both an average tipping angle and quantum fluctuation (either longitudinal or transverse) at the initiating stage. This comprehensive review also encompasses rigorously the effects of pump dynamics on the SF evolution. The terminology is unified. Specification of certain pump beam initial conditions at a given frequency results in specific SF characteristics at another frequency as recently observed in CH_3F and Ba. Pump dynamics are studied in both the average value of the tipping angle and quantum fluctuation at the initiation stage.

Important Remarks

At this time, I wish to express my appreciation and give credit to Gibbs, McCall and Feld in the two-level analysis and Dr. C.M. Bowden and Dr. C.C. Sung in the three-level analysis and for their many contributions in the form of numerous relevant discussions, preparatory analytical work and help in selecting details of realistic models based on their close contact with laboratory results. In addition, Dr. Gibbs and Dr. C.M. Bowden's participation in carrying the two-level and three-level SF calculations respectively accelerated the rate of progress in my research. Let me take this occasion to thank Dr. Gibbs, Dr. McCall, Dr. Feld and Dr. Bowden for their energetic and enthusiastic collaboration.

Introduction

Spontaneous emission by an excited atom is a random process in which the stored energy is emitted in the natural lifetime τ_{sp} of the excited state. In 1954 Dicke predicted that under certain conditions all the energy could be released cooperatively in a much shorter time τ_{sp}/N , where N is the effective number of excited atoms.¹ In this process, which he called superradiance, the atoms would decay cooperatively, instead of independently. The emission intensity would be then in proportion to N^2 , instead of N as expected for incoherent radiation.

The concept of N^2 emission in an array of driven electrical or magnetic dipoles is well known. For instance, when the dipoles are confined to a volume with linear dimensions smaller than the wavelength of the driving field they oscillate in phase. The resulting emission is proportional to the square of the number of dipoles. Such N^2 intensities have been known in the field of NMR, for example in spin echoes²², the pulses are much shorter than the lifetime divided by N because the lifetime of an individual spin is enormously long and there are always some broadening mechanisms. Experimental verification of Dicke superradiance only became feasible with the advent of sources of intense laser radiation, albeit with volumes large compared to 2 cubic wavelengths, and resultant qualifications. Friedberg and Hartmann²³ noted a high gain requirement to insure that coherent decay processes dominate over incoherent decay $\alpha L \geq 1$ and superradiance to occur.

The first experiment to demonstrate Dicke superradiance was reported in 1973 by Skribanowitz, Herman, MacGillivray and Feld in rotational transitions of HF gas.³ Like all subsequent superradiance experiments⁴⁻⁶ a long optically thick vapor of two level atoms (an HF rotational transition in this case) was prepared in a state of total inversion by indirectly (i.e., incoherent) pumping the upper level with a short light pulse, in this case via a coupled ground state transit (Fig. 1). There is no optical cavity and stray feedback is negligible. In the first aspect of the paper, as in most theoretical treatments, the dynamical effect of the pump is not considered. Only the relaxation process from the state of complete inversion in a two-level manifold is treated. After a relatively long delay, proportional to $1/N$, an intense pulse or radiation was emitted at the superradiant transition, which totally de-excited the sample. The peak intensity was found to be proportional to N^2 , and the emission process was completed in a time six orders of magnitude smaller than the radiative lifetime. Under many experiment conditions the emitted pulses exhibited strong ringing. This interesting feature, not predicted by theories developed at that time,¹⁰ was attributed to propagation

† Part of this work was performed at the MIT Regional Laser Center which is a National Science Foundation Regional Instrumentation facility.

†† Partially supported by the US Army Research Office DAAG23-79-C-0148, Battelle Columbus Lab, and the Office of Naval Research N000-14-80-C0174; presently on extended leave of absence from Polytechnic Institute of New York.

effects.^{3,11,12} These results were interpreted by means of a propagation model based on the coupled Maxwell-Schrodinger ("semiclassical") formalism.^{3,13} For simplicity, the superradiant pulse was assumed to be in the form of a plane wave ("one dimensional" model). The theory was found to predict all the observed features, and be in reasonable agreement with the data.

A noteworthy feature of these experiments is that the atoms are prepared in an inverted state, hence initially do not possess a macroscopic polarization. Classically, the sample would not radiate except in the presence of black body radiation. The triggering of the superradiant emission process is, in fact a fundamental quantum phenomenon, brought about by random spontaneous emission events and/or black body radiation. Hence, the consequent fluctuations in delay time, peak intensity, and pulse shape provide information about quantum statistics.⁸ In the semiclassical propagation model these fluctuations are simulated by a small initiating pulse of area ("tipping angle") θ_0 ,³ or by a polarization source distributed throughout the medium.¹³ Dicke superradiance emitted by an initially inverted sample is often called superfluorescence (SF).¹⁴ All observations of Dicke superradiance to date have been of this type.

Following the HF studies, SF was studied in several atomic⁴ and molecular⁵ systems, and the general features of the initial observation were confirmed: pulse intensities N^2 , pulse delays $1/N$, and ringing (see Fig. 2).

In 1976 Gibbs and Vrehe carried a careful set of quantitative observations on the $7P_{3/2} - 7S_{1/2}$ transition of atomic Cs at $2.33\mu\text{m}$ in a 3KG magnetic field.⁶ The transition chosen was free of M-degeneracies and the experimental parameters obeyed a set of conditions formulated in the mean field theory (MFT) approximation of Bonifacio et al.¹⁴ Mean field theories inherently excluded propagation, and generally predicted "single pulse" (i.e., no ringing) emission. The Cs experiment established the existence of a regime of single pulse emission (Fig. 3), in qualitative agreement with the MFT, but the observed pulse widths and delays did not agree.⁷ Under conditions of higher densities, however, some ringing was observed.

Furthermore the SF output was shown to fluctuate from shot to shot, i.e., when the sample is repeatedly prepared with the atoms in the excited state. These fluctuations, both in delay time and shape, are of quantum origin (as it has been shown by Haake et al.¹⁷ and Vrehe et al.¹⁸); they correspond to the initial quantum uncertainties in the state of the field and the atomic system. SF thus offers the unique possibility of studying microscopic quantum fluctuation in the time domain as it was observed by Vrehe et al.^{7b}

Thus an open question in SF experiments was raised: Why the output pulse is sometimes smooth, but at other times exhibits multiple structure or ringing. MacGillivray and Feld proposed that the lack of ringing was due to the non-plane wave nature of the evolving SF pulse,^{15,16} but this idea was not pursued.

Another explanation put forth was that the initial tipping angle θ_0 is of the order of 10^{-2} , which is much larger than the generally accepted value of $< 10^{-4}$. The propagational model predicted that such a large value would greatly curtail the ringing and reduce the decay. However, a direct measurement of θ_0 by Vrehe and Schuurmans^{8a} showed that such a large value could be excluded.

In 1977 two quantized field treatments which rigorously incorporated propagation effects and described the quantum initiation process, were developed by Glauber and Haake¹⁷ and the other by Polder, Schuurmans and Vrehe.¹⁸ These treatments were developed to describe the observed statistical fluctuations and hopefully, to account for the lack of ringing. The predicted fluctuations agreed with the Cs observations but due to the plane wave nature of the theory, the lack of ringing could not be accounted for. These quantized field treatments confirmed the validity of using the semiclassical approach, and showed that the quantum initiation process could be properly included in the propagational model by means of a set of initiating polarization sources or fields randomly distributed throughout the medium.¹⁹

By this time it was generally accepted that the lack of ringing was due to the non-plane nature of the evolving SF pulse. Bonifacio, Farina and Narducci²⁰ examined transverse effects in the MFT approximation, while MacGillivray and Feld²¹ (see Fig. 4) and Bullough, Saunders and Feuillade²² included a loss term in the Maxwell equation to describe diffraction. The results of these treatments gave qualitative support to the role of diffraction in reducing the ringing, but quantitative agreement with single pulse observations was poor.

Beginning in 1980, Mattar, Gibbs, McCall and Feld^{23,24} rigorously extended the propagational model of SF to the non-plane wave regime. Mattar's model, which included a transverse Laplacian term in the reduced Maxwell equation, have been developed for describing transverse (i.e. non-plane wave)²⁵ field variations self-induced-transparency (SIT);²⁶ its validity has been confirmed by several SIT experiments.^{27,28} The results of the non-plane wave SF analysis provided the first complete explanation of the absence of ringing at lower densities and, for the first time, quantitative agreement with the Cs experiments (Fig. 3).

Transverse effects influence the SF pulse evolution process in two major ways, one of which is spatial averaging. In SF experiments the initial inversion density is radially dependent, since the pump light pulse which inverts the sample has typically a Gaussian-like profile. In the absence of diffraction the resulting cylinder of inverted atoms can be thought of as a set of concentric cylindrical shells, each with its own density, initial conditions and delay time. The radiation is a sum of plane-wave intensities; when the entire output signal is viewed the ringing averages out, resulting in an asymmetric pulse with a long tail.¹⁵

A second transverse effect, diffraction is unavoidable in any SF situation. Diffraction becomes important in samples with small Fresnel number $F = A/AL$, with L the cylinder length and A the cross-section. This effect causes light emitted by one shell to affect the emission from adjacent shells. It couples together atoms in various parts of the cylindrical cross-section, so that they tend to emit at the same time. This coupling mechanism causes transverse energy flow. Furthermore, this effect slightly increases the delay and reduces the tail and asymmetry.

SF is thus an inherent transverse effect problem even for large F samples since the off-axis modes develop and diffraction couples them together. This work is a collaboration with Gibbs, McCall and Feld^{23,24} and was the first one to correctly include this crucial element long sought for.²⁹

The propagational model automatically includes the effects of both spatial averaging and diffraction coupling. The first calculations described a geometry with cylindrical symmetry (two spatial dimensions). Subsequent calculations have been extended to the more complex case where azimuthal symmetry is absent and two transverse dimensions are required. The latter model is needed to describe short-scale-length phase and amplitude fluctuations which result in multiple transverse mode initiation and lead to multi-directional output with hot spots. This effect is only important in samples with large Fresnel numbers, since diffraction singles out a smooth phase front in small F samples.

Extension of the propagational model to include non-plane wave effects has many advantages. Homogeneous and Doppler broadening are readily included. Quantum fluctuations are incorporated by means of suitable random initial conditions, as in the plane wave treatment of Refs. 17 and 18. As shown in Fig. 5, these refinements lead to improved agreement with the experiments.^{30,32} The reader is referred to recent SF reviews of both experimental and plane wave theory achievements.³³

The second aspect of this article features the effect of indirect pumping which produces the initial population inversion on the SF emission. In all experiments to date a long cylindrical sample is pumped along its axis. This gives rise to a front of inversion density which moves down the sample at the speed of light. A key question was to investigate the effect of gain to diffraction-loss balance³⁴ in the swept-gain case that is responsible in the plane wave regime for stabilizing the energy and power.³⁵

Furthermore, as found by Bowden and Sung,³⁶ when τ_R is comparable or larger than τ_p the process of coherent optical pumping on a three-level system can have dramatic effects on the SF. In particular, as the SF pulse grows and propagates down the medium, its delay (relative to the pump pulse) decreases. Therefore, in a sufficiently long sample, an overlap will occur between the pump and the evolving pulse, resulting in a strong interaction which depletes the pump and reshapes the evolving pulse similar to the Raman process. Thus the full nonlinear co-proportional aspects of the injected pump pulse, together with the SF which evolves must be treated explicitly in the calculation as presented by Mattar and Bowden.³⁷ To analyze the pump dynamics, the physical model must encompass three-level atoms instead of the two-level. The Λ -configuration is considered. The $1 \leftrightarrow 3$ transition is induced by a coherent injection pulse of frequency nearly tuned to the identical transition. The properties of this pumping pulse are specified initially in terms of the initial and boundary conditions. The transition $3 \leftrightarrow 2$ evolves by spontaneous emission at frequency ω . It is assumed that the energy-level spacing is such that $\epsilon_3 > \epsilon_2 \gg \epsilon_1$ (see Fig. 1) so that the fields at frequencies ω_0 and ω can be treated by separate wave equations. However the nonlinear material closely intertwines the two fields. The energy levels $2 \leftrightarrow 1$ are not coupled radiatively due to parity considerations. Further, we neglect spontaneous relaxation in the $3 \leftrightarrow 1$ transition, and the spontaneous relaxation in the $3 \leftrightarrow 2$ transition is simulated by the choice of a small but nonzero, initial transverse polarization characterized by the parameter $\psi_0 \sim 10^{-3}$. The initial condition is chosen consistent with the particular choice of ψ with nearly all the population in the ground state and the initial values of the other atomic variables chosen consistently³⁸ according to the initial equilibrium properties of the system.⁴⁷ The initiation of the three-level system is described in the appendix of Ref. 37. The results do not depend upon nominal variations of this parameter. The full statistical treatment of the quantum initiation process with resulting temporal fluctuations utilize an additional driving Langevin force in the material Bloch equation as was recently derived by Bowden and Sung.³⁸ In particular, it was shown that the injected coherent pump-pulse initial characteristics, such as on-axis area, temporal and radial width and shape, can have significant deterministic effects on the SF pulse delay-time, peak intensity, temporal width and shape. Thus by specifying certain initial properties of the injected pump pulse, the superfluorescent pulse can be shaped and altered both for an average initial tipping angle³⁷ as well as an ensemble of (quantum) fluctuation initialization.⁴⁰ The full nonlinear set of results predict the conditions under which an injected light pulse of a given frequency can be used to generate, shape and control a second light pulse of a different frequency via a nonlinear medium, thus demonstrating a new aspect of the phenomenon of light control by light even with random initiation. Three specific regions are encountered; the SF buildup, the full development of SF with the pump depleted, and the highly nonlinear regime where the SF and the pump overlap significantly, if not totally.

This phenomenon known as pump dynamics³⁵ is interesting because the characteristics of the superradiant pulse emitted at one frequency can be controlled by specifying certain characteristics of the pump pulse injected at a different frequency.³⁷ Thus a new aspect of light control by light, was demonstrated.³⁷ Recently the quantum fluctuations for three-levels was derived by Bowden and Sung. In particular they presented in Ref. 38 a more comprehensive treatment of SF in the linearized regime of SF initiation by combining coherent pump dynamics on the three-level system and simultaneous as well as subsequent, quantum mechanical initiation of the SF emission. Their attention, as well as ours, is confined to situations satisfying

$\tau_p < \tau_R$, which is the condition where the effects of SF quantum are expected to be most important in terms of subsequent temporal fluctuation. Using their initiation through a Langevin force as additional driving forces in the material (generalized three level Bloch equations), we study numerically the nonlinear regimes which include propagation, transverse and diffraction effects and found that the light control by light remains.⁴⁰

Synthesis of Results

In summary, the primary objective of this paper is to review how the various refinements in the propagation model in a two-level optically thick medium lead to an increasingly accurate description of the observed SF pulse shapes, delays and fluctuations. New results of swept gain superradiance and pump dynamics are also presented. Uniform plane-wave Maxwell-Bloch solutions have been performed by Haake et al.³¹ for hundreds of such statistical initial conditions. These yield about 12% for the standard deviation $\sigma(\tau_D)$ in the delay-time in good agreement with the expression $2.3/2nN$ derived by Polder⁴² et. al. Vreken et al. have measured $(10 \pm 2)\%$ for Fresnel number $F = 0.8$, $(6 \pm 2)\%$ for $F = 4$, and 4% for $F = 18$. Note that the plane-waves theoretical value of $\sigma(\tau_D) = (13.5 \pm 3.6)\%$ for $F = 1$ in satisfactory agreement with the experiment, i.e. the jittering of the calculated delays fall within the experimental uncertainty from shot-to-shot. These fluctuations reduce the tail of the output obtained with transverse effects alone, thus improving the agreement with Cs data. It curtails the amount of on-axis ringing even for a single shot.

When one considers simultaneously transverse effects, quantum initiation and inhomogeneous broadening, one finds excellent agreement between the propagation theory and experiment. In particular, the ringing disappears and the Fresnel dependency of computer delays agree more uniformly with the experimental data. More specifically, the Fresnel dependency of the uncertainty in delay time normalized to the average delay is different for $F < 1$ from what it is for $F > 1$. The curve peaks for $F = 1$, ascertaining the competition between diffraction-loss and medium gains as the consideration of the two transverse effects, spacial averaging of the concentric shells and communication between the various shells through the Laplacian coupling.

The effects presented in the second part of the analysis clearly demonstrate in this part the control effect of coherence pump for both deterministic³⁵ or random initialization^{38,39} on SF pulse evolution.³⁸ It is suggested that effects of the type discussed here may have in fact been operative in SF experiments and their results. The pump pulse was taken as purely coherent in these calculations. To determine whether or not effects of the nature reported here are indeed operative in a given experiment it is crucial to determine the degree of coherence of the pumping process as well as its temporal duration even for an ensemble of shots. Furthermore, and perhaps of greater importance, we have demonstrated the control and shaping of SF pulse which evolves by specification of particular initial characteristics and conditions for the pumping pulse which is injected into the nonlinear medium to initiate SF emission in a three-level media randomly polarized. These manifestations and others of the same class we call the control of light by light via a nonlinear medium. This phenomenon constitutes a method for nonlinear information encoding, or information transfer, from the injection pulse initial characteristics at a given frequency to corresponding SF pulse characteristics which evolve at another frequency due to propagation and interaction in the nonlinear medium⁴⁰. This idea can be transposed to Raman (or blue-green conversion) studies.

Physical Principles

As explained in the introduction, the rate of cooperative spontaneous emission is much more rapid than the single atom decay rate. This can be understood by considering the radiative decay of two excited atoms. If the separation between the atoms is large they will decay incoherently in a time τ_{sp} . However, if the two atoms are brought close they radiate in a much different manner. A system of two two-level atoms separated by a distance much smaller than the wavelength λ of the emitted radiation must be properly symmetrized; as such they emit cooperatively, not independently. Thus, the emission process takes the system from the fully excited state ($\uparrow\uparrow$) to the triplet intermediate state $(\uparrow\uparrow\uparrow)/2$, and then to ground state ($\uparrow\uparrow$). The radiation rate for each of these steps is twice that of isolated atoms. The emitted intensity is thus four times as great as in the single atom case. Hence the cooperative lifetime $\tau_R (N = 2) = \tau_{sp}/2$.

Similarly, for the case of N closely spaced atoms the total wave function must be symmetrized. The state with the maximum emission rate is the totally symmetric state which has zero population difference. Its radiation rate is $N/4$ times greater than that of N independent atoms: $\tau_R(N) = \tau_{sp}/(N/4)$. This state of maximum emission corresponds to the arrangement of atoms in which the net dipole moment is maximized.

All observations of SF to date have occurred in extended samples, where both the sample length L and the transverse dimension (e.g., r_p) $\gg \lambda$. The radiation is emitted into a small solid angle $\Delta\Omega/4\pi$ along the cylinder axis, in contrast to the isotropic radiation pattern of ordinary spontaneous emission. For a large F sample with an initial inversion density n the solid angle is determined by geometry: $\Delta\Omega/4\pi = \lambda^2/4\pi A$, and the characteristic cooperative radiation time

$$\tau_R = \tau_{sp}/(n\lambda^2 L/8\pi). \quad (1)$$

This enhancement factor can be interpreted as the effective number of radiators $(n\lambda^2 L/8\pi)$ ($\Delta\Omega/4\pi$) which can participate cooperatively in the emission process.

Consider an extended optically thick sample initially prepared in a totally inverted state. Due to spontaneous emission, random photons will be emitted at the wavelength of the SF transition. The first photon to be emitted along the axis of the sample will induce a small macroscopic polarization which acts as a source to create a small electric field. This field induces additional polarization, which tends to build up regeneratively. Thus, an SF state slowly evolves over a sizeable portion of the sample. When the polarization becomes sufficiently large in a particular region the regeneration process becomes rapid, and the sample emits energy at greatly enhanced rate. This leads to a rapid de-excitation of that region of the sample, after which all of the population is transferred to the lower level. De-excited regions can then be re-excited by radiation from other parts of the sample, which gives rise to the ringing.

Statistical fluctuations in the initiation process give rise to corresponding fluctuations in the output characteristics of the SF pulses.

A unique feature of SF emission is that virtually all the energy stored in the sample is released in the form of coherently emitted light. In this respect it differs greatly from other cooperative emission effects in which only a fraction of the stored energy is emitted coherently. Examples include photon echoes and free induction decay. In these phenomena the sample is essentially unaffected by the cooperative emission and its decays by incoherent processes. MacGillivray and Feld¹³ termed these effects as 'limited superradiance'.

Although the initiation of such system is inherently quantum mechanical, its subsequent evolution can be described semi-classically. The system is analogous to an array of coupled pendulums, all initially balanced on end. The motion of the system can be triggered by disturbing any one pendulum from its unstable equilibrium position. Coupling will cause the entire array of pendula to respond together and follow the motion. For a relatively long time the tipping angle remains small, and the system evolves slowly. However, when the angle becomes sufficiently large, perhaps of the order of a few degrees, the pendula will swing rapidly. As the pendula swing they collectively emit radiation, and thereby lose energy. Eventually they are completely de-activated and, come to rest. If the various initiating perturbations are not identical, the motion of the pendula will vary somewhat from one shot to another.

In a simplified form of the semi-classical theory, these fluctuations are approximated by an initial tipping angle. The quantum mechanical theory shows that the initial fluctuations can be accurately modeled by assigning random initial tipping angle to the individual pendula.

If the simple (one-dimensional) pendula described above are replaced by conical pendula the motion becomes two-dimensional. In this case the initiating tipping angle will have two components. (θ_0 and ϕ). From one shot to another both components of the initiation will vary. To enhance this point, picture a child on a swing. If the child is pushed at the exact center of his back, his motion will be planar. But if the push is off center, the motion is conical, i.e., nonplanar like a Foucault pendulum. (See Fig. 6b).

The SF process is a unique macroscopic manifestation of quantum fluctuations, even though they are proportional to the inverse of N , the number of atoms. One usually does not expect that these small microscopical fluctuations could be seen for N greater than 10. However, in superfluorescence one can easily (macroscopically) see this 10% fluctuation for N as large as $N = 10^6$.

Equations of Motion for the Two-level Analysis

A - Three dimensional problem.

In the slowly varying envelope approximation, the normalized field-matter equations read:

$$\dot{\epsilon} = \text{Re} \{ \dot{E} \exp [i (\omega t - Kz)] \} \quad (2)$$

$$\dot{P} = \text{Re} \{ i \dot{P} \exp [i (\omega t - Kz)] \} \quad (3)$$

$$E = (2\mu E/\hbar) \tau_R, \quad P = \tilde{P}/\mu \quad (4)$$

$$\tau = (t - z/c)/\tau_R \quad (5)$$

$$\eta = z/l, \quad \text{the cell length.} \quad (6)$$

where E and P are the slowly varying complex amplitudes of the electric field and polarization, respectively; ω is the population difference; τ is the retarded time; η or ξ the normalized axial coordinate; μ is the transition dipole moment matrix element; and T_1 and T_2 are the population relaxation and polarization dephasing times; T_D the Doppler Broadening time and τ_R the radiation time

$$-\frac{1}{4\pi} \nabla_T^2 E + \frac{\partial E}{\partial \eta} = (\sigma_R \tau_R) d \int P(\Delta\Omega) g(\Delta\Omega) d(\Delta\Omega) \quad (7)$$

$$\text{If } \xi = z/\sigma_R \quad (8)$$

instead, one obtains

$$-\frac{i}{4F_g} \nabla_T^2 E + \frac{\partial E}{\partial t} = d \int P(\Delta\Omega) g(\Delta\Omega) d(\Delta\Omega) \quad (9)$$

However, if one identifies l as the pulse extent (i.e., $l = c\tau_p$) one recovers the SIT normalisation; whereas should l be taken as the cooperation length $l = c\tau_R$, the two normalisations eqs. (6) and (8) become equivalent.

$$\partial_T P + (i\Delta\Omega + 1/\tau_2) P = EW \quad (10)$$

$$\partial_T W + (W+1)/\tau_1 = -\frac{1}{2} (E^*P + P^*E)$$

$$\tau_R = \hbar\lambda/4\pi^2\mu^2\eta\delta L = 8\pi\tau_0/3\eta\delta\lambda^2 L \quad (11)$$

$$\tau_1 = T_1/\tau_R \quad (12)$$

$$\tau_2 = T_2/\tau_R \quad (13)$$

$$\tau_2^* = T_2^*/\tau_R \quad (14)$$

$$\Delta\Omega = (w_0 - w)\tau_R \quad (15)$$

$$\int_{-\infty}^{\infty} g(\Delta\Omega) d(\Delta\Omega) = \sqrt{\pi/\tau_2^*} \int_{-\infty}^{\infty} \exp \{ - [(\Delta\Omega)\tau_2^*]^2 \} d(\Delta\Omega) = 1 \quad (16)$$

$$d = \exp [- (\rho/\rho_N)^m] = \frac{N(\rho)}{N(0)} \quad (17)$$

$d = 1$, uniform density

for $m > 0$ the radial population density distribution for active atoms is variable, say, for an atomic beam

$m = 2$, gaussian density profile

$m = 4$, super-gaussian density profile

$m = 6$, hyper-gaussian density profile

ρ_N is $(1/e)$ radius of the atomic density N distribution

The relationships of σ_R and τ_R leads directly to

$$\sigma_R L = 1 \quad (18)$$

As noted previously in the plane wave regime, a universal scaling of the equation exists. The gain length Fresnel number F_g qualifies the competition between diffraction (i.e., transverse effects) and the nonlinear gain of the SF system as it did in SIT²⁵. Drummond and Eberly⁵¹ also recently recognized this scaling.

Following 17-19, we interpret the equations of motion as c-number representation of the corresponding operator equations.

- Energy consideration for sharp line $g(\Delta\Omega) = \delta(\Delta\omega)$

$$\frac{i}{F_g} \nabla_T (E \nabla_T E^* - E^* \nabla_T E) + \partial_T |E|^2 = d(E^*P + EP^*) \quad (19)$$

$$\nabla \cdot J = -2d [\partial_T W + (W+1)/\tau_1] \quad (20)$$

where using the polar representation of the complex envelope, we have

$$E = A \exp(i\phi) \quad (21)$$

$$J_z = A^2 \quad \text{and} \quad J_T = \frac{2i}{F_g} A^2 \nabla_T \phi \quad (22)$$

for cylindrical geometry $J_T = \frac{2i}{F_g} A^2 \frac{\partial \phi}{\partial \rho}$ (23) whereas for Cartesian geometry

$$J_x = \frac{2}{F_g} A^2 \partial_x \phi \quad \text{and} \quad J_y = \frac{2}{F_g} A^2 \partial_y \phi \quad (24)$$

The components J_z and J_T represents the longitudinal and transverse energy current flow. Thus, the existence of transverse energy flow is clearly associated with the radial variation of the phase ϕ of the complex field amplitude. When J_T is negative [i.e., $\nabla_T \phi > 0$], self-induced focusing dominates diffraction spreading.

One may rewrite the energy continuity equation, Eq. (20) in the laboratory frame to recover its familiar form:

$$\nabla \cdot J = -d \left\{ \frac{\partial}{\partial t} \left[2W_0 + \frac{1}{c\tau_R \sigma_R} A^2 \right] - \frac{W - W_0}{\tau_1} \right\} \quad (25)$$

The material equations are subjected to the following initial conditions

$$P = W_0 \sin \theta_0 \exp(i\phi) \quad (26)$$

$$W = W_0 \cos \theta_0$$

for an initially inverted medium $W_0 = +1.0$

$$\theta_0 = 2/\sqrt{N} = 2/\sqrt{n_0 \pi r_p^2 L} \quad (27)$$

$$0 \leq \phi \leq 2\pi \quad (28)$$

θ_0 and ϕ are the amplitude and phase of the average (i.e., deterministic) uniform along the cell axis initiating tipping angle.

$n_0(r) = n_0 \exp[-2n_2(r^2/r_p^2)]$ (29) the inversion density with r_p the HWHM radius; L the sample length, $r^2 = x^2 + y^2$; $F = \pi r_p^2 / \lambda L$ (30), the geometric Fresnel number; $\Delta\Omega = [(\omega_0 - \omega)\tau_R]$ the normalized frequency offset.

Diffraction is taken into account by the transverse Laplacian ∇_T^2

$$= \frac{1}{\rho} \frac{\partial}{\partial \rho} \left(\rho \frac{\partial}{\partial \rho} \right) \quad \text{with } \rho = r/r_p \quad \text{for cylindrical geometry}$$

$$= \frac{\partial^2}{\partial \xi^2} + \frac{\partial^2}{\partial \zeta^2} \quad \text{with } \xi = X/r_p \quad \text{and } \zeta = Y/r_p \quad \text{for cartesian geometry} \quad (31)$$

Furthermore, diffraction is also explicitly taken into account by the boundary condition that $\rho = \rho_{\max}$ (or, $\xi = \xi_{\max}$ and $\zeta = \zeta_{\max}$) corresponds to completely absorbing walls. To insure that (1) the entire field is accurately simulated, (2) no artificial reflections are introduced at the numerical boundary $\rho_{\max} \gg r_p^2$, and (3) fine diffraction variations near the axis are resolved; the sample cross-section is divided into non-uniform stretching cells.^{47,50}

If $\alpha_R^\dagger = \frac{\omega_0 \mu^2}{n h c} N \tau_R$ (32) the on-axis effective gain then $F_g = \frac{\pi r_p^2}{\lambda \alpha_R^\dagger - 1}$ (33) is the gain length Fresnel number

F_g is related to the usual Fresnel number by $F_g/F = \alpha_R L$ (34) (i.e. the total gain of the medium); F_g can be thought as effective gain α_R^{-1} to diffraction loss ratio, κ^{-1} ; whereas F can correspondingly be thought of as the reciprocal of the strength of the diffraction loss κ for a length L .^{34,37}

$$\kappa = \lambda / \pi r_p^2 \quad (35)$$

$$F_g = \alpha_R / \kappa \quad (36) \quad \text{and} \quad F = (\kappa L)^{-1} \quad (37)$$

α_R^\dagger is the effective Beer length as defined by Gibbs and Slusher⁴⁶ in SIT for sharp line atomic system but with T_2 replaced by τ_R i.e. $\alpha_R = \frac{2\pi \mu^2 \omega_0 N}{h c} \tau_R$

B - Simplified one-dimensional problem

Let us consider the uniform plane wave solution where the variations transverse to the direction of propagation are neglected ($F = \infty$) and where the medium spectral line response is sharp ($\tau_2 = \infty$). The relaxation times are negligible ($\tau_1 = \tau_2 = \infty$). The input field is collimated; if the input field is pure real, the evolving field and polarisation will be real.

The equations reduced to the one which describe the familiar array of nonlinear pendulum initially tipped at a uniform small angle, which fall as a phased array. Approximate solutions can be derived as summarized in Table 1.

TABLE 1

$\alpha_{\tau_2} = \frac{4\pi 2}{\lambda} \frac{\mu^2}{h}$	$n_0 \tau_2 = (\tau_2 / \tau_{sp}) (n_0 \lambda^2 L) / 8\pi$
high gain $\alpha L \geq \frac{1}{2} \ln N$ (see Friedberg and Hartman ^{2(b)})	
$\tau_R = \tau_{sp} (8\pi / n_0 \lambda^2 L) = \tau_2 / \alpha L$	
$\tau_c = (c\alpha)^{-1}$	Arrechi-Courtens maximum cooperation time defined in Ref. 10a
$\tau_E = 2Lc^{-1}$	Photon escape time
$\theta_0 = \mu \tau_R E (z = 0, \tau) / h$	
peak intensity	$I_p \sim \frac{4N\hbar\omega}{\tau_R \ln(2\pi/\theta_0) ^2} \propto N^2$
(a highly directional dependence i.e., with the radiation pattern similar to that of an 'end fire' antenna array)	
pulse width	$\tau_w \sim \tau_R \ln(2\pi/\theta_0) \propto N^{-1}$
delay time	$\tau_D \sim \tau_R \ln(2\pi/\theta_0) ^2 \propto N^{-1}$

It is noteworthy scaling relation describes the basic characteristics of superradiant emission: the duration of the radiation pulse varies inversely with both the inversion density of the sample and its length, and the peak output power increases as the square of each of these parameters. Furthermore, the delay as well as the pulse width can be expressed in terms of τ_R as seen in Fig. 5. The time scales as τ_R and the intensity scales as τ_R^2 . The shape of the normalized output curve depends on the tipping angle.

C - Cylindrical SF simulations.

(i) Average constant initial tipping angle. Computational methods developed earlier⁴³ and discussed elsewhere⁴⁴ were applied to compute the effect of transverse effects on the SF evolution. The result presented here demonstrate many effects of transverse variations and how inherent they are to the problem of SF. The initiating quantum fluctuations are first approximated by a uniform tipping angle.

The graphic of Fig. 7(a) displays results where spatial averaging is present but diffraction is absent, by setting $F = \infty$ in the field equation. In this figure the emitted power of SF pulses is plotted for samples with uniform and Gaussian profiles $n_0(r)$ and $\theta_0(r)$. First, we studied ringing reduction due to spatial averaging of independent concentric shells, each emitting in a plane-wave fashion. The case in which n_0 and θ_0 are both constant (curve 1), the uniform plane-wave limit, exhibits strong ringing. In curve II, in which n_0 is Gaussian $\{n_0(r) = n_0 \exp[-\ln 2(r/r_p)^2]\}$ (38) and θ_0 is uniform, the ringing is largely averaged out, resulting in an asymmetric pulse with a tail. An essentially identical result (Curve III), is obtained for the case in which n_0 and θ_0 are both Gaussian $\{\theta_0 = \theta_0 \times \exp[0.5 \ln 2 (r/r_p)^2]\}$ (39), showing that the ringing is predominantly removed by a Gaussian n_0 regardless of the radial dependence of θ_0 . This is expected, since the output-pulse parameters are all dependent only on $\ln \theta_0$. As shown in Fig. 7(b) with uniform n_0 and θ_0 but with diffraction included, the output-pulse is almost symmetrical, and also nearly free of ringing for $F \leq 0.4$. Fig. 7(c) shows the same output power but with different detector apertures: The narrow detector aperture (i) shows the ringing observed by the HF experiment and the large aperture (iv) shows no ringing in agreement with C_0 ; the intermediate apertures (ii) (iii) display partial averaging of the ringing and cross-talk of the concentric shells.

In Fig. 8a, the effect of diffraction on the SF pulse shapes is studied by varying F with the use of a Gaussian n_0 as in the figure showing Curve 6(a). Reducing F curtails the oscillatory structure and makes the output-pulse more symmetrical, since the outer portions of the gain cylinder are stimulated to emit earlier because of diffraction from the inner portions. Diffraction through the Laplacian term establishes mode coupling between high gain to lower gain regions; it induces the different modes to pull together and superfluoresce concomitantly; subsequently, this leads to the reduction in tail which brings the output pulse shape into greater conformity with the experimental data. Thus diffraction becomes more important as F decreases. Figure 8b is an isometric graph of the intensity build up for a sample with $F = 1$. The radial variations of intensity peaks, delay and ringing, illustrate how different gain shells contribute independently to the net power. Each shell exhibits a different Burham-Chiao^(b,c) ringing pattern. Accordingly, their contributions to the net signal interfere and reduce the ringing. However, the central portion of the output pulse should exhibit strong plane-wave ringing. In fact, the ringing observed in the HF-gas experiments may have been just that, since the detector viewed a small area in the near field of the beam.

Figure 9 compares the normalized Cs SF data (for which $F \sim 0.7$, with uncertainty ranging from 0.35 to 1.4) to the theory (including relaxation terms). The data were fitted with the use of Gaussian n_0 and a uniform θ_0 with nominal value $\theta_0 = 2(n_0 \pi r_p^2 L)^{1/2}$ (40), n_0 being adjusted to yield the observed delays (1.6-2.8 times the experimental n_0 values). However, the experimental curve published at each density was the one with the shortest delay. The experimental average delay is $\sim 30\%$ greater at each density (see Footnote 13 of ref. 8a). Thus, the effective ratios of our computed densities to the experimental ones range from 1.2 to 2.2, compared with the $+60\%$, -40% quoted experimental uncertainties.

The quantum calculations^{17,18} actually yield $\theta = (2/\sqrt{N})[\ln(2N)]^{1/2}$ (41), a 9% correction which further reduces the range to 1.14-2.0. If one sets $\theta_0 = 6/\sqrt{N}$ (42), as suggested by the small injection experiment,^{8a} the range is 1-1.8, in still better agreement.

The calculated shapes are in good agreement with the data and are within the range of shot-to-shot fluctuation. The only discrepancy is that the simulations predict more of a tail than observed in the experiments. For comparison, this figure also plots the fit of the one-dimensional Maxwell-Schrodinger theory. As can be seen, the present theory gives a more accurate fit, illustrating the necessity of including transverse effects. The pulse tails are further curtailed by reducing F within the range of experimental uncertainties (which used a $1/e$ rather than a half width at half maximum definition as r_p). Note that often a Fresnel number F' defined as $r_p^2/\lambda L$, is used; diffraction effects become important when $F' = 1$ (i.e., when $F = 0.36$). Finally, the simulations predicted large ringing for a small detector placed in the center of the Fresnel number ($F=1$)SF¹ output

Figure 10 clearly displays the propagational theory of SF as outlined by Feld et al. [13]. The fluency (energy current) and the field energy are shown as isometric in τ and ρ for different distances z in the cell. The build up of the field as driven by the initiating polarison is seen to be dependent on ρ and z . With a uniform tipping angle, the energy current is always positive (i.e., the beam diffracts and blooms and do not experience self-focusing).

(ii) Quantum fluctuations. The initiation process is treated rigorously. The emission begins by incoherent spontaneous emission; only the geometry of the inverted medium leads to directed emission. Quantum effects occur during the very beginning of the pulse evolution when the problem is still linear i.e., with coupled Maxwell-Bloch solutions. The quantum initiation is then described by a statistical ensemble of initial conditions for Maxwell-Bloch solutions. One adopts an initial polarization source at each z position with random phase ϕ (relative to the coherent emission electric field which eventually develops) and with tipping angle θ which is a bivariate Gaussian with RMS value $2/\sqrt{N}$ where N is the number of atoms in each step in Z . There are two experiments by Vreken et al.^{45a} and Carlson et al.^{45b} that indicate that θ_0 is about this size; they show that injected pulses must have input pulse areas larger than θ_0 in order to shorten the SF delay time.

In particular the polarization magnitude is determined by a Gaussian distribution

$$P(u,v)dudv = \frac{1}{\pi\sigma^2} \exp [-(u^2+v^2)/\sigma^2] dudv \quad (43)$$

Where u and v are the transverse components of the Bloch vector (i.e., the real and imaginary part of the polarization) and

$$\sigma = \langle \theta^2 \rangle^{1/2} = 2/\sqrt{N} \quad (44)$$

to represent the quantum initiation properly (following Glauber & Hooke;¹⁷ Polder, Vreken Shuurmans¹⁸ and Hopf).¹⁹ The angular brackets denote an ensemble average. Equation (2) is easily checked using

$$u^2 + v^2 = 1 - w^2 \approx \sin^2 \theta \approx \theta^2 \quad (45)$$

For small θ as assumed here; then

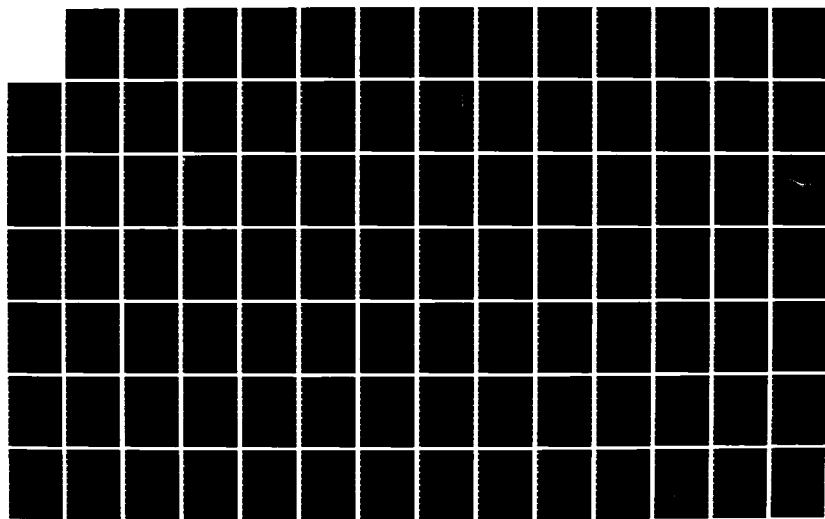
AD-A136 906

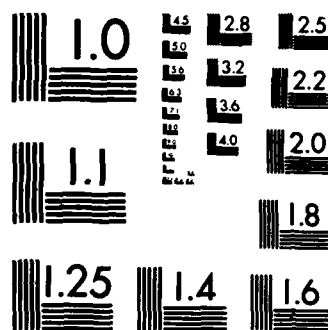
TRANSVERSE AND QUANTUM EFFECTS IN LIGHT CONTROL BY
LIGHT; (A) PARALLEL BE. (U) POLYTECHNIC INST OF NEW
YORK BROOKLYN DEPT OF MECHANICAL AND A. F P MATTAR
1983 POLY-M/AE-83-4 N00014-80-C-0174 F/G 20/6

5/6

UNCLASSIFIED

NL





MICROCOPY RESOLUTION TEST CHART
NATIONAL BUREAU OF STANDARDS-1963-A

$$P(\theta^2)d\theta^2 = \frac{1}{\sigma^2} \exp \left[-\theta^2/\sigma^2 \right] d\theta^2 \quad (46)$$

the probability that θ^2 is less than θ_0^2 is

$$\int_0^{\theta_0^2} P(\theta^2)d\theta^2 = 1 - \exp \left[-\theta_0^2/\sigma^2 \right] \quad (47)$$

So that Eq. (5) can be set equal to $1 - R$, when R is a random number R between 0 and 1, or alternatively $\exp \left[-\theta_0^2/\sigma^2 \right]$ can be set equal to R . This leads to

$$\theta_0 = \frac{2}{\sqrt{N}} \left(\ln \frac{1}{R} \right)^{1/2}. \quad (48)$$

When the population inverted medium is divided into smaller volume elements, N is replaced by the number of atoms in each volume element, i.e.,

$$\theta_0^i = \frac{2}{\sqrt{N_i}} \left[\ln \left(\frac{1}{R} \right) \right]^{1/2} \quad (49a)$$

is the initial tipping angle for the i th volume element containing N_i atoms. N_i is the fractional density contained in the i th planar shell (i.e., ring over the density contained in a unit volume (i.e., $1 = \Delta z$).

$$N_i = N(\rho_i) = \frac{\exp \left[-(\rho_i/\rho_N)^m \right] \left\{ \pi(\rho_{i+1/2}^2 - \rho_{i-1/2}^2) \right\}}{\pi\rho_{i/2}^2 + \sum_{j=2}^{N\rho-1} \exp \left[-(\rho_j/\rho_N)^m \right] \left\{ \pi(\rho_{j+1/2}^2 - \rho_{j-1/2}^2) \right\} + \left\{ \exp \left[-(\rho/\rho_N)^m \right] \pi(\rho_N^2 - \rho_{N\rho-1/2}^2) \right\}} \quad (49b)$$

With m the index of the exponential density distribution (for a gaussian profile $m = 2$; for a super-gaussian, $m = 4$; and for a hyper-gaussian $m = 6$) and $N\rho$ the number of radial shell. If we study large Fresnel numbers the geometry changes from cylinder to Cartesian parallelepiped. The localized area of the computational cell becomes $4(x_{i+1/2} y_{i+1/2} - x_{i-1/2} y_{i-1/2})$ (51). The smaller the volume element the larger the initial tipping angle and the fluctuations for that element, but also the smaller their effect.

The random numbers R used in Eq. (48) and the one used in defining ϕ between 0 and 2π are uniform; they are obtained from a table of random numbers. The starting address in the table is changed at the beginning of each run to simulate the variation from shot-to-shot.

The simulation parameters (except as noted) were essentially those of the Cs single-pulse experiment,²³ namely, $\lambda = 2.931 \mu\text{m}$, $L = 2 \text{ cm}$, $T_1 = 70 \text{ ns}$, $T_2 = 80 \text{ ns}$, $\tau_R = 8\pi\tau_0/3n_0\lambda^2 L$ (52), $\tau_0 = 551 \text{ ns}$, $n_0 = 1.8 \times 10^{11} \text{ cm}^{-3}$, and $F = 1$. The initial gain profile is Gaussian, i.e., $n(r) = n_0 \exp[-(r/r_0)^2 \ln 2]$ (53) so the spatial width is narrower for smaller F , but the peak gain remains the same.

III. QUANTUM FLUCTUATION SIMULATION RESULTS

Uniform plane-wave Maxwell-Bloch solutions have been performed by Haake et al.¹⁷ for hundreds of such statistical initial conditions. These yield about 10% for the standard deviation $\sigma[\tau_D]$ in the delay time in good agreement with the expression $2.3/nM$ derived by Polder, Schuurman and Vreken.^{18b} Vreken and Van der Weduwe⁴¹ have measured $10 \pm 2\%$ for Fresnel number $F = 0.8$, $6 \pm 2\%$ for $F = 4$, and 4% for $F = 18$. Note that the plane-wave's theoretical value of $\sigma[\tau_D]$ is in good agreement with the $F = 0.8$ experimental value. We find that when both quantum initiation and transverse effects are included $\sigma[\tau_D] = 13.5 \pm 3.6\%$ for $F = 1$ in satisfactory agreement with the experiment, i.e. the jittering of the calculated delays fall within the experimental uncertainty form shot-to-shot. These fluctuations reduce the tail of the output obtained with transverse effects alone, thus improving the agreement with the Cs data. It curtails the amount of on-axis ringing even for a single shot.^{30,31}

A. SF Pulse Shapes

Figure 11 is a summation of fourteen output pulses in the plane-wave case with quantum fluctuations. The ringing is still very pronounced so quantum fluctuations alone do not remove it as was found by Haake et al.¹⁷ Figure 12(b) illustrates the fact that for $F = 1$ transverse effects alone do largely remove ringing.^{23,24} Figures 12(c) through 12(f) show that transverse effects and quantum fluctuations together result in fluctuating output pulses with very little ringing that encompass the published Cs pulse shapes (one is shown in Fig. 12(a)). Figure 13 illustrates that on the average (17 runs) the tail of the pulse is lower with fluctuations than without.

Figure 14 displays isometric plots of the SF intensity and its associated fluency ($J_T = |E|^2 \frac{\partial \phi}{\partial p}$, where ϕ is the phase of the electric field as a function of p and r for elements of the statistical ensemble. One finds that the transverse energy current J_T occasionally flows inwardly causing hot spots in the output beam as was sometimes observed in the Cs experiments. The previous transverse calculations^{23,24} involving uniform tipping angle never displayed inward-transverse energy flow. Figure 14 also shows the radially integrated output SF intensity as a function of r for the four shots of the statistical ensemble.

B. Delay Time Fluctuations

Figure 15(a) is a histogram showing the fluctuations in delay time τ_D when quantum fluctuations are included in the plane-wave approximation. These 57 runs yield

$$\frac{\sigma(\tau_D)}{\bar{\tau}_D} = \frac{\sum_{i=1}^{NR} (\tau_D^i - \bar{\tau}_D)^2 / NR}{\bar{\tau}_D} \left\{ 1 \pm \frac{1}{\sqrt{NR-1}} \right\} = (9.9 \pm 1.3)\% \quad \text{with NR the number of runs} \quad (50)$$

compared with 12% from the formula $2/3\ln N$ derived by Polder et al.¹⁸ and from numerical simulations of a larger number of trajectories.¹⁷ Figures 5(b) and 5(c) are similar histograms for cylindrical symmetry transverse simulations for $F = 1$ and $F = \pi^2$, respectively;

$$\sigma(\tau_D, F=1)/\bar{\tau}_D = (13.0 \pm 3.6)\%$$

for 13 trajectories and $(7.2 \pm 1.8)\%$ for $F = \pi^2$ and 16 trajectories. Figure 16 summarizes the Fresnel number dependence over the range $F = 0.3$ to 1.5. The curve is drawn through the points to guide the eye. Because the same starting point was used in the same random number table for the five black-dot points, the Fresnel number dependence of $\sigma(\tau_D)/\bar{\tau}_D$ is probably determined much better than the error bars would suggest. The curve yields $12 \pm 4\%$ for $F = 0.8$ compared with $(10 \pm 2)\%$ reported by Vrehen and der Weduwe for Cs.^{19a} Drummond and Eberly have more extensive calculations of $\sigma(\tau_D)$ for $F = 1$ to 16.⁵¹

Figure 17 illustrates a difficulty encountered in calculating $\phi(\tau_D)$. Occasionally, the first "peak" is not the highest peak. If one uses the highest peak for determining τ_D for just one trajectory in a set of 10, the value of $\sigma(\tau_D)$ is dominated by that one trajectory. Consequently, in Fig. 6, τ_D is measured to the first peak even if it is only an inflection on the leading edge of the pulse as in Fig. 7(d). Trajectories as unusual as those of Fig. 7 occurred perhaps every 20 to 30 trajectories, and they can be interpreted as phase waves discussed by Hopf.^{19b}

C. Full Three-Dimensional Quantum Fluctuations--Cartesian Geometry

The cylindrical symmetry was removed to allow fluctuations in all three spatial dimensions. This permits treatment of the large Fresnel number case in which there may be competition between transverse modes not possessing cylindrical symmetry. This additional degree of freedom has little effect on pulse shapes integrated over transverse dimensions (Fig. 18), but it elucidates fluctuations in SF angular distributions (Fig. 19). For small Fresnel numbers the diffraction term strongly couples the various parts of the beam, so the beam behaves as a unit. On the other hand, the output for large Fresnel numbers is completely irregular and highly asymmetrical; see Fig. 19 for the energy isometric near the peak of the output pulse. This is due to the loose coupling between the various portions of the beam as well as the short-scale fluctuations. Nevertheless, Fig. 19(b) shows that the (transversely) integrated output signals remain smooth, as observed by the detector in the experiment. Fig. 20 compares seven different outputs showing quantum fluctuations in the full 3D Cartesian case.

For seven shots, figure 21 displays the field energy and the associated transverse fluxes J_x and J_y at the end of the cell. Some of the fluxes are negative (i.e., flowing inwardly) indicating the onset of hot points (self-lensing effects).

Figure 22 illustrates for $F = 0.7$, seven of the output elements of our statistical ensemble. Both the energy and the transverse energy flux are contrasted isometrically as a function of x and r or y and r . One can see that for some of the elements of the statistical ensemble, the phase curvature is such that the energy is flowing inwardly, leading to self-focusing hot-spots across the beam as observed experimentally. Whereas, for other elements the fluency is only flowing outwardly, thus diffracting as in the physical situation with transverse effects alone.

D. Inhomogeneous Broadening

Fluctuations in the medium initiation and inhomogeneous broadening in the plane-wave limit have been calculated by Haake, King, Schroeder, Haus, and Glauber.⁸ Their results show that simulations, including both inhomogeneous broadening (T_2^*) and fluctuations but ignoring transverse effects, do not explain the absence of ringing in the Cs data. Without fluctuations or transverse effects, Fig. 12 shows that $T_2^* \approx 32$ ns

as in the Cs data has little effect on the ringing. Elimination of ringing is shown in Fig. 23 using a T_2 almost as short as τ_{SF} . Fig. 24 shows that adding $T_2 = 32$ to the previous simulations including fluctuations and transverse effects changes the pulse shapes very little.

IV. Conclusions of Two Level Superfluorescence

The addition of quantum fluctuations in the initial conditions of SF calculations does not greatly alter the general shape of the total output pulse integrated over the transverse dimension. It does result in noticeable macroscopic pulse-shape fluctuations similar to those observed. It does reduce the tail, on the average, improving the agreement with the Cs data. It reduces the amount of on-axis ringing even for a single shot. The standard deviation in delay time is consistent with the measured value, but the uncertainties in both the simulations and experiments are large. The Cs data are encompassed by the changes in output pulse shapes calculated including both fluctuations and transverse effects as summarized in Ref. 30 to 32.

V. Pump Dynamics Effects in Three-level Superfluorescence

In this section we present a model and calculational results and analysis for the effects of coherent pump dynamics, quantum initiation, propagation, transverse and diffraction effects on superfluorescent (SF) emission from a collection of N optically-pumped three-level systems. The full, nonlinear, co-propagational aspects of the injected pump pulse, together with the SF which evolves, are explicitly treated in the calculation.

The model upon which the calculation is based is the semiclassical version^{36,37} of the fully quantum mechanical model used to derive the effects of quantum initiation in the linearized region of SF in a coherently-pumped three-level system³⁸ (i.e., during and subsequent to the pump pulse time frame). The semiclassical aspects amounts to representing the SF and pump fields by classical fields determined by Maxwell's equations, including the transverse contribution, and representing the Langevin force fluctuation terms responsible for spontaneous relaxation and quantum initiation by complex valued c -numbers.³⁹ The amplitudes and phases of the complex-valued fluctuation terms are determined by Gaussian and uniform statistics, respectively, which are derived from the fully quantum model.^{38,39}

The first model for the study of dynamical effects of coherent pumping on SF evolution was the three-level model proposed by Bowden and Sung.³⁶ The model is comprised of a collection of identical three-level atoms, each having the energy level scheme such that the $1 \leftrightarrow 3$ transition is induced by a coherent electromagnetic field pulse of frequency ω_0 and wave vector k_0 . The transition $3 \leftrightarrow 2$ evolves by spontaneous emission at a much lower frequency ω . It is assumed that the energy level spacing is such that $\epsilon_3 > \epsilon_2 \gg \epsilon_1$, and we also retain spontaneous relaxation in the pump transition $1 \leftrightarrow 3$ for generality. The energy levels ϵ_2 and ϵ_1 are not coupled radiatively due to parity considerations. The injected pump field is treated as a coherent state.³³

The Hamiltonian which describes the system and the corresponding equations of motion have been discussed in References 37 to 39, and the reader is referred to those equations.

The normally-ordered Heisenberg equations of motion for the SF fluorescence field obtained from the Hamiltonian for the system^{38,39} are formally integrated, and then separated into the contribution due to the self-field of the atom, the vacuum contribution and the contribution due to the presence of all the other atoms (i.e., the extended dipole contribution). The first mentioned separated field leads to natural atomic relaxation γ^{-1} for the $3 \leftrightarrow 2$ transition in the normally-ordered Heisenberg equations and the vacuum contribution leads to Langevin force terms $f(\tau)$ which satisfy the ensemble average over the vacuum fluctuations (i.e., which are delta correlated):

$$\langle f_{a,b}(\tau) f_{a,b}^*(\tau') \rangle = \frac{1}{N \tau_{RP,SF}} \delta(\tau - \tau') \quad (54)$$

$$\langle f_{a,b}^*(\tau) f_{a,b}(\tau') \rangle = 0 \quad (55)$$

where N is the total number of atoms and τ_{RP} , τ_{SF} are the characteristic pump and SF time (i.e., the time for which, on the average, one cooperative photon is emitted), and is given by

$$\tau_{RP,SF} = \frac{L}{c} \left[\frac{2\pi |\mu_{P,SF}|^2}{k} N \right]^{-1} \quad (56)$$

Here, N is the atomic density, L is the longitudinal length of the medium, and $\mu_{P,SF}$ is the atom-field coupling in the neighborhood of the resonance for the pump and the SF transition respectively. The Maxwell equations in retarded time coordinates are derived in a manner similar to that leading to Eq. (36) of Reference 16. The details of the derivations were presented elsewhere.

Both field operators variables E_a and E_b and the atomic operators variables P_a , P_b , Q , W_a and W_b are to be understood as functions of z and t , and the fluctuating force terms f_b and f_a which are responsible for quantum initiation can be shown to be functions of retarded time τ only.^{17,18}

The Langevin terms f_a corresponding to the $1 \leftrightarrow 3$ transition obey relations identical to those of f_b (54,55), but with τ_{RSF} replaced by τ_{RP} . The Langevin forces terms in the Heisenberg equations of motion³⁸ give rise to Gaussian random quantum initiation statistics in both allowed transitions.³⁹ The pumping field³⁹ envelope E_A is taken as a rightward propagating pulse which is injected into the medium with specified initial and boundary conditions and in general is described by a classical Maxwell equation.

Classical Equations of Motion and Computational Method

The calculation of SF pulse evolution in the nonlinear regime is necessarily a calculational problem if propagation is explicitly included. We use an algorithm presented elsewhere⁴⁴ and the model defined by the equations of motion^{38,39} to analyze the effects of coherent pump dynamics, propagation, transverse and diffraction effects on SF emission. To facilitate numerical calculation, the equations of motion are taken in their factorized, semiclassical form³⁷ with the field operator replaced by its classical representation which is described by Maxwell's equation. The pump field and fluorescence field operator are determined dynamically and specially in retarded time, by initial and boundary conditions and the equations (The variables transformations and normalization are identical to those for the two-level SF study)

$$\begin{aligned} -\frac{1}{F_{gp}} \nabla_T^2 E_a + \partial_{\zeta P} E_a &= d P_a \\ -\frac{1}{F_{gsf}} \nabla_T^2 E_b + \partial_{\zeta S} E_b &= d P_b \end{aligned} \quad (57)$$

In the above equations, cylindrical symmetry was assumed with

$$\zeta_{p,s} = z \alpha_{RP,RSF}; \quad \alpha_{RP,PSF} = \frac{\{w_0 \mu^2_{SF}\} N}{n \hbar c} \tau_{RP,RSF}; \quad g_{P,SF}^\dagger = \frac{\alpha_{RP,PSF} R_2}{\tau_{RP,RSF}} \quad (59)$$

Equivalently, one solves numerically

$$\begin{aligned} -i F_{gp}^{-1} \nabla_T^2 E_a + \partial_{\zeta P} E_a &= d P_a \\ -i \left(\frac{\alpha_{RSF}}{\alpha_{RP}} \right) F_{gsf}^{-1} \nabla_T^2 E_b + \partial_{\zeta P} E_b &= d \left(\frac{\alpha_{RSF}}{\alpha_{RP}} \right) P_b \end{aligned} \quad (60)$$

The c-number Bloch equation for the 3 Level Superfluorescence reads as follows:

$$\begin{aligned} \frac{\partial P_a}{\partial \tau} + \beta_a P_a &= E_a W_a - \frac{1}{2} E_b Q - f_b Q + f_a W_a & \beta_a &= \frac{1}{\tau_2} + i \Delta \omega_a \\ \frac{\partial P_b}{\partial \tau} + \beta_b P_b &= E_b W_b - \frac{1}{2} E_a Q^* - f_a Q^* + f_b W_b & \beta_b &= \frac{1}{\tau_2} + i \Delta \omega_b \\ \frac{\partial Q}{\partial \tau} + \beta_c Q &= \frac{1}{2} (E_a P_b^* + E_b P_a^*) + f_a P_a^* + f_b P_b^* & \beta_c &= \frac{1}{\tau_2} + i \Delta \omega_c \\ \frac{\partial W_a}{\partial \tau} + \gamma_a (W_a - W_a^0) &= -\frac{1}{2} (E_a^* P_a + E_a P_a^*) - \frac{1}{4} (E_b^* P_b + E_b P_b^*) - 2(f_a^* P_a + f_a P_a^*) - (f_b^* P_b + f_b P_b^*) & \gamma_a &= \frac{1}{\tau_1}, \quad \gamma_b = \frac{1}{\tau_1} \\ \frac{\partial W_b}{\partial \tau} + \gamma_b (W_b - W_b^0) &= -\frac{1}{2} (E_b^* P_b + E_b P_b^*) - \frac{1}{4} (E_a^* P_a + E_a P_a^*) - (f_a^* P_a + f_a P_a^*) - 2(f_b^* P_b + f_b P_b^*) & & \end{aligned} \quad (61)$$

† This definition is more commonly used to normalize z : $\eta_{P,SF} = (\epsilon_{P,SF} F_{EP,ES}) \alpha_{RP,RSF}^{-1}$ (see ref 37).

where $f_{a,b} = |f_{a,b}| \exp(i\phi_{a,b})$ (62), $0 \leq \phi_{a,b} \leq 2\pi$ (63)

$$|f_a| = f_p \quad (64), \quad P(f_p^2) = \pi^{-1} \sigma_p^{-1} \exp \left[-\left(\frac{f_p}{\sigma_p}\right)^2 \right] \quad (65)$$

$$|f_b| = h_{SF} \quad (66), \quad P(h_{SF}^2) = \pi^{-1} \sigma_{SF}^{-1} \exp \left[-\left(\frac{h_{SF}}{\sigma_{SF}}\right)^2 \right] \quad (67)$$

$$\sigma_p^2 = \frac{\tau_n^2}{(\tau_{RP} L/C) N_i} = \frac{\tau_n^2}{\tau_{RP} \tau_E N_i} = \frac{\tau_n^2}{N_i \tau_c} \quad (68)$$

$\tau_c^2 = \tau_{RP} \tau_E$ with τ_E escape time and τ_c the cooperation time.

$$\sigma_{SF}^2 = \frac{\tau_n^2}{(\tau_{RSF} L/C) N_i} \quad (69)$$

$$\tau_{RP} = \frac{L}{c} \left[\frac{2\pi |\mu_p|^2}{h} N_i \right]^{-1} \quad \mu_p = \mu_a \quad (70)$$

$$\tau_{RSF} = \frac{L}{c} \left[\frac{2\pi |\mu_{SF}|^2}{h} N_i \right]^{-1} \quad \mu_{SF} = \mu_b \quad (71)$$

For deterministic calculations the langevin forces are taken either as constant or as zero, such that the initial conditions are chosen to establish a small, but nonzero transverse polarization for the $3 \leftrightarrow 2$ transition with almost the entire population in the ground state. This requires the specification of two small parameters, $\psi \sim 10^{-4}$, for the ground state initial population deficit, and $\delta \sim 10^{-4}$ for the tipping angle for the initial transverse polarization for the $3 \leftrightarrow 2$ transition. The derivation for the initial values for the various matrix elements is presented elsewhere,³⁸ and the results are as follows:

$$\begin{aligned} W_A &= 2\psi - 1 \\ W_B &= \psi \\ \text{Re } P_B &= 0 \\ \text{Im } P_B &= \psi\delta \\ \text{Re } P_A &= m \sin \phi_p \\ \text{Im } P_A &= m \cos \phi_p \\ \text{Re } Q &= -2 \text{Im } P_A \\ \text{Im } Q &= 2 \text{Re } P_A \end{aligned} \quad (72)$$

where $m = \cos^{-1}(2\psi - 1)$ and the phase ϕ_p is arbitrary, and we have chosen the phase ϕ_s to be zero.

The Langevin force fluctuation terms f and f_0 , responsible for quantum initiation and relaxation, are taken as complex valued c-numbers,

where $f_{a,b} = |f_{a,b}| \exp(i\phi_{a,b})$ (73), $0 \leq \phi_{a,b} \leq 2\pi$ (74)

$$|f_a| = f_p \quad (75) \quad P(f_p^2) = \pi^{-1} \sigma_p^{-1} \exp \left[-\left(\frac{f_p}{\sigma_p}\right)^2 \right] \quad (76)$$

$$|f_b| = h_{SF} \quad (77) \quad P(h_{SF}^2) = \pi^{-1} \sigma_{SF}^{-1} \exp \left[-\left(\frac{h_{SF}}{\sigma_{SF}}\right)^2 \right] \quad (78)$$

$$\sigma_p^2 = \frac{\tau_n^2}{\tau_{RP}(L/C)N_i} \quad (79)$$

$$\sigma_{SF}^2 = \frac{\tau_n^2}{\tau_{RSF}(L/C)N_i} \quad (80)$$

The Langevin force contributions to the semiclassical equations of motion give rise to initiation of fluorescence in the $3 \leftrightarrow 2$ transition when the $3 \leftrightarrow 1$ transition is coupled by the pumping field E_A . Normally, one can ignore fluorescence in the $3 \leftrightarrow 1$ transition, i.e., ignore contributions from f_a .

Thus, by utilizing the relations (73-80), a complete ensemble simulation can be constructed, and in this way the manifestations of amplified quantum initiation can be computationally analyzed over the full range of dynamical SF evolution. This amounts to generating the calculational results, using the semiclassical representation of the Heisenberg equations of motion³⁷ for specified initial and boundary conditions, for each of the values selected for $|f_a|$, $|f_b|$, ϕ_a and ϕ_b according to the statistical distributions (73-80). In the computation N in (59) is taken as N_i for each volume element or cell in each computational state (it is noted that $\tau_R L/c = \tau_c$ (81) which is invariant with volume). One then must take the ensemble averages and associated variances. For the results presented here, we have ignored fluorescence in the pump transition. The material parameters chosen for these calculations are arbitrary, but correspond roughly to those for optically-pumped metal vapors.

The initial and boundary conditions are such that all the atomic population is in the ground state ϵ_1 at $\tau = 0$. The pumping pulse which pumps the $1 \leftrightarrow 3$ transition is injected at $z = 0$ and is rightward propagating, and its initial characteristics are specified at $z = 0$. The SF pulse subsequently evolves in z , ρ , and τ due to the initiation of fluorescence instigated by $|f|$ and ϕ as indicated in the equations of motion³ in their semiclassical form discussed above.¹ The pump pulse, whose initial characteristics are specified at injection and the SF pulse co-propagate and interact via the nonlinear medium.

III. Deterministic effects of Pump Dynamics in the Nonlinear Regions of SF

More specifically, we computed the effects on SF pulse evolution for various initial conditions for the injected (pump) pulse. The results presented here demonstrate many facets of the control and shaping of the SF signal by control of the input signal initial characteristics. The material parameters chosen for these calculations are arbitrary, but correspond roughly to those for optically pumped metal vapors in the regime $\tau_p > \tau_R$.

Thus although the simulation inherently yields numerically accurate results for particular experimental design, the results reported here must be taken as qualitative. Our main purpose here is to demonstrate and analyze specific correlations between the initial and boundary conditions associated with the injected pump pulse and characteristics of the SF pulse which evolve. In many of the cases which follow, rules are established through the analysis which can be used to predict quantitative results for any particular experimental conditions. Our choice of particular initial and boundary conditions has been motivated in part by processes which may have been operative in experiments which have been reported^{3, 9} and in part by the feasibility of experimental selection or specification. In connection with the latter, we demonstrate the control of one light signal by another via a nonlinear medium, thus encoding nonlinear information transfer and pulse shaping of the SF from specific initial and boundary conditions associated with the pump injection signal.

Since the average values of τ_D and the peak SF intensity are important quantities for interpreting experimental results with theories of SF,^{1, 14, 18} the manner in which the pump-pulse coherence and initial on-axis area affects these quantities is seen to be of extreme importance in any analysis.

The simulation parameters (except so noted) are as follows: The injected pulses are initially gaussian in ρ and τ with widths (FWHM) $r_p = 0.24$ cm and $\tau_D = 4$ nsec respectively; the level spacings are such that $(\epsilon_3 - \epsilon_1)/(\epsilon_3 - \epsilon_2) = 126.6$. The effective gain for the pump is $\alpha_{RP} = 0.364$ ($g_p = 17$) cm^{-1} that for the SF transition $\alpha_{RSF} = 0.171$ ($g_{SF} = 291.7$) cm^{-1} . The gain-length Fresnel numbers for the two transitions $F_{gp} = 359.72$ ($p = 16800$) and $F_{gs} = 1.334$ ($s = 2278$). The relaxation and dephasing times are taken identical for all transitions and are given as $T = 80$ nsec and $T = 70$ nsec, respectively.

Figure 25a shows the effect upon the SF pulse of variation in the initial temporal width of the injected pulse τ_w becomes smaller, the SF delay time τ_D increases, whereas the peak SF intensity decreases, and the SF temporal width τ_s remains very closely fixed.

It is clear from these results that there exists an approximate linear relationship between the time delay τ_D is plotted versus the corresponding pump-pulse initial temporal width, from Fig. 25b. These results generate the following empirical formula for τ_D as a function of τ_p :

$$\tau_D = 0.375 \tau_R [\ln(4\pi/\psi)]^2 - 4\tau_R \gamma_1 (\gamma_R/4\gamma_1 - 1) \tau_p \quad (84)$$

where²⁰

$$\tau_R = \frac{2T_2}{g_s^2} \quad (\text{or equivalently, } \frac{\alpha_{RSF,RP}}{g_{SF,P}} = \frac{\tau_{RSF,RP}}{T_2})$$

is the characteristic superfluorescence time,^{1,14} and ψ is a parameter adjusted to give a best fit to the calculational results. For the case treated here, $\tau_R = 41$ psec, $T_2 = 70$ nsec, and $\gamma = 10^{-8}$, and the geometric Fresnel number $F = 1.47$.

The relation (84) is at least in qualitative agreement with the analytical prediction made in Ref. 36(b), Eq. (5.1), based upon mean-field theory. The first term in (84) was chosen to conform with the quantum-mechanical SF initiation result.¹⁷ The quantity ψ can be interpreted as the "effective tipping angle" for an equivalent π -initial impulse excitation, i.e., for $\tau_p \rightarrow 0$, which initiates subsequent superfluorescence. It is to be noted that the value for ψ is dependent upon our choice of δ (see the Appendix of Ref. 37); however, τ_D varies less than 25% for order-of-magnitude changes in δ for $|\delta| < 10^{-2}$. The choice of δ is simply an artificial way of instigating the semiclassical numerical calculation, and reasonable variations in its value do not strongly affect the results. The physical parameter is, then, ψ , which, interpreted on the basis of (84), is generated through the dynamics caused by the pumping process and represents quantum SF initiation. The full statistical treatment for three-level superfluorescence with pump dynamics included was presented in the fifth Coherent and Quantum Optics Conference.⁴⁰

These results emphasize the importance of the initiating pulse characteristics in SF pulse evolution, and the effect of SF pulse narrowing with approximate pulse shape invariance by increasing the initial temporal width of the injected pulse. It is emphasized that all other parameters, including the initial value for the injected pulse on-axis area, are identical among these sets of curves.

The initial radial width r_0 of the injected pulse was varied and the effect upon the sf pulse evolution is shown in Fig. 26. There is clearly indicated an optimum value for r_0 for which the SF peak intensity is a maximum and the SF temporal width τ_s is a minimum. If the relation (34) is used in conjunction with the values of the parameters given in Fig. 26 and its caption, it is seen that optimization occurs for a value for the conventional Fresnel number F_0 for the SF transition $F_s \approx 1$. Thus from (34) and $F_s = 1$, we have

$$F_{gs} = \alpha_{RSF} z_{\max}^2 \quad (84)$$

for the gain-length Fresnel number. Since $F_{gs} \sim 1/2$, the implication is that Eq. (84) gives the penetration depth z_{\max} at which the SF peak intensity reaches a maximum in terms of the ratio F_{gs}/α_{RSF} . Since this takes both transverse and diffraction explicitly into account as well as propagation, this is indeed a profound statement.

Further insight into the implication of (84) can be obtained by considering a one-spacial dimension analogy. If the linear field loss is taken to be entirely due to diffraction, then the one-dimensional linear loss κ corresponding to the two-dimensional case specified by F_{SF} is given by

$$\kappa_{SF} = \frac{\lambda_s}{2\pi\delta} \quad (85)$$

Then, from (36),

$$F_{gsF} = \frac{\alpha_{RSF}}{\kappa_{SF}} \quad (\text{or equivalently } S = \frac{g_{SF}}{\kappa_{SF}} \text{ as equ. (3.5) of ref. 37}) \quad (86)$$

is the effective gain α_{RSF} to loss κ_{SF} ratio. From the condition (84),

$$z_{\max} = (\kappa_{SF}^{-1}), \quad (87)$$

i.e., z_{\max} is the penetration depth at which the SF peak intensity is a maximum and corresponds to one effective diffraction length, as defined by (85). Carrying the one-dimensional analogy one step further, (86) used in (34) gives

$$F = (\kappa z)^{-1}. \quad (88)$$

From (86) and (87) we have exhibited the significance of the Fresnel numbers F_0 and F in terms of diffraction loss, i.e., F_0 can be thought of as gain to loss ratio, Eq. (86), whereas F can correspondingly be thought of as the reciprocal of the strength of the diffraction loss, Eq. (87).

The effect of changing the effective gain for the SF transition α_{RSF} and hence the relative oscillator strength between the SF transition and the pump transition is demonstrated in the results of Figs. 26-30. Each of these figures corresponds to a different on-axis initial area θ_p for the injection pulse. Consistent among the entire set of results is that increasing the effective gain α_{RSF} results in a nearly linear increase

in the SF peak intensity as well as decrease in the delay time τ_D . Also, the smaller area initiating pulse causes a narrower SF pulse to evolve and with apparently less ringing.

Figure 31 shows the effect of variation of the density N of active atoms. The effective gains α_{RSF} and α_{RP} are changed proportionally, corresponding to a density variation N . The ratio of the SF intensities is $I_c/I_b = 1.76$ and $I_b/I_a = 2.06$; these ratios are larger than the corresponding density ratios squared, $(N_c/N_b)^2 = 1.40$ and $(N_b/N_a)^2 = 1.49$. This difference from the predictions from previous theories of SF^{1,3} may be due to self-focusing, especially since the values of the effective gains used in this case are quite high. However, the ratio of the temporal widths τ_s , FWHM, are within 15% of the corresponding inverse ratios of the densities; the same is true for the delay time τ_D of the SF intensity peak with respect to the pump intensity peak. These results compare qualitatively reasonably well with the mean-field predictions for SF in two-level systems initially prepared in a state of complete inversion.¹⁴

A comparison of the effects upon the injection pulse of variation in oscillator strengths between the SF and pump transition (variation of α_{RSF}) as contrasted to effects upon the pump pulse of a density variation (variation of both α_{RP} and α_{RSF} proportionally) is given in Figs. 32 and 33, respectively. It is seen that the respective effects in the pump-pulse reshaping are quite distinct. The variation in oscillator strengths, Fig. 32, essentially causes "hole burning" in the following edge of the pump pulse, whereas the variation in density, Fig. 33, affects the whole pump pulse. This contrast has an analogy as an inhomogeneous, Fig. 32, as opposed to a homogeneous, Fig. 33, effect on the pump pulse. This effect might be used for the purposes of pulse shaping under suitable conditions.

Shown in Fig. 34 is the transverse integrated SF pulse intensity versus retarded time τ (curve 2) together with the transverse integrated pump-pulse intensity versus τ (curve 1) for a gain and propagation depth chosen so that the pulses temporally overlap. Under these conditions the two pulses strongly interact with each other via the nonlinear medium, and the two-photon processes (resonant, coherent Raman-RCR), which transfer populations directly between levels ϵ_2 and ϵ_1 , make strong contributions to the mutual pulse development.³⁶ The importance of the RCR in SF dynamical evolution in an optically pumped three-level system was pointed out for the first time in Ref. 36. Indeed, the SF pulse evolution demonstrated here has greater nonlinearity than SF in a two-level system which has been prepared initially by an impulse excitation. What is remarkable is that this is an example where the SF pulse temporal width τ_s is much less than the pump width τ_p even though the two pulses temporally overlap, i.e., the SF process gets started late and terminates early with respect to the pump time duration. Pulses of this type have been observed⁵ in Co_2 -pumped CH_3F .

IV. Conclusions of Deterministic Three Level SF

The effects presented here clearly demonstrate the coherence and deterministic effects on SF pulse evolution of injection pump-pulse characteristics and conditions in the regime $\tau_p < \tau_R$. It is suggested that effects of the type discussed here may have in fact been operative in SF experiments and their results which were published earlier.³⁻⁹ The pump pulse was taken as purely coherent in these calculations. To determine whether or not effects of the nature reported here are indeed operative in a given experiment, it is crucial to determine the degree of coherence of the pumping process as well as its temporal duration.³⁶

Furthermore, and perhaps of greater importance, we have demonstrated the control and shaping of the SF pulse which evolves by specification of particular initial characteristics and conditions for the pumping pulse which is injected into the nonlinear medium to initiate SF emission. These manifestations and others of the same class we call the control of light by light via a nonlinear medium. This phenomenon constitutes a method for nonlinear information encoding, or information transfer, from the injection pulse initial characteristics to corresponding SF pulse characteristics which evolve due to propagation and interaction in the nonlinear medium.³⁷

Calculational Results and Delay-Time Statistics

Amplified quantum initiation statistics in the highly nonlinear regime of SF pulse evolution are presented in the figure for the separation in retarded time τ of the main peak of the SF pulse from that of the pump pulse. Here we have plotted the initial temporal width of the pumping pulse τ_p vs. ϵ , where (see Eq. 50)

$$\epsilon = \frac{\sigma}{\bar{\tau}_D} \pm \frac{\sigma}{\bar{\tau}_D \sqrt{NR-1}} \quad (89)$$

where $\bar{\tau}_D$ is the mean value of the (SF) pulse peak delay from the pump pulse peak, σ is the standard deviation and NR is the number of elements in the ensemble, which in this case, $NR = 10$.

Since the size of the ensemble is quite small the statistics presented here can at best give trends, so we regard these results as quite preliminary. The case here is referred to as the highly nonlinear regime, since the pump pulse and the SF pulse completely overlap for each member of the ensemble. Thus, the two pulses are strongly interacting in this regime via the nonlinear medium and two-photon processes which enhance the Q matrix elements are strongly operative. The highly nonlinear regime does not correspond to SF as studied previously, but is quite interesting in itself. As preliminary results, the calculation is far less expensive than that needed to analyze the nonlinear regime of well-separated pulses. This, of course, will soon follow.⁵⁴

The main deduction from Figure 35 is that the quantum statistics of initiation are manifestly important only for the pump pulses corresponding to the shorter initial temporal duration τ_p . This supports our earlier hypothesis that amplified quantum initiation is important only for conditions such that $\tau_p/\tau_R \leq 1$.

For the condition that $\tau_p/\tau_R \gg 1$, the coherence of the pump itself overwhelms the fluctuations due to quantum initiation which would otherwise become amplified in the nonlinear regime.

An interesting effect is evident in our computations in that significant statistical variation of the pump pulse peak from turn-on (i.e., $\tau = 0$) was observed. Thus, the pump pulse statistics are also important, at least in the highly nonlinear regime, as well as statistics for the SF pulse. Of course, statistics of both pulses are mutually incorporated in the figure.

The Fresnel variation of the standard deviation normalized to either the average delay difference or the average of the arithmetic mean of the two delays $\langle \tau \rangle = \frac{1}{2}(\tau_p + \tau_{SF}) = \frac{1}{2}[\langle \tau_p \rangle + \langle \tau_{SF} \rangle]$ (90) for three different regions of propagations: Fig. 37(a) the SF buildup; Fig. 37(b) the SF completely evolved partially overlapping the pump pulse and Fig. 37(c) the highly nonlinear regime where the two pulses completely overlap (additional nonlinear two-photon processes are also taking place and compete with the SF process). For simplicity the error bars are shown in a table instead of being introduced in the graphs.

F_{gsf}	$(1/\tau_p)$	$\sigma(\Delta\tau_D)/\langle \Delta\tau_D \rangle$	$\sigma(\Delta\tau_D)/\{1/2(\tau_{DP} + \tau_{DSF})\}$
1.62	2.35	(40.44 ± 13.48)	(3.09 ± 1.03)
1.07	2.9	(29.35 ± 9.78)	(3.25 ± 1.08)
0.72	3.257	(35.81 ± 11.94)	(3.94 ± 1.31)
0.59	3.9	(28.89 ± 9.63)	(3.76 ± 1.25)
0.495	4.237	(28.69 ± 9.50)	(3.92 ± 1.31)
0.27	5.5771	(31.04 ± 10.25)	(6.41 ± 2.14)
0.23	6.25191	(34.34 ± 11.44)	(8.73 ± 2.91)
0.12	8.7	(40.81 ± 13.60)	(13.73 ± 4.58)

(# A 1) SF with partially developed nonlinear region.

1.94	2.35	142.63 ± 47.54	1.881 ± 0.604
1.28	2.9	122.57 ± 40.86	2.07 ± 0.690
0.683	3.527	65.57 ± 21.86	2.31 ± 0.77
0.704	3.9	59.82 ± 19.94	2.37 ± 0.79
0.593	4.237	65.23 ± 21.74	3.04 ± 1.01
0.322	5.5771	58.87 ± 12.95	3.55 ± 1.183
0.275	6.25191	36.87 ± 12.29	4.28 ± 1.429
0.142	8.7	49.13 ± 16.38	10.67 ± 3.56
0.086	11.1542	5.690 ± 1.896	1.37 ± 0.46

#B nonlinear region full SF evolution (partial overlapping between SF and pump pulses)

2.26	2.35	40.89 ± 13.63	1.161 ± 0.387
1.49	2.9	73.72 ± 24.57	1.463 ± 0.488
1.005	3.527	73.27 ± 24.57	1.463 ± 0.488
0.82	3.9	91.967 ± 30.65	1.692 ± 0.564
0.69	4.237	213.57 ± 80.72	1.512 ± 0.571
0.375	5.5771	83.47 ± 27.82	2.266 ± 0.755
0.320	6.25191	43.90 ± 14.63	2.147 ± 0.716
0.165	8.7	27.742 ± 77.80	3.202 ± 1.059
0.100	11.1542	11.24 ± 3.746	2.552 ± 0.852

C highly nonlinear region (strong-overlapping)

The first dependence (which is plotted $\langle \text{dif del} \rangle = \langle |\tau_p - \tau_{SF}| \rangle$ (91) see Fig. 36) varies totally from one zone to the other zone illustrating the occurrence of different nonlinear processes concomitantly; whereas the second dependence (see Fig. 37) which is an exponential decay does not vary in shape.

Further work is continuing, both for the nonlinear regime as well as the highly nonlinear regime and will appear.⁵⁴

References

Preliminary presentation were made by F.P. Mattar, Abstract Digest of the European Conference on Atomic Physics, Heidelberg, 1981, edited by J. Kowalski, G. Zupulitz, and H.G. Weber (European Physical Society, Geneva, 1981), Vol. VA; Laser Spectroscopy V, edited by B. Stoicheff et al. (Springer, Heidelberg, 1982); U.S. Army Research Office Workshop on Coupled Nonlinear Oscillators invited paper, Los Alamos, 1981 (unpublished); Proceedings of the Los Alamos Conference on Optics, Los Alamos, 1981 (Society of Photo-optic Instrumentation Engineers, Bellingham, Washington, 1981), Vol. 288, pp. 364-371; E. A. Watson, H.M. Gibbs, F.P. Mattar, M. Cormier, S. L. McCall, and M.S. Feld, J. Opt. Soc. Am. **71**, 1589. AM. Phy. Soc. DEAP annual meeting, Dec. 1981, New York, NY (unpublished); International Conference on Laser (invited paper) Dec. 1981, New Orleans, LA (see Abstract Digest) (Paper unpublished).

1. (a) R.H. Dicke, Phys. Rev. **93**, 99 (1954) and in Proc. Third Int. Conf. on Quantum Electronics Paris (1963), ed. by P. Grivet and N. Bloembergen, Pub. by Columbia University Press, NY (1964); (b) S.L. McCall, Ph.D. Thesis in Physics, Univ. of California, Berkeley (1968); (c) D.C. Burnham and R.Y. Chiao, Phys. Rev. **188**, 667 (1969).
2. (a) E.L. Hahn, Phys. Rev. **80**, 580 (1950); (b) R. Friedberg and S.R. Hartman, Phys. Lett **A37**, 285 (1971) and Ibid **A38**, 227 (1972).
3. N. Skribanowitz, I.P. Herman, J.C. MacGillivray and M.S. Feld, Phys. Rev. Lett. **30**, 309 (1973). I.P. Herman, J.C. MacGillivray, N. Skribanowitz and M.S. Feld, in Laser Spectroscopy, R.G. Brewer and A. Mooradian, eds. (Plenum, NY, 1974).
4. M. Gross, C. Fabre, P. Pillet, S. Haroche: Phys. Rev. Lett **36**, 1035 (1976); A. Flusberg, T. Mossberg and S.R. Hartmann, Phys. Lett. **58A**, 373 (1976) and Phys. Rev. Lett. **38**, 59 (1977). Q.H.F. Vrehen, H.M.J. Hikspoors and H.M. Gibbs, Phys. Rev. Lett. **38**, 764 (1977); M. Gross, J.M. Raimond and S. Haroche, Phys. Rev. Lett. **40**, 1711 (1978); J. Okada, K. Ikeda and M. Matsuoka, Optics Comm. **27**, 321 (1978); and A. Crubellier, S. Liberman and P. Pillet, Phys. Rev. Lett. **41**, 1237 (1978).
5. A.T. Rosenberger, S.J. Petuchowski and T.A. DeTemple, in Cooperative Effects in Matter and Radiation, edited by C.M. Bowden, D.W. Howgate and H.R. Robl (Plenum Press, New York, 1977), p. 15. J.J. Ehrlich, C.M. Bowden, D.W. Howgate, S.H. Lehnigk, A.T. Rosenberg and T.A. DeTemple in Coherence and Quantum Optics IV, edited by L. Mandel and E. Wolf (Plenum, New York, 1978); and A.T. Rosenberg and T.A. DeTemple Phys. Rev. **A24**, 868 (1981).
6. H.M. Gibbs, Q.H.F. Vrehen and H.M.J. Hikspoors, Phys. Rev. Lett. **39**, 547 (1977).
7. H.M. Gibbs, Q.H.F. Vrehen, H.M.J. Hikspoors: In Laser Spectroscopy III, eds. by J.L. Hall, J.L. Carsten, Springer Series in Optical Science, Vol. 7 (Springer, Berlin, Heidelberg, and New York 1977) p. 213; Q.H.F. Vrehen, H.M.J. Hikspoors, and H.M. Gibbs, in Coherence and Quantum Optics IV (Plenum, NY, 1978). L. Mandel and E. Wolf, eds., p. 543, H.M. Gibbs, NATO Advanced Study Institute as 'Superfluorescence Experiments' in Coherence in Spectroscopy and Modern Physics ed. F.T. Arecchi, R. Bonifacio and M.D. Scully, Plenum Press, 1978, p. 121.
8. a) Q.H.F. Vrehen and M.F.H. Schuurmans, Phys. Rev. Lett. **42**, 224 (1979); b) Q.H.F. Vrehen in Laser Spectroscopy IV, edited by H. Walther and K.W. Rothe (Springer-Verlag, Berlin-Heidelberg-New York, 1979); p. 471.
9. M. Gross, P. Goy, C. Fabre, S. Haroche and J.M. Raimond, Phys. Rev. Lett. **43**, 343 (1979); C. Brehignac, Ph. Cahuzac: J. Phys. Paris Lett. **40**, L-123 (1979) Ph. Cahuzac, H. Sontag, P.E. Toschek, Opt. Commun. **31**, 37 (1979); A. Crubellier, S. Liberman, D. Mayors, P. Pillet and M.G. Schweighjer, Opt. Lett. **7**, 16 (1982).
10. F.T. Arecchi, E. Courtens, Phys. Rev. **A2**, 1730 (1970); N.E. Rehler, J.H. Eberly, Phys. Rev. **A3**, 1735 (1971); J.H. Eberly, Am. J. Phys. **40**, 1374 (1972).
11. S.L. McCall, Dissertation, University of California, 1968.
12. D.C. Burnham and R.Y. Chiao, Phys. Rev. **188**, 667 (1969).
13. J.C. MacGillivray, M.S. Feld: Phys. Rev. **A14**, 1169 (1976).
14. R. Bonifacio, P. Schwendimann and F. Haake, Phys. Rev. **A4**, 302 (1971); and **4**, 858 (1971); R. Bonifacio and L.A. Lugiato, Ibid **11**, 1507 (1975) and **12**, 587 (1975); see also Ref. 5.
15. (a) J.C. MacGillivray and M.S. Feld in Cooperative Effects in Matter and Radiation (Ref. 5) p. 1 and in Applications of Lasers to Atomic, Molecular and Nuclear Physics, edited by Institute of Spectroscopy, U.S.S.R. Academy of Science ("Nauka", Moscow, 1979); 117-130; (b) In 1977, J.C. MacGillivray and M.S. Feld showed that a gaussian average of plane wave solutions removes most of the ringing but results in a much longer tail than observed (private correspondence to H.M. Gibbs, Spring 1977; (c) J.C. MacGillivray, D.Sc. Thesis 1980, Physics Department, M.I.T.

16. N.E. Rehler and J.H. Eberly, *Phys. Rev. A* **3**, 1735 (1971).
17. R. Glauber and F. Haake, *Phys. Lett.* **68A**, 29 (1978); F. Haake, H. King, G. Schroder, J. Haus, R. Glauber and F. Hopf, *Phys. Rev. Lett.* **42**, 1740 (1979); F. Haake, J. Haus, H. King, G. Schroder, R. Glauber, *Phys. Rev. Lett.* **45**, 558 (1980); and F. Haake, in *Laser Spectroscopy IV*, (Ref. 17), p. 451.
18. M.F.H. Schuurmans, D. Polder and Q.H.F. Vrehen, *J. Opt. Soc. Am.* **68**, 699 (1978). D. Polder, M.F.H. Schuurmans and Q.H.F. Vrehen, *Phys. Rev. A* **19**, 1192 (1979).
19. a) Q.H.F. Vrehen and J.J. der Weduwe, *Phys. Rev. A* **24**, 2857 (1981); b) F.A. Hopf, *Phys. Rev. A* **20**, 2054 (1979).
20. ¹⁰R. Bonifacio, J.D. Farina and L.M. Narducci, *Opt. Commun.* **31** 377 (1979). This paper uses the mean-field theory (MFT), which neglects propagation and predicts no ringing for the low-density Cs regime. Therefore the mode-competition transverse effects that they treat apply only to high-density MFT oscillatory SF and are not directly relevant to the Cs data.
21. M.S. Feld and J.C. MacGillivray in *Advances in Coherent Nonlinear Optics*, M.S. Feld and V.S. Letokhov, eds., (Springer-Verlag, Berlin, 1980).
22. R.K. Bullough, R. Saunders, and C. Feuillade, in *Coherence and Quantum Optics IV* (1980).
23. F.P. Mattar and H.M. Gibbs, *Proceedings of the International Conference on Lasers*, December 15-19, 1980, p. 777.
24. F.P. Mattar, H.M. Gibbs, S.L. McCall and M.S. Feld, *Phys. Rev. Lett.* **46**, 1121 (1981).
25. F.P. Mattar and M.C. Newstein, *IEEE QE-13*, 507 (1977) and in *Cooperative Effects in Matter and Radiation* (Ref. 5).
26. S.L. McCall and E.L. Hahn, *Phys. Rev.* **183**, 457 (1969).
27. H.M. Gibbs, B. Bölgner, F.P. Mattar, M.C. Newstein, G. Forster and P.E. Toschek, *Phys. Rev. Lett.* **37**, 1743 (1976).
28. J.J. Bannister, H.J. Baker, T.A. King and W.G. McNaught, *Phys. Rev. Lett.* **44** 1062 (1980).
29. Panel discussion in *Cooperative Effects in Matter and Radiation*, ed. by C.M. Bowden, D.W. Howgate and H.R. Robl (Plenum Press, NY 1977).
30. (a) F.P. Mattar, Abstract Digest of European Conference of Atomic Physics, Heidelberg F.R. Germany (April 1981) ed. J. Kowolski, G. Zuputlitz and H.G. Weber pub. European Physical Soc., Geneva 1981; (b) F.P. Mattar, Los Alamos conference on Optics (April 1981) Proceedings published SPIE vol. 288 p. 353.
31. F.P. Mattar, M. Cormier, H.M. Gibbs, E. Watson, S.L. McCall and M.S. Feld (post deadline paper) *Fifth International Conference on Laser Spectroscopy*, Jasper, Alberta; Canada, ARO Workshop on Nonlinear Oscillators, Los Alamos, Proceeding to be published in *Physics D*, North Holland.
32. E.A. Watson, H.M. Gibbs, F.P. Mattar, M. Cormier, S.L. McCall and M.S. Feld, *J. Opt. Soc. Am.* **71**, 1589 (1981); and E.A. Watson, H.M. Gibbs, F.P. Mattar, M. Cormier, Y. Claude and M.S. Feld *Phys. Rev. A* **27**, 1427 (1983).
33. Reviews of SF: M.S. Feld and J.C. MacGillivray in *Coherent Nonlinear Optics* ed. by M.S. Feld and V.S. Setokhov (Springer, Berlin 1980) p. 7; Q.H.F. Vrehen and H.M. Gibbs in *Dissipative Systems in Quantum Optics*, ed by R. Bonifacio (Springer, Berlin, 1981) p. 11; M.F.H. Schuurmans, Q.H.F. Vrehen, D. Polder and H.M. Gibbs in *Advances in Atomic and molecular Physics* ed. by D.R. Bates and B. Bederson (Academic Press, NY 1981) p. 168; M. Grass and S. Haroche, *Phys. Repts. Dec.* (1982).
34. C.M. Bowden and F.P. Mattar, Los Alamos Conference on Optics (April 1981) Proceeding published by SPIE vol. 288, p. 364 *International Conference on Excited States and Multi-Resonant Nonlinear Optical Processes*, Aussois, France (March 1981); F.P. Mattar, C.M. Bowden, Y. Claude and M. Cormier, *Opt. Soc. Am.* **71**, 1589 (1981).
35. R. Bonifacio, F.A. Hopf, P. Meystre and M.O. Scully, *Phys. Rev. A* **12**, 2568 (1975).
36. C.M. Bowden and C.C. Sung, *Phys. Rev. A* **18**, 1558 (1978) and *Phys. Rev. A* **20**, 2033 (1979).
37. F.P. Mattar and C.M. Bowden, *Topics in Current Physics* ed. by C.D. Cantrell (Springer-Verlag 1983); and *Phys. Rev. A* **27**, 345 (1983).

38. C.M. Bowden and C.C. Sung, Phys. Rev. Lett. 50, 156 (1983); and Optics Commu. 45, 273 (1983).
39. C.M. Bowden in Proceedings of the Third New Zealand Symposium on Laser Physics ed. by D.F. Walls and J.D. Harvey, Lecture Notes in Physics series Vol. 182, pp. 95-212 (Springer-Verlag 1983).
40. F.P. Mattar, C.M. Bowden and C.C. Sung (to be published in Proceedings on Rochester Fifth Conference on Quantum Optics (1983)).
41. See Ibid 17.
42. See Ibid 18.
43. See Ibid 25.
44. F.P. Mattar, Appl. Phys. 17, 53 (1978); and F.P. Mattar and M.C. Newstein, comp. Phys. Comm. 20, 139 (1980).
45. (a) see Ibid Ref. 8a; (b) N.W. Carlson, D.J. Jackson, A.L. Schawlow, M. Gross and S. Harache, Opt. Commun. 32, 350 (1980).
46. H.M. Gibbs and R.E. Slusher, Phys. Rev. A5, 1634 (1972); Ibid A6, 2326 (1972).
47. J.R.R. Leite, R.S. Sheffield, M. Duclay, R.D. Sharma and M.S. Feld, Phys. Rev. A14, 1151 (1976).
48. F.P. Mattar, in Optical Bistability, ed. by C.M. Bowden, M. Ciftan and H.R. Robl (Pienum Press, 1981) p. 503, in Proceedings Tenth Simulation and Modeling Conference, Pittsburgh 1978, ed. by W. Vogt and M. Mickle (Instrument Society of America, Pittsburg, 1979).
49. M. Cormier, Y. Claude, P. Cadieux and F.P. Mattar, Proceedings of the International Conference on Laser 1981, ed. by C-B. Collins (STS, MacLean, Virginia) pp. 1085-1115.
50. H.C. Van de Hulst, Light scattering by small particles, publ. John Wiley, NY (1957) pp. 179-183.
51. P.D. Drummond and J.H. Eberly, Rapid Commn. Phys. Rev. A25, 3446 (1982).
52. A.T. Rosenberger and T.A. DeTemple, Phys. Rev. A24, 868 (1981).
53. R.J. Glauber, Phys. Rev. 130, 2529 (1963); Ibid 131, 2766 (1963).
54. F.P. Mattar and C.M. Bowden Rochester Fifth Quantum and coherence optic conference June 1983, U. of . Rochester, NY)

38. C.M. Bowden and C.C. Sung, Phys. Rev. Lett. 50, 156 (1983); and Optics Commu. 45, 273 (1983).
39. C.M. Bowden in Proceedings of the Third New Zealand Symposium on Laser Physics ed. by D.F. Walls and J.D. Harvey, Lecture Notes in Physics series Vol. 182, pp. 95-212 (Springer-Verlag 1983).
40. F.P. Mattar, C.M. Bowden and C.C. Sung (to be published in Proceedings on Rochester Fifth Conference on Quantum Optics (1983)).
41. See Ibid 17.
42. See Ibid 18.
43. See Ibid 25.
44. F.P. Mattar, Appl. Phys. 17, 53 (1978); and F.P. Mattar and M.C. Newstein, comp. Phys. Comm. 20, 139 (1980).
45. (a) see Ibid Ref. 8a; (b) N.W. Carlson, D.J. Jackson, A.L. Schawlow, M. Gross and S. Harache, Opt. Commun. 32, 350 (1980).
46. H.M. Gibbs and R.E. Slusher, Phys. Rev. A5, 1634 (1972); Ibid A6, 2326 (1972).
47. J.R.R. Leite, R.S. Sheffield, M. Duclay, R.D. Sharma and M.S. Feld, Phys. Rev. A14, 1151 (1976).
48. F.P. Mattar, in Optical Bistability, ed. by C.M. Bowden, M. Ciftan and H.R. Robl (Plenum Press, 1981) p. 503, in Proceedings Tenth Simulation and Modeling Conference, Pittsburgh 1978, ed. by W. Vogt and M. Mickle (Instrument Society of America, Pittsburg, 1979).
49. M. Cormier, Y. Claude, P. Cadieux and F.P. Mattar, Proceedings of the International Conference on Laser 1981, ed. by C-B. Collins (STS, MacLean, Virginia) pp. 1085-1115.
50. H.C. Van de Hulst, Light scattering by small particles, publ. John Wiley, NY (1957) pp. 179-183.
51. P.D. Drummond and J.H. Eberly, Rapid Commn. Phys. Rev. A25, 3446 (1982).
52. A.T. Rosenberger and T.A. DeTemple, Phys. Rev. A24, 868 (1981).
53. R.J. Glauber, Phys. Rev. 130, 2529 (1963); Ibid 131, 2766 (1963).
54. F.P. Mattar and C.M. Bowden Rochester Fifth Quantum and coherence optic conference June 1983, U. of . Rochester, NY)

FIGURE CAPTIONS

Fig. 1. Model three-level atomic system and electric field tunings under consideration. For the results reported here, the injected pulse is tuned to the $1 \rightarrow 3$ transition, the SF emission radiates at the $3 \rightarrow 2$ transition.

Fig. 2. Sketch of the temporal and geometric emission characteristics of a superfluorescing pencil.

Fig. 3. Oscilloscope trace of superradiant pulse at $84 \mu\text{m}$ ($J = 3 \rightarrow 2$), pumped by the $R_1(2)$ laser line, and theoretical fit. The parameters are $I = 1 \text{ kW/cm}^2$, $p = 1.3 \text{ mTorr}$, and $\kappa L = 2.5$ for $l = 100 \text{ cm}$. The small peak on the scope trace at $\gamma = 0$ is the $3\text{-}\mu\text{m}$ pump pulse, highly attenuated.

Fig. 4. Normalized single-shot pulse shapes for several cesium densities n ; Fresnel number $F = 1$. Uncertainties in the values of n are estimated to be (+60, -40% (Gibbs et al., 1977a).

Fig. 4. Normalized output curve. This curve is the output response to a small rectangular input pulse of area θ_0 in a nondegenerate system where $T_2 = T_2^* = \infty$ and $\kappa L = 0$. The time scales as τ_R and the intensity scales as τ_R^2 . Note that the shape of the normalized output curve depends on θ_0 . I_p , τ_D , and τ_U can all be expressed in terms of τ_R and θ_0 (see Table 1).

Fig. 6a. Computer results showing the influence of parameters on output intensity. The same intensity scale is used throughout. (a) A theoretical fit with parameters $\tau_R = 6.1 \text{ nsec}$, $T_2^* = 330 \text{ nsec}$, $T_2 = 5.4 \mu\text{sec}$, $\kappa L = 2.5$, $J_{\text{lower}} = 2$. All parameters have the same values as in the curve except when stated otherwise. (b) No level degeneracy, $T_2 = T_2^* = \infty$, $\kappa L = 0$. (c) $T_2 = \infty$. (d) $T_2^* = \infty$. (e) $\kappa L = 0$. (f) $\kappa L = 5$. (g) No level degeneracy.

Fig. 6b. Foucault pendulum to illustrate the two tipping angle θ and ϕ .

Fig. 7. Normalized SF output power vs. τ/τ_R , $\epsilon_0^2 = 2 \times 10^{-4}$, $T_1 = T_2 = T_2^* = \infty$, $L/c\tau_R = 3.9$. (a) $F = \infty$. For the uniform profiles the excited state density $n_0(r) = n_0^0$ and $\theta_0(r) = \theta_0^0$; for Gaussian profiles $n_0(r) = n_0^0 \exp[-\ln 2(r/r_p)^2]$ and $\theta_0(r) = \theta_0^0 \exp[0.5 \ln 2(r/r_p)^2]$. [(i) n_0, θ_0 uniform; (ii) n_0 Gaussian, θ_0 uniform; (iii) n_0, θ_0 Gaussian; (iv) n_0 uniform, θ_0 Gaussian.] (b) Same as (a) but with diffraction ($F = \pi r_p^2 / \lambda_0 L$) included and uniform $n_0(r)$ and $\theta_0(r)$; $F = \infty$ (—), $F = 1.0$ (---), $F = 0.4$ (— — —), $F = 0.06$ (— — —).

Fig. 8. Influence of diffraction on SF pulse shapes. Parameters are the same as in Fig. 7a, with n_0 Gaussian and θ_0 uniform. (a) Emitted power: $F = \infty$, 11(—); $F = 1.0$ (---); $F = 0.4$ (— — —); $F = 0.1$ (— — —). (b) Isometric graph of intensity vs. $r/c\tau_R$ and τ/τ_R for $F=1$ case of Fig. 8a.

Fig. 9. Theoretical fits to Cs data of Ref. 22. The two dashed-line curves in (a) indicate typical experimental shot-to-shot variation. $F = 1$, $L = 2 \text{ cm}$, $T_1 = 70 \text{ ns}$, $T_2 = 80 \text{ ns}$, $\lambda = 2.931 \mu\text{m}$, $\tau_0 = 551 \text{ ns}$, θ_0 is uniform or Gaussian, and $n_0(r)$ is Gaussian. The following give $\theta_0^0(\text{fit})$, $n_0^0(\text{fit})$, $n_0^0(\text{exp})$, with θ_0^0 in units of $10^{-1}/\text{cm}^3$ and n_0^0 in units of $10^{10}/\text{cm}^3$: (a) 1.07, 31, 19; (b) 1.37, 18, 7.6; (c) 1.69, 11.9, 3.8; (d) 1.96, 8.85, 3.1. The broken-line curve in (b) is the one-dimensional fit of Ref. 7a, with $\theta_0^0 = 1.69$ and $n_0^0 = 12$.

Fig. 10. An isometric plot of the transverse energy current and the energy versus r and ρ for different distance of propagation ρ to illustrate the build up of SF and the propagational theory. Note that the transverse flux is always positive (i.e., not flowing inwardly).

Fig. 11. Intensity as a function of time for the average of 14 output pulses in the plane-wave case with quantum fluctuations such that $\epsilon_0^2 = 10^{-4}$ and $n_0^0 = 11.6 \times 10^{10} \text{ cm}^{-3}$.

Fig. 12. Intensity integrated over the transverse cylindrical coordinate as a function of time for single trajectories. (a) Cs data for $n_0 = 7.6 \times 10^{10} \text{ cm}^{-3}$. (b) Simulation with transverse effects, but no fluctuations: $n_0 = 18.2 \times 10^{10} \text{ cm}^{-3}$, $\theta_0 = 1.37 \times 10^{-4} \text{ rad}$, and Fresnel number $F = 1$. (c)-(f) Simulations with transverse effects and fluctuations for $n_0 = 18.2 \times 10^{10} \text{ cm}^{-3}$, $\langle \theta_0^2 \rangle^{1/2} = 1.37 \times 10^{-4} \text{ rad}$, and $F = 1$.

Fig. 13. Effect of fluctuations on the average pulse shape. Average over 17 trajectories with fluctuations (solid curve) has a slightly shorter delay and a smaller tail than the dashed curve with no fluctuations and a uniform θ_0 . Here, $n_0 = 18.2 \times 10^{10} \text{ cm}^{-3}$, $\langle \theta_0^2 \rangle^{1/2} = 1.37 \times 10^{-4} \text{ rad}$, and $F = 0.32$.

Fig. 14. Transverse energy current J_T and intensity are plotted isometrically for four shots in a statistical ensemble. In some of the shots the phase curvature is such that the associated energy flux flows inwardly; i.e., the transverse energy current is negative, which could lead to self-focusing. Inward energy flow never occurred for simulations using a homogeneous initial tipping angle (without quantum initiation) for any value of the Fresnel number. Here, $n_0 = 9.5 \times 10^{10} \text{ cm}^{-3}$, $F = 1.49$, and $10^4 \langle \theta_0^2 \rangle^{1/2} = 2.15, 1.63, 1.79$, and 1.16 rad , respectively, from top to bottom. Note the fluctuations in peak maximum and its associated delay in the output integrated over ρ (last column).

Fig. 15. Histogram showing the number of occurrences of a particular delay time. Points do not occur at integral values of τ_D because of the nonlinear time mesh. (a) Plane-wave case for $n_0 = 11.8 \times 10^{10} \text{ cm}^{-3}$ and $\langle \theta_0^2 \rangle^{1/2} = 1.69 \times 10^{-4} \text{ rad}$. (b) and (c) Cylindrical-symmetric transverse case for $n_0 = 18.2 \times 10^{10} \text{ cm}^{-3}$, and $\langle \theta_0^2 \rangle^{1/2} = 1.37 \times 10^{-4} \text{ rad}$. (b) $F = 1$. (c) $F = \pi^{-1}$. Each arrow denotes $\bar{\tau}_D$.

Fig. 16. Fresnel-number dependence of the uncertainty in delay time normalized to the average delay. Points are as follows: o, seven trajectories with $n_0 = 9.5 \times 10^{10} \text{ cm}^{-3}$ and $\langle \theta_0^2 \rangle^{1/2} = 1.89 \times 10^{-4} \text{ rad}$; □, $n_0 = 18 \times 10^{10} \text{ cm}^{-3}$ and $\langle \theta_0^2 \rangle^{1/2} = 1.37 \times 10^{-4} \text{ rad}$, for 13 trajectories for $F = 1$, and for 16 trajectories for $F = \pi^{-1}$; Δ, experimental value for 468 trajectories. A peak close to $F = 1$ can be argued as follows: For small F , strong diffractive coupling reduces fluctuations in the overall output. For large F , so many transverse modes compete that a good average is obtained on every shot. For ≈ 1 , competition of a few modes is maximal, resulting in large fluctuations. Meaningful calculations for large F require an increasing number of transverse steps, and so we avoid the large- F region.

Fig. 17. Phase waves. Fluctuations can result in the second peak exceeding the first. $n_0 = 9.5 \times 10^{10} \text{ cm}^{-3}$. (a) $F = 1.49$, $\langle \theta_0^2 \rangle^{1/2} = 1.21 \times 10^{-4} \text{ rad}$; (b) $F = 1.49$, $\langle \theta_0^2 \rangle^{1/2} = 1.24 \times 10^{-4} \text{ rad}$; (c) $F = 0.165$, $\langle \theta_0^2 \rangle^{1/2} = 2.22 \times 10^{-4} \text{ rad}$; (d) $F = 0.165$, $\langle \theta_0^2 \rangle^{1/2} = 1.79 \times 10^{-4} \text{ rad}$.

Fig. 18. Effect of Cartesian vs. cylindrical geometry for the sum over shots of the transversely integrated intensity for quantum-fluctuation calculations. Curve a holds for $F = 1.37$ for a cartesian geometry. $F = 0.11$ for both curves b and c; curve b involves cylindrical geometry while curve c is Cartesian (parallelepiped). Note that the delay with $F = 1.37$ (curve a) is shorter than the delay with $F = 0.11$ (curve c), just as it was for cylindrical geometry and no fluctuations (Ref. 24). Strong diffraction increases the delay because of energy lost transversely, but the tail is greatly reduced because the diffraction makes the sample superfluoresce as a unit. Curves a'-c' show the same curves normalized for pulse-shape comparisons. $n_0 = 18.2 \times 10^{10} \text{ cm}^{-3}$ and $\langle \theta_0^2 \rangle^{1/2}$ is about $1.56 \times 10^{-4} \text{ rad}$.

Fig. 19. Transverse fluctuations for a full three-spatial-dimension calculation with quantum initiation. (a) Field energy is displayed isometrically at a time near the peak of the pulse [see also Fig. 12(b)]. In (a), the transversely integrated energy is displayed. Actually (a) and (b) were identical at $L = 1.5 \text{ cm}$.

Fig. 20. Comparison of seven output energy profiles. $F = 1.37$, $n_0 = 18.2 \times 10^{10} \text{ cm}^{-3}$, and $\langle \theta_0 \rangle = 1.56 \times 10^{-4} \text{ rad}$.

Fig. 21(a). Isometric display of field energy and associated transverse fluxes J_x and J_y versus x and y at the end of the atomic cell; (b) the radially integrated energy (output power) is displayed as a function of t to illustrate the smoothness of the output detected and how no rings appear in this (x, y, z, t) calculation; (c) the same function energy and J_x are plotted versus t for a given y ; whereas they are plotted the energy and J_y are plotted versus t for a given x .

Fig. 22. Effects of inhomogeneous broadening in the uniform plane-wave case with homogeneous initial tipping angle. a: $T_2^* = \infty$. B and c: $T_2^* = 32 \text{ ns}$ in the formulas (for b) $g(\Delta\omega) = (T_2^*/\pi) \exp[-(T_2^*(\Delta\omega)/\pi)^2]$ and (for c) $g(\Delta\omega) = (T_2^*/\pi^{3/2}) \{1 + [T_2^*(\Delta\omega)/\pi]^2\}^{-1}$ corresponding closely to the value in the Cs experiment. Notice that including T_2^* damps the field energy amplitude and reduces the tail. Delay is also affected slightly. $n_0 = 9.5 \times 10^{10} \text{ cm}^{-3}$ and $\theta_0 = 1.89 \times 10^{-4} \text{ rad}$.

Fig. 23. Removal of ringing by inhomogeneous broadening. Parameters: Same as Fig. 22 with $T_2^* = 0.67 \text{ ns}$.

Fig. 24. Transverse effects and inhomogeneous broadening. Parameters: Same as Fig. 24 except that transverse effects ($F = 0.27$) are now considered. Including T_2^* in the Cs simulation is seen to be a small refinement which does suppress the tail slightly. (a) Relative integrated outputs. (b) Normalized integrated outputs with peaks shifted to coincide with each other to simplify pulse-shape comparisons.

Fig. 25a. Radially integrated normalized intensity profiles for the SF and injected pulses at $z = 5.3\text{-cm}$ penetration depth for five different values for the initial temporal width of the injected pulse. The initial on-axis area of the injected pulse is $\theta_p = \pi$, and the pump transition and SF effective gains are $\alpha_{RP} = 0.376(g_p = 17.5) \text{ cm}^{-1}$ and $\alpha_{RSF} = 0.376(g_{SF} = 641.7) \text{ cm}^{-1}$, respectively. The injected pulse initial temporal widths at half maximum are (A) $\tau_p = 4 \text{ nsec}$, (B) $\tau_p = 3.3 \text{ nsec}$, (C) $\tau_p = 2.9 \text{ nsec}$, (D) $\tau_p = 2.5 \text{ nsec}$, and (E) $\tau_p = 2.2 \text{ nsec}$.

Fig. 25b. Delay time τ_D of the SF peak intensity from the corresponding pump-pulse peak intensity vs. the pump-pulse initial full temporal width at half maximum intensity τ_p according to Fig. 25a.

Fig. 26. Radially integrated normalized intensity profiles for the SF and injected pulses at $z = 5.3\text{-cm}$ penetration depth for seven different values for the injected pulse initial radial width at half maximum r_0 . The initial on-axis area θ_p of the injection pulse is $\theta_p = 2\pi$; the SF effective gain $\alpha_{RSF} = 0.444(g_{SF} = 758.3) \text{ cm}^{-1}$, and the pump transition effective gain $\alpha_{RP} = 0.313(g_p = 14.6) \text{ cm}^{-1}$. The initial radial widths at half maximum for the injected pulses are (a) $r_0 = 0.57 \text{ cm}$, (b) $r_0 = 0.41 \text{ cm}$, (c) $r_0 = 0.24 \text{ cm}$, (d) $r_0 = 0.18 \text{ cm}$, (e) $r_0 = 0.15 \text{ cm}$, (f) $r_0 = 0.11 \text{ cm}$, and (g) $r_0 = 0.09 \text{ cm}$. The corresponding geometrical Fresnel numbers are (a) $F_{SF} = 8.46$, (b) $F_{SF} = 4.79$, (c) $F_{SF} = 1.47$, (d) $F_{SF} = 0.85$, (e) $F_{SF} = 0.57$, (f) $F_{SF} = 0.35$, and (g) $F_{SF} = 0.21$.

Fig. 27. Radially integrated normalized intensity profiles for the SF and injected pulses at $z = 5.3\text{-cm}$ penetration depth for three different values for the SF transition effective gain $\alpha_{RSF}(g_{SF})$. The on-axis initial area θ_p for the injected pulse is $\theta_p = \pi$. All other parameters are the same as those for Fig. 26(c). The SF transition effective gain is (a) $\alpha_{RSF} = 0.3075(g_{SF} = 525.0) \text{ cm}^{-1}$, (b) $\alpha_{RSF} = 0.444(g_{SF} = 758.3) \text{ cm}^{-1}$, and (c) $\alpha_{RSF} = 0.444(g_{SF} = 758.3) \text{ cm}^{-1}$.

Fig. 28. Radially integrated normalized intensity profiles for the SF and injected pulses at $z = 5.3$ -cm penetration depth for three different values for the SF transition effective gain $\alpha_{RSF}(g_s)$. The on-axis initial area θ_p for the injected pulse is $\theta_p = 2\pi$. All other parameters are the same as for Fig. 27.

Fig. 29. Radially integrated normalized intensity profiles for the SF and injected pulses at $z = 5.3$ -cm penetration depth for three different values for the SF transition effective gain $\alpha_{RSF}(g_s)$. The on-axis initial area θ_p for the injected pulse is $\theta_p = 3\pi$. All other parameters are the same as for Fig. 27.

Fig. 30. Radially integrated normalized intensity profiles for the SF and injected pulses at $z = 5.3$ -cm penetration depth for three different values for the SF transition effective gain $\alpha_{RSF}(g_s)$. The on-axis initial area θ_p for the injected pulse is $\theta_p = 4\pi$. All other parameters are the same as for Fig. 27.

Fig. 31. Radially integrated normalized intensity profiles for the SF and injected pulses at $z = 5.3$ -cm penetration depth for three different values for the density ρ of atoms. The on-axis initial area θ_p for the injected pulse is $\theta_p = 2\pi$. Except for the effective gains and Fresnel numbers, the values for all other parameters are the same as for Fig. 26(c). For each set of curves, the gain values are (b) $\alpha_{RSF} = 0.3075(g_{SF} = 525.0) \text{ cm}^{-1}$, $\alpha_{RP} = 0.564(g_p = 26.3) \text{ cm}^{-1}$; (c) $\alpha_{RSF} = 0.376(g_{SF} = 641.7) \text{ cm}^{-1}$, $\alpha_{RP} = 0.688(g_p = 32.1) \text{ cm}^{-1}$; and (d) $\alpha_{RSF} = 0.444(g_{SF} = 758.3) \text{ cm}^{-1}$, $\alpha_{RP} = 0.812(g_p = 37.9) \text{ cm}^{-1}$. The corresponding gain length Fresnel numbers are (b) $F_{gp} = 557.4$ ($F_p = 25992$), $F_{sSF} = 2.40$ ($F_s = 4100) \text{ cm}^{-1}$; (c) $F_{gp} = 679.94$ ($F_p = 31724$), $F_{sSF} = 2.94$ ($F_s = 5010) \text{ cm}^{-1}$; and (d) $F_{gp} = 802.5$ ($F_p = 37456$), $F_{sSF} = 3.47$ ($F_s = 5922) \text{ cm}^{-1}$.

Fig. 32. Radially integrated normalized intensity profiles for the SF and injected pulses at $z = 5.3$ -cm penetration depth for four different values for the SF transition effective gain $\alpha_{RSF}(g_{SF})$. The initial on-axis area for the injected pulse is $\theta_p = \pi$, and the effective gain for the pump transition $\alpha_{RP} = 0.375$ ($g_p = 17.5) \text{ cm}^{-1}$. Except for the effective gain $\alpha_{RSF}(g_{SF})$, all other parameters are the same as those for Fig. 26(c). The SF transition effective gain g_s for each set of curves is (a) $\alpha_{RSF} = 0.1708(g_{SF} = 291.7) \text{ cm}^{-1}$, (b) $\alpha_{RSF} = 0.239(g_{SF} = 408.3) \text{ cm}^{-1}$, (c) $\alpha_{RSF} = 0.3075(g_{SF} = 525.0) \text{ cm}^{-1}$, and (d) $\alpha_{RSF} = 0.376(g_{SF} = 641.7) \text{ cm}^{-1}$.

Fig. 33. Radially integrated normalized intensity profiles for the SF and injected pulse at $z = 5.3$ -cm penetration depth for four different values for the density ρ of atoms. The on-axis initial area θ_p for the injected pulse is $\theta_p = \pi$. Except for the effective gains and gain length Fresnel numbers, the values for all other parameters are the same as for Fig. 26(c). For each set of curves, the gain values are (a) $\alpha_{RSF} = 0.1708(g_{SF} = 291.7) \text{ cm}^{-1}$, $\alpha_{RP} = 0.375(g_p = 17.5) \text{ cm}^{-1}$; (b) $\alpha_{RSF} = 0.239(g_{SF} = 408.3) \text{ cm}^{-1}$, $\alpha_{RP} = 0.525(g_p = 24.5) \text{ cm}^{-1}$; (c) $\alpha_{RSF} = 0.3075(g_{SF} = 525.0) \text{ cm}^{-1}$, $\alpha_{RP} = 0.675(g_p = 31.5) \text{ cm}^{-1}$; and (d) $\alpha_{RSF} = 0.376(g_{SF} = 641.7) \text{ cm}^{-1}$, $\alpha_{RP} = 0.825(g_p = 38.5) \text{ cm}^{-1}$. The corresponding Fresnel numbers are (a) $F_{ps} = 370.63$ ($F_p = 17296$), $F_{sSF} = 1.334$ ($F_s = 2278$); (b) $F_{gp} = 518.83$ ($F_p = 24212$), $F_{sSF} = 1.866$ ($F_s = 3188$); (c) $F_{gp} = 667.07$ ($F_p = 31130$), $F_{sSF} = 2.401$ ($F_s = 4100$); and (d) $F_{gp} = 815.31$ ($F_p = 38048$), $F_{sSF} = 2.94$ ($F_s = 5010$).

Fig. 34. Radially integrated intensity profiles in units of Rabi frequency, for the SF(2) and injected pulse (1) at a penetration depth of $z = 5.3$ cm. The effective gain for the pump transition and the SF transition are $\alpha_{RP} = 0.3643(g_p = 17) \text{ cm}^{-1}$ and $\alpha_{RSF} = 0.376(g_s = 641.7) \text{ cm}^{-1}$, respectively. The initial on-axis area for the injected pulse is $\theta_p = \pi$.

Fig. 35. Pump pulse initial temporal width τ_p vs. ϵ . $F = 0.7$; pump pulse initial on-axis area $\theta_p = 2\pi$; $T_1 = 80$ nsec; $T_2 = 70$ nsec; $\tau_{RSF} = 19.5$ psec; $L = 5.6$ cm.

Fig. 36. Fresnel variation of the SF delay-statistics standard variation versus the average delay difference between the peak of the pump pulse and the first peak of the SF pulse (not always the largest when phase wave appears) for the three region of interest (a) build up SF; (b) partial overlap of SF pulse completely evolved and pump pulse; (c) highly nonlinear regime: the two pulses completely overlap.

Fig. 37. Fresnel variation of the SF delay-statistics standard variation versus the the arithmetic mean of the two average delays of pump and SF between the peak of the pump pulse and the first peak of the SF pulse (not always the largest when phase wave appears) for the three region of interest (a) build up SF; (b) partial overlap of SF pulse completely evolved and pump pulse; (c) highly nonlinear regime: the two pulses completely overlap.

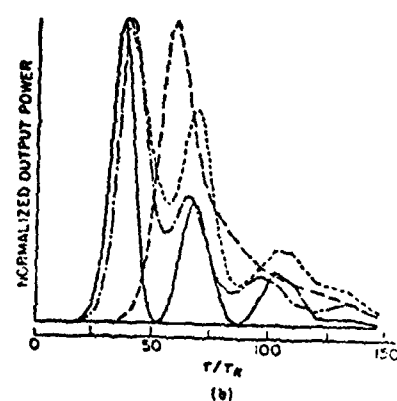
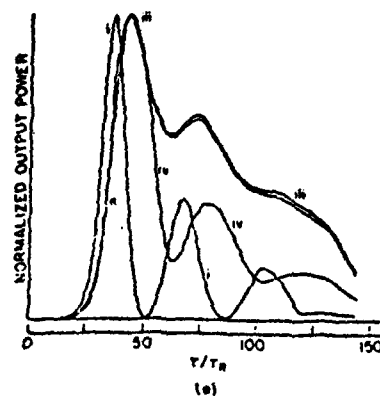
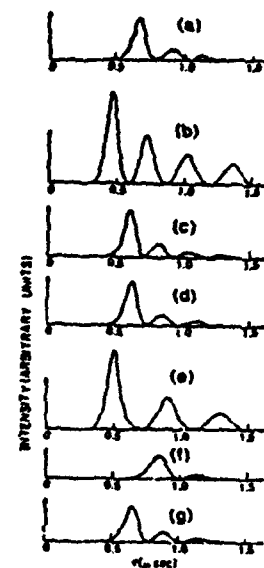
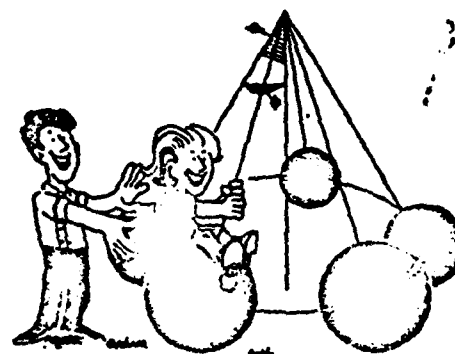
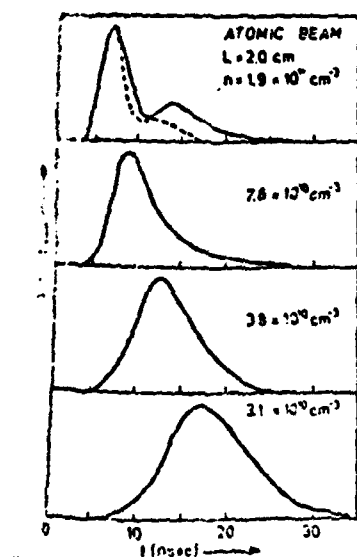
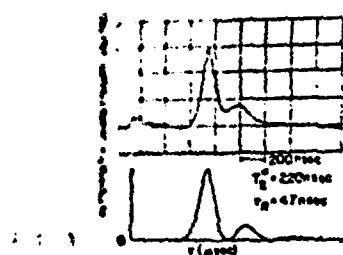
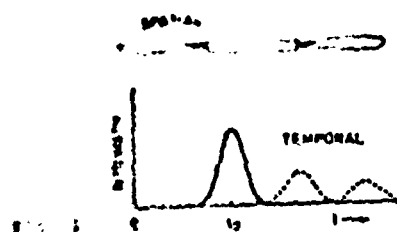
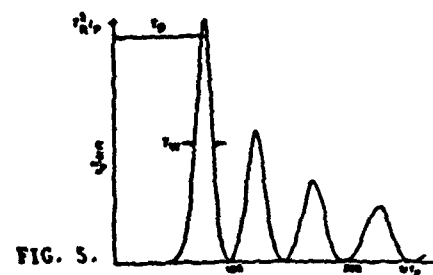
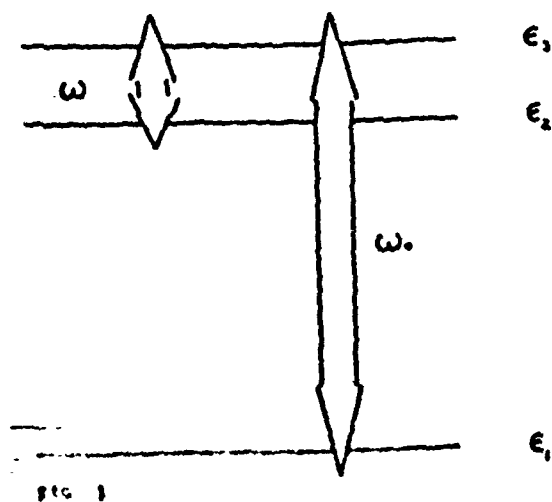
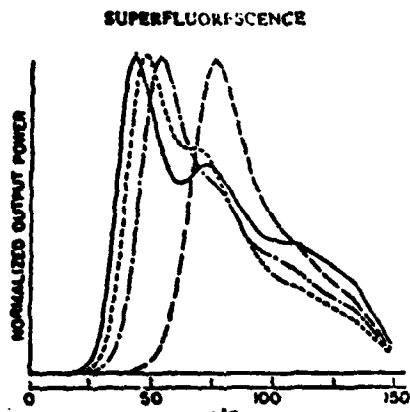
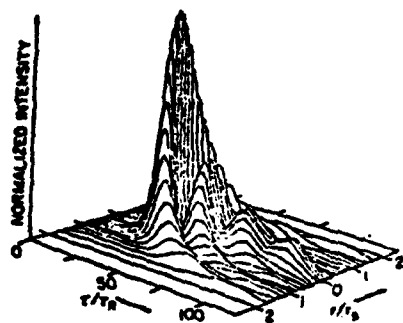


FIG. 7.

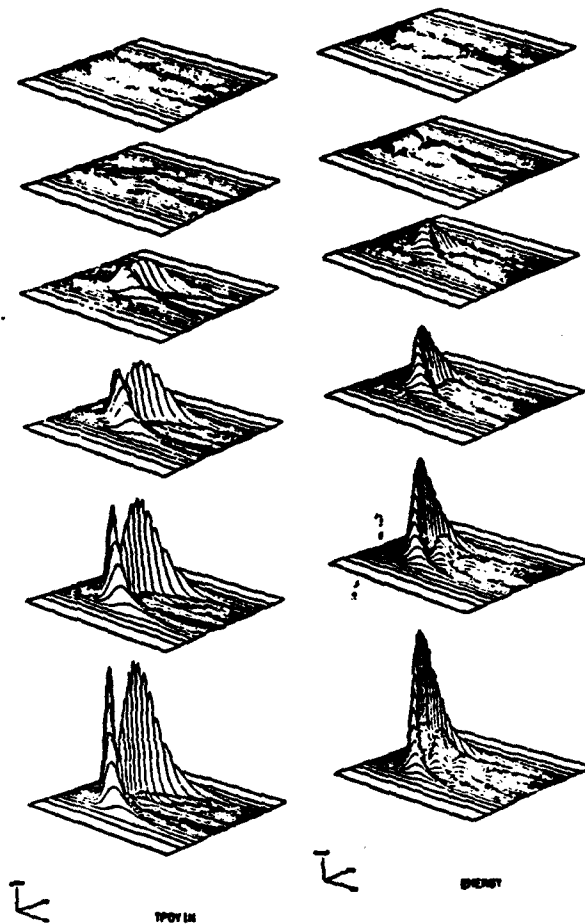


(a)

FIG. 8.



(b)



(c)

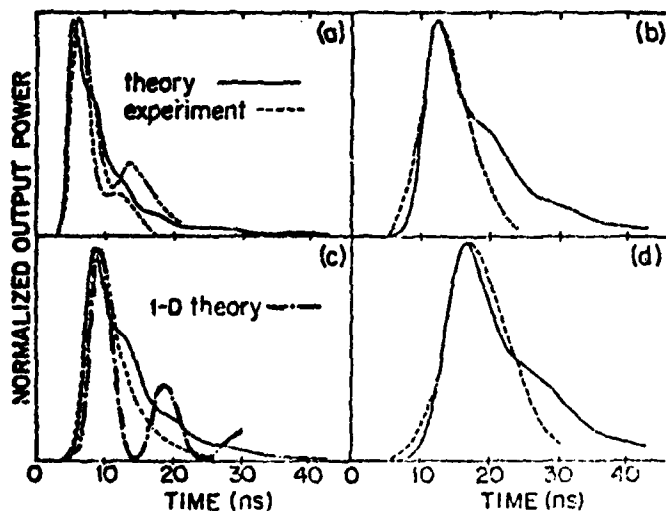


FIG. 9.

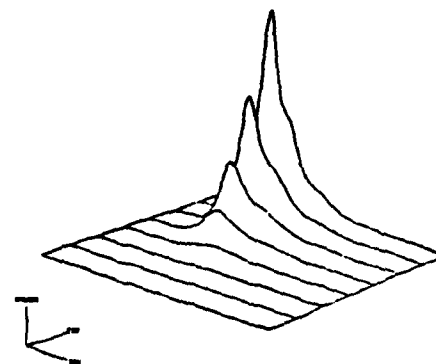


FIG. 10.

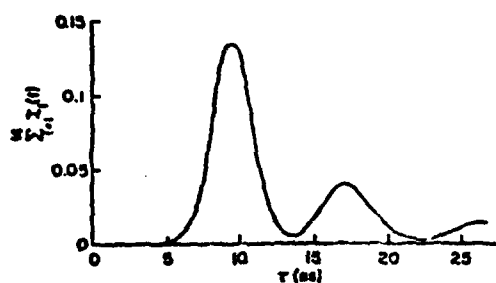


FIG. 11.

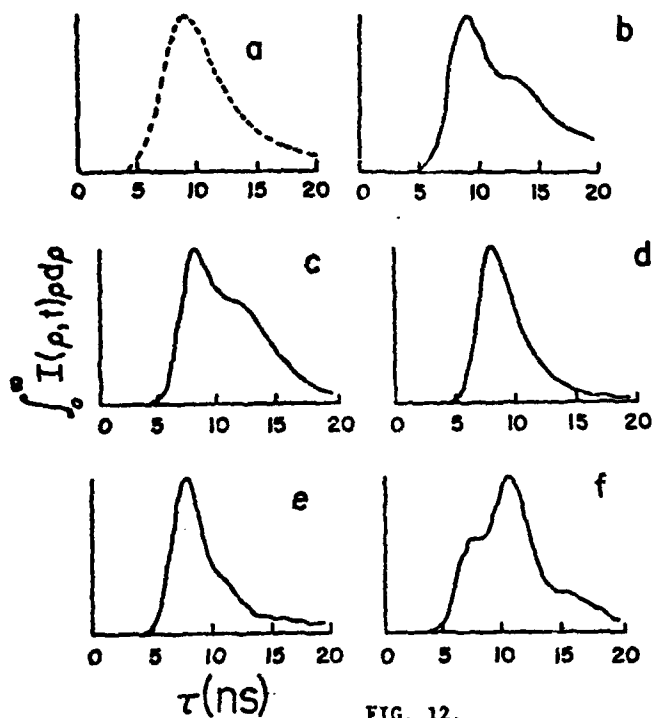


FIG. 12.

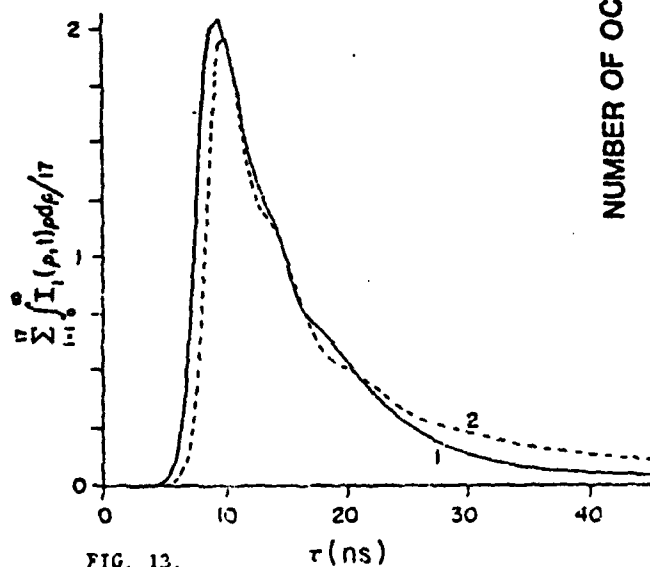


FIG. 13.

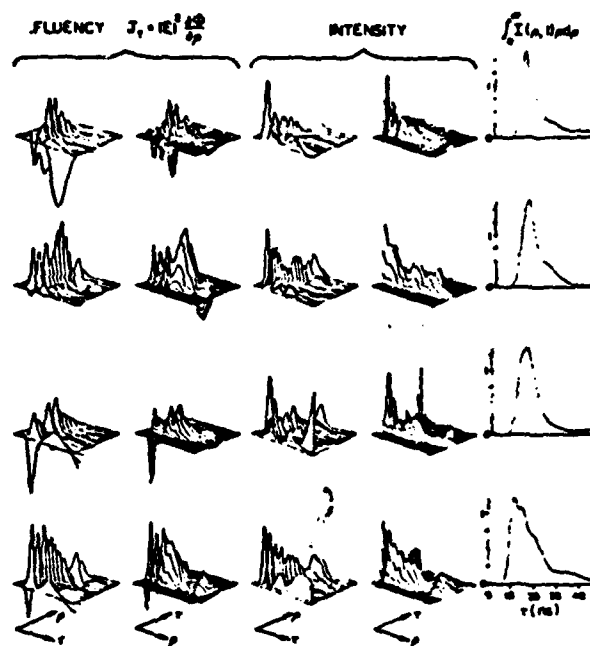


FIG. 14.

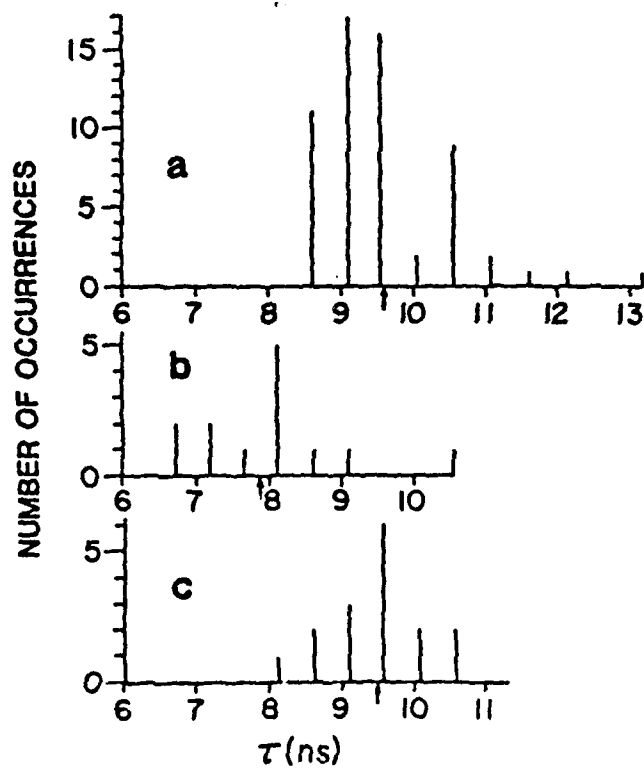


FIG. 15.

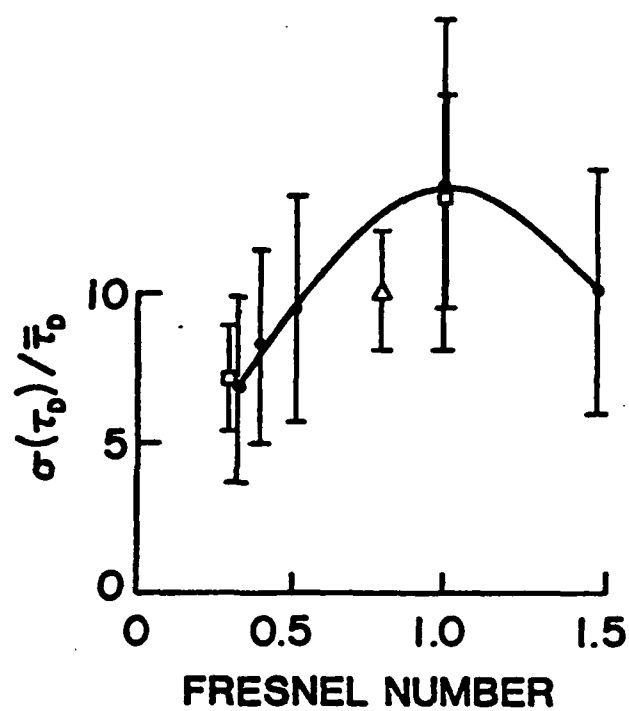


FIG. 16.

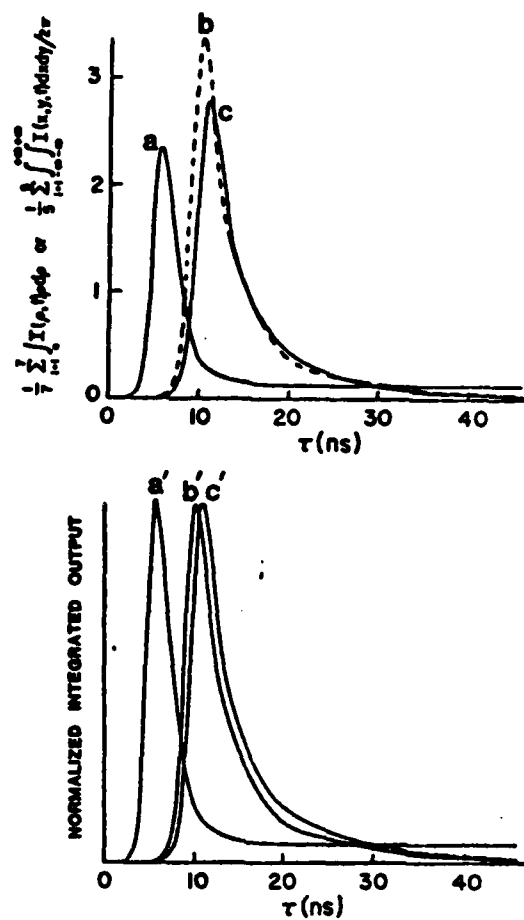


FIG. 18.

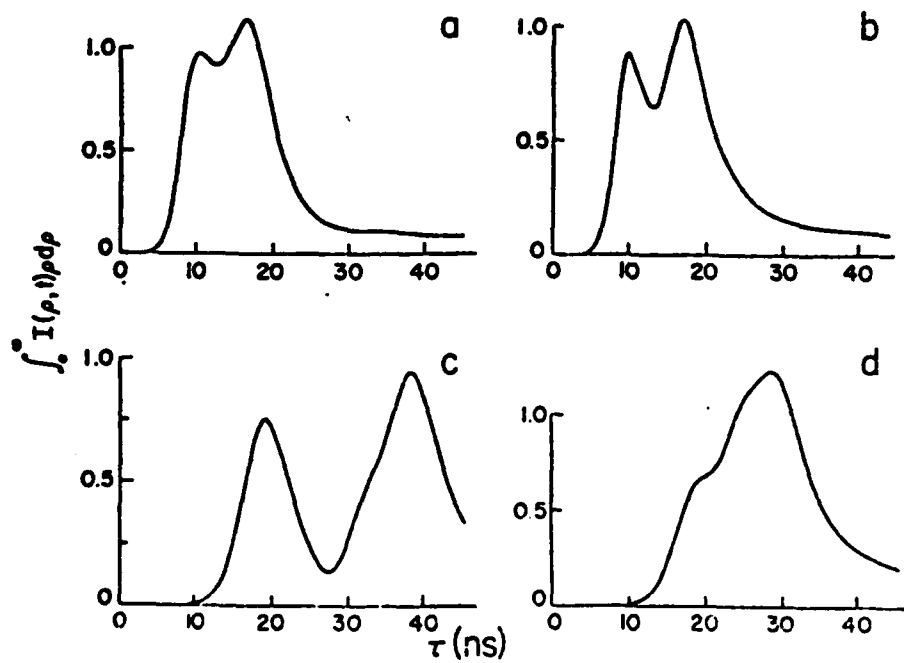


FIG. 17.

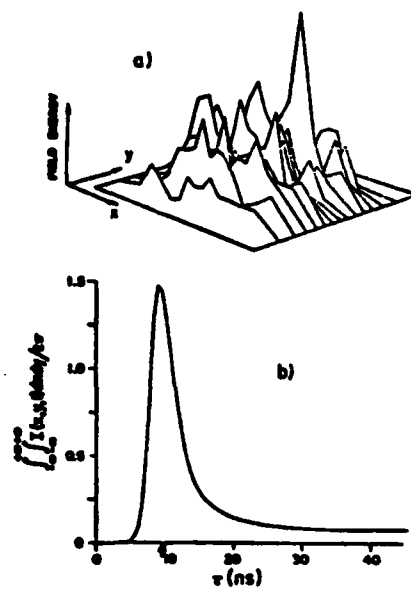


FIG. 19.

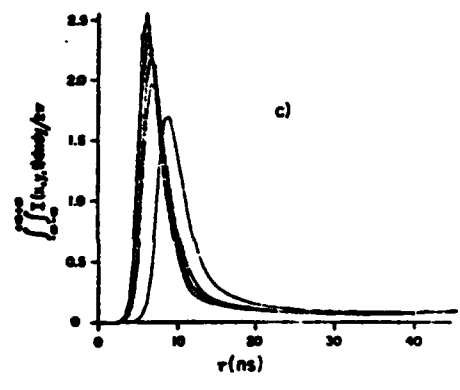


FIG. 20.

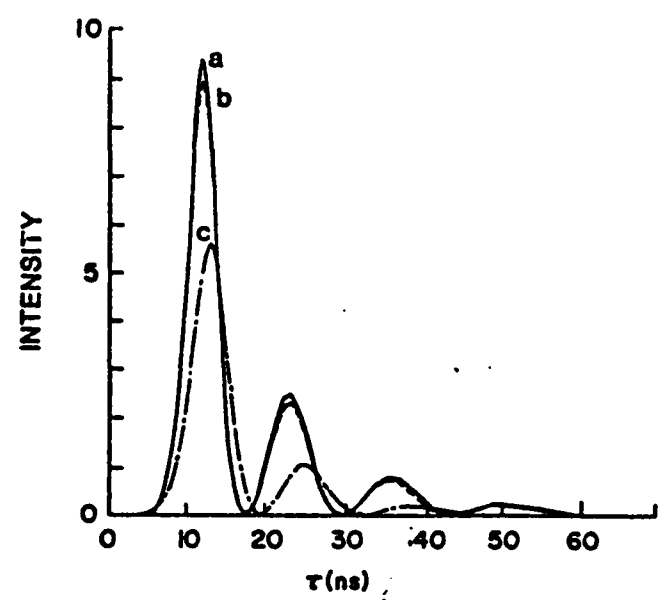


FIG. 22.

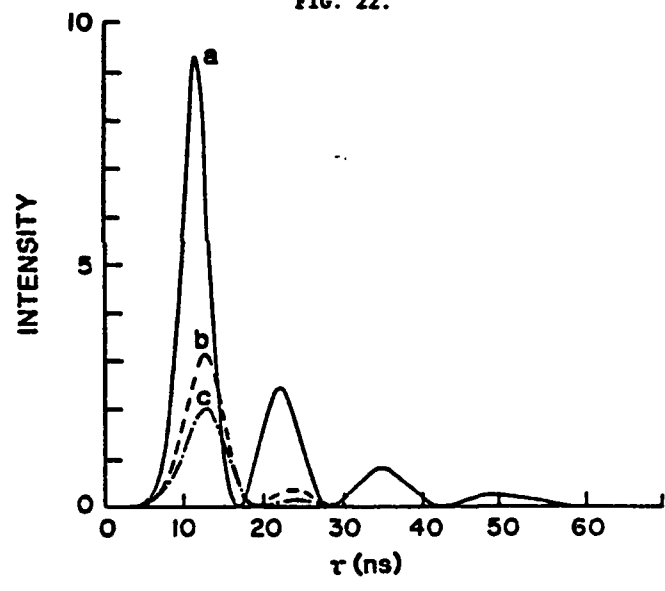


FIG. 23.

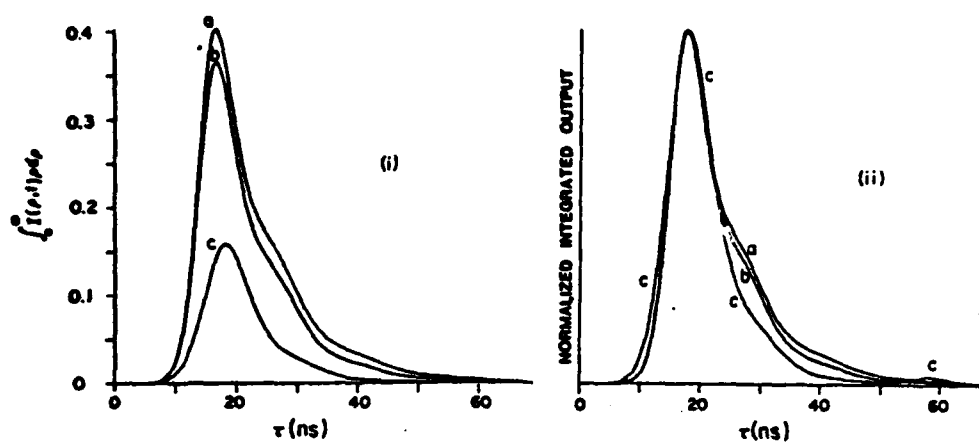


FIG. 24.

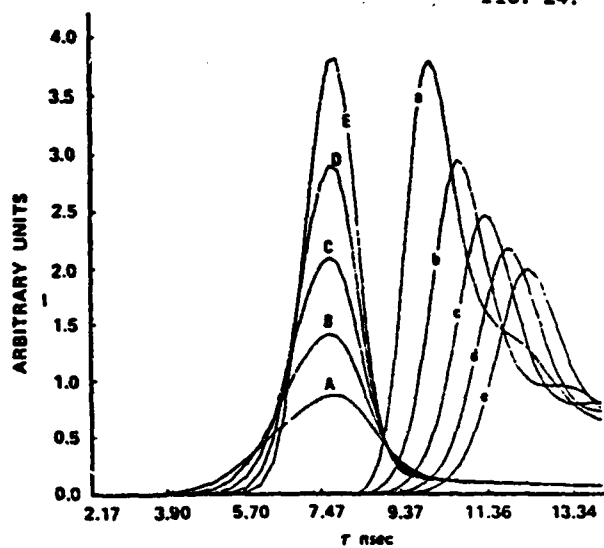


FIG. 25a.

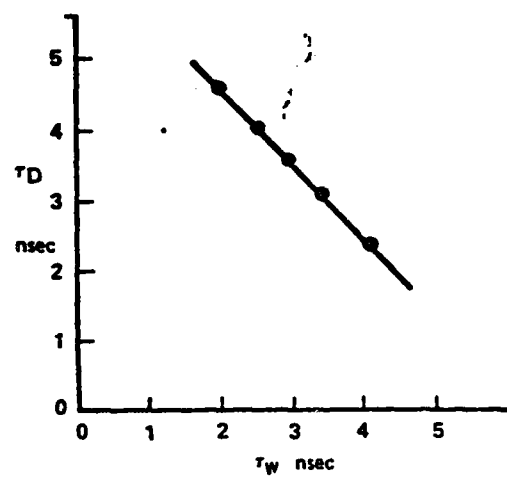


FIG. 25b.

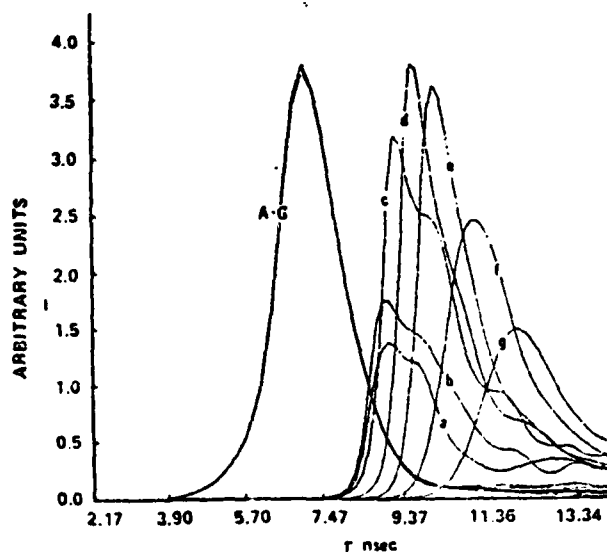


FIG. 26.

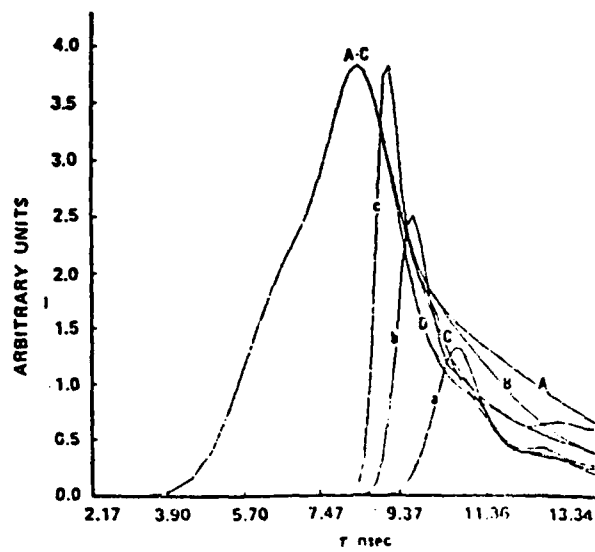


FIG. 27.

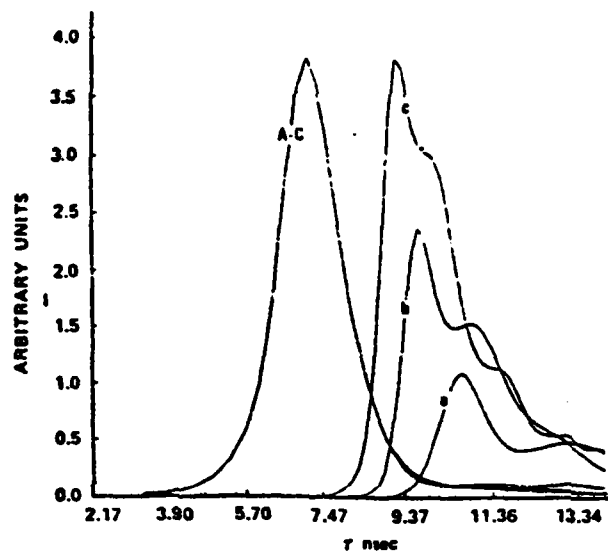


FIG. 28.

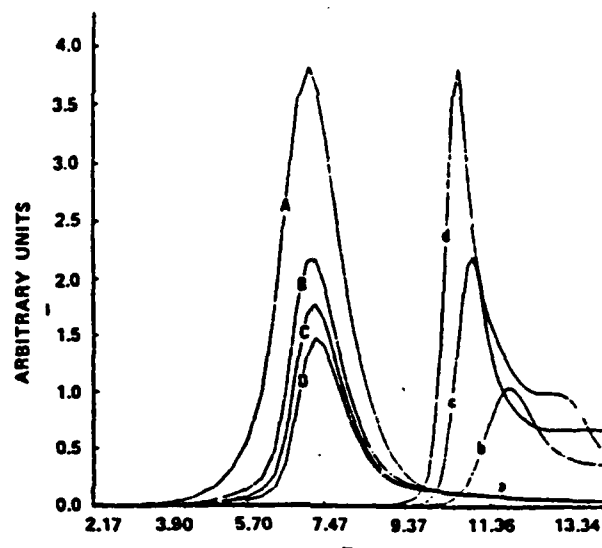


FIG. 31.

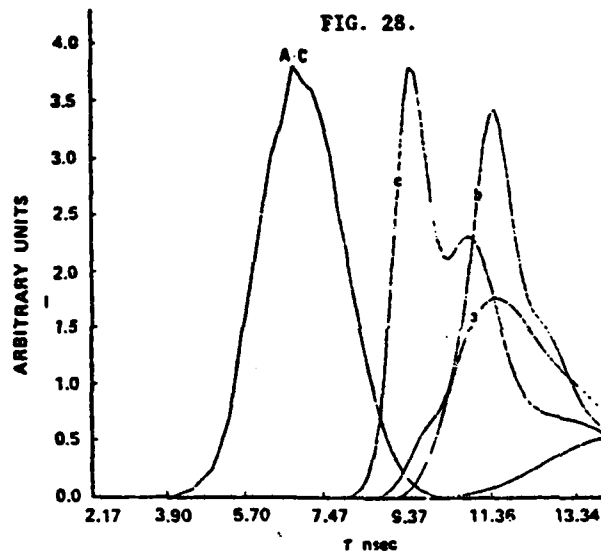


FIG. 29.

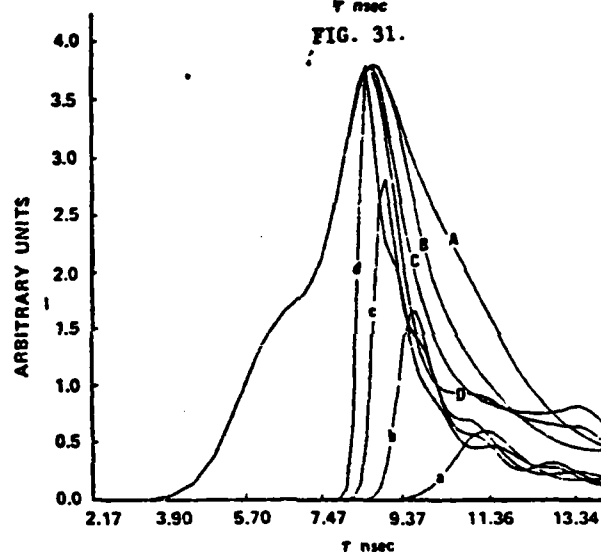


FIG. 32.

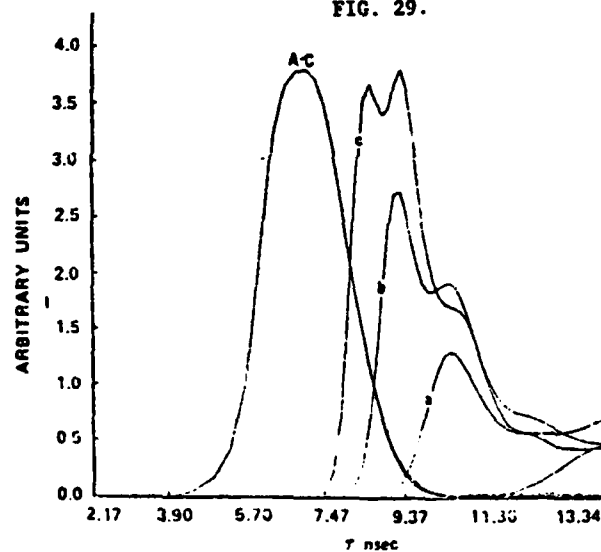


FIG. 30.

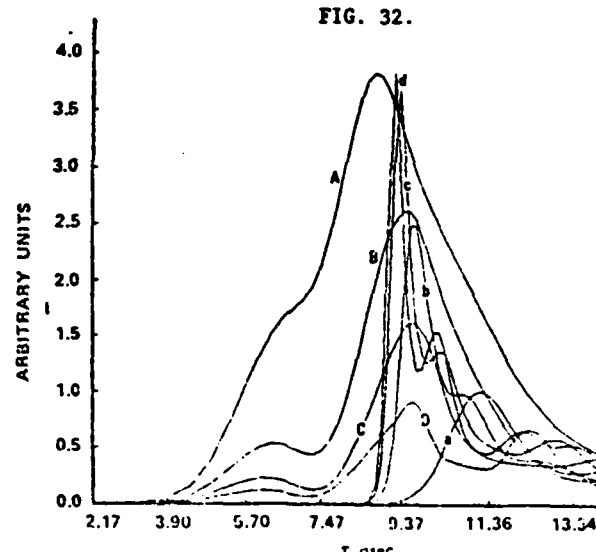


FIG. 33.

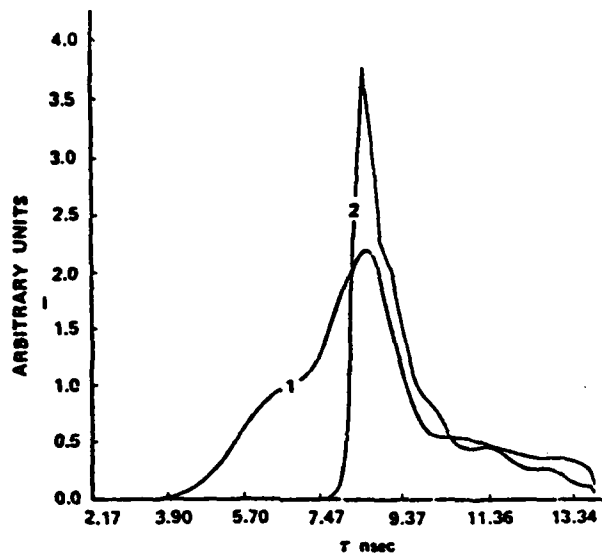


FIG. 34.

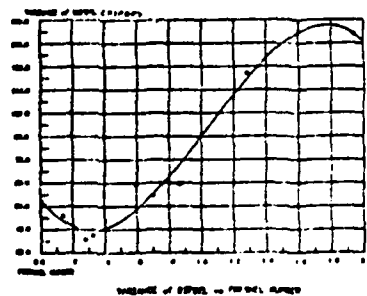
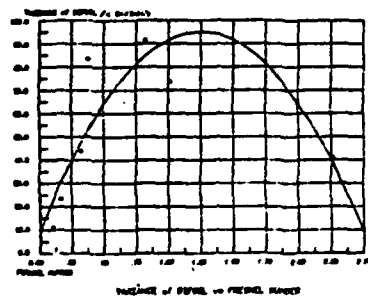
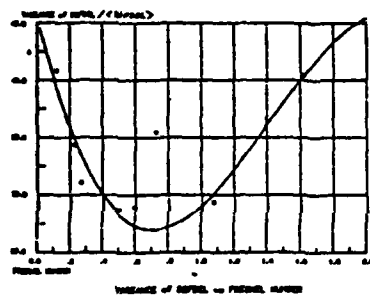


FIG. 36

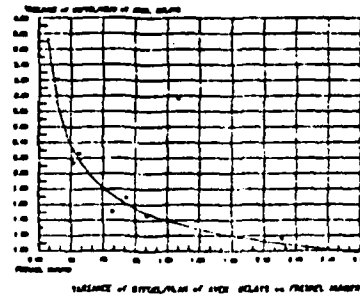
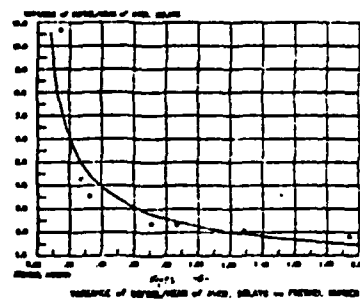
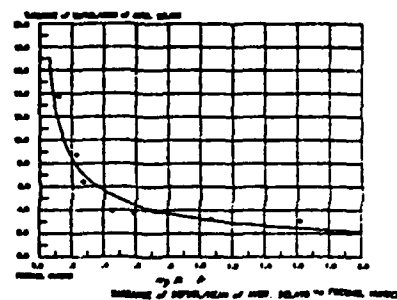


FIG. 37

COMMENTS ON P.D. DRUMMOND'S
CENTRAL PARTIAL DIFFERENCE PROPAGATION ALGORITHMS

F.P. Mattar*

Physics Department, New York University

New York, New York 10003

and

Spectroscopy Lab, Massachusetts Institute of Technology

Cambridge, Massachusetts 02139

and

M.C. Newstein

Department of Electrical Engineering, Polytechnic Institute of New York

Farmingdale, New York 11735

Drummond [1] has erroneously indicated that Mattar and Newstein's [2] algorithm is only a predictor-corrector technique similar to that of Icsevgi and Lamb's [3] together with an explicit finite difference approximation to a cylindrically symmetric Laplacian. He stated that this technique is limited by the extra overhead memory required as well as the lack of parallelism and the reduced stability of explicit algorithms. He fails to reference Tappert [4], Fleck's [5]

* Supported by the U.S. Office of Naval Research; on extended leave from Polytechnic Institute of New York.

COMMENTS ON P.D. DRUMMOND'S
CENTRAL PARTIAL DIFFERENCE PROPAGATION ALGORITHMS

F.P. Mattar*

Physics Department, New York University

New York, New York 10003

and

Spectroscopy Lab, Massachusetts Institute of Technology

Cambridge, Massachusetts 02139

and

M.C. Newstein

Department of Electrical Engineering, Polytechnic Institute of New York

Farmingdale, New York 11735

Drummond [1] has erroneously indicated that Mattar and Newstein's [2] algorithm is only a predictor-corrector technique similar to that of I.C. Sevgi and Lamb's [3] together with an explicit finite difference approximation to a cylindrically symmetric ~~L~~aplacian. He stated that this technique is limited by the extra overhead memory required as well as the lack of parallelism and the reduced stability of explicit algorithms. He fails to reference Tappert [4], Fleck's [5]

* Supported by the U.S. Office of Naval Research; on extended leave from Polytechnic Institute of New York.

recent published algorithms using Fast Fourier transform [5] and enclosed references [6-14] treating Thermal Blooming as well as Lax work [15]. Furthermore, Drummond fails to recognize the important techniques of dynamic automatically adaptive grids [2, 11-18] determined by the calculation itself.

Mattar and Newstein's computational strategy as illustrated in the articles referenced, however apparently not read, by Drummond consist in a modification of MacCormack's [19] two-level predictor-corrector method widely used in the gas dynamic computation such as those carried out by Moretti [16-18]. MacCormack's predictor-corrector method requires only one preceding plane to march along the direction of propagation precisely as in the various implicit scheme. Thus, the memory requirements are identical.

By reading Mattar and Newstein's algorithm description the reader can appreciate that the correction of the predicted field variables is done in terms of the yet-to-be computed corrected values of the material variables and not in terms of the predicted material values. Similarly, the material functions are assessed in terms of the corrected values of the field and not the predicted values. A set of implicit algebraic equations results which must be solved to compute the various variables. This technique insured that both material and field functions are simultaneously accurate to the second order in space coordinates and temporal grid.

It is advised to respect the criterion of stability of the explicit method to ensure that the physical problem is correctly simulated instead of being mis-calculated by using a mesh incompatible with the Fresnel number defined in terms of the nonlinear medium characteristic length which is a physical limiting parameter.

By adopting non-uniform meshes instead of the straight-forward computation grids a greater computational efficiency and reliability is achieved. Evenly spaced grids in the computational frame are adjustably mapped from variable non-uniform grids, in the physical frame by stretching and rezoning techniques such that the computational effort is clustered around the points of physical interest and less dense in the region where the physical function varies slowly.

More explicitly, the rationale these adaptive coordinate changes and function transformation is to enhance both the accuracy and the efficiency of the computation. This procedure removes, for example, the necessity for sampling the high frequency oscillation induced in the plane by focussing. Suydam and Mattar recently presented a full implicit code with adaptive stretching and rezoning techniques [20].

The coordinate transformations alter the independent variables so that the dependent variables take a different functional form at equivalent points in time and space in the two-coordinate systems. The altered functional form is smoother, easier and more economical to calculate. This refined algorithm while requiring more calculation per step, actually is less expensive of computer memory and time for a given problem than the brute force orthogonal mesh.

Mattar and Newstein's algorithm was used to simulate various physical situations [such as the (1) propagation of light in nonlinear media displaying a novel transient self-lensing effect [20]; (2) the build up of coherent emission from noise (superfluorescence) [21]; (3) the prediction of light control by light [23]; (4) the evolution of optically pumped superfluorescence [24]; (5) two-color superfluorescence [25] and various amplifiers [26] as well as (6) multi-level propa-

gation for laser isotopic separation studies [27] and (7) cw phase encoding that lead to on-axis intensity self-enhancement [28]] that quantitative, agree with experimental observation [29-37].

References

1. P.D. Drummond, Comput. Phys. Commun., 29, 211 (1983).
2. F.P. Mattar, Appl. Phys., 17, 53 (1978).
F.P. Mattar and M.C. Newstein, Comput. Phys. Commun., 20, 139 (1980).
3. A. Icsevigi and W.W. Lamb, Jr., Phys. Rev., 185, 517 (1969).
4. F.D. Tappert, Amer. Math. Soc. Lectures in Applied Mathematics, 15, 1151 (1974).
5. J.A. Fleck, Jr., J.R. Morris and M.D. Feit, Appl. Phys., 10, 129 (1976); and ibid. 14, 99 (1977); and M.D. Feit, J.A. Fleck, Jr., and J.R. Morris, J. Appl. Phys., 48, 3301 (1977).
6. A. Edwards, M.D. Feit and J.A. Fleck, Jr., Lawrence Livermore Laboratory Report, UCRL-52174 (1976), J. Appl. Phys., 50, 4307 (1979).
7. P.B. Ulrich, Numerical Methods in High Power Laser Application, AGARD Conf. Proceedings, No. 183, Optical Propagation in the Atmosphere (October, 1975) (National Technical Information Service, Springfield, Va. 22151).
8. P.B. Ulrich, "A Numerical Calculation of Thermal Booming of Pulse, Focused Laser Beams," Naval Resch. Lab. Rept., 7382 (December, 1971).
9. P.B. Ulrich, "PROP-I: An Efficient Implicit Algorithm for Calculating Nonlinear Scalar Wave Propagation in the Fresnel Approximation," Naval Resch. Lab. Rept., 7706, (May, 1974).
10. L.C. Bradley and J. Herrman, J. Opt. Soc. Am., 61, 668 (1971) and 'Numerical Calculation of Light Propagation,' MIT-Lincoln Lab. Rept., Laser Technology Program, LTP-10, (July, 1971).
11. L.C. Bradley and J. Herrmann, 'Notes on the Lincoln Lab Propagation' Code (1974), unpublished notes.
12. H.J. Breaux, 'An Analysis of Mathematical Transformation and a Comparison of Numerical Techniques for Computation of High Energy CW Laser Propagation in An Inhomogeneous Medium,' U.S. Army Ballistic Resch. Lab. Rept., 1723, (June, 1974).
13. K.G. Whitney and J.L. Mader, SSPRAMA: A Nonlinear, Wave Optics Multiple Pulse (and CW) Steady State Propagation Code With Adaptive Coordinates, NRL Rept., 8074, (February, 1977).

14. J.L. Walsh and P.B. Ulrich "Thermal Blooming in the Atmosphere," in Laser Beam Propagation in the Atmosphere, ed., J.W. Strohbehn, Topics in Applied Physics, Vol. 25, p. 226, Springer Verlag, (1978).
15. M. Lax, J.H. Batteh and G.P. Agrawal, J. App. Phys., 52, 109 (1981).
16. G. Moretti, Proc. 1974, Heat Transfer and Fluid Mechanics Institute, Stanford University Press, Stanford, California, (1974); Polytechnic Institute of New York Tech. Rept.: Poly-AE/AM 74-9 (December, 1974), ibid. 73-18 (August, 1973); ibid. 69-26 (July, 1969); ibid. 70-48 (November, 1970); ibid. 71-25 (September, 1971); ibid. 74-15 (September, 1974); ibid. 76-06 (March, 1976); and ibid. 68-25 (July, 1969).
17. G. Moretti, Proc. Symp. Trans-sonicum II, Gottingen, (September, 1975), Fed. Rep. Germany; Springer Verlag, (1976).
18. G. Moretti, "Proc. IBM Scientific Computing Symposium on Large Scale Problems in Physics," IBM Research Center, Yorktown Heights, New York, (December, 1963).
19. R.W. MacCormack, AIAA, Hypervelocity Impact Conf. 1969, paper 69-354; and Lecture Notes in Physics, Vol. 59, Proceedings of the Fifth International Conference on Numerical Methods in Fluid Dynamics, Springer Verlag, (1971), p. 307.
20. B.R. Suydam and F.P. Mattar, Los Alamos National Lab., Tech. Rept. T-7 LA-UR-82 3370, (November, 1982) and Los Alamos Optics Conf., (April, 1983), Proceedings to be Published by SPIE.
21. F.P. Mattar and H.H. Gibbs, Proceedings International Conf. on Lasers, New Orleans, Louisiana, p. 777, (December, 1980); F.P. Mattar, H.M. Gibbs, S.L. McCall and M.S. Feld, Phys. Rev. Lett. 46, 1123 (1981)
22. C.M. Bowden and F.P. Mattar, Proceedings Los Alamos Conference on Optics, Los Alamos, New Mexico, SPIE, Vol. 288, p. 364.
23. F.P. Mattar and C.M. Bowden, Phys. Rev. A, 345, (1983) and Opt. Soc. Am., 71, 1589, (1981) and to appear in Topics in Current Physics, ed. C.D. Cantrell, Srpinger Verlag, (1984).
24. F.P. Mattar and C.M. Bowden, Appl. Phys., (1982).
25. F.P. Mattar, M. Raymer and I. Wesley (submitted to IEEE International Conf. of Quantum Electronics, (June, 1984).
26. F.P. Mattar, International Conf. of Lasers, New Orleans, Louisiana, December, 1982 and Progress Report to DAAD, Bonn, F.R. Germany, F. Haake, R. Reibold and F.P. Mattar (submitted to IEEE International Conference of Quantum Electronics, June, 1984).
27. C.D. Cantrell, F.A. Rebentrost, W.H. Louisell and F.P. Mattar, Proceedings International Conf. on Lasers, December, 1981, STS Press, p. 270.

14. J.L. Walsh and P.B. Ulrich "Thermal Blooming in the Atmosphere," in Laser Beam Propagation in the Atmosphere, ed., J.W. Strohbehm, Topics in Applied Physics, Vol. 25, p. 226, Springer Verlag, (1978).
15. M. Lax, J.H. Batteh and G.P. Agrawal, J. App. Phys., 52, 109 (1981).
16. G. Moretti, Proc. 1974, Heat Transfer and Fluid Mechanics Institute, Stanford University Press, Stanford, California, (1974); Polytechnic Institute of New York Tech. Rept.: Poly-AE/AM 74-9 (December, 1974), ibid. 73-18 (August, 1973); ibid. 69-26 (July, 1969); ibid. 70-48 (November, 1970); ibid. 71-25 (September, 1971); ibid. 74-15 (September, 1974); ibid. 76-06 (March, 1976); and ibid. 68-25 (July, 1969).
17. G. Moretti, Proc. Symp. Trans-sonicum II, Gottingen, (September, 1975), Fed. Rep. Germany; Springer Verlag, (1976).
18. G. Moretti, "Proc. IBM Scientific Computing Symposium on Large Scale Problems in Physics," IBM Research Center, Yorktown Heights, New York, (December, 1963).
19. R.W. MacCormack, AIAA, Hypervelocity Impact Conf. 1969, paper 69-354; and Lecture Notes in Physics, Vol. 59, Proceedings of the Fifth International Conference on Numerical Methods in Fluid Dynamics, Springer Verlag, (1971), p. 307.
20. B.R. Suydam and F.P. Mattar, Los Alamos National Lab., Tech. Rept. T-7 LA-UR-82 3370, (November, 1982) and Los Alamos Optics Conf., (April, 1983), Proceedings to be Published by SPIE.
21. F.P. Mattar and H.H. Gibbs, Proceedings International Conf. on Lasers, New Orleans, Louisiana, p. 777, (December, 1980); F.P. Mattar, H.M. Gibbs, S.L. McCall and M.S. Feld, Phys. Rev. Lett., 46, 1123 (1981).
22. C.M. Bowden and F.P. Mattar, Proceedings Los Alamos Conference on Optics, Los Alamos, New Mexico, SPIE, Vol. 288, p. 364.
23. F.P. Mattar and C.M. Bowden, Phys. Rev. A, 345, (1983) and Opt. Soc. Am., 71, 1589, (1981) and to appear in Topics in Current Physics, ed. C.D. Cantrell, Springer Verlag, (1984).
24. F.P. Mattar and C.M. Bowden, Appl. Phys., (1982).
25. F.P. Mattar, M. Raymer and I. Wesley (submitted to IEEE International Conf. of Quantum Electronics, (June, 1984).
26. F.P. Mattar, International Conf. of Lasers, New Orleans, Louisiana, December, 1982 and Progress Report to DAAD, Bonn, F.R. Germany, F. Haake, R. Reibold and F.P. Mattar (submitted to IEEE International Conference of Quantum Electronics, June, 1984).
27. C.D. Cantrell, F.A. Rebentrost, W.H. Louisell and F.P. Mattar, Proceedings International Conf. on Lasers, December, 1981, STS Press, p. 270.

28. M. LeBerre, F.P. Mattar, E. Ressayre and A. Tallet, Proceeding of the Max Born Centenary Conference, publ. by SPIE paper 36901, (September, 1982).
29. H.M. Gibbs, B. Bolger and L. Baade, Opt. Comm. 18, 99 (1976).
30. H.M. Gibbs, B. Bolger, F.P. Mattar, M.C. Newstein, G. Forster and P.E. Toshek, Phy. Rev. Lett., 37, 1743, (1976).
31. F.P. Mattar, G. Forster and P.E. Toshek, Kvantovaya Elektronika, 5, 1819 (1978).
32. J.J. Bannister, H.J. Baker, T.A. King and W.G. McNaught, Phys. Rev. Lett., 44, 1062, (1980).
33. A.T. Rosenberg and T.A. DeTemple, Phys. Rev., A24, 868, (1981).
34. F.P. Mattar, Abstract Digest European Conf. Atomic Physics Heidelberg, F.R. Germany (April, 1981), ed. J. Kowolski, G. Zuputlitg and H. Weber, (EPS, Geneva, 1981); Proceedings of the Los Alamos Conference on Optics, SPIE, Vol. 288, p. 383 (1981).
35. E. Watson, H.M. Gibbs, F.P. Mattar, M. Cormier, Y. Claude, S.L. McCall and M.S. Feld, Phys. Rev., A27, 1427, (1983).
36. M. LeBerre, E. Ressayre, A. Tallet, H.M. Gibbs, M.C. Rushford and F.P. Mattar, Fifth Rochester Conference on Coherence and Quantum Optics, (June, 1983).
37. R. Florian, L.O. Schwan and D. Schmid, Solid State Comm., 42, 55 (1982).

Acknowledgements

The author gratefully thanks Professor H.A. Haus, Professor G. Moretti, Dr. J. Herrmann and Dr. P. Ulrich for introducing him to the physics and computation of nonlinear propagation effects.

*Canadian Association of
Physicists and Canadian Astrophysics Soc.
Victoria, British Columbia, Canada (June 82)*

THE PERTURBATION THEORY OF THE SELF-FOCUSING OF A CW OPTICAL BEAM ON RESONANCE

Jiří Teichmann

University of Montreal, Physics Department, Montreal

and

Farrès P. Mattar

Spectroscopy Laboratory, Massachusetts Institute of Technology
Cambridge, Massachusetts

Recently Boshier and Sandle /1/ reported via the numerical simulations a new phenomenon of CW on-resonance self-focusing for very intense beam having intensity larger than the saturation one. The analytical discussion of this self-focusing by LeBerre et al /2a,b/ led to controversy due to the neglecting of the off-axis effects in /2a/. The self-focusing in the purely absorptive propagation was demonstrated in /3/.

In the present study we develop a detailed analytical treatment of the beam stripping in the off-axis regions, occurring during the early stage of the beam reshaping.

Introducing into the evolution equation for the field amplitude $e(\rho, z)$

$$\frac{\partial}{\partial z} e - i f \nabla_T^2 e = -\frac{1}{2} \frac{e}{1 + \beta |e|^2} \quad (1)$$

(where β depends on dipole momentum and relaxation times in the corresponding Bloch equation and $f \ll 1$ is a reciprocal characteristic Fresnel number) the expansion

$$e(\rho, z) = \sum_n f^{2n} e_{2n}(\rho, z) + i \sum_n f^{(2n+1)} e_{(2n+1)}(\rho, z) \quad (2)$$

leads to the hierarchy of solutions for $e_n(\rho, z)$:

$$e_n(\rho, z) = e_0(\rho, z) \int_0^z dz' \left\{ (-1)^{n+1} \nabla_T^2 e_{n-1}(\rho, z') + F_n(e_0(\rho, z') \dots e_{n-1}(\rho, z')) \right. \\ \left. \cdot \left[\frac{1 + \beta e_0^2(\rho, z)}{1 + \beta e_0^2(\rho, z')} \right]^{\frac{1}{2}(1 + (-1)^n)} \right\} e_0^{-1}(\rho, z') \quad (3)$$

These solutions show the competing effect of the beam diffraction (the Laplacian in (3)) and the nonlinear absorption of the medium expressed via the nonlinear response $F_n(e_j(\rho, z))$. The zeroth order solution to eq. (1), $e_0(\rho, z)$, was given by Icsevci and Lamb in [4]. In the case of very intense CW beam, the on-axis intensity $\beta I_0 \gg 1$ and the amplitude $e_0(\rho, z)$ can be approximated in the on-axis domain by (the initial beam profile is Gaussian):

$$e_0(\rho, z) = \left\{ I_0 e^{-2\rho^2} - \frac{z}{\beta} - \frac{1}{\beta} \ln \left(1 - \frac{z}{\beta I_0} e^{2\rho^2} \right) \right\}^{\frac{1}{2}} \quad (4)$$

To analyse the beam reshaping and stripping near the outer region where $I_0(\rho, z) \sim 1$, $e_0(\rho, z)$ is expressed by:

$$e_0(\rho, z) = 1 + \sum_{n=1}^{\infty} p_n G^n(\rho, z) \quad (5)$$

where $G(\rho, z) = (1 + \beta)^{-1} \left\{ \ln K - \frac{1}{2}\beta \right\}$, $K \equiv I_0^{\frac{1}{2}} e^{-\rho^2} e^{\frac{1}{2}\beta I_0} e^{-2\rho^2} e^{-\frac{1}{2}z}$.

Finally near the edges of the beam where $I_0(\rho, z) \ll 1$ the following approximation is suitable

$$e_0(\rho, z) = \sum_{m=0}^{\infty} p_{2m+1} K^{(2m+1)} \quad (6)$$

Using these explicit functions in their domains of validity we have calculated the amplitudes $e_n(\rho, z)$ up to the third order both analytically and numerically. The beam evolution is also characterized by the effective beam radius (in the Marburger's definition):

$$\rho_{eff} \approx \left\{ \frac{\int [(e_0 + f^2 e_2)^2 + f^2 e_1^2] \rho d\rho}{\int \{ [\nabla_T(e_0 + f^2 e_2)]^2 + f^2 [\nabla_T e_1]^2 \} \rho d\rho} \right\}^{\frac{1}{2}} \quad (7)$$

and by the radial energy flow $J_t(\rho, z)$:

$$J_t(\rho, z) = |e|^2 \frac{\partial \phi}{\partial \rho}, \quad \phi \approx \tan \phi = \frac{e_1 + f^2 e_3}{e_0 + f^2 e_2} f \quad (8)$$

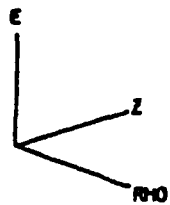
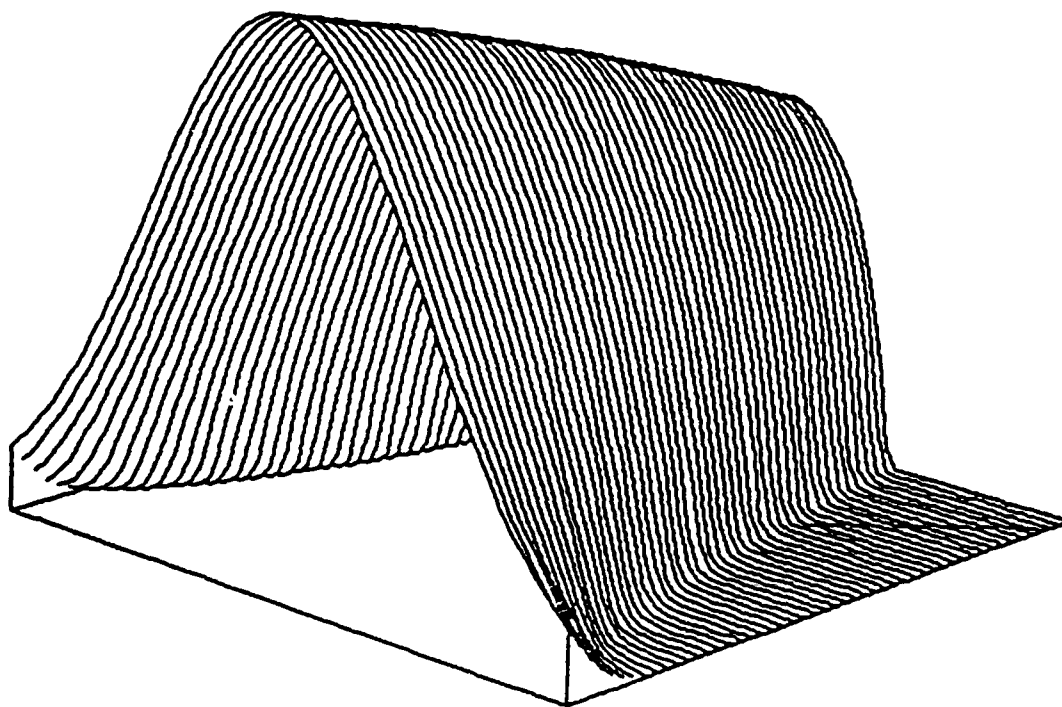
The radius ρ_{eff} , the phase ϕ and its radial variation $\frac{\partial \phi}{\partial \rho}$

were also calculated. To compare our results with /1/ we have plotted $e_0(\rho, z)$ (Fig.1.), $e_1(\rho, z)$ (Fig.2.), $e_n(\rho, z)$, $\phi(\rho, z)$, $J_t(\rho, z)$ and the radius $\rho_{eff}(z)$ for $\beta=1$, $f=1/300$ and $I_0=225$. The analysis shows that for sufficiently large penetration depth z the nonlinearity predominates over the diffraction as the energy flow changes the direction toward the center of the beam. At first the beam transverse structure is reshaped and stripped near the edges giving rise to the radially dependent wave front. The phase changes rapidly in the outer regions of the beam. As z increases, substantial reshaping in the near-axis domain takes place. Even the zeroth order beam intensity, being initially Gaussian, becomes peaky with increasing z .

Our results corroborate the numerical simulations /1/.

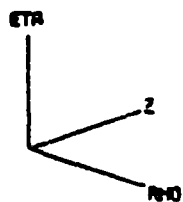
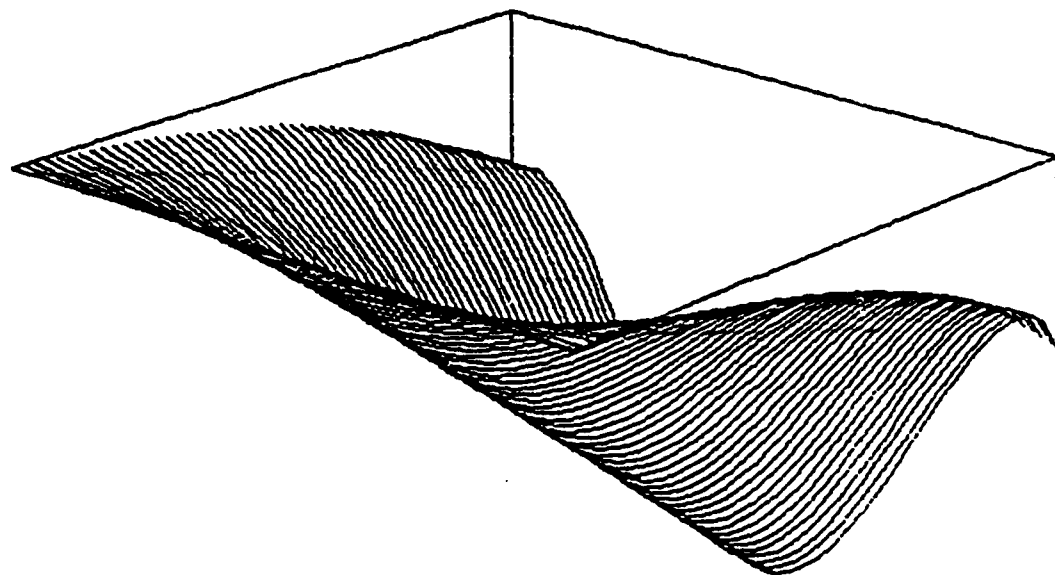
References :

- /1/ M.G. Boshier and W.J. Sandle, Opt. Comm. 42,371(1982)
- /2/ M. LeBerre-Rousseau, E. Ressayre and A. Tallet
a. Abstract Digest, b. Proceedings, Coherent and Quantum Optics Conference V., Rochester (1983)
- /3/ J. Teichmann and F.P. Mattar, Congress, Canadian Association of Physicists and Canadian Astronomical Society, Victoria (1983)
- /4/ A. Icsevgi and W.E. Lamb Jr. , Phys. Rev. 185,517(1968)



E

Fig.1.



ETA

Fig.2.

ON THE PERTURBATIVE THEORY OF THE ONSET OF THESELF FOCUSING IN
THE PURELY ABSORPTIVE CW OPTICAL BEAM PROPAGATION†

Jiri Teichmann

Department de physique, Universite de Montreal
P.O. Box 6128, Montreal, Canada

and

Yves Claude

Department d'Informatique, Universite de Montreal
P.O. Box 6128, Montreal, Canada

Farrès P. Mattar††

Department de Physico-Chimie, Centre d'Etudes Nucleaires
de Saclay, Gif-sur-Yvette, France and Spectroscopy Laboratory,
Massachusetts Institute of Technology Cambridge, Massachusetts 02139

Revision Received September 23, 1983

ABSTRACT

The onset of the self-focusing of very intense CW optical beam on resonance is studied analytically using perturbational methods. The competitive effects of radially dependent nonlinear absorption of the media and the diffraction spread of the initially gaussian beam are analyzed. The radial variations of the field components, phase and effective beam radius show the beam reshaping and stripping effects in agreement with numerical simulations.

Introduction.

Recently Boshier and Sandle [1] reported a new phenomenon of CW on-resonance self focusing for very intense beams having intensity larger than the saturation one. This new phenomenon has not occur previously as reviewed by Marburger [2] where less intense beams were studied: The nonlinear susceptibility χ_{NL} vanishes on-resonance excluding the occurrence of self-focusing as observed by Bjorkholm et al [3];

† The development of the numerical program applied to this study was sponsored by the U.S. Army Research office (DAAG23-79-C-0148) and the U.S. office of Naval Research (N000-14-80-C-0175)

†† On extended leave of absence from the Polytechnic Institute of New York, Brooklyn, New York 11201

either below the resonance or above the resonance the beam experiences self lensing phenomenon as predicted by Javan and Kelly [4] and observed by Irishkowsky et al [5]. The coherent (pulsed) on-resonant self-focusing predicted by Newstein et al [6,7] and subsequently ascertained in Sodium [8,9] Neon [9,10] and Iodine [11] could be understood in terms of an instantaneous frequency offset ($\Delta\Omega = \partial\phi/\partial t$), which results from the phase variation initiation due to diffraction. Similar methodology to the one developed by Newstein et al for the transient case [12,13] to treat the diffraction as a perturbation, elucidate the development of the radially dependent phase in the CW regime as shown by LeBerre et al in [4,15]. LeBerre et al used for a base Içsevçi and Lamb's plane wave (CW) implicit solution [17] instead of McCall and Hahn SIT (pulse) solution [18]. The phase curvature was obtained by the competitive effects of radially dependent nonlinear absorption of the medium and the diffraction spreading of the input gaussian beam. A Fresnel number, defined in terms of the (nonlinear medium) Beer length instead of the cell length, characterizes completely with the ratio of the input intensity to the saturation intensity the beam evolution and reshaping. Particular care must be taken in the perturbation treatment to approximate correctly the canonical plane wave solution and to include the transverse boundary edge effects. Le Berre et al [16] in their first analysis missed the stripping* process that takes place at the edge of the canonical solution profile and concluded that this CW self-focusing was a computer artifact. Our attempt was to understand both results and illustrate the physics. Our present approach is perturbational both analytically using two power series

* The physical mechanism of stripping was first recognized by McCall and Hahn [18] in their pulse analysis in resonant media. They understood that the pulse entering into the resonant medium is not uniform in intensity across its profile. They assumed that the plane-wave analysis of the transparency effect is applicable to small patches of the light wave front anywhere on the profile a modification of the pulse intensity output across the beam profile can be described along the rod. They stated that at a particular radius $r_c \leq r$ where the pulse area falls below π , the light will be absorbed for all $r_c < r$ within a few Beer's lengths α^{-1} . Consequently, the outer periphery of the original pencil of light should be stripped away.

development to treat rigorously the edge effect and numerically where the basic solution is exactly solved using implicit algorithm. The analysis led us to understand the evolution of the onset of the self-focusing from the transverse energy current associated with the phase curvature induced by the amplitude abrupt variation (i.e., stripping [18] at the edge. The phase and amplitude structures which arise from the perturbation are such that if the beam propagates through free space, it will experience an enhancement (magnification) on-axis. The trend of our perturbational results was conform with our rigorous solution [19] as well as with those by Tai [20], Drummond [21] and Le Berre et al (though not accepted as real) [22] and the Saclay [30] calculation as well as with a recent modified theoretical analysis by Le Berre et al [23] that takes into account of the stripping process.

Equations of motions.

Thus, in recent papers, LeBerre et al [14-16] discussed analytically the beam reshaping in the case of a CW beam propagating in a purely absorptive medium. Recently, Le Berre et al [16] attempted to demonstrate analytically that the self-focusing, obtained previously by Boshier et al [1] by numerical simulations is due solely to computational artifact despite their obtaining a mesh independent self-focusing with a simplified non-adaptive mesh version of Mattar code [24]. Nevertheless the beam reshaping was thoroughly shown by other numerical approaches [19-23, 30].

We have therefore reexamined the analytical solution to the propagation problem of CW laser beam in absorbing media using the perturbative treatment.

The propagation of an intense CW light beam in an absorptive medium is described by equation:

$$\frac{\partial}{\partial z} e - i f \nabla_T^2 e = - \frac{1}{2} \frac{e}{1 + \beta |e|^2}$$

where the parameter $\beta = \frac{|\bar{\mu}|^2}{h^2} \tau_1 \tau_2$, $\bar{\mu}$ being the dipole moment for

atom, $\tau_1 \tau_2$ relaxation times in the corresponding Bloch equation. The other parameter, $f \ll 1$, represents the relative magnitude of diffraction with respect to absorption, $f = (1/2 k w_0^2)^{-1}$ the ' $1/2 k w_0^2$ ' is the in-

verse diffraction length z_d , while α is the Beer absorption reciprocal length and w_0 being the waist thickness of the beam, $z = (1/2) \alpha \bar{z}$, \bar{z} is the penetration depth in physical units, $\rho = \frac{r}{T}$, ∇^2 is the transverse Laplacian in ρ . The complex field amplitude is $e(\rho, z)$.

Thus f as first recognized by Mattar and Newstein [7,13] is a reciprocal characteristic medium length Fresnel number whereas the geometric

reciprocal Fresnel number is $f_g = \frac{z}{kw_0^2}$. Their ratio $f/f_g = \alpha \bar{z}$ total absorption in a medium of length \bar{z} [25].

Using the usual perturbation method [26], we expand the field amplitude $e(\rho, z)$ in terms of the expansion [2]:

$$e(\rho, z) = \sum_{j=1} f^{2j} e_{2j}(\rho, z) + i \sum_{j=1} f^{(2j+1)} e_{(2j+1)}(\rho, z) \quad (2)$$

with $e_j(\rho, z)$ being real. Introducing eq. (2) into eq. (1), one obtains the following hierarchy of evolution equations

$$\frac{\partial}{\partial z} e_0 = - \frac{1}{2} \frac{e_0}{1 + \beta e_0^2}$$

$$\frac{\partial}{\partial z} e_1 - \nabla_T^2 e_0 = - \frac{1}{2} \frac{1}{1 + \beta e_0^2} e_1$$

$$\frac{\partial}{\partial z} e_2 + \nabla_T^2 e_1 = - \frac{1}{2} \frac{1 - \beta e_0^2}{(1 + \beta e_0^2)^2} e_2 + \frac{1}{2} \frac{\beta e_0}{(1 + \beta e_0^2)^2} e_1^2$$

$$\frac{\partial}{\partial z} e_3 - \nabla_T^2 e_2 = - \frac{1}{2} \frac{1}{1 + \beta e_0^2} e_3 + \frac{\beta e_0}{(1 + \beta e_0^2)^2} e_1 e_2 + \frac{1}{2} \frac{\beta}{(1 + \beta e_0^2)^2} e_1^3$$

The first three equations coincide with eq. (9) in [14-13] for $\beta=1$.

The zeroth order approximation in (3) has a well known solution given by Icsevgi and Lamb [17]:

$$e_0 \exp \left[\frac{1}{2} \beta e_0^2 \right] = I_0^{1/2} \exp[-\rho^2] \exp \left[\frac{1}{2} \beta I_0 \exp\{-2\rho^2\} \right] \exp\left[-\frac{1}{2} z\right] \quad (4)$$

Assuming this solution, $e_0(\rho, z)$ as a known function of the normalized variables ρ and z , we obtain for higher order approximations.

$$\begin{aligned}
 e_1(z) &= e_0(z) \int_0^z [\nabla_T^2 e_0(z')] \frac{1}{e_0(z')} dz' \\
 e_2(z) &= \frac{e_0(z)}{[1+\beta e_0^2(z)]} \int_0^z [-\nabla_T^2 e_z(z') + \frac{\beta}{2} \frac{e_0(z') e_1^2(z')}{[1+\beta e_0^2(z')]^2}] \frac{1+\beta e_0^2(z')}{e_0(z')} dz' \\
 e_3(z) &= e_0(z) \int_0^z [\nabla_T^2 e_z(z') + \frac{\beta e_0(z') e_1(z') e_2(z')}{[1+\beta e_0^2(z')]^2} + \frac{1}{2} \frac{\beta e_1^3(z')}{[1+\beta e_0^2(z')]^2}] \dots \\
 &\quad \cdot \frac{1}{e_0(z')} dz' \quad (5)
 \end{aligned}$$

Here we have assumed that $e_j(\rho, z) = 0$ for $j \neq 0$ at $z = 0$. In the case of very intense CW beam, as considered in [14-16,23], where the on-axis input intensity $I_0 \gg 1$, the solutions (5) can be rather simplified.

For $\beta I_0 \gg 1$, the Icsevgi-Lamb solution (4) can be following ref [16] approximated for an initially gaussian profile by:

$$I(\rho, z) = I_0 \exp[-2\rho^2] - \frac{z}{\beta} \quad (6)$$

which is a good approximation for the near axis region if

$$\frac{z}{\beta} < I_0 \exp[-2\rho^2]$$

Then

$$e_0(\rho, z) = [I_0 \exp[-2\rho^2] - \frac{z}{\beta}]^{\frac{1}{2}} \quad (7)$$

with exception of the close vicinity of the point $\frac{z}{\beta} = I_0 \exp[-2\rho^2]$. For the first order solution we have:

$$\begin{aligned}
 e_1(\rho, z) &= 4\beta I_0 \{(1-2\rho^2) \exp[-2\rho^2] \ln [1 - (z/\beta I_0) \exp[2\rho^2]] \dots \\
 &\quad - \rho^2 \frac{(z/\beta I_0)}{1 - (z/\beta I_0) \exp[2\rho^2]} \} \cdot \{I_0 \exp[-2\rho^2] - z/\beta\}^{\frac{1}{2}} \quad (8)
 \end{aligned}$$

$$\begin{aligned}
 e_2(\rho, z) = & \frac{8\beta^2 I_0}{(1 - \frac{z}{\beta I_0} \exp(2\rho^2))^{\frac{1}{2}}} \left\{ - (1-2\rho^2)^2 \left(1 - \frac{z}{\beta I_0} \exp(2\rho^2)\right) \ln^2 \left(1 - \frac{z}{\beta I_0} \exp(2\rho^2)\right) \dots \right. \\
 & + [(-6\rho^2 + 20\rho^4) + (14\rho^2 - 12\rho^4) \left(1 - \frac{z}{\beta I_0} \exp(2\rho^2)\right) - 4(1 - 4\rho^2 + 2\rho^4) \left(1 - \frac{z}{\beta I_0} \exp(2\rho^2)\right)^2] \cdot \\
 & \cdot \ln \left(1 - \frac{z}{\beta I_0} \exp(2\rho^2)\right) + (-4 + 24\rho^2 - 7\rho^4) \frac{z}{\beta I_0} \exp(2\rho^2) + (5 - 34\rho^2 + 24\rho^4) \frac{z^2}{\beta^2 I_0^2} \exp(4\rho^2) \\
 & \left. + 7\rho^4 \frac{\frac{z}{\beta I_0} \exp(2\rho^2)}{\left(1 - \frac{z}{\beta I_0} \exp(2\rho^2)\right)} \right\} \quad (9)
 \end{aligned}$$

and similarly for higher order terms. All useful information on the beam evolution gives the radial energy flow, defined as

$$J_T(\rho, z) = |e|^2 \frac{\partial \phi}{\partial \rho}, \quad \phi \cong \tan \phi = \frac{\text{Im}[e(\rho, z)]}{\text{Re}[e(\rho, z)]} = \frac{e_1(\rho, z) + 0(f^2)}{e_0(\rho, z) + 0(f^2)} \quad (10)$$

If we neglect terms of the order of f^2 , the phase can be calculated using eqs. (6) to (8). This leads to

$$\begin{aligned}
 \phi(\rho, z) = & f 4 \beta I_0 \left\{ (1-2\rho^2) \exp[-2\rho^2] \ln \left(1 - \frac{z}{\beta I_0} \exp[2\rho^2]\right) - \rho^2 \frac{\frac{z}{\beta I_0}}{1 - \frac{z}{\beta I_0} \exp[2\rho^2]} \right\} \\
 & \quad (11)
 \end{aligned}$$

$$\begin{aligned}
 \frac{\partial \phi}{\partial \rho}(\rho, z) = & f 8 \beta I_0 \rho \left\{ -4(1-\rho^2) \exp[-2\rho^2] \ln \left(1 - \frac{z}{\beta I_0} \exp[2\rho^2]\right) \right. \\
 & \left. - (3-4\rho^2) \frac{\frac{z}{\beta I_0}}{1 - \frac{z}{\beta I_0} \exp[2\rho^2]} - 2\rho^2 \exp[2\rho^2] \frac{\frac{z^2}{\beta^2 I_0^2}}{\left(1 - \frac{z}{\beta I_0} \exp[2\rho^2]\right)^2} \right\}
 \end{aligned}$$

Following Marburger [2] we define an effective beam width in terms of the phase curvature (i.e., the phase gradient)

$$\rho_H = \left\{ \frac{\int |\nabla_T e|^2 \rho d\rho}{\int |\nabla_T e|^2 \rho d\rho} \right\}^{\frac{1}{2}} = \left\{ \frac{\int e e^* \rho d\rho}{\int (\nabla_T e)(\nabla_T e)^* \rho d\rho} \right\}^{\frac{1}{2}} \quad (12)$$

The Marburger effective radius up to the order of f^2 is:

$$\rho_{M_2} = \left[\frac{\int \{e_0 + f^2 e_2\}^2 + f^2 (e_1^2) \} \rho d\rho}{(\nabla_T e_0 + f^2 \nabla_T e_2)^2 + f^2 [(\nabla_T e_1)^2]} \right]^{1/2}$$

To analyze the beam reshaping in the out of axis region, where βI_0 becomes small, the Iscevgi-Lamb solution is approximated by [27]

$$e_0(\rho, z) = \sum_{m=0}^{\infty} p_{2m+1} \kappa^{(2m+1)}(\rho, z) \quad (13)$$

with the first five terms

$$e_0(\rho, z) = I_0 R^{1/2} \exp(-\frac{1}{2}z) - \frac{1}{2} \beta I_0 R^{3/2} \exp(-\frac{3}{2}z) + \frac{5}{8} \beta^2 I_0 R^{5/2} \exp(-\frac{5}{2}z) - \frac{49}{48} \beta^3 I_0 R^{7/2} \exp(-\frac{7}{2}z) + \frac{243}{128} \beta^4 I_0 R^{9/2} \exp(-\frac{9}{2}z) \quad (14)$$

where $R \equiv \exp(-\rho^2) \exp\{\frac{1}{2}\beta I_0 \exp(-2\rho^2)\}$, and $Z = \exp[-\frac{1}{2}z]$ the series is valid for small βI_0 verifying the convergence condition. The approximation (13) is particularly useful for studying the beam stripping behavior at the edges where $\{I = I_0 \exp(-2\rho^2)\}$ is small enough. Introducing (13) in (10), we have

$$\frac{1}{f} \phi(\rho, z) = H_1 z + \frac{1}{2} \beta I_0 R^2 H_3 (\exp(-z) - 1) - \frac{1}{8} \beta^2 I_0^2 R^4 H_5 (\exp(-2z) - 1) + \frac{1}{48} \beta^3 I_0^3 R^6 H_7 (\exp(-3z) - 1) - \frac{1}{384} \beta^4 I_0^4 R^8 H_9 (\exp(-4z) - 1) \quad (15)$$

where (a_j, b_j, c_j) are numerical constants):

$$H_j(\rho, z) = -a_j (1 + \beta \bar{I}_0) + b_j \rho^2 (1 + \beta \bar{I}_0)^2 + c_j \rho^2 \beta \bar{I}_0 \quad (16)$$

The radial structure is such that the transverse energy flux is inward which illustrates the onset of on-axis energy magnification should the beam propagate either in free space or in free space or in the nonlinear medium [6] using numerical methods. The continuation of the two-level medium beyond the validity of the perturbation will enhance the on-axis

magnification sooner [6,7]. To compare our results with [1, 14-16] we have plotted $e_0(\rho, z)$ (Fig. 1.), $\phi(\rho, z)$ (Fig. 2), $e_2(\rho, z)$ (Fig. 3) and $e_2(\rho, z)$ (Fig. 4.) for $\beta = 1$, $f = 1/300$ and $I_0 = 225$.

All graphs as well as our other analysis for different approximations to $e_0(\rho, z)$ show clearly, that for sufficiently large z , the non-linearity predominates over the diffraction as the energy flow changes the direction toward the center of the beam. First, the beam transverse structure reshaped and stripped giving rise to a radially dependent wave-front; for larger values of z beyond the range of validity of the perturbation a small self-focusing takes place also for the inner region of the beam. The zeroth order solution e_0 has only at the input plane ($z=0$) a gaussian profile, later the beam narrows and the profile e_0 is first "peaky" then it develops transverse structure (e.g., radial rings) in the rim of the beam. The trend of inward radial flow is established for the first time both analytically and numerically. Thus, our results confirm the numerical simulations [1, 19-23]. More detailed analytical and numerical solutions will be given elsewhere.

ADDENDUM: At the Fifth Rochester Conference, LeBerre et al. retracted their conjecture that the $C\bar{W}$ on-resonance self-focusing was a computational artifact. They realized that the stripping process had to be included in the analysis [23].

Gibbs et al. have recently observed in highly absorbing sodium vapor [28] the $C\bar{W}$ on-resonance on-axis enhancement (CORE) and is reporting qualitative agreement with the different theoretical studies [29]. Furthermore, J.P. Babuel-Peyrissac, C. Bardin, J.P. Marignier [30] have recently duplicated Boshier's results.

ACKNOWLEDGEMENT: The authors are grateful for the extensive discussions with Prof. H.M. Gibbs and Dr. B.R. Suydam. Awareness of K. Tai and P. Drummond computational results is joyfully acknowledged. The diligent word processing effort of M. Patterson is joyfully appreciated.

REFERENCES

- [1] M.G. Boshier and W.J. Sandle, *Opt. Comm.* 42 371 (1982).
- [2] J.H. Marburger, *Progress in Quantum Electronics*, vol. 4, eds. J.H. Sanders and S. Stenholm (Pergamon Press 1975) p. 35.
- [3] J. G. Bjorkholm and A. Ashkin *Phys. Rev. Lett* 32, 129 (1974).
- [4] A. Javan and P. Kelly *IEEE J. Quantum Electron.* QE-2, 470 (1966).
- [5] D. Grischkowsky *Phys. Rev. Lett.* 24, 866 (1970); D. Grischkowsky and J. Armstrong, *Proc. 3rd Conf. Quantum Optics* (University of Rochester, NY, June 1972), ed. L. Mandel and E. Wolf, pub. by Plenum Press, p. 829; *ibid Phys. Rev. A*, 1566 (1972).
- [6] N. Wright and M.C. Newstein, *Opt. Commun.* 1, 8 (1973).
- [7] F.P. Mattar and M.C. Newstein, *Opt. Comm.* 18, 70 (1976); *Proceedings of the X Congress of the International Commission for Optics, Prague (1975): Recent Advances in Optical Physics*, eds. B. Havelka and J. Blabla, Soc. of Czechoslovak Math. and Phys. (Prague 1975) p. 299; and F.P. Mattar and M.C. Newstein, *IEEE J. Quantum Electronics* QE-13, 507 (1977).
- [8] H.M. Gibbs, B. Bolger and L. Baade, *Opt. Commun.* 18, 199 (1976).
- [9] H.M. Gibbs, B. Bolger, F.P. Mattar, M.C. Newstein, G. Forster and P.E. Toshek, *Phys. Lett.* 37, 1743 (1976).
- [10] F.P. Mattar, G. Forster and P.E. Toshek, *Kvantovaya Elektronika* 5, 1819 (1978).
- [11] J.J. Bannister, H.J. Baker, T.A. Kurg and W.G. McNaught, *Phys. Rev. Lett.* 44, 1062 (1980).
- [12] M.C. Newstein and N. Wright, *IEEE J. Quantum Electronics*, QE10 743 (1974).
- [13] M.C. Newstein and F.P. Mattar, *Laser TAC Meeting*, RLE-MIT, Cambridge, Massachusetts, ed. by S. Ezechieli (1975) and *J. Opt-Soc. Am* 65, 1181 (1975); and F.P. Mattar and M.C. Newstein in *Cooperative Effects in Matter and Radiation* ed. by C.M. Bowden, D.W. Howgate and H.R. Robl (Plenum Press 1977) p. 139.
- [14] M. Le Berre-Rousseau, E. Ressayre and A. Tallet, *Phys. Rev. A* 25 (1982), 1604.

- [15](a) M. LeBerre-Rousseau, F.P. Mattar, E. Ressayre and A. Tallet, Proceedings of the Max Born Centenary Conf., (publ. by SPIE Paper 36901) Sept., 1982; (b) M. Le Berre, E. Ressayre, A. Tallet, H.M. Gibbs, M.C. Rushford, and F.P. Mattar, Fifth Rochester Conference on Coherence and Quantum Optics, 1983.
- [16] M. LeBerre, E. Ressayre and A. Tallet, (a) unpublished report (private communication to H.M. Gibbs and F.P. Mattar, Spring, 1982); and (b) in 'A Purely Absorptive Self-Focusing Does Not Exist.' Abstract digest of Coherent and Quantum Optics Conference V, in Rochester, ed. L. Mandel and E. Wolf, p. 102 (U. of Rochester, Rochester NY.)
- [17] A. Icsevgi and W.E. Lamb Jr., Phys. Rev. 185, 517 (1968).
- [18] S.L. McCall and E.L. Hahn, Phys. Rev. Lett. 28, 308 (1967); and Phys. Rev. 183, 487 (1969).
- [19] F.P. Mattar, Y. Claude and J. Teichman, Calculations with 64-128 points to be published with i) uniform, ii) prescribed rezoned and iii) adaptive rezoned mesh algorithms (see ref. 24).
- [20] H.M. Gibbs and Tai: Using a modification of M. Lax's CFT code for optical resonators studies duplicated Boshier's results, U. of Arizona at Tucson Ariz. Private communication to FPM.
- [21] P. Drummond implicit code reproduced Boshier's on-resonance results with 500-1000 radial points, U. of Rochester, Rochester, NY. Private Communication to FPM.
- [22] See ibid Ref. 16. In the discussion section, LeBerre et al state clearly without any ambiguity that they duplicated the numerical results of Boshier et al [1] using a CW simplified version with uniform mesh of Mattar's code [24]. LeBerre et al tested the stability of the results by changing the integration steps (from 64 to 128 radial shells) and verified that the following two constants of motion continuity of total energy in plane wave and first moment of total energy transport for large Fresnel numbers do hold.
- [23] M. LeBerre, E. Ressayre and A. Tallet, Proceedings of Coherent and Quantum Optics Conference V in Rochester, ed. L. Mandel and E. Wolf (to be published by Plenum Press).
- [24](a) F.P. Mattar, Appl. Phys. 17, 53 (1978), and F.P. Mattar and M.C. Newstein: Proceedings of 7th Conf. on Numerical Simulation of Plasmas, Courant Institute of Mathematical Studies, New York Univ. (June 1975) p. 223; and Comp. Phys. Comm. 20 13 (1980); (b) F.P. Mattar and B.R. Suydam 'A novel rezoned implicit algorithm for the coherent propagation of light in a multi-level System,' Los Alamos National Lab, Tech. Report T-7 LA-UR-82-3370 (Nov. 1982) Los Alamos, New Mexico (to appear in IEEE J. Quantum Electronics) and references herein.

- [25] C.M. Bowden and F.P. Mattar in Proceedings Los Alamos Conference on Optics SPIE 288 364 (1981); and F.P. Mattar and C.M. Bowden, Phys. Rev. A27 345 (1983).
- [27] (a) F.P. Mattar, Ph.D. Thesis, Polytechnic Institute of New York, Brooklyn, NY (Dec. 1975) Appendix A, B and D. (Copies can be obtained from University Microfilm, Ann Arbor, Michigan.)
(b) Private Communication M. LeBerre, E. Ressayre and A. Tallet.
- [27] J. Teichmann and F.P. Mattar, Annual meeting Canadian Physics Association of Physicist and Canadian Astrophysics Society, Victoria, BC, Canada (June, 1983).
- [28] K. Tai, M.C. Rushford, N. Peyghambarian and H.M. Gibbs, Optical Physics Technical Group Discussion at the Annual Meeting of the American Optical Society in New Orleans (October, 1983).
- [29] K. Tai, H.M. Gibbs, M.C. Rushford, N. Peyghambarian, M. Leberre, E. Ressayre, A. Tallet, W.J. Sandle, J. Teichman, F.P. Mattar and P.D. Drummond (submitted to Phys. Rev. Lett.).
- [30] J.P. Babuel-Peyrissac, C. Bardin, J.P. Marignier, DPC (CEN-SACLAY) using F.P. Mattar code with rezoning and stretching [24]. Private communication.

FIGURE CAPTIONS

- Fig. 1 The Zeroth order approximation of the field amplitude $e_0(\rho, z)$ is shown as a functional of z the propagational distance for different values of ρ between $\rho = 0$ and $\rho = 1.5$.
- Fig 2 The profile of the phase $\phi(\rho, z)$ is plotted for different z (for $z=0$, $\phi=0$) a negative curvature is seen to develop as the depth of penetration in the medium increases.
- Fig. 3 The profile of the amplitude $e_1(\rho, z)$, the imaginary component of the field which develops due to the diffraction coupling, is displayed as a function of z . Note the radial variation forming as z increases.
- Fig. 4 The profile of the amplitude $e_2(\rho, z)$. As the penetration depth increases, $e_2(\rho, z)$ increases at the edges of the beam due to the beam stripping.

QUANTUM FLUCTUATIONS IN TWO-COLOR SUPERFLUORESCENCE (SF)
FROM THREE-LEVEL SYSTEM

F. Haake and R. Reibold
Fachbereich Physik, Universität Essen-Gesamthochschule
Essen, F.R. Germany

and

F.P. Mattar*
Physics Department, New York University, New York,
New York 10003, and Spectroscopy Laboratory,
Massachusetts Institute of Technology, Cambridge, Mass. 02139

Abstract

The concomitant effect of dynamic diffraction coupling and quantum initiation are examined rigorously in two-colour SF. The synchronisation of the delays associated with the two-colour SF pulses as observed by Florian et al is reproduced in the plane wave regime and for small Fresnel number per gain length F . Feld's propagation model for SF and Eberly's simulton theory are ascertained by the calculations. The variance of synchronisation is shown as a function of F .

* Jointly supported by DAAD (F.R. Germany) KFA-Julich and U.S.-ONR

QUANTUM FLUCTUATIONS IN TWO-COLOR SUPERFLUORESCENCE
(SF) FROM THREE LEVEL SYSTEMS

F. Haake and R. Reibold
Fachbereich Physik, Universität Essen-Gesamthochschule
Essen, F.R. Germany

and

F.P. Mattar
Physics department, New York University, New York,
New York 10003 and Spectroscopy Laboratory,
Massachusetts Institute of Technology, Cambridge, Massachusetts 02139

Summary

Results of a rigorous numerical simulation of diffraction coupling, radial density variations and quantum initiation are discussed for two-color superfluorescence from a three-level system of a configuration. The calculations agree and interpret for the first time Florian et al's recent experimental observation [1]. The model consists of two-scalar field equations closely intertwined in the generalized three-level ~~inverted~~ Bloch equations [2,3]. The two-transitions are initially inverted. The effect of coherent pump dynamic [4] is not considered here [4] of Feld's propagational model [5] is shown to be relevant to the physical interpretation and modeling as it was for the two-level case studied by Mattar et al [6]. A synchronisation of the delays associated with the two-color SF is always achieved in agreement with Florian's measurements, thus confirming Eberly et al's [7] simulation prediction.

Moreover, when phase and transverse variations are included the synchronisation is altered according to the Fresnel number per gain length F . The physical meaning of F is the ratio of nonlinear medium gain to diffraction loss [9]. For small F the synchronisation prevails however for somewhat large Fresnel where short-scale-length phase and amplitude mode initiations lead to multi-directional output with hot-spots and to the reduction of delays synchronisation. The delay difference statistics are consistent with those of Haake et al [9] for the two level counterpart their Fresnel variation also conformed with Mattar et al [10], Drummond et al [11] and Mostowski et al [12] studies.

1. R. Florian, L.O. Schwan and D. Schmid, Solid State Commun. 42, 55 (1982).
2. F. Haake and R. Reibold, Physics Letters 92A, 29 (1982).
3. F.P. Mattar and J.H. Eberly, Physics and Chemistry of Laser Induced Processes, ed. by R. L. Kompo and B.D. Smith, Springer Verlag 1979; and F.P. Mattar The International Conference on Lasers 1982 (to be published).
4. F.P. Mattar and C.M. Bowden, Phys. Rev. A27, 345 (1983) and Rochester Fifth Quantum and Coherences Optic Conf. (June 1983).
5. J.C. MacGillivray and M.S. Feld, Phys. Rev. A14, 1169 (1976).
6. F.P. Mattar, H.M. Gibbs, S.L. McCall and M.S. Feld, Phys. Rev. Lett. 46, 1123 (1981).
7. M. Konopnicki and J.H. Eberly, Phys. Rev. A24, 313 (1981).
8. C.M. Bowden and F.P. Mattar, Los Alamos Conf. on Optics (April 1981), proceedings published by SPIE, vol. 288, p. 364; International Conference on Excited States and Multi-Resonant Nonlinear Optical Processes, Aussois, France (March 1981) and to be published.
9. F. Haake, S. Haus, H. King, G. Schöber and R. Glauber, Phys. Review A20, 2047 (1979) and ibid A23, 1322 (1981).
10. F.P. Mattar, M. Cormier, Y. Claude, H.M. Gibbs, E. Watson, S.L. McCall and M.S. Feld, Joint U.S. Army-Center for Nonlinear Studies Workshop on Coupled Nonlinear Oscillators held in Los Alamos, New Mexico July 1981 (invited paper) and J. Opt. Soc. Am. 71, 1589 (81); International Conference of Laser, 1981, New Orleans, Louisiana, (invited paper); Phys. Rev. A27, 1427, (1983) and Fifth Rochester Conference on Coherence and Quantum Optics (June 1983).
11. P. Drummond and J.H. Eberly, J. Opt. Soc. Am. 71, 1588 (81) International Conference of Laser 1981, (invited paper); and Rapid Commun. Phys. Rev. A25, 3446 (1982).
12. Mostowski and Sobolewska, Fifth Rochester Conference on Coherence and Quantum Optics, (June 1983).

ON THE PERTURBATIVE THEORY OF THE ONSET OF THE SELF FOCUSING IN
THE PURELY ABSORPTIVE CW OPTICAL BEAM PROPAGATION>

Jiri Teichmann

Department de physique, Universite de Montreal

P.O. Box 6128, Montreal, Canada

and

Yves Claude

Department d'Informatique, Universite de Montreal

P.O. Box 6128, Montreal, Canada

Farrès P. Mattar††

Department de Physico-Chimie, Centre d'Etudes Nucleaires
de Saclay, Gif-sur-Yvette, France and Spectroscopy Laboratory,
Massachusetts Institute of Technology Cambridge, Massachusetts 02139

ABSTRACT

The self-focusing onset of very intense CW optical beam on resonance is studied analytically using perturbational methods. The competitive effects of radially dependent nonlinear absorption of the media and the diffraction spread of the initially gaussian beam are analyzed. The radial variations of the field components, phase and effective beam radius show the beam reshaping and stripping effects in agreement with numerical simulations.

† The development of the numerical program applied to this study was sponsored by the U.S. Army Research office (DAAG23-79-C-0148) and the U.S. office of Naval Research (N000-14-80-C-0175)

†† On extended leave of absence from the Polytechnic Institute of New York, Brooklyn, New York 11201

Introduction.

Recently Boshier and Sandle [1] reported a new phenomenon of CW on-resonance self focusing for very intense beams having intensity larger than the saturation one. This new phenomenon has not occur previously as reviewed by Marburger [2] where less intense beams were studied: The nonlinear susceptibility χ_{NL} vanishes on-resonance excluding the occurrence of self-focusing as observed by Bjorkholm et al [3]; either below the resonance or above the resonance the beam experiences self-lensing phenomenon as predicted by Javan and Kelly [4] and observed by Grishkowsky et al [5]. The coherent (pulsed) on-resonant self-focusing predicted by Newstein et al [6,7] and subsequently ascertained in Sodium [8,9] Neon [9,10] and Iodine [11] could be understood in terms of an instantaneous frequency offset ($\Delta\Omega = \partial\phi/\partial t$), which results from the phase variation initiation due to diffraction. Similar methodology to the one developed by Newstein et al for the transient case [12,13] to treat the diffraction as a perturbation, elucidate the development of the radially dependent phase in the CW regime as shown by LeBerre et al in [14,15]. LeBerre et al used for a base Icsevigi and Lamb's plane wave (CW) implicit solution [17] instead of McCall and Hahn SIT (pulse) solution [18]. The phase curvature was obtained by the competitive effects of radially dependent nonlinear absorption of the medium and the diffraction spreading of the input gaussian beam. A Fresnel number, defined in terms of the (nonlinear medium) Beer length instead of the cell length, characterizes completely with the ratio of the input intensity to the saturation intensity the beam evolution and reshaping. Particular care must be taken in the perturbation treatment to approximate correctly the canonical plane wave solution and to include the transverse boundary edge effects.

Le Berre et al [16] in their first analysis missed the stripping[†] process that takes place at the edge of the canonical solution profile and concluded that this CW self-focusing was a computer artifact. Our attempt was to understand both results and illustrate the physics. Our present approach is perturbational both analytically using two power series development to treat rigorously the edge effect and numerically where the basic solution is exactly solved using implicit algorithm. The analysis led us to understand the evolution of the onset self-focusing from the transverse energy current associated with the phase curvature induced by the amplitude abrupt variation at the edge. The phase and amplitude structures which arise from the perturbation are such that if the beam propagates through free space it will experience an enhancement (magnification) on-axis. Our perturbational results was conform with our rigorous solution [19] as well as with those by Tai [20], Drummond [21] and Le Berre et al (though not accepted as real) [22] and with a recent modified theoretical analysis by Le Berre et al [23] that takes into account of the stripping process.

Equations of motions.

Thus, in recent papers, LeBerre et al [28] discussed analytically

† The stripping mechanism was first recognized by McCall and Hahn [18] in their pulse analysis. They understood that the pulse entering into the resonant medium is not uniform in intensity across its profile. They assumed that the plane-wave analysis of the transparency effect is applicable to small patches of the light wave front anywhere on the profile a modification of the pulse intensity output across the beam profile can be described along the rod. They stated that at a particular radius $r_c \leq r$ where the pulse area falls below π , the light will be absorbed for all $r_c \leq r$ within a few Beer's lengths α^{-1} . Consequently, the outer periphery of the original pencil of light should be stripped away.

the beam reshaping in the case of a CW beam propagating in a purely absorptive medium. Recently, Le Berre et al attempted to demonstrate analytically that the self-focusing, obtained previously by Boshier et al [29] by numerical simulations is due solely to computational artifact despite their obtaining a mesh independent self-focusing with a simplified non-adaptive mesh version of Mattar code [30]. Nevertheless the beam reshaping was thoroughly shown by other numerical approaches [31].

We have therefore reexamined the analytical solution to the propagation problem of CW laser beam in absorbing media using the perturbative treatment.

The propagation of an intense CW light beam in an absorptive medium is described by equation.

$$\frac{\partial}{\partial z} e - i f \nabla_T^2 e = - \frac{1}{2} \frac{e}{1 + \beta |e|^2} \quad (1)$$

where the parameter $\beta = - \frac{|\mu|^2}{\hbar^2} \tau_1 \tau_2$, μ being the dipole moment for atom, τ_1, τ_2 relaxation times in the corresponding Bloch equation. The other parameter, $f \ll 1$, represents the relative magnitude of diffraction with respect to absorption, $f = (1/2 k \alpha w_0^2)^{-1}$, with ' $1/2 k w_0^2$ ' is the inverse diffraction length z_d , while α is the Beer absorption reciprocal length and w_0 being the waist thickness of the beam, $z = (1/2) \alpha \bar{z}$, \bar{z} is the

penetration depth in physical units, $\rho = \frac{r}{w_0}$, ∇_T^2 is the transverse Laplacian in ρ . The complex field amplitude is $e(\rho, z)$.

Thus f as first recognized by Mattar and Newstein (34) is a reciprocal characteristic medium length Fresnel number whereas the geometric reciprocal Fresnel number is $f_g = \frac{z}{k w_0^2}$. Their ratio $f/f_g = \alpha \bar{z}$ total absorption in a medium of length \bar{z} [35].

Using the usual perturbation method, we expand the field amplitude $e(\rho, z)$ in terms of the expansion [36]:

$$e(\rho, z) = \sum_{j=1}^{\infty} f^{2j} e_{2j}(\rho, z) + i \sum_{j=1}^{\infty} f^{(2j+1)} e_{(2j+1)}(\rho, z) \quad (2)$$

$e_j(\rho, z)$ being real.

Introducing eq. (2) into eq. (1), one obtains the following hierarchy of evolution equations [37]

$$\frac{\partial}{\partial z} e_0 = - \frac{1}{2} \frac{e_0}{1 + \beta e_0^2}$$

$$\frac{\partial}{\partial z} e_1 - \nabla_T^2 e_0 = - \frac{1}{2} \frac{1}{1 + \beta e_0^2} e_1$$

$$\frac{\partial}{\partial z} e_2 + \nabla_T^2 e_1 = - \frac{1}{2} \frac{1 - \beta e_0^2}{(1 + \beta e_0^2)^2} e_2 + \frac{1}{2} \frac{\beta e_0}{(1 + \beta e_0^2)^2} e_1^2$$

$$\frac{\partial}{\partial z} e_3 - \nabla_T^2 e_2 = - \frac{1}{2} \frac{1}{1 + \beta e_0^2} e_3 + \frac{\beta e_0}{(1 + \beta e_0^2)^2} e_1 e_2 + \frac{1}{2} \frac{\beta}{(1 + \beta e_0^2)^2} e_1^3$$

$$\begin{aligned} \frac{\partial}{\partial z} e_4 + \nabla_T^2 e_3 = & - \frac{1}{2} \frac{1 - \beta e_0^2}{(1 + \beta e_0^2)^2} e_4 + \frac{1}{2} \beta \frac{3e_0 - \beta e_0^3}{(1 + \beta e_0^2)^3} e_1^2 e_2 \\ & + \beta \frac{e_0}{(1 + \beta e_0^2)^2} e_1 e_3 + \frac{1}{2} \beta \frac{1 - 2\beta e_0^2 - 3\beta^2 e_0^4}{(1 + \beta e_0^2)^4} e_1^2 e_2 \\ & - \frac{1}{2} \beta^2 \frac{e_0 + 2\beta e_0^3 + \beta^2 e_0^5}{(1 + \beta e_0^2)^5} e_1^4 \end{aligned}$$

$$\frac{\partial}{\partial z} e_3 - \nabla_T^2 e_4 = -\frac{1}{2} \frac{1}{(1+\beta e_0^2)} e_5 + \frac{1}{2} \frac{\beta e_0}{(1+\beta e_0^2)^2} (2e_1 e_4 + 2e_2 e_3) + \frac{1}{2} \frac{\beta(e_1 e_2^2 + 3e_2^2 e_3 - \beta^2 e_0^2(3e_1 e_2^2 - 3e_2^2 e_3) - 2\beta^2 e_0 e_1^2 e_2)}{(1+\beta e_0^2)^3} + \frac{\beta^2}{(1+\beta e_0^2)^3} e_1^5 \quad (3)$$

The first three equations coincide with eq. (9) in [36] for $\beta=1$.

The zeroth order approximation in (3) has a well known solution given by Icsevci and Lamb [37]:

$$e_0 \exp \left[\frac{1}{2} \beta e_0^2 \right] = I_0 \exp[-\rho^2] \exp \left[\frac{1}{2} \beta I_0 \exp\{-2\rho^2\} \right] \exp\left[-\frac{1}{2}z\right]$$

Assuming this solution, $e_0(\rho, z)$ as a known function of the normalized variables ρ and z , we obtain for higher order approximations.

$$e_1(z) = e_0(z) \int_0^z [\nabla_T^2 e_0(z')] \frac{1}{e_0(z')} dz'$$

$$e_2(z) = \frac{e_0(z)}{[1+\beta e_0^2(z)]} \int_0^z \left[-\nabla_T^2 e_2(z') + \frac{\beta}{2} \frac{e_0(z') e_1^2(z')}{[1+\beta e_0^2(z')]^2} \right] \frac{1+\beta e_0^2(z')}{e_0(z')} dz'$$

$$e_3(z) = e_0(z) \int_0^z \left[\nabla_T^2 e_3(z') + \frac{\beta e_0(z') e_1(z') e_2(z')}{[1+\beta e_0^2(z')]^2} + \frac{1}{2} \frac{\beta e_1^3(z')}{[1+\beta e_0^2(z')]^2} \right] \dots \cdot \frac{1}{e_0(z')} dz'$$

$$e_4(z) = \frac{e_0(z)}{[1+\beta e_0^2(z)]} \int_0^z \left[-\nabla_T^2 e_4(z') + \frac{1}{2\beta} \frac{3e_0(z') - \beta e_0^3(z')}{[1+\beta e_0^2(z')]^3} e_2^2(z') + \beta \frac{e_0(z') e_1(z') e_3(z')}{[1+\beta e_0^2(z')]^2} + \frac{1}{2\beta} \frac{1-2\beta e_0^2(z') - 3\beta^2 e_0^4(z')}{[1+\beta e_0^2(z')]^4} e_1^2(z') e_2(z') - \frac{1}{2\beta^2} \frac{e_0(z') + 2\beta e_0^3(z') + \beta^2 e_0^5(z')}{[1+\beta e_0^2(z')]^5} e_1^4(z') \right] \frac{1+\beta e_0^2(z')}{e_0(z')} dz'$$

$$\begin{aligned}
 e_3(z) = & e_0(z) \int_0^z \left\{ \nabla_T^2 e_4(z') + \frac{1}{2} \beta \frac{e_0(z') [2e_1(z')e_4(z') + 2e_2(z')e_3(z')]}{(1+\beta e_0^2(z'))^2} \right. \\
 & + \frac{1}{2} \beta \frac{(e_1(z')e_2^2(z') + 3e_1^2(z')e_3(z')) - \beta e_0^2(z') (3e_1(z')e_2^2(z') - 3e_1^2(z')e_3(z')) - 2\beta e_0(z')e_1^3(z')e_2(z')}{[1+\beta e_0^2(z')]^3} \\
 & \left. + \frac{\beta^2}{(1+\beta e_0^2(z'))^3} e_1^5(z') \right\} \frac{1}{e_0(z')} dz' \quad (4)
 \end{aligned}$$

Here we have assumed that $e_j(\rho, z) = 0$ for $j \neq 0$ at $z = 0$. In the case of very intense CW beam, as considered in [38] where the on-axis input intensity $I_0 \gg 1$, the solutions (4) can be rather simplified.

$$\begin{aligned}
 e_1(z) &= e_0(z) \int_0^z [\nabla_T^2 e_0(z')] \frac{1}{e_0(z')} dz' \\
 e_2(z) &\cong \frac{1}{e_0(z)} \int_0^z [-\nabla_T^2 e_1(z') + \frac{1}{2} \frac{1}{\beta} \frac{e_1^2(z')}{e_0^3(z')}] e_0(z') dz' \\
 e_3(z) &\cong e_0(z) \int_0^z [\nabla_T^2 e_2(z') + \frac{1}{\beta} \frac{e_1(z')e_2(z')}{e_0^3(z')} + \frac{1}{2} \frac{1}{\beta} \frac{e_1^3(z')}{e_0^4(z')}] \frac{1}{e_0(z')} dz' \\
 e_4(z) &\cong \frac{1}{e_0(z)} \int_0^z [-\nabla_T^2 e_3(z') + \frac{1}{2} \frac{1}{\beta^2} \frac{3-\beta e_0^2(z')}{e_0^5(z')} e_2^2(z') + \frac{1}{\beta} \frac{e_1(z')e_3(z')}{e_0^3(z')} \\
 &\quad + \frac{1}{2} \frac{1}{\beta^3} \frac{1-2\beta e_0^2(z')-3\beta^2 e_0^4(z')}{e_0^8(z')} e_1^2(z')e_2(z') \\
 &\quad - \frac{1}{2} \frac{1}{\beta^3} \frac{1+2\beta e_0^2(z')+\beta^2 e_0^4(z')}{e_0^9(z')} e_1^4(z')] e_0(z') dz' \\
 e_5(z) &\cong e_0(z) \int_0^z [\nabla_T^2 e_4(z') + (\frac{e_1(z')e_4(z') + e_2(z')e_3(z')}{\beta e_0^3})
 \end{aligned}$$

$$\begin{aligned}
 & + \frac{1}{2} \{ \beta e_1(z') e_2^2(z') + 3 e_1^2(z') e_3(z') - \beta^2 e_0^2(z') (3 e_1(z') e_2^2(z') - 3 e_1^2(z') e_3(z')) \\
 & - 2 \beta^2 e_0(z') e_1^3(z') e_2(z') + e_1^5(z') \} / \beta^3 e_0^3(z') \} \frac{1}{e_0(z')} dz'
 \end{aligned} \quad (5)$$

For $\beta I_0 \gg 1$, the Icsevgi-Lamb solution (5) can be following ref [39] approximated for an initially gaussian profile by:

$$\begin{aligned}
 I(\rho, z) &= I_0(\rho, z=0) - \frac{z}{\beta} \\
 I(\rho, z) &= I_0 \exp[-2\rho^2] - \frac{z}{\beta}
 \end{aligned} \quad (6)$$

which is a good approximation for the central region of the beam, where

$$\frac{z}{\beta} < I_0 \exp[-2\rho^2]$$

Then

$$e_0(\rho, z) = [I_0 \exp[-2\rho^2] - \frac{z}{\beta}]^{\frac{1}{2}}$$

with exception of the close vicinity of the point $\frac{z}{\beta} = I_0 \exp[-2\rho^2]$. For the first order solution we have:

$$\begin{aligned}
 e_1(\rho, z) &= 4\beta I_0 \{ (1-2\rho^2) \exp[-2\rho^2] \ln [1 - (z/\beta I_0) \exp[2\rho^2]] \dots \\
 &\quad - \rho^2 \frac{(z/\beta I_0)}{1 - (z/\beta I_0) \exp[2\rho^2]} \} \cdot \{ I_0 \exp[-2\rho^2] - z/\beta \}^{\frac{1}{2}}
 \end{aligned} \quad (7)$$

$$\begin{aligned}
 e_2(\rho, z) &= \frac{8\beta^2 I_0}{(1 - \frac{z}{\beta I_0} \exp[2\rho^2])^{\frac{5}{2}}} \exp[-5\rho^2] \{ -(1-2\rho^2)^2 (1 - \frac{z}{\beta I_0} \exp[2\rho^2]) \ln^2 (1 - \frac{z}{\beta I_0} \exp[2\rho^2]) \dots \\
 &\quad + [(-6\rho^2 + 20\rho^4) + (14\rho^2 - 12\rho^4) (1 - \frac{z}{\beta I_0} \exp[2\rho^2]) - 4(1 - 4\rho^2 + 2\rho^4) (1 - \frac{z}{\beta I_0} \exp[2\rho^2])^2] \cdot
 \end{aligned}$$

$$\begin{aligned} & \cdot \ln(1 - \frac{z}{\beta I_0} \exp(2\rho^2)) + (-4 + 24\rho^2 - 7\rho^4) \frac{z}{\beta I_0} \exp(2\rho^2) + (5 - 34\rho^2 + 24\rho^4) \frac{z^2}{\beta^2 I_0^2} \exp(4\rho^2) \\ & + 7\rho^4 \frac{\frac{z}{\beta I_0} \exp(2\rho^2)}{(1 - \frac{z}{\beta I_0} \exp(2\rho^2))} \} \end{aligned} \quad (8)$$

and similarly for higher order terms. All useful information on the beam evolution gives the radial energy flow, defined as

$$J_T(\rho, z) = |e|^2 \frac{\partial \phi}{\partial \rho}, \quad \phi \cong \tan \phi = \frac{\text{Im}[e(\rho, z)]}{\text{Re}[e(\rho, z)]} = \frac{e_1(\rho, z) + \sigma(f^2)}{e_0(\rho, z) + \delta(f^2)} \quad (9)$$

If we neglect terms of the order of f^2 , the phase can be calculated using eqs. (6) to (8). This leads to

$$\phi(\rho, z) \cong f 4 \beta I_0 \{ (1 - 2\rho^2) \exp[-2\rho^2] \ln(1 - \frac{z}{\beta I_0} \exp[2\rho^2]) - \rho^2 \frac{\frac{z}{\beta I_0}}{1 - \frac{z}{\beta I_0} \exp[2\rho^2]} \} \quad (10)$$

$$\begin{aligned} \frac{\partial \phi}{\partial \rho}(\rho, z) & \cong f 8 \beta I_0 \rho \{ -4(1 - \rho^2) \exp[-2\rho^2] \ln(1 - \frac{z}{\beta I_0} \exp[2\rho^2]) \\ & - (3 - 4\rho^2) \frac{\frac{z}{\beta I_0}}{1 - \frac{z}{\beta I_0} \exp[2\rho^2]} - 2\rho^2 \exp[2\rho^2] \frac{\frac{z^2}{\beta^2 I_0^2}}{(1 - \frac{z}{\beta I_0} \exp[2\rho^2])^2} \} \end{aligned}$$

Following Marburger [40] we define an effective beam width in terms of the phase curvature (i.e., the phase gradient)

$$\rho_M = \left\{ \frac{\int |e|^2 \rho d\rho}{\int |\nabla_T e|^2 \rho d\rho} \right\}^{\frac{1}{2}} = \left\{ \frac{\int e e^* \rho d\rho}{\int (\nabla_T e) (\nabla_T e)^* \rho d\rho} \right\}^{\frac{1}{2}}$$

The zero order Marburger effective radius is

$$\rho_{H_0} = \left[\frac{\int e_0^2 \rho d\rho}{\int |\nabla_T e_0|^2 \rho d\rho} \right]^{\frac{1}{2}} = \left\{ \frac{[1 - \exp[-\rho_{\max}^2] - (z/2\beta)\rho_{\max}^2]}{2[1 + \exp[-4\rho_{\max}^2]\{4\rho_{\max}^{-1}\}]} \right\}^{\frac{1}{2}}$$

the refined radii up to the f and f^2 order in e are:

$$\begin{aligned} \rho_{H_1} &\cong \left[\frac{\int (e_0^2 + f^2 e_1^2) \rho d\rho}{\int \{(\nabla_T e_0)^2 + f^2 (\nabla_T e_1)^2\} \rho d\rho} \right]^{\frac{1}{2}} \\ &= \left[\frac{\int e_0^2 (1 + f^2 \phi^2) \rho d\rho}{\int \{(\partial_\rho e_0)^2 + f^2 (\phi \partial_\rho e_0 + e_0 \partial_\rho \phi)^2\} \rho d\rho} \right]^{\frac{1}{2}} \\ &\quad \int \{e_0 + f^2 e_2\}^2 + f^2 (e_1^2) \rho d\rho \\ \rho_{H_2} &= \left[\frac{\int (e_0 + f^2 e_2)^2 + f^2 (e_1^2) \rho d\rho}{(\nabla_T e_0 + f^2 \nabla_T e_2)^2 + f^2 (\nabla_T e_1)^2} \right]^{\frac{1}{2}} \end{aligned}$$

To compare our results [40] with [41], we have plotted $\frac{\partial \phi}{\partial \rho}(\rho, z)$, $J_T(\rho, z)$, $\rho_H(z)$ for $f = \frac{1}{30}$, $I = 100$, $0 \leq \rho \leq 1.2$, $0 \leq z \leq 10-15$ neglecting terms $\sim f^2$ in (8) (such that $e_0 \geq f e_1 \geq f^2 e_2$. e_2 and e_T are also plotted to the order of f^4 and also for $f = 1/500$. All graphs as well as our other analysis for different approximations to $e_0(\rho, z)$ show clearly, that for sufficiently large z , the nonlinearity predominates over the diffraction as the energy flow changes the direction toward the center of the beam. First, the beam transverse structure reshaped and stripped giving rise to a radially dependent wave-front; for larger values of z the self-focusing takes place also for the inner region of the beam. Thus, one can conclude that, in case of propagation of the optical beam in purely absorptive media, reshaping and self-trapping takes place for intense beam ($I_0 \gg 1$).

To ascertain this conclusion, the profile of the most pertinent function is displayed for different penetrations distances $z = 0, 1, 10, 20, 30, 40, 50$. Should one use Leberre et al's approach outlined in reference 16a the validity of all calculations and graphs is controlled by the condition $z/\beta < I_0 \exp[2\rho^2]$. To maintain the precision to several percent we one would have to discontinue the calculations for larger z as soon as ' $z/\beta = 0.95 I_0 \exp[-2\rho^2]$ ' is reached. Thus the validity of the theory LeBerre et al in ref [16a] is radially dependent. All the processes of interest develop before the validity condition breaks down. The zeroth order solution e_0 has only a gaussian profile, at the input plane ($z=0$) later on the beam narrows and the profile e_0 is first "peaky" then it develops transverse structure (e.g., radial rings) in the rim of the beam as shown in Fig. 7.

The most interesting process such as rapid variation of the phase, field components ($e_j(\rho, z)$) and radial energy flux takes place near the edges of the beam. To be able to describe these stripping effects accurately one has to use more precise approximation for the zeroth-order field $e_0(\rho, z)$ than as given in eq. (6) from the Icsevgi-Lamb solution [17] for $e_0(\rho, z)$, namely

$$I(\rho, z) \exp[\beta I(\rho, z)]^n = I_0(\rho, z) \exp[\beta I_0(\rho, z_0)] \exp[-z] \quad (11)$$

we can construct via the method of consecutive approximations the next order approximation to the expression (6):

$$e_0(\rho, z) = \{I_0 \exp[-2\rho^2] - \frac{z}{\beta} - \frac{1}{\beta} \ln(1 - \frac{z}{\beta I_0} \exp[+2\rho^2])\}^{1/2} \quad (12)$$

where again I_0 is the initial beam intensity at $z=0$. This approximation gives better description of processes in the central region and in the vicinity of beam edges. E.g. the phase $\phi_1(\rho, z)$ is given now by

$$\phi(\rho, z) = \frac{1}{2} f \cdot \nabla_T^2 \int_0^z \ln F(\rho, z) dz + \frac{1}{4} f \cdot \int_0^z \left(\frac{\partial}{\partial \rho} \ln F(\rho, z) \right)^2 dz \quad (13)$$

$$\text{where } F_1(\rho, z) = I_0 \exp[2\rho^2] - \frac{z}{\beta} - \frac{1}{\beta} \ln \left(1 - \frac{z}{\beta I_0} \exp[2\rho^2] \right) \quad (14)$$

$$\text{or } \phi(\rho, z) = f \cdot \int_0^z \left\{ 8\rho^2 \frac{F_3}{F_1} - 4\rho^2 \frac{F_2^2}{F_1^2} - 4 \frac{F_2}{F_1} \right\} dz \quad (15)$$

$$\text{where } F_2 = I_0 \exp[-2\rho^2] + \frac{z}{\beta^2 I_0} \frac{1}{\frac{z}{\beta I_0} - \exp[-2\rho^2]} \quad (16)$$

$$F_3 = I_0 \exp[-2\rho^2] + \frac{z}{\beta^2 I_0} \frac{\exp[-2\rho^2]}{\left(\frac{z}{\beta I_0} - \exp[2\rho^2] \right)} \quad (17)$$

Still better approximation to the zeroth order field $\rho_0(\rho, z)$ at the beam edges, can be obtained by developing the Icsevgi and Lamb' solution in a series.

Instead, one should solve rigorously the Icsevgi and Lamb' solution [17] for small values of βI by using numerical methods or by developing the Icsevgi and Lamb' solution, namely

$$e_0 \exp \left[\frac{1}{2} \beta e_0^2 \right] = I_0 \exp[-\rho^2] \exp \left[\frac{1}{2} \beta I_0 \exp\{-2\rho^2\} \right] \exp\left[-\frac{1}{2} z\right] \quad (18)$$

in a series for $\rho > 0.95 \rho_c$

with $\rho_c = \min \left(\rho_{\max}, \sqrt{0.5 \ln \left(\frac{\beta I_0}{z} \right)} \right)$

$$e_0(\rho, z) = \sum_{m=0}^{\infty} p_{2m+1} K^{(2m+1)}(\rho, z) \quad (19)$$

with $K = I_0 R Z^{1/2}$

with the first five terms

$$e_0(\rho, z) = I_0 R \exp(-\frac{1}{2}z) - \frac{1}{2}\beta I_0^3 R^3 \exp(-\frac{3}{2}z) + \frac{5}{8}\beta^2 I_0^5 R^5 \exp(-\frac{5}{2}z) - \frac{49}{48}\beta^3 I_0^7 R^7 \exp(-\frac{7}{2}z) + \frac{243}{128}\beta^4 I_0^9 R^9 \exp(-\frac{9}{2}z) \quad (20)$$

where $R \equiv \exp(-\rho^2) \exp\{\frac{1}{2}\beta I_0 \exp(-2\rho^2)\}$ and $Z = \exp[-\frac{1}{2}z]$. The series is valid for small βI_0 verifying the convergence condition

$$\beta I_0 R^2 \exp(-z) \ll 1 \quad (21)$$

The approximation (20) is particularly useful for studying the beam stripping behavior at the edges where $\bar{I}_0 = I_0 \exp(-2\rho^2)$ is small enough (is near the edges). Introducing (20) in (9),

$$\begin{aligned} \frac{1}{f} \phi(\rho, z) = & H_1 z + \frac{1}{2} \beta I_0 R^2 H_3 (\exp(-z)-1) - \frac{1}{8} \beta^2 I_0^3 R^4 H_5 (\exp(-2z)-1) \\ & + \frac{1}{48} \beta^3 I_0^5 R^6 H_7 (\exp(-3z)-1) - \frac{1}{384} \beta^4 I_0^7 R^8 H_9 (\exp(-4z)-1) \end{aligned} \quad (22)$$

where:

$$H_j(\rho, z) = -a_j(1+\beta\bar{I}_0) + b_j\rho^2(1+\beta\bar{I}_0)^2 + c_j\rho^2\beta\bar{I}_0 \quad (23)$$

$$H'_j = \frac{\partial H_j}{\partial \rho} = 2b_j\rho(1+\beta\bar{I}_0)^2 - 8b_j\rho^3(1+\beta\bar{I}_0)\beta\bar{I}_0 + (4a_j + 2c_j)\rho\beta\bar{I}_0 - 4c_j\rho^3\beta\bar{I}_0 \quad (24)$$

and

$$\begin{aligned} \nabla_T^2 H_j &= 4b_j(1+\beta\bar{I}_0)^2 - 48b_j\rho^2(1+\beta\bar{I}_0)\beta\bar{I}_0 + 4(2a_j + c_j)\beta\bar{I}_0 - 8(2a_j + 3c_j)\rho^2\beta\bar{I}_0 \\ &+ 32b_j\rho^4(1+\beta\bar{I}_0)\beta\bar{I}_0 + 32b_j\rho^4\beta^2(\bar{I}_0)^2 + 16c_j\rho^4\beta\bar{I}_0 \end{aligned} \quad (25)$$

Consequently the phase gradient we obtain is,

$$\begin{aligned} \frac{1}{f} \frac{\partial \phi(\rho, z)}{\partial \rho} &= H'_1 z + \frac{1}{2} \beta I_0 R^2 (H'_3 - 4\rho(1+\beta\bar{I}_0)H_3) (\exp(-z)-1) \\ &- \frac{1}{8} \beta^2 I_0^2 R^4 (H'_5 - 8\rho(1+\beta\bar{I}_0)H_5) (\exp(-2z)-1) \\ &+ \frac{1}{48} \beta^3 I_0^3 R^6 (H'_7 - 12\rho(1+\beta\bar{I}_0)H_7) (\exp(-3z)-1) \\ &- \frac{1}{384} \beta^4 I_0^4 R^8 (H'_9 - 16\rho(1+\beta\bar{I}_0)H_9) (\exp(-4z)-1) \end{aligned} \quad (26)$$

For the first order field term, we have simply from equation (10)

$$e_1(\rho, z) = e_0(\rho, z) \cdot \frac{1}{f} \phi(\rho, z)$$

The multiplication of the series (20) and (22) gives then

$$e_1(\rho, z) = \sum_{m=1}^4 z A_m \exp\left(-\frac{(2m-1)z}{2}\right) + \sum_{m=1}^7 B_m \exp\left(-\frac{(2m-1)z}{2}\right) \quad (27)$$

where $A_j = A_j(\rho)$, $B_j = B_j(\rho)$, are defined from (20), (22), see ref [49]

for details. The next order field for $\beta e_0^2 \ll 1$ is given by

$$e_2(\rho, z) = e_0(\rho, z) \int_0^z \{ (-\nabla_T^2 e_1(\rho, z)) e_0^{-1}(\rho, z) + \frac{\beta}{2} e_1^2(\rho, z) \} dz \quad (28)$$

by integrating, one obtains for

$$e_2(\rho, z) = e_0(\rho, z) \Psi_E(\rho, z) \quad (E \text{ stands for edge of numerical grid}) \quad (29)$$

$$\begin{aligned} \Psi_E(\rho, z) = & -I_0^{-1/2} R^{-1} (\nabla_T^2 B_1) z - \frac{1}{2} I_0^{-1/2} R^{-1} (\nabla_T^2 A_1) z^2 \\ & + (I_0^{-1/2} R^{-1} (\nabla_T^2 A_2) + \frac{\beta}{2} I_0^{+1/2} R (\nabla_T^2 A_1) - \beta A_1 B_1) ((1+z) \exp(-z) - 1) \\ & + (I_0^{-1/2} R^{-1} (\nabla_T^2 A_3) + \frac{\beta}{2} I_0^{+1/2} R (\nabla_T^2 A_2) - \frac{3}{8} \beta^2 I_0^{3/2} R^3 (\nabla_T^2 A_1) - \beta A_1 B_2 - \beta A_2 B_1) \cdot \\ & \quad ((\frac{1}{4} + \frac{z}{2}) \exp(-2z) - \frac{1}{4}) \\ & - \frac{\beta}{2} A_1^2 ((z^2 + 2z + 2) \exp(-z) - 2) - \frac{\beta}{2} A_1 A_2 ((z^2 + z + 1) \exp(-2z) - \frac{1}{2}) \\ & + (I_0^{-1/2} R^{-1} (\nabla_T^2 B_2) + \frac{\beta}{2} I_0^{1/2} R (\nabla_T^2 B_1) - \frac{\beta}{2} B_1^2) \exp(-z) - 1) \\ & + \frac{1}{2} (I_0^{-1/2} R^{-1} (\nabla_T^2 B_3) + \frac{\beta}{2} I_0^{1/2} R (\nabla_T^2 B_2) - \frac{3}{8} \beta^2 I_0^{3/2} R^3 (\nabla_T^2 B_1) - \frac{1}{2} \beta \beta_1 \beta_2) \\ & \quad (\exp(-2z) - 1) \end{aligned} \quad (30)$$

$$\begin{aligned} A_1 &= I_0^{1/2} H_1 R, \quad A_2 = -\frac{\beta}{2} I_0^{3/2} R^3 H_1, \quad A_3 = \frac{5}{8} \beta^2 I_0^{5/2} R^5 H_1, \\ B_1 &= -\frac{1}{2} \beta I_0^{3/2} R^3 H_3 + \frac{1}{8} \beta^2 I_0^{5/2} R^5 H_5 - \frac{1}{48} \beta^3 I_0^{7/2} R^7 H_7 \\ B_2 &= \frac{1}{4} \beta^2 I_0^{5/2} R^5 H_3 - \frac{1}{16} \beta^3 I_0^{7/2} R^7 H_5 - \frac{1}{96} \beta^4 I_0^{9/2} R^9 H_7 \\ B_3 &= -\frac{5}{16} \beta^3 I_0^{7/2} R^7 H_3 + \frac{5}{64} \beta^4 I_0^{9/2} R^9 H_5 - \frac{5}{384} \beta^5 I_0^{11/2} R^{11} H_7 \end{aligned} \quad (31)$$

Another power series is needed to be developed for the transition region where $2.0 < e_0 < 0.5$ to insure continuity of the derivatives. The intermediate region solution was obtained by developing into power

series the logarithm of Icsevgi and Lamb's exact implicit solution. (See fig. 15) Take the logarithm of both sides of equation (18)

$$\ln e_0 + \frac{1}{2} \beta e_0^2 = \ln I_0^{\frac{1}{2}} + (\frac{1}{2} \beta I_0 \exp[-2\rho^2] - \frac{1}{2} z - \rho^2) = \ln K \quad (32)$$

For $e_0 < 2$ we have

$$\ln e_0 = + \sum_{n=1}^{\infty} (-1)^{n+1} \left(\frac{e_0 - 1}{n} \right)^n \quad (33)$$

equivalently,

$$e_0(\rho, z) = 1 + \sum_{n=1}^{\infty} p_n F^n \quad (27) \quad F \equiv (1 + \beta)^{-1} [\ln K - \frac{1}{2} \beta] \quad (34)$$

or explicitly

$$F = (1 + \beta)^{-1} [\ln I_0^{\frac{1}{2}} - \frac{1}{2} \beta] + (1 + \beta)^{-1} [\frac{1}{2} \beta I_0 \exp[-2\rho^2] - \rho^2] + (1 + \beta)^{-1} (-\frac{1}{2} z) \quad (35)$$

the first coefficients of the series (34)

$$\begin{aligned} p_1 &= 1; \quad p_2 = \frac{1}{2} \frac{(1-\beta)}{(1+\beta)}; \quad p_3 = \frac{1}{2} \left(\frac{1-\beta}{1+\beta} \right)^2 - \frac{1}{3(1+\beta)} \\ p_4 &= \frac{5}{6} \frac{(\beta-1)}{(1+\beta)^2} + \frac{1}{4(1+\beta)} - \frac{5}{8} \frac{(\beta-1)^3}{(\beta+1)^3} \\ p_5 &= \frac{3}{4} \frac{1-\beta}{(1+\beta)^2} + \frac{1}{3} \frac{1}{(1+\beta)^2} + \frac{7}{8} \frac{(1-\beta)^4}{(1+\beta)^4} - \frac{1}{5(1+\beta)} - \frac{7}{4} \frac{(1-\beta)^2}{(1+\beta)^3} \end{aligned} \quad (36)$$

For $\beta = 1$ we have simply

$$F \equiv \left(\frac{1}{2} \ln I_0 - \frac{1}{4} \right) + \left(\frac{1}{4} I_0 \exp[-2\rho^2] - \frac{1}{2} \rho^2 \right) - \frac{1}{4} z \quad (37)$$

for $2.0 \geq e_0 \geq 0.5$

To calculate the higher order field components, we need the Laplacian which can be defined as

$$(\nabla_T^2 e_0) = \sum_{n=0}^{\infty} A_n F^n \quad (38)$$

with

$$A_n = (n+1) P_{n+1} (\nabla_T^2 F) + (n+2) (n+1) P_{n+2} \left(\frac{\partial F}{\partial \rho}\right)^2 \quad (39)$$

Where

$$(\nabla_T^2 F) = \frac{4}{1+\beta} [2\rho^2 \beta \bar{I}_0 - \beta \bar{I}_0 - 1]; \quad (40)$$

$$\frac{\partial F}{\partial \rho} = - \frac{2\rho}{1+\beta} [1+\beta \bar{I}_0], \quad \bar{I}_0 = I_0 \exp(-2\rho^2) \quad (41)$$

furthermore, for component e_1 with

$$e_0^{-1}(\rho, z) = 1 + c_1 F + c_2 F^2 + \dots = \sum_{n=0}^{\infty} c_n F^n \quad (42)$$

where

$$\begin{aligned} c_0 &= 1, \quad c_1 = -p_1, \quad c_2 = p_1^2 - p_2, \quad c_3 = -p_3 + 2p_1 p_2 - p_1^3, \\ c_4 &= -p_1 (2p_1 p_2 - p_3 - p_1^3) - p_2 (p_1^2 - p_2) + p_1 p_3 - p_4 \end{aligned} \quad (43)$$

Substituting the approximation (29) for e_0 and using (33) we have by analogy to eq (9) for the phase $(F(\rho, z) = \Phi(\rho) - \frac{1}{2(1+\beta)} z)$

Then

$$f^{-1} \Phi(\rho, z) = A_0 z + (A_1 + c_1 A_0) \left(\Phi \cdot z - \frac{1}{4(1+\beta)} z^2\right)$$

$$\begin{aligned}
 & + (A_2 + c_1 A_1 + c_2 A_0) (\phi^2 z - \phi \frac{1}{2(1+\beta)} z^2 + \frac{1}{12(1+\beta)^2} z^3) + \\
 & + (A_3 + c_1 A_2 + c_2 A_1 + c_3 A_0) (\phi^3 z - \frac{3}{4} \phi^2 \frac{z^2}{(1+\beta)} + \frac{1}{4} \phi \frac{z^3}{(1+\beta)^2} \\
 & - \frac{1}{32} \frac{z^4}{(1+\beta)^3}) + \dots
 \end{aligned} \tag{44}$$

$$\text{with } \phi(\rho) = \frac{\ln I_0^{1/2} - 1/2\beta}{1+\beta} + \frac{1/2\beta I_0 \exp[-2\rho^2] - \rho^2}{1+\beta} \tag{45}$$

Finally, for the component e_1

$$e_1(\rho, z) = \frac{1}{f} \phi(\rho, z) e_0(\rho, z) \tag{46}$$

with

$$e_1(\rho, z) = \sum_{n=1}^{\infty} B_n z^n \quad (47), \quad B_n = B_n(\rho), \quad A_j = A_j(\rho), \quad \phi = \phi(\rho) \tag{47}$$

where

$$B_1 = [A_0 + (A_1 + c_1 A_0) \phi + (A_2 + c_1 A_1 + c_2 A_0) \phi^2 + (A_3 + c_1 A_2 + c_2 A_1 + c_3 A_0) \phi^3 + \dots] \cdot$$

$$\cdot [1 + p_1 \phi + p_2 \phi^2 + p_3 \phi^3 + \dots]$$

$$B_2 = - \frac{1}{1+\beta} \left[\frac{1}{4} (A_1 + c_1 A_0) + \frac{1}{2} (A_2 + c_1 A_1 + c_2 A_0) \phi + \frac{3}{4} (A_3 + c_1 A_2 + c_2 A_1 + c_3 A_0) \phi^2 \right] \cdot$$

$$\cdot [1 + p_1 \phi + p_2 \phi^2 + p_3 \phi^3 + \dots]$$

$$- \frac{1}{1+\beta} \left[\frac{1}{2} p_1 + p_2 \phi + \frac{3}{2} p_3 \phi^2 + \dots \right] [A_0 + (A_1 + c_1 A_0) \phi +$$

$$+ (A_2 + c_1 A_1 + c_2 A_0) \phi^2 + (A_3 + c_1 A_2 + c_2 A_1 + c_3 A_0) \phi^3 + \dots]$$

$$B_3 = \frac{1}{(1+\beta)^2} \left[\frac{1}{12} (A_2 + c_1 A_1 + c_2 A_0) + \frac{1}{4} (A_3 + c_1 A_2 + c_2 A_1 + c_3 A_0) \phi + \dots \right] \cdot$$

$$\cdot [1 + p_1 \phi + p_2 \phi^2 + p_3 \phi^3]$$

$$\begin{aligned}
 & + \frac{1}{(1+\beta)^2} \left[\frac{1}{4} (A_1 + c_1 A_0) + \frac{1}{2} (A_2 + c_1 A_1 + c_2 A_0) \phi + \frac{3}{4} (A_3 + c_1 A_2 + c_2 A_1 + c_3 A_0) \phi^2 \right] \cdot \\
 & \quad \cdot \left[\frac{1}{2} p_1 + p_2 \phi + \frac{3}{2} p_3 \phi^2 + \dots \right] \\
 & + \frac{1}{(1+\beta)^2} \left[\frac{1}{4} p_2 + \frac{3}{4} p_3 \phi \right] [A_0 + (A_1 + c_1 A_0) \phi + (A_2 + c_1 A_1 + c_2 A_0) \phi^2 \\
 & + (A_3 + c_1 A_2 + c_2 A_1 + c_3 A_0) \phi^3] \\
 B_4 = & \frac{-1}{(1+\beta)^3} [(A_0 + (A_1 + c_1 A_0) \phi + (A_2 + c_1 A_1 + c_2 A_0) \phi^2 \\
 & + (A_3 + c_1 A_2 + c_2 A_1 + c_3 A_0) \phi^3 + \dots) \left[\frac{1}{8} p_3 + \frac{1}{2} p_4 \phi + \dots \right] \\
 & \frac{-1}{(1+\beta)^3} \left[\frac{1}{2} (A_1 + c_1 A_0) + \frac{1}{2} (A_2 + c_1 A_1 + c_2 A_0) \phi + \frac{3}{4} (A_3 + c_1 A_2 + c_2 A_1 + c_3 A_0) \phi^2 \right] \cdot \\
 & \left[\frac{1}{4} p_2 + \frac{3}{4} p_3 \phi + \dots \right] \quad \dots \quad (\text{continuation next page}) \\
 & \frac{-1}{(1+\beta)^3} \left[\frac{1}{12} (A_2 + c_1 A_1 + c_2 A_0) + \frac{1}{4} (A_3 + c_1 A_2 + c_2 A_1 + c_3 A_0) \phi + \dots \right] \cdot \\
 & \left[\frac{1}{2} p_1 + p_2 \phi + \frac{3}{2} p_3 \phi^2 + 2 p_4 \phi^3 + \dots \right] \\
 & \frac{-1}{(1+\beta)^3} \left[\frac{1}{32} (A_3 + c_1 A_2 + c_2 A_1 + c_3 A_0) + \frac{1}{8} (A_4 + c_1 A_3 + c_2 A_2 + c_3 A_1 + c_4 A_0) \phi + \dots \right] \cdot \\
 & \left[1 + p_1 \phi + p_2 \phi^2 + p_3 \phi^3 + \dots \right]
 \end{aligned} \tag{48}$$

there A_j and ϕ are functions of ρ

For small $e_0 \ll 1$

$$e_2(\rho, z) \simeq e_0 \int_0^z \left[(-\nabla_T^2 e_1) \frac{1}{e_0} + \frac{\beta}{2} e_1^2 \right] dz \tag{49}$$

$$\approx e_0(\phi, z) \psi_I(p, z) \quad (\psi_I \text{ stands for the intermediate case}) \quad (50)$$

$$\begin{aligned} \psi_I(\phi, z) \approx & \left\{ -\frac{1}{2} [(1+c_1\phi+c_2\phi^2+c_3\phi^3)(\nabla_T^2 B_1)] \right\} z^2 \\ & - \frac{1}{3} \left\{ \frac{-1}{1+\beta} (\frac{1}{2}c_1+c_2\phi+\frac{3}{2}c_3\phi^2)(\nabla_T^2 B_1) \right\} \\ & + (1+c_1\phi+c_2\phi^2+c_3\phi^3)(\nabla_T^2 B_2) - \frac{\beta}{2} B_1^2 \} z^3 \\ & - \frac{1}{4} \left\{ \left[\frac{1}{(1+\beta)^2} (\frac{1}{4}c_2 + \frac{3}{4}c_3\phi)(\nabla_T^2 B_1) - \frac{1}{1+\beta} (\frac{1}{2}c_1+c_2\phi + \frac{3}{2}c_3\phi^2)(\nabla_T^2 B_2) \right. \right. \\ & \left. \left. + (1+c_1\phi + c_2\phi^2 + c_3\phi^3)(\nabla_T^2 B_3) \right] - \beta B_1 B_2 \right\} z^4 \\ & - \frac{1}{5} \left\{ - \frac{1}{(1+\beta)^3} (\frac{1}{8}c_3)(\nabla_T^2 B_1) + \frac{1}{(1+\beta)^2} (\frac{1}{4}c_2 + \frac{3}{4}c_3\phi)(\nabla_T^2 B_2) \right. \\ & \left. - \frac{1}{1+\beta} (\frac{1}{2}c_1+c_2\phi + \frac{3}{2}c_3\phi^2)(\nabla_T^2 B_3) + (1+c_1\phi + c_2\phi^2 + c_3\phi^3)(\nabla_T^2 B_4) \right\} \\ & - \frac{\beta}{2} -(2B_1 B_3 + B_2) \} z^5 + \dots \end{aligned} \quad (52)$$

Fig. 8a and Fig. 8b display the phase and the imaginary part of the field both arising from the coupling between the various shells each of intensity e_0 . Accordingly, the initial phase is zero. However, the transverse Laplacian associated with the gaussian variation from one shell to the other does not vanish; its accumulation increases along the penetration depth. Both the field e_0 and the perturbation e_1 experience abrupt changes along $\rho = \rho_c(z)$ as shown isometrically in Fig. 10. Through numerical calculation the stripping effect is clearly demonstrated.

Figs. 9, 10 and 12 display the self-action process such as self-phase modulation which lead to the onset of self-lensing (here, on-axis magnification self-focusing) phenomena. The radial structure of the

amplitude and phase will lead to an energy bunching (beam narrowing) in free space. The trend of self-focusing is indicated; it gets accentuated as the beam propagates further into the medium.

Fig. 8 summarizes the profile of the total field in the approximation of Ref 1. The field grows at the center but more rapidly at the edges of the beam. Here, one is severely constrained by the validity of the analytical treatment. Thus, one may not include all the energy at the wings that could flow toward the axis (due to the change of amplitude at the stripping edge which leads into phase gradient evolution).

Fig. 13 shows the on-axis total energy as a function of the propagation distance for various f . The energy is seen to decrease first (i.e., depress to a minimum) then increase (i.e., getting enhanced) establishing a trend conforming to the rigorous calculation of Boshier et al. [5]. The smaller the f , the stronger are the diffraction and the radial absorption as well as the stripping mechanism. Thus, the stronger is the trend to focus and the shorter is the enhancement length should the beam be allowed to propagate through the free space as suggested by Leberre et al in reference [14]. However, if one follows Newstein and Wright [12] and follow the beam propagation in the non-linear medium the trend of on-axis magnification is accentuated. Either propagation beyond the validity of the perturbation theory must be carried out numerically.

Our results confirm the numerical simulations [42]. The discrepancy between the conclusion of [42] and our results (as well as results of numerical simulations) consist in their neglecting the stripping effect and confining the extent of radial width to where the approximation in the solution $e_0(\rho, z)$ is valid as given by equation 6. We have found that the dependence of the phase on ρ and z is rather sensitive on the form of $e_0(\rho, z)$.

The validity of the perturbation holds as long as $e_0 \gg fe_1 \gg f^2e_2 \gg f^3e_3 \gg f^4e_4 \dots$ when any of the inequalities is not satisfied, the range of the validity has been exceeded. At most, the total on-axis field strength builds up to $\sqrt{2}e_0$ or $\sqrt{5}e_0$ if e_0 or e_1 and e_2 orders are included. As in SIT, this perturbational holds as long as the dynamic diffraction can be treated as a small quantity. Fig. 14 displays isometrically the field energy to the second order in e as a function of z . The one-axis enhancement is clearly illustrated. At best, this approach outlines a trend of self-lensing [44] but can never hold in a focal region; as a matter of fact, for tight focusing the paraxial approximation (i.e., the rigorous equation) does not even hold and a corrective longitudinal field correction, as derived by Lax et al [45], must also be calculated. Furthermore, the lack of computational resolution for evaluating correctly the dynamic diffraction term around the focal region has been treated in both Thermal Blooming [46] and SIT Self-focusing [47]. The latter treatment was referenced by Leberre et al. though not studied. An extension outlined in ref [57] deals with the clustering of points not only near the axis but also near the stripping radii when the abrupt changes in amplitude lead to phase variations and transverse energy flux.

Conclusion

The onset of the CW on-resonant self-focusing (on-axis magnification) as computed by Boshier et al, has been elucidated using a perturbational treatment of the diffraction coupling and multiple series developments across the beam profile to map the stripping process at the beam edges. The evolving radial variation of the amplitude and phase will

✓ lead to a subsequent energy on-axis build up (i.e., enhancement and beam narrowing) should the beam be allowed to propagate further in either free space or a nonlinear medium.

ADDENDUM: At the Fifth Rochester Conference, LeBerre et al. retracted their conjecture that the CW on-resonance self-focusing was a computational artifact. They realized that the stripping process had to be included in the analysis. [50]

ACKNOWLEDGEMENT: The authors are grateful for the extensive discussions with Prof. H.M. Gibbs and Dr. B.R. Suydam. Awareness of K. Tai and P. Drummond computational results is joyfully acknowledged. The diligent word processing effort of Fatmatta Kay-Kamara is joyfully appreciated.

REFERENCES

- [1] M.G. Boshier and W.J. Sandle, Opt. Comm. 42 371 (1982).
- [2] J.H. Marburger, Progress in Quantum Electronics, vol. 4, eds. J.H. Sanders and S. Stenholm (Pergamon Press 1975) p. 35.
- [3] J. G. Bjorkholm and A. Ashkin, Phys. Rev. Lett. 32, 129 (1974).
- [4] A. Javan and P. Kelly, IEEE J. Quantum Electron. QE-2, 470 (1966).
- [5] D. Grischkowsky, Phys. Rev. Lett. 24, 866 (1970); D. Grischkowsky and J. Armstrong Proc. 3rd Conf. Quantum Optics (University of Rochester, NY June 1972) ed. L. Mandel and E. Wolf, pub. by Plenum Press p. 829; *ibid* Phys. Rev. A, 1566 (1972).
- [6] N. Wright and M.C. Newstein, Optic Commun. 1, 8 (1973).

- [7] F.P. Mattar and M.C. Newstein, Opt. Comm. 18, 70 (1976); Recent Advances in Optical Physics, eds. B. Havelka and Blabla Soc. of Czechoslovak Math. and Phys. Prague 1975) p. 299; and F.P. Mattar and M.C. Newstein IEEE J. Quantum Electronics QE-13, 507 (1977).
- [8] H.M. Gibbs, B. Bölger and L. Baade, Opt. Commun. 18, 199 (1976).
- [9] H.M. Gibbs, B. Bölger, F.P. Mattar, M.C. Newstein, G. Forster and P.E. Toshek, Phys. Lett. 37, 1743 (1976).
- [10] F.P. Mattar, G. Forster and P.E. Toshek, Kvantovaya Elektronika 5, 1819 (1978).
- [11] J.J. Bannister, H.J. Baker, T.A. Kurg and W.G. McNaught, Phys. Rev. Lett. 44, 1062 (1980).
- [12] M.C. Newstein and N. Wright, IEEE J. Quantum Electronics, QE10 743 (1974).
- [13] M.C. Newstein and F.P. Mattar, Laser TAC meeting, RLE-MIT ed. by S. Ezechieli (1975) and J. Opt-Soc. Am 65, 1181 (1975); and F.P. Mattar and M.C. Newstein in Cooperative Effects in Matter and Radiation ed by C.M. Bowden, D.W. Howgate and H.R. Robl (Plenum Press 1977) p. 139.
- [14] M. Le Berre-Rousseau, E. Ressayre and A. Tallet, Phys. rev. A-25 (1982), 1604.
- [15] (a) M. LeBerre-Rousseau, F.P. Mattar, E. Ressayre and A. Tallet, Proceedings of the Max Born Centenary Conf., (publ. by SPIE Paper 36901) Sept. 1982; (b) M. Le Berre, E. Ressayre, A. Tallet, H.M. Gibbs, M.C. Rushford, and F.P. Mattar, Fifth Rochester Conference on Coherence and Quantum Optics, 1983.
- [16] M. LeBerre, E. Ressayre and A. Tallet, (a) unpublished report; and (b) in 'A Purely Absorptive Self-Focusing Does Not Exist'. Abstract digest of Coherent and Quantum Optics Conference V in Rochester ed. L. Mandel and E. Wolf p. 102 (U. of Rochester, Rochester NY.)
- [17] A. Icsevigi and W.E. Lamb Jr., Phys. Rev. 185, 517 (1968).
- [18] S.L. McCall and E.L. Hahn, Phys Rev. Lett. 28 308 (1967); and Phys. Rev. 183 487 (1969).
- [19] F.P. Mattar, Y. Claude and J. Teichman, Calculations with 64-128 points to be published with i) uniform, ii) prescribed rezoned and iii) adaptive rezoned mesh algorithms:

- [20] H.M. Gibbs and K. Tai: Using a modification of M. Lax's CFT code for optical resonators studies duplicated Boshier's results, U. of Arizona at Tucson Ariz. Private communication to FPM.
- [21] P. Drummond implicit code reproduced Boshier's on-resonance results with 500-1000 radial points, U. of Rochester, Rochester, NY, Private Communication to FPM.
- [22] see ibid Ref. 16 In the discussion section, LeBerre et al state clearly without any ambiguity that they duplicated the numerical results of Boshier et al [1] using a CW simplified version with uniform mesh of Mattar's code [24]. LeBerre et al tested the stability of the results by changing the integration steps (from 64 to 128 radial shells) and verified that the following two constants of motion continuity of total energy in plane wave and first moment of total energy transport for large Fresnel numbers do hold.
- [23] M. LeBerre, E. Ressayre and A. Tallet, Proceedings of Coherent and Quantum Optics Conference V in Rochester ed. L. Mandel and E. Wolf (to be published by Plenum Press).
- [24] (a) F.P. Mattar, Appl. Phys. 17, 53 (1978), and F.P. Mattar and M.C. Newstein: Proceedings of 7th Conf. on Numerical Simulation of Plasmas, Courant Institute of Mathematical Studies, New York Univ. (June 1975) p. 223; and Comp. Phys. Comm. 20 13 (1980); (b) F.P. Mattar and B.R. Suydam' A novel rezoned implicit algorithm for the coherent propagation of light in a multi-level System', Los Alamos National Lab, Tech. Report T-7 LA-UR-82-3370 (Nov. 1982) Los Alamos, New Mexico.
- [25] P.M. Ulrich, Naval Research Lab, Washington, D.C. NRL Tech. Rept. 7706 (1974); K.G. Whiteney, G.L. Nader and P.B. Ulrich, NRL Tech. Rept. 2074 (1977).
- [26] J. Herrman and L. Bradley III, MIT-Lincoln Lab, Laser Technology Program Tech. Rept. LTP-10, and internal note on "Changes of reference wavefront in in the MIT CW nonlinear optics propagation code" (1974) (private communication to FPM).
- [27] H. Breaux, Ballistic Research Laboratory, Tech. Rept., 1723 (1974) Aberdeen Proving Grounds, MD.
- [28] See ibid ref. 14-16
- [29] See ibid ref. 12-13
- [30] See ibid ref. 16a
- [31] See ibid ref. 1
- [32] See ibid ref. 24

- [35] C.M. Bowden and F.P. Mattar in Proceedings Los Alamos Conference on Optics SPIE 288 364 (1981); and F.P. Mattar and C.M. Bowden, Phys. Rev. A27 345 (1983).
- [36] (a) F.P. Mattar, Ph.D. Thesis, Polytechnic Institute of New York, Brooklyn, NY (Dec. 1975) Appendix A, B and D. (Copies can be obtained from University Microfilm, Ann Arbor, Michigan.)
(b) Private Communication M. LeBerre, E. Ressayre and A. Tallet. See *ibid* ref. 16a.
- [37] J. Teichmann and F.P. Mattar, Annual meeting Canadian Physics Association of Physicist and Canadian Astrophysics Society, Victoria, BC, Canada (June 1983).
- [38] See *ibid* ref. 14-16
- [39] See *ibid* ref. 17
- [40] See *ibid* ref. 37; and F.P. Mattar, Y. Claude and J. Teichman (to be published).
- [41] See *ibid* ref. 1; and *ibid* from ref. 14 to ref. 16.
- [42] See *ibid* ref. 25 to ref. 27.
- [43] See *ibid* ref. 16.
- [44] See *ibid* ref. 36a.
- [45] See *ibid* ref. 23.
- [46] M. Lax, W.H. Louisell and W.B. McKnight Phys. Rev. A11, 1365 (1975).
- [47] See *ibid* ref. 25-27.
- [48] See *ibid* ref. 6-13.
- [49] See *ibid* ref. 246.
- [50] See *ibid* ref. 23.

FIGURE CAPTIONS

- Fig. 1 The Zeroth order approximation of the field Intensity $I_0(\rho, z)$ is shown as a functional of z the propagational distance for different values of ρ between $\rho=0$ and $\rho=1.2$ in step of 0.2.
- Fig. 2 The Zeroth order field strength $e_0(\rho, z)$ is shown as a function of z for $0 \leq \rho \leq 1.2$ in steps of $\rho = 0.2$. The graphs are stopped at $z = 0.95$ of the zeros of the theoretical approximation of I_0 described in ref [1].
- Fig. 3. The phase curvature $\frac{\partial \phi}{\partial \rho}$ is shown as a function of z for various radii $0.2 \leq \rho \leq 1.2$. The larger the radius, the quick the phase curvature changes sign from positive to negative value even though $\rho < \rho_c$ as in Ref. [1].
- Fig. 4. The energy flux or transverse energy current J_T is shown as a function of z for various radii $0.2 \leq \rho \leq 1.2$. One can clearly see negative values of energy current which indicate the begining of inflow energy towards the axis (i.e., a tendency of beam self-focusing) despite the fact that $\rho < \rho_c$.
- Fig. 5. The imaginary part of the field e_1 , which is of order f , is plotted as a function of z for various radii up to $\rho < \rho_c$ as in Ref. [1].
- Fig. 6. Marburger's radius $\rho_M = \left[\frac{\int |e|^2 \rho d\rho}{\int |\nabla_T e|^2 \rho d\rho} \right]^{1/2}$ is shown as a function of z for the Iscevgi and Lamb's solution and for the fe_1 correction. Beam stripping and beam narrowing are respectively illustrated.
- Fig. 7 The approximated solution of Iscevgi and Lamb $e_0(\rho, z) \cong I_0^{1/2} \exp[-\rho^2] \{1 - (z/\beta I_0) \exp[+2\rho^2]\}^{1/2}$ is shown as a function of ρ for different values of $z = 0, 10, 20, 30, 40, 50$ up to $\rho < \rho_c$ as in Ref. [1].

- Fig. 8a. The profile of the phase $\phi(\rho, z)$ is plotted for different $z = 10, 20, 30, 40, 50$ (for $z=0$, $\phi=0$) a negative curvature is seen to develop as the depth of penetration in the medium increases up to $\rho < \rho_c$ as in Ref. [1].
- Fig. 8b. The profile of the amplitude $e_1(\rho, z)$, the imaginary component of the field which develops due to the diffraction coupling, is displayed as a function of $z = 10, 20, 30, 40, 50$. Note the radial variation forming as z increases even though $\rho < \rho_c$ as in Ref. [1].
- Fig. 9 The field strengths e_0 and e_1 are shown as isometrics plots in ρ and z to illustrate the physical process of stripping for $I_0 = 100$, and $I_0 = 225$.
- Fig. 10 The wave front $\partial\phi/\partial\rho$ profile is drawn as a function of $z = 10, 20, 30, 40, 50$. The negative value illustrates the self-lensing trend even though $\rho < \rho_c$ as in Ref. [1].
- Fig. 11 The total field $(e_0^2 + f^2 e_1^2)^{1/2}$ profile is drawn for different penetration distances $z = 10, 20, 30, 40, 50$ for $\rho < \rho_c$ as in Ref. [1].
- Fig. 12 The transverse energy current (radial flux) J_T is plotted versus ρ for different z . The rapidity of the change of curvature into negative value is striking even though $\rho < \rho_c$ as in Ref. [1].
- Fig. 13 The on-axis total field is plotted versus z to display first a decrease then subsequently an enhancement (i.e., the onset of the self-focusing as seen by Boshier et al. [5]. This is done for different values of f .
- Fig. 14 The total field energy $\{e^2 = (e_0 + f^2 e_2)^2 + f^2 e_1^2\}$ is plotted isometrically versus ρ and z clearly displaying the onset of a self-focusing (i.e., on-axis magnification).

Fig. 15 Profile of the canonical field e_0 for three distance of propagations illustrating the two power series development around the stripping region - part a of the grap represent the approximation of Icsevgi and Lamb solution as outlined by LeBerre et al (see ref. 16); part b represent the intermediate region defined $2.0 \geq e_0 \geq 0.5$; part c represent the edge when $e_0 \leq 0.5$.

ACKNOWLEDGMENTS

Extensive discussions with Prof. H.M. Gibbs are gratefully appreciated. Availability of Tai and Drummond's computational results is joyfully acknowledged.

FIG 1

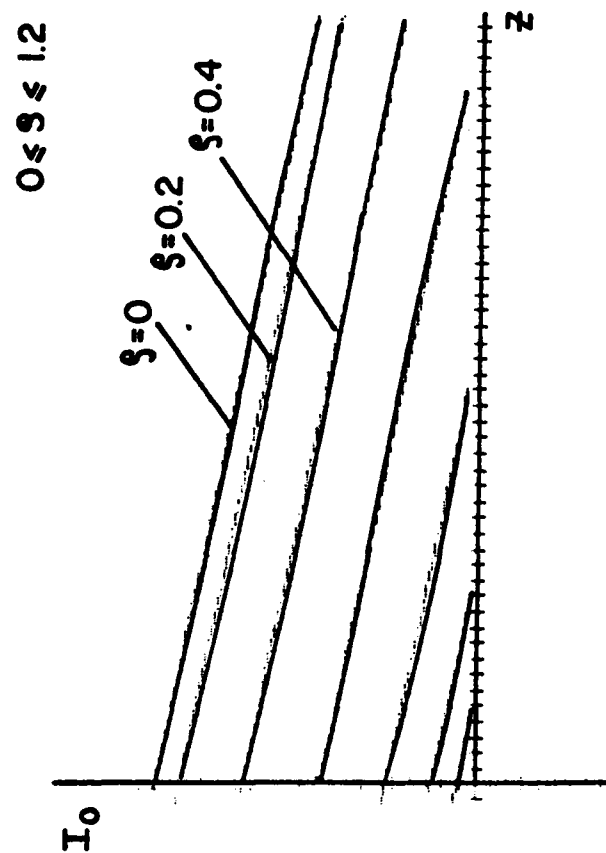


FIG 2

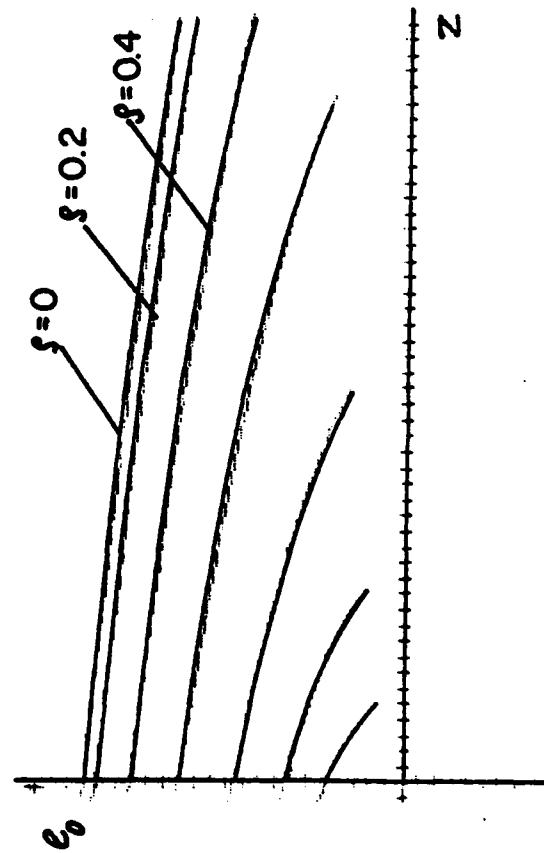


FIG 3

$\frac{\partial \phi}{\partial z}$

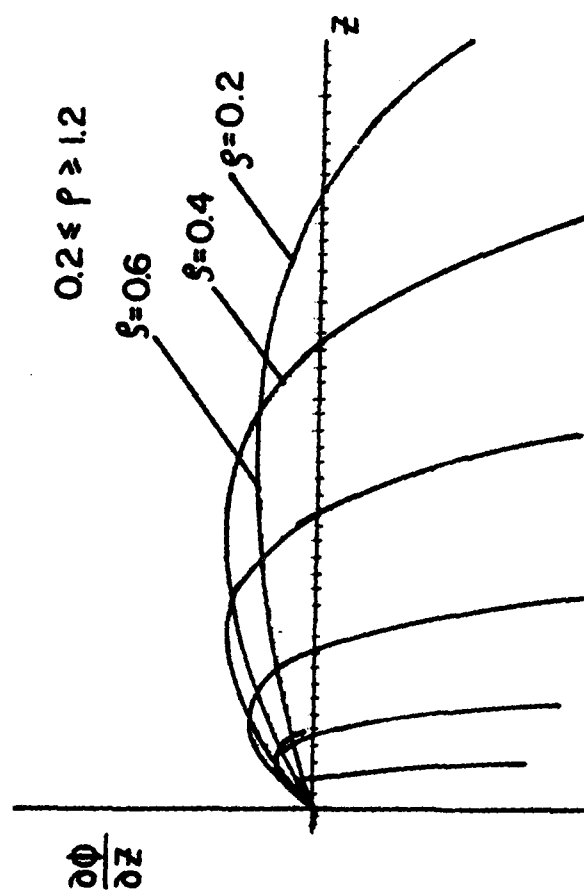


FIG 4

FIG 4

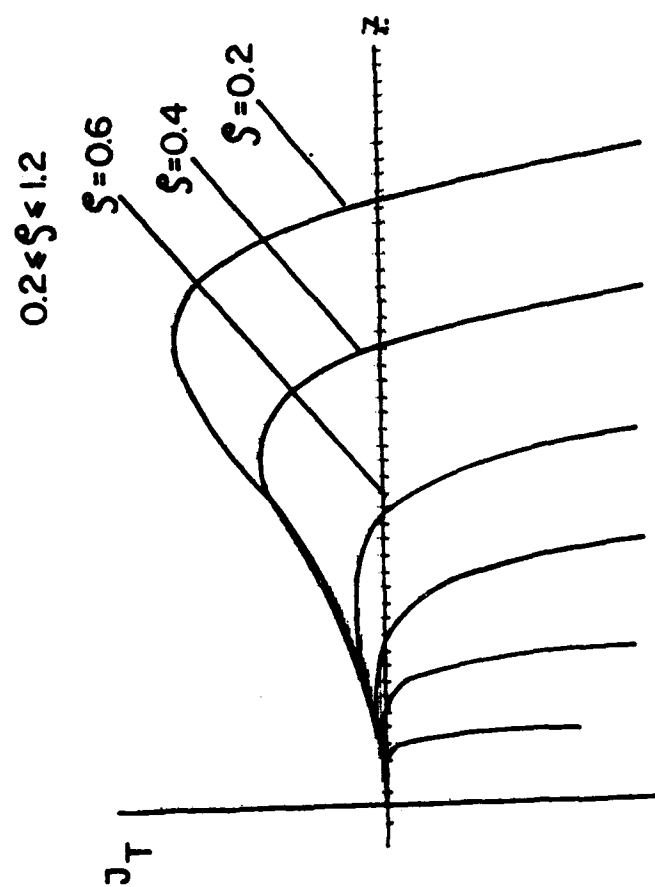
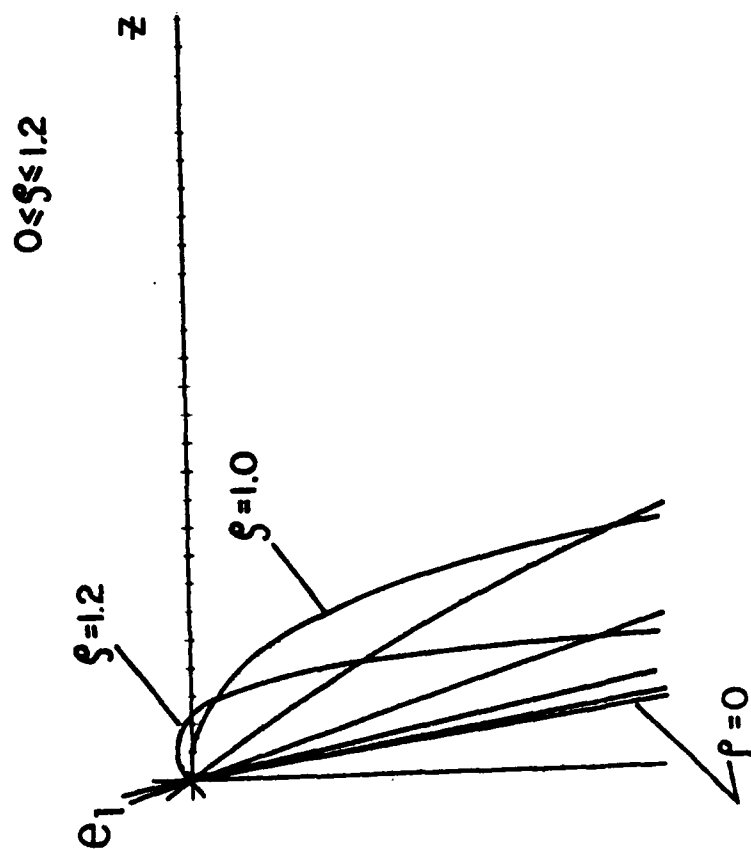


Fig 5
h_me₁

FIG 5



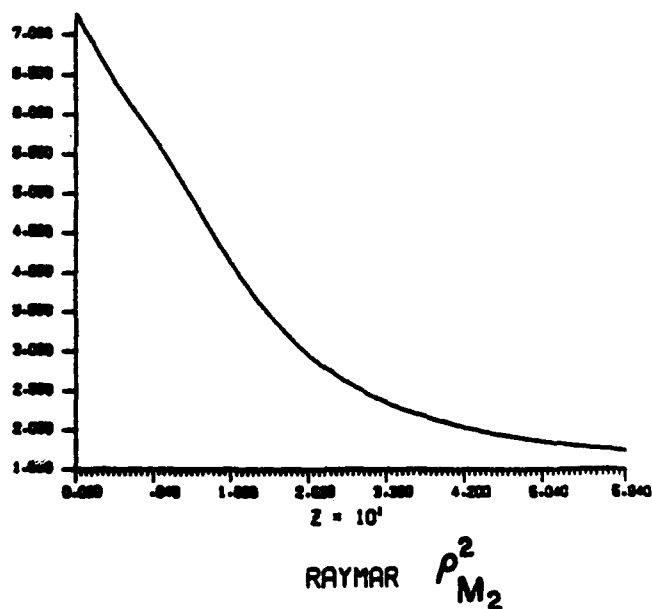
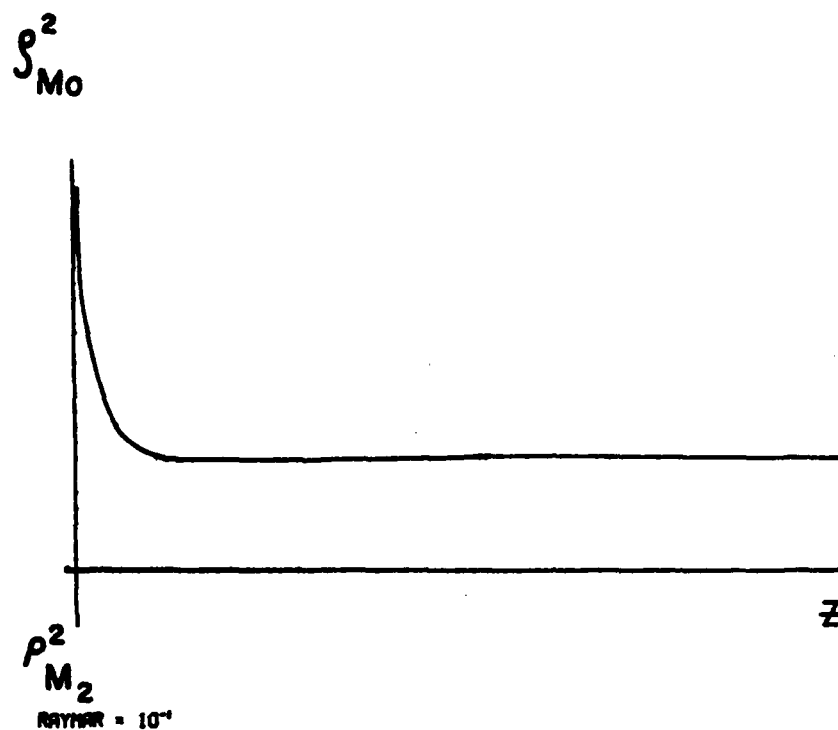


FIG 6

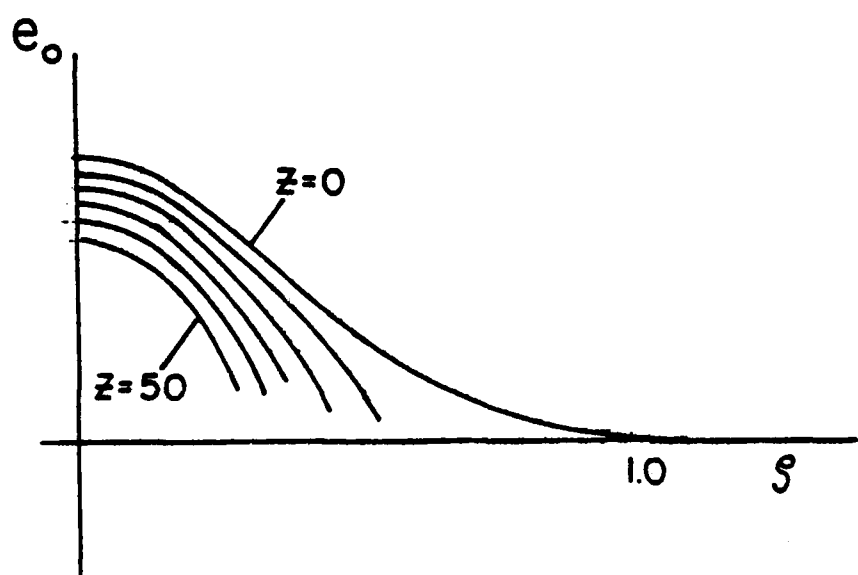


Fig 7

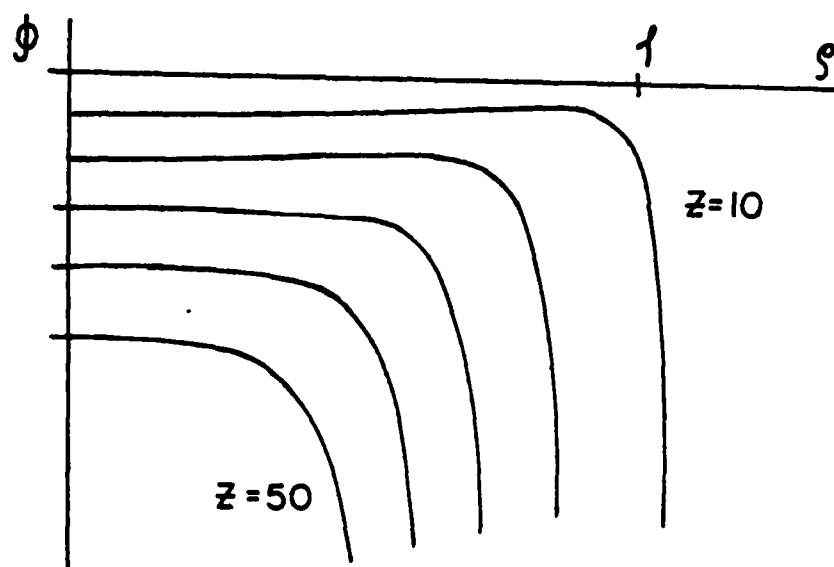


FIG 8a

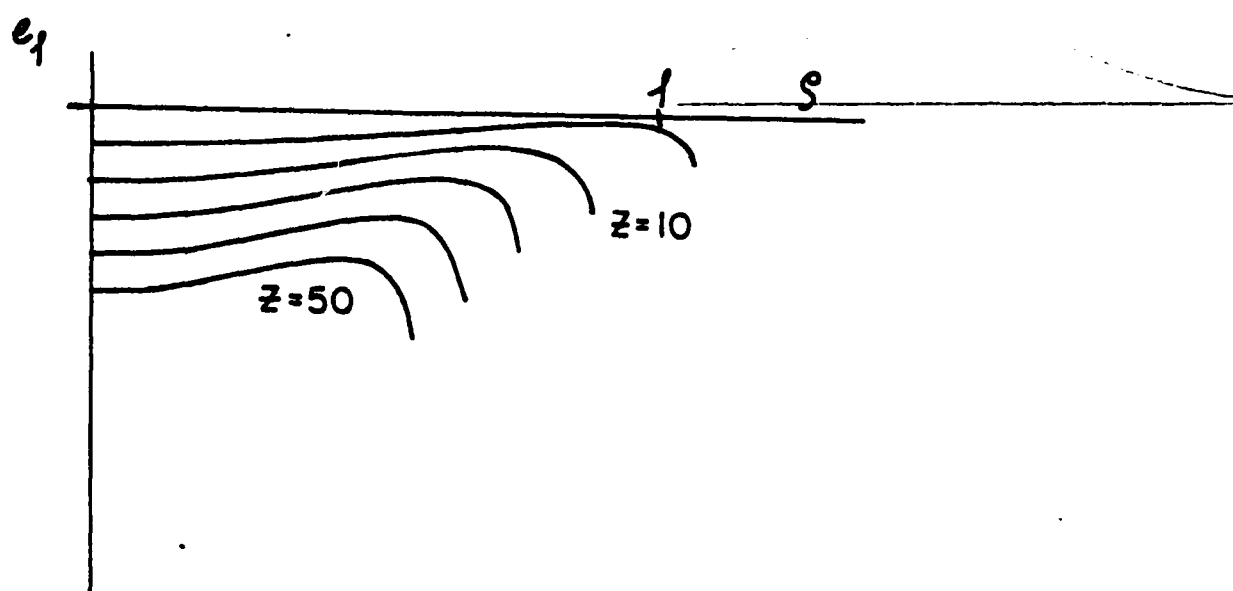


FIG 8b

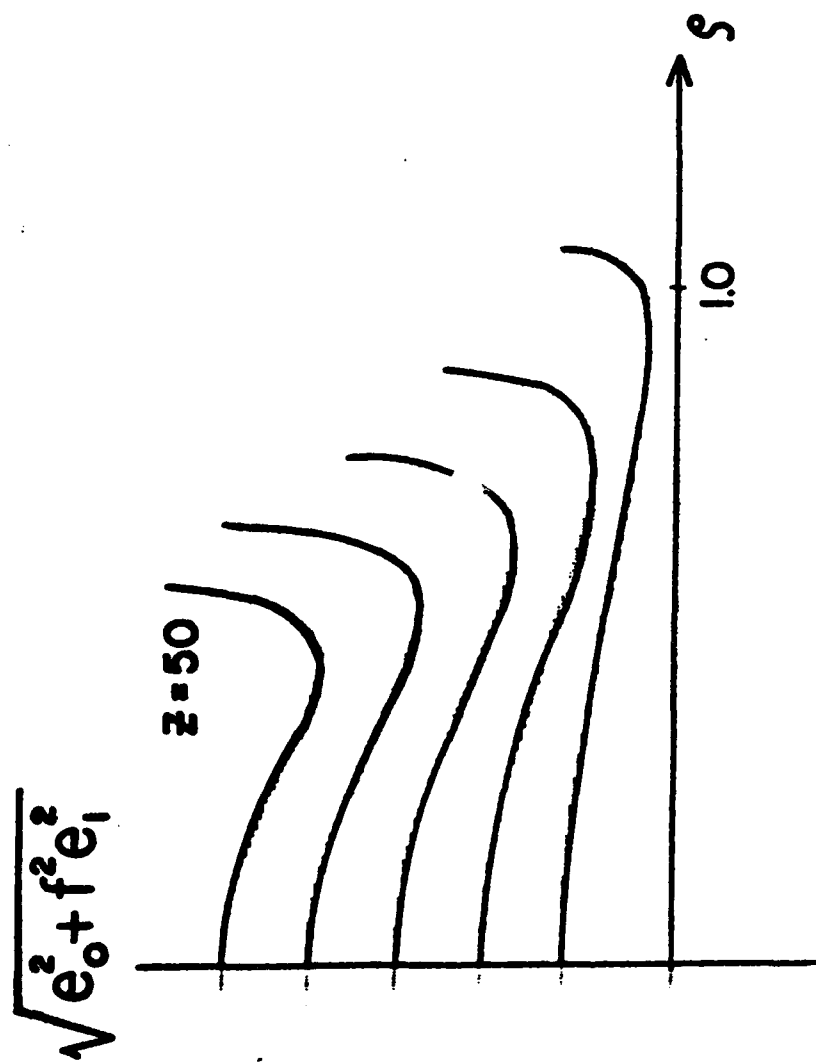


FIG 11

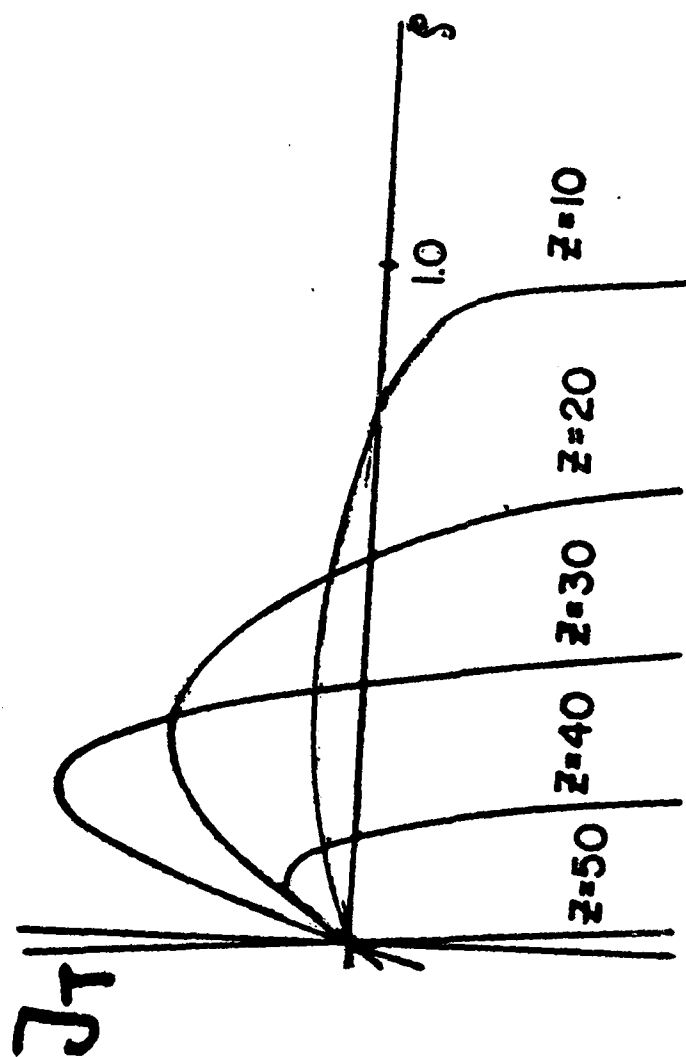


Fig 12

AD-A136 906

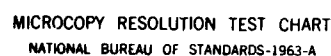
TRANSVERSE AND QUANTUM EFFECTS IN LIGHT CONTROL BY
LIGHT; (A) PARALLEL BE. (U) POLYTECHNIC INST OF NEW
YORK BROOKLYN DEPT OF MECHANICAL AND A. F P MATTAR
1983 POLY-M/AE-83-4 N00014-80-C-0174 F/G 20/6

6/6

UNCLASSIFIED

NL

END



MICROCOPY RESOLUTION TEST CHART
NATIONAL BUREAU OF STANDARDS-1963-A

Fig 9(b)

REVISED

1.1

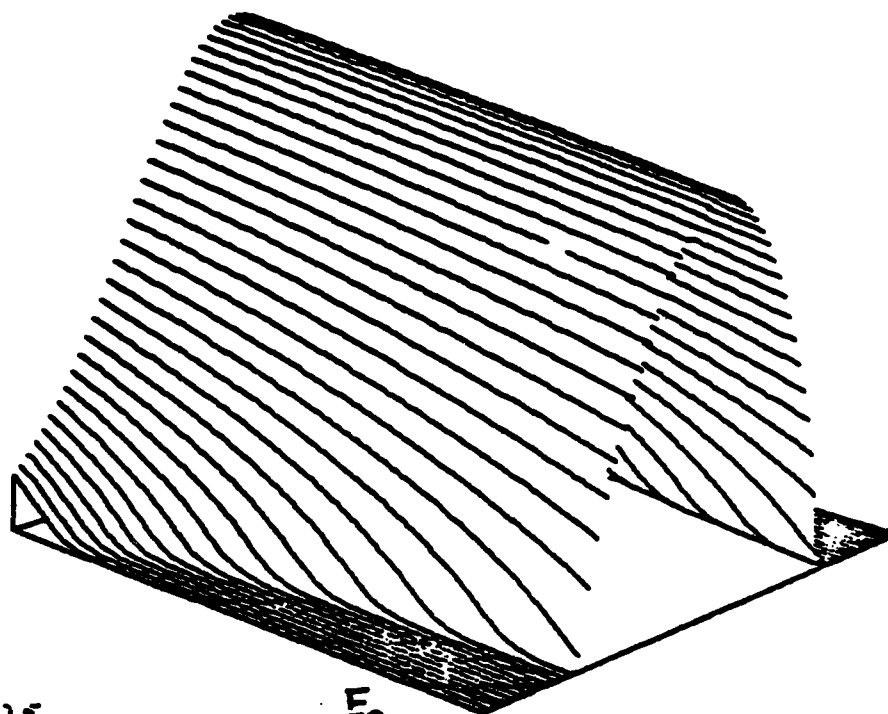
03/08/08

04-60.41

PAGE 3

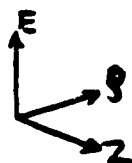
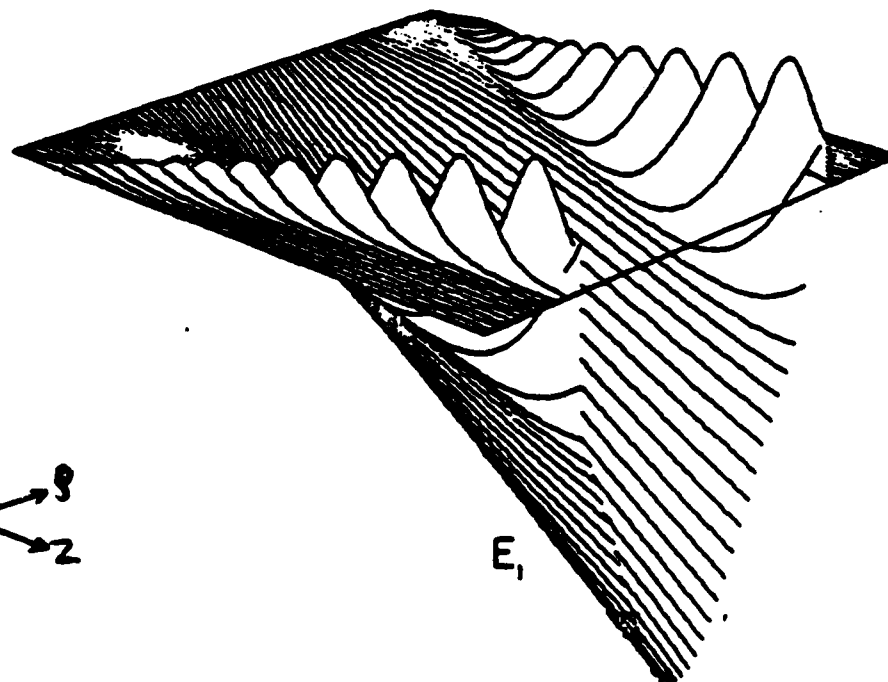
LRPERT SIMULATION NO. 20

$I_0 = 225$



$I_0 = 225$

E_0



E_1

DEGRES 1.1

83/06/04 12.21.29 PAGE 33

LRPERT SIMULATION NO. 21

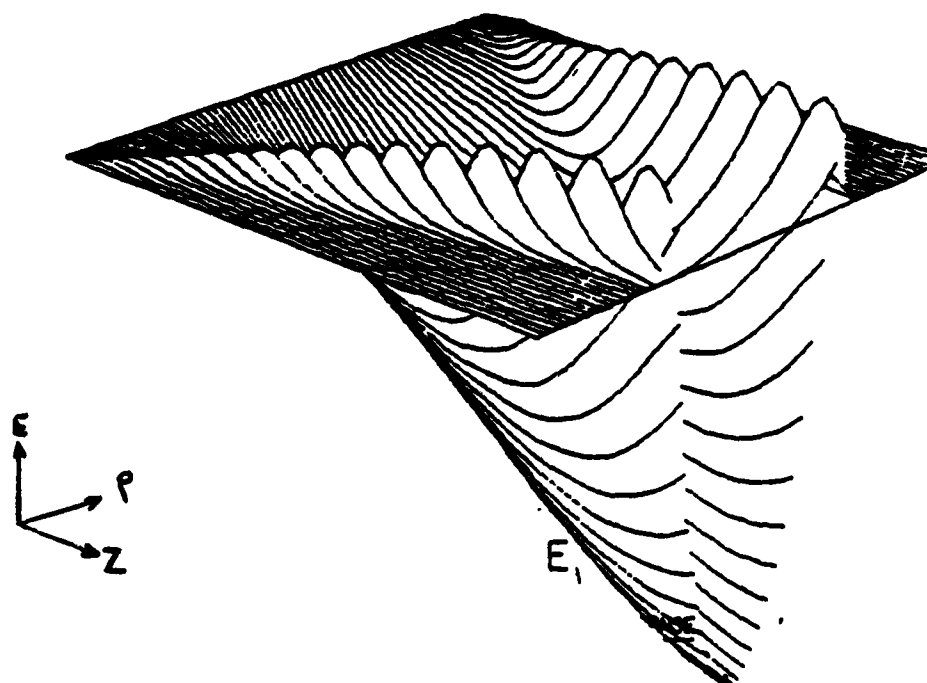
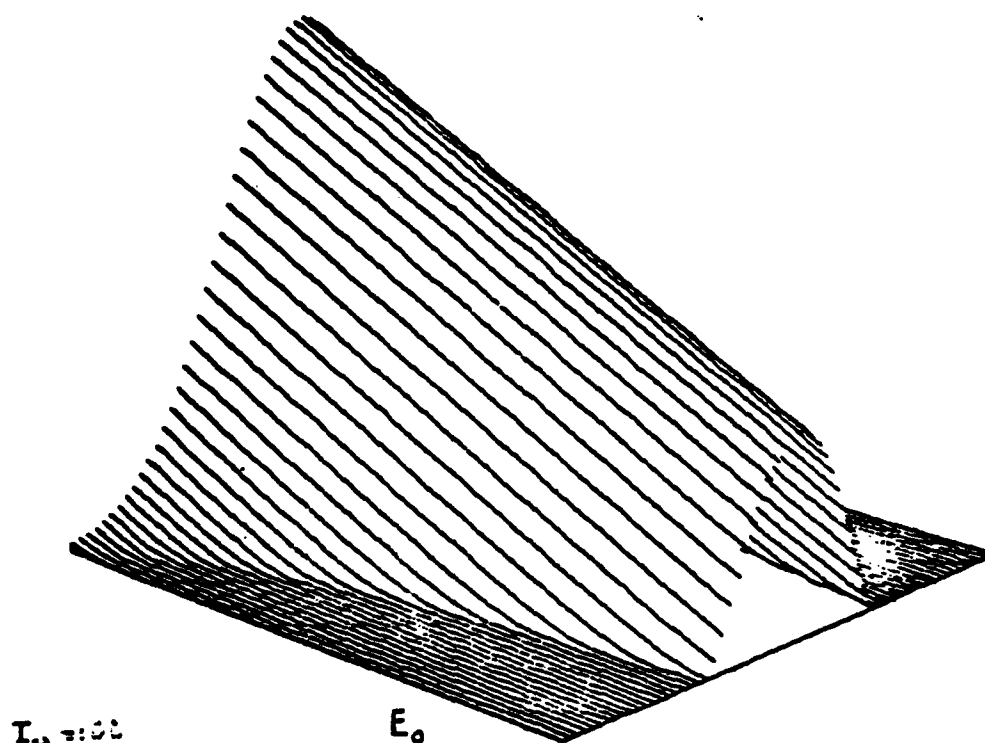
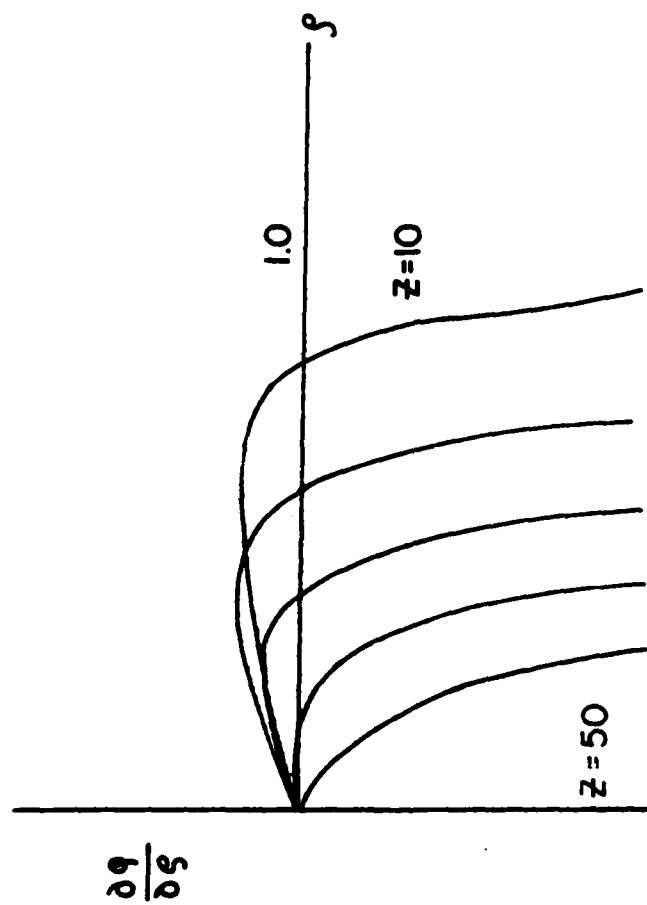
 $I_0 = 100$ 

FIG 10



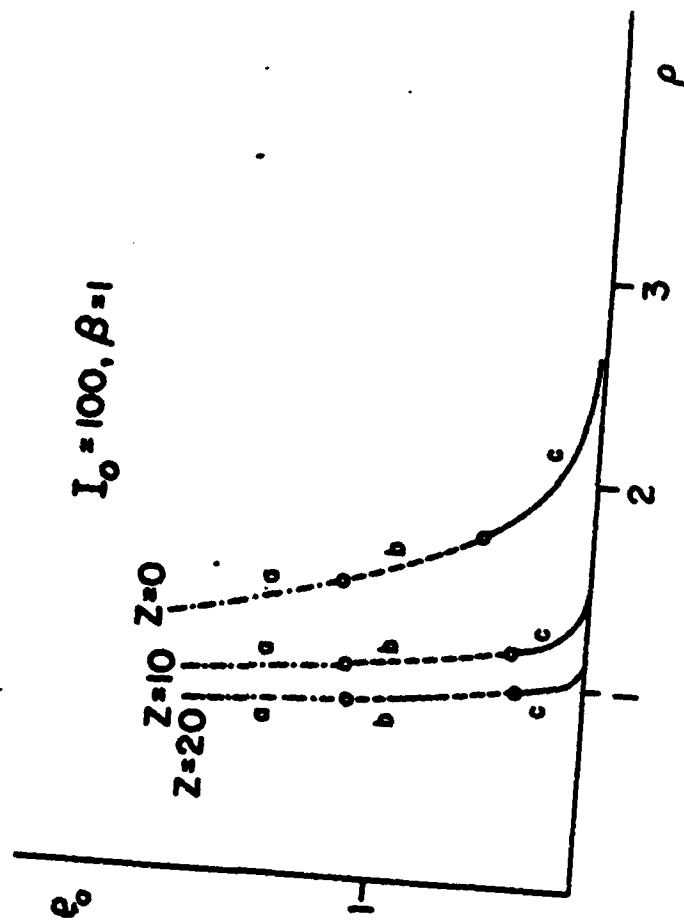


Fig 15

F-P. Matlay : small Trend in Counterf.
One strong, one weak beam interaction

STANDING WAVE EFFECTS

$$E^+(\rho, z, t) = e^+(\rho, z, t) \exp[i(\omega t - kz)] + \text{c.c.}$$

$$E^-(\rho, z, t) = e^-(\rho, z, t) \exp[i(\omega t + kz)] + \text{c.c.}$$

$$P(\rho, z, t) = P(\rho, z, t) \exp(i\omega t)$$

e^+ , e^- slowly varying $\omega_0 t$ exponential

$$-iFV_T^2 e^+ + \frac{\partial e^+}{\partial t} + \frac{\partial e^+}{\partial z} = +g^+ \langle P \exp(ikz) \rangle$$

$$-iFV_T^2 e^- + \frac{\partial e^-}{\partial t} - \frac{\partial e^-}{\partial z} = +g^- \langle P \exp(+ikz) \rangle$$

The quantity in the R.H.S. undergo rapid spatial variations

\longleftrightarrow spatial average of these quantities over a few wavelengths

BUT

$$\frac{\partial P}{\partial t} + (-i(\Delta\Omega) + \tau_2^{-1})P = + \{W(e^+ + e^-)\}$$

$$\frac{\partial W}{\partial t} + \tau_1^{-1}(W_0 - W) = - \frac{1}{2} (P + P^*) (E^+ + E^-)$$

$$\therefore \frac{\partial P}{\partial t} = (-i(\Delta\Omega) + \tau_2^{-1}) P = W[e^+ \exp(-ikz) + e^- \exp(+ikz)]$$

$$\frac{\partial W}{\partial t} + \tau_1^{-1}(W^e - W) = - \frac{1}{2} (Pe^{+*} \exp(ikz) + Pe^{-*} \exp(-ikz) + \text{c.c.})$$

The presence of opposing waves leads to a quasi-standing wave pattern in the field intensity over a half-wave length.

$$P = \exp(-ikz) \sum_{p=0}^{\infty} P_{(2p+1)}^+ \exp(-i2pkz) + \exp(+ikz) \sum_{p=0}^{\infty} P_{(2p+1)}^- \exp(+i2pkz)$$

$$W = W_0 + \sum_{p=1} [W_{2p} \exp(-i2pkz) + \text{c.c.}]$$

with W_0 a real number

$$-iFV_T^2 e^{\pm} + \partial_t e^{\pm} \pm \partial_z e^{\pm} = g^{\pm} P_1^{\pm}$$

$$\partial_{\tau} P_1^+ + P_1^+/\tau_2 = W_0 e^+ + W_2 e^-;$$

$$\partial_{\tau} P_3^+ + P_3^+/\tau_2 = W_2 e^+ + W_4 e^-;$$

... ..

$$\partial_{\tau} P_{(2p+1)}^+ + P_{(2p+1)}^+/\tau_2 = W_{2p} e^+ + W_{2(p+1)} e^-; \text{ and}$$

$$\partial_{\tau} P_1^- + P_1^-/\tau_2 = W_0 e^- + W_2^* e^+$$

$$\partial_{\tau} P_3^- + P_3^-/\tau_2 = W_2 e^- + W_4^* e^+$$

... ..

$$\partial_{\tau} P_{(2p+1)}^- + P_{(2p+1)}^-/\tau_2 = W_{2p}^* e^- + W_{2(p+1)}^* e^+$$

$$\partial_{\tau} W_0 + (W_0 - W_0^e)/\tau_1 = -\frac{1}{2}(e^{-*} P_1^- + e^{+*} P_1^+ + \text{c.c.})$$

$$\partial_{\tau} W_0 + (W_0 - W_0^e)/\tau_1 = -\frac{1}{2}(e^{-*} P_1^- + e^{+*} P_1^+ + \text{c.c.})$$

$$\partial_{\tau} W_2 + W_2/\tau_1 = -\frac{1}{2}(e^{-*} P_1^+ + e^{+*} P_3^+ + e^+ P_1^{-*} + e^- P_3^{-*})$$

$$\partial_{\tau} W_{2p} + W_{2p}/\tau_1 = -\frac{1}{2}(e^{-*} P_1^+ + e^+ P_{2p+1}^+ + e^+ P_{2p+1}^{-*} + e^{-*} P_{2p+1}^{-*})$$

Perturbation

e^+ Strong Beam e^- Weak Beam

Mathematically, this translates

$$e^-/e^+ = \mathcal{O}(\delta) ; \quad P_{2p+1}^-/P_{2p+1}^+ = \mathcal{O}(\delta);$$

$$P_{2p+3}^+/P_{2p+1}^+ = \mathcal{O}(\delta); \quad W_{2p}/W_{2(p+1)} = \mathcal{O}(\delta),$$

$$\text{and } P_{2p+3}^-/P_{2p+1}^+ = \mathcal{O}(\delta^2)$$

Case A. (In the diffractionless limit ($F = 0$, ∞) e_0^+ , P_{10}^+ and W_0 represent the S.I.T. limit.)

$$e^+ = e_0^+ + \delta e_1^+ + \delta^2 e_2^+ + \delta^3 e_3^+ + \dots$$

$$e^- = \delta w_1^- + \delta^2 e_2^- + \delta^3 e_3^- + \dots$$

$$P_1 = P_{10}^+ + \delta P_{11}^+ + \delta^2 P_{12}^+ + \delta^3 P_{13}^+ + \dots$$

$$P_1^- = \delta P_{11}^- + \delta^2 P_{12}^- + \delta^3 P_{13}^- + \dots$$

$$P_3^+ = \delta P_{31}^+ + \delta^2 P_{32}^+ + \delta^3 P_{33}^+ + \dots$$

$$P_5^+ = \delta^2 P_{52}^+ + \delta^3 P_{53}^+ + \dots$$

$$P_3^- = \delta^2 P_{32}^- + \delta^3 P_{33}^+ + \dots$$

$$P_5^- = \delta^3 P_{53}^+ + \dots$$

$$W_0 = W_{00} + \delta W_{01} + \delta^2 W_{02} + \delta^3 W_{03} + \dots$$

$$W_2 = \delta W_{21} + \delta^2 W_{22} + \delta^3 W_{23} + \dots$$

$$W_4 = \delta^2 W_{42} + \delta^3 W_{43} + \dots$$

Zero order of δ : $\square(\delta^0)$ as in S.I.T.

$$\partial_\tau e_0^+ + \partial_z e_0^+ = g^+ P_{10}^+$$

$$\partial_\tau P_{10}^+ + P_{10}^+/\tau_2 = W_{00} e_0^+$$

$$\partial_\tau W_{00} + (W_{00} - W_{00}^e)/\tau_1 = -\frac{1}{2}(e_0^{+*} P_{10}^+ + e_0^+ P_{10}^{+*})$$

First order of δ : $\square(\delta)$

$$\partial_\tau e_1^+ + \partial_z e_1^+ = g^- P_{11}^+$$

$$\partial_\tau e_1^- - \partial_z e_1^- = g^- P_{11}^-$$

$$\partial_\tau P_{11}^+ + P_{11}^+/\tau_2 = W_{01} e_0^+ + W_{00} e_1^+$$

$$\partial_\tau P_{11}^- + P_{11}^-/\tau_2 = W_{00} e_1^- + W_{21}^* e_0^+$$

$$\partial_\tau P_{31}^+ + P_{31}^+/\tau_2 = W_{21} e_0^+$$

$$\partial_\tau W_{01} + W_{01}/\tau_1 = -\frac{1}{2}(e_0^{+*} P_{11}^+ + e_1^{+*} P_{10}^+ + \text{c.c.})$$

$$\partial_\tau W_{21} + W_{21}/\tau_1 = -\frac{1}{2}(e_1^{-*} P_{10}^+ + e_0^{+*} P_{31}^+ + e_0^+ P_{11}^{-*} + e_0^+ P_{11}^+ + e_1^+ P_{10}^+)$$

2nd order of δ : $\square(\delta^2)$

$$\partial_\tau e_2^+ + \partial_z e_2^+ = g^+ P_{12}^+$$

$$\partial_\tau e_2^- - \partial_z e_2^- = g^- P_{12}^-$$

$$\partial_\tau P_{12}^+ + P_{12}^+/\tau_2 = W_{02} e_0^+ + W_{01} e_1^+ + W_{00} e_2^+ + W_{21} e_1^-$$

$$\partial_\tau P_{12}^- + P_{12}^-/\tau_2 = W_{00} e_2^- + W_{01} e_1^- + W_{21}^* e_1^+ + W_{22}^* e_0^+$$

$$\partial_\tau P_{32}^+ + P_{32}^+/\tau_2 = W_{22} e_0^+ + W_{21} e_1^+$$

$$\partial_{\tau} P_{52}^{+} + P_{52}^{+}/\tau_2 = W_{42} e_0^{+}$$

$$\partial_{\tau} P_{32}^{-} + P_{32}^{-}/\tau_2 = W_{22}^{*} e_0^{-}$$

$$\partial_{\tau} W_{22} = -\frac{1}{2} [(e_2^{+*} P_{10}^{+} + e_1^{+*} P_{11}^{+} + e_0^{+*} P_{12}^{+}) + (e_1^{-*} P_{11}^{-}) + \text{c.c.}]$$

$$\partial_{\tau} W_{22} = -\frac{1}{2} [(e_1^{-*} P_{11}^{+} + e_2^{-*} P_{10}^{+}) + (e_0^{+*} P_{32}) + (e_1^{+*} P_{11}^{-*} + e_0^{+*} P_{12}^{-})]$$

$$\partial_{\tau} W_{42} = -\frac{1}{2} (e_1^{-*} P_{31}^{+} + e_0^{+} P_{32}^{+} + e_1^{+} P_{31}^{+})$$

Steady State

$$\partial_z e_o^+ = g^+ P_{10}^+$$

$$P_{10}^+ = \tau_2 W_{oo} e_o^+$$

$$W_{oo} - W_{oo}^e = -\tau_1/2 [e_o^{++} P_{10}^+ + e_o^+ P_{10}^{++}]$$

$$W_{oo} = W_{oo}^e - \frac{\tau_1}{2} [e_o^{++} (\tau_2 W_{oo} e_o^+) + e_o^+ (\tau_2 W_{oo} e_o^{++})]$$

$$= W_{oo}^2 - \frac{\tau_1}{2} [\tau_2 W_{oo} |e_o^+|^2 + \tau_2 W_{oo} |e_o^+|^2]$$

$$= W_{oo}^2 - \tau_1 \tau_2 W_{oo} |e_o^+|^2$$

$$W_{oo} = W_{oo}^2 / [1 + \tau_1 \tau_2 |e_o^+|^2]$$

$$\partial_z e_o^+ = g^+ \tau_2 \frac{W_{oo}^e e_o^+}{1 + \tau_1 \tau_2 |e_o^+|^2}$$

$$\text{with } e_S = (\tau_1 \tau_2)^{-1/2} \quad \text{and } e_o^+ \text{ real}$$

$$\partial_z e_o^+ = \tau_2 W_{oo}^e e_o^+ / [1 + (e_o^+ / e_S)^2]$$

$$d e_o^+ [1 + (e_o^+ / e_S)^2]^{+1} = [\tau_2 W_{oo}^2 e_o^+] dz$$

$$[(1/e_o^+) + (e_o^+ / e_S^2)] d e_o^+ = \tau_2 W_{oo}^2 dz$$

$$\ln \left[\frac{e_o^+}{e_S} \right] + \frac{[e_o^+(z)]^2 - [e_o^+(0)]^2}{2 e_S^2} = \tau_2 (\int W_{oo}^2 dz)$$

$$+ \frac{\partial e_1^+}{\partial z} = g^+ P_{11}^+$$

$$- \frac{\partial e_1^-}{\partial z} = g^- P_{11}^-$$

$$P_{11}^+ = \tau_2 (W_{01} e_0^+ + W_{00} e_1^+)$$

$$P_{11}^- = \tau_2 (W_{00} e_0^- + W_{21}^* e_0^+)$$

$$P_{31}^+ = \tau_2 W_{21} e_0^+$$

$$W_{01} = -\tau_1/2 (e_0^{+*} P_{11} + e_1^{+*} P_{10} + \text{c.c.})$$

$$W_{21} = -\tau_1/2 (e_1^{-*} P_{10}^+ + e_0^{+*} P_{31}^+ + e_0^+ P_{11}^{-*})$$

$$W_{21}' = -\tau_1/2 (e_1^{-*} P_{10}^+ + e_0^{+*} \tau_2 W_{21} e_0^+ + e_0^+ + e_0^+ P_{11}^*)$$

$$W_{21} = -\tau_1/2 (e_1^{-*} P_{10}^+ + \tau_2 W_{21} |e_0^+|^2 + e_0^+ P_{11}^{-*})$$

$$\therefore W_{21} = \frac{e_1^{-*} P_{10}^+ + e_0^+ P_{11}^{-*}}{1 + \frac{\tau_1 \tau_2}{2} |e_0^+|^2} = \frac{e_1^{-*} P_{10}^+ + e_0^+ P_{11}^{-*}}{1 + \frac{1}{2} \frac{|e_0^+|^2}{e_5^2}}$$

substituting for P_{11}^{-*} , one obtains e_5^2

$$W_{21}^* = -\frac{\tau_1}{2} (e_1^- P_{10}^{+*} + \tau_2 W_{21}^* |e_0^+|^2 + e_0^{+*} \tau_2 (W_{00} e_1^- + W_{21}^* e_0^{+*}))$$

$$W_{21}^* (1 + \frac{\tau_1 \tau_2}{2} \{|e_0^+|^2 + (e_0^{+*})^2\})$$

$$= -\frac{\tau_1}{2} (P_{10}^{+*} + \tau_2 W_{00} e_0^{+*}) e_1^-$$

$$W_{21}^* = \frac{-\frac{\tau_1}{2} (P_{10}^{+*} + \tau_2 W_{00} e_0^{+*}) e_1^-}{[1 + \frac{\tau_1 \tau_2}{2} \{|e_0^+|^2 + |e_0^{+*}|^2\}]}$$

$$-\frac{1}{e_1^-} \frac{\partial e_1^-}{\partial z} = g^- \tau_2 [W_{00} + \frac{W_{21}^*}{e_1^-} e_0^+]$$

REPORT DOCUMENTATION PAGE		READ INSTRUCTIONS BEFORE COMPLETING FORM
1. REPORT NUMBER	2. GOVT ACCESSION NO.	3. RECIPIENT'S CATALOG NUMBER
4. TITLE (and Subtitle) Transverse and quantum effects in light control by light (a) parallel beams: pump dynamics for three-level superfluorescence; (b) counterflow beams: an algorithm for transverse, full transient effects in optical bistability in a		5. TYPE OF REPORT & PERIOD COVERED Final - December, 1979 to July 31, 1983
7. AUTHOR(s) Fabry-Perot Cavity F. P. MATTAR		6. PERFORMING ORG. REPORT NUMBER
9. PERFORMING ORGANIZATION NAME AND ADDRESS Polytechnic Institute of New York 333 Jay St.; Brooklyn, NY 11201		8. CONTRACT OR GRANT NUMBER(s) N000-1480-C-0174
11. CONTROLLING OFFICE NAME AND ADDRESS U.S. Office of Naval Research 800 Quincy Road Washington, D.C. 22217 Arlington, Virginia		10. PROGRAM ELEMENT, PROJECT, TASK AREA & WORK UNIT NUMBERS
14. MONITORING AGENCY NAME & ADDRESS (if different from Controlling Office) Office of Naval Research, RR NY Area Office, 750 Broadway, N.Y.C. 10003		12. REPORT DATE Fall, 1983
		13. NUMBER OF PAGES
		15. SECURITY CLASS. (of this report) Unclassified
		15a. DECLASSIFICATION/DOWNGRADING SCHEDULE
16. DISTRIBUTION STATEMENT (of this Report) Approved for public release Distribution unlimited		
17. DISTRIBUTION STATEMENT (of the abstract entered in Block 20, if different from Report) 1179		
18. SUPPLEMENTARY NOTES The view, opinions, and/or findings contained in this report are those of the author(s) and should not be construed as an official Department of the Navy position, policy, or decision, unless so designated by other documentation		
19. KEY WORDS (Continue on reverse side if necessary and identify by block number) Transverse Quantum Effects; Light Control by Light; Three Level Superfluorescence Algorithm for Optical Bistability		
20. ABSTRACT (Continue on reverse side if necessary and identify by block number) I. <u>Methodology</u> : Computational methodologies were developed to treat rigorously (i) transverse boundary in an inverted (amplifying) media; (ii) to treat quantum fluctuations in an initial boundary condition in the light-matter interactions problem; (iii) construct a two-laser three-level code to study light control by light effect; (iv) construction of a data base that (a) would manage the production of different types of laser calculations: cylindrical, cylindrical with atomic frequency broadening, cartesian geometry; (all of the above with quantum me-		

1. Methodology: Computational methodologies were developed to treat rigorously (i) transverse boundary in an inverted (amplifying) media; (ii) to treat quantum fluctuations in an initial boundary condition in the light-matter interactions problem; (iii) construct a two-laser three-level code to study light control by light effect; (iv) construction of a data base that (a) would manage the production of different types of laser calculations: cylindrical, cylindrical with atomic frequency broadening, cartesian geometry; (all of the above with quantum mechanical initiation), (b) allow parametric comparison within the same type of calculations, by establishing a unifying protocol of software storage, of the various refinements of the model could be contrasted among themselves and with experiment; (v) construct an algorithm for counterbeam transient studies for optical bistability and optical oscillator studies.

A. Transverse propagation effects in an inverted medium were studied. Special care had to be taken to treat the boundary reflection conditions. If ill-posed, they can obscure the emergence of any new physical results. The two transverse effects considered are (1) the 'spatial averaging' associated with the initial atomic inversion density being radially dependent (since the pump which inverts the sample has typically a Gaussian-like profile); and (2) the "diffraction coupling" (which permits the various parts of the cylindrical cross-section to communicate, interact and emit at the same time). The first effect is important for large Fresnel numbers, whereas the second predominant for small Fresnel numbers.

The study of output energy stabilization between diffraction spreading and nonlinear self-action due to the non-uniform gain of the active media was also carried out to reach an understanding of the various physical processes that take place in coherent resonant amplifiers.

B. Physical Results: i. The Study of three-level systems exhibited that injected coherent-pump initial characteristic (such as on-axis area, temporal and radial width and shape) injected at one frequency can have significant deterministic effects on the evolution of the superfluorescence at another frequency and its pulse delay time, peak intensity, temporal width and shape. The importance of Resonant Coherent Raman processes was clearly demonstrated in an example where the evolving superfluorescence pulse temporal width τ_s is much less than the reshaped coherent pump width τ_p , even though the two pulses temporarily overlap (i.e., the superfluorescence process gets started late and terminates early with respect to the pump time duration). The results of the three-level calculations are in quantitative agreement with observation in CO_2 pumped CH_3F by A.T. Rosenberg and T.A. DeTemple (Phys. Rev., A24, 868 (1981)).

ii. Additional calculations incorporating fluctuations in both pump and superfluorescence transitions were carried out to study the output pulse delay statistics. The fluctuations operators were introduced as langevin operators in the matter (density matrix) operators. In the average c-number semi-classical regime the fluctuations appear as additional driving forces in the Bloch equations acting for all p , z and τ .

iii. Two color superfluorescence was subsequently studied in collaboration with Professor F. Haake. The propagation theory of M. Feld was shown to prevail over the Mean-Field theory of Bonifacio et al. The main result of the calculation displayed for the plane wave regime is a pulse synchronisation which ascertains Eberly et al's theory of 'simultons.' However for quantum fluctuations during the initiation and strong phase evolution in the beam (i.e., large Fresnel number) the synchronisation decreases and the standard deviation of the delay difference between the two peaks normalized to the average delay becomes larger.

iv. Elucidating the physical processes [namely, (a) the dynamic diffraction, (b) the non-uniform absorption (i.e., refraction) and (c) beam stripping] that lead to the on-axis manifestation predicted by Boshier and Sandle calculation [see Optic Commu., 42, 371 (1982)]. This effort was carried out in collaboration with Professor J. Teichmann.

V. The development of an implicit algorithm which self-adaptive non-uniform computational grids. This effort was carried out in collaboration with Dr. B.R. Suydam. These new codes represent a combination of Snyder code in Los Alamos and Mattar stretching and rezoning techniques to treat self-lensing effects.

END

FILMED

2-84

DTIC